11th

Australian Conference on Nuclear Techniques of Analysis

The Australian Institute of Nuclear Science and Engineering, Lucas Heights, NSW.

24-26 November 1999

PROCEEDINGS

5th

VACUUM SOCIETY OF AUSTRALIA CONGRESS

ISSN 1325-1694

11th Australian Conference on Nuclear Techniques of Analysis & 5th Vacuum Society of Australia Congress

AINSE
Lucas Heights NSW

24 – 26 November 1999

PROCEEDINGS

Conference Planning Committee

Dr David Cohen, Conference Chairman	ANSTO
Dr Rob Elliman	Australian National University
Dr Peter Johnston	Royal Melbourne Institute of Technology
A/Prof John O'Connor	University of Newcastle
Dr Soey Sie	CSIRO
A/Prof David Jamieson	University of Melbourne
Prof Ron MacDonald	University of Newcastle
Dr Dennis Mather	AINSE
Mrs Irene Parker	AINSE

SPONSORS AND EXHIBITORS

Alphatech International Pty Ltd

Andrew Young & Co

AVT Services Pty Ltd

Balzers Australia Pty Ltd

Coherent Scientific Pty Ltd

Javac Pty Ltd

National Electrostatics Corp

Scientific Technology Pty Ltd

Stanton Scientific

Thermo Optek Australia Pty Ltd

University of Surrey Ion Beam Centre

NEC ion electron BEAM SYSTEMS

THE WORLD LEADER IN MEGAVOLT ACCELERATOR TECHNOLOGY

NATIONAL ELECTROSTATICS CORP.

AMS

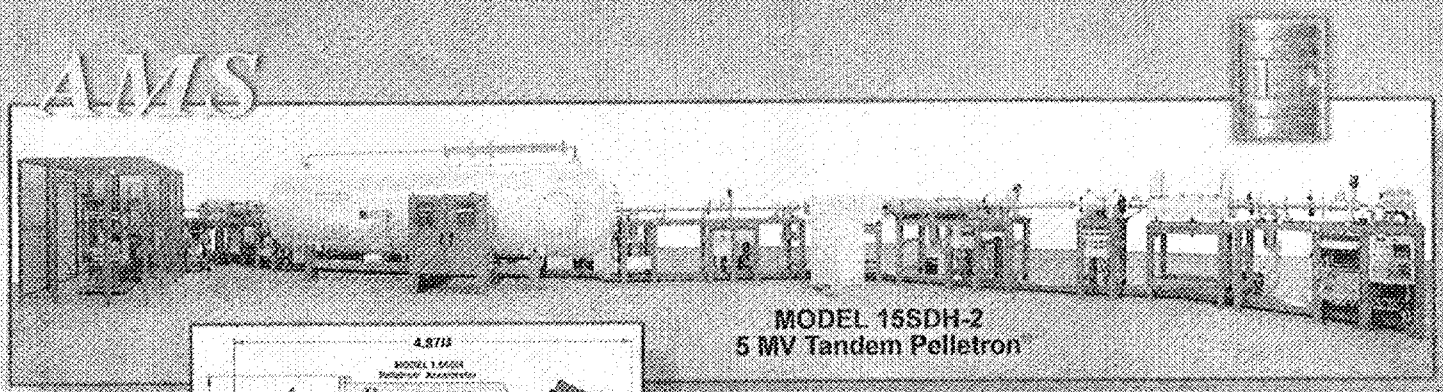

MODEL 15SDH-2
5 MV Tandem Pelletron

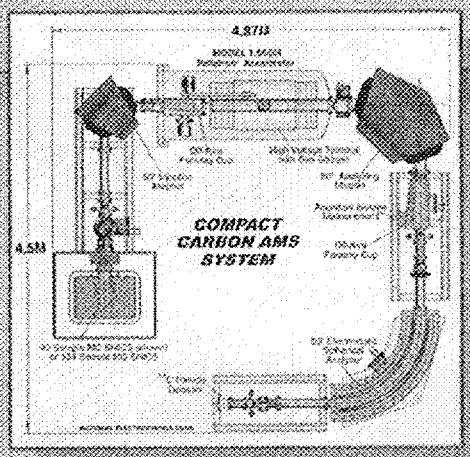

RBS/PIXE

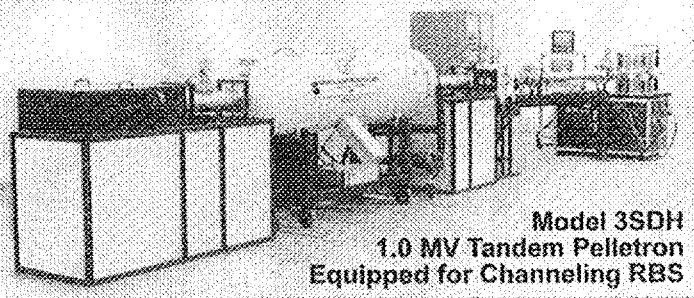

Model 3SDH
1.0 MV Tandem Pelletron
Equipped for Channeling RBS

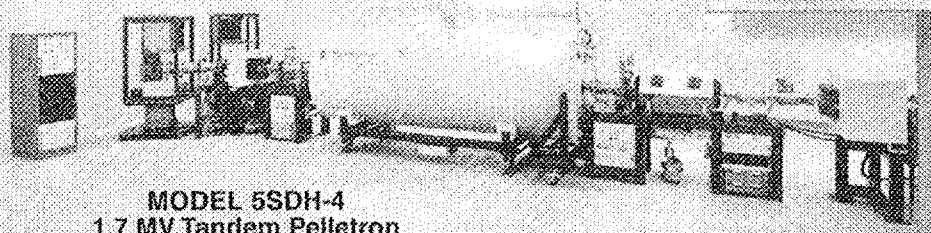

MODEL 5SDH-4
1.7 MV Tandem Pelletron

Ion Implant/Analysis

NEC Pelletron Accelerator Systems provide high quality ion and electron beams with energies from 10's of keV to 100's of MeV for a wide variety of applications. Complete turnkey systems are available for research implantation, RBS, channeling, ERD, PIXE, NRA and AMS.

Contact NEC for information about systems and ion beam handling and vacuum components.

7540 GRABER ROAD, P.O. BOX 620310, MIDDLETON, WI 53562-0310 U.S.A.
TELEPHONE: 608-831-7600 ◆ FAX: 608-256-4103 ◆ E-MAIL: nec@pelletron.com ◆ WEB SITE: http://www.pelletron.com

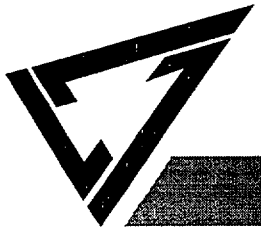

AVT Services Pty Limited

ACN 056 503 461

Vacuum & Cryogenics

Alcatel

Woosung

Leybold

Sargent Welch

Weire

Pfeiffer

Polycold

Stokes

Veeco

Ebara

CTI

SERVICE AND SUPPORT FOR ALL BRANDS OF VACUUM PUMPS AND EQUIPMENT

Edwards

Austin Scientific

Vacuubrand

Busch

Balzers

Varian

Siemens

Kinney

Thomas

Rotant

Kashiyama

Head Office: 16/35 Foundry Road Seven Hills NSW 2147

Phone 02 9674 6711 Fax 02 9674 7358 Email avtserv@bigpond.com

Web page www.avt.net.au

Andrew Young & Co Pty Limited

A.C.N. 075 764 313
18 Bowerman Place Cherrybrook NSW 2126
Telephone (02) 9484 5720 Facsimile (02) 9980 8920
ayoung@wr.com.au

REPRESENTING

AML	**UHV Equipment** Gauging Stepper Motors Stages Goniometers
Cressington	**Coaters** Sputter Coaters Carbon Coaters Thickness Monitors
Tectra	Research Physics Equipment Effusion Cell IonEtch , Ion Guns Atom Sources e-flux, Electron Beam Evaporator e-Beam Heating Power Supply Plasma Ion Sources Mini Coater micro MBE
VG Scientific	Surface Analysis Systems ESCA, VG ESCALAB Auger, VG Microlab
VG Semicon	Molecular Beam Epitaxy Systems Components for MBE MBE for Research MBE for Production

VARIAN VACUUM TECHNOLOGIES

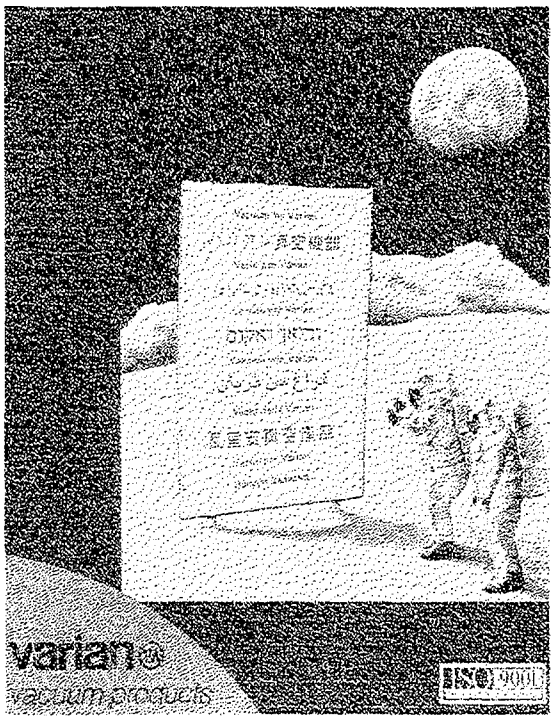

Now Represented By Scientific Technology Pty Ltd

NOVEMBER 24TH 1999

- Scientific Technology
- PO Box 914
- Toronto NSW 2283
- 02-4959-9780 email jpgdn@bigpond.com

Harry Shorrock

John Gordon

- ☐ Spectra Sensortech Residual Gas Analysers.
- ☐ Kratos Electron Spectrometers.
- ☐ MALDI-ToF Mass Spectrometers
- ☐ GC-MS ToF Systems.
- ☐ C/D/N Stable Isotopes.

JAVAC
Vacuum Solutions

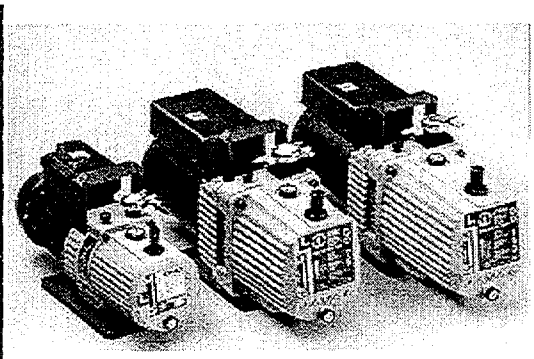

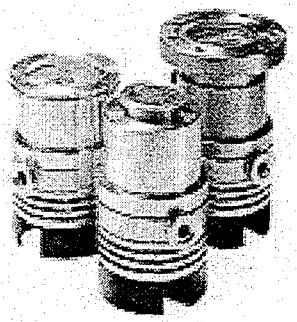

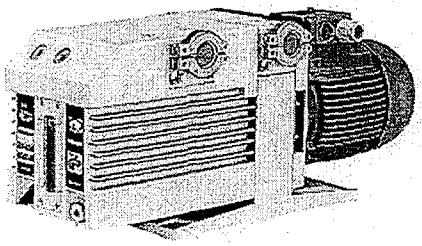

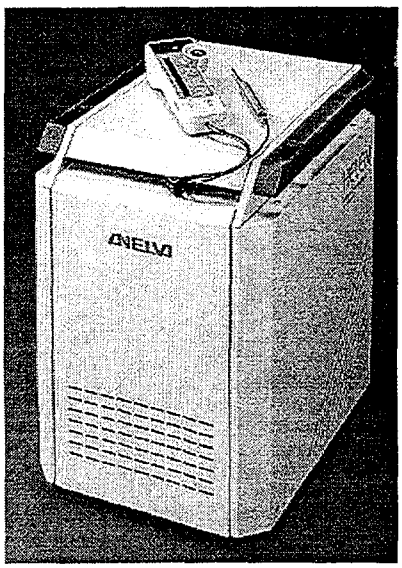

- **Rotary Vane Pumps**
  - Javac
  - Leybold
  - DVP
- **Diaphragm Vacuum / Pressure Pumps**
  - KNF Neuberger
  - Welch Vacuum
- **Air & Liquid Sampling Pumps**
  - KNF Neuberger
  - KNF Flodos
- **Turbomolecular & Cryopumps**
  - Leybold
- **Leak Detectors**
  - Anelva
  - Inficon
- **Vacuum Gauges & Fittings**
  - Javac
  - Leybold
- **Service & Advice**
  - We Service all Types of Vacuum Equipment
  - Service Contracts
  - On-Site Service
  - Custom Design & Manufacture

Head Office:
54 Rushdale Street
Knoxfield
VIC 3180
Ph: (03) 9763 7633
Fax: (03) 9763 2756
Email: javac@javac.com.au

Unit 30, 112 Benaroon Rd
Belmore
NSW 2192
Ph: (02) 9758 9743
Fax (02) 9758 9763
Email: javac.nsw@bigpond.com.au

VACUUM PRODUCTS FROM .....

COHERENT SCIENTIFIC

STANFORD RESEARCH SYSTEMS

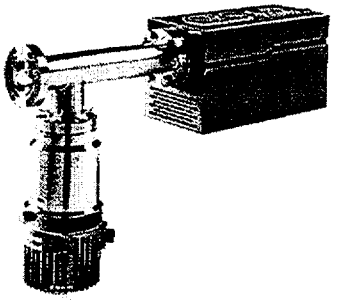

⇒ RGA Series Residual Gas Analysers

⇒ QMS Series Quadrupole Mass Sampler Systems

⇒ PPR Series Vacuum Process Monitoring Systems

⇒ Closed Ion Source Gas Analysers

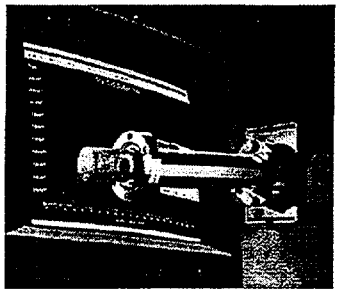

BURLE ELECTRO-OPTICS (Previously GALILEO)

⇒ "Channeltron" Electron Multipliers

⇒ Single Microchannel Plates

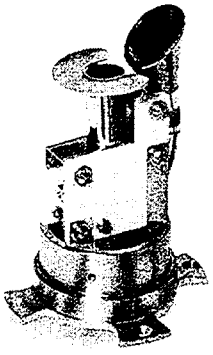

⇒ Chevron Tested Microchannel Plates

⇒ Z-stack Microchannel Plates

⇒ Advanced Detector Assemblies

116 Burbridge Road – Hilton – South Australia – 5033
Phone: (08) 8150 5200 Fax: (08) 8352 2020
E-mail: sales@cohsci.com.au Web: www.cohsci.com.au

Coherent SCIENTIFIC

The *IBA DataFurnace*

A new tool for thin film depth profiling from the University of Surrey

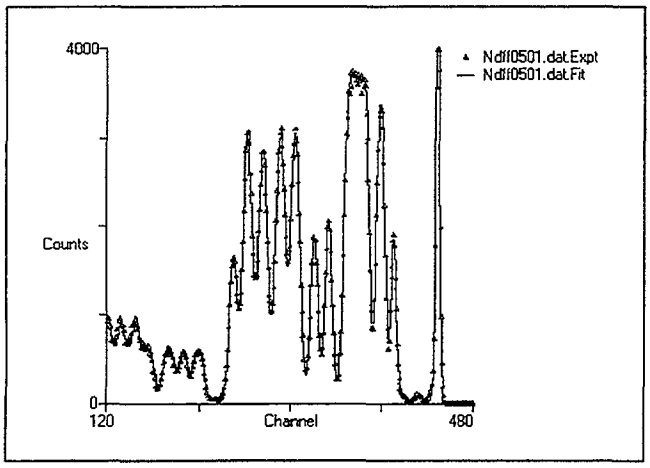

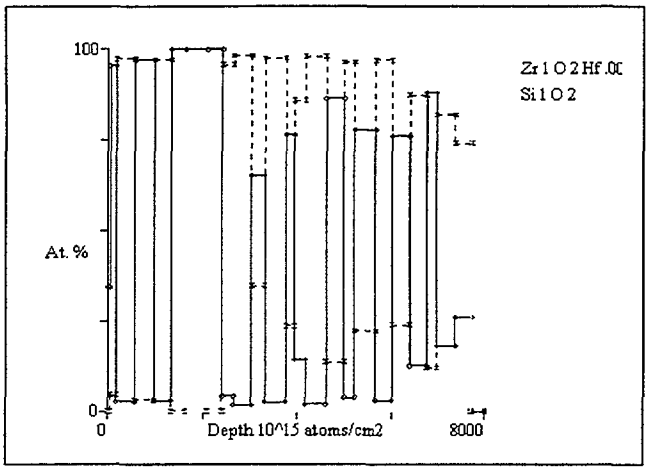

Depth profile of antireflection coating

2.2MeV RBS of a 22 layer zirconia/silica multilayer on glass. Spectrum and DataFurnace fit (above) and calculated depth profile (below: the glass substrate is omitted for clarity). DataFurnace requires only element names: in this case we supply the *molecules*. The zirconia has some Hf. This multilayer has typical layer thickness of 40nm, which is determined to about 5% precision. Energy straggling must be correctly included for this multilayer coating.

What is the DataFurnace?
It is a new code that can extract the depth profile from RBS, ERD and some NRA data.

But I do that already with RUMP (or something)!
RUMP is a simulator. *You* have to guess the profile. Of course, DataFurnace has a simulator equivalent to RUMP, but you don't specify any layer structure!

How does it do that?
It uses the Simulated Annealing algorithm to find a *global* minimum of the difference between the data and the fit. Magic, if you prefer!

For further information contact Chris Jeynes at
c.jeynes@surrey.ac.uk
http://www.ee.surrey.ac.uk/Research/SCRIBA/ndf/

NTA/VSA Program 1999

Wednesday 24 November		
8.30 – 10.00	Registration including late registrations, AINSE Foyer Coffee on arrival	
Session 1	**Chair: David Cohen**	
10.00 – 10.15	Conference Opening, AINSE Theatre Prof Ron MacDonald, University of Newcastle	
10.15 – 10.45	Invited T R Ophel *NTA since 1955 – a nostalgic review*	
10.45 – 11.15	J W Boldeman *Boomerang – The Australian light source*	
Session 2	**Geology**	**Chair: Soey Sie**
11.15 – 11.35	C J Ryan *Progress of the new CSIRO-GEMOC Nuclear Microprobe: First results, performance and recent applications*	
11.35 – 11.55	M Zaw *Application of Ion Microprobe (SHRIMP II) and Synchrotron XRF techniques to the study of uranium series disequilibria in natural samples*	
11.55 – 12.15	H Jackson *Analysis of clays from a Hellenistic housing insula in North Syria*	
12.15 – 12.35	A P Radlinski *Application of small angle neutron scattering to petroleum geology*	
12.35 – 2.00	Lunch, ANSTO Canteen	
Session 3	**Ion Beam Analysis – 1**	**Chair: Heiko Timmers**
2.00 – 2.30	Invited B Trompetter *Depth profile analysis of thin TiO_xN_y films using standard ion beam analysis techniques and HERDA*	
2.30 – 2.50	T D M Weijers *Heavy ion ERD analysis of doped-silica films for integrated photonics*	
2.50 – 3.10	R Siegele *Elemental mapping with the ANSTO high energy heavy ion microprobe*	
3.10 – 3.30	S Jones *Compositional analysis of YbaCuO superconducting films with ion beam analysis techniques*	
3.30 – 3.50	Coffee Break, Gymnasium	
Session 4	**Poster Session I, Gymnasium**	
3.50 – 5.45	Poster Session I, drinks and nibbles	
6.00 – 9.00	Barbeque, ANSTO Pool area	

Thursday 25 November 1999

Session 5	**Thin films**	**Chair: Peter Johnston**
9.00 – 9.30	Invited A Macleod *Sensitivity to contamination of optical coatings*	
9.30 – 9.50	V A Sashin *Electronic structure of the alkali earth metals and their oxides*	
9.50 – 10.10	N Singh *Surface studies of chlorine chemisorption on CVD diamond*	
10.10 – 10.30	J Quinton *Adsorption oscillations in organosilane film growth on metal oxide surfaces*	
10.30 – 11.00	Coffee Break	
Session 6	**Environment**	**Chair: Bill Trompetter**
11.00 – 11.20	B Ben-Nissan *Production and Analysis of Hydroxyapatite from Australian Corals via Hydrothermal Process*	
11.20 – 11.40	D D Cohen *IBA and synchrotron methods for sub-micron fine particle characterisation*	
11.40 – 12.00	G D McOrist *Trace elements associated with atmospheric particulate matter in the upper Hunter Valley – A preliminary study*	
12.00 – 12.20	R Szymczak *Applications of nuclear tracer techniques in coastal zone process studies*	
12.20 – 12.40	R Jeffree *The application of nuclear localisation technologies in environmental biology*	
12.40 – 2.00	Lunch	
1.00 – 2.00	***VSA Annual General Meeting***	
Session 7	**IBMM Chair: Trevor Ophel**	**Surfaces Chair: John O'Connor**
2.00 – 2.20	B C Johnson *Influence of pre-existing structures and ion-implantation conditions on the formation of amorphous silicon*	A Bilic *The computer simulation of the structure of transition metal surface alloys*
2.20 – 2.40	L Morpeth *Characterisation of Ti:Al_2O_3 created by the co-implantation of sapphire with Ti and O*	F Gard *Quantitative study of elemental inter-diffusion across ZnSe/GaAs interface by using SIMS*
2.40 – 3.00	J O Orwa *Diamond nanocrystals formed by implanting fused quartz with carbon ions*	J Xi *Depth profiling surfaces with atomic layer resolution*
3.00 – 3.20	S Cheylan *The effect of ion-irradiation and annealing on the luminescence of Si nanocrystals in SiO2*	D Hoxley *MeV ion-induced electron emission from carbon allotropes*
3.20 – 4.00		A C Y Liu *A novel method for fabricating quantum wire in silicon*
4.00 – 4.30	Coffee Break	
Session 8	**Poster Session II, Gymnasium**	
4.30 – 5.30	Poster Session II	
5.30 – 10.30	Conference Dinner – Harbour Cruise	

NTA/VSA Program 1999 contd

Friday 26 November 1999

Session 9	**Ion Beam Analysis – 2**	**Chair: Chris Ryan**
9.00 – 9.30	Invited R Clark *Quantum Computers*	
9.30 – 9.50	C Jeynes *Hydrogen isotope profiling of functionalised polystyrene blends using RBS/ERD and RBS/NRA with simulated annealing data analysis*	
9.50 – 10.10	T R Ophel *High resolution measurement of hydrogen in thin films*	
10.10 – 10.30	M Ghantasala *Characterisation of magnetron sputtered $SmCo_5$ thin films*	
10.30 – 11.00	Coffee Break	
Session 10	**Ion Beam Analysis – 3**	**Chair: Leszek Wielunski**
11.00 – 11.20	H Timmers *Simplifying position-sensitive gas-ionisation detectors for heavy ion elastic recoil detection*	
11.20 – 11.40	A P Byrne *Ion beam induced amorphisation in semiconductors studied using pertubred angular correlations*	
11.40 – 12.00	M Vos *A new high-energy (e,2e) spectrometer for the study of the electronic structure of materials*	
12.00 – 12.20	D N Jamieson *Surface Studies : Corrosion, lattice orientation, hydrogen content and charge transport in materials and devices*	
12.20 – 1.30	Lunch, ANSTO Canteen	
Session 11	**Isotopic Techniques**	**Chair: Rainer Siegele**
1.30 – 1.50	S H Sie *Precision Pb and S isotopic ratio measurements by microbeam AMS*	
1.50 – 2.10	A M Smith *^{10}Be concentrations in recent firn and ice from Law Dome Antarctica*	
2.10 – 2.30	P Hausladen *Ultra-sensitive detection of technetium-99 by Accelerator Mass Spectrometry*	
2.30 – 2.50	R J McKenzie *Developing a method for the retrospective estimation of radon exposure from In Vivo measurements of ^{210}Pb activity in bone*	
2.50 – 3.10	D Fink *The latest news from the ANTARES AMS facility*	
Session 12	**Conference Closing**	**Chair: David Cohen**
3.10 – 3.40	H Garnett *Status of Replacement Reactor* Prizes and concluding remarks	
3.40	Conference close	

Oral Papers

Poster Papers

SESSION 1

Chair – David Cohen

NTA Since 1955 - A Nostalgic Review

T. R. Ophel

Department of Nuclear Physics, Research School of Physical Sciences and Engineering,
Australian National University, Canberra 0200

INTRODUCTION

Often, the applications of nuclear techniques of analysis (NTA) are (or at least have been in the past) seen as an a field quite separate from the basic research that initially provided the underlying methodology. Alternatively, it is sometimes cynically observed that NTA are an indulgence of nuclear physicists in their twilight years. Indeed, even the author unwisely shunned the early NTA conferences, believing them to be a forum for a different - far be it to say an inferior, activity to that catered for by the companion AINSE nuclear physics conferences. Times, attitudes and perceptions do change though. Here, NTA are championed as an essential section of nuclear research.

A review of a forty five year involvement in mainly nuclear research serves to highlight the errors of both earlier viewpoints and to underscore the changing University attitudes over the years to areas of endeavour like NTA. Research and applications are now closely integrated at the ANU, providing good examples of the important synergies that prevail - especially if both are pursued within the same laboratory.

Since it not possible to be in any way comprehensive, a number of episodes, perhaps chosen with a dash of historical whimsy, are used to illustrate the changing role and expansion of NTA. For those who feel the past is allowed to loom too largely, several current and likely future developments are included.

MOISTURE MEASUREMENTS - 1955

For various reasons of chance, the author - then a brash young student, newly-arrived at ANU, became aware of the measurement of moisture in soils by means of the thermalization of neutrons. One Sunday afternoon, a test arrangement was contrived to demonstrate the technique to several staff from Land Research, CSIRO for possible implementation in the field. It was almost certainly the first time that the arcane research skills of RSPhysS were directed toward anything useful. Of course, in those innocent days, none present for the trial would have comprehended such terms as intellectual property, commercial-in-confidence and sunrise industry.

The simple method worked spectacularly well as water was poured into sand-filled waste paper bins, housing a BF_3 detector and a fast neutron source. Apparently the results of the afternoon did lead to field units. However next day, the newly-fledged moisture-measuring expert was in dire trouble. Not only was every bin in the laboratory filled with wet sand, but spilled water and mud sullied the pristine control room of the Cockcroft-Walton accelerator. An angry head technician had to be mollified. Far worse was the stern condemnation of a senior academic - "such activity is entirely inappropriate in a research laboratory". It would be fair to say that this would have been a unanimous, widely held view then and for some years to come. Certainly, one pioneering and possibly promising career in NTA was firmly nipped in the bud.

NITROGEN PROFILING - 1967

A common technique for preparing nitrogen targets is the nitriding of tantalum. The process provides robust targets, stable when bombarded with intense beams. The thickness of the targets is readily measured using the 15N(p,$\alpha\gamma$) reaction at the 429 keV resonance. Invariably, a slowly increasing yield of gamma rays observed above the resonance was attributed to the tails of higher resonances. However, measurements in 1966/7 of the 14N(p,γ) reaction above the two resonances at 2.38 and 2.46 MeV produced quite bewildering results until a newly-acquired Ge(Li) detector was used instead of NaI. With the much improved resolution, it became possible to observe gamma rays with the discrete energies corresponding to the resonances when the bombarding energy was well above the resonant energies. Clearly a substantial fraction of the tail yield was due to diffused nitrogen at considerable depth. Regrettably, the significant finding was merely used to correct the results in hand and never published. In the years thereafter, several measurements in other laboratories using such targets have been shown to have been affected by the same problem. The episode is indicative of the indifference researchers often had to wider use of what they did. A solution to a problem, likely to be experienced more widely or applicable elsewhere, was not disseminated.

In retrospect, it is surprising that Ge(Li) detectors are not used more widely for NTA than appears to be the case. For example, it is generally considered that hydrogen depth profiling using ^{19}F or ^{15}N beams is restricted in depth because of the existence of resonances at higher energies. A Ge(Li) detector can uniquely identify resonances either by the Doppler-broadened line shapes (which reflect the α-γ correlation) for both reactions [1], and by the relative gamma ray yields in the case of $^{1}H(^{19}F,\alpha)$.

THE COMING OF AMS - 1985

Involvement by the author with a plainly identified NTA activity began in 1985 - surely at the high noon of his career, when ^{36}Cl measurements using the 14 UD accelerator were initiated in collaboration with Roger Bird as an ANU/AAEC/CSIRO joint venture. Misgivings remained though. A strongly expressed intention to participate only until a measurement capability was achieved, was in fact only honoured in part. Frequent interaction with the AMS group, now led by Keith Fifield, that embraces a suite of cosmogenic and anthropogenic isotopes (^{10}Be, ^{14}C, ^{26}Al, ^{32}Si, ^{36}Cl, ^{59}Ni, ^{99}Tc, ^{129}I and the planetary elements Pu and Np) has continued.

An excellent detailed account of the sometimes stormy path of development of AMS is already available [2] so that it unnecessary to dwell on it further here. However, two aspects are noteworthy. First, AMS was quickly implemented because of the infrastructure in place in the laboratory for "proper" nuclear research programs. Aside from the accelerator itself, with near ultra-high vacuum throughout and foil stripping, detectors were provided by the heavy ion reactions group, fast chopping at the ion source was a contribution from the gamma ray nuclear structure group, and a high quality GVM control system had been developed by a group that investigated ion-solid interactions. Problems with specific isotopes that arose were overcome using equipment established for research purposes or techniques developed for them.

Subsequently though, the flow of benefits was reversed. Developments required to enhance AMS capability have generally provided at least equal benefits to research capabilities. In particular, the upgraded injection system installed in 1991, replacement of damaged coils (a legacy of events in 1974) in the 90 degree analyzing magnet in 1995 to

restore the mass-energy product to 200, the multi-sample (32), high-intensity SNICS source that came into operation in 1996, and an upgraded terminal stripping configuration in 1998 stemmed largely from initiatives by Fifield and others with AMS needs foremost as justification. A number of current nuclear research projects (and ERDA mentioned below) would not have been feasible without one or other of these developments. With perceived benefits for the two areas of activity, proposals for funding of the new equipment were treated more favourably than would have been the case for either acting alone.

Secondly, John Carver, the Director of RSPhysSE, was a strong advocate of the attraction of external income. Thus he embraced the AMS project enthusiastically from the outset. Often, to the dismay of the Department of Nuclear Physics, his presentations on the work of the School concentrated very much on AMS, the "more important" research achievements being accorded scant mention. So much for the intellectual snobbery of 1955!

ELASTIC RECOILS - FRIEND OR FOE?

In recent times, there has been substantial interest in elastic recoil analysis of thin films, whereby constituent elements ejected after the scattering of heavier beams are detected and identified. Facilities have been established at ANSTO, using time of flight techniques, at CSIRO, North Ryde with alpha particles to obtain hydrogen profiles, and at ANU with a large solid angle gas ionization detector. With the latter, simultaneous depth profiles are obtained for a wide range of elements with 250 MeV ^{197}Au beams. For example, measurements of high temperature superconductors span elements from hydrogen to barium. Recoil analysis has become a powerful technique and a worthy addition to the armamentarium of NTA. However it is hardly a new phenomenon. Elastic recoils have been intertwined with many measurements undertaken at ANU over the years - most commonly as a curse, until the transition to become a blessing as an analysis tool.

Hydrogen recoils have always been a familiar problem for users of magnetic spectrometers. At forward angles, reaction products of interest would be swamped by the recoils that extended over a wide region of the focal plane or, in the case of narrow range devices, over a considerable range of magnetic field. Because of their relatively low energy, such recoil protons are highly dispersed. A typical measurement with a deuteron beam [3] is shown in Figure 1.

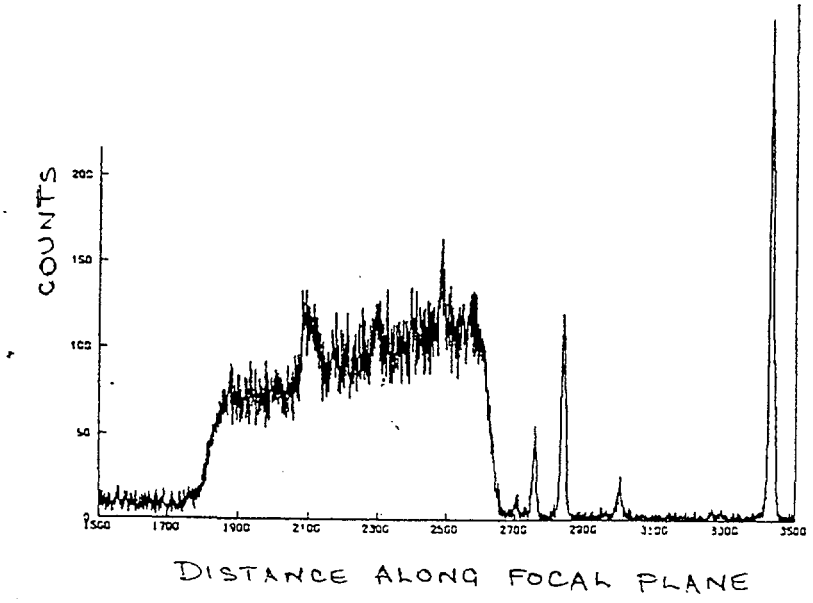

Figure 1. Elastic recoil protons produced by 18 MeV deuterons.

The sought after tritons (less than 1% of the yield) were largely obscured by the profile of hydrogen in the target of ^{54}Fe evaporated onto a carbon foil. Separation of the inelastic deuterons and tritons was dependent on companion energy loss information. "True" researchers were of course indifferent to the hydrogen composition of carbon foils, or of anything else for that matter, but did manage to extract some profit from the kinematic effect. Comparison of the recoil proton energy produced by a heavy ion beam with alpha particles from a source provided a reasonably accurate measure of the energy of the beam [4].

Far greater problems from elastic recoil effects lurked within ionization detectors, although recognition of them was a slow process. Universally, it was found that the detection of monoenergetic ions with a gas detector yielded a well-defined peak containing about 99.8% of the incident particles; the remainder were within a continuously distributed tail extending to low energies. Usually unimportant, such an effect tended to be attributed to recombination of some of the initial electron-ion pairs in the gas, but otherwise was ignored. It became evident at ANU both that the magnitude of the tail was essentially independent of ion type and therefore unlikely to be due to recombination, and that the anomalous events could not be ignored, First, attempts to identify the exotic nucleus ^{20}N and measure its mass were frustrated by a background from tails in the gas-filled, focal plane detector due to the much more prolific ^{17}O. Secondly, AMS was being established at about the same time. It was found that the ultimate sensitivity for the detection of ^{36}Cl was determined by the presence of anomalous events from the intense flux of ^{36}S ions, detected simultaneously in a small, multi-anode gas ionization detector. Though both problems stemmed from anomalous events within gas detectors, the nature of the troublesome events was quite different. For the former, the prohibitive background was due to ^{17}O ions within the tail that yielded only about 80% of their actual energy, so that both their apparent energy and dE/dx mimicked an ^{20}N ion for any given magnetic rigidity. With AMS, the equivalent energy-degraded tail could be readily distinguished from ^{36}Cl ions. Instead, a background arose from ^{36}S ions which deposited their correct total energy, but lost more of that energy than normal prior to the final sensing electrode (designated Eres for residual energy), and therefore correspondingly less beneath that electrode (Fig. 2).

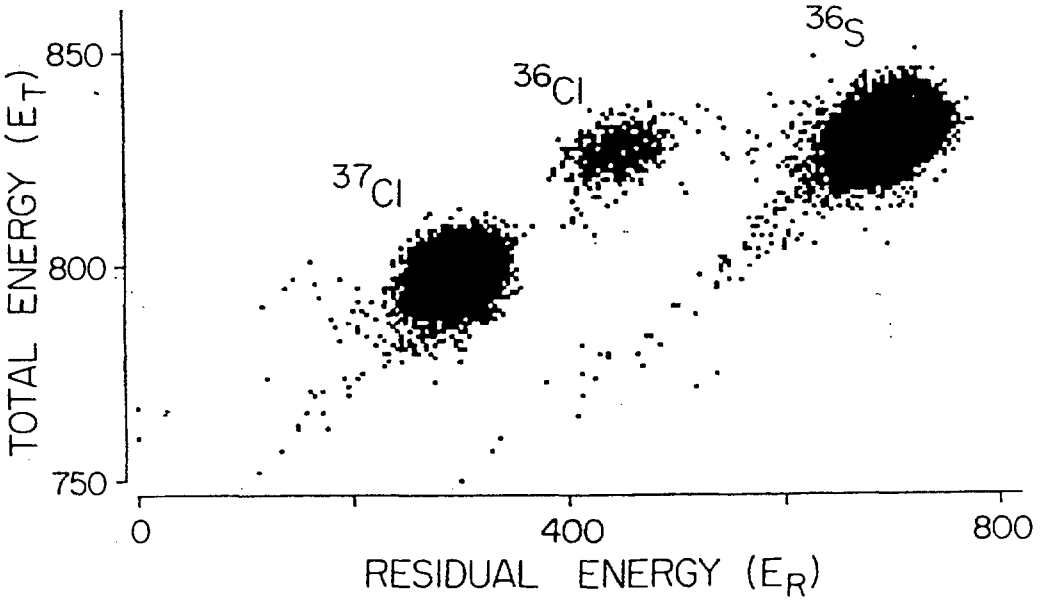

Figure 2. A ^{36}Cl measurement showing background events if only the residual energy (ER) is measured.

Extensive investigations were made over a number of years using two focal plane detectors, useful because both several energy loss measurements and as many as three position determinations could be made along each ion trajectory, and a small special purpose AMS detector developed initially for ^{36}Cl identification. In the present context, the outcome of some truly elegant observations [5] is obvious. The anomalous events proved to be due the consequences of hydrogen and carbon recoils produced when some of the incident ions were scattered by the hydrocarbon stopping gas (initially isobutane, later propane). The overall effects become complex because the elastic recoils are produced over a wide range of energies as the incident ions are slowed and stopped, and of course all kinematically allowed scattering angles are possible. After scattering, the direction and dE/dx of the primary ions differ from those of the unscattered ions and the elastic recoils will in general not deposit all of their energy in the gas. For large scattering angles, either the primary ions or the recoils may strike the detector electrodes. However, it is possible to provide a schematic typical response for any section of the anode plane with identification of both the location and the nature of the scattering (Fig.3).

A solution was devised to both problems in the form of a narrow electrode within the anode, such that at an appropriate gas pressure, the electrode sampled the energy loss at the Bragg peak of the interfering ion type. A typical measurement with the electrode is given in Figure 4. Clearly, no ^{36}S ions lose less than normal energy under the electrode, but still yield the correct total energy. Accordingly, the region where the ^{36}Cl events occur is free of any ^{36}S-induced background. Thus a highly successful AMS detector that has remained unchanged for more than a decade to measure thousands of samples at optimum sensitivity, and an almost background-free measurement of the mass of ^{20}N eventuated from a joint venture involving both applied and basic research.

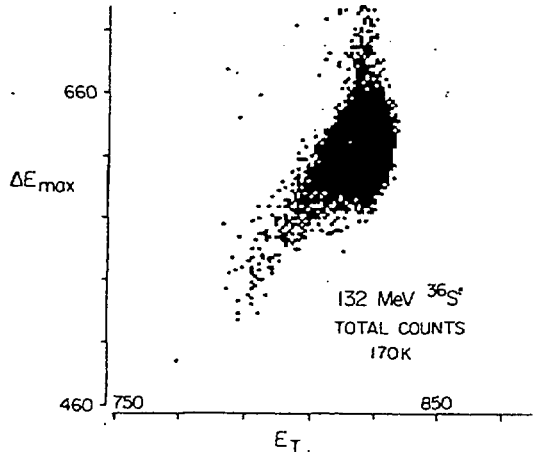

Figure 3. - see text

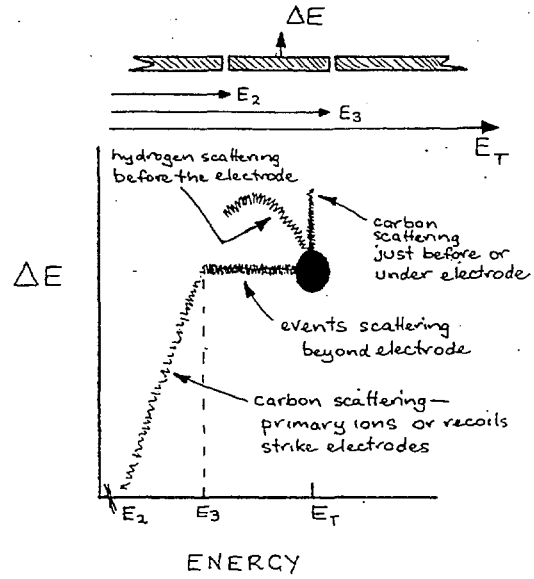

Figure 4. - see text

A similar cycle of inter-related benefits has flowed from elastic recoil analysis (ERDA), now that elastic recoils have been harnessed for good purpose. Again, ERDA was established in a short time at ANU, using the existing infrastructure and the experience gained with focal plane and AMS detectors. Nonetheless, a new class of problems quickly emerged. With a large acceptance solid angle and a range of heavy ions differing widely in mass and energy to be detected, shortcomings in earlier detector designs became apparent. In particular, energy loss and spatial measurements were found to be critically dependent on the entrance

window geometry and associated field configuration. These and other problems have been solved, leading to much improved and species-independent spatial determination, and innovative alternatives methods for the simultaneous measurement of several energy losses and the total energy of ions. Usually, the total energy is obtained by summing all of the signals from the anode, necessarily divided to measure energy losses of ions along their trajectory. This entails careful gain matching for optimum results. Instead, a second grid electrode, between the usual Frisch grid and the anode has been demonstrated [6] to provide a true total energy measurement with a resolution only slightly inferior to that obtained by summing the anode signals (currently four in the ANU detector, with the possibility of one more). Such a development immediately suggests an inversion, whereby a divided second grid is used to measure the energy losses, for which the resolution is not critical, so that an entire undivided anode can provide a simple total energy measurement. The concept has already been tested successfully, but not yet put to actual use. Clearly, the fresh approaches stimulated by ERDA to the design of gridded ionization detectors will certainly be reflected in any new detectors built for ERDA, AMS or heavy ion research at ANU or elsewhere.

Further, a second activity within the ERDA program promises future mutual benefits too. A large, high-resolution Bragg detector has been built for heavy ion RBS and possible ERDA use. The latter would require companion spatial information for kinematic correction, a feature not previously available from such detectors. Investigations into the feasibility of using gridded electrodes within the Bragg detector have been encouraging. It would seem likely that the scattering angle can indeed be measured. More importantly though, the gridded electrodes can also provide energy loss information to supplement the total energy and Bragg peak information normally obtained. Thus it may be possible to eliminate the troublesome anomalous events described above from Bragg detectors as well. Until now, the inability to identify and reject such backgrounds has meant that Bragg detectors are less than ideal for AMS.

SUMMARY

NTA have achieved respectability in the last decade or so, becoming a worthy partner of basic research in nuclear physics. The field continues to expand productively, with both AMS and ERDA now well-established. Two old war-horses, the 2 MV and 3 MV Van de Graaffs of the early sixties at ANU and ANSTO, both of which did much to pioneer NTA in Australia, are about to be replaced with modern counterparts - ample proof of the essential role that NTA now play in many disciplines.

REFERENCES

1. S.D. Cloud and T.R. Ophel, Nuclear Phys A135 (1969) 647.
   C.H. Osman, ANU Thesis (1968).
2. A Tower of Strength - a history of the Department of Nuclear Physics, T.R. Ophel, 236 pp (1968).
3. J.B.A. England, T.R. Ophel, A. Johnston and A.F. Zeller, J. Phys. G 6 (1980) 1553.
4. D.K. Olsen, N.H. Merrill, S.F. Biagi, W.R. Phillips and A.R. Barnett, Nuclear Inst. and Meth. 114 (1974) 615.
5. T.R. Ophel, L.K. Fifield, W.N. Catford, N.A. Orr, C.L. Woods, A. Harding and G.P Clarkson, Nuclear Inst. and Meth. A 272 (1988) 734.
6. New design features of gas ionization detectors used for elastic recoil detection, H. Timmers, R.G. Elliman and T.R. Ophel, (to be published).
   H. Timmers, T.R. Ophel and R.G. Elliman, Nuclear Inst. and Meth. B 156 (1999) 236.

BOOMERANG - The Australian light source

J.W. Boldeman and R.L. Garrett
Australian Nuclear Science and Technology Organisation,
PMB 1, Menai, NSW 2234

1. *Introduction*

A proposal has been prepared for the installation in Australia of a national high performance synchrotron light facility called **Boomerang**. The Boomerang proposal had its origin in the establishment of the Australian Synchrotron Research Program (ASRP) which was one of the seven Major National Research Facilities announced by the Federal Government in December 1995. The ASRP provides the opportunity and funding for Australian researchers to access international synchrotron facilities, specifically two consortia at the Advanced Photon Source (APS) at the Argonne National Laboratory, USA and continued interaction with the Photon Factory at the KEK Laboratory in Japan. The ASRP was the successor to the Australian National Beamline Facility project (ANBF) which began in 1991 following the ASTEC inquiry titled "Small Country - Big Science".

The Federal Government also provided funding for a Feasibility Study to determine the value of establishing an Australian-based synchrotron radiation facility. The Feasibility Study was completed in August 1998 and endorsed by the institutional members of the ASRP and the research community in general. The study concluded that, on the data available in Australia, there was a strong case for the installation of an Australian-based facility. The study considered several options for an Australian-based facility and recommended that these options and the data supporting the general conclusions receive further investigation. A mission was arranged to a select group of overseas laboratories to explore these questions in detail. The review team included a mix of scientific and industrial experience and also represented the interests of the ASRP and an Industrial Synchrotron Consortium based in Victoria. Based on the conclusions of the overseas mission and incorporating the advice of all international specialists in the design and use of synchrotron facilities consulted during the mission, the most cost-effective option was an extended version of 'ANKA', a synchrotron facility that is currently under construction at Karlsruhe, Germany.

2. *Specifications for Boomerang*

The lattice of the parent ANKA facility, currently under construction, comprises four cells each having a dual Double Bend Achromat giving a total of 16 dipoles in the ring. The extended version of ANKA, Boomerang, has six cells and thus 24 dipole magnets in the storage ring. As for the ANKA storage ring, the spacing between the six cells in the proposed facility is different from the internal spacing between the DBAs in each cell, thereby reducing the overall size of the lattice without any compromise in performance. The configuration of Boomerang is shown in Figure 1. The injector and booster are identical to those on ANKA and the RF system is also the same. However, the positioning of the two RF sections has been changed for more efficient operation. Although the extension of the original ANKA design leads to a modest increase in cost, the overall cost of the facility remains attractive because of the use of many of the components from the ANKA facility. The principal specifications of Boomerang are also shown in Figure 1.

The extension of the design has a number of consequences:

- The number of long straight sections is increased to 6 allowing up to 6 insertion devices of traditional design;
- the number of available short sections is increased to 3;

- the circumference of the ring is now 163.8 m;
- with the same magnet field strength of 1.5 T for the dipoles, the energy of the ring increases to 3 GeV making the facility very competitive with other third generation storage rings under construction;
- the emittance of the ring with distributed dispersion is reduced to 16 nm rad which will produce very high brilliance beams.
- Beam current is maintained at 300mA.

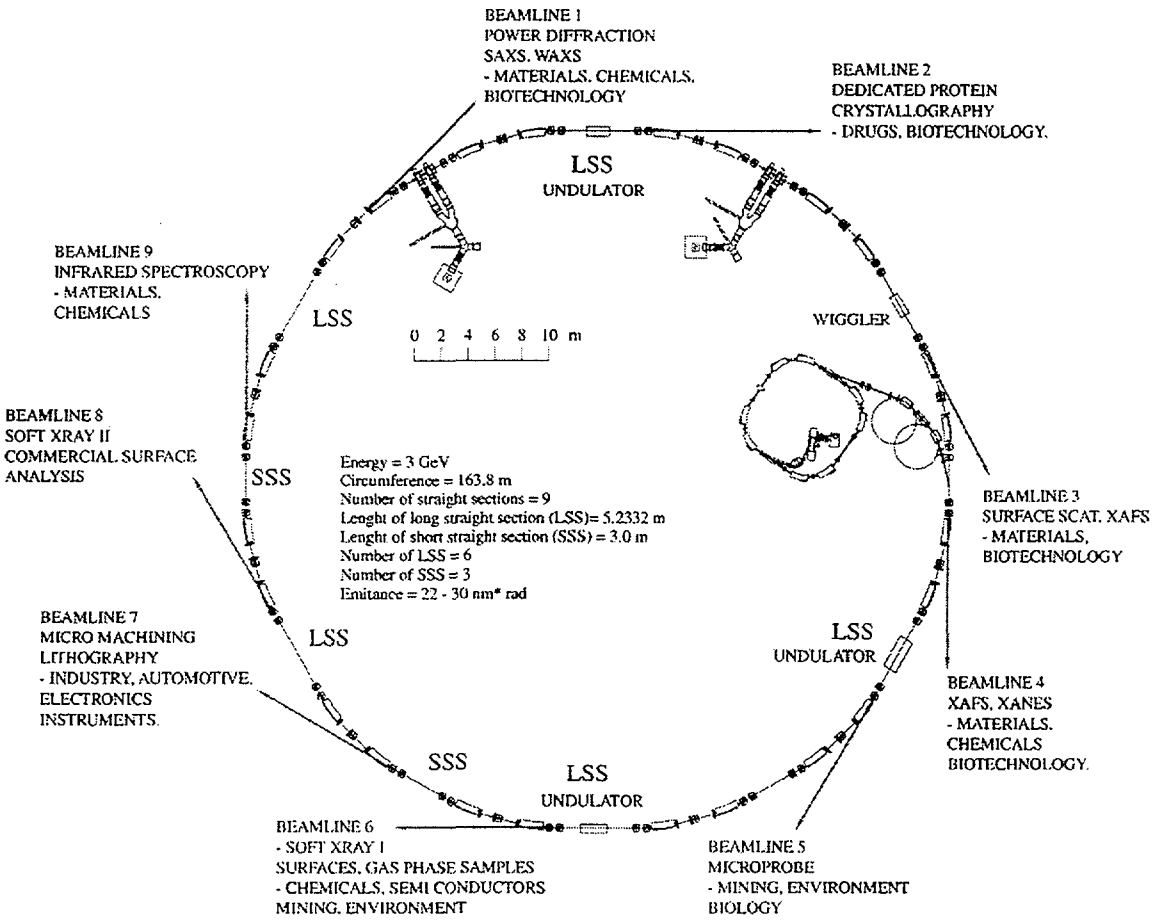

Figure 1 - Configuration of Boomerang

2.1 Beam Optics Calculations

The optics of the proposed lattice have been evaluated using the MAD program, developed at CERN, and the program DIMET, developed by the Stanford Synchrotron Radiation Laboratory. The optics of strong focussing storage rings is now a mature science and the optics calculations provide a very accurate evaluation of an actual storage ring particularly in the hands of experienced designers. Figure 2 shows the optical functions for non zero dispersion in the straight sections. When Boomerang is operated in this fashion, the performance is very competitive with that of other facilities currently in operation. Figure 3 compares the brightness from the Boomerang dipoles with that from the dipoles of the APS and the Photon Factory.

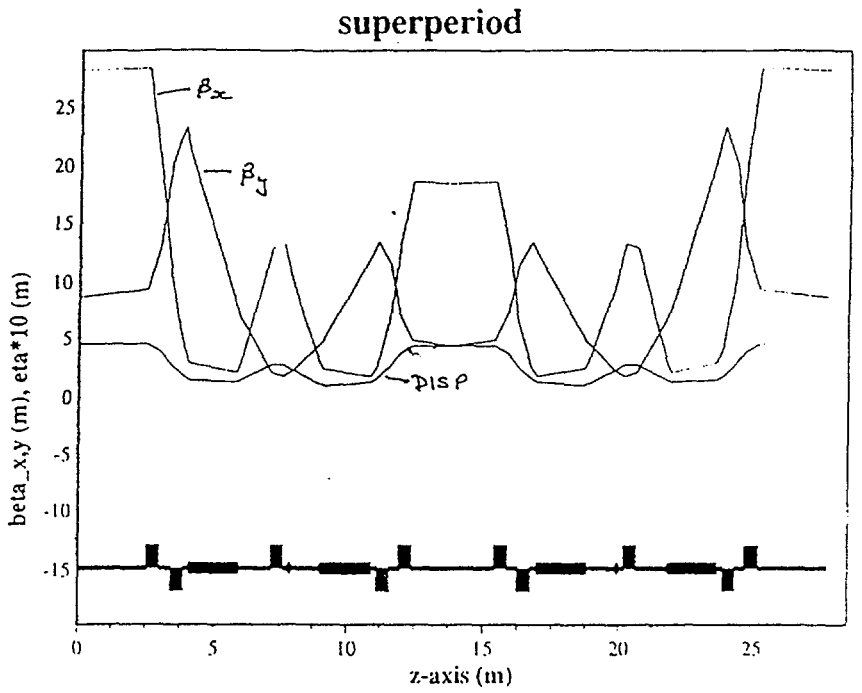

Figure 2 - Variation of the Machine Optics Parameters with Non Zero Dispersion

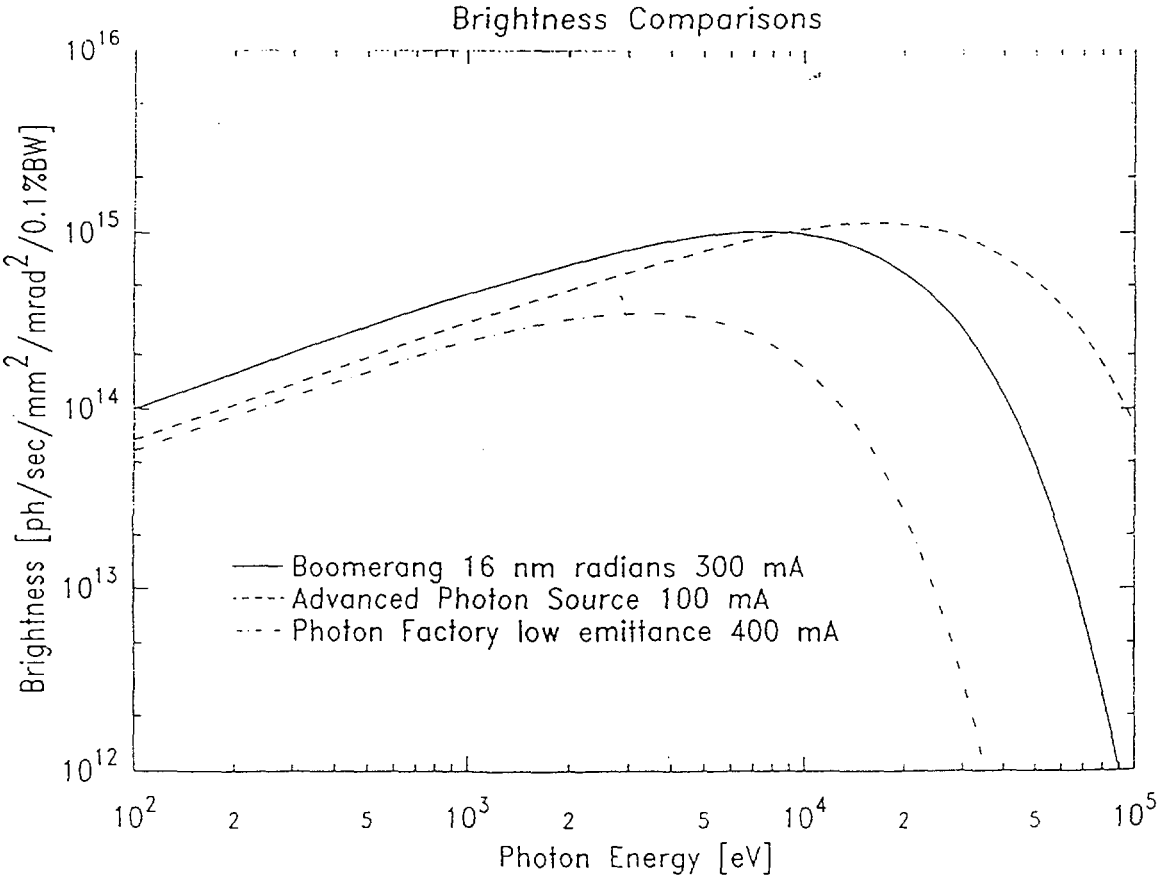

Figure 3. - Brightness Comparisons

2.2 Beamlines and Experimental Stations

Boomerang is capable of supporting as many as 60 experimental stations with perhaps 15 stations on insertion devices. It has therefore been designed to cater for the long term development of the applications of synchrotron radiation in Australia. However the cost per instrument station is approximately $2-4M and ultimately the major investment on the facility will be in associated equipment. A preliminary survey of current users in Australia has suggested that the limited instrument station package shown in Table 1 will cater for approximately 95% of the present and anticipated Australian usage in the first 5 years of operation. The package includes three undulator insertion devices plus a wiggler. The insertion devices and the bend magnets will provide photons to 9 experiment stations.

Table 11 - Beamlines and Instrument Stations

	Source	**Capabilities**
Beamline 1	Bending Magnet	Powder Diffraction, SAXS, WAXS
Beamline 2	Undulator	Protein Crystallography
Beamline 3	Wiggler	Surface Scattering/Dilute XAS
Beamline 4	Bending Magnet	General X-ray Absorption Spectroscopy
Beamline 5	Undulator	Fluorescence Microprobe/Coherence
Beamline 6	Undulator	Soft X-ray I
Beamline 7	Bending Magnet	Micro-machining & Lithography
Beamline 8	Bending Magnet	Soft X-ray II
Beamline 9	Bending Magnet	Infra Red

2.3 Site, Staff and Total Cost

The Boomerang storage ring and associated beamlines will be housed in a large warehouse type structure, 75m by 85m in size. An associated office and laboratory complex will be constructed adjacent to the warehouse building. Office accommodation will include 40 rooms, each with an area of $20m^2$. Five specialist laboratories, $40m^2$, will also be included. The storage ring itself will be enclosed in an airconditioned concrete tunnel. The Boomerang Complex includes a dormitory with 30 double rooms and associated conference and parking facilities. The approximate dimensions of the site are 110m by 220m.

It is proposed that the facility be constructed by Australian staff supported by 7 specialist synchrotron designers from the FZK laboratory. A project engineer will be appointed. The Australian staff, recruited during the construction stage, will become the operational staff of the facility. To operate, promote and fully exploit the capability of the facility will require approximately 52 staff members.

The facility will be operated as a national facility with scientific access following peer review. A strong emphasis will be given to industrial use. The estimated cost over the first 10 years of the facility, including the construction period of 4 years, is $160M. At this time no site has been selected. The philosophy is to submit this proposal to the Federal Government as a national facility and recommend to the government that they seek expressions of interest to house the facility.

3. *Summary of the Scientific and Economic Consequences*

A comprehensive analysis has been made of the scientific and economic benefits that should arise from the installation of Boomerang. Some of the relevant benefits are as follows:

Synchrotron radiation research has evolved from an esoteric endeavour practiced by a small number of scientists primarily from the fields of solid state physics and surface science to a mainstream activity which provides essential information in the materials and chemical sciences, the life sciences, molecular environmental science, the geosciences, nascent technology and defence related research among many fields.

Based on the experience in OECD countries, the Australian scientific community involved in the applications of synchrotron radiation could be expected to reach 1200 registered users by the year 2010 if Boomerang is installed.

Boomerang would become the premier research tool in Australia for the training of a scientifically advanced community.

Synchrotron facilities are the most versatile of all major research facilities and therefore the installation of Boomerang would allow Australian researchers to participate in many emerging technologies.

Boomerang is expected to become a major Pacific Rim research facility and could attract investment from neighbouring nations such as New Zealand, South Africa, Malaysia and perhaps Indonesia.

Australian science with a rapidly growing community of internationally respected protein crystallographers would be extremely well placed to capture the benefits in biological science following the installation of a synchrotron facility. The installation of Boomerang would provide the opportunity for Australia to compete on a level playing field as a pharmaceutical supplier in the next century. It could be expected that products based on the generation of Intellectual Property by Australian researchers at Boomerang could generate annual revenue of as much as $2B. Appropriate investment could capture much of this revenue for Australian based companies.

The installation of Boomerang could supplement existing capabilities for the manufacture of microstructure products. The potential annual revenue from the provision of comprehensive capabilities in this industrial activity could be up to $60-120M based on an expected world market of more than $60B in the early part of the next century.

It is expected that synchrotron radiation will play an important role in diagnostic and perhaps therapeutic medicine in the 21st century. It is also apparent that Australian scientists have the tradition and expertise to exploit these opportunities when they arise. For any application in medicine it is not conceivable to consider the use of international facilities.

Boomerang should assist the Australian mining and exploration industry by providing state of the art analytical X-ray capabilities. At a time when the decline in commodity prices is placing pressure on this major Australian industry, it would be a wise strategic decision to have access to state of the art analytical facilities available at short notice to protect these industries.

Internationally with more than 80 facilities planned or operational, Australia is by far the largest trading nation without a home based facility.

SESSION 2

Chair – Soey Sie

Geology

Progress of the new CSIRO-GEMOC nuclear microprobe: first results, performance and recent applications

C.G. Ryan[1], D.N. Jamieson[2], W.L. Griffin[3,1], G. Cripps[1], S.H. Sie[1] and G.F. Suter[1]
[1] CSIRO Exploration and Mining, North Ryde NSW 2113, Australia.
[2] MARC, University of Melbourne, Parkville VIC 3052, Australia.
[3] GEMOC, Macquarie University, Sydney NSW 2109, Australia.

The new CSIRO-GEMOC Nuclear Microprobe (NMP) features a number of technical advances for high resolution, high sensitivity microanalysis. It was designed at the CSIRO and developed as collaboration between the CSIRO, the GEMOC key-centre at Macquarie University and the MARC group of the University of Melbourne. For imaging applications, it also features a software system using a powerful algorithm called *Dynamic Analysis*, developed at the CSIRO for unmixing elemental signatures in proton induced X-ray emission (PIXE) data, to provide a tool for rapid quantitative imaging of trace and major element spatial distribution in minerals. This paper reports on the performance of the NMP and examples of its application over the past 6 months since completion.

System Overview The NMP uses a new design that closely integrates the beam forming lens system with the chamber, microscope and detector systems (Fig. 1) to provide good focussing performance and large solid-angle detectors while featuring a high quality normal-viewing microscope coaxial with the beam [1,2]. The key to this design is a unique magnetic quadrupole quintuplet lens system, a distributed 5 lens configuration, which uses a novel design for each quadrupole. Further features of the new probe include: large area X-ray, γ-ray and particle detectors, digital signal processors, electrostatic on-demand beam-switching and scanning, Questar long-range normal-viewing microscope with coaxial reflected light illumination, CCD camera and remote control, computer-controlled sample goniometer (X,Y,Z,θ,ϕ), sample-change vacuum-lock, anti-vibration mounting, and efficient beam shaping using computer-controlled object and divergence limiting slits.

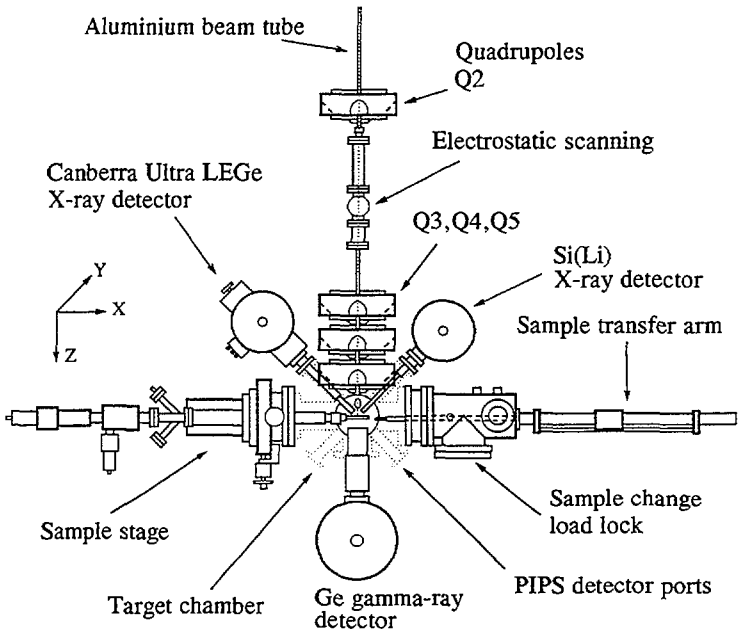

Fig. 1 Top view of NMP target chamber showing the close lens-detector-target geometry and general layout.

Quadrupole Lens Design A distinguishing feature of the new lens system is the design of each quadrupole lens, developed as collaboration between CSIRO and the MARC group, University of Melbourne. The quadrupole yokes are shaped with pole-tip extensions, which bring the quadrupole fields 30 mm closer to the target. Also, to accommodate unrestricted detector access at 135° to the beam, the yokes have cutouts between poles for symmetric detector ports. The cutouts permit these ports to fit between coil windings, and four cutouts are used to maintain four-fold symmetry. The result is an effective working distance of 80 mm despite a large yoke outer diameter of 270 mm and an ample bore of 14 mm [3].

Quintuplet Lens Configuration The lens configuration uses a unique separated quadrupole quintuplet, with a coupling of +A+A-A-A+B. The drift spaces between the first 3 quadrupoles have been used to reduce spherical aberration, especially the cross-terms, increase demagnification, reduce lens excitation, and approach equal demagnification in the X and Y planes. This configuration has a demagnification of 67 in X and Y (despite a short overall system length of 4.7 m), low total spherical aberration for this demagnification, and has all its significant aberration contributions concentrated into $x|\theta^n$ terms.

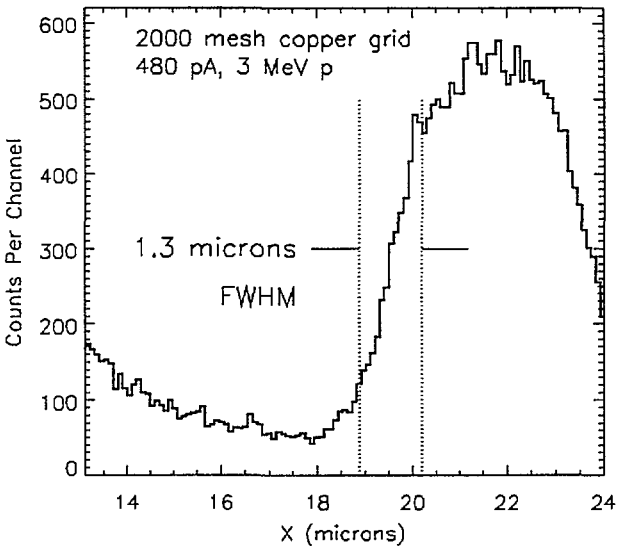

Figure 2 Scan across a grid bar of a 2000 mesh Cu grid, using 480pA of 3MeV protons.

Beam Shaping Controls Computer-controlled object and divergence limiting slits control phase-space acceptance. The object slits are formed by polished W rods and allow the slit-gap to be continuously varied from 0 to 1200 μm. There are also fixed apertures of 1, 2 and 5 mm. The divergence slits are positioned at 2.6 m following the object slits [2].

The lens system has most aberration terms concentrated into terms of the form $x|\theta^n$ [3]. This means that controlling the ratio of θ/ϕ, via the divergence slit gap ratio X/Y, can be used to control the degree of aberration in the focussed beam-spot, at constant beam current. To facilitate this adjustment, the computer control of each slit-group is done via a graphical user interface on the Amiga control computer. Slider controls can manipulate the X/Y ratio, or adjust X and Y slit gaps together at constant X/Y, or control object and divergence slits together. Once set-up, this enables the user to simply slide one control to the desired beam current.

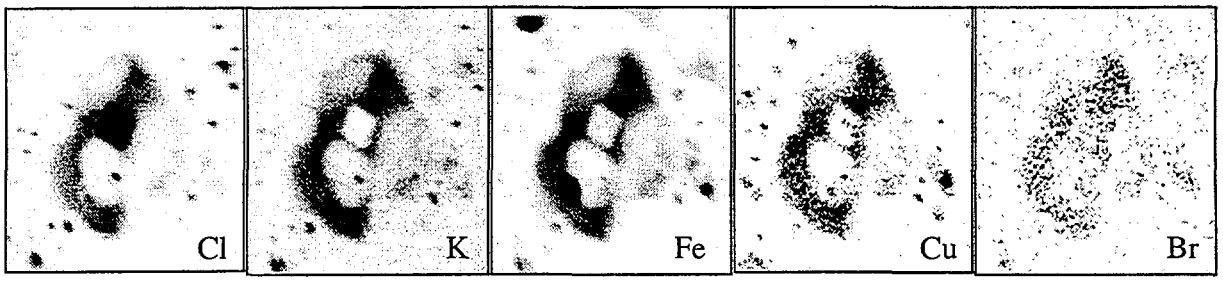

Figure 3 PIXE images of a 70 μm fluid inclusion in quartz (100 x 100 μm^2 scan area). Note the large cubic halite daughter crystal (high Cl, low K, Mn, Fe), the sylvite crystals (high K and Cl) to the left of the halite, the hematite crystal (high Fe) and a small chalcopyrite daughter crystal on the far right (high Cu, Fe). Images also obtained for Ca, Zn, Rb, Sr, As, Ba and Pb.

Data Acquisition and Analysis Data Acquisition uses the MicroDAS interface, developed by the MARC group at Melbourne University. For every event recorded by a detector, an E,X,Y triplet is saved, tagged by the detector number, as a record of the energy (E) and coordinate (X,Y) of the event in the image area. This event data stream is analysed using a new GUI version of the CSIRO GeoPIXE system for quantitative analysis of PIXE data in order to image element distribution using *Dynamic Analysis* (DA). The latter is a powerful algorithm for unmixing elemental spectral signatures in PIXE data, in order to project

quantitative images of trace and major element spatial distribution in the sample under study [4,5].

Performance The theoretical performance of this new configuration [3], suggests that sub-micron beam spot-sizes at 100pA beam current can be achieved, at the low brightness of the CSIRO tandem accelerator (~1pA/[μm^2.$mrad^2$.MeV]). A spot-size of 1.3μm was obtained on the first day with beam (Figure 2), at a beam current suitable for trace element work (480pA). As the acceptance of the system is increased, and the beam current grows to ~20nA, the modelling suggests a slow rate of spot-size growth with a spot size of ~3μm possible at these high currents. This is observed in practice with the spot-size growing to only 1.8μm at 10nA, an ideal current for trace element imaging in silicates (eg. Figure 4).

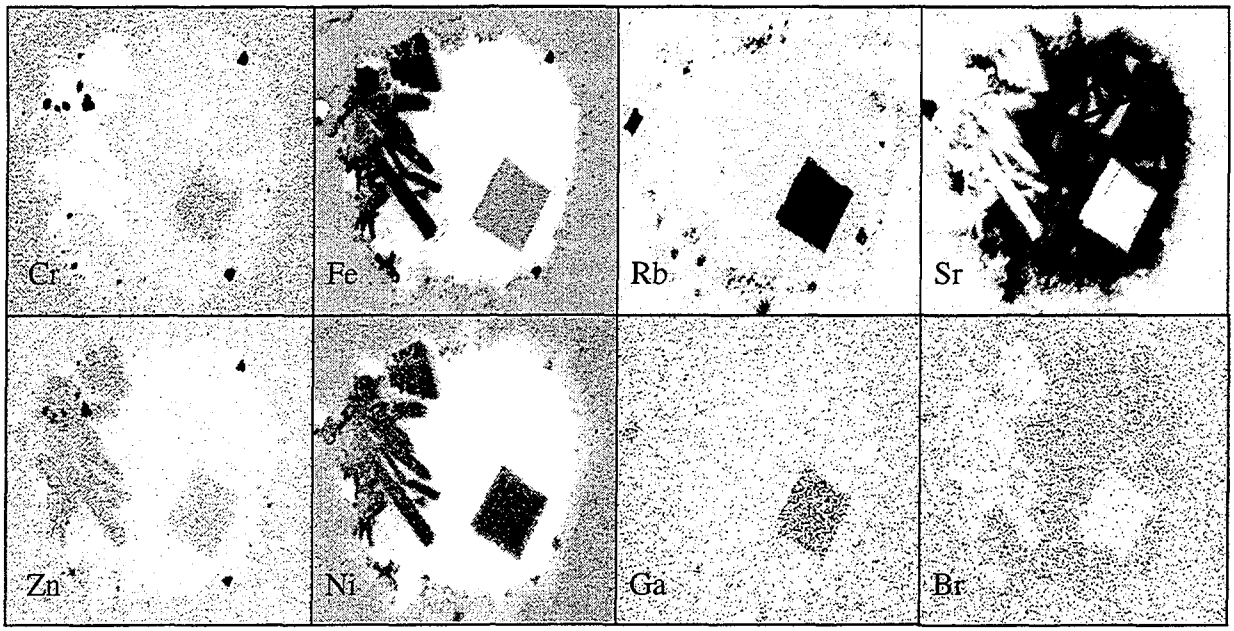

Figure. 4 Quantitative DA PIXE images of a carbonatitic melt inclusion in clinopyroxene from the Slave Craton, Canada (1.4 x 1.4 mm^2 scan area, Q = 138.4 μC). Images also obtained for Mn, Cu, Zn, Ga, Ge, Br, Zr, Nb, Ag, Th, Ta, La, Ce, Sn and Pb. Average concentrations over the inclusion sub-region include: Fe 2.75%, Sr 0.6%, Rb 48 ppm, Zn 17 ppm, Ga 3.0 ppm and Br 0.5 ppm. Detection limit for Ga. Br is 0.24 ppm.

NMP applications Several features of the new NMP are proving very useful for efficient geological application: (1) High beam currents into <2μm beam-spots for high sensitivity. (2) Large area, close geometry, Ge X-ray detector for high efficiency. (3) Quantitative PIXE imaging using *Dynamic Analysis*. (4) High quality normal-viewing microscope optics. (5) Convenient computer control of sample stage and beam-shaping. These result in high-resolution images of more than 20 elements per sample (eg. figure 4,5), detection limits in extracted areas for many elements below 0.3 ppm (eg. figure 4), analysis and imaging of REE (eg. figure 5), *in situ* imaging of the contents of individual fluid inclusions in minerals (eg. figure 3), and the analysis of precious metals in sulfides (eg. figure 6).

The Future Ongoing development is being directed towards: (1) Light element detection using proton induced γ-rays (PIGE). (2) The integration of the PIXE analysis software and the *Dynamic Analysis* approach with the new data acquisition system to enable on-line unmixing of PIXE (and later PIGE) image data for the *real-time* display of quantitative images. (3) Development of methods to cope with the volume of data generated by the new NMP (~3-6 Gbytes per month).

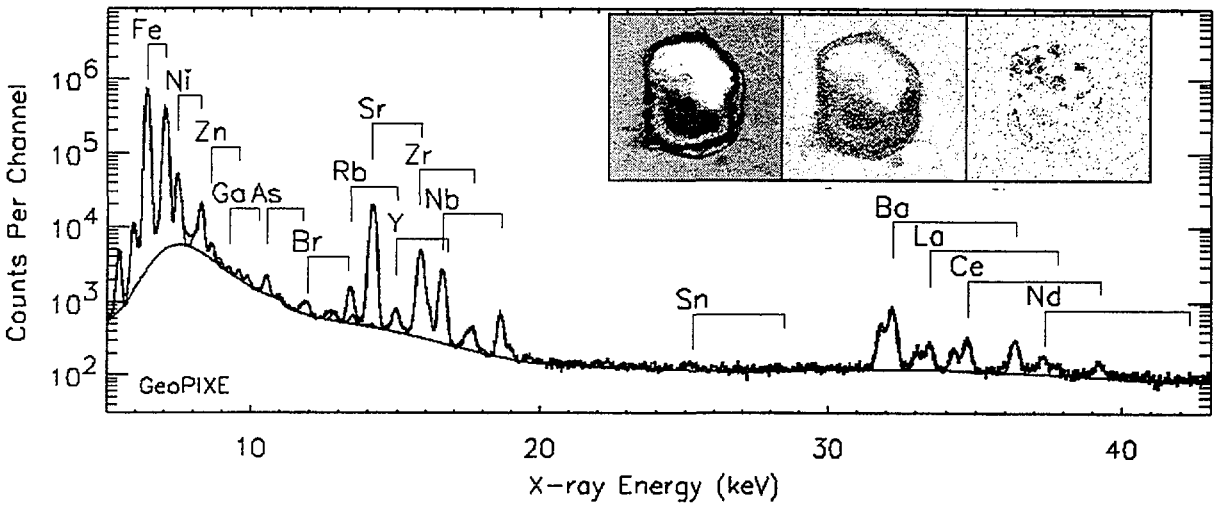

Figure 5 Spectrum extracted from a sub-region of a scan area containing a kimberlitic melt inclusion in xenocrystic clinopyroxene from the Slave Craton, Canada (1.4 x 1.3 mm^2 scan area, Ge X-ray detector). Images also obtained for Cr, Mn, Ni, Cu, Zn, Ga, Ge, As, Br, Rb, Sr, Y, Zr, Mo, Ag, Th, Ta, Ba, La, Nd, Sn and Pb. The detection limits for elements such as Ga, Ge, As and Br is 0.3-0.4 ppm, and for Ce is 6 ppm. Charge for the sub-region enclosing the inclusion is 47 uC.

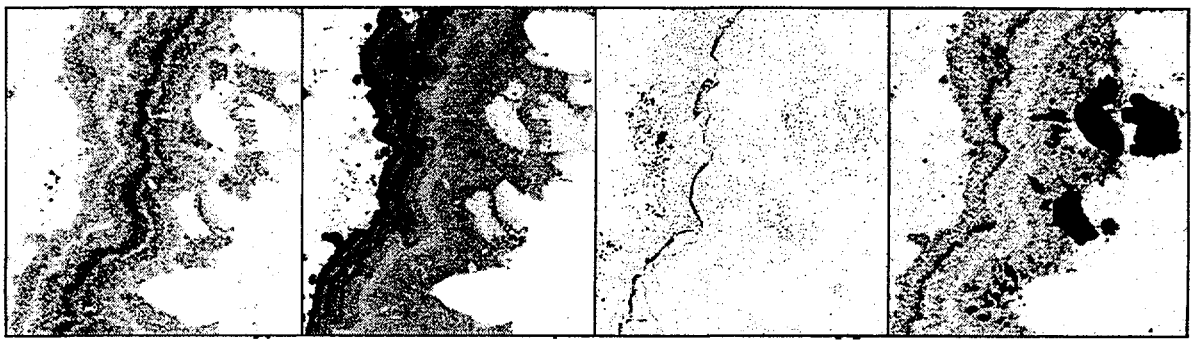

Figure 6 DA PIXE images of a 2 x 2 mm^2 section through an epithermal sulfide ore vein in quartz from the Emperor Mine, Fiji (acquisition time 45 minutes). Note the gold-silver tellurides (on right in Au image) and trace gold zonation at 200-6000 ppm. Gold zonation follows As in general terms, but not in detail. Images also obtained for Fe, Ni, Zn, Se, Sr, Y, Sb and Te.

[1] C.G. Ryan, D.N. Jamieson, W.L. Griffin, S.H. Sie, G. Cripps and G.F. Suter, "The new CSIRO-GEMOC Nuclear Microprobe: A new highly integrated design for geoscience applications", proceedings of 10th Australian Conf. on Nuclear Techniques of Analysis, Canberra, ISSN 1329-8437 (1997) NTA/VSA8.

[2] C.G. Ryan, D.N. Jamieson, W.L. Griffin and G. Cripps, "The CSIRO-GEMOC Nuclear Microprobe: A high-performance system based on a new closely integrated design", Nucl. Instr. Meth. B158 (1999) 97-106.

[3] C.G. Ryan and D.N. Jamieson, "A high-performance quadrupole quintuplet lens system for the CSIRO-GEMOC Nuclear Microprobe", Nucl. Instr. Meth. B158 (1999) 18-23.

[4] C.G. Ryan and D.N. Jamieson, "Dynamic Analysis: On-line Quantitative PIXE Microanalysis and its Use in Overlap-Resolved Elemental Mapping", Nucl. Instr. Meth. B77 (1993) 203-214.

[5] C.G. Ryan, E. van Achterbergh, D.N. Jamieson and C.L. Churms, "Overlap corrected on-line PIXE imaging using the Proton Microprobe", Nucl, Instr. Meth. B109/110 (1996) 154-160.

[6] E. van Achterbergh, W.L. Griffin, K. Kivi, N.J. Pearson and S.Y. O'Reilly, "Carbonatites at 200 km: Quenched melt inclusions in megacrystalline lherzolite xenoliths, Slave Craton, Canada, Proc. of 9th V.M.. Goldschmidt Conf., Cambridge, Massachusetts (1999) 304-305.

Application of ion microprobe (SHRIMP II) and synchrotron X-ray fluorescence techniques to the study of uranium series disequilibria in natural samples

Myint Zaw[1], Peter Airey[1], Timothy Payne[1], Ian Williams[2], Tsutomu Sato[3] and Tetsushi Nagano[4]

[1] Australian Nuclear Science and Technology Organisation, [2] Australian National University, [3] Kanazawa University, Japan and [4] Japan Atomic Energy Research Institute.

Introduction

This research was part of an international project coordinated by the Organisation for Economic Corporation and Development / Nuclear Energy Agency to study the Koongarra uranium deposit in the Northern Territory of Australia as a natural analogue of radioactive waste repositories. There is particular interest in the migration and retention mechanisms of uranium (U) and its daughter products including thorium (Th) and lead (Pb) isotopes in the natural environment. The most direct source of evidence comes from the measured $^{234}U/^{238}U$, $^{230}Th/^{234}U$, $^{206}Pb/^{238}U$ and lead isotope ratios in selected mineral phases. The spatial distribution of the $^{234}U/^{238}U$ and the lead isotope ratios can be studied on a petrological slide (resolution 5 to 30μm) using the Sensitive High Resolution Ion Microprobe (SHRIMP) at the Australian National University. The aim of the Advanced Photon Source (APS) investigation was to explore whether it is possible to obtain normalising factors to convert the uncorrected $^{230}Th/^{234}U$ and $^{206}Pb/^{238}U$ SHRIMP count ratios into activity ratios. A uniform Tanzania uraninite sample which is at secular radioactive equilibrium (Sato *et al*, 1998) was used to validate the concept.

Experimental

SHRIMP measurement - The SHRIMP is optimised for high sensitivity when operating at high mass resolution, which is achieved by the combination of wide slits and a large secondary mass analyser. In the SHRIMP measurements, a primary beam of O_2^- at 10kV accelerating voltage and 5-10nA beam current was focused to a spot of about 30μm in diameter on the polished thin section, which was coated with a ~5nm layer of gold to overcome charging. Each analysis comprised sequential ion count rate measurements at several mass-stations. The main target nuclides were Pb (^{204}Pb, ^{206}Pb, ^{207}Pb and ^{208}Pb), Th (^{230}Th and ^{232}Th) and U (^{234}U, ^{235}U, $^{250}(UO)$ and $^{251}(UO)$). Count rates of ^{235}U (rather than ^{238}U) were measured because the count rates of ^{238}U exceeded the capacity of the ion counter. Count rates of ^{238}U were calculated from the measured ^{235}U count rates using a $^{238}U/^{235}U$ atomic ratio of 137.88. The time required per spot was about 20 minutes, including two minutes to sputter-clean the target area of the polished section prior to analysis. The ratios of isotopes of a given element may be calculated directly from the observed count rates. However, direct measurements of the $^{230}Th/^{234}U$ and $^{206}Pb/^{238}U$ using the SHRIMP are not possible, because of significant differences in the sputtering factors for the different elements (Sato *et al*, 1998; Nagano *et al*, 1999).

Advanced Photon Source measurement - The Synchrotron beamline of the SRI-CAT at the Advanced Photon Source (Chicago, USA) was used for fluorescence trace analysis of a reference sample of Tanzania uraninite which was mounted on a glass slide and epoxy resin. The X-ray microprobe beamline consisted of a primary aperture, a double crystal Si(111) monochromator, a flat focusing mirror, and a four-jaw slit assembly. The analysed spot size on the sample was ~20μm in diameter. The intensity of the incident beam was monitored with an ion chamber, and the resulting Pb (Lα1 and Lα2), Th (Lα2) and U (Lα1) fluorescence

signals were detected using a Ge energy-dispersive detector at 90° to the incident X-ray beam. An optical microscope was used for viewing and positioning the sample in the X-ray beam. X-ray fluorescence (XRF) spectra of the reference Tanzania uraninite which had been previously analysed using the SHRIMP were taken and analysed for the count ratios of Th/U and Pb/U. Spectra were obtained around the emission energies of the peaks of Pb, Th and U as shown in Table 1. Fluorescence lines of Pb (Lα1 and Lα2, Lβ1 and Lβ2), Th (Lα2) and U (Lα1) were measured within the energy ranges of 10.2 to 14.1keV using the SRI-CAT at the APS.

Table 1. Summary of the analysis emission lines and experimental parameters of Pb, Th and U.

Element	Line	Emission energy (keV)	Energy ranges (keV)	Channels
Pb	Lα1	10.5515	10.213-10.908	770-823
	Lα2	10.4495		
	Lβ1	12.6137		
	Lβ2	12.6226		
Th	Lα2	12.8096	12.444-12.930	940-977
U	Lα1	13.6147	13.166-14.085	995-1065

Results and Discussion

The net counts of Pb or U in the APS were obtained directly from the experimental data within the corresponding channels (ie. within the corresponding energy ranges). However, the net counts of Th from the APS were obtained indirectly because the Th emission line Lα2 overlaps with Pb emission lines of Lβ1 and Lβ2. The procedure for Th was as follows:

- The XRF spectrum of the standard reference material SRM1833 was obtained as shown in Figure 1(a). The composition of this sample is also shown inside the Figure.
- The count ratio of Pb2 (from Lβ1 and Lβ2) to Pb1 (from Lα1 and Lα2) was measured using standard reference material as shown in Figure 1(a). The value was 0.4295.
- The interference Pb counts in standard Tanzania uraninite (Figure 1(b)) in the energy range of 12.444 and 12.930keV can be obtained from the Pb counts of energy range of 10.213 and 10.908keV multiplied by 0.4295.
- Hence the net counts of Th in the energy range of 12.444 and 12.930keV were obtained from the difference of the total measured counts and the corresponding interference Pb counts.

The overall elemental net count intensity from the APS was compared with the sum of all the isotopic count rates of each element obtained from the SHRIMP. Hence the total count rate of Th in SHRIMP measurement is the sum of count rates for ^{230}Th and ^{232}Th. Similarly the total count rate of U in SHRIMP measurement is the sum of count rates for ^{234}U, ^{235}U and ^{238}U. The correction factor thus obtained was applied to correct the apparent isotope count ratio obtained from the SHRIMP (eg SHRIMP ^{230}Th/^{234}U) to obtain the normalised isotope ratio. The data were expressed as mass ratios and activity ratios as shown in Table 2.

Table 2. The computation of APS and SHRIMP data of Tanzania uraninite to obtain normalised data of $^{230}Th/^{234}U$ and $^{206}Pb/^{238}U$.

Parameters	Isotope and isotope Ratios	Tanzania uraninite			
		APS (counts)	SHRIMP-1 (cps)	SHRIMP-2 (cps)	SHRIMP-3 (cps)
SHRIMP Measurements	^{230}Th		8.6	19	20
	^{234}U		80	152	162
	^{206}Pb		920000	850000	770000
	^{238}U		1516680	2619720	2895480
	$^{230}Th/^{234}U$		0.1075	0.1267	0.1250
	$^{206}Pb/^{238}U$		0.6066	0.3245	0.2659
Counts (cps)	Pb	671623.3	977206.6	903207.4	818312
	Th	28090.6	1708.6	3619	3820
	U	9863492	1527760	2638870	2916640
Count ratios	Pb/U	0.0681	0.6396	0.3423	0.2806
	Th/U	0.0028	0.0011	0.0014	0.0013
Normalising factors	$(Pb/U)_{SHRIMP}/(Pb/U)_{APS}$		9.3937	5.0266	4.1204
	$(Th/U)_{SHRIMP}/(Th/U)_{APS}$		0.3927	0.4815	0.4599
SHRIMP mass ratios	$^{230}Th/^{234}U$ (normalised)		0.2737	0.2630	0.2718
	$^{230}Th/^{234}U$ (error)		0.0870	0.0450	0.0450
	$^{206}Pb/^{238}U$ (normalised)		0.0646	0.0645	0.0645
	$^{206}Pb/^{238}U$ (error)		0.0010	0.0080	0.0010
SHRIMP activity ratios	$^{230}Th/^{234}U$ (normalised)		0.8916	0.8567	0.8852
	$^{230}Th/^{234}U$ (error)		0.2827	0.1462	0.1462

Notes: (1) SHRIMP-1, -2 and -3 indicate different spots on the same sample. Cps indicates counts per second.
(2) For SHRIMP total Pb = (^{204}Pb + ^{206}Pb + ^{207}Pb + ^{208}Pb), Th =(^{230}Th + ^{232}Th) and U=(^{234}U + ^{235}U + ^{238}U).

The XRF data were then used to convert the SHRIMP count ratios of ^{230}Th and ^{234}U. For example, the uncorrected SHRIMP count ratio of $^{230}Th/^{234}U$ for one measurement spot was 0.108 ± 0.034. The measured normalising ratio $(Th/U)_{SHRIMP}/(Th/U)_{APS}$ (at the same spot) was determined to be 0.393. Hence the normalised $^{230}Th/^{234}U$ atomic ratio was 0.274 ± 0.087. The observed range for all measuring spots was 0.263-0.274. Therefore the activity ratios of $^{230}Th/^{234}U$ for the Tanzania uraninite were 0.857-0.892 (errors 0.146 to 0.283). This is consistent with equilibrium within experimental error, and thus validates the concept. Further refinements of the measurements would be required for the routine use of this procedure.

Conclusions

The following conclusions were drawn. (1) The concept of using XRF measurements from the APS to normalise the uncorrected $^{230}Th/^{234}U$ from the SHRIMP appears to be valid. Extension of the work to $^{206}Pb/^{238}U$ is possible, although the Pb/U measured by APS (0.065) is less than that expected from the uraninite's $^{207}Pb/^{206}Pb$ age of 640 Ma (0.104), and the Pb/U measured by SHRIMP varied, both indicating that the uraninite has lost Pb. (2) Higher energy emission lines for Th (Lβ or Lγ) may be required to reduce the lead interference in Th counts, which limited the precision of the APS estimates of the $^{230}Th/^{234}U$ ratios. (3) In designing a comprehensive investigation of uranium series disequilibria on the micro scale, care will be needed to ensure that the levels of the daughter radionuclides are sufficient to obtain adequate measurement statistics with SHRIMP. (4) Measurements on natural samples were undertaken. However the count rates were very low and the uncertainties high. Further work is necessary.

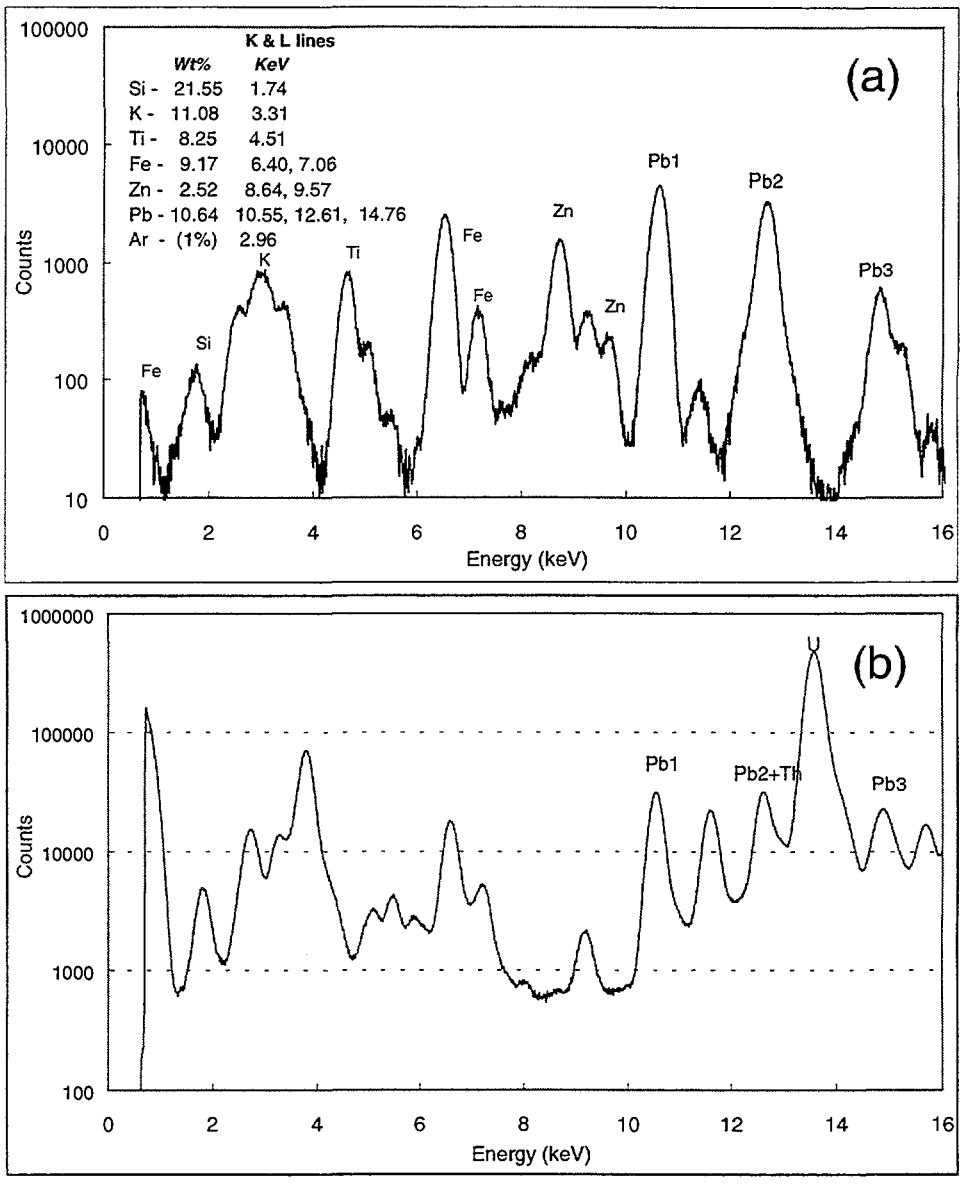

Figure 1. X-ray fluorescence spectra of (a) the standard reference material SRM1833 and (b) the standard Tanzania uraninite compound as a function of emission energies.

Acknowledgment

This work was supported by the Australian Synchrotron Research Program, which is funded by the Commonwealth of Australia under the Major National Research Facilities program. Use of the Advanced Photon Source was supported by the U.S. Department of Energy, Basic Energy Sciences, Office of Energy Research, under Contract No. W-31-109-Eng-38. The authors acknowledge with gratitude the assistance of the staff from SRI-CAT.

References

Sato, T., Yanase, N., Williams, I. S., Compston, W., Zaw, M., Payne, T. E. and Airey, P. L. (1998) Uranium Micro-isotopic Analysis of Weathered Rock by a Sensitive High Resolution Ion Microprobe (SHRIMP II). *Radiochim. Acta.* **82**, 335-340.

Nagano, T., Sato, T., Yanase, N., Isobe, H., Ohnuki, T., Williams, T. S., Zaw, M., Payne, T. E., and Airey, P. L. (1999) Analogue Studies in the Alligator Rivers Region - *In-situ* Measurement of Uranium Series Nuclides with SHRIMP. Japan Atomic Energy Research Institute - Research, 99-024, March. 52 pp.

Analysis of clays from a Hellenistic housing insula in North Syria.

Heather Jackson[1], Graeme Bailey[2], Eric Clayton[2], Ed Stelcer[2]

[1]University of Melbourne, Parkville, VIC, 3052
[2]ANSTO

Jebel Khalid, on the West bank of the Euphrates River in Northern Syria, has been excavated by an Australian team from Canberra and Melbourne Universities since 1987. It is a Seleucid settlement ie. probably founded by Seleucus I (one of Alexander's generals who 'inherited' a large tract of his empire) or one of his successors in the early third century BCE. The coin evidence shows that the site had a life of about two hundred years and was slowly abandoned in the first half of the first century BCE. It is built on a steep, twin-peaked mountain and its principle purpose must have been defensive, to judge by the Circuit Wall of 4-5 kilometres and the twenty-eight towers dispersed along it. What was it defending? One strong probability is the river crossing and the concomitant trade route, which is relevant to the study of the pottery and artefacts from the site. The importance of the site apart from this lies in its being a 'virgin' Hellenistic site with no contamination by Roman settlement. Not a great deal is known or has been published about Hellenistic sites in Syria.

The pottery which is the main subject of this report was all excavated from the housing area, which lies on a south-facing slope facing the higher peak, on which stood the Governor's Palace. Very few whole pots were excavated so we have to rely on diagnostic sherds to re-create the types of vessels used. The volume and range is enormous; it covers large amphorae and jars, cooking pots, kitchen vessels and tableware which can be quite fine. Some of the latter is imported and easily identified as such by its appearance, particularly the even surface of glossy black or glossy red. The majority, however, if painted at all, has a dull red surface, with drips running down. This is what we tend to call 'local' pottery without really knowing where it was made. No kilns have been found on site but would surely have been down in the valley with the source of the clay, near the river for water supply.

North Syria has long been suspected of having an important role in pottery production during the Hellenistic period, but no specific site has been proved. Antioch-on-the-Orontes is a strong contender and it seems likely that at least some of the Jebel Khalid pottery was brought in from there. But there must have been a nearer source and we cannot determine the extent and range of imports from Antioch until we can distinguish between the clays. Publications of pottery from Syrian Hellenistic sites (including Antioch) tend to date from early in the century when such analysis was not available, or are often given less attention because they are incidental to the excavation of another earlier period. Where clays are described, it is in terms of colour, a highly subjective approach, and inclusions seen with the naked eye. Where some analysis has occurred, far more attention has been given to the Fine Wares than to the much more numerous Common Wares.

Aims of the 'pilot' analysis

To establish the diagnostic composition of the different clays used for:

1. Commonware vessels at Jebel Khalid.

2. Semi-fine, perhaps local, tableware.

3. Clay lamps.

4. Clay figurines.

With the welcome aid of an AINSE pilot grant, we were able to send 30 samples through the PIXE/PIGME process of analysis. These were made up as follows:

Samples 1-10 were fragments of large coarseware jars and amphorae, of different shapes and of two different clay colours. All were excavated together from a hoard of pots in one room and must be contemporary.

Samples 11-21 were fragments of semi-fine painted table ware (mainly small plates and bowls), with two of these samples being 'planted' as suspected imports.

Samples 22-26 were fragments of terracotta lamps, covering two different types. One type was thought to be Antiochene (the rosette on the base being a trademark of Antioch lamps), the other possibly a local type exclusive to Jebel Khalid and found in great numbers.

Samples 27-30 were fragments of terracotta figurines, two of Greek style made in a double mould and two of 'Persian rider' figurines, a Near Eastern hand-made type.

Results to date

Dr. Eric Clayton has been invaluable in interpreting the results for us. He has found three distinct groups or clusters:

1. The clearest distinct cluster is small: it comprises two of the lamp fragments and two of the figurine fragments. The lamps are the suspected Antiochene imports and the figurine fragments are of the moulded Greek-style.

2. A larger cluster (seven fragments) comprising three large jars, all of different profile, three semi-fine table ware bowls and, surprisingly in this group, one of the Near Eastern figurines.

3. The largest group also comprises a mixture of fragments of large jars of different shapes, some red-painted semi-fine bowls, the possibly 'local' lamp fragments and the other Near Eastern-style figurine.

Obviously far more samples need to be tested before one can come to confident conclusions. Tentative observations may be made:

1. That some lamps and Greek-style figurines were not locally made but imported, perhaps from Antioch.

2. That the two larger groups both produced large jars as well as tableware. This does not necessarily mean that the jars and tableware were made in the same workshop, just that the same or similar clay was used for both. It does mean that we have two different sources of clay. Which, if any, is local? It is interesting that the Near Eastern-style figurines have a sample in each group, which tends to suggest that neither source is far to the West, where Greek-style figurines predominate. It also suggests that the coroplastic workshop/s making this type of figurine were linked with the pottery industry.

3. The largest group contains all three lamp fragments apart from those in Group 1. This group seems the most likely group to be a local product, although to the eye, the range of clay colour and the strong mica content (gold and white) look much the same in both groups 2 and 3. Group 2 looks better levigated; it may well represent a source of slightly finer pottery not very far away.

Future testing hopes to include:

1. Samples from Tell Ahmar, an important centre 40 kilometres up-river.

2. Samples of imported fine wares, such as fine black-glaze (from Attica and East Greece) and Eastern Sigillata A (source unknown but suspected to be in the Antioch area).

3. Samples of a wider range of lamps and figurines.

4. Collaboration with Princeton University who have in their possession some pottery from Antioch.

Radlinski

A. P. Radlinski[1] and E. Z. Radlinska[2]

[1] Petroleum and Marine Division, Australian Geological Survey Organisation, GPO Box 378, Canberra, ACT 2601

[2] Department of Applied Mathematics, The Australian National University, GPO Box 4, Canberra, ACT 0200

Abstract

Sedimentary rocks are complex and somewhat ill-defined "dirty" systems. Typical rock may be described as a water-saturated, highly compacted fine mixture of many different oxides of light elements, numerous trace elements, and hundreds of species of fossil organic molecules. Hydrocarbons are generated in such rocks by thermal maturation - a process of temperature-driven decomposition of organic macromolecules deposited in the pore space of the inorganic rock matrix. The consequent increase in molecular volume leads to the overpressure, formation of micro-cracks and transport of generated hydrocarbons through the network of conduits (interconnected pores) out of source rocks and into the more porous reservoir rocks, where commercial hydrocarbon accumulations are formed.

The microstructure of sedimentary rocks has strong influence on the oil and gas generation and retention, and the fluid flow properties in geological formations. SANS and SAXS are two techniques best suited to study the microstructure of complex porous systems: they are non-invasive and average over relatively large sample volume. They can be applied to studies of sedimentary rocks in the entire range of organic matter content, from lean shales to coals.

We present examples of absolute measurements of SAXS and SANS from sedimentary rocks (natural hydrocarbon source rocks [1, 2], artificially pyrolysed source rocks [3], laboratory-prepared rocks, and coals [4,5]), including data obtained using Bonse-Hart geometry instruments. We discuss the multi-phase character of rock microstructure and its perception by SAXS and SANS, the question of contrast, scattering by fractals, the origin of fractality in rocks, and the advantages of small angle scattering in petroleum exploration.

References

[1] A.P. Radlinski, E.Z. Radlinska, M. Agamalian, G.D. Wignall, P. Lindner and O.G. Randl, *Phys. Rev. Letters* **82**, 3078 (1999).

[2] A.P. Radlinski, C.J. Boreham, G.D. Wignall and J.-S. Lin, *Phys. Rev. B*, **53**, 14152 (1996).

[3] A.P. Radlinski, C.J. Boreham, P. Lindner, O.G. Randl, G.D. Wignall and J.M. Hope, *Organic Geochemistry*, in press.

[4] A.P. Radlinski, E.Z. Radlinska and J.-S. Lin, in preparation.

[5] A.P. Radlinski and E.Z. Radlinska, in: *Coalbed Methane: Scientific, Environmental and Economic Evaluation*, eds. M. Mastalerz, M. Glikson and S.D. Golding, Kluvier Academic Publishers, in press.

SESSION 3

Chair – Heiko

Ion Beam Analysis-1

Depth profile analysis of thin TiO_xN_y films using standard ion beam analysis techniques and HERDA

A. Markwitz[1], A. Bittar[2], L. J. Törnquist[2], N. Dytlewski[3] and D. Cohen[3]

1. Institute of Geological & Nuclear Sciences Ltd., Environmental Group, PO Box 30-312, Lower Hutt, New Zealand, 2 Industrial Research, PO Box 31-310, Lower Hutt, New Zealand, 3 ANSTO, Physics Division, PMB 1, Menai, NSW 2234, Australia

Ion beam assisted deposition is used to fabricate thin titanium oxynitride films (TiO_xN_y) at Industrial Research (typical film thickness 100nm). At the Institute of Geological and Nuclear Sciences, the thin films are analysed using non-destructive standard ion beam analysis (IBA) techniques. High-resolution titanium depth profiles are measured with RBS using 1.5MeV $^4He^+$ ions. Non-resonant nuclear reaction analysis (NRA) is performed for investigating the amounts of O and N in the deposited films using the reactions $^{16}O(d,p)^{17}O$ at 920keV and $^{14}N(d,\alpha)^{12}C$ at 1.4MeV. Using a combination of these nuclear techniques, the stoichiometry as well as the thickness of the layers is revealed. However, when oxygen and nitrogen depth profiles are required for investigating stoichiometric changes in the films, additional nuclear analysis techniques such as heavy ion elastic recoil detection (HERDA) have to be applied. With HERDA, depth profiles of N, O, and Ti are measured simultaneously. In this paper comparative IBA measurements of TiO_xN_y films with different compositions are presented and discussed.

1 Introduction

Ion beam assisted deposition is used to fabricate thin titanium oxynitride films (TiO_xN_y) at Industrial Research. Thin films (typical film thickness 100nm) of TiO_xN_y deposited onto substrates of copper are of considerable interest for use as solar selective surfaces [1]. Such films have been previously investigated at ANSTO with HERDA and SIMS [2-5]. They showed a degradation upon annealing in air at temperatures of 200°C as a result of copper migration through the thin film. To stop this diffusion, an additional diffusion barrier layer and also a capping layer have been investigated by the same means. These barriers have been shown to delay the degradation to approximately 300°C [3].

2 Sample preparation

The thin (~100nm) TiO_xN_y films were deposited onto substrates of copper-coated glass slides. The substrates were cleaned with alcohol and ion beam sputtering prior to the evaporation to remove surface contaminants. The TiO_xN_y films were produced by evaporation of Ti and simultaneous bombardment with ionic mixtures of oxygen and nitrogen (Ion Assisted Deposition). Ti was deposited with an electron gun at a constant deposition rate of approximately $2Å s^{-1}$. During ion bombardment, the measured TiO_xN_y deposition rate was approximately $1Å s^{-1}$, indicating some removal (or sputtering) of material by the ion beam. A Kaufmann type ion gun was used to bombard/implant nitrogen and oxygen in the films. Dry air, 20% oxygen and 80% nitrogen, was ionised and accelerated to 605eV by the ion gun. The current density was measured by a faraday cup located beside the samples and was held at $0.20mA cm^{-2}$. This method produces TiO_xN_y films with near equistoichiometric composition. The films have suitable optical properties for solar thermal applications. The film preparation is described in more detail elsewhere [1].

3 Ion beam analysis techniques

At the Institute of Geological and Nuclear Sciences, the thin TiO_xN_y films were analysed using non-destructive standard ion beam analysis (IBA) techniques. High-resolution titanium

depth profiles are measured with RBS. Non-resonant nuclear reaction analysis (NRA) is performed for investigating the absolute amounts of O and N. Using a combination of these nuclear techniques, the stoichiometry and the thickness of the layers is revealed. However, when particular O and N depth profiles are required, additional nuclear analysis techniques such as HERDA are applied. With HERDA performed at ANSTO, depth profiles of N, O, and Ti were measured simultaneously.

3.1 RBS – Ti depth profiling

For measuring high-resolution titanium depth profiles, the non-destructive nuclear analysis technique RBS was performed. In the experiment, the ion beam energy was adjusted at 1.5MeV to provide a high depth resolution at surface (~ 10nm) and a large depth of analysis of at least 1μm. A silicon surface barrier detector (12keV FWHM) was placed at the backscattering angle of 170°. As RBS spectra may be fully calculated using known physical parameters such as ion sort, ion energy, backscattering angle, collected charge, beam current etc., titanium depth profiles were extracted from the experimental spectra with the RUMP code [6] by unfolding by means of an iterative simulation process.

3.2 Non-resonant Nuclear Reaction Analysis (NRA) – Detecting N, O & C

Thin film non-resonant nuclear reaction analysis (NRA) was performed for investigating the absolute amounts of O and N in the samples via the $^{16}O(d,p)^{17}O$ reaction at 920keV [7] and $^{14}N(d,\alpha)^{12}C$ at 1.4MeV [8], respectively. In the experiment, a 7.6μm Mylar foil was attached in front of the surface barrier detector, which was placed at a backscattering angle of 150° to stop the scattered deuterium particles. Using this set-up, the p_0 and α_0 particles emitted from the nuclear reactions are located in the background free region of the energy spectrum. Reference samples were used to quantify the elemental concentration in areal density. The limit of detection of O and N is usually about 20ppm [9]. NRA was also used to test for carbon. At 920keV, the cross-section of the excitation function of the nuclear reaction $^{12}C(d,p)^{13}C$ [10] enables also the detection of a low level (~ 20 atomic layers). However, since IBA itself could introduce several atomic layers of carbon during the analysis, it is important to have another means of detecting carbon, eg. Raman spectroscopy. Combined NRA-RAMAN analyses are described for example in [11].

3.3 Heavy ion ERD (HERDA) – Ti, O and N depth profiling

When the mass of the incident ion is higher than the mass of the substrate atom, recoiling of the latter occurs in forward scattering geometry. To measure depth profiles of the elements in the surface of thin TiO_xN_y films, in particular Ti, O and N, time of flight HERDA using 77MeV iodine ions was applied [12,13]. Although the depth resolution at the surface is about the same as in RBS and the limit of detection is also only about 0.05 at.%, the major advantage of HERDA is the ability to measure independent depth profiles of may elements, simultaneously. However, due to the usage of heavy ions, sputtering can occur. In the case of thin TiO_xN_y films produced by ion beam assisted deposition, the ion beam damage has not to be underestimated. To ensure reliable measurements, series of analyses were performed with different accumulated charge. It was found, that HERDA insignificantly sputters the surfaces during analysis for a reasonably low accumulated charge.

4 Results

RBS and NRA were used to investigate thin TiO_xN_y films deposited on various substrates. As an example, figure 1 shows a RBS spectrum of a thin film deposited on Cu on top of glass. As can be seen in the energy spectrum, the Ti peak, located between 1.08 and about 1.0MeV, is sitting on top of the signal of the Cu signal located in the spectrum between 1.17 and about 0.55MeV. By simulating the spectrum, the thickness of the TiO_xN_y film is determined to 550

x $10^{15}cm^{-2}$ (40 ± 2 at.% Ti). Taking a density of 3.5 x $10^{22}cm^{-3}$ into consideration, the thickness of the TiO_xN_y film is 160nm. In the spectrum, however, the signals from O and N are located at 543 and 467keV and cannot be analysed sophistically.

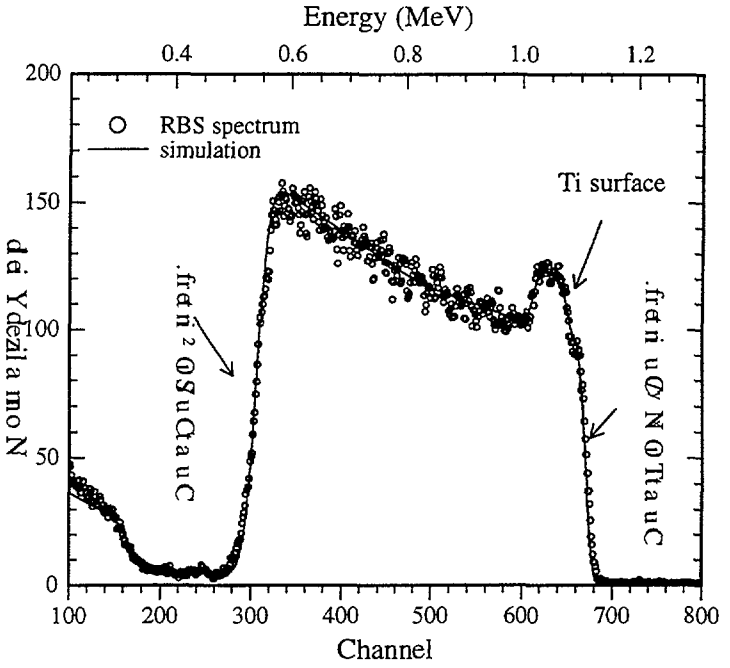

Figure 1: RBS spectrum (sample #04-S1) of a TiO_xN_y film deposited on 500nm Cu/SiO_2

In the next stage of IBA analysis, the N and O concentration in the films were analysed. The results of RBS and NRA are listed in table 1.

Sample #	thick. (nm) ± 5	Ti [at.%] ± 2	N conc [$10^{15}cm^{-2}$] ± 20	N (at.%) ± 2	O conc [$10^{15}cm^{-2}$] ± 20	O (at.%) ± 2
02-s1	180	40	520	31	330	30
03-s1	165	45	515	30	275	25
04-s1	160	40	480	30	230	22
05-s1	115	40	375	33	205	27
06-s1	200	55	385	20	305	26
07-s2	150	41	410	28	255	30
08-s2a	180	35	745	43	305	26
09-s2	150	40	470	31	290	31
010-s1	135	40	385	29	265	31

Table 1: Nitrogen and O concentrations measured with NRA. The thickness of the films and the Ti concentrations were determined with RBS

The combined RBS-NRA analysis revealed the composition and the thickness of the TiO_xN_y films. As can be seen in the table, the sample preparation process influences the composition and the thickness of the films produced under different conditions.

In a further IBA analysis the C concentration in the films was measured. Table 2 shows the C concentration of the films described in Table 1.

Sample #	C conc $[10^{15}cm^{-2}]$ ± 20	**C (at.%) ± 2**
02-s1	17	**2**
03-s1	10	**1**
04-s1	11	**1**
05-s1	11	**1**
06-s1	34	**3**
07-s2	9	**1**
08-s2a	14	**1**
09-s2	8	**1**
010-s1	8	**1**

Table 2: Carbon concentrations measured with NRA

As shown in table 2, the C concentration in the TiO_xN_y films is insignificant and independent on the sample preparation process.

In order to measure depth profiles of N and O, HERDA analysis were performed. Figure 2 shows a typical TOF-ERD 2D plot.

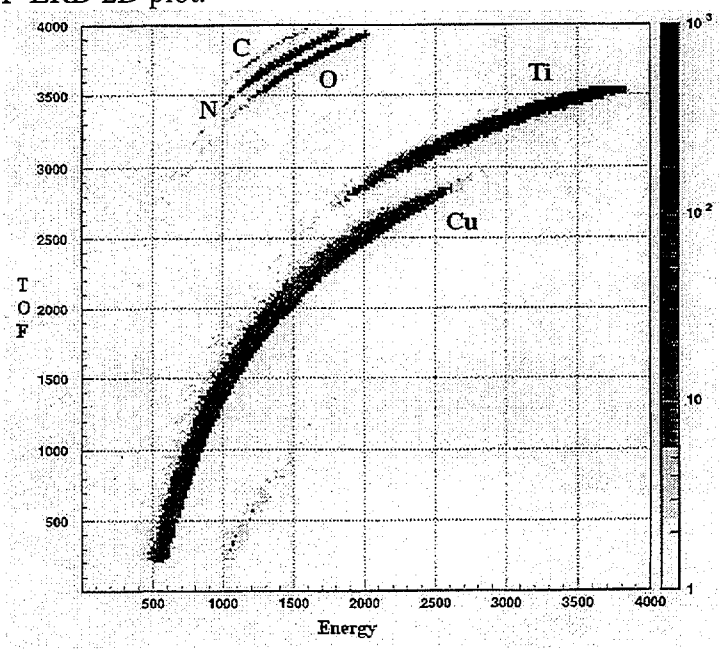

Figure 2: Typical TOF-ERD plot of the TiO_xN_y film #04-S1a deposited on Cu/SiO_2

Figure 2 shows perfectly well separated curves of C, N, O, Ti, and Cu. Differences in the grey scale indicate different levels of concentration. In the figure, the grey scale is plotted additionally.

In the first step of the HERDA analysis, separated curves are plotted for each element (units: counts vs. energy). Figure 3 shows N, O, Ti and Cu depth profiles of sample #04-S1a.

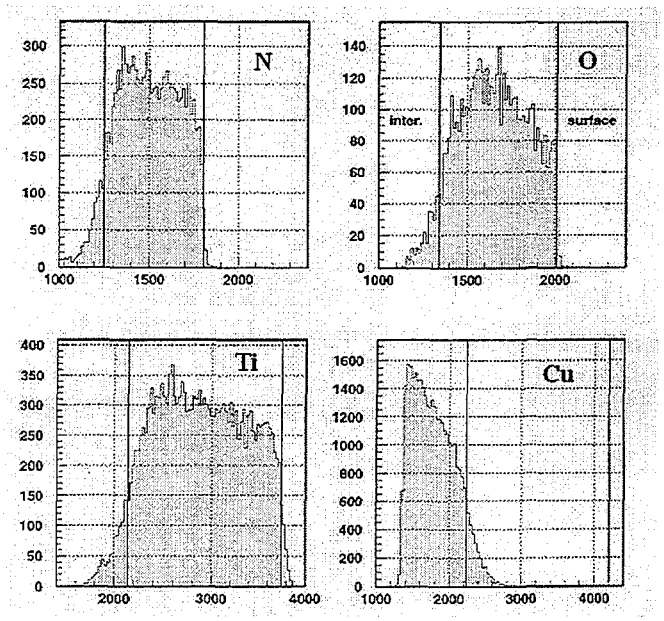

Figure 3: N, O, Ti and Cu depth profiles of sample #04-S1a

Preliminary simulations of the N, O and Ti depth profiles indicate that the composition of the film is almost uniform in the entire TiO_xN_y layer. This is indicated in figure 3 by an increase of the number of counts with increasing depth of analysis. However, the Cu profile shows a slight diffusion of Cu at the Cu/SiO_2 interface into the TiO_xN_y layer. The markers in figure 3 indicate the position of the surface (front marker, high energy) and the TiO_xN_y/Cu interface (back marker, low energy).

5 Conclusion

In this paper comparative IBA measurements of TiO_xN_y films with different compositions are presented and discussed. The IBA techniques of RBS, NRA and HERDA have allowed the determination of the thickness, the elemental depth profiles of Ti, O, and N, and the stoichiometry of the titanium oxynitrides.

6 Acknowledgements

This work was performed under research contracts to the New Zealand Foundation for Research, Science and Technology and with the aid of the Australian Institute of Nuclear Science and Engineering (AINSE) grant #59. We thank Bill Trompetter and Chris Purcell for technical assistance.

7 References

[1] A. Bittar, D. Cochrane, S. Caughley, I. Vickridge, J. Vac. Sci. Technol. A15 (1997) 223

[2] L.J. Törnquist, A. Bittar and I. Vickridge, Solar 97, ANZSES conference proceedings, Canberra, Australia (1997)

[3] L.J. Törnquist, J.B. Metson, K.E. Prince and A. Bittar, In proceedings of Solar '99, Geelong, Australia, December 1999.

[4] J.B Metson, K.E. Prince, A. Bittar and L.J. Törnquist, *Surface and Interface Analysis*, To be published.

[5] J.B Metson, K.E. Prince, L.J. Törnquist and A. Bittar, *Surface and Interface Analysis*, Accepted for publication.

[6] L. Doolittle, Nucl. Instr. and Meth. B9 (1985) 334

[7] J.-P. Thomas, J. Engerran, A. Charard and J. Tardy, Nucl. Instr. Meth. 119 (1974) 373
[8] C. Olivier, M. Peisach and T. B. Pierce, J. Radiologie Chem. 32 (1976) 71
[9] J. R. Bird and J. S. Williams: in ion beams for materials analysis, Academic Press, Australia, 1989
[10] G. Amsel, J. P. Nadai, E. d'Artemare,D. David, E. Girard and J. Moulin, Nucl. Instr. Meth. 92 (1971) 481
[11] A. Markwitz, P.B. Johnson, P.W. Gilberd, D. Cohen and G.A. Collins, accepted for publication in Nucl. Instr. And Meth. B
[12] J.W. Martin, D.D. Cohen, N. Dytlewski, D.B. Garton, H.J. Whitlow, G.J. Russell, Nucl. Instr. and Meth. B94 (1994) 277
[13] J.W. Martin, D.D. Cohen, G.J. Russell, N. Dytlewski, Nucl. Instr. and Meth. B118 (1996) 201

Heavy-ion elastic-recoil detection analysis of doped-silica films for integrated photonics

T.D.M. Weijers[a,b], K. Gaff[c], H. Timmers[a,b], T.R. Ophel[b] and R.G. Elliman[a]

Departments of [a]Electronic Materials Engineering, [b]Nuclear Physics, and [c]Optical Sciences Centre, Research School of Physical Sciences and Engineering, Australian National University, Canberra, Australia

1. Introduction

Photosensitive silica films, in which a permanent refractive index change is induced by exposure to ultra-violet (UV) light, are of interest for the fabrication of integrated photonic devices and circuits [1]. Such films, consisting of Ge- and Sn-doped silica, are being fabricated at the Australian National University (ANU) by a plasma assisted deposition technique known as Helicon Assisted Reactive Evaporation (HARE) [2]. The initial refractive index of these films is related to their stoichiometry and can be altered further by controlled exposure to UV light. Contaminants introduced into the films during deposition can degrade their optical properties and are therefore also of interest. Hydrogen is of particular concern as it causes optical absorption in the wavelength range of interest for communications applications (1.3-1.5μm).

High-energy heavy ion elastic recoil detection (ERD) analysis enables the detection of a broad range of elements with almost constant sensitivity. A variety of recoil detection systems have been developed for this purpose, including time-of-flight systems [3], magnetic spectrometers [4], and quadrupole spectrometers [5]. However, these are often restricted to small acceptance solid angles. Beam-induced sample modification, such as hydrogen release, can therefore be a serious limitation [6]. The use of a position sensitive gas ionization detector [7] overcomes these limitations for a range of important applications by operating with a large solid angle and correcting the kinematic energy spread of the ions over large acceptance angles to provide $\leq 1\%$ energy resolution.

In this study, heavy-ion ERD employing a novel position sensitive gas ionization detector is used to characterize the composition, thickness, uniformity and hydrogen content of Ge- and Sn- doped silica films. The technique is shown to provide this information in a single measurement.

2. Experimental Details

For the measurements reported here, 214 or 241MeV ^{197}Au projectile beams were produced using the 14UD pelletron accelerator at the ANU. Recoiled ions were detected at a scattering angle of 45° with a large-solid angle (~4 msr) position sensitive gas ionization detector. The detector had a 0.5μm Mylar window and was operated with a flowing propane ambient maintained at a pressure of 70 mbar. The detector [8-10] has an anode that is partitioned into two ΔE segments and a residual energy (Eres) segment. The second of the ΔE segments is further segmented to provide position information in the scattering plane. The detector also incorporates a grid electrode, located between the Frisch grid and the anode, which provides a total energy signal. Elemental separation is achieved by plotting the energy loss of the recoils over one (or both) of the ΔE segments, against the ion energy determined from either the sum of the anode signals or directly from the grid electrode.

Hydrogen was detected either with a surface barrier detector located at the back of the ionization detector or by the ionization detector itself. The ionization detector can be used in several modes for hydrogen detection [11]. In the present case, it was used in a transmission mode, where the recoiling protons passed through the detector and their energy loss was determined from the residual energy electrode, with hydrogen being separated from low

energy heavy ions by gating with a signal from the grid electrode. Both signals were amplified with high gain for this purpose.

3. Results and Discussion

3.1 Stoichiometry and Thickness

Figure 1 shows a two-dimensional ΔE-E spectrum obtained from a nominally 1.25μm thick Ge-doped film. Ge, Ar, Si and O recoils can be identified; Ar is used to maintain the O plasma during deposition. For thicknesses ≤ 1.25μm the film is resolved, and the stoichiometry can be extracted from the total number of counts for each element after normalisation with the respective recoil cross-sections. This assumes that all elements are distributed uniformly throughout the film, which was found to be the case for most of the films studied

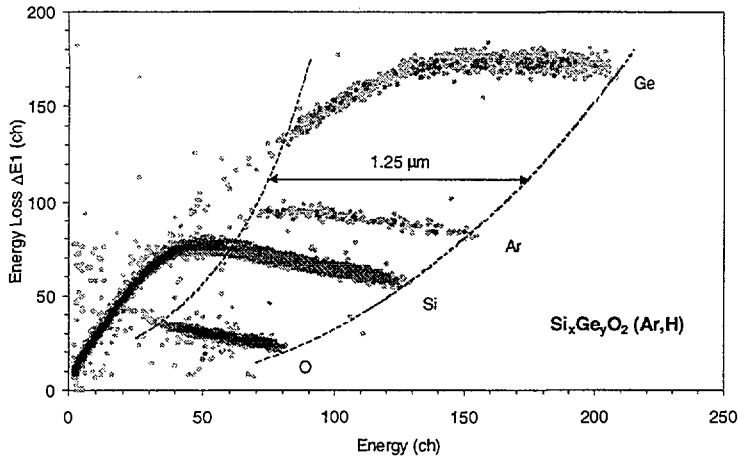

Figure 1. The energy loss of recoils over the first section (ΔE_1) of the gas detector plotted against their total energies for a Ge-doped SiO_2 film irradiated with 241MeV ^{197}Au using a scattering angle of 45°. Ge, O, Si and Ar recoils are easily separated.

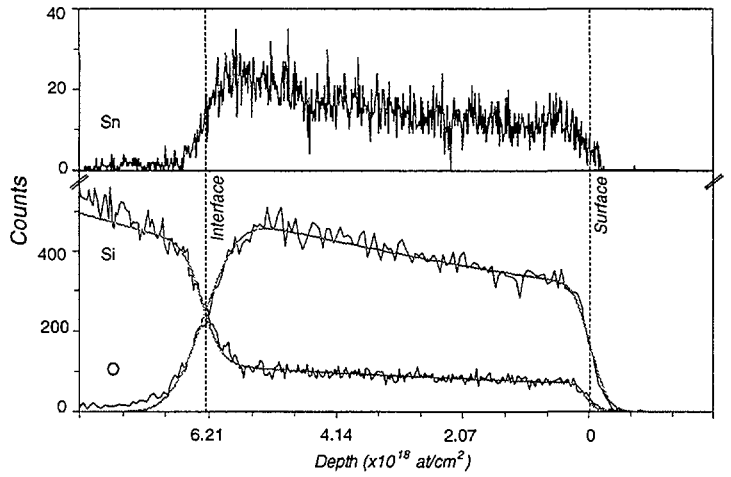

Figure 2. Energy spectra for Sn (top), Si and O (bottom) recoils, gated from a 2-D spectrum such as that depicted in figure 1. Smooth lines represent simulations of the data with the RUMP code.

The uncertainty in the stoichiometry is then dominated by the counting statistics and the identification of the film-substrate interface in the Si spectrum. The average dopant fraction was determined to better than 2% using this technique, and the stoichiometry of the films was shown to be $Ge_xSi_{1-x}O_{2.00\pm0.04}$. (Ar was present at ~2 at.%.). Similar results were determined for Sn-doped films.

For non-uniform films and those thicker than ~1.25μm, analysis was based on the full energy spectrum for each element. The raw data were corrected for the kinematic energy spread over the detector acceptance angle by using the position information recorded for each recoil. Figure 2 shows typical O, Si and Sn spectra measured for a Sn-doped film. The increase in the yields with depth is consistent with the expected increase in scattering cross-sections, confirming the compositional uniformity of the layer.

Figure 3 shows the refractive index of Ge- and Sn-doped films, obtained from ellipsometry measurements, plotted against the dopant oxide fraction determined from heavy-ion ERD. The two datum points for 'pure' SiO_2 correspond to layers deposited under conditions similar to those of the corresponding doped set.

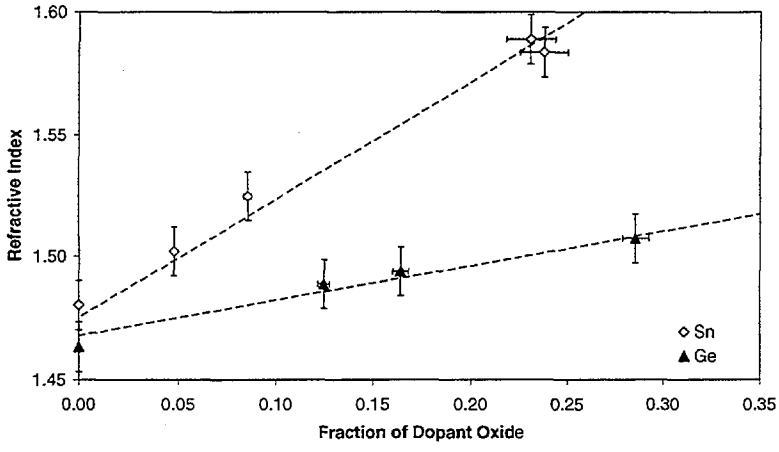

Figure 3. The refractive index (ellipsometry) plotted against the dopant oxide fraction (heavy ion ERD) for Ge and Sn-doped silica samples. The dotted lines show linear least squares fits through the data.

3.2 Hydrogen Content

Figure 4 shows proton spectra measured by the Eres electrode. In general, these spectra include high energy protons that pass through the detector, as well as lower energy protons that stop under the Eres electrode. These two contributions have to be distinguished in a two-dimensional plot of Eres and Grid signals. In this case, the silica films examined are sufficiently thin that all the recoiled protons passed through the gas detector and the total hydrogen content can readily be determined by integration of the spectrum.

The inset in figure 4 shows the hydrogen content of three Sn-doped films determined from the surface barrier detector and as described above. The data show consistent results for both detection methods. However, the acceptance solid angle of gas detector is almost 12 times greater than that of the surface barrier detector.

In order to extract depth profiles from the measured spectra, the response function of the Eres electrode was determined by measuring the uniform hydrogen distribution in a Kapton film. This response function is also shown in figure 4. It reflects the relationship between the energy loss detected by the Eres electrode and the total proton energy, a point which is highlighted by the black circles that indicate equal total-energy increments (157keV). The film thicknesses determined with this information were found to be consistent with those obtained from the heavy ion data.

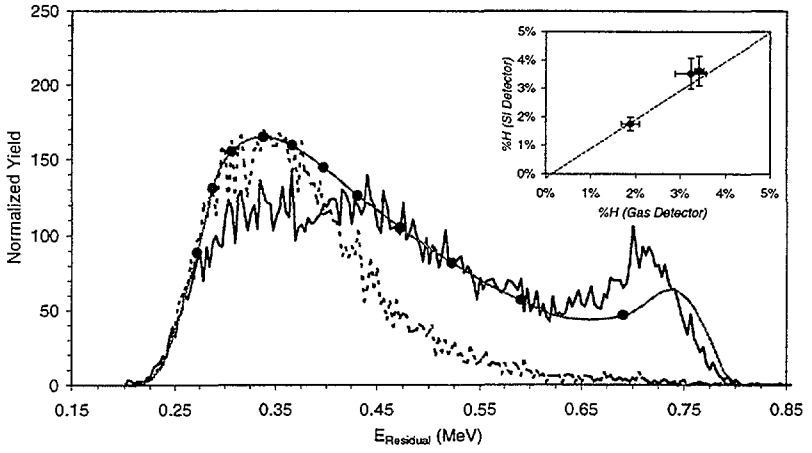

Figure 4. H spectra from the Eres electrode. Spectra shown are for a thick (~1.7μm) (solid line) and a thin (~1.25μm) (dotted line) sample. The response of the detector to a constant H concentration was determined by measuring the H distribution in a uniform Kapton film (smooth curve). The filled circles correspond to equal increments (157keV) of total proton energy. The inset shows the H concentration measured by the gas ionisation detector and the surface barrier detector for three Sn-doped samples.

4. Conclusions

Heavy ion ERD employing a position sensitive gas ionisation detector was shown to provide important information for the characterisation of Ge- or Sn-doped silica films developed for integrated photonics applications. This includes film stoichiometry, uniformity and thickness, as well as the concentration of contaminants such as Ar and H, which were all obtained with a single measurement. The average stoichiometry of thinner films (≤ 1.25μm) was determined to better than 2% accuracy by integration of the total yield for each element. Hydrogen detection with the gas ionisation detector was demonstrated to yield the total hydrogen content of the film and some information about the depth distribution.

References

[1] M. V. Bazylenko, M. Gross, P. L. Chu, and D. Moss, Electronics Letters 32 (1996) 1198

[2] A. Durandet, C. A. Davis, and R. W. Boswell, Appl. Phys. Lett. 70 (1997) 1814

[3] R. Groleau, S. C. Gujrathi, and J. P. Martin, Nucl. Instr. Meth. B218 (1983) 11

[4] B. L. Doyle and N. D. Wing, IEEE Trans. Nuclear Science 30 (1983) 1214

[5] C. R. Gossett, Nucl. Instr. and Meth. B15 (1986) 481

[6] M. E. Adel, O. Amir, R. Kalish, and L. C. Feldman, J. Appl. Phys. 66 (1989) 3248

[7] W. Assmann, H. Huber, C. Steinhausen, M. Dobler, H. Gluckler, and A. Weidinger, Nucl. Instr. Meth. B89 (1994) 131

[8] H. Timmers, R. G. Elliman, G. R. Palmer, T. R. Ophel, and D. J. O'Connor, B138 (1998) 611

[9] H. Timmers, T. R. Ophel, and R. G. Elliman, Nucl. Instr. and Meth. B156 (1999) 236

[10] H. Timmers, T. R. Ophel, and R. G. Elliman, accepted for publication in Nucl. Instr. and Meth. B

[11] R. G. Elliman, H. Timmers, T. R. Ophel, T. D. M. Weijers, L. S. Wielunski, and G. L. Harding, accepted for publication in Nucl. Instr. and Meth. B

Elemental mapping with the ANSTO high energy heavy ion microprobe

Rainer Siegele, David D. Cohen and Chris Waring

Physics & Environment Division ANSTO, PMB 1, Menai 2234, NSW, Australia.

Introduction

ANSTO was among the first laboratories to use microscopic beams in Ion Beam Analysis. In these early experiments apertures were used to minimise the beam spot size rather than active focusing elements[1], such as quadrupoles. This tradition was continued with the ANSTO Milliprobe, which also uses apertures and has produced many interesting results for beam spot sizes down to 50μm.

However, in order to be able to achieve the smallest spot sizes and use a wide range of IBA techniques on a microprobe, focussing of the ion beam with either electrostatic or magnetic quadrupoles is required. The high energy, heavy ion microprobe is intended to fill this gap in ANSTO's IBA facilities[2]. The aim was not to duplicate existing proton microprobe facilities in Australia or internationally, but to design a microprobe that would utilise IBA techniques at high energies using heavy ions, which have become more common in the IBA community in recent years. These methods include high energy nuclear reactions and resonances as well as heavy ion elastic recoil detection analysis (ERDA)[3]. They are particularly useful to analyse the lighter elements such as, H, C, N and O.

The primary aim was to establish the use of heavy ion techniques on an ion microprobe using spot sizes between 5-20μm, with sufficient beam current to perform an IBA measurement in a reasonable time.

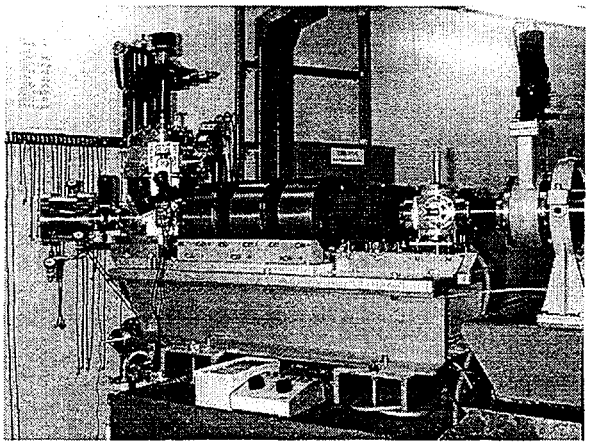

Figure 1: The picture shows the microprobe end station with the quadrupole triplet, beam scanning system and the target chamber.

Reducing the beam spot size generally reduces the target current and thus the count rate in the detector. This of course increases the measurement time, which can be overcome in different ways; 1) by a higher ion source brightness, 2) by larger solid angle detectors or 3) using IBA techniques with higher reaction cross sections.

The reaction cross sections of Ion Beam Analysis techniques increases proportionally to the square of the atomic number of the incident ion, thus making the use of heavy ions advantageous in microprobes. In X-ray fluorescence there is a 10-100 fold increase in the X-ray production cross section rate from protons to carbon, while the increase in cross section is about the same from 2MeV He RBS to 80MeV Br ERDA[2].

Because of the higher cross sections and the possibility to separate the signal resulting from different target atoms[1], heavy ion ERDA has certain advantages over RBS in the detection of light elements in a heavy matrix. Thus a heavy ion microprobe can make use of higher cross section over the full range of elements by employing heavy ion ERDA and heavy ion PIXE, compared to RBS and proton PIXE. The focusing quadrupoles for the High Energy Heavy Ion Microprobe were obtained from Oxford Microbeams in 1998. The microprobe was designed to for a wide range of ions at various energies, with a maximum mass energy product ME/q^2 of 100MeV amu. This results in interesting new applications and allows for the application of a wide variety of ion beam analysis techniques in the microprobe field.

Microprobe Facility

The belt charging system of the ANSTO tandem accelerator was in 1996 upgraded to a pelletron system, which produced improved terminal voltage stability to less than 1kV at 8MV. The tandem accelerator is equipped with two sputter ion sources and a charge exchange RF ion source. Hence most elements of the periodic table can be accelerated with reasonably high intensity

The total length of the microprobe, from object slits to the centre of the target chamber is about 7m. The high energy ion beam coming from the accelerator is analysed and switched by a single 30° deflection magnet. The deflection is large enough to separate different charge states as well as neighbouring isotopes for most of the common ions used. Tests showed ion beam currents up to a few microamps are readily available at the entrance to the microprobe system.

The ion beam enters the microprobe through a set of pre-slits, which limit the beam current impinging on the object slits. Object and collimating slits are 6.1m apart and are 4-jaw rectangular beam defining apertures, consisting of highly polished stainless steel cylinders, in order to reduce the effects of surface roughness and scattering. To prevent vibrations the object slits are decoupled from the beamline by membrane bellows and mounted separately on a large solid concrete block.

The collimating apertures, beam scanning system, quadrupole triplet and the target chamber are all mounted on the same baseplate and mechanically isolated from the rest of the beamline by membrane bellows, as shown in figure 1. This whole end-station assembly is mounted on a concrete block, sitting on a layer of sand to prevent transmission of vibrations through the floor. The pumping system is mechanically isolated form the target chamber by a bellows system.

The collimating slits are immediately followed by the beam scanning system. A scanning system, designed to scan ion beams with a mass energy product of ME/q^2 of 100MeV amu over an area of $1x1mm^2$ has recently been installed. The microprobe lens system consists of a magnetic quadrupole triplet with a high focusing power, due a small pole gap of 8mm. The quadrupole triplet can focus ion beams with a ME/q^2 greater than 100MeV amu at a working distance of 150mm.

Experimental

The samples were analysed with both He induced X-ray emission and RBS using a 7.62MeV He beam. At this energy ^{16}O shows a broad resonance with a cross section that is ~100 times greater than that for Rutherford scattering [4]. At the same time this energy is well suited for X-ray fluorescence analysis, since He has a high X-ray excitation cross section. All samples were measured with the beam at normal incidence. In all the measurements the ion beam was focussed to spot size between 10-15μm. The beam spot size was measured by scanning over the edge of a Au-layer deposited on a silicon wafer.

In order to demonstrate the simultaneous use of He induced X-ray emission and (α,α) resonance analysis, specimens of mineral sands were prepared. The samples consisted of a mixture of grains of ilmenite ($TiFeO_3$), pyrite (FeS_2), rutile (TiO_2), magnetite (Fe_3O_4) and zircon ($ZrSiO_4$). This covers a wide range of elements, which will enable us to evaluate whether a combination of the two techniques can cover a wider range of elements. The size of the grains in the specimen is between 50 and 100• m.

Results and Discussion

Figure 2 shows a typical X-ray spectrum of the specimen. The spectrum was taken with 7.62MeV He ions and is the total spectrum for a scan over a 1 x 1mm^2 area. The spectrum clearly shows X-ray peaks for titanium, chromium, iron, zirconium and sulfur. Sulfur is only just visible in the spectrum because of the small fraction of pyrite in the mineral sand.

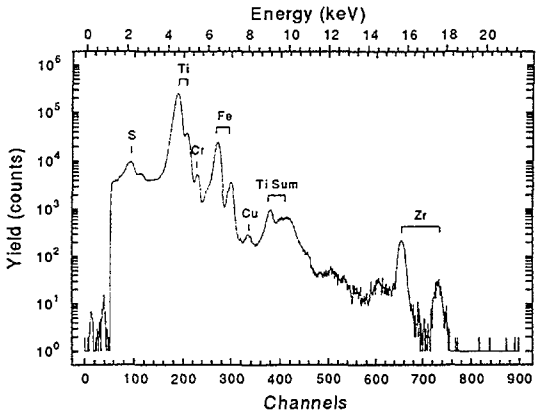

Figure 2: Total X-ray spectrum of a scan over a 1 x 1mm^2 area on a mineral sands specimen, containing grains of ilmenite ($TiFeO_3$), pyrite (FeS_2), magnetite (Fe_3O_2), zircon ($ZrSiO_4$) and rutile (TiO_2). Clearly visible are the X-ray peaks of the mayor elements S, Ti, Fe and Zr in the mineral.

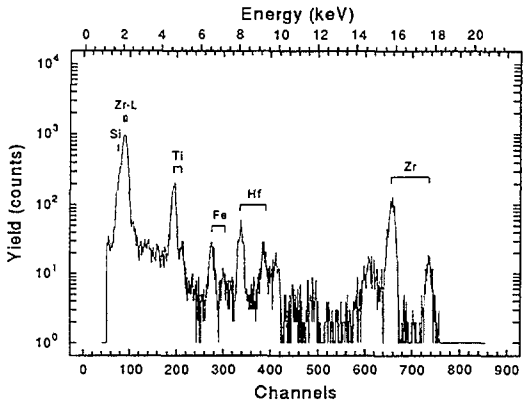

Figure 4: X-ray spectrum of a spot measurement on the zircon grain visible in the upper right corner of figure 3

The elemental maps of the major elements corresponding to the above spectrum are shown in figure 3. The maps show the number of X-rays at the characteristic energy for these elements covering an area of 1 x 1mm^2. The maps clearly show the individual grains in the sample. From these maps the different minerals present in the sample can be distinguished. For example, from the sulfur and iron maps the pyrite grains can easily be identified. As expected, at locations with high Fe and S concentrations none of the other elements are present. However, the sulfur maps also show a high count rate in areas where Ti and Zr are present. At locations where Zr is present, this is due to the Zr L-lines, which appear at the same energy as sulfur. Figure 4 shows a spectrum taken as a spot measurement on the zircon grain in the upper right corner of figure 3. The spectrum clearly shows the major elements of zircon, Zr and Si, but also traces of hafnium, which is known to be present in zircon.

Figure 5 shows the backscattering spectrum taken simultaneously with the X-ray spectrum of figure 2. The part of backscattering spectrum originating from light elements is no longer Rutherford, due to the high energy of the incident beam. This results in the large peaks in the low energy part of the spectrum. Indicated in the figure are the energies for the projectiles backscattered from different target elements. The surface edges for Zr, Fe, Ti and Si are visible.

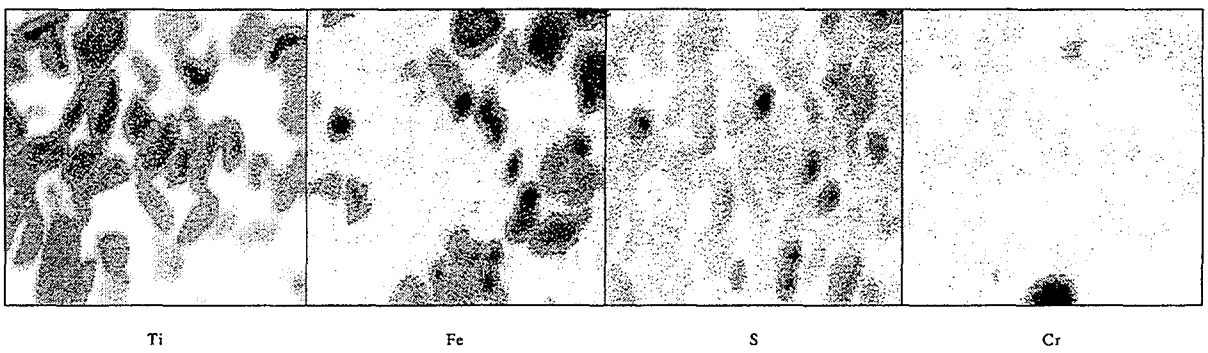

Figure 3: Elemental maps of titanium, iron, sulfur, chromium and zirconium in a mineral sands specimen taken from X-ray spectrum. The area of the scan is 1 x 1mm^2.

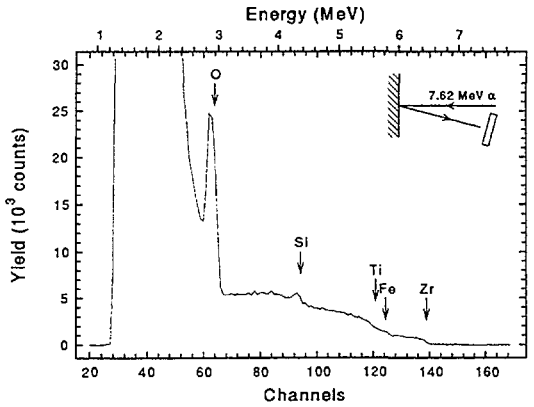

Figure 5: Backscattering spectrum of mineral sands specimen taken with 7.62MeV He. The edges for Zr and the O peak, which has the enhanced cross section at this energy, are clearly visible.

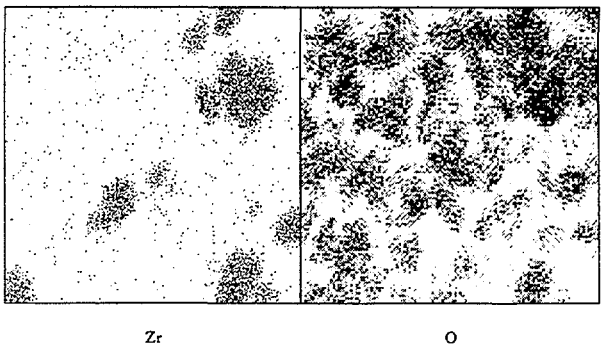

Figure 6: Elemental maps of zirconium and oxygen obtained from the backscattering spectrum of figure 5. The total scan area is 1 x 1mm^2

The scattering of both Si and O are no longer Rutherford, which causes the structure in the spectrum at lower energies. However, the much enhanced cross section for oxygen makes it possible to measure oxygen in the presence of heavier elements. Regions around the surface energies for O and Zr were taken and are shown as a function of the beam position in the elemental maps of figure 6. The Zr maps agree very well with the maps obtained from the X-ray spectrum. For heavy elements such as Zr, these maps have much better statistics compared to the X-ray maps because of the high scattering cross section of the heavy elements.

In the oxygen maps the higher oxygen content in the zircon grains is clearly visible. Furthermore the complete absence of oxygen in pyrite grains is also apparent.

Summary

These results show that both X-ray fluorescence and high energy resonance can be used simultaneously to map both light and heavy elements. More important however is the fact that once elemental maps have been obtained, these can be used to perform spot measurements of selected regions. These spot measurements will lead to quantitative results, since the cross sections of the $^{16}O(\alpha,\alpha)^{16}O$ resonance at 7.62MeV[1] are very well known over a wide energy range. Furthermore oxygen depth profiles can be extracted from such a measurement.

Acknowledgments

The authors would also like to thank Hans Noorman, David Garton and Alex Croal for their help in constructing the beamline and the Tandem Accelerator Operations Team for their efforts.

References

[1] B.K. Mak, J.R. Bird and T.M. Sabine, *Nature* **211** (1996) 738.

[2] R. Siegele and D.D. Cohen, Nucl. Instr. and Meth. In print.

[3] J.W. Martin, D.D. Cohen, N. Dytlewski, D.B. Garton, H.J. Withlow, G.J. Russel, *Nucl. Instr. and Methods* **B94** (1994) 277.

[4] J.A. Davies, F.J.D. Almeida, H.K. Haugen, R. Siegele, J.S. Forster and T.E. Jackman, *Nucl. Instr. and Methods* **B85** (1994) 28.

Compositional analysis of YBaCuO superconducting films with ion beam analysis techniques

Stephen Jones[a,b], H. Timmers[a,b], T.R. Ophel[a], R.G. Elliman[b]

Departments of Nuclear Physics[a] and Electronic Materials Engineering[b]
Research School of Physical Sciences and Engineering Australian National University, Canberra, ACT 0200

1. Introduction

High-T_c $YBa_xCu_yO_{7-\delta}$ superconducting films are being developed for applications such as superconducting quantum interference devices. The carrier concentration, critical current density J_c and critical temperature T_c of these films depend sensitively on the oxygen content. Stoichiometry, uniformity with depth, homogeneity across the sample and film thickness are also important quantities for their characterisation. It has been shown, for example, that the stoichiometry of the metallic elements affects the growth characteristics and surface morphology of the films [1]. With the deposition techniques used, reproducibility of film properties is difficult.

The characterisation of $YBa_xCu_yO_{7-\delta}$ films with ion beam analysis techniques is complex. Whereas the three metallic elements can be detected with helium beams and Rutherford Backscattering (RBS), the oxygen signal is generally obscured by that from substrate elements [2]. It can be better detected using resonant backscattering with 3.04MeV ^{4}He ions or nuclear reaction analysis. Elastic Recoil Detection (ERD) with high-energetic (1MeV/amu), heavy beams (Z > 120), enables all elements to be detected and separated in a single experiment [3,4]. It is well established that ion bombardment induces vacancies in the oxygen sub-lattice, driving the material to change from crystalline to amorphous, the latter phase having a reduced oxygen content [5]. In previous heavy ion ERD measurements of $YBa_xCu_yO_z$ films with 200MeV ^{127}I beams [6], the opaque films became transparent in the beam spot area, indicative of the amorphous phase. The accuracy of the oxygen measurement is therefore questionable. Indeed, using Raman spectroscopy, distortions of the crystalline structure above a fluence of 5 x 10^{11} ion/cm^2 and for higher doses some signatures of a reduction in oxygen content have been observed for such beams [7]. It appears therefore that a correct determination of the oxygen content requires either a drastic reduction in fluence or a containment of the oxygen inside the film.

In the present study a series of $YBa_xCu_yO_{7-\delta}$ films have been analysed with heavy ion ERD using ^{197}Au beams and a gas ionisation detector with large acceptance angle. RBS with ^{4}He and ^{28}Si projectiles was also performed. The results from these three techniques have been compared and the reliability of the oxygen measurement with heavy ion ERD has been evaluated.

2. Experimental Details

The samples were crystalline layers of $YBa_xCu_yO_{7-\delta}$, deposited on a MgO substrate in an argon-oxygen atmosphere with the magnetron sputtering technique [8,9]. Three different sputter targets (T10, T11, T13) with ideal stoichiometry for the metals ($YBa_2Cu_3O_{7-\delta}$) were used to make 5 different samples, subsequently referred to as T10a, T10b, T10c, T11 and T13. The deposition parameters were similar. After deposition the samples were kept for 1h in a pressurised oxygen atmosphere. On sample T10c a thin film of Au was evaporated to seal the surface and suppress loss of material due to sputtering during ion beam analysis. Prior to the ion beam measurements, the films were characterised with x-ray diffraction and measurements of T_c and J_c. All films were high-T_c superconductors with T_c = 84.8-86.3K and J_c = 0.5-3.4 10^6Acm^{-2}.

For heavy ion ERD, beams of ^{197}Au at 212.4MeV, 216MeV and 243.6MeV were produced with the 14UD pelletron accelerator and collimated (slit dimensions 1 × 3mm). Recoil ions were detected with a position-sensitive, gas ionisation detector (solid angle 4 msr) which was located inside a scattering chamber (radius 1m) at an angle of $\theta = 45°$ relative to the beam direction [10]. The sample normal was 67.5° relative to the beam and in plane with detector axis and beam. The films were typically exposed to a dose of 5×10^{12} ions.cm^{-2}. The beam spot area on the irradiated samples was approximately 7mm^2. Two energy loss signals (ΔE1 and ΔE2) and a residual energy signal (Eres) were detected to identify the atomic number Z of the ions. All relevant elements can be distinguished in a projection of ΔE2 versus Eres (Figure 1a). The total energy of the recoil ions was measured by summing ΔE1, ΔE2 and the residual energy, and in addition directly using a grid electrode. The position information was used to correct the kinematic energy broadening over the acceptance angle.

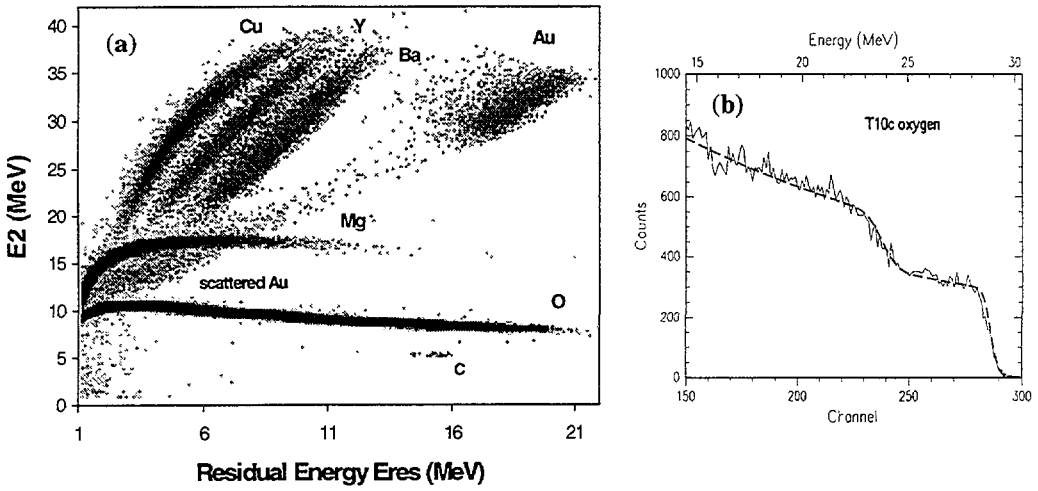

Figure 1 Heavy ion ERD results for the film T10c. (a) Energy loss ΔE2 versus residual energy Eres.

Samples T10c and T13 were analysed with heavy ion RBS using a 52.9MeV ^{28}Si beam from the 14UD accelerator (Si-RBS). The energy of the backscattered ions was measured at $\theta = 110°$ with a Bragg ionisation detector. The angle between sample normal and beam was 45°. Additional RBS measurements were performed on all samples with a 1.83MeV ^4He beam from a 2MV van-de-Graaff machine (He-RBS). Scattered ions were detected at θ =98° and 168° with silicon surface barrier detectors. Sample orientations were between +5° and –5° relative to the beam, chosen to allow channelled (He-RBS-c) and random entry.

3. Data Analysis

In the data analysis the stoichiometric ratios of the metallic elements in the film (Y,Ba,Cu) were determined first. As illustrated in Figures 1a and 2a, the metals are resolved with heavy ion ERD and Si-RBS. Ratios have thus been extracted by dividing the number of counts and normalising with the respective scattering cross-sections. The accuracy of this technique is only limited by statistical uncertainties. In addition, theoretical simulations have been adapted (heavy ion ERD) or fitted (Si-RBS) to the energy spectra using the code RUMP [11]. Since the stoichiometric ratios of the metals are not affected by these parameters, fluence, film thickness and straggling were allowed to deviate from the actual value and O and Mg were ignored in the calculations. Uniform stoichiometry throughout the film was assumed. The ratios obtained this way are, in addition to the statistical uncertainty, affected by the uncertainty of the adaptation. With He-RBS the metallic elements were not fully separated (Figure 2b). In the spectra (random entry) from the backward detector at 169° surface and

interface edges associated with these elements can, however, be clearly identified. This allowed sensible fits of this part of the spectrum using RUMP. The experimental ratios obtained with the different techniques, are consistent for each sample (Figure 3a). For each sample the measured ratios were weighted by uncertainty and the average value was adopted.

Due to the scattering kinematics, oxygen cannot be detected with Si-RBS. In the He-RBS spectra the oxygen signal is obscured by that from magnesium. In the case of heavy ion ERD, oxygen is separated from the other elements and the interface edge between film and substrate can be identified (Figure 1b). Using the adopted stoichiometries for Y, Ba and Cu, the oxygen content of the films was determined by integrating the oxygen spectra between surface edge and interface and also by fitting the spectrum in this range using RUMP. Since it is difficult to identify the exact position of the interface edge, the latter produced more accurate results. Again, weighted averages were adopted as the results shown in Figure 3b.

Finally, using the measured film stoichiometries, the heavy ion ERD spectra were compared with simulations using RUMP. Film thickness, straggling and fluence were treated as free parameters. The substrate composition was assumed to be stoichiometric MgO. No film

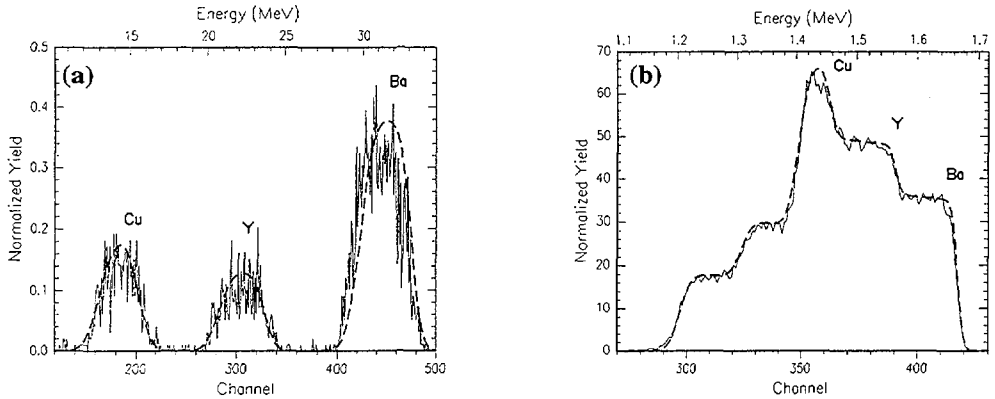

Figure 2 (a) Silicon RBS spectra of T13. (b) Helium RBS spectra of T10b. Th e dashed line in each case is the RUMP simulation.

shows depth variations of the stoichiometry.

4. Discussion

All samples show a change from opaque to transparent in the beam spot area. He-RBS-c orientation confirmed the crystallinity of the films. However, the minimum yields in the ERD beam spot area are only slightly less than those for random orientation indicating amorphisation. A fluence reduction by an order of magnitude would be necessary to limit crystal damage. This may be achieved, with an acceptable deterioration of the energy resolution, by doubling the detector solid angle and the width of the collimation slit and also using a shallower angle between sample surface and beam.

With the exception of T11, the ratios of the metallic elements are similar for all samples. Although in all cases sputter targets with the ideal stoichiometric ratios for the metals (YBa_2Cu_3) were used in the film deposition, the measured Ba/Y and Cu/Y ratios are both smaller than those expected for ideal stoichiometry, while the Ba/Cu ratio agrees with that value. The ratios for sample T10c, which has a Au surface film, are consistent with those for T10a and T10b which were made from the same sputter target, but have no Au film. For all films the results from the different ion beam techniques agree. This indicates that sputtering of metallic elements during ion beam analysis, which would be beam and energy dependent, is

insignificant. The deficiency of Ba and Cu relative to Y is likely to be due to the deposition process. A possible cause may be sputtering of the film surface by plasma particles during deposition, which can lead to a preferential loss of these elements [12]. For sample T11 the Ba/Cu and Cu/Y ratios are consistent with stoichiometric composition, while the Ba/Y ratio is only slightly smaller.

The results for the oxygen content reflect those for the metals. The O/Cu ratios are constant and in agreement with stoichiometric composition and the O/Ba ratios are only slightly larger than the ideal value. In contrast, again with the exception of T11 for which it is almost stoichiometric, the O/Y ratio is considerably smaller. It may be assumed that oxygen loss during ion beam analysis of a stoichiometric sample would reduce the ratio of oxygen to all three metals. With the exception of Yttrium such a reduction is not observed. For sample T11 the ratios of all elements are consistent with those expected for a superconductor with close-to-ideal stoichiometry. The reduced O/Y ratio for the other samples is consistent with the observation of an excess presence of yttrium relative to the other two metals. This suggests that, despite the amorphisation of the film, the oxygen content measured with heavy ion ERD is accurate and that any loss during the analysis is insignificant.

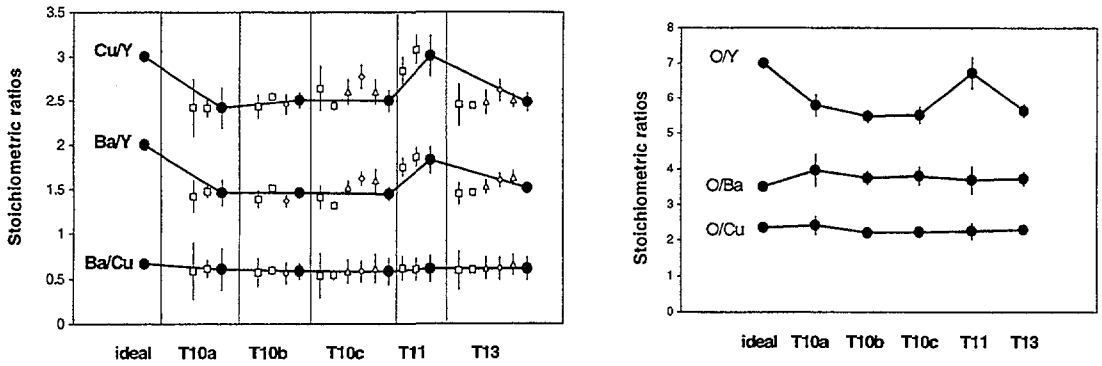

(a) (b)

Figure 3 (a) The experimental ratios of Y, Ba and Cu determined with heavy ion ERD (square), Si-RBS (triangle) and He-RBS (rhombus). The large filled circles are averages, weighted by uncertainty. (b) The ratios of O and the three metallic elements as measured with heavy ion ERD.

Acknowledgements

We would like thank Dr C. Foley, Dr B. Sankrithyan and Dr. L. Wielunski for making the $YBa_xCu_yO_z$ samples available and for their contributions to this work .

References

[1] F. Baudenbacher et al., *Physica C* 185-189 (1991) 2177-2178.

[2] J. Keinonen et al., in *Studies of high temperature superconductors*, Vol.4, ed. A. Narlikar, Nova Science Publishers, New York 239-262.

[3] J.P. Stoquert et al., *Nucl. Instr. Meth.* B44 (1989) 184-194.

[4] J.W. Martin et al., *Nucl. Instr. Meth.* B94 (1994) 277-290.

[5] H. Bernas et al., *Nucl. Instr. Meth.* B46 (1990) 269-275.

[6] W. Assmann et al., *Nucl. Instr. Meth.* B118 (1996) 242-250.

[7] R. Vlastou et al., *Nucl. Instr. Meth.* B136-138 (1998) 1286-1290.

[8] The samples were made at CSIRO, Telecommunications & Industrial Physics, Lindfield, Australia.

[9] N. Savvides and A. Katasaros, *Appl. Phys. Lett.* 62 (5) (1993) 528-530.

[10] H. Timmers et al., *Nucl. Instr. Meth.* B156 (1999) 236-243.

[11] RUMP ion beam analysis package http://www.genplot.com/

[12] N. Savvides et al., *Mater. Res. Soc. Symp. Proc.* 169 (1999) 655.

SESSION 5

Chair – Peter Johnston

Thin Films

Sensitivity to Contamination of Optical Coatings

Angus Macleod

Thin Film Center Inc
2745 E Via Rotonda
Tucson, AZ 85716-5227, USA
angus@thinfilmcenter.com

Summary

A simple theory is presented of the sensitivity to contamination of optical coatings, which permits prediction of performance degradation in the presence of small deposits of absorbing material. Although a major objective is the ability to compare the sensitivities of different coating types, absolute values can be made possible by adopting a standard contamination layer consisting of a 1Å thickness of carbon. Results are quoted for a number of common thin-film coatings and filters and are sometimes surprising. The common high-reflectance coating is the quarterwave stack and, at its reference wavelength, it has very low sensitivity to contamination. Although minor constructional errors have little effect on the reflectance, they can seriously affect the contamination sensitivity. Further, the level of contamination determines the maximum reflectance it is possible to achieve, regardless of the number of layers in the coating. The admittance diagram helps in understanding the reasons for the very large variations in sensitivity between coatings with quite similar reflectance.

Abstract

Optical coatings are rarely used in an ideal environment. They are subjected to all kinds of environmental disturbances ranging from abrasion to high temperature and humidity. These cause performance degradation that mostly originates in an actual irreversible and usually visible destruction of the layers. However, performance may be degraded in a rather less spectacular way by the simple acquisition of a contaminant that may have no aggressive effect on the layers other than a reduction of the level of performance of the coating as a whole. The action of water vapor that is adsorbed by a process of capillary condensation and causes a spectral shift of the coating is well known. Here we are concerned with much smaller amounts of absorbing material such as carbon in the form of sub-molecular thicknesses either at some point during the construction of the coating or, more usually, over the surface after deposition.

Although there are many tests for the assessment of the resistance of a coating to most environmental disturbances there is no standard test for the measurement of susceptibility to contamination. Yet it can be shown [1] that the response of coatings can vary enormously, depending on many factors including design, wavelength, and even on errors committed during deposition. The reason may be that, often, careful cleaning will restore the performance but this does not avoid the degradation in between cleanings, and more frequent cleanings are required for more susceptible coatings.

Fortunately it is possible to make some predictions of coating response to low levels of contamination and, especially, to make assessments of comparative sensitivity. Electric field distribution and potential absorption are the keys to understanding the phenomenon.

The irradiance absorbed is a thin layer can be shown [2, 3] to be

$$I_{absorbed} = \frac{2\pi nkd}{\lambda} \cdot \mathcal{Y} \cdot \mathcal{E} \tag{1}$$

where the symbols have their usual meaning. Note that the losses are proportional to the *product* of n and k and the square of the electric field amplitude, $\mathcal{E}$. Both n and k must be nonzero for absorption to occur. The absorption will be small both for a metal with vanishingly small n and a dielectric with vanishingly small k.

But we need to find the contribution to the absorptance A of the multilayer. For this we make use of the concepts of potential transmittance and potential absorptance.

The potential transmittance [4], ψ, of any element of a coating system is defined as the ratio of the output to the input irradiances, the input being the net irradiance rather than the incident. Potential transmittance has several advantages over transmittance when dealing with absorbing systems because it completely avoids any problems associated with the mixed Poynting vector in absorbing media. The potential transmittance of a complete system is simply the product of the individual potential transmittances.

$$\psi = \frac{I_{out}}{I_{in}} \tag{2}$$

$$\psi_{system} = \psi_1 \cdot \psi_2 \cdot \psi_3 \cdot \psi_4 \cdot \psi_5 \cdots \psi_q$$

with the eventual overall transmittance given by

$$T = (1 - R) \cdot \psi_{system} \tag{3}$$

We return to our thin element. From the complex form of the Poynting vector

$$I_{in} = \frac{1}{2} \mathcal{Y} \cdot \mathrm{Re}(Y) \cdot \mathcal{E}^2 \tag{4}$$

where Y is the admittance of the structure in free space units at the element in question, and $\mathcal{Y}$ is the admittance of free space. Then

$$\psi = \frac{I_{in} - I_{absorbed}}{I_{in}} = 1 - \frac{2\pi nkd}{\lambda} \cdot \frac{2}{\mathrm{Re}\ Y} \tag{5}$$

Potential absorptance is the complement of potential transmittance. The potential absorptance, $\mathcal{A}$, is defined as the ratio of what is absorbed in the element to the input irradiance.

$$\psi + \mathcal{A} = 1.0 \tag{6}$$

so that for our thin element

$$\mathcal{A} = \frac{2\pi nkd}{\lambda} \cdot \frac{2}{\mathrm{Re}} \tag{7}$$

Amongst other things, this result allows interpretation of an admittance locus in terms of potential absorption.

Let us now limit ourselves to contamination on the front surface of an optical coating. The contamination receives the full irradiance that enters the multilayer and the admittance at the contamination layer determines the reflectance as well as the potential absorptance. The absorptance, A, is therefore given by:

$$\begin{aligned} A &= (1 - R) \cdot \mathcal{A} \\ &= \frac{4\pi nkd}{\lambda} \cdot \frac{1}{\mathrm{Re}(Y)} \cdot \left\{ 1 - \frac{\left[y_0 - \mathrm{Re}(Y)\right]^2 + \left[\mathrm{Im}(Y)\right]^2}{\left[y_0 + \mathrm{Re}(Y)\right]^2 + \left[\mathrm{Im}(Y)\right]^2} \right\} \\ &= \frac{4\pi nkd}{\lambda} \cdot \frac{4y_0}{\left[y_0 + \mathrm{Re}(Y)\right]^2 + \left[\mathrm{Im}(Y)\right]^2} \end{aligned} \tag{8}$$

and equation (8) permits us to put contours of absorption due to contamination on the admittance diagram. Before we draw actual lines we need to define some of the quantities. It is simplest to use numbers that allow us to scale the diagram easily. We therefore simplify the expression by defining the quantity K for our absorbing element.

$$\frac{16\pi nkd}{\lambda} = K \tag{9}$$

Then, from (8),

$$A = K \cdot \frac{y_0}{\left[y_0 + \mathrm{Re}(Y)\right]^2 + \left[\mathrm{Im}(Y)\right]^2} \tag{10}$$

And if we replace Y by $x + iz$ then the equation giving the contours of constant A/K is

$$\left(y_0 + x\right)^2 + z^2 = y_0 \cdot \frac{K}{A} \tag{11}$$

that is, a circle with center at the point $(-y_0,0)$ on the negative branch of the real axis.

To simplify matters we take the value of y_0 as 1.00. Then Figure 1 shows contour lines of constant A/K. Now to assess the sensitivity of a system to contamination we simply have to see where the admittance locus ends.

We can make some immediate general deductions from this diagram. Antireflection coatings all have loci that terminate as closely as possible to the point corresponding to y_0, 1.0 in this case. This means that all have virtually identical sensitivity to contamination and that nothing can be done to modify it because a movement away from the point y_0 implies an increase in reflectance. High reflectance coatings, on the other hand, have a termination point that could be anywhere on an isoreflectance circle centered on the real axis. If we are dealing with a quarterwave stack that terminates with a high-index quarterwave then the termination point is at a high admittance on the real axis and therefore the sensitivity to contamination is low. A quarterwave stack that is terminated with a low index, on the other hand, has an enhanced sensitivity to contamination.

As an example of the magnitude of K we can take the values of amorphous carbon given by Palik[5, 6] that is optical constants of 2.26-i1.025 at 1000nm, and assume a thickness of 0.1nm.

A plot of K is shown in Figure 2 and over most of the wavelength region shown it is between 0.01 and 0.02.

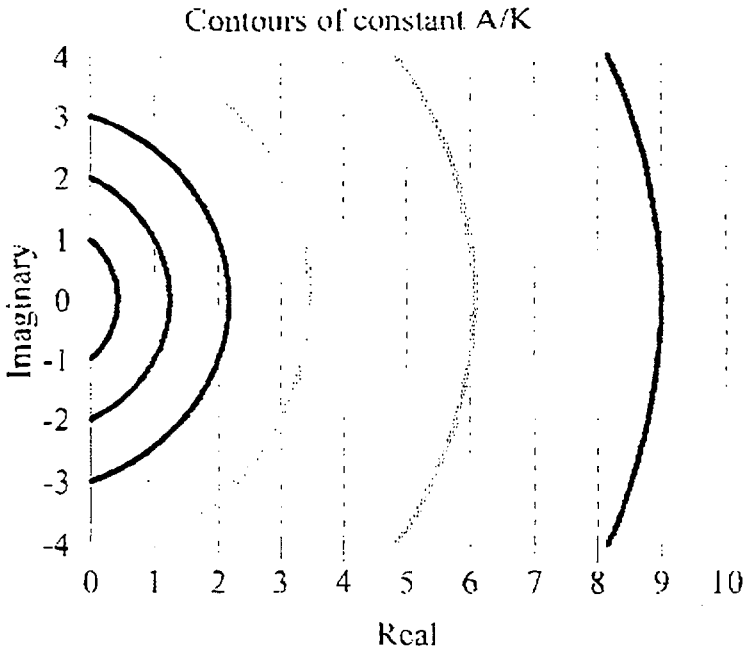

Figure 1. The contour lines of constant A/K in the admittance diagram assuming that μ_0 is 1.00. From left to right (inner to outer circle) the values of A/K are 0.5, 0.2, 0.1, 0.05, 0.02, 0.01. The origin corresponds to a value of A/K of 1.00.

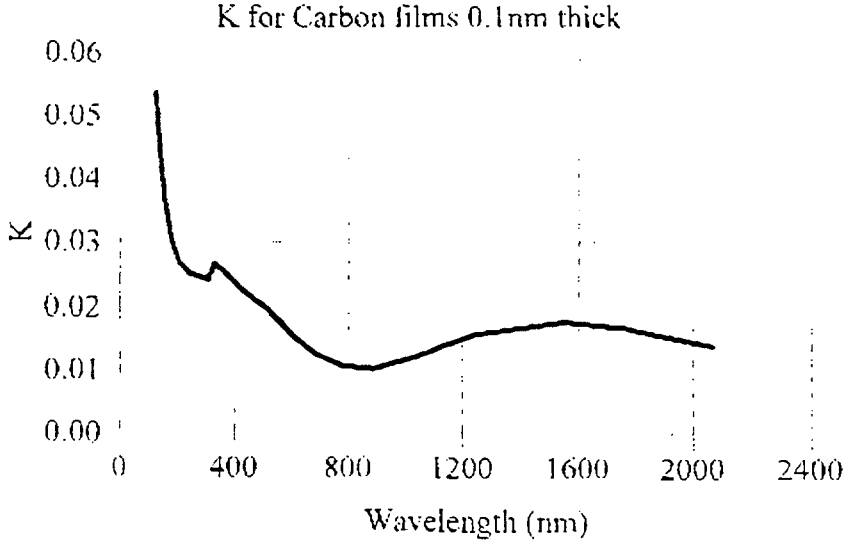

Figure 2. Plot of K against wavelength for 0.1nm thickness of carbon film.

It turns out that given a certain level of contamination there is no point in trying to increase reflectance by adding layers to a quarterwave stack. The reflectance simply stays constant. This appears to contradict the simple theory but is actually a consequence of a curious interference effect in even the very thin less than monomolecular thickness of the contaminant. Also extended-zone high-reflectance coatings have regions where the sensitivity to contamination is considerably enhanced. The halfwave protecting layer of silica over a front-surface aluminized mirror is almost the best arrangement possible from the point of view of contamination sensitivity.

These and other curious effects will be discussed. They do have quite serious implications and especially when performance levels tend towards the achievable limits.

References

1. Macleod, Angus and Christopher Clark. *Assessing contamination sensitivity in optical coatings*. In *42nd Annual Technical Conference Proceedings*. 1999. Chicago: Society of Vacuum Coaters. p. 232-236.
2. Macleod, H A and C Clark. *Electric field distribution as a tool in optical coating design*. In *40th Annual Technical Conference Proceedings*. 1997. New Orleans: Society of Vacuum Coaters. p. 221-226.
3. Macleod, Angus and Christopher Clark. *How sensitive are coatings to contamination?* In *Eleventh International Conference on Vacuum Web Coatings*. 1997. Miami, Florida: Bakish Materials Corporation, New Jersey. p. 176-186.
4. Berning, P H and A F Turner. *Induced transmission in absorbing films applied to band pass filter design*. Journal of the Optical Society of America. 1957. 47: p. 230-239.
5. Palik, E D. ed. *Handbook of Optical Constants of Solids*. . 1985. Academic Press Inc.
6. Palik, Edward D. *Handbook of Optical Constants of Solids II*. 1991. San Diego and London: Academic Press.

Electronic structure of the alkali earth metals and their oxides

V.A. Sashin, M.J. Ford, M A Bolorizadeh

Physics Dept., Flinders University of South Australia, GPO Box 2100, SA 5001, Australia

A.S. Kheifets

Research School of Physical Sciences and Engineering, Institute of Advanced Studies, ANU, Canberra ACT 0200, Australia.

The alkali-earth oxides are of considerable interest due to their technological importance in areas ranging from catalysis to microelectronics and because they are important constituents of the Earth's lower mantle. A number of band structure calculations for these materials have been reported in the literature (see for example Pandey et al [1]) using a range of theoretical methods. In contrast the available experimental data is more limited, band gaps have been measured with optical reflectance techniques [2] and density of states with photoelectron spectroscopy [3]. Different theoretical models can reproduce different aspects of the experimental data, but a comprehensive understanding of the electronic structure of these materials is still being developed. Measurement of the full band-dispersions by angle resolved photoelectron spectroscopy might be expected to give considerable insight into this problem and provide a complete data set with which to compare the various calculations. One such measurement has been previously reported [4], although the difficulty of applying the technique to these highly insulating oxides and interpretation of the results has perhaps hampered progress in this direction. In this paper we present our experimental measurements of the electronic structures of Be, Mg, Ca and their oxides. We have also performed *ab-intio* calculations for these systems within the linear muffin-tin orbital approximation. The magnesium experiment and calculations is also published elsewhere [5].

The experiments have been performed using electron momentum spectroscopy [6]. This technique uses electron impact ionisation to measure directly the energy-momentum resolved densities of a solid target, in other words band dispersion together with band occupation. These experiments can provide a sensitive test of theoretical models and the technique can be applied equally well to amorphous and polycrystalline targets as well as single crystals. The samples used in our experiment have been prepared by evaporating of the order of 2nm of the appropriate metallic species onto an ultrathin carbon membrane (3nm in thickness). Since our experiments are performed in transmission mode the overall thickness of the target must be kept below 10nm in order to avoid the signal being dominated by multiple scattering effects. The geometry of the apparatus also means the measured EMS signal originates essentially from the outermost 2nm of the target. Hence it is not sensitive to relatively small amounts of surface contamination, yet is sensitive enough that the carbon substrate does not contribute to the measured spectrum. The metallic samples prepared in this way are expected to be polycrystalline, auger electron spectra of the samples indicates that the level of surface contamination is small. The oxide samples are prepared by a similar process, except that the evaporation is performed in an oxygen background of typically 10^{-6}Torr. Sample preparation and Auger measurements are all performed in situ, with the EMS measurement being performed under ultra-high vacuum conditions, typically 10^{-10}Torr.

The experimental and calculated band structures for CaO and BeO are shown in figures 1 and 2 respectively. In each figure the upper left panel shows the experimentally determined energy-momentum resolved density. The upper right panel is the corresponding LMTO calculation. The calculation has been spherically averaged over crystal directions in order to take account of the polycrystalline nature of the targets used in the experiment. The calculation has also been convoluted with gaussians of 1.0eV (FWHM) and 0.1au (FWHM) to match the experimental energy and momentum resolutions. Measured binding energies are with respect to the vacuum level whereas the calculation is performed with respect to the

valence band maximum, and so the binding energies in the calculations have been shifted to align the upper valence band with the experiment. The lower panel in each figure shows the experimental and theoretical binding energy curve over the momentum range 0.8 to 1.0au. The measured and calculated energy and intensity of the O 2p upper valence band peak have been normalised to each other in these plots. These plots are derived by taking vertical slices through the energy-momentum densities integrated over a 0.2 au. momentum interval.

The results for CaO (figure 1) clearly show bands derived from O 2p, O 2s, Ca 3p and Ca 3s states at approximately 10eV, 25eV, 28eV and 48eV respectively. The dispersion range of the bands is relatively small as is expected of these ionic compound. Although the calculation reproduces the experimental dispersions relatively well there is a noticeable disagreement for the energy gap between the upper and lower oxygen derived valence bands, with the calculation underestimating this gap by about 3eV. The calculated and measured intensities of the bands are also different. The results for BeO, where the two oxygen derived valence bands are clearly visible (figure 2), show the same characteristics. In the experimental results a relatively high intensity is seen in the upper valence band at close to zero momentum. This is rather surprising given that this band is derived predominantly from O 2p states and is not reproduced in the calculations. The origin of this intensity is unclear, though may result from combination of the finite resolution and multiple scattering. Similar feature were observed for MgO [5].

Our experimental measurements for the metallic states show the characteristic free-electron like parabola, and are in reasonable agreement with the calculations The spectra show a significant contribution from multiple scattering effects making a quantitative comparison of experiment and theory more difficult.

References

[1] Pandey R, Jaffe J E, and Kunz A B 1991 *Phys. Rev. B* **43** 9228

[2] Whited R C, Flaten C J, and Walker W C 1973 *Solid State Commun.* **13** 1903

[3] Fiermans L, Hoogewijs R, de Meyer G, and Vennik J 1980 *Phys. Status Solidi A* **59** 569

[4] Tjeng L H, Vos A R, and Sawatzky G A 1990 *Surf. Sci.* **235** 269

[5] Canney S A, Sashin V A, Ford M J, and Kheifets AS 1999 *J. Phys.: Condens. Matter* **11** 7507

[6] McCarthy I E and Weigold E 1991 *Rep. Prog. Phys.* **51** 299

Spectral Momentum Density in CaO

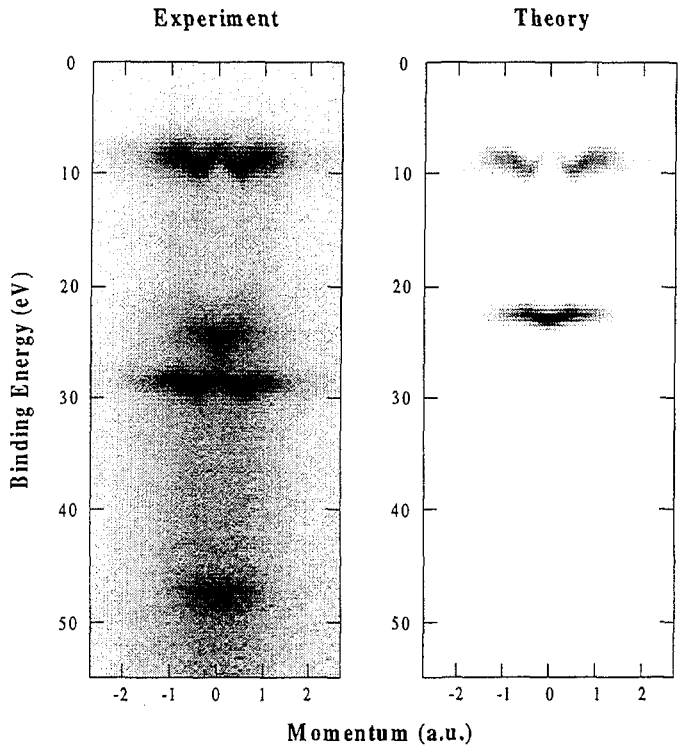

Binding Energy Spectrum for 0.8 a.u. Momentum

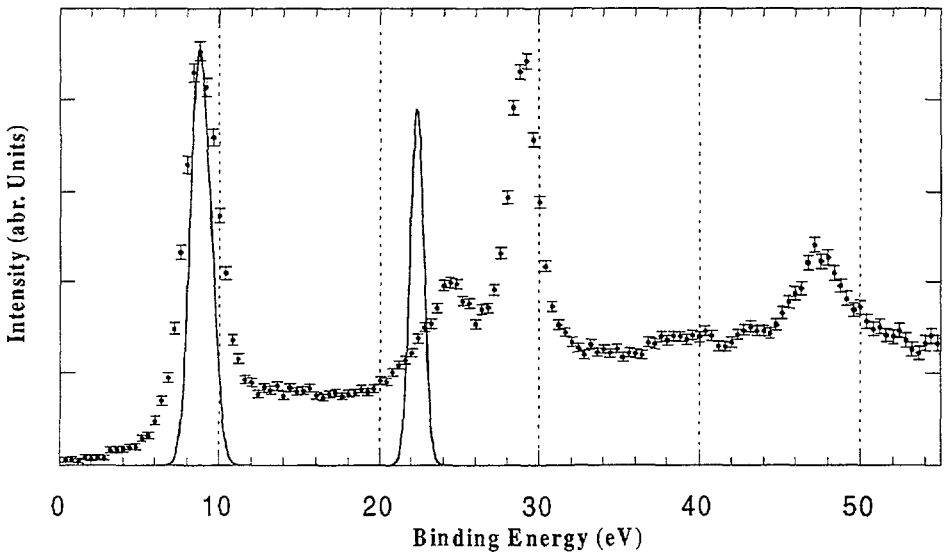

Figure 1

Spectral Momentum Density in BeO

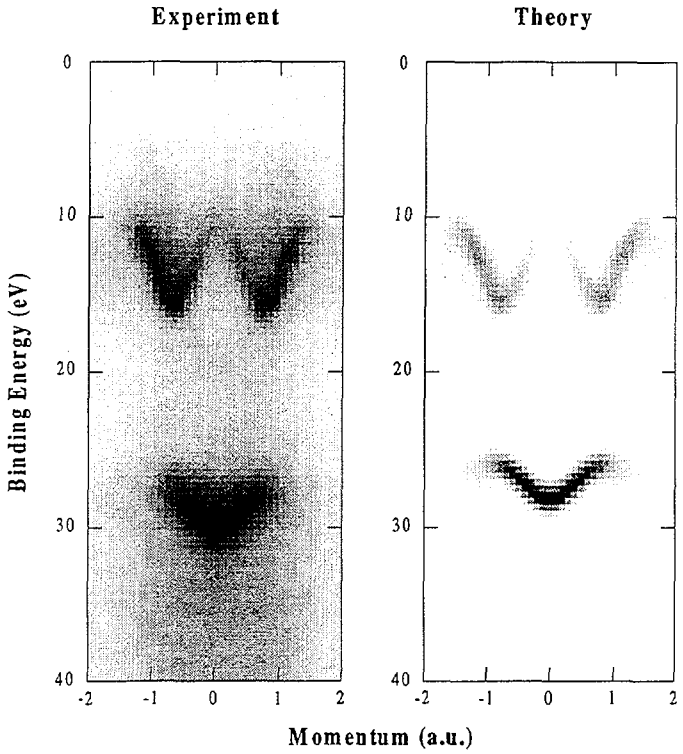

Binding Energy Spectrum for 0.8 a.u. Momentum

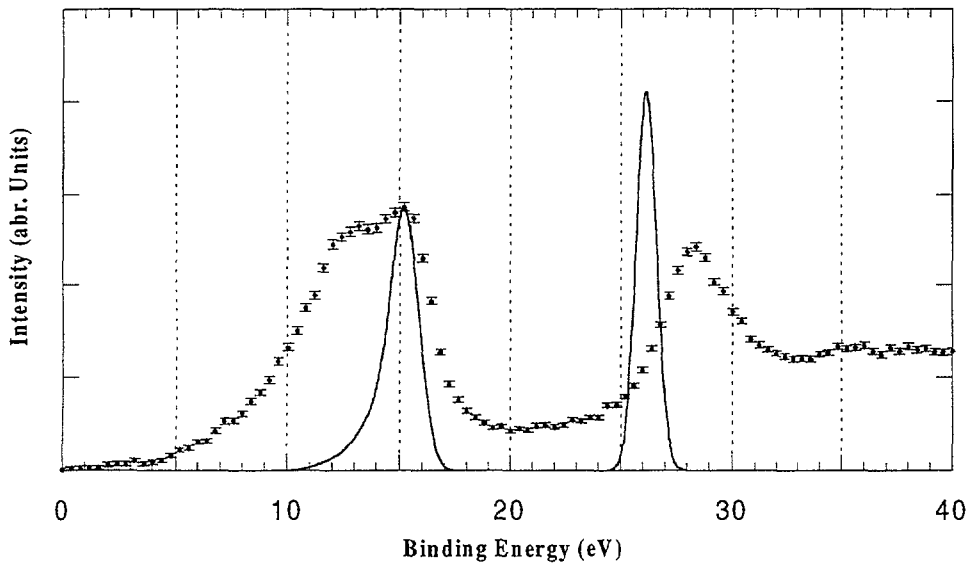

Figure 2

Surface studies of Cl_2 chemisorption on CVD diamond

Nathan Paris & Nagindar Singh

School of Chemistry, The University of New South Wales, Sydney, NSW 2052.

Abstract

The technique of X–ray photoelectron spectroscopy has been used to study the interactions of molecular chlorine with CVD diamond surfaces. Chlorine is found to adsorb onto the clean surface with a sticking probability of ~0.001 at 25°C, although this can be enhanced by pre–hydrogenation of the surface. Adsorbed chlorine desorbs from the surface over a wide temperature range below 500°C. It can also be very efficiently etched away by atomic hydrogen. In this paper we present results obtained in the investigation, and discuss their implications in diamond growth mechanisms, in particular to the development of low temperature growth models using halogen–based precursors.

Introduction

Diamond thin films find applications in such areas as thermal management of electronic chips, optical windows and radiation detectors [1]. High quality thin films of diamond are now routinely grown by the technique of Chemical Vapour Deposition (CVD) using low pressures of hydrocarbon/hydrogen mixtures [see for example [2]), either excited by plasma or a hot filament. A major disadvantage of this technique, however, is that it requires high substrate temperatures, typically 900°C, to achieve a reasonable growth rate. Substrates that cannot withstand high temperatures, either because they melt or undergo problematic phase changes therefore cannot be employed. Interest exists in the development of practical CVD diamond processes that provide significant growth rates at lowered growth temperatures. This can be achieved by modifying the hydrocarbon/hydrogen feedstock in the CVD reactor by addition of oxygen or halogen based compounds, and this method has shown [3, 4] to lower the growth temperature by several hundred degrees.

The growth mechanism of CVD diamond from hydrocarbon in hydrogen mixtures has been the subject of extensive investigation, both experimentally and theoretically (see, for example [5] and references therein). A reasonable consensus exists concerning the broad nature of the gas phase and surface chemical processes responsible for deposition. We have extended this general understanding to the use of chlorine–based feedstocks. This requires a knowledge of the changes in gas phase composition, which arise when chlorine–based compounds are introduced, the interactions of any new gas phase species generated with the surface of the growing film, and the surface processes involving any new species. Free Cl species are known to be produced in the gas phase when chlorinated compounds are used during diamond growth, and these are expected to chemisorb onto a diamond surface; the occurrence of bound surface Cl species has indeed been observed [3]. It follows that the surface properties of bound Cl species, their thermal properties and the extent they can be etched with atomic hydrogen need to be understood if reliable growth models are to be produced from relevant precursor mixtures. In this paper we report on the interactions of molecular chlorine with CVD diamond at room temperature.

Experimental Procedures

All experiments were carried out in an ultra–high vacuum chamber equipped with a mass spectrometer for gas phase analysis, and an X-ray source and concentric hemispherical analyser (VSW HA100) for X–ray photoelectron spectroscopy. The diamond sample was a high quality boron–doped randomly oriented CVD film of 10μm thickness, grown by plasma assisted CVD onto boron–doped Si(100) substrate. *In situ* sample cleaning was performed initially by slowly annealing to 1300K, and subsequently by repeated cycles of flashing to

1300K. This procedure was repeated until the XP spectrum showed the presence of a good diamond plasmon structure (surface and bulk) in the 305 – 325eV binding energy region in addition to the C 1s peak at 285eV, and did not show the O 1s peak at 530eV. Atomic hydrogen for etching experiments and for hydrogenating the diamond surface was generated *in situ* by thermal cracking, over a hot (2200°C) coiled tantalum filament, of high purity hydrogen (99.995%, BOC) at a fixed pressure of $1x10^{-4}$ mbar. The sample to tantalum filament distance was maintained at 3cm during surface hydrogen dosing to ensure that the sample temperature did not rise above 90°C. Molecular chlorine (99.5% purity, Argo International) was delivered via an *ex situ* leak valve and stainless steel dosing line, the tip of which was 5mm from the substrate surface. Dosing was carried out at substrate temperatures below 80°C. For the study of the chlorine uptake behaviour dosing was carried out at a chlorine pressure of $1x10^{-4}$mbar for known (fixed) lengths of time, and aliquot dosing was continued up to saturation coverage of 30L. In the case of etching experiments, the initial chlorine saturated surface was formed by exposing the clean surface to chlorine at $1x10^{-4}$mbar for half an hour, which ensured that the surface was fully saturated with chlorine.

Results

The first series of experiments studied the kinetics of chlorine uptake by the diamond surface and the thermal desorption behaviour of the surface chlorine, using XPS. Exposure of chlorine to the clean diamond surface shows a peak at 210eV binding energy. In Figure 1(a) we show the variation in this Cl 2p signal with increasing exposures of chlorine gas. We detect a slight chemical shift with the binding energy decreasing to approximately 209.5eV at saturation coverage.

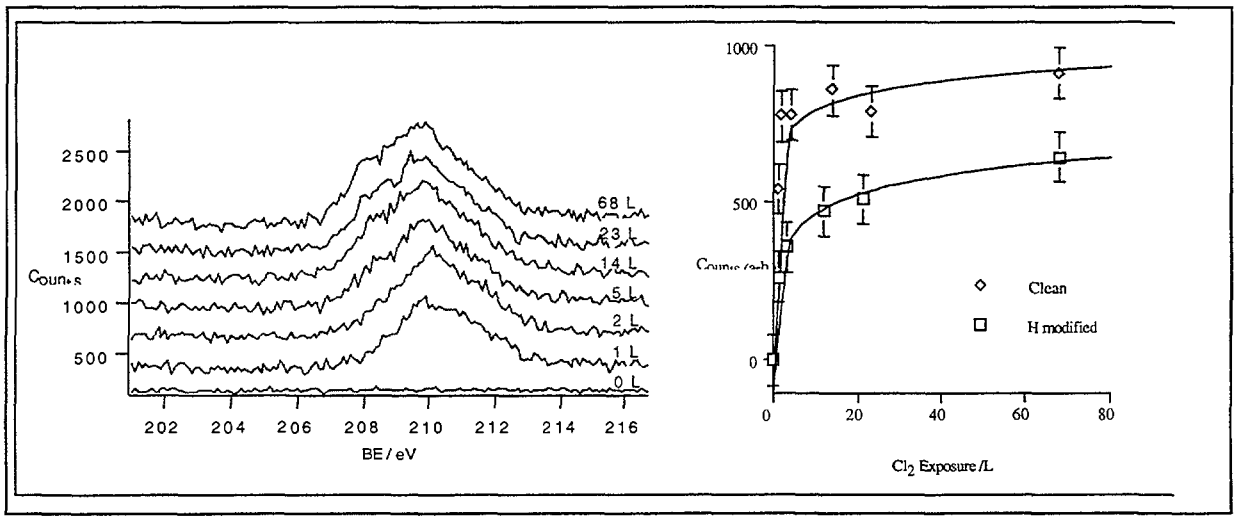

Figure 1(a). Cl 2p photoelectron peak monitored as a function of increasing chlorine exposure at room temperature, figure 1(b) Cl 2p peak intensity plotted as a function of chlorine exposure on clean and pre–hydrogenated surfaces.

As expected, the intensity of the peak increases with exposure, and a plot of the peak intensity as a function of Cl_2 exposure (Figure 1(b)) shows that there is an initial rapid uptake of chlorine by the surface followed by a slow increase up to saturation coverage. The chlorine uptake experiments on a fully H–terminated surface (also plotted in Figure 1(b)), carried out in a similar manner to that on the clean surface, again showed an initial rapid uptake followed by a slow uptake until no further increase in the chlorine coverage was observed. Close inspection of the initial uptake shows that the uptake on the hydrogen saturated surface is more rapid than on a clean surface. Calculations of chlorine sticking probabilities in a related study [6] showed them to be low, being approximately 0.001, which increased to two times this value for adsorption on a pre–hydrogenated surface. However, the maximum chlorine coverage attainable on this surface corresponded to approximately 70% of the saturation

coverage of the clean surface. Surprisingly the C 1s region of the spectrum did not show the presence of the chemically shifted carbon peaks, and we deduce from this that the surface chlorine concentration is low.

The thermal stability of the adsorbed chlorine was examined and in Figure 2 below we show the thermal desorption behavior from clean and H–terminated surfaces. Samples were prepared by exposing both hydrogen free and hydrogen terminated surfaces to chlorine to the saturation dose of molecular chlorine. Upon heating we see initial slow decreases in the surface chlorine concentrations in both cases, up to a temperature of 350K, followed by more rapid decreases. For temperatures greater than 450K the decreases in surface concentrations slow down significantly, and the surface coverage corresponds to approximately 40% of the initial chlorine coverage. Although the desorption behavior from both surfaces show similar trends, differences exist in the desorption temperatures. In the case of chlorine adsorbed onto a clean surface the chlorine coverage drops to 50% of the initial value following heating to 475K and all the chlorine desorbs from the surface at approximately 1100K. In the case of desorption from H–terminated surface 50% of the initial chlorine coverage is reached following heating to a lower temperature of 400K, and complete chlorine desorption occurs by 650K. In a previous investigation [7] adsorbed chlorine from diamond (100) substrates was also observed to desorb completely by 600K, and our value is in reasonable agreement with the value observed in that study.

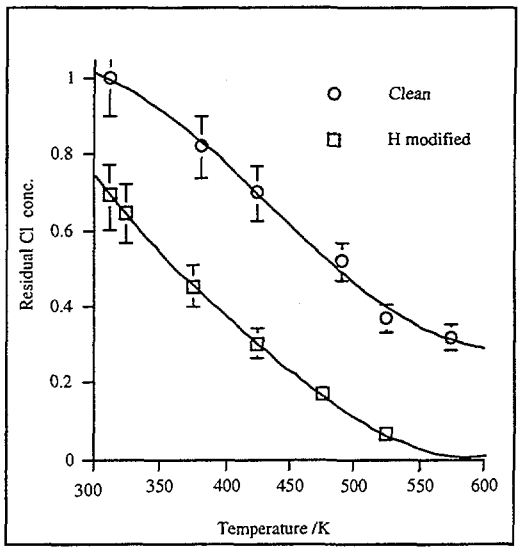

Figure 2. Residual chlorine concentration following thermal desorption from saturated surfaces.

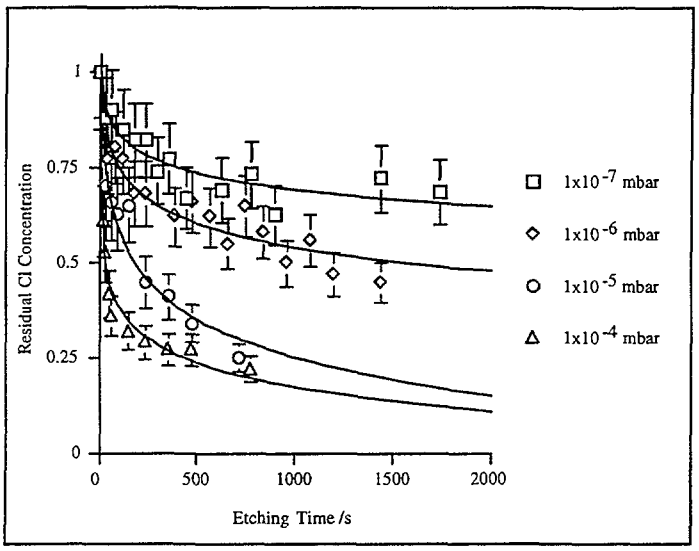

Figure 3. Residual chlorine concentration versus etching times for hydrogen pressures indicated.

The etching of chlorinated diamond surfaces with atomic hydrogen was also studied. Saturated surfaces were formed as above by exposure to molecular chlorine. These surfaces were then exposed to different pressures of atomic hydrogen for increasing lengths of time. XPS analysis of the remaining bound chlorine yielded the data presented in Figure 3, for hydrogen pressures ranging from $1x10^{-7}$mbar to $1x10^{-4}$mbar. Etching of chlorine by atomic hydrogen is clearly seen for all hydrogen pressures, and it is the initial exposure to hydrogen that causes by far the most rapid chlorine loss. We also find that with increasing hydrogen pressure the rate of this initial loss increases, and hence the largest decrease in the surface chlorine concentration was observed for $1x10^{-4}$mbar atomic hydrogen pressure. In all cases the rapid loss (region I) is followed by a slow decrease (region II), and for etching times greater than 1000s the surface chlorine concentration does not change significantly, but appears to become a constant. for each hydrogen pressure. If the rate of loss of chlorine from the surface was proportional to the Cl coverage then a plot of *ln* (Cl intensity) against time should be linear, showing first order desorption kinetics. No such relationship was found, the

etching rate at long reaction times dropping off significantly faster than first order kinetics would suggest. However, the etching rate is proportional to the atomic hydrogen pressure.

Discussion

Our results show that molecular chlorine reacts with both clean and pre–hydrogenated surface. However the sticking probabilities are rather low, emphasizing the inertness of the diamond surface to closed shell molecules. In contrast, sticking probabilities of halogens with silicon surfaces determined under similar experimental conditions typically lie close to unity. The observation that chlorine adsorption occurs on a fully pre–hydrogenated surface suggests that on this surface it is the actual hydrogenated surface sites which are reacting with chlorine, presumably via a substitutional process, involving the formation of a gas phase H or HCl species. The partial dehydrogenation produces vacant radical sites which are capable of reacting with impinging Cl_2 molecules. This process appears more favourable than the reaction of Cl_2 with a clean hydrogen–free, and consequently reconstructed surface, since on that surface C–C bonds will need to be broken to make available radical sites at which reaction can occur.

The thermal desorption of chlorine from the hydrogen–free CVD surface (figure 2) is quite similar to that seen on the diamond (100) surface [8, 9]. Important characteristics here are a fairly low adsorption energy, as indicated by the relatively low temperatures at which chlorine is lost from the surface, and a wide desorption temperature range indicative of a wide range of desorption energies. We also see that the adsorbed chlorine can also be efficiently removed by etching with atomic hydrogen. The two regions observed in the etch plots (figure 3) most probably correspond to etching of Cl from two different environments. The rapid drop in surface Cl concentration (region I) corresponds to removal of chlorine from a carbon site bonded to two Cl atoms at saturation or near saturation coverages, while region II corresponds to removal of Cl atoms bound singly to the surface sites at sub–monolayer coverages. These two environments account for the decreasing binding energy of the Cl 2p peak as the surface coverage of chlorine increases to saturation coverages.

Our results show that surface chlorine can be lost from the surface either by thermal desorption or by etching with atomic hydrogen. Thermal desorption at low temperatures could obviously be one of the reasons why chlorine is good at promoting low temperature growth since it is clearly able to displace hydrogen from the surface at low temperatures thus freeing surface sites to permit diamond growth. However, in a CVD diamond reactor, with the high hydrogen concentration, etching with atomic hydrogen is probably the more predominant process for the removal of surface chlorine in the regime of low temperature diamond growth.

References

[1] R. Sussman, J. Brandon, S. Coe, C. Pickles, C. Sweeney, A. Wasenczuk, C. Wort and C. Dodge, *Industrial Diamond Review*, 58 (1998) 69.

[2] H. Maeda, M. Irie, T. Hino, K. Kusakabe, S. Marooka, *Diamond and Related Materials*, 3 (1994) 1072.

[3] M. Admann, J. Heberlein, E. Pfender, *Diamond and Related Materials*, 8 (1999) 1.

[4] I. Schmidt, F. Hentschel, C. Benndorf, *Solid State Ionics*, 101 (1997) 97.

[5] E. Dawnkaski, D. Srivastava, B. Garrison, *J. Chem Phys.*, 104 (1996) 5997.

[6] S. Proffitt, C. H. B. Thompson, A. Guttierez–Sosa, N. Paris, N. K. Singh, R. B. Jackman, J. S. Foord, *Diamond and Related Materials*, (1999) in press.

[7] A. Freedman, C. D. Stinespring, *Appl. Phys. Lett.*, 57 (1990), 1194.

[8] A. Freedman, *J. Appl. Phys.*, 75 (1994) 3112.

[9] S. Hadenfeldt, C. Benndorf, *Surf. Sci.*, 402 (1998) 227.

Adsorption oscillations in organosilane film growth on metal oxides

J.S. Quinton and P.C. Dastoor
Department of Physics, University of Newcastle, Callaghan, NSW 2308, Australia

Abstract

The kinetics of adsorption of propyltrimethoxysilane (PTMS) and aminopropyltriethoxysilane (APS) onto polycrystalline metal oxide surfaces have been investigated using X-ray photoelectron spectroscopy (XPS) and Static Time of Flight Secondary Ion Mass Spectrometry (ToFSIMS). In each case, the adsorption kinetics does not follow the behaviour predicted by classic adsorption models. Non-linear oscillations are observed in every case, which indicate that the mechanism is quite complex.
Based on the processes that can occur on the surface and dynamics theory, a mechanism model has been developed for PTMS adsorption. Using this and the results of the two complimentary surface analysis techniques, an insight into the surface adsorption processes with both silanes has been obtained.

Introduction

Silane coupling agents are commonly employed to promote adhesion between dissimilar materials [**1**] in a wide number of industries, including aerospace, automotive and construction. γ-Aminopropyltriethoxysilane (APS) has been the coupling agent of choice in many investigations and applications [**2** - **5**], with a particular focus on corrosion protection of iron and steel surfaces [**6**].
Previous work in this laboratory has systematically studied the adsorption of propyltrimethoxysilane (PTMS), which has a relatively inert propyl organofunctional group, with aluminium, iron, chromium and zinc oxide surfaces. Despite its relatively simple chemical structure, the adsorption of PTMS was found to be complex and exhibited so-called oscillatory adsorption, whereby the surface coverage of PTMS was found to oscillate as a function of adsorption time [**7**]. Indeed, the nature of this oscillatory adsorption, and its underlying mechanism, has been the subject of continued investigation [**8**, **9**, **10**].
The situation for hydrolysed APS, however, is complicated since each molecule possesses two moieties, an aminopropyl group and a silanol species, that can interact with an oxide surface. Investigations of the adsorption of APS on iron and steel oxide surfaces have been reported previously and both moieties are known to interact with the surface [**3**, **4**]. However, previous work describing the characterisation of APS films deposited under specific conditions has not focussed on the dynamic behaviour of adsorbing films.

Experimental

The procedures used to obtain and prepare the metal surfaces are described in detail elsewhere [**9**]. PTMS solutions of 0.75% and APS solutions of 1% concentration by volume were prepared by stirring the required quantity of organosilane into de-ionised water for a period of five minutes, by which time the silane had dissolved completely and was considered to be hydrolysed. The pH of each solution was pH3 for PTMS (by addition of acetic acid) and natural pH (10.4) in the case of APS. After dipping, the samples were blown dry with nitrogen and stored under a nitrogen atmosphere to prevent reaction of amine groups (in the case of APS films) with CO_2 in air to form ammonium carbamates [**11**], which may alter the film structure.
After coating, the samples were characterised with XPS using a PHI-550 surface analysis system with a base pressure of better than 2 x 10^{-10} Torr. The XPS spectra were taken with

400W Al K_α radiation and a double pass cylindrical mirror analyser with a pass energy of 100eV. Data analysis involved fitting core level peaks with Lorentzian-Gaussian peak shapes. The calibrated atomic sensitivity factors for the PHI 550 surface analysis system were applied to the measured peak areas to obtain atomic surface concentration [**12**].
Following XPS analysis, each APS coated sample was characterised with a Kratos prism ToFSIMS analysis system, with a base pressure better than 5 x 10^{-9} Torr. Positive spectra were taken with 25keV Ga^+ ions and a pulse width of 100ns, for masses ranging from 0 to 500 m/e (Daltons). The total integrated ion dose was about 10^{12} ions/cm^2, which is below the generally accepted upper limit (5 x 10^{12} ions/cm^2) of static SIMS [**4**]. Each spectrum was calibrated using the masses of known peaks, namely Fe^+ (mass 56) and Si^+ (mass 28), which were strong intensity peaks in each ToFSIMS spectrum. The spectra were normalised by the total integrated ion count, to allow comparisons to be made between samples.

Results and Discussion

In accordance with previous adsorption kinetics studies, the silicon:(silicon + metal) concentration ratio, as measured by XPS, has been taken as an indication of normalised adsorbate coverage on the metal surface. The time dependence of PTMS adsorption on iron and aluminium oxide surfaces has been reported previously [**8**], but is reproduced in Figures 1 and 2. In each case, the coverage does not increase monotonically as predicted by known adsorption theories, but rather exhibit an oscillatory nature.

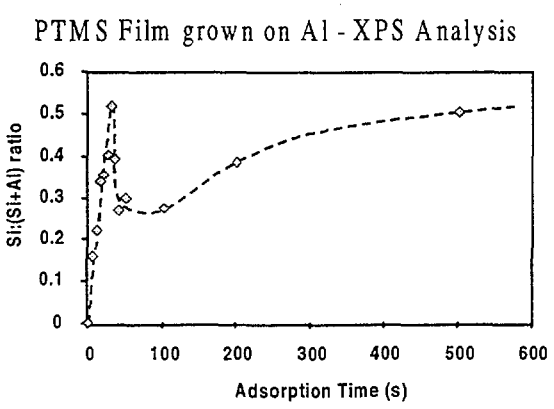

Figure 1. PTMS film growth on Al

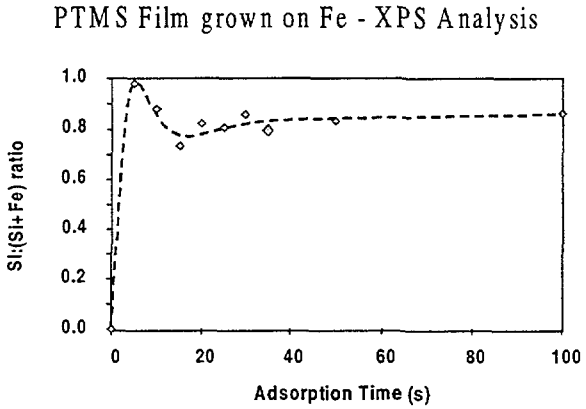

Figure 2. PTMS film growth on Fe

The time dependence of APS adsorption on a native iron oxide surface, as measured by XPS, is illustrated in Figure 3, clearly demonstrating non-linear oscillations in organosilane coverage as the exposure time of the iron substrate to the APS solution increases. Furthermore, the Si:Si+Metal ratio for Figures 1 to 3 is less than unity throughout the adsorption (indicating a strong substrate presence), suggesting that on average, an organosilane film of the order of a monolayer is formed across the surface. The observed oscillatory nature of the adsorption of APS on iron oxide is confirmed by the results of ToFSIMS surface characterisation shown in Figure 4. For the positive ToFSIMS data, the same concentration ratio has been plotted using the intensity of the mass 28 and mass 56 fragments as an indication of the silicon and iron surface concentrations respectively, in accordance with other SIMS investigations of organosilane adsorption [5].
Oscillatory adsorption was first reported for the adsorption of PTMS, a model organosilane species, on aluminium oxide surfaces. Indeed, in a series of related investigations, it was shown that this phenomenon occurred for PTMS adsorbing on a variety of metal oxide surfaces and the nature of the oscillations was shown to be a strong function of a number of experimental parameters [9, 10]. To date, however, the existence of oscillatory adsorption has not been reported for an industrially relevant organosilane coupling-agent, such as APS. It

would seem therefore that the phenomenon of oscillatory adsorption is a general behaviour of organosilane species adsorbing onto oxide surfaces from the liquid phase.

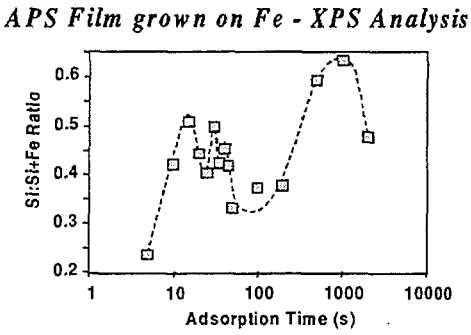

Figure 3. APS film growth on Fe

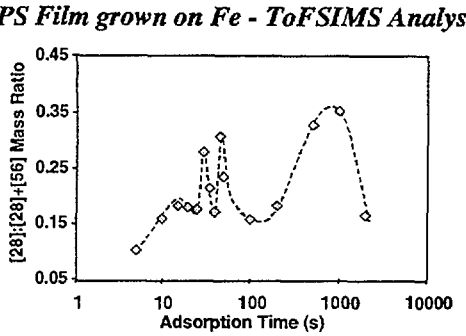

Figure 4. APS Film growth on Fe

Since oscillatory adsorption does not exhibit behaviour predicted by known adsorption theories, models must be developed to describe the dynamical nature of film growth. For PTMS adsorption on aluminium and iron as described in Figures 1 and 2, a semi-quantitative model has been developed to identify the rates of film growth and allow comparison between substrates. Careful scrutiny of each adsorption curve indicates that there are at least three distinct phases of the film growth process, identifiable as an initial rapid adsorption process followed by desorption, and then a slower adsorption process. An expression for the fractional surface coverage, θ, derived from a superposition of these processes [**13**], is given by

$$\theta = A - Be^{-k_1 t} + Be^{-k_2 t} - Ae^{-k_3 t} \qquad (1)$$

where each exponential term in succession represents the rapid adsorption, desorption and slower adsorption of the experimental curve, with individual rate constants k_1, k_2 and k_3.

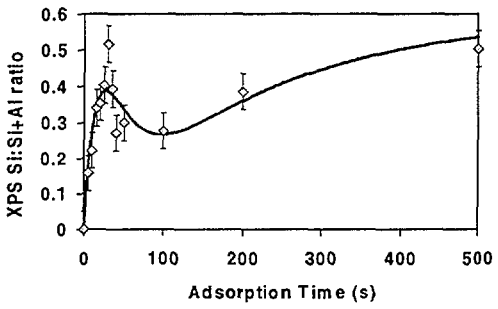

Figure 5. Model Fit to PTMS on Al

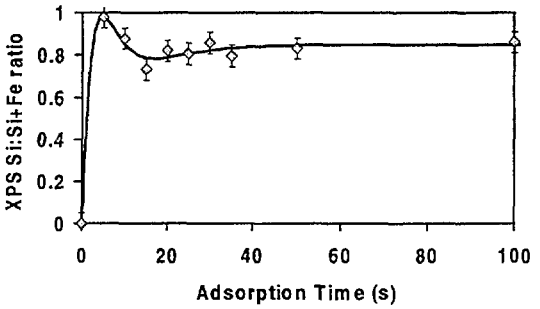

Figure 6. Model fit to PTMS on Fe

Equation 1 has been employed with a least-squares fitting algorithm to fit the PTMS adsorption curves, as plotted in Figures 5 and 6. The values for the fitted parameters are illustrated in table 1, and indicate that all processes occur much more rapidly on the iron surface, as expected. The model function adequately fits the iron data curve, but is less successful with the aluminium data curve because the gradient of the desorption process is of similar magnitude to the initial adsorption.

Fitted Parameter	A	B	k_1	k_2	k_3
Al - Fitted Value	0.56	17.9	0.046	0.044	0.0053
Fe - Fitted Value	0.86	139.4	0.299	0.295	0.1129

Table 1. Fitted values to Least squares fitted data

Conclusions

Oscillatory adsorption has been observed for the adsorption of both PTMS, a model silane coupling agent, and APS, a widely used industrial coupling agent, on metal oxide surfaces, illustrating that the phenomenon may be general to organosilanes. The adsorption oscillations observed during PTMS film growth have been modelled using a mathematical construction with three distinct terms, based upon a superposition of adsorption and desorption processes. The simple model presented here illustrates the non-monotonic behaviour of the film-coverage time dependence, the non-linear character of the adsorption kinetics of the system and provides a possible mechanism for film restructuring or reordering.

Acknowledgements

The authors are grateful to the Surface Science and Technology Centre at the University of New South Wales, Sydney, Australia, for access to their Kratos ToFSIMS instrument.

References

1. E.P. Plueddemann, "*Silane Coupling Agents*", Plenum Press, New York, (1991).
2. B.N. Eldridge, L.P. Buchwalter, C.A. Chess, M.J. Goldberg, R.D. Goldblatt, and F.P. Novak, in *Silanes and Other Coupling Agents*, K.L. Mittal (Ed.), pp. 305 – 321, VSP, Utrecht, The Netherlands, (1992).
3. M.R Horner, F.J. Boerio, and H.M. Clearfield, in *Silanes and Other Coupling Agents*, K.L. Mittal (Ed.), pp. 241 – 262, VSP, Utrecht, The Netherlands, (1992).
4. W.J. van Ooij, and A. Sabata, in *Silanes and Other Coupling Agents*, K.L. Mittal (Ed.), pp. 323 – 343, VSP, Utrecht, The Netherlands, (1992).
5. W.J. van Ooij and A. Sabata, *Surf. Interface Anal.*, **20**, 475, (1993).
6. W.J. van Ooij and A. Sabata, *Scand. J. Metall.*, **21**, 32, (1992).
7. J.S. Quinton, L. Thomsen and P.C. Dastoor, *Surf. Interface Anal.*, **25**, 931, (1997).
8. J.S. Quinton, P.C. Dastoor, and W. Allison, *Surf. Sci.*, **402 – 404**, 66, (1998).
9. J.S. Quinton and P.C. Dastoor, *Surf. Interface Anal.*, accepted for publication, (1999).
10. J.S. Quinton and P.C. Dastoor, *Mat. Sci. Lett.*, accepted for publication, (1999).
11. K.P. Battjes, A.M. Barolo and P. Dreyfuss, in *Silanes and Other Coupling Agents*, K.L. Mittal (Ed.), pp. 199 – 213, VSP, Utrecht, The Netherlands, (1992).
12. C.D. Wagner, W.M. Riggs, L.E. Davis, J.F. Moulder, and G.E. Muilenberg, *Handbook of X-ray Photoelectron Spectroscopy*, Perkin-Elmer Corporation, Physical Electronics Division, Minnesota, USA, (1979).
13. J.S. Quinton and P.C. Dastoor, *Surf. Interface Anal.*, submitted, (1999).

SESSION 6

Chair – Bill Trompetter

Environment

Production and analysis of hydroxyapatite from Australian corals via hydrothermal process

J. Hu*, J. Russell*, R. Vago**, and B. Ben-Nissan*

* Department of Chemistry, Materials and Forensic Science
University of Technology, Sydney, Broadway 2007, Australia
** Australian Institute of Marine Science, Townsville MC, Queensland 4810, Australia

Introduction

Since the 1970s it is well known that if a biocompatible ceramic prosthesis with appropriate interconnected pores is used, growth of hard and soft tissue into the surface pores will be observed. A very strong attachment and hence the resultant mechanical and chemical bond to the existing surrounding tissue will be produced.

Current artificial eyes although widely used encounter various problems due to the their motility and fail to deliver natural movement. They also cause sagging of the lids due to unsupported weight of the prosthesis. It is expected that application of a porous bioceramic such as the hydroxyapatite can generate good bonding to the tissue and hence a life-like eye movement [1].

Hydroxyapatite (HAp) and related calcium phosphates have been studied for many years as implant materials, due to their similarity with the mineral phase of bone. From the point of view of biocompatibility, HAp seems to be the most suitable ceramic material for tissue replacement implants. Hydroxyapatite ceramics do not exhibit any cytoxic effects. It shows excellent biocompatibility with hard and soft tissues. Moreover, HAp can directly bond to the bone [2].

Various preparation methods for HAp including the hydrothermal method have been used. The hydrothermal method was first used for hydroxyapatite formation directly from corals in 1974 by Roy and Linnehan [3]. Complete replacement of aragonite by phosphatic material was achieved under 270°C and 103MPa using the hydrothermal process. This process has the disadvantage that the hydrothermal treatment must be carried out at a relatively high temperature under very high pressure. In 1996, HAp derived from Indian coral using hydrothermal process was developed by Sivakumar *et al.* [4]. However, the resultant material was in the form of a powder.

Australia has rich variety of corals. Their application for implants have been studied very little. In this study, Australian corals selected were used for hydroxyapatite conversion. A new hydrothermal process of hydroxyapatite formation has been developed. Systematic characterisation of various coral species and converted hydroxyapatite has also been carried out.

This paper represents a comparison of the physical properties of Australian coral before and after hydrothermal conversion to hydroxyapatite (HAp). In the present study an improved hydrothermal process has been developed which produces a HAp material having greater strength. This enables the resultant material to be shaped after conversion. Hydroxyapatite produced from corals has applications to many types of implants.

Materials and Methods

The coral, similar to the genus Goniopora, was obtained from the Australian Great Barrier Reef. It was shaped into the form of a block or sphere and prepared according to the hydrothermal method used by Roy and Linnehan [3].

The coral was studied before heat treatment, after heat treatment and after hydrothermal conversion. A number of characterisation techniques including Fourier transform infrared spectroscopy (FTIR), nuclear magnetic resonance (NMR), X-ray diffraction (XRD), scanning electron microscopy (SEM) and thermogravimetric and differential thermal analysis (TGA/DTA) were used. Infrared spectra were recorded on a BIO-RAD FTS-7 Fourier transform spectrophotometer. Samples were mounted on KBr discs and were routinely recorded using a resolution of $2cm^{-1}$ and 64 scans. ^{31}P NMR solid-state spectra were recorded on a Bruker MAS-300 spectrometer operating at 121.49MHz. The reference used was external 85% H_3PO_4. The morphology of the coral was studied using a JEOL 6300F FEG SEM operated at 8kV. The phase composition of the coral and heated samples were examined by X-ray diffraction (XRD) using the Siemens D-5000 (Karlsruhe, Germany), employing graphite-monochromated Cu-Kα radiation. The XRD scan was from 2 Theta = 20.000 to 60.000 in 0.020 steps with a step time of 2.0s. Thermogravimetric and differential analyses were performed on a TA Instruments SDT 2960 Simultaneous DTA-TGA at a heating rate of 10°C/min.

Results and Discussion

The IR spectra of the coralline hydroxyapatite showed absorption bands P-O at 1091, 1060sh, 964, 602, 564 and $476cm^{-1}$, and at 358 and $636cm^{-1}$ are indicative of the O-H functional group.

Solid ^{31}P NMR spectrum of the coralline hydroxyapatite exhibited one single peak at 2.89ppm relative to 85% H_3PO_4, indicating the absence of any impurities.

The products after hydrothermal process were identified by powder X-ray diffraction to be single phase of hydroxyapatite (JCPDS 9-0432). The XRD pattern of converted hydroxyapatite demonstrated high crystallinity. No peaks corresponding to $CaCO_3$ or CaO were found (Figure 1).

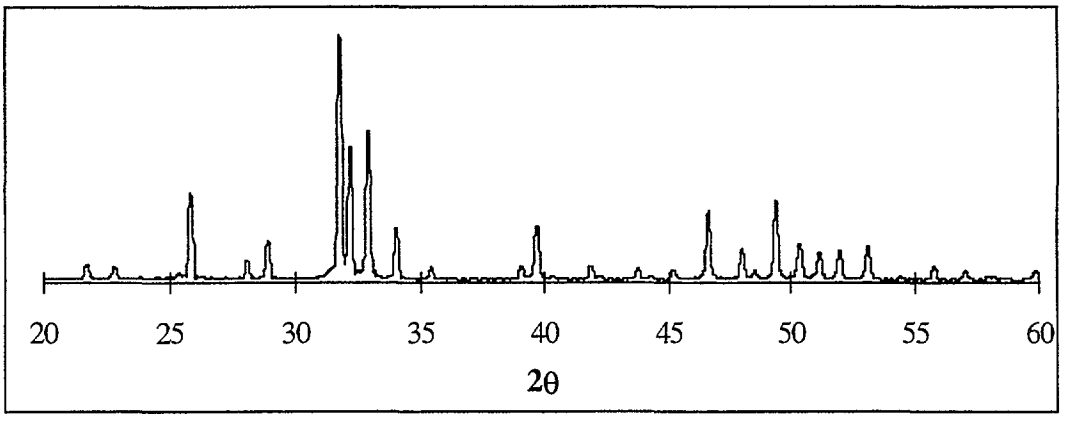

Figure 1. XRD pattern of a coralline hydroxyapatite.

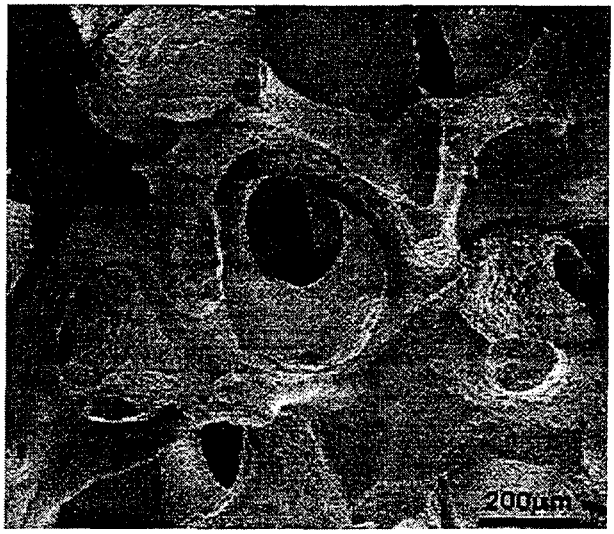

Figure 2: SEM image of Australian coral after hydrothermal conversion.

The morphology of the coral before and after conversion was studied using SEM. An SEM image of Australian coral after conversion is given in Figure 2. The pores in the structure were found to increase in size after hydrothermal conversion. Even with the increased pore size the interconnecting material is substantial enough to maintain the strength of the coral.

Thermal analysis was used to further characterise hydroxyapatite formation from coral. The weight loss of the product at 1000°C was observed as only 1.4%. This indicates that the hydroxyapatite product converted from Australian coral under hydrothermal treatment has a low concentration of impurities.

Conclusion

This work has demonstrated that under a controlled hydrothermal exchange, strong and porous coralline hydroxyapatite from Australian coral can be produced at relatively low pressure. The hydroxyapatite obtained retains the structure and strength of coral.

Acknowledgments

The authors would like to thank Mr. D. Green of UTS for assistance in XRD and NMR and the Microstructural Analysis Unit at UTS for use of XRD and SEM equipment. Funding provided by the UTS internal grants scheme is also gratefully acknowledged.

References

1. E. White and C. Shors, *Dental Clinics of North America*, **30** (1986) 49.
2. K. De Groot, Degradable Ceramics, in Biocompatibility of Clinical Implant Materials, Vol. 1, D. F. Williams, ED., CRC Press, Boca Raton, FL, (1984) 199.
3. D. M. Roy and S. K. Linnehan, *Nature*, **247** (1974) 220.
4. M. Sivakumar, T. S. Sampath Kumar, K. L. Shantha, K. Panduranga Rao, *Biomaterials*, **17** (1996) 1709.

IBA and synchrotron methods for sub-micron fine particle characterisation

David D. Cohen[a], Rainer Siegele[a], Anton Stampfl[a], Z. Cai[b], P. Ilinski[b], W. Rodrigues[b], D.G. Legnini[b], W. Yun[b], B. Lai[b].

[a]Physics Division, ANSTO, Private Mail Bag 1, Menai, NSW, Australia, 2234.
[b] Experimental Facilities Division, APS, Argonne National Lab, Argonne, IL, USA

Introduction

Fine air-borne particles, whose average diameters are 2.5 μm and less (PM2.5), are known to play significant roles in a number of human and environmental issues. They may penetrate deep into the human lung system and are believed, due to their small size or due to toxins adsorbed onto their surfaces, to be responsible for up to 60,000 and 10,000 deaths in the U.S. and U.K. respectively [1,2]. Health studies within NSW, Australia carried out by the NSW EPA, have shown increased hospital admissions and excess deaths related to high fine particle pollution episodes.

A number of environmental issues are affected by the amount and type of fine-particles in the air. The white and brown hazes that occur in populated cities causing poor visibility are due to light scattering from fine particles. These same particles are easily transported large distances in the lower atmosphere playing a key role in global pollution and climate forcing [3].

Current knowledge of fine-particle concentrations and constituents is very limited. Sources of fine particles are both natural and man-made. Over the past few years considerable work on the characterisation of these particles has been going on at ANSTO using accelerator based ion beam analysis (IBA) methods [4-6]. X-ray fluorescence using ion beams from accelerators and synchrotron fluorescence are complementary techniques. This is well demonstrated by the plot of figure 1. PIXE has higher cross sections for low Z elements, but for high Z elements closer to the excitation energy (16keV) synchrotron radiation cross sections are larger. Both techniques are multi-elemental analysis techniques.

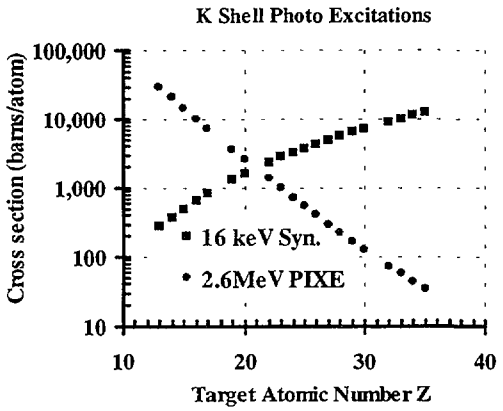

Figure 1. Comparison of ionisation cross sections for 2.6MeV PIXE (circles) and 16keV Synchrotron excitation (squares) against trace element atomic number Z.

Synchrotron induced X-ray emission has three distinct advantages over other more conventional multi-elemental methods such as XRF and PIXE. These include (i) very high brightness source with low emittance, which makes for high sensitivity for elements close to the excitation energy, (ii) an ability to tune the excitation energy from a few keV to tens of keV, thus spanning a large fraction of the period table for trace element analysis, and (iii) the ability to focus down to spot sizes of the order of 0.1μm diameter with sufficient intensity to perform real time analyses. For our particle sizes (0.1-2.5μm) this was critical.

The experiment reported here uses all three of these major assets of synchrotron radiation and utilises the previous PIXE analyses to make the synchrotron results quantitative.

The Experiment

Hundreds of fine particle (PM2.5) samples were collected on 25mm stretched Teflon filters from in the Sydney Basin and around coal fired power stations producing power for the Sydney region. All filters were analysed by simultaneous IBA methods for most of the commonly occurring elements including H, C, N, O, F, Na, Al, Si, P, S, Cl, K, Ca, Ti, V, Cr, Mn, Fe, Co, Ni, Cu, Zn, Br and Pb at concentrations down to 1 ng/m^3 of air sampled [4-6]. Typically, filter sampling areas were 2.27cm^2 and sampling volumes were 32 m^3 over the 24 hour period so a concentration of 1ng.m^{-3} of air sampled corresponded to only 14ng.cm^{-2} of material on the filter itself.

Of the 24 or so elements analysed by IBA methods some key elements related to significant fine particle sources were not present. Coal burning produces elemental carbon and sulfur but these elements are also produced by other sources such as motor vehicles, particularly diesel driven vehicles. So to distinguish coal sources from motor vehicles sources we need to included other characteristic tracer like Se and As, however for PIXE analysis these are completely swamped by Br and Pb from petrol driven motor vehicles. Typically the Pb and Br concentrations are 50 to 100 times larger than the As and Se concentrations measured in the Sydney region. By appropriate tuning of the synchrotron excitation energy this problem can be overcome.

Broad Beam Tuned Excitations

The broad beam synchrotron studies were carried out using an 8 x 3mm beam with run times between 300 and 500 seconds for each Teflon filter sample. Two beam excitation energies, one at 13.5keV, above the Pb and Br absorption edges, and one at 12.9keV below the Pb and Br absorption edges, but above the As and Se edges were required to separate the As and Se from coal burning from the higher concentrations of Pb and Br from motor vehicles. Figures 2 and 3 show X-ray spectra for these two situations for a 24 hour sample on the same Teflon filter acquired at the Richmond site in the Sydney Basin on 9 March 1999. Each spectrum has been background subtracted and contains two curves, the original data and a gaussian peak fit to this data.

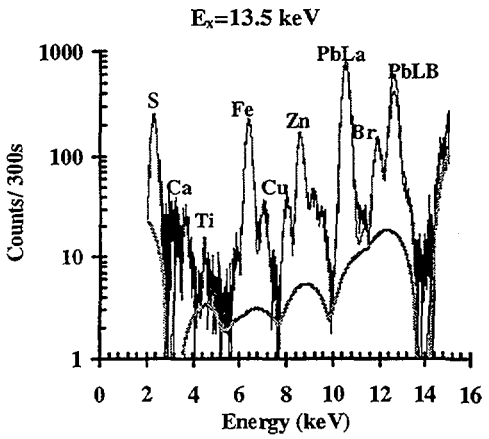

Figure 2 A typical fitted PIXE spectrum for synchrotron excitation energy E_x=13.5keV.

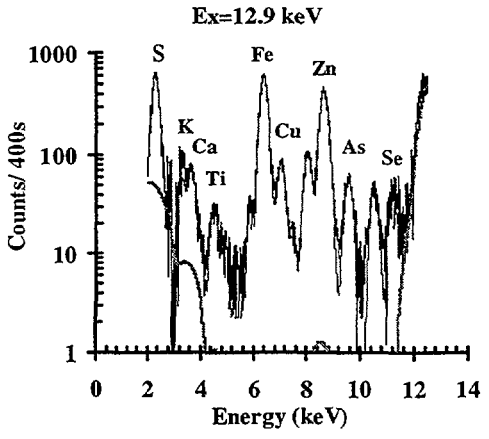

Figure 3 A typical fitted PIXE spectrum for synchrotron excitation energy E_x=12.9keV.

For figure 2 with E_x=13.5keV the excitation energy is above the Pb and Br edges and these trace elements at concentrations of 100 and 50ng.m^{-3} are clearly seen. Peaks corresponding to

As (under Pb) and Se (under Br) are too small to be observed. However, for E_x=12.9keV, figure 3, which is above the As and Se K edges but below the Pb and Br edges we see that the contributions from Pb and Br are reduced to zero and that As and Se peaks are considerably enhanced since the excitation energy is even closer to their K edges. The As and Se concentrations correspond to values below 1ng.m^{-3}, that is about two orders of magnitude below the Pb and Br concentrations in the same sample.

Over 230 filters were run under similar conditions. These represented samples for a full 12 months from one of the coal-fired power stations at Muswellbrook and selected months from one site in the Sydney basin at Richmond. All these filters had previously been analysed by IBA methods for the absolute concentrations of the 24 or so elements mentioned above. So it was possible to use these results to determine a conversion factor to provided absolute concentrations for all the synchrotron results similar to those of figures 2 and 3. Figure 4 shows the synchrotron counts/ ngm^{-3}/ sec for trace elements with a given characteristic X-ray energy for a synchrotron excitation energy of E_x=12.9keV. A similar plot was obtained for the 13.5keV excitation data. These data were obtained by comparing PIXE concentrations for major trace elements like S, Fe, Zn, Pb and Br shown in Figs 2 and 3, for hundreds of filters, with the measured synchrotron yields. A polynomial fit to the data allowed interpolation and extrapolation to estimate the concentration of elements measured by synchrotron excitation over the characteristic X-ray energy range from 2 to 12keV. This included all elements from sulfur to selenium. As with figure 1 we see that the synchrotron yield of figure 4 falls off rapidly as one moves away from the excitation energy. The sulfur peaks in Figs 2 and 3 only appear larger

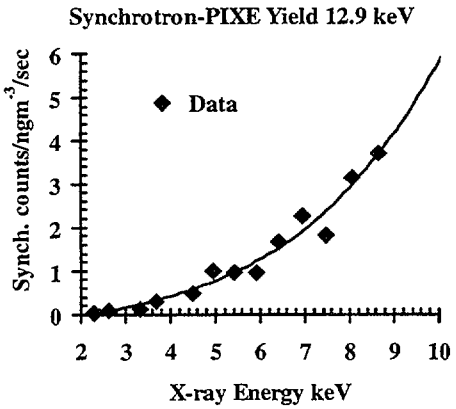

Figure 4. Calibration plot for E_x=12.9keV for synchrotron counts/ ng.m^{-3}.s^{-1} for a given trace element X-ray energy.

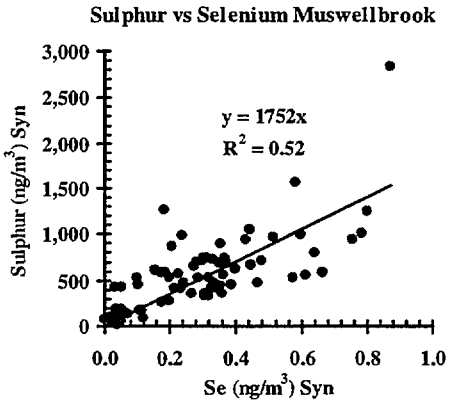

Figure 5. A plot of Sulfur versus Selenium concentrations for filters affected by a coal-fired power station near Muswellbrook, NSW.

relative to the other trace elements because of the higher sulfur concentrations (3,000ng.m^{-3}) found in these fine particle samples. This again demonstrates the complementarity of PIXE and synchrotron methods. Use of curves like figure 4 allow concentration estimates for trace elements like As and Se not previously seen by IBA methods. For the 230 filters measured at the APS the average As and Se concentrations were (0.4±0.4)ng/m^3 and (0.3±0.4)ng.m^{-3} respectively. If Se and As originate from

coal burning then these elements should correlate with sulfur also present in coal. Figure 5 is a plot of the sulfur versus selenium concentrations for a full year at Muswellbrook site in NSW which was influenced by coal combustion from near by power stations. The plot shows a reasonable sulfur-selenium correlation (R^2=0.52) over the full selenium concentration range from 0 to 1ng.m^{-3}. This is a strong suggestion that sulfur and selenium originate from the same source at this site during the study period. This plot could not have been obtained by

conventional X-ray (IBA, XRF) methods. Figure 5 not only demonstrates the association between these two key elements but

also provides us with a quantitative relationship, namely [S/Se]= (1752±350), which can be used in source fingerprinting estimates [5,6] at other sites affected by coal combustion.

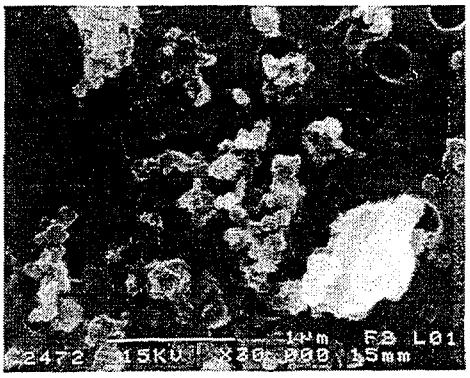

Figure 6. Scanning electron micrograph (SEM) of typical fine particles (PM2.5). Mag 30,000x.

Focused Beam Excitations

The principles described above for broad beam synchrotron excitations are directly applicable to focused sub-microbeam studies. The high brightness allows the X-ray beam to be focused to less than 0.2 x 0.2μm spot sizes. Scanning electron micrographs (SEM) of typical fine particle filters show two distinct groups of particles are generally collected. Namely, fine particles, with diameters much less than 1 μm, from combustion sources such as motor vehicles and power stations, and coarser particles, much greater than 1 μm in diameter, from mechanical sources such as windblown dust and seaspray. This is clearly shown in the SEM of figure 6 of PM2.5 particles, where, over an area of approximately 3 x 4μm you see a large soil particle in the bottom right with many other fine combustion particles with diameters between 0.1 and 0.2μm. Similar areas and particles can be scanned at the SRI-CAT facility at the APS. The advantage being that the X-ray beam energy can be tuned, as with the broad beam studies to only include trace elements of interest. Figures 7 and 8 show sub-microbeam scans over similar areas to that of figure 6 for the elements S and Pb at the two different excitation energies, 12.9keV and 13.5keV. Each scan took 6 hours using a beam spot size of about 0.2 x 0.2μm scanned over 3.2 x 3.2μm. Full energy X-ray spectra were obtained for 100 seconds at each of 256 pixels in each scan and can be further analysed off line for all the elements shown in figures 2 and 3.

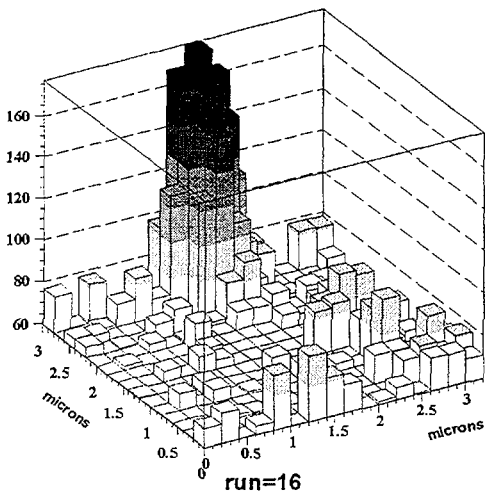

Figure 7. A typical 3D spectrum with a 0.2x0.2 μm spot size for S for E_x=12.9keV.

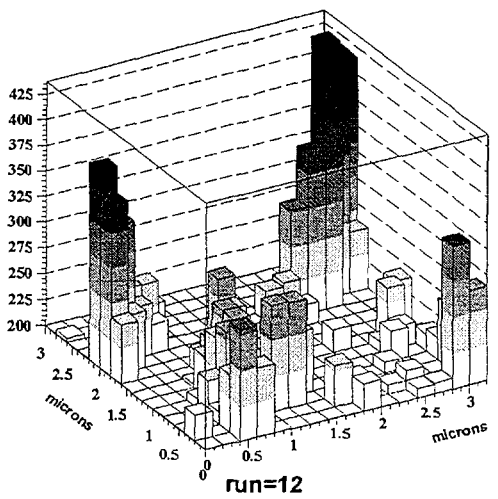

Figure 8. A typical 3D spectrum with a 0.2x0.2 μm spot size for Pb for E_x=13.5keV.

Summary

This paper describes some preliminary synchrotron X-ray microbeam studies which yielded many new results regarding the elemental and spatial character of atmospheric fine particles and compares them with the PIXE results previously obtained at ANSTO. Absolute elemental concentrations were obtained for elements not seen by PIXE and for elements within sub-micron particles. The SRI-CAT facility at the APS, in Chicago, clearly has the brightness and hence the sensitivity to detect trace elements of interest, not detected by other X-ray methods, in a few minutes of running even for submicron beam spot sizes on individual particles. Furthermore, the ability of the beam energy to be finely tuned to excluded elements above selected K edges provides a unique opportunity to overcome some adjacent element interferences present in other techniques.

Acknowledgements

We would like to acknowledge funding from the Australian Synchrotron Research Program which allowed DDC and RS to perform these experiments at the APS, Argonne Labs, Chicago. We also thank, G. Bailey, P. Johnston, D. Garton, E. Stelcer, A. Croal for assistance in the PIXE data analysis and for operating the 3MV Van de Graaff accelerator throughout many aspects this work.

References

[1] D. W. Dockery, C. A. Pope, X. Xu, J. D. Spengler, J.H. Ware, M. E. Fay, B. G. Ferris, F.E. Speizer, New England Journal of Medicine, 329 (1993) 1753-59.

[2] C. A. Pope, J. Schwartz and M. Ransom, Arch. of Environ. Health, 47 (1992) 211-217.

[3] Climate Change 1995; The Science of Climate Change, Report of Working Group I to the Intergovernmental Panel on Climate Change, IPCC-XI, Rome, 11-15 December 1995.

[4] D. D. Cohen, Nucl. Instr. and Meth., B79 (1993) 385-388.

[5] D.D. Cohen, , G. M. Bailey and R. Kondepudi, Nucl. Instru. and Methods, B109 (1996) 218-226.

[6] D.D. Cohen, Nucl. Instru. and Methods, B136(1998)14.

Trace elements associated with atmospheric particulate matter in the upper Hunter Valley – a preliminary study

Gordon D. McOrist
Environmental Radiochemistry Group, Environment Division, ANSTO, PMB 1, Menai, 2234.

Karabi Farhana
Dept. of Geography and Environmental Science, University of Newcastle, Callaghan, 2308.

Summary

The concentration of trace elements associated with airborne particulate matter in the Upper Hunter Valley in NSW was studied. This preliminary study, which took place in early in 1999, analysed air filter and soil samples from 5 sampling sites in close proximity to the Bayswater Colliery Company (results from only two of the sites were considered here).

Objectives included measuring relative amounts of particulate during this period, identifying associated trace elements and possibly identifying their source. (Is visible particulate "fallout" on certain surfaces of nearby homesteads associated activities at the nearby colliery?)

Results from this study indicate that there was no clear indication that particulate "fallout" was associated with colliery activities. Although some interesting data relating to total TSP and PM_{10} particulate and associated trace elements was obtained, more work is needed.

Introduction

Airborne particulate matter is one of the most important constituents of the atmosphere. Particulate pollutants consist of finely divided solids or liquids such as smoke, dust, fumes, mist, fog, smog and sprays [1]. Natural processes injecting particulate matter into the atmosphere include volcanic eruptions, wind blown dust and soil and spray from marine source [2]. Anthropogenic (man-made) sources include power plant emissions and activities associated with mining.

Airborne particulate matter usually consists of discrete particles ranging in size from molecular clusters of 0.005μm to coarse particles in the order of 100μm. This particulate matter may vary in chemical and physical properties (time, region, meteorology, source). It usually adversely affects climate, visibility, vegetation, human and animal health.

The Hunter Valley is located 200km northwest of Sydney, between Singleton and Scone, in New South Wales. Within this region, the Muswellbrook shire is embraced by large and diverse agricultural activities, power generation and open cut mining operations. Airborne particulate matter has been previously identified as a potential problem within this region.

A preliminary study was commenced that would evaluate, among other things –

- The total concentration of TSP (total suspended particulate) and PM_{10} (particulate matter of < 10μm aerodynamic diameter).
- Determining the atmospheric concentrations of some of the trace elements associated with airborne particulate.
- Identifying the potential sources of these trace elements.

(As a result of this preliminary study, a large amount of data was collected and comprehensively evaluated by the co-author [3]. For logistical reasons results from only two of the sites will be considered here).

Experimental

The two sites chosen were Windmill ("down wind" from Bayswater Colliery during the sampling period) and Edderton (the only upwind site – the "baseline" site).

TSP and PM_{10} air filter samples were taken at each site for 48 hours (a weekend when no mining operations took place) followed by 4 approximately 21-hour consecutive samples at each site (during normal colliery working hours). The trace element distribution for filters from the same site for the 5 periods were studied. Filters from the same sampling period at each site were also compared.

Soil samples were taken from the surface at each site (following a significant period without rain) and at a depth of 10-20cm (supposedly uncontaminated by air particulate) at the same location. A number of samples of overburden material were also taken at the colliery. The trace elements in each sample were determined in order to establish any possible relationship between overburden and particulate.

Filter samples (6 x 2cm cut from each filter) and standard reference material (NBS 1632a coal) were placed in a clean polythene bags, irradiated in HIFAR for 9hrs at a thermal flux of $5 \times 10^{12} ncm^{-2}s^{-1}$ and counted after 7 and 28 days decay.

Soil samples were dried, homogenised and, along with standard reference material (NBS 1633a fly ash), weighed into cleaned polythene containers. All were irradiated in HIFAR for 1 min at a thermal flux of $1.7 \times 10^{12} ncm^{-2}s^{-1}$ and counted after 20 min and 24 hrs decay. Samples and standards were then irradiated in HIFAR for 9hrs at a thermal flux of $5 \times 10^{12} ncm^{-2}s^{-1}$ and counted after 7 and 28 days decay.

Results and Discussion

Fifteen trace elements, Sc, Cr, Fe, Co, Zn, Br, Cs, Ba, La, Ce, Nd, Hf, Ce, Th and U were analysed in most soil and/or filter samples allowing a reasonable degree of comparison within analysis error. The trace element data for filters can be found in Tables 1 and 2. Results for soil samples are summarised in Table 3.

Filter results

The overall results for trace elements on filters were less than conclusive for a number of reasons. The glass fibre filters used (already being routinely used by mining and university staff before our trial commenced) had quite high and variable levels of impurities. When blank filter data was subtracted zero or negative results occurred. The filters were also high in Na that did not allow many important short half-life elements to be determined. Due to other time constraints the filters could not be changed (although this will be avoidable with a more comprehensive future study).

Although visually the total amount of particulate on both TSP and PM_{10} filters sampled at Edderton (reference site) was less than those from Windmill (down wind site), the trace element data in general showed few significant differences (Tables 1 and 2). It was assumed that the concentration of trace elements on filters at Windmill over the weekend (when no mining activities took place) would be noticeably lower than weekday results. However, from Table 2 it can be seen that, with the exception of Sc and Br in PM_{10} at Windmill, all trace element results for the two sites were similar for the same periods.

Table 1: Concentration ($ng.m^{-3}$) of trace elements in TSP (and PM_{10}) at Edderton

Element	w/e 30/1/99	18/2/99	22/2/99	23/2/99	25/2/99
Sc	0.14 (0.11)	0.19 (0.25)	0.56 (0.51)	0.40 (0.23)	0.30
Cr	14 (11)	13 (18)	11 (10)	nd	9.0
Fe	3600 (3600)	2200 (4800)	4600 (3300)	nd	900
Co	1.8 (1.9)	1.1 (2.6)	2.4 (1.5)	0.5	0.3
Zn	40 (37)	43 (48)	22 (18)	nd	36
Br	2.8 (9.2)	8.9 (9.2)	4.1 (4.8)	nd	9.0
Cs	0.36 (0.31)	0.64 (nd)	0.61 (0.58)	Nd (0.44)	0.63
Ce	1.1 (0.11)	1.1 (0.8)	2.7 (1.3)	nd	0.9
Hf	2.7 (2.3)	2.7 (2.8)	1.2 (1.3)	nd	2.1
Th	0.11 (0.11)	nd (0.3)	0.5 (0.3)	nd	nd

Table 2: Concentration ($ng.m^{-3}$) of trace elements in TSP (and PM_{10}) at Windmill

Element	w/e 30/1/99	18/2/99	22/2/99	23/2/99	25/2/99
Sc	0.08 (0.29)	0.19 (1.2)	0.29 (1.2)	0.21 (1.5)	nd (0.66)
Cr	11 (10)	15 (13)	15 (13)	9.0 (7.9)	14 (13)
Fe	1900 (2400)	2100 (3700)	3100 (2100)	Nd (1000)	2400 (3400)
Co	1.0 (1.2)	1.3 (1.9)	1.9 (1.8)	0.5 (0.5)	1.3 (1.9)
Zn	28 (28)	16 (15)	41 (38)	nd (nd)	34 (33)
Br	5.9 (12)	5.1 (16)	4.5 (nd)	nd (12)	2.2 (16)
Cs	nd (nd)	0.3 (0.25)	0.3 (nd)	0.3 (nd)	nd (nd)
Ce	1.5 (0.8)	1.1 (1.0)	2.4 (2.3)	nd	0.3 (0.3)
Hf	1.9 (1.9)	1.3 (1.3)	2.9 (2.8)	nd	1.9 (1.8)
Th	0.11 (0.11)	0.26 (0.3)	0.29 (0.3)	nd	nd

Soil results

It was assumed that the particulate "fallout" observed at most of the downwind sampling sites was associated with as a result of mining activities at the nearby colliery and would also settle on top of nearby soil. Since there had been no rain immediately before or during the sampling period, the top soil at Windmill *should* have trace elements similar in concentration to mine site overburden and probably at elevated levels when compared with samples taken 10cm or so below the surface. [It is important to note that trace element results for air filters and soil samples cannot be directly related due to differences in enrichment factors].

From Table 3 it can be clearly seen that results for Cr, Fe, Co, As and Zn in overburden are significantly lower than either Edderton (upwind) or Windmill downwind) soils with all other results similar. It is therefore reasonable to suggest that activities at the colliery are not the source of so-called particulate fallout and are more likely a result of emissions (stack or fly ash dams) from the nearby Bayswater and Liddell power stations.

Table 3: Trace element data for soils

Element	Edderton top soil		Windmill top soil		Windmill 10cm soil		Mine site Overburden*	
	µg/g	error	µg/g	error	µg/g	error	µg/g	error
Sc	16	1	11	1	14	1	14	1
Cr	180	10	130	10	150	10	56	3
Fe	43000	1000	35000	1000	45000	1000	29000	1000
Co	19	1	17	1	24	1	13	1
Zn	90	10	140	10	90	10	72	16
As	8.4	2.3	6.9	1.7	7.4	1.1	6.2	1.3
Br	23	3	18	3	17	1	-	
Cs	6.9	0.6	4.7	0.6	5.5	0.5	5.2	0.6
Ba	250	110	450	60	550	80	490	90
La	32	1	24	1	28	1	28	1
Ce	67	2	50	2	60	2	57	2
Sm	6.0	0.8	4.4	0.6	4.9	0.6	5.0	0.6
Eu	1.4	0.1	1.1	0.1	1.3	0.1	1.2	0.1
Dy	5	1	2.7	0.5	4.2	0.5	4.3	0.5
Yb	3.4	0.2	2.5	0.1	2.6	0.1	2.8	0.2
Th	10	1	7.5	0.2	8.4	0.3	9.0	0.3
U	2.2	0.9	1.8	0.7	2.3	0.9	2.7	1.2

Note: * Mean result for overburden, 1st and 2nd strip.

Conclusion

Although a significant amount of particulate (both TSP and PM_{10}) was observed on filters taken at the "downwind" site at Windmill, the source of this particulate could not be confidently determined. When compared with the Edderton site and with weekend data, only Sc and Br were noticeably higher. Analysis of samples of overburden and soil from site indicated that the colliery was unlikely to be associated with particulate fallout observed.

References

[1] Dara S.S., "A Textbook of Environmental Chemistry and Pollution Control", Chand and Co., New Delhi, 1995.

[2] De A.K., "Environmental Chemistry", Wiley Eastern Ltd, New Delhi, 1993.

[3] Farhana B.K., "Atmospheric Particulate Concentration and Trace Element Chemistry in the Upper Hunter Valley, NSW (Thesis accepted for publication in Water, Air and Soil Pollution)

Applications of nuclear tracer techniques in coastal zone process studies

Ron Szymczak

Australian Nuclear Science & Technology Organisation, PMB 1, Menai, NSW 2234 Australia

Introduction

Radioactivity is a natural part of the environment, arising mainly from primordial elements such as uranium and thorium and their daughter products, and those being constantly produced in the atmosphere by interactions with solar radiation. Of the more than 5000 nuclides (atoms) recognised by science today about 95% are radioactive [1] and scientists can use these natural radioactive atoms to study environmental processes and thereby gain a better understanding of the world we live in. Some of the earliest applications of radioisotopes as tracers of environmental processes were carried out by workers from Harwell (UK) approximately 40 years ago to study the fate of dredge spoil in the Thames River estuary. Developments since that time have been such that today highly accurate and specific information on physical, chemical and biological processes in rivers, estuaries and coastal environments may be obtained, often in real time, by selection of a proxy isotope with the appropriate properties. Radiotracers may be naturally occurring isotopes characteristic of the particular process under investigation, artificial isotopes introduced as analogues of natural products, or artificial labels on substances retrieved from nature.

Physical Processes

Sand Mobility Studies - Sand movements on the continental shelf, along or offshore beaches, within estuaries and river systems have been characterised using radiotracers [2]. Briefly, the technique involves the preparation of the labelled material, its injection and subsequent monitoring. Investigations may extend from a few days to over a year depending on the coastal process of interest. Particular isotopes are chosen to suit the duration of the investigation including; ^{198}Au (useful life 2 weeks), ^{51}Cr (4 months), ^{192}Ir (8 months), ^{46}Sc (9 months) and ^{110m}Ag (>1 year). The isotope is either adsorbed onto the surface of the natural material or incorporated into glass and ground and sieved to match the particle size distributions of the natural material. The radioactively labelled material is released used remote handling techniques and monitored on the sea bed with calibrated probes attached to a sled or other device to ensure reproducible geometry [2]. Quantitative estimates of the rate of bed load transport can be made.

Offshore sewage dispersion studies - An extensive evaluation of the deep water ocean outfalls at Malabar (NSW) has been undertaken for the NSWEPA by ANSTO in collaboration with UNSW-WRL (formally AWACS) [3]. Tracer radioisotopes were typically metered in to the sewage flow at the Sydney Water Corporation's Malabar Treatment Plant over a three hour period. The dilution of sewage is monitored at the diffusers, located at a depth of 80m and 4km out to sea, and its fate then studied over the next several hours to days. Depending on the local current and oceanographic conditions, the sewage was traced to either rise to the surface or remain trapped at depth and/or migrate northward or southward along the NSW coast [3]. Two isotopes are normally used for these studies, tritium (^{3}H) and gold (^{198}Au). The gamma emitting ^{198}Au can be measured in situ with submersible probes. The information is combined with accurate positioning and depth data to provide a 3 dimensional picture of the dispersing plume. Also, separate isotope labels may be placed on distinct plume components, such as tritium (^{3}H) for the aqueous or dissolved phase, chromium (^{51}Cr) for particulate material and gold (^{198}Au) for the grease component [4]. Water samples are typically collected within the

plume for subsequent chemical, radiochemical and microbiological analyses at the laboratory. The transport and dispersal data were used for the validation of the mathematical models for offshore sewage flow developed by AWACS.

Chemical Processes

The in situ behaviour of manganese has been studied in detail (Figure 1) utilising an artificial isotope (^{54}Mn) to follow chemical behaviour at extremely low concentrations, typical of natural levels [5]. Along with iron, this element is an important chemical scavenger in the ocean and thereby influences the geochemistry of several other trace metals [6]. Briefly, ferromanganous and organic coatings on marine particles provide sites for adsorption and complexation of dissolved trace metals and in general terms, marine particles grow through accumulation of successive layers of these oxyhydroxide precipitates with surface-bound organic and inorganic species. Once formed, particles may remain in suspension as small colloids, aggregate or associate with other particles until their density is such that they fall vertically through the water column [7]. These chemical processes account for, in part, the removal of trace metals from surface waters to sea floor sediments.

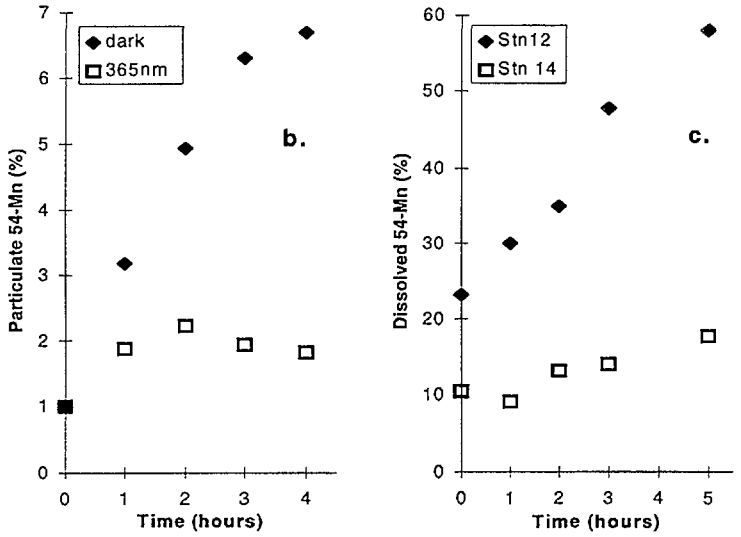

Figure 1. Results of experiments of (a) ^{54}Mn particle formation, and (b) 365nm light photolysis on ^{54}Mn particle formation and (c) particulate ^{54}Mn dissolution on 365nm photolysis, modified from [5].

Further understanding of ocean particle scavenging processes has developed through studies of naturally occurring radionuclides as tracers. Particularly suited to studies of chemical scavenging in marine systems is the observed disequilibrium in ^{234}Th/^{238}U activities. ^{234}Th, a daughter isotope of ^{238}U with a half-life of 24.1 days, provides a mechanism to trace processes with temporal ranges of days to months. The activity of this tracer (Figure 2a) has been applied to determine the residence times of particles in seawater (Figure 2b) and interpret the behaviour of several dissolved trace elements (Figure 3). The residence times (τ) of suspended marine particles is calculated from measurements of the ^{234}Th/^{238}U activity ratio using the following equation [7];

$$\tau = \tau_m \times R / (1-R) \qquad (1)$$

where τ_m is the mean-life of ^{234}Th (1/decay constant = 34.8 days), and R is the ^{234}Th/^{238}U activity ratio. ^{234}U activity is relatively constant at 2.41dpm/L. Removal Rates (Ψ) are the inverse of τ.

Residence times (Figure 2b) deduced for suspended particles in Australian coastal waters varied considerably (0.66 - 9.2 days for particles >10μm and 4.2 - 23.4 days when all particles

>0.5μm were considered) over a period of five consecutive days [8]. Dissolved residence times ranged from 30 to 64 days [8]. At each sample site the residence time of dissolved ^{234}Th was much longer than that of particulate ^{234}Th implying the rate of uptake is much slower than the rate of removal and limits the ultimate scavenging of ^{234}Th from the water column. These results are comparable to data from the North Atlantic [9], rather than coastal and shelf systems [7] reflecting the extremely oligotrophic nature of tropical northern Australian coastal waters.

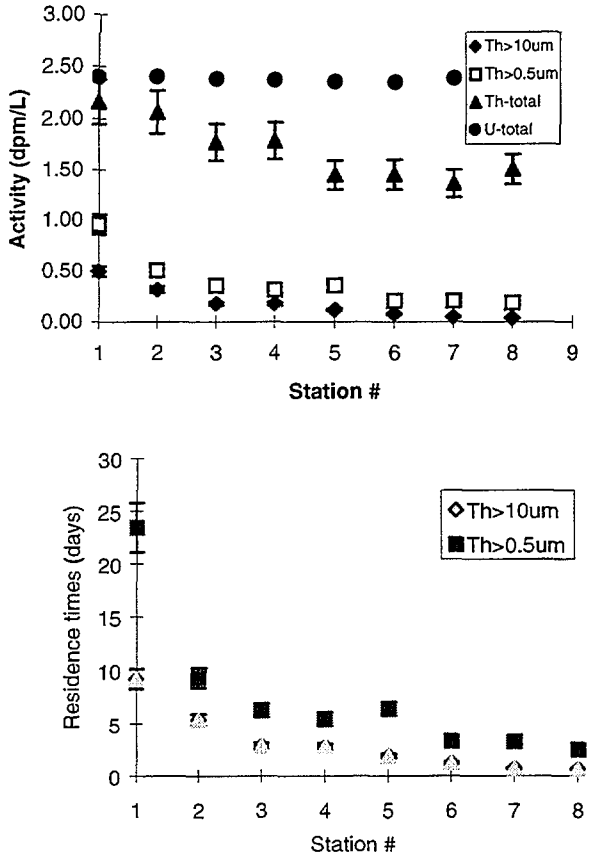

Figure 2. (a) Gamma activities of ^{234}Th in Total, >10μm and >0.5μm particulate size fractions and (b) dissolved trace element concentrations relative to Particle Removal (Flux) rates [12].

The concentrations of dissolved trace metals in samples corresponding to ^{234}Th sites (Figure 3) varied from values typical of urbanised coastal and shelf waters to very low values typical of open ocean systems [10]. All metals analysed decreased in concentration in synchrony with observations of decreasing particulate ^{234}Th residence times, however, differences in scavenging efficiency and possibly mechanisms were evident. Dissolved Cr, Ni and Pb were removed at a relatively constant rate (Figure 3a), while for Co, Mn and Cd an initial period of rapid removal was observed, followed by a considerably reduced removal rate (Figure 3b).

Many coastal water bodies are impacted by human activities, and despite recent advances in surface and solution chemistry, it is still not possible to deduce residence times for trace metals in seawater from model calculations. It is therefore important to assess the chemical residence times, or "self cleansing ability" of these waters according to the nature of discharges and in situ biogeochemical scavenging processes. These processes allow natural water bodies to cope with some level of disturbance, however, if the rate of chemical discharges exceeds the rate of removal, deleterious impacts may occur. Radiotracer techniques can quantify this balance.

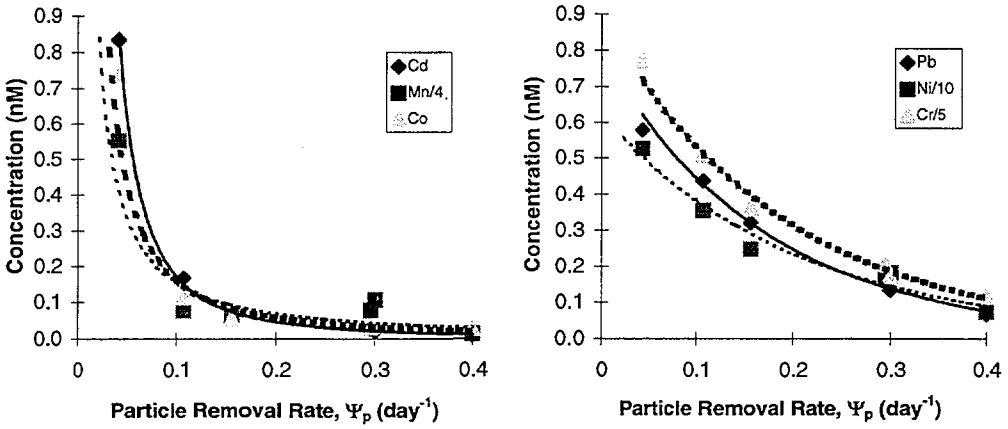

Figure 3. Dissolved trace element conc. as a function of the Particle Removal Rate (ψ_p), from [14].

Conclusions

Nuclear techniques have a wide utility in coastal zone studies. Applications include studies of the offshore dispersal of sewage, the migration of sand and sediment, and processes important to the biogeochemical cycling of elements in the marine environment. They are particularly suited to elucidation of the compartmentalisation and rates of processes, both presently occurring and in past times. Many studies are designed to contribute to the scientific basis, or development of engineering concepts, for sustainable development in coastal regions where population densities are high and there are potential conflicts in the exploitation of resources. Other studies are aimed at developing an understanding of specific interactions within coastal ecosystems and the rates at which these processes occur. These radiotracer techniques provide a mechanism of fine tuning concepts and equations (models) in order to achieve a balance between man's activities and his impact on the environment.

References

[1] Baxter, M.S. (1993) Environmental radioactivity: A perspective on industrial contributions, *International Atomic Energy Agency Bulletin,* 2, 33-38.

[2] Davison, A., Szymczak, R. and Cox, R. (1995) *Report to the International Atomic Energy Agency on IAEA/RCA Seminar (Colombo Dec '94) - Applications of Nuclear Techniques to Coastal Engineering RAS/8/069-08 Isotopes and Radiation in Industry and the Environment,* ANSTO Report # C465.

[4] Davison, A., Easey, J.F. and Seatonberry, B.W. (1981) Radioisotope studies on the paradox in dispersion and agglomeration of sewage greases discharged from ocean outfalls, *Proc. 9th Federal Convention of the Australian Water and Wastewater Association* (Perth), p.23-28.

[5] Waite, T.D. and Szymczak, R. (1993) Manganese dynamics in surface waters of the eastern Caribbean Sea, *Journal of Geophysical Research,* 98 (C2), 2361-2369.

[6] Landing, M.L. and Bruland, K.W. (1987) The contrasting biogeochemistry of iron and manganese in the Pacific Ocean, *Geochimica et Cosmochimica Acta* 51, 29-43.

[7] Baskaran, M. and Santschi, P.H. (1993) The role of particles and colloids in the transport of radionuclides in coastal environments of Texas, *Marine Chemistry, 43* (1993) 95-114.

[8] Szymczak, R., Short, S., Waite, T.D. and Furnas, M.J. (1996) $^{234}Th/^{238}U$ inventories and the dynamic cycling of trace metals in shelf waters of tropical northern Australia (in prep.)

[9] Buesseler, K.O., Bacon, P.B., Cochran, J.K. and Livingston, H.D. (1992) Carbon and nitrogen export during the JGOFS North Atlantic Bloom Experiment estimated from $^{234}Th/^{238}U$ disequilibria , *Deep-Sea Research* **38** (1992) 1115-1137.

[10] Jeffree, R.A. and Szymczak, R. (1999) Enhancing effect of marine oligotrophy on environmental concentrations of particle-reactive trace elements, *Science of the Total Environment*, (submitted Jun '99).

The application of nuclear localisation technologies in environmental biology

Ross A. Jeffree,
Leader, Radioecology Affinity Group, Environment Division, ANSTO, PMB 1, Menai, 2234
raj@ansto.gov.au

Nuclear and related localisation technologies at ANSTO have been applied to a range biological matrices, in relation to specific environmental questions. Several of these applications are summarised below.

The major sites of radium-226 accumulation in the tissue of tropical freshwater bivalves

Experimental and field investigations of accumulation of Ra-226 in bivalve tissue had indicated atypical uptake and loss patterns coupled with an ability to concentrate this natural nuclide to unusually high concentrations under natural conditions within the Kakadu national park. The alpha-track solid-state detector CR-39, was used to conclusively demonstrate that Ra-226 and other alpha-emitters were located in extracellular granules, which associated electron microprobe analyses demonstrated were predominantly composed of Ca phosphate, and contained various other metals in abundance. The demonstration of co-location of Ca and its metabolic analogue Ra-226 led to the further development of a theoretical model of the bioaccumulation of alkaline-earth and other elements in the tissues of Australian freshwater bivalves, based on the relative solubilities of elements as phosphates. This information was also fundamental to explaining how Ra-226 was accumulated to such high tissue concentrations under natural conditions, which were not appreciably altered by mining activities at the Ranger uranium mine.

Localisation of Pb and other elements in crocodile osteoderms

Estuarine crocodiles (*Crocodylus porosus*) from Kakadu National Park, Northern Australia, consume waterfowl hunted by the traditional Aboriginal owners, who have used lead shot ammunition since the 1950s. Their exposure to anthropogenic Pb, not previously reported for crocodilians, was monitored in individual animals using osteoderms and samples of flesh, whose Pb concentrations were also relevant to human consumption. Osteoderm Pb concentrations were an order magnitude higher ($P<0.001$) in crocodiles from two populations, *a priori* identified as at risk of enhanced exposure, compared to many other populations sampled within the Park. IBA and SIMS were used to measure the ratios of Pb:Ca signals, across the internal structure of the osteoderms from crocodiles with enhanced Pb burdens. These localised analyses showed a consistently enhanced signal from the primordial to most recently constructed lamination. This pattern was consistent with continual Pb exposure over the animals' lives of up to 18 years.

Validation of bivalve shell micro-laminations as archival monitors of pollution signals

SIMS and other localisation technologies have been used to demonstrate that the micro-laminations in the shells of freshwater bivalves have the capability to record and archive an elevated water concentration of manganese, a contaminant typically associated with uranium mining. In this application the depth-profiling operational mode of the ANSTO SIMS was used to demonstrate a pattern of enhanced Mn concentration in the most recently deposited micro-laminar shell material.

References

Jeffree R.A. & Simpson R.D. (1984). Radium-226 is accumulated in calcium granules in the tissues of the freshwater mussel, *Velesunio angasi*: support for a metabolic analogue hypothesis? Comparative Biochemistry & Physiology, 79A(I) 61-72.

Jeffree R.A. & Simpson R.D. (1986). An experimental study of the uptake and loss of Ra-226 by the tropical freshwater mussel *Velesunio angasi* (Sowerby) under varying Ca and Mg water concentrations. Hydrobiologia, 139, 59-80.

Jeffree R.A. (1988). Patterns of accumulation of alkaline-earth metals in the tissue of the freshwater mussel *Velesunio angasi* (Sowerby). Archives of Hydrobiology. 112(1), 67-90.

Jeffree R. A., Markich S. L, Lefebvre R, Thellier M. and Ripoll C. (1995). Shell microlaminations in the freshwater bivalve Hyridella depressa (Lamarck) as an archival monitor of manganese water concentration: Experimental validation by depth profiling using secondary ion mass spectrometry (SIMS). Experientia 51, 838-848.

Twining J. R., Markich S. J., Prince K. E. and Jeffree R. A. (in press). Osteoderms of estuarine crocodiles record their enhanced Pb exposure in Kakadu National Park. Environmental Science and Technology.

SESSION 7

Chair – Trevor Ophel

IBMM

Influence of Pre-Existing Structures and Ion-Implantation Conditions on the Formation of Amorphous Silicon

B.C. Johnson, A.C.Y. Liu, J.C. McCallum

Microanalytical Research Center, School of Physics, University of Melbourne, Parkville, Vic. 3010

Introduction

Stable defects are introduced into Si by nuclear collisions in ion beam processing. These defects are known to be pernicious to semiconductor devices and so have become a major issue as the integrated circuit industry moves towards smaller device dimensions and lower thermal budgets. It is essential then to understand the influence that ion implantation has on the structure of the target material in order to minimize defects in the active device region and to further understand their role in materials.

Previous studies have shown that the implant temperature and the ion fluence has a strong effect over the type and amount of irradiation induced disorder.[1] Therefore, these parameters will be varied over a wide range in order to better understand this influence. Also, we can study the role of defects in a controlled environment via the use of structural relaxation which has in part been attributed to the annihilation of non-equilibrium defects.[2] Structural relaxation has the effect of decreasing the strain energy and is related to the topology of the material which can be described by the RMS bond angle deviation. This can be measured directly by Raman spectroscopy.[3]

The conditions under which the Si substrates were prepared involved varying the substrate temperature during implantation and the self-ion-implantation dosages at a fixed energy. The implants were performed into both crystalline silicon (c-Si) and relaxed amorphous silicon (a-Si). The structure of the silicon was then characterized by it's vibrational properties as measured by the Raman spectrometer. Rutherford Backscattering Spectrometry and Channeling (RBS-C) was also used to determine the density and layer thickness of the samples giving us further information about its amorphous state.

In surveying a range of ion induced effects we are also investigating the influence that pre-existing nanocavity structures have on the formation of a-Si. In particular, Raman Spectroscopy will be used to characterize the formation of amorphous material around the cavities at different ion doses. Nanocavities are used for the gettering of transition metal impurities and defects and are found to collapse upon irradiation due to plastic flow in a-Si.[4] Again, RBS-C will be employed to record the effect of ion implantation.

The following paper will only present our results on ion-implantation into relaxed a-Si and c-Si at an implant temperature of 77K.

Experiment

In this study Cz Si(100) p-type wafers of a resistivity ranging between $1 - 10\Omega$cm were used. A thick amorphous layer was prepared by ion implantation of $^{28}Si^{+}$ ions at energies of 0.5, 1.0 and 2.0 MeV using a 1.7 MeV NEC ion implanter. During these implants the substrates were affixed to a stage held at 77K with silver dag to ensure good thermal contact. The samples were then annealed for 45 minutes at a temperature of $500°C$ in vacuum. This had the effect of relaxing the amorphous layer. A region

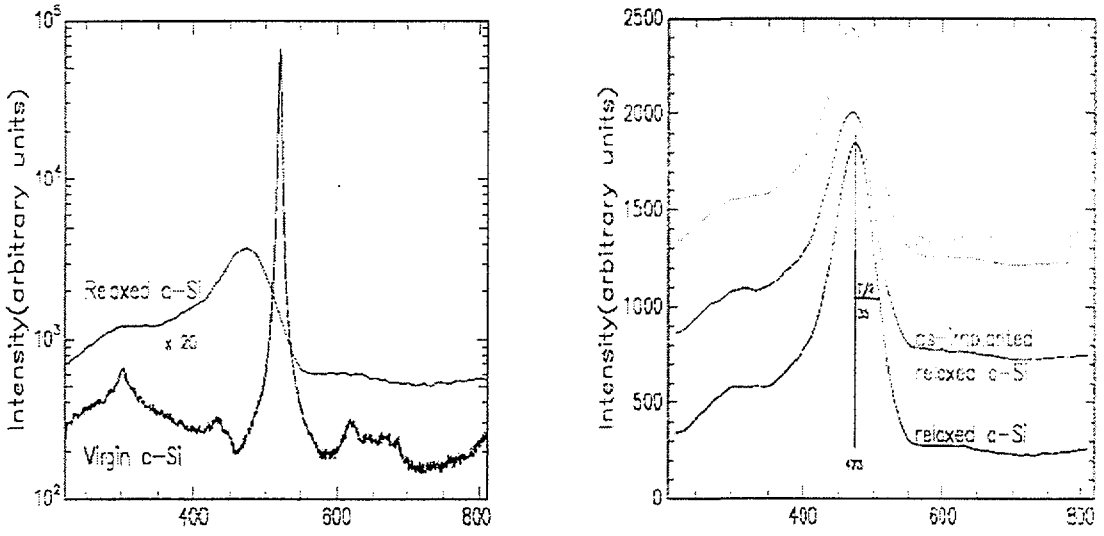

Figure 1: a) The Stokes Raman Spectra for relaxed a-Si (top) and c-Si (bottom). b) The Stokes Raman spectra for relaxed a-Si (bottom), implanted relaxed a-Si (100keV $^{28}Si^{+}$ ions to a fluence of 1×10^{17} at 77K), and the same implant into c-Si (top). Indicated are the peak position and peak half width.

which overlapped both relaxed a-Si and c-Si was then irradiated with 100keV $^{28}Si^{+}$ ions to fluences ranging from 1×10^{13} to $1 \times 10^{17} cm^{-2}$ while the substrates were held at temperatures of 77K, 293K, or 373K.

Raman spectra were then taken using the University of Melbourne Dispersive Raman Microprobe at integration times of 1000s. The 514.5nm line of a continuous wave Ar^{+} ion laser was used to irradiate the sample in a backscattering geometry. The Raman laser had a spot size of $1\mu m \times 1\mu m$ with a power of 0.6mW at the sample surface to avoid heating effects. The scattered light was spectrally resolved onto a CCD camera where the gratings were arranged in a double subtractive mode.

Results and Discussion

Raman Spectroscopy is quite sensitive to transformations from the crystalline to amorphous phase. This point is illustrated in Figure 1(a) which shows typical spectra for relaxed a-Si and c-Si. The c-Si Raman spectrum is determined by wavevector selection rules. A strong single one-phonon band at $520.2 cm^{-1}$ dominates the underlying second-order Raman characteristics. The intensity of this peak is polarization dependent and is attributed to the creation of the triply degenerate long wavelength optical phonons. On irradiation the intensity of this line will decrease as more light will be scattered from a disordered material. It's general shape will also become skewed and shift towards lower wavenumbers with the build up of damage and the ultimate breakdown of selection rules. These effects will be studied more closely in the nanocavity Raman spectra with the use of the Phonon Confinement Model.[5]

The a-Si spectrum reflects the full vibrational Density-of-States (DOS). It consists

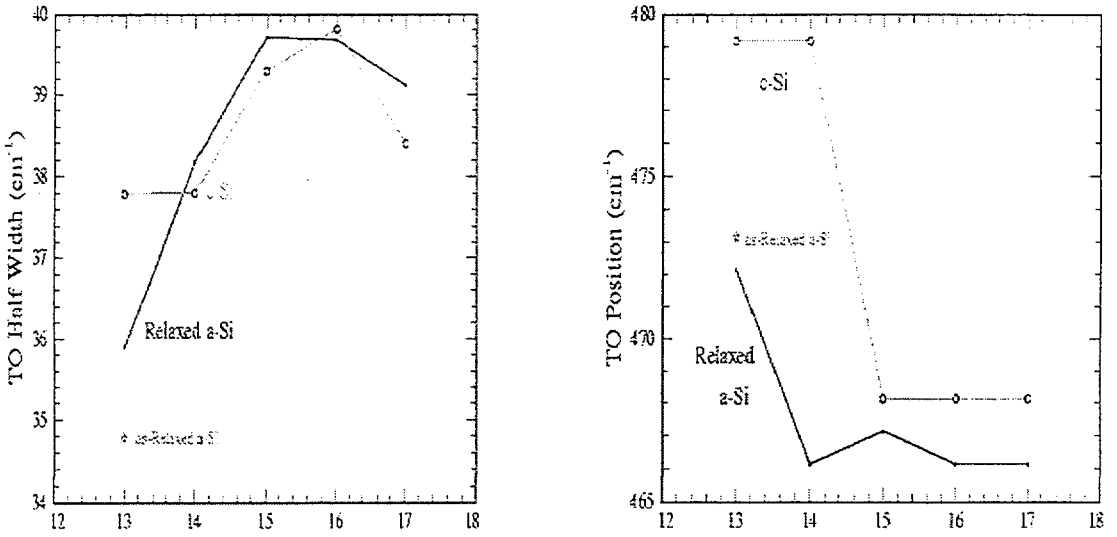

Figure 2: a) Half width of the TO Raman peak as a function of dose for both relaxed a-Si and c-Si (open circles) irradiated at a temperature of 77K. b) Position of the TO Raman peak as a function of dose. Indicated are typical values of Relaxed a-Si.

of a transverse optical (TO) phonon peak at $\sim 470cm^{-1}$ whose existence requires tetrahedral symmetry to be present in the amorphous structure.[6] Features on the lower wavenumber shoulder of the TO peak are attributed to longitudinal optical (LO) and longitudinal acoustic (LA) phonon bands.

The evolution of the TO peak was followed as the ion dose was increased. In particular, its peak position shift and half width. The half width to the high wavenumber side of the peak was measured (as indicated in Figure 1b) to avoid the LO and LA like features. It can be seen that once the relaxed a-Si is irradiated to high doses its Raman spectra becomes identical to that of its as-implanted counterpart.

The range of 100keV Si ions in Si is 1500Å with the peak in $(\frac{dE}{dx})_{nuclear}$ occurring at a depth of $\sim$ 1000Å as calculated by SRIM.[8] These depths are within the expected probe depth ($\sim$ 1600Å) of the Ar laser in a-Si. For implantation into relaxed a-Si, the 100keV ions cause de-relaxation of the continuous random network (CRN) structure. This leads to increased bond-angle distortion and defect incorporation and results in the observed shift in the TO position and width, as shown in figure 2. For implantation into c-Si the 100keV ions initially generate isolated zones of a-Si which coalesce into a continuous amorphous layer with increasing dose. Amorphous layers produced at elevated implantation temperatures where dynamic annealing may play a vital role are yet to be analyzed.

The trends observed here are qualitatively similar to those observed by Roorda *et al.*[7] for 5.5MeV implantation into relaxed a-Si where the ion range is far beyond the probe depth of the laser. As expected, in the case of our 100keV implants, the relatively small depth range of the ions causes the range at which the TO position exhibits the

most dramatic shift to occur at lower doses than that observed by Roorda. We are currently examining our data in more detail to see if the differences between data sets can be related to the expected changes in the a-Si network. We expect that the trends observed in samples implanted at room temperature and above will provide a better picture of what is happening in the material.

Conclusion

This study investigated the influence of ion implantation conditions on the structure of a-Si. It was found that keV implants display qualitatively similar behaviour to the MeV implants produced by Roorda *et al.* as seen by Raman analysis. Using this tool we will be able to characterize the effect of ion induced damage at a range of ion doses and temperatures where dynamical annealing may play a vital role in determining the resultant structure.

Samples produced with different ion doses and at different ion implantation temperatures are yet to be analyzed. Subsequent RBS-C spectra will be obtained in order to determine the density and layer thickness of the samples to correlate this with the Raman spectra. Thus, the effect of ion implantation temperature and dose on the resultant amorphous structure will be determined as well as a comparison between keV and MeV implants.

Using the same analytical tools as above the collapse of nanocavities is yet to be examined.

REFERENCES

[1] J. S. Williams *Advanced Materials '93, IV Laser and Ion Beam Modification of Materials, ed. I. Yamada et al. Trans. Mat Res. Soc. Jpn.***17**, *4545 (1994)*

[2] S. Roorda, J.M. Poate, D.C. Jacobson, D.J. Eaglesham, B.S. Dennis, S. Dierker. *Solid State Communications. 75 (3), 197 (1990)*

[3] D. Beeman, R. Tsu, M.F. Thorpe. *Phys. Rev. B 32 (2), 874 (1985)*

[4] X. Zhu, J. S. Williams, D. J. Llewellyn, J. C. McCallum. *Appl. Phys. Lett. 74 (16), 2313 (1999)*

[5] X. Huang, F. Ninio, L. J. Brown, S. Prawer. *J. Appl. Phys. 77 (11), 5910 (1995)*

[6] R. Alben, D. Weaire, J. E. Smith, M. H. Brodski. *Phys. Rev. B. 11 (6), 2271 (1975)*

[7] S. Roorda, J.M. Poate, D.C. Jacobson, D.J. Eaglesham, B.S. Dennis, S. Dierker. *Appl. Phys. Lett. 56 (21), 2097 (1990)*

[8] J. P. Biersack, L. G. Haggmark. *Nucl. Instr. Meth. 174 (1980) 257.*

CHARACTERISATION OF Ti:Al_2O_3 CREATED BY THE CO-IMPLANTATION OF SAPPHIRE WITH TI AND O

L.D.Morpeth and J.C.McCallum.
MicroAnalytical Research Centre, School of Physics, University of Melbourne, Parkville, Victoria 3052, Australia. ldm@physics.unimelb.edu.au

INTRODUCTION

The development of a Titanium Sapphire laser in a waveguide geometry would yield an elegant, compact, versatile and highly tunable light source useful for applications in spectroscopy and optical telecommunications. We are investigating whether Ion Implantation techniques can be utilised to produce suitable crystal quality and waveguide geometry for fabrication of a Ti:Al_2O_3 waveguide laser.

The implantation of Ti and O ions into c-axis oriented α-Al_2O_3 followed by subsequent thermal annealing under various conditions has been investigated as a means of forming the waveguide and optimising the fraction of Ti ions that have the correct oxidation state required for laser operation. A Raman Microprobe is being used to investigate the photo-luminscence associated with the Ti^{3+} ion. Current measurements indicate optimal implantation and annealing parameteres for Ti^{3+} formation.

Auger Electron Spectroscopy (AES) and X-Ray Photoelectron Spectroscopy (XPS) are currently being utilised to determine chemical information pertaining to the oxidation state of the implanted titanium ion. An α-Step profiler has been used to observe no change in density of annealed samples, indicating a chance of favourable refractive index modification by ion implantation.

Rutherford Backscattering and Ion Channeling (RBS-C) analysis have been used to study the crystal struture of the samples following implantation and annealing. This has enabled the optimisation of implantation parameters and annealing conditions, to minimise defect levels, which would otherwise limit the ability of light to propagate in the Ti:Al_2O_3 waveguide.

EXPERIMENT

Uniform overlapping concentration profiles of Ti and O were produced over the depth range $\sim$ 0.5–0.7 μm in c-axis oriented α-Al_2O_3 crystals by multiple energy implants using a 1.7 MV NEC ion implanter. During implantation, the substrates were mounted on a temperature controlled stage using Ag paste to ensure good thermal contact. They were also tilted 7° from normal incidence to avoid channeling implantation. The implants were performed either at room temperature (RT) or at -195°C . The Ti implants were performed first. The implanted samples were annealed at 1100°C in a tube furnace using controlled ambients of O_2 or forming gas (96% Ar, 4% H). Photoluminescence (PL) measurements were performed with a DILOR XY confocal micro-Raman spectrometer using the 514 nm line of an Ar ion laser as the excitation source.

RESULTS & DISCUSSION

Figure 1a shows PROFILE [1] code calculations of the Ti and O profiles expected from an implantation schedule of Ti(1310 keV, 6.0×10^{15} .cm^{-2} + 910 keV, 3.1×10^{15} .cm^{-2}) followed by O(700 keV, 5.5×10^{15} .cm^{-2} + 545 keV, 3.0×10^{15} .cm^{-2} + 440 keV, 2.8×10^{15} .cm^{-2}) into Al_2O_3 . The resultant Ti and O implant profiles are relatively

uniform over the depth range $\sim$ 0.5–0.7 μm . The Ti concentration profile depicted in Fig. 1a corresponds to 0.2 at.% Ti. The Ti/O concentrations are in the ratio of 2:3 so that if all of the Ti is present in the 3+ oxidation state the implant profile is equivalent to 0.7 wt.%. Ti_2O_3 in Al_2O_3 . Other Ti and O concentrations used in our experiments were obtained by appropriate scaling of the doses given above. Rutherford backscattering and ion channeling (RBSC) measurements show that in samples implanted at -195°C with this schedule of doses, a buried layer is produced which is highly damaged but not amorphous.

Elsewhere, we have established that Ti^{3+} is not only present within the implanted samples but is responsible to the observed photoluminescence. [2–4]. The spectral response of the PL detection system we use gives the Ti^{3+} luminescence a peak of around 700nm. Relative luminescence measurements, such as those shown in the following figures, are made using the recorded luminesence observed at 700nm. The excitation source is the 514nm line of an argon ion laser.

Figure 1b shows the variation in the relative luminescence intensity as a function of Ti concentration for thermally annealed samples. For Ti concentrations greater than $\sim$ 0.1 at.% there is a marked roll-off in the rate of increase of the luminescence intensity with increasing Ti concentration, reaching a plateau at $\sim$ 0.2 at.%. This indicates that the concentration of Ti in the 3+ oxidation state reaches saturation. Given that the Ti^{3+} concentration in commercial Ti:sapphire lasers is typically 0.03 at.%, the saturation above $\sim$ 0.1 at.% is not expected to limit our endeavours to produce a waveguide laser by ion implantation. However, please note that we have quoted the implanted Ti concentration and that the fraction of Ti present in each oxidation state is not yet known.

Figure 2a shows the variation in the PL intensity as a function of the O/Ti ratio for a fixed Ti concentration of $\sim$ 0.2 at.% in samples implanted at -195°C and then thermally annealed at 1050°C for 4 h, in an ambient of either O_2 (triangles) or forming gas (circles). This data shows that the luminescence yield due to Ti^{3+} is quite strongly peaked at an O/Ti ratio of 2:1 and that small increases in the O stoichiometry beyond this ratio result in a dramatic reduction in the yield. Similar results were obtained for

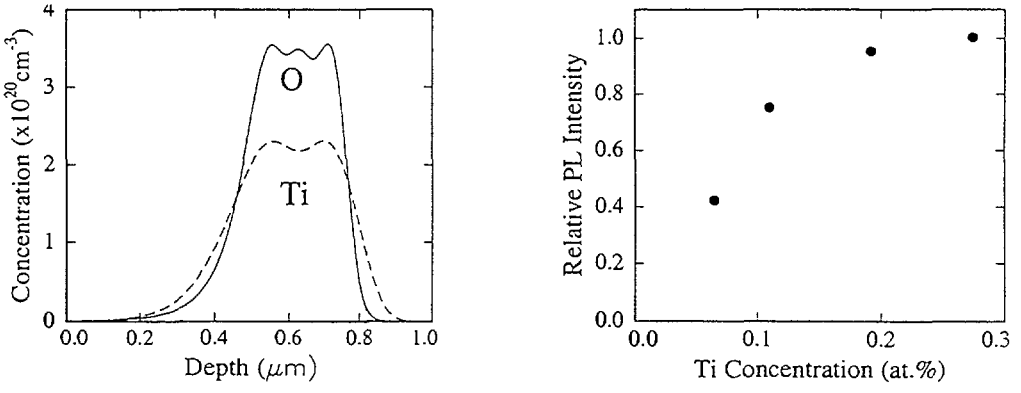

Figure 1: (a) Calculated concentration profiles for implantation of Ti and O into Al_2O_3 at multiple energies and doses as quoted in the text. The resultant Ti and O concentrations are equivalent to 0.7 wt.Ti_2O_3 in Al_2O_3 over the depth range $\sim$ 0.5–0.7 μm . (b) Variation in the PL intensity as a function of Ti concentration for samples implanted at -195°C with a Ti/O ratio of 2:3 and annealed at 1100°C for 4 hr, in O_2 .

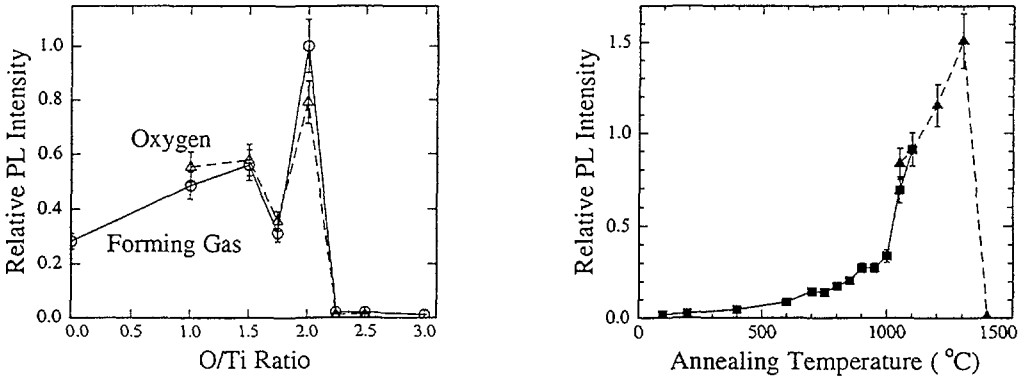

Figure 2: (a) Peak PL intensity as a function of O/Ti ratio for a fixed Ti concentration of 0.2 at%. Samples were implanted at -195°C and then thermally annealed at 1050°C 4 h, in an ambient of either O_2 (triangles) or forming gas (circles). Lines are guides to the eye. (b) Peak PL intensity as a function of annealing temperature for samples containing a Ti concentration of 0.14 at.% and an O/Ti ratio of 3:2, annealed for 4 h in forming gas (squares) or 1 h in air (triangles).

both annealing ambients although there is some variation in the maximum yield for the two environments. An O/Ti ratio of 2:1 would provide the Ti with sufficient implanted O to form the optically-inactive 4+ oxidation state (TiO_2) and yet, surprisingly, our results suggest that the Ti^{3+} content is maximised under these conditions. In one other study involving high energy co-implantation of Ti and O ions into sapphire evidence of formation of TiO_2 (rutile) microcrystals was found in co-implanted samples but not in samples implanted with Ti alone. [5] In that work, the peak Ti concentration was $\sim$ 1.4 at.% which is considerably higher than the concentration regime we are interested in, and single-energy overlapping Ti and O implants were used, giving an O/Ti ratio of $\sim$ 3:1 at the peak of the profile and greater than 2:1 over much of the depth range. However, comparison of the two sets of results would suggest that as the O/Ti ratio is increased, an increasing proportion of the Ti is present in the higher 3+ and 4+ oxidation states and that for O/Ti ratios greater than 2:1 it is present mainly as optically-inactive Ti^{4+} . What is not clear is why an over-stoichiometry of O (2:1 instead of 3:2 O/Ti) is needed to maximise the Ti^{3+} content.

The dependence of the PL intensity on annealing temperature is illustrated in Fig 2b which shows data from samples implanted with 0.14 at.% Ti and an O/Ti ratio of 3:2, annealed for 4 h in forming gas (squares) or 1 h in air (triangles). The peak PL intensity is observed for anneals at $\sim$ 1300°C and there is a dramatic reduction in the PL intensity for anneals performed at higher temperatures. In an ion channeling study of the annealing behaviour of sapphire implanted with 150 keV Ti ions, Naramoto et al.[6] found that the substitutional fraction of Ti increased substantially for anneals in the temperature range 1200–1300°C and then it decreased again with further annealing to 1500°C accompanied by Ti redistribution and precipitation. The peak at 1300°C in our PL versus temperature data is consistent with this observation since Ti^{3+} is expected to occupy Al lattice sites in sapphire. Phillips et al.[7] showed that thermal annealing of Ti-doped sapphire crystals at 1400°C in air results in precipitation of TiO_2 . This explains the low PL yield we obtained for annealing at 1400°C . Clearly, Ti^{3+} formation is maximised in a narrow temperature band near 1300°C and processing at

higher temperatures leads to conversion of the Ti to the 4+ state. To explore this further, we are planning to measure the fraction of Ti present in each oxidation state using X-ray absorption and photoelectron spectroscopies.

Preliminary studies of the residual defect levels have been made with Rutherford Backscattering and Ion Channeling (RBS-C). The spectra (not shown) indicate significant damage recovery during a 4hr anneal at 1100 °C in the presence of forming gas. The temperature dependence of this recovery process, in particular at higher temperatures where Ti^{3+} formation is optimised is currently being investigated. We intend to obtain lattice site and post anneal distribution imformation from Proton Induced X-Ray Emission (PIXE) and Secondary Ion Mass Spectrometry (SIMS) respectively.

An α-Step profiler has been used to observe no change in density of annealed samples, indicating a chance of favourable refractive index modification by ion implantation. We shall use ellipsometry to hoepfully observe the refractive index change in recently formed channel like guides. Currently, attempts are also being made to quantify the change with a Metricon. Results from oxidation state, defects and refractive index considerations is soon be published.

CONCLUSION

In conclusion, we have found that co-implantaton of Ti and O into c-axis oriented α-Al_2O_3 can be used to substantially increase the fraction of Ti stabilised in the optically-active 3+ oxidation state. Following thermal annealing in the temperature range $\sim$ 1050–1300°C strong luminescence due to Ti^{3+} is observed over the wavelength range $\sim$ 600–900 nm, accompanied by the characteristic absorption band at 450–550 nm. The luminescence yield is strongly dependent on the ratio of implanted O/Ti and on the annealing temperature. Maximum luminescence is obtained for an O/Ti ratio near 2:1 with further increases in O content leading to a sharp reduction in the luminescence yield, presumably due to conversion of the Ti to the 4+ state. Similarly, the peak PL yield is obtained for annealing at temperatures near 1300°C while higher temperatures result in low luminescence yields consistent with TiO_2 formation.

This research is supported by a fellowship and research grant from the Australian Research Council. The Department of Electronics Materials Engineering at the Australian National University is gratefully acknowledged for support in providing access to ion implantation facilites.

REFERENCES

[1] Implant Sciences Corporation, Wakefield, MA, USA.

[2] J.C.McCallum and L.D.Morpeth, Synthesis of Ti:sapphire by ion implantation. Nucl. Inst. Meth. B, **148**: 726-729, 1999

[3] L.D.Morpeth and J.C.McCallum, Formation of Ti^{3+} in spphire by co-implantation of Ti and O ions, Applied Physics Letters, to be published

[4] L.D.Morpeth, Synthesis of Titanium Sapphire by high energy ion implantation, honours thesis, Melbourne Univestity, 1997

[5] S. Nakao, M. Ikeyama, M. Tazawa, P. Jin, H. Niwa, S. Tanemura, Y. Miyagawa, S. Miyagawa and K. Saitoh, Materials Chemistry and Physics **54**, 342 (1998).

[6] H. Naramoto, C. J. McHargue, C. W. White, J. M. Williams, O. W. Holland, M. M. Abraham and B. R. Appleton, Nucl. Instr. and Meth. in Phys. Res. **209/210**, 1159 (1983).

[7] D. S. Phillips, A. H. Heuer and T. E. Mitchell, Phil. Mag. A **42**, 385 (1980).

Diamond nanocrystals formed by implanting fused quartz with carbon ions

J.O. Orwa*, S. Prawer, J.C. McCallum, D.N. Jamieson, P. Julin and K.W. Nugent

MARC, School of Physics, The University of Melbourne, Parkville, Victoria 3052

1. Introduction

Recently, there have been many studies involving the synthesis and characterisation of nanometer sized clusters of various materials embedded by ion implantation in both amorphous and crystalline substrates [1]. The main feature of these clusters is an observed variation in their band gaps with size which allows for the tuning of luminescence wavelengths according to desired applications. Although highly desirable, synthesis of diamond directly from carbon has so far been an elusive goal. In addition to applications involving band gap engineering, the added characteristic of negative electron affinity [2] promises that diamond nanoclusters may eventually find use as cold cathode emitters [3]. This study investigates the synthesis of diamond nanocrystals by implanting fused quartz with carbon and annealing in a furnace under different ambients.

2. Experimental

1MeV carbon ions were implanted into fused quartz to doses of $5 \times 10^{16}cm^{-2}$, $1 \times 10^{17}cm^{-2}$, $2 \times 10^{17}cm^{-2}$ and $5 \times 10^{17}cm^{-2}$ at room temperature. Each implant uniformly covered an area of $1cm^2$ and had a projected range (range straggling) estimated using Transport of Ions in Matter (TRIM) code [4] of $R_p \pm (\Delta R_p) = 1.45 \pm (0.12)\mu m$. As a control, 1MeV argon ions were implanted into quartz to a dose of $1 \times 10^{17}cm^{-2}$ and subjected to identical annealing treatments as the carbon implanted samples.

Each sample was thermally annealed at 1100°C for 1 hour, 4 hours and 16 hours in flowing forming gas (4% hydrogen in argon), argon and oxygen. Absorption spectroscopy was performed using a Cary 5 spectrophotometer in the double beam configuration and with unimplanted substrates as references. To identify the nature of the carbon structures created we performed both visible and UV Raman spectroscopy. The visible Raman signal was excited by 2mW of the 514.5nm line of an argon-ion laser focused to a 1μm spot and detected using a DILOR XY Confocal micro-Raman spectrometer with optical multi-channel collection. The UV Raman spectra were excited by the 244nm line of a frequency doubled 488nm line of an argon ion laser.

Cross sectional TEM samples were prepared using a planar Gattan hand grinder, dimple grinder and an ion beam thinner. The TEM system used was the University of Melbourne's 400kV JEOL 4000EX coupled with a JEOL EELS spectrometer. After loading the samples onto the microscope stage, the column was evacuated to a pressure of $\sim 2 \times 10^{-7}$ Torr.?? ?? Using the 2mm aperture of the spectrometer, the sample was imaged with a magnification of 120,000×.

* joo@physics.unimelb.edu.au

3. Experimental results

3.1 Absorption Measurements:

Figure 1 shows absorption spectra for fused quartz samples that were implanted to a dose of $5 \times 10^{17}cm^{-2}$ and annealed in forming gas for various durations. A spectrum of a sample that was implanted with argon to a dose of $1 \times 10^{17}cm^{-2}$ and annealed under similar conditions for 1 hour is shown for comparison. The peak observed at around 5.2eV in the annealed carbon implants only appears as a shoulder in the as-implanted sample and is absent in the argon implant which suggests that the peak is due to the presence of carbon clusters. The absence of a definite peak in the unannealed carbon implanted sample thus points to the lack of any significant clustering before annealing.

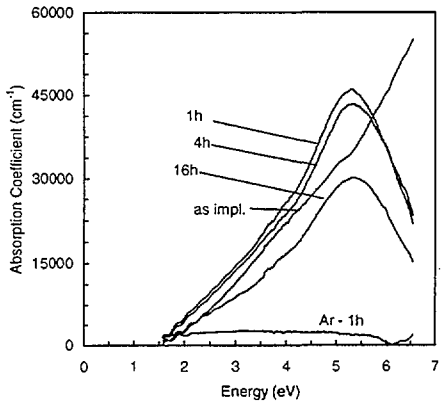

Figure 1 Absorption spectra for 1MeV carbon ions implanted into fused quartz to a dose of 5×10^{17} cm^{-2} and annealed for various durations at 1100°C in forming gas. Spectra of an unannealed quartz and quartz implanted with argon to a dose of 1×10^{17} cm^{-2} and annealed for 1 hour in forming gas are included for comparison.

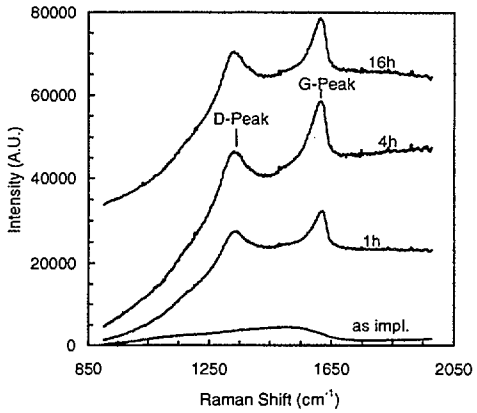

Figure 2 Raman spectra for 5×10^{17} cm^{-2} samples annealed in forming gas. The spectrum for an unannealed sample implanted to the same dose is shown for comparison

We observed that both the absorption coefficient and peak energy increased with dose as did the absorption peak energy. We comment on these findings in section 4.

3.2 Visible Raman Measurements

Having established from absorption data that the peak at 5eV is due to carbon clusters, we turn to Raman spectroscopy to determine the bonding in the clusters. Figure 2 shows Raman spectra of a sample implanted to a dose of $5 \times 10^{17}cm^{-2}$ and annealed for various durations in forming gas. A spectrum of the sample implanted to a dose of $5 \times 10^{17}cm^{-2}$ but unannealed is included for comparison. The single Raman peak in the unannealed sample at around $1500cm^{-1}$ indicates that the carbon exists mainly in amorphous form. After 1 hour annealing, the Raman D and G peaks located at $1350cm^{-1}$ and $1580cm^{-1}$, respectively, appear, suggesting that the implanted carbon has formed into sp^2-bonded micro-clusters.

3.3 UV Raman measurements

UV Raman spectroscopy was performed to aid in the detection of the presence of sp^3 bonded carbon. Because of the close proximity in the energy of the exciting wavelength to the bandgap of sp^3 bonded carbon, resonance enhancement of the Raman spectra is expected compared to visible wavelength excitation. The spectra for all carbon implanted but unannealed samples and for the sample implanted with argon showed broad identical features which suggests that they are due to damage induced fluorescence from the quartz substrate.

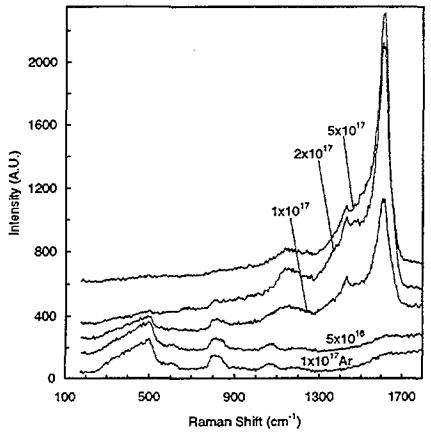

Figure 3 U.V Raman spectra for carbon implanted quartz samples annealed at 1100°C for 1 hour in forming gas. The spectrum for argon implanted quartz sample is included for comparison.

Figure 3 shows UV Raman spectra of selected carbon implanted quartz samples annealed in forming gas at 1100°C for 1 hour. The spectrum of a quartz sample implanted with argon is included for comparison. Three interesting peaks occur in these spectra at around 1150, 1425 and between 1600 and 1615cm^{-1}. These peaks are not observed when the carbon dose is very low as in the 5×10^{16}cm^{-2} implant. We comment on the origins of these peaks in the discussion.

3.4 TEM, Diffraction and PEELS results

TEM micrographs, diffraction patterns and PEEL spectra all showed the presence of diamond nanoclusters embedded in a quartz matrix. It was found that the size of the clusters increased with implanted carbon dose and that the smaller clusters were more defect free than the larger ones.

4 Discussion

The peak observed at 5.2eV in the absorption spectra is due to the presence of carbon clusters. However, the origin of the peak is uncertain. The increase in the peak position with ion dose is an unexpected result because increasing the ion dose should cause the formation of larger clusters which, according to predictions from quantum confinement, should have smaller band gaps. The opposite trend observed thus suggests that the transition corresponding to the 5eV peak is not simply due to band to band transition in a diamond nano-cluster. Rather, the peak at 5eV may be due to transitions between defect states associated with the nano-clusters. The occurrence of an absorption peak and not an absorption edge further suggests that the absorption is dominated by defects. The defects may be associated with the surface of the clusters, or may be due to interstitial defects (such as the so-called split-interstitial or dumbbell defect) or vacancy or vacancy clusters. The energy levels of these defects may well depend on the cluster size and even shape. The broadness of the 5eV peak may be explained by the presence of defects and possible irregularities relating to size and shape which may cause small variations in the band gap of the clusters.

The peak observed at 1140cm^{-1} has been observed in nanocrystalline diamond and has been known to be associated with sp^3 bonded carbon [5-7]. The peak just over 1600cm^{-1} is of the same origin as the G-peak but is believed to be shifted to higher frequencies as a result of the stiffening of the sp^2 bonds by their sp^3 neighbours [5] whose presence are predicted by the peak at 1150cm^{-1}.

After annealing for 1 hour at 1100°C, the 5×10^{16}cm^{-2} sample shows a spectrum similar to that of unimplanted quartz and the argon implant. When annealed at 800 °C for the same duration, the 5×10^{16}cm^{-2} sample shows the presence of the 1140 and 1600cm^{-1} peaks. This, together with the observation that after annealing for 4 hours in forming gas, the 1×10^{17}cm^{-2} sample spectrum looks more like virgin quartz suggests that annealing results in some loss of carbon. We noted that the loss was much more dramatic when the sample was annealed in oxygen.

5 Conclusions and future work

Direct synthesis of nanocrystalline diamond by implanting carbon into fused quartz was found to be possible when the samples were annealed in forming gas (4% hydrogen in argon). The diamond formed was more defect free in smaller clusters compared to larger ones. The long term motivation for this work was to create low energy electron emitters for applications in flat panel displays and to eventually produce high frequency photon emitters for applications in opto-electronics. Having synthesised the nanocrystalline diamond, the focus should now be on determining their electrical and optical characteristics.

References

[1] C.W. White, J.D. Budai, S.P. Withrow, J.G. Zhu, S.J. Pennycook, R.A. Zuhr, D.M. Hembree Jr., D.O. Henderson, R.H. Magruder, M.J. Yacaman, G. Mondragon and S. Prawer, *Nuclear Instruments and Methods in Physics Research B,* **127/128** (1997) 545.

[2] J. Van der Weide, Z. Zhang, P.K. Baumann, M.G. Wensell, J. Benholc and R.J. Nemanich, P*hys. Rev. B,* **50** (1994) 5803.

[3] A.A. Talin, L.S. Pan, K.F. McCarty, T.E. Felter, H.J. Doerr and R.F. Bunshah, *Applied Physics Letters,* **29** (1996) 3842.

[4] J.F. Ziegler, J.P. Biersack and U. Littmak, *The Stopping Powers and Ranges of Ions in Matter*, Permagon Press, (1985).

[5] V.I. Merkulov, J.S. Lannin, C.H. Munro, S.A. Asher, V.S. Veerasamy and W.I. Milne, *Phys. Rev. Lett.*, **78** (1997) 4869.

[6] A.V. Khomich, V.I. Merkulov, P.I. Perov, V.P. Varnin, I.G. Teremetskaya, B.G. Balakirev and E.D. Obraztsova, *Mat. Res. Soc. Proc.*, **423** (1996) 723

[7] S. Prawer and K.W. Nugent in *"Amorphous Carbon: State of the Art"*, - Proceedings of the 1st International Specialist Meeting on Amorphous Carbon (SMAC '97) – Eds. S.R.P. Silva, J. Robertson, W.I. Milne and G.A.J. Amaratunga - July 1997, pp.199.

The effect of ion-irradiation and annealing on the luminescence of si nanocrystals in SiO_2

S. Cheylan, N. Langford, R.G. Elliman

Department of Electronic Materials Engineering, Research School of Physical Sciences and Engineering, Australian National University, Canberra ACT 0200, Australia

Abstract: SiO_2 layers containing Si nanocrystals were irradiated with either 400keV or 3MeV Si ions to determine the effect of nuclear and electronic energy loss processes on defect production and luminescence. Irradiation reduced the nanocrystal-related luminescence at 806nm and produced a well-known defect emission at 640nm. Irradiation had a similar dose dependence for both 400keV and 3MeV ions, despite significant differences in the magnitude and nature of their energy loss. The nanocrystal emission was being quenched to 4% of its initial value following irradiation to $5x10^{12}Si.cm^{-2}$ and saturating for fluences $\geq 5x10^{13}Si.cm^{-2}$ (0.18dpa). This is discussed in terms of a previously proposed model in which point defects produced by irradiation accumulate at the nanocrystal surface leading to amorphisation at low displacement rates
(0.1 – 0.2dpa). In this model, quenching of the nanocrystal emission and its sensitivity to dose are assumed to result from the preferential accumulation of point-defect at the nanocrystal-SiO_2 interface, an effect which is predicated on the assumption that such defect act as non-radiative recombination centres. The existence of such defects is shown to be supported by the annealing behaviour of the nanocrystal and defect emissions.

Introduction

Strong visible photoluminescence (PL) is observed from Si nanocrystals in SiO_2[1-6]. As a consequence, this material system is of considerable technological interest for optoelectronic device applications[7]. Light emission is known to be associated with the presence of Si nanocrystals but its origin remains controversial[9-10]. It has variously been speculated to result from recombination of excitons within the nanocrystal itself[4,6-8] or from defect recombination in the SiO_2 matrix or Si-SiO_2 interface[12-14]. The role of defects is therefore an important issue.

Irradiation-induced defects in SiO_2 have been studied extensively[17,18]. It is well known that defects can be created by both nuclear and electronic energy loss processes and that the rate of defect production is much higher for nuclear processes[17]. It is also known that a class of paramagnetic defects, generally associated with O-deficient centres, give rise to a PL emission band around 640nm.

In this study, the role of defects is assessed by irradiating samples containing nanocrystals with low (400keV) and high (3MeV) energy Si ions. The magnitude and nature of the energy loss is very different for these two cases and this provides an opportunity to distinguish any differences associated with the energy loss mechanism. The thermal stability of irradiation induced changes is also examined.

Experimental

SiO_2 films, 0.98μm thick grown on Si wafers, were implanted at room temperature with $1.0x10^{17}Si.cm^{-2}$ at 400keV (Si distribution peak ~ 700nm[18] and excess Si concentration peak ~5 at.%). Nanocrystals were formed by annealing the samples at 1100°C for 60min in a N_2 ambient, followed by a second anneal at 500°C in forming gas (95% N_2+5%H_2).

of the nanocrystal distribution (700nm) and correspond to 140eV/nm. In contrast, the energy loss of 3MeV ions is dominated by electronic energy loss (~1500eV/nm, nuclear energy loss ~ 30eV/nm). Although the total energy loss is 5.5 times greater for 3MeV ions than for 400keV ions, it is important to note that the nuclear energy loss is 4.7 times greater for 400keV ions and the electronic energy loss 11 times greater for 3MeV ions. The relative contribution of nuclear and electronic energy losses is therefore very different for the two cases.

The stability of the damage was assessed by comparing PL spectra after successive isochronal (60 min) annealing at 200°C up to 1000°C in a N_2 ambient. All PL spectra were measured at room temperature using a monochromator (Digikrom model DK480) and a GaAs photomultiplier (Himamatsu R943-02). The excitation source consisted was the 488nm line of an Ar ion laser and the PL emission was collected using a quartz light pipe. Standard lock-in detection techniques were used to maximise the signal-to-noise ratio and all spectra were corrected for the system response.

Results and Discussion

The as-implanted sample exhibits two main peaks, a well-known[2,4] defect peak at around 640nm and a second at around 780nm. The second peak is close to that observed for nanocrystal-based emission[2,4,8] and is believed to result from nanocrystal nuclei formed during implantation. Following annealing at 1100°C, the PL emission is dominated by nanocrystal-based emission centred at 806nm. The peak emission wavelength is consistent[9,20] with emission from nanocrystals of mean diameter ~3nm, giving a nanocrystal density of ~3 - $4x10^{18}cm^{-3}$. The nanocrystal emission is further enhanced by annealing in forming gas and exhibits a slight red-shift, as previously reported[21]. The increase in emission suggests that non-radiative defects remain after annealing at 1100°C and have a significant effect on the emission intensity.

Effect of Irradiation

Figure 1a compares the PL intensities of the defect and nanocrystal emission peaks for samples irradiated with 3MeV ions. Irradiation reduces the nanocrystal emission at 806nm and increases the defect emission at 640nm. For the lowest dose, $5x10^{12}Si.cm^{-2}$, only the nanocrystal emission is present but its intensity is already reduced to ~4% of that measured for the unirradiated sample. [This corresponds to ~20% of the unpassivated intensity]. Defect emission (640nm) is only observed for doses $\geq 1x10^{13}Si.cm^{-2}$. This suggests that irradiation creates two types of defect, the well known radiative centre which give rise to the emission at 640nm and a non-radiative defect that quenches the nanocrystal emission.

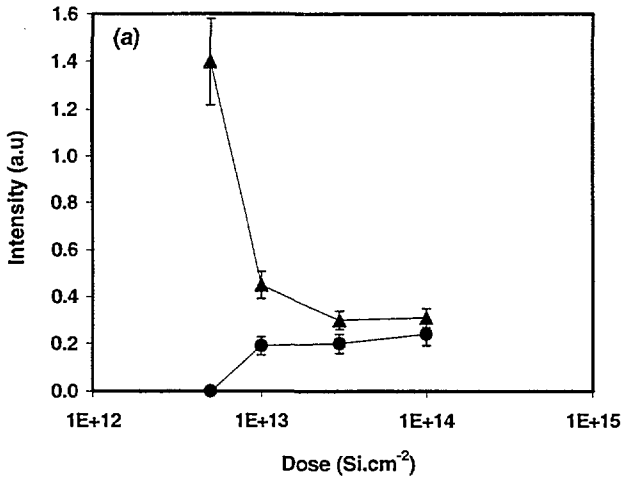

Figure 1. Peak emission intensity as a function of implant dose for: a) nanocrystal emission at 780nm (circles), and b) defect emission at 640nm (triangles). Data for 3.0MeV.

The nanocrystal emission continues to decrease for higher doses but saturates for doses ≥ $3x10^{13}Si.cm^{-2}$. It has previously been shown[20] that Si nanocrystals can be amorphised at displacement rates of 0.1-0.2dpa, more than two orders of magnitude lower than that required to amorphise bulk Si. For 400keV Si ions this corresponds to a dose of between $3x10^{13}Si.cm^{-2}$ (~0.06dpa) and $1x10^{14}Si.cm^{-2}$ (0.18 dpa), in the range where the nanocrystal emission saturates. The mode of amorphisation was attributed to the accumulation of point defects at the Si-SiO_2 interface[20], a process which in its initial stages was speculated to cause the observed reduction in nanocrystal emission. ie. The point defects were assumed to form non-radiative defect centres at the nanocrystal-SiO_2 interface, quenching the nanocrystal emission. The present results are consistent with this model.

Surprisingly, the reduction in nanocrystal emission and the increase in defect emission (figure 1a) shows a similar dose dependence for both 400keV and 3MeV irradiations, despite significant differences in the magnitude and mechanism of energy loss. For this to be the case, the defects responsible must be produced at similar rates in both cases. It is well known[17] that defects are created more efficiently in SiO_2 by nuclear energy loss processes than by electronic energy loss processes. This can account for the present results if it is assumed that defect production is ~10 times lower for electronic than for nuclear energy loss.

Annealing Behaviour

Figure 1b shows the effect of annealing on the intensity of the defect and nanocrystal emissions for a sample irradiated to a dose of $1x10^{13}Si.cm^{-2}$. As the temperature increases the defect-related peak gradually decreases and the nanocrystal-related peak increases in intensity. Again, the results show similar trends for samples damaged by 400keV and 3MeV ions. The defect emission is already reduced by annealing at 200°C and is eliminated by annealing to temperatures in the range 600–800°C. The preexistence of nanocrystals does not appear to significantly affect this behaviour.

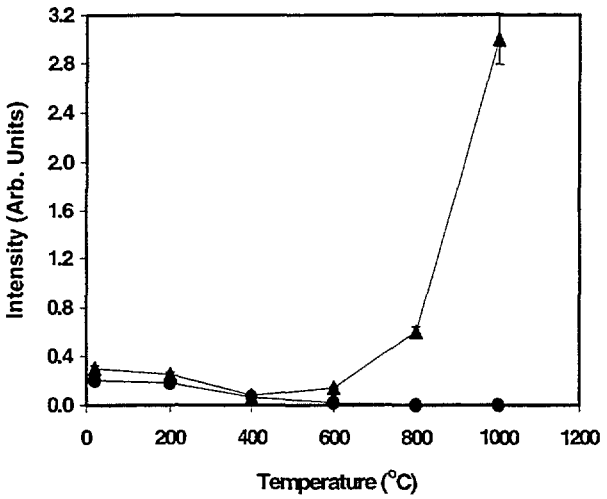

Figure 4: Peak emission intensity as a function of annealing temperature for a sample irradiated to a fluence of $1x10^{13}Si.cm^{-2}$:
a) nanocrystal emission at 780nm (circles), and
b) defect emission at 640nm (triangles). Data for 3.0MeV.

The nanocrystal emission remains largely unaffected by annealing up to 600°C, but increases rapidly for temperatures between 800°C and 1000°C. Previous experiments[22] have shown that nanocrystals rendered amorphous by irradiation do not recrystallise below ~775°C. This would suggest that the recovery of the nanocrystal emission for temperatures in the range 600-800°C is associated with such crystallisation, at least for samples irradiated to higher fluences. This is supported by the fact that recovery occurs at much lower temperatures (400 – 600°C) for samples irradiated to the lowest dose. The extent of recovery after annealing to 1000°C also depends on the irradiation dose, being greater for samples irradiated to lower doses. This supports evidence from H-passivation experiments that non-radiative defects remain after annealing at 1000°C.

Summary and Conclusions

Irradiation of SiO_2 layers containing Si nanocrystals with 400keV or 3.0MeV Si ions was shown to reduce the nanocrystal-based luminescence at 806nm and produce defect-based emission at 640nm. Irradiation has a similar dose dependence for both irradiations, despite significant differences in the magnitude and nature of the energy loss processes. It was shown that this could be reconciled by assuming that the defect production rate from electronic energy loss processes was ~10% of that for nuclear processes. The nanocrystal emission was shown to be particularly sensitive to irradiation, being quenched to 4% of its initial value following irradiation to $5x10^{12}Si.cm^{-2}$ and saturating for fluences $\geq 5x10^{13}Si.cm^{-2}$ (0.18 dpa). This was shown to be consistent with a previously proposed model[22] in which point defects produced by irradiation accumulate at the nanocrystal surface, leading to amorphisation at low displacement rates (0.1 – 0.2dpa). Quenching of the nanocrystal emission and its sensitivity to dose were shown to be consistent with the preferential accumulation of non-radiative defects at the nanocrystal-SiO_2 interface. The existence of such defects was also supported by the annealing behaviour of the nanocrystal and defect emissions.

These showed distinctly different temperature dependencies, with the defect emission eliminated by annealing to temperatures in the range 600 – 800°C, and the nanocrystal emission showing only partial recovery after annealing to 1000°C.

References

[1] H.Z. Song, X. M. Bao, N. S. Li, and J. Y. Zhang, J. Appl. Phys. 82, (1997), 4028

[2] S. Guha, J. Appl. Phys. 84, (1998), 5210

[3] J. Y. Zhang, X. M. Bao, N. S. Li, and H. Z. Song, J. Appl. Phys. 83, (1998), 3609

[4] K. S. Min, K. V. Shcheglov, C. M. Yang, H. A. Atwater, M. L. Brongersma, and A. Polman, Appl. Phys. Lett. 69, (1996), 2033

[5] T. Shimizu-Iwayama, K. Fujita, M. Akai, S. Nakao, and K. Saitoh, J. of Non Crystalline Solids 187, (1995), 112

[6] H. Z. Song and X. M. Bao, Physical Review B55, (1997), 6988-6993

[7] *Materials and Devices for Silicon-Based Optoelectronics*, Vol. 486, edited by S. Coffa and A. Polman (Materials Research Society, 1998).

[8] Y. Kanazawa, T. Kageyama, S. Takeoka, M. Fujii, S. Hayashi, and K. Yamamoto, Solid State Communications 102, (1997), 533

[9] P.F. Trwoga, A. J. Kenyon, and C. W. Pitt, J. Appl. Phys. 83, (1998), 3789

[10] M. L. Brongersma, A. Polman, K. S Min, E. Boer, T. Tambo, and H. A. Atwater, Appl. Phys. Lett 72, (1998), 2577

[11] A. D. Lan, B. X. Liu, and X. D. Bai, J. Appl. Phys. 82, (1997), 5144

[12] C. Delerue, G. Allan, and M. Lannoo, Phys. Rev. B48, (1993), 11024

[13] M. L. Brongersma, A. Polman, K. S. min, E. Boer, T. Tambo, and H. A. Atwater, Appl. Phys. Lett. 72, (1998), 2577

[14] K. Kimura, and S. Iwasaki, J. Appl. Phys. 83, (1998), 1345

[15] S. K. Ma and J. T. Lue, Thin Solid Films 304, (1997), 353

[16] A. Lan, B. X. Liu, and X. D. Bai, J. Appl. Phys. 82, (1994), 378

[17] R. A. B. Devine, Nucl. Inst. Meth. B91, (1994), 378

[18] D. L. Griscom, J. Non Cryst. Solids 73, (1985), 51

[19] J. F. Ziegler, J. P. Biersack, and U. Littmark, *The stopping of Ions in Solids* (Pergamon Press, New York, 1985).

[20] Y. Kanzawa, T. Kageyama, S. Takeoka, M. Fujii, S. Hayashi, and K. Yamamoto, Solid State Communications 102, (1997), 533

[21] S. Cheylan and R. G. Elliman, Nucl. Instr. & Meth. B148, (1999), 213

[22] G. A. Kachurin, M. O. Ruault, A. K. Gutakovsky, O. Kaitasov, S. G. Yanovskaya, K. S. Zhuravlev, and H. Bernas, Nucl. Instr. & Meth. B147, (1999), 356

SESSION 7

Chair – John O'Connor

Surfaces

The computer simulation of the structure of transition metal surface alloys

A. Bilić, B.V. King, D.J. O'Connor
Department of Physics, University of Newcastle, NSW 2308

1. Introduction

In recent years interest has arisen in connection with the thin alloy films of Al and Pd. Such films are created by deposition of ≥ 0.5 ML of Al onto Pd(001) and annealing to 750-950 K. The structure has been investigated using LEIS [1] and shows a p(2×2)-p4g clock reconstruction. A structure was proposed consisting of a clock-rotated Pd top layer over a c(2×2) Al-Pd underlayer. This paper presents a simulation study of the structure and energetics of Al dissolution into the Pd(001) surface using the embedded atom method (EAM) [2].

2. Method and Results

There is only one set of EAM potentials for aluminum-palladium systems in the literature [3], referred as the CY set. In this work we also make use of Al and Pd potentials of Johnson and Oh (JO) [4] and those of Voter [5]. Since they have not fitted the cross interaction between Pd and Al we use geometric mean for the cross term. To establish the exact interatomic Al-Pd potentials, parameters in

Table 1: The heat of formation or solution ΔH for Al-Pd phases, given in eV, obtained with the use of various potential sets, and from Miedema alloy theory. a is the lattice constant of the phase calculated for each of the potentials while the last column is its value predicted by the Vegard law. The units of a are Å.

	CY		JO		Voter		Mied.	Veg.
binary phase	ΔH	a	ΔH	a	ΔH	a	ΔH	a
Al_3Pd ($L1_2$)	-0.48	4.038	-1.06	3.98	-0.44	3.91	-0.57	4.00
AlPd (B2)	-0.43	3.23	-1.73	3.12	-0.60	3.06	-0.87	3.14
AlPd ($L1_0$)	-0.64	4.012	-1.73	3.94	-0.64	3.86	-0.87	3.96
$AlPd_3$ ($L1_2$)	-0.44	3.970	-1.50	3.88	-0.49	3.86	-0.54	3.93
Al in Pd	-2.92		-8.60		-1.98		-1.83	
Pd in Al	-3.25		-4.39		-1.83		-1.94	

the potentials should be changed until the structure predicted by the potential agrees with known Al-Pd structures. However, there is a lack of experimental data suitable for fitting the Al-Pd interaction. This was overcome by assuming the existence of predicted (but not observed) cubic structures such as Al_3Pd and $AlPd_3$ which have a $L1_2$ structure, AlPd with $L1_0$ and B2 structures, and fitting the results of simulations to the alloy heats of formation, taken from Miedema theory of alloys [6]. Since this work is primarily motivated with modeling clock reconstruction on Al/Pd(001), the JO set for Al and Pd were combined so as to reproduce the surface reconstruction. This has not been possible with the use of the Voter potentials. On the other hand the Voter potentials give a good

agreement with Miedema alloy theory. In Table 1 the heats of formation of the predicted Al-Pd phases as obtained with the use of CY, JO, and Voter set are compared with those predicted from Miedema alloy theory. The values for the lattice parameters are also given as calculated from these potential sets and the Vegard law (i.e. the volume of the alloy unit cell is the sum of the volumes of the elemental unit cells).

Once the potentials are known, Monte Carlo (MC) simulations and molecular statics (MS) calculations of Al mixing into the surface and subsurface layers of Pd(001) are carried out in order to find the optimum structure.

In order to simulate the Pd(001) surface a slab geometry is employed. The calculations utilize a $p(10 \times 10)$ supercell with periodic boundary conditions in the two directions parallel to the surface. The cell consists of ten atomic layers. As a first step the zero-temperature energetics of a single Al substitutional atom in a layer of the Pd(001) cell are computed by MS. In MC two types of modifications are taken into account. First, the atoms are spatially displaced in random directions. Second, every atom is allowed to change its chemical identity during the course of simulations. Each simulation considered the total of forty million modifications. The simulations are performed at temperatures of 300, 600, 750 and 900 K, with spatial displacements of the atoms up to 0.2 Å allowed. Initially the periodic cell contains only Pd atoms, while the Al atoms are created in the course of a simulation.

Table 2 presents the energy of a substitutional Al impurity atom in top three layers of the Pd(001) slab relative to the energy of that impurity in the bulk, calculated by MS. The CY set appears to favor a bulk mixture of Al in Pd, while the JO set strongly favors Al in the second layer. The differences are much less significant with the Voter set. None of the sets favors the impurity in the first layer, consistently with experiments. MC simulations reveal that the CY

Table 2: The total energy (in eV) of a single Al impurity in the first three layers of the Pd(001) slab relative to the energy of the impurity in the bulk.

Atomic layer	CY	JO	Voter
1	0.68	0.47	0.23
2	0.77	-0.71	0.03
3	0.21	-0.02	-0.02

set does not prefer intermixing of these two elements at all. Regardless of the temperature and the choice of chemical potentials, using the CY set the result is the segregation of Al and Pd phases or, at low Al concentrations, agglomeration of Al. However, with the use of Voter set, an ordered multilayer surface alloy consisting of alternating pure Pd layers and c(2×2) Al-Pd layers is created by MC simulation throughout the unconstrained layers of the slab. If the chemical potentials are chosen to generate the Al concentration equivalent to 0.5 ML, the MC run produces a structure with a c(2×2) Al-Pd underlayer under a pure unreconstructed Pd top layer. After subsequent MS relaxation it is found that Pd atoms in the underlayer are buckled upward by 0.02 Å relative to Al. The use of the JO set also results in the creation of Al in certain layers. However, it is

interesting to note that, with the use of JO set, the structure of the second layer becomes more regular c(2×2) as the temperature increases from 300 to 900 K, as shown in Fig 1. Likewise, the clock reconstruction of the top layer becomes more clear with the increase of temperature. After MS optimization a clock-displacement of 0.38 Å is obtained in the top layer, with a Pd upward buckling of 0.08 Å in the second layer. The JO set is the only alloy potential that reproduces the experimentally observed Pd(001)-p(2×2)-p4g-Al structure.

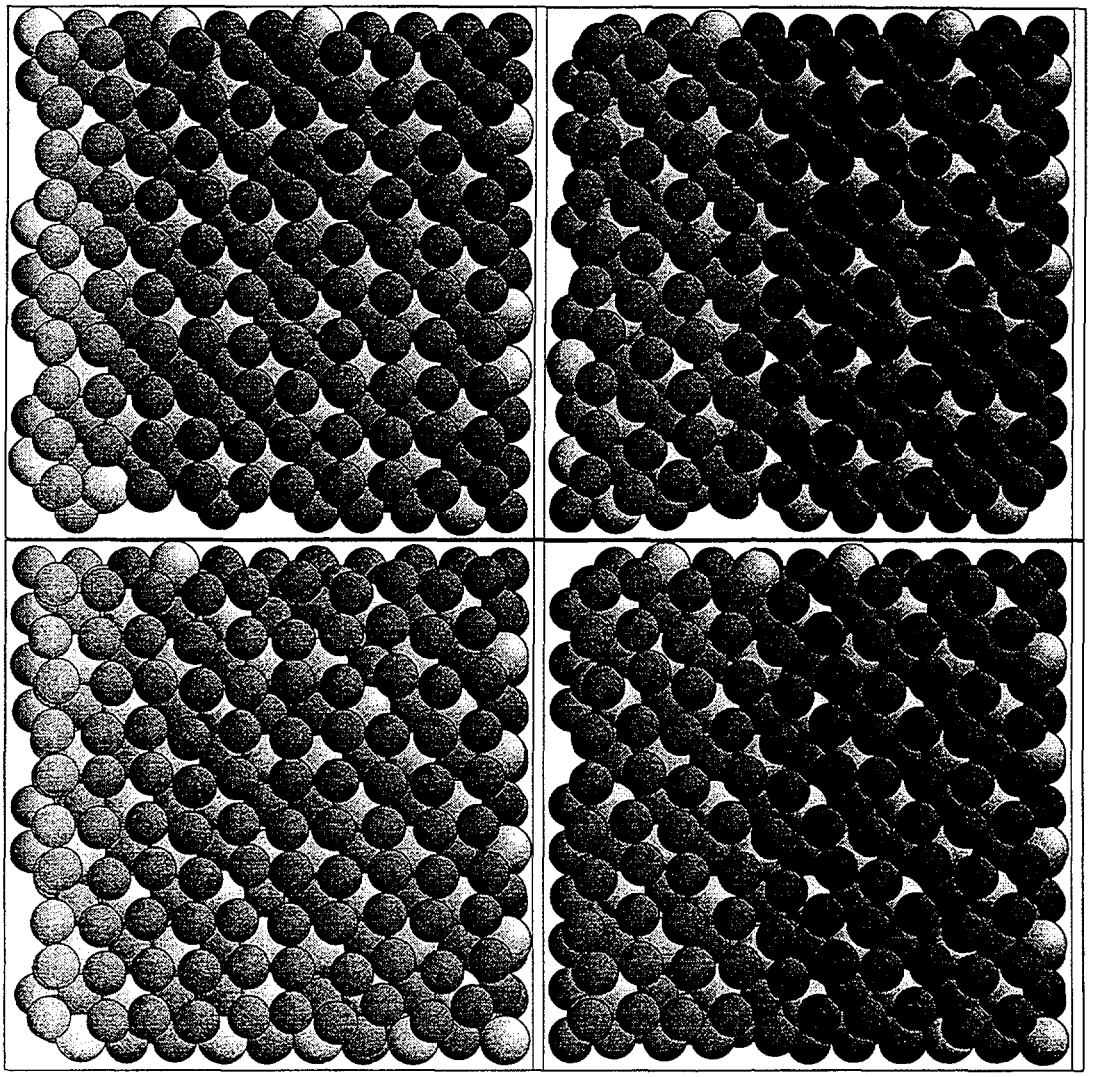

Figure 1: The snapshots of a randomly selected configuration from the MC simulations of the Al/Pd(001) surface at different temperatures using the JO potential set. The dark (light) spheres are Pd (Al) atoms. Upper left panel - T = 300 K. Upper right panel - T = 600 K. Lower left panel - T = 750 K. Lower right panel - T = 900 K.

4. Discussion and Summary

No reliable alloy potential for Al-Pd systems has yet been published in the literature. The only published potential, the CY set, in this work gave less satisfactory results than two potentials (Voter and JO) which have been generated in a simple manner from elemental Al and Pd potentials. For example, for the B2 phase the experimental lattice parameter of 3.05 Å is noticeably smaller than that of the Vegard law. On the other hand Table 1 shows that the CY set yields lattice parameters which are too big, exceeding those of the Vegard law. The CY set also favors segregation rather than the mixing between Al and Pd. The results from the Voter set are in a good agreement with Miedema alloy theory. The Voter set also gives a lattice constant for the B2 phase in a good agreement with the experimental value, while the other lattice parameters are also below the Vegard law values. The JO set is in good agreement with the Vegard law, but the values for the heats of formation and solution greatly exceed those of Miedema.

Only the JO set has given partially good results when applied to Al/Pd(001) alloying. Firstly, it strongly favors the creation of Al impurities in the second layer. Secondly, it is capable of reproducing the desired top layer reconstruction, with the second layer stoichiometry as in the experiment. It is interesting to note that this structure becomes more ordered with the increase of temperature up to 900 K. Larger buckling of Pd in the second layer is obtained with the JO set compared to that obtained with the Voter set. This may imply that the top layer reconstruction is a consequence of buckling. Since the experimental data for the Al-Pd alloys are insufficient to generate such a potential, more data must be extracted from first principles calculations.

References

[1] Y.G. Shen, J. Yao, D.J. O'Connor, B.V. King and R.J. MacDonald, Phys. Rev. B 56 (1997) 9894.

[2] S.M. Foiles, M.I. Baskes and M.S. Daw, Phys. Rev. B 33 (1986) 7983.

[3] J. Cai and Y.Y. Ye, Phys. Rev. B 54 (1996) 8398.

[4] D.J. Oh and R.A. Johnson, in *Atomistic Simulation of Materials: Beyond Pair Potentials*, edited by V. Vitek and D.J. Srolovitz, (Plenum Press, New York, 1989), p. 233.

[5] A.F. Voter, Los Alamos Unclassified Technical Report # LA-UR-93-3901.

[6] F.R. de Boer, R. Boom, W.C.M. Mattens, A.R. Miedema and A.K. Niessen, *Cohesion in Metals*, (North-Holland, Amsterdam 1988).

Quantitative study of elemental inter-diffusion across ZnSe/GaAs interface by using SIMS

Faramarz S. Gard* & John Riley* & Brian F. Usher#
La Trobe University, School of Physics* & School of Electronic Engineering# Bundoora Vic. 3083
Kathryn Prince & Patrick Burke
Environmental Science, ANSTO, Private Bag 1, Menai NSW 2234, Australia

ZnSe and related II-VI materials are wide bandgap semiconductors, which are expected to be used for blue/green lasers. However, the maximum lifetime of the devices has not been increased beyond 400 hours for the last 3 years [1]. In this time commercial GaN-based devices have been successfully introduced to market [2]. However GaN-based devices do not cover the whole range of green region, due to their bandgaps [3]. Molecular Beam Epitaxy (MBE) of ZnSe-based materials has overcome some of the problems traditionally encountered in producing high-quality crystalline ZnSe. Controlled doping of ZnSe to produce n- and p-type material has made it possible to develop high efficiency pin diodes for use in the visible region [4]. ZnSe-based materials still have a technological future, however remaining problems are yet to be solved.

This paper presents data obtained from ZnSe epilayers grown on GaAs substrates by MBE. We seek to answer the following fundamental questions about ZnSe growth on GaAs substrates by using SIMS:

- How sharp is the ZnSe/GaAs interface?
- Is there any elemental interdiffusion across the ZnSe/GaAs interface?
- What is the form of dopant profiles (i.e. concentration as a function of depth)?
- Does the dopant profile show abrupt transition between different concentration levels?
- Are spurious electrically active impurity elements present?

SIMS measurements were performed using a Cameca IMS-5f ion microscope at the Australian Institute of Nuclear Science and Engineering, (AINSE). The experimental conditions for Static-SIMS (S-SIMS) and Dynamic-SIMS (D-SIMS) are summarised in Table 1. Positive secondary ion depth profiles were taken with a 15nA Cs^+ primary Ion Current at 1.33keV, rastered over a 250 x 250μm area.

Several investigations have shown that for different samples, employing Cs^+ ion bombardment and detecting MCs^+ molecular ions can drastically reduce matrix effects in SIMS, where M designates the elements to be analysed [5]. Several pieces of evidence support the notion that this reduction of matrix effects is largely due to the MCs^+ formation mechanism: the association of Cs^+ ion and a neutral M atom in a double collision sputtering event. [6] Under steady state conditions, the flux of sputtered M represents the bulk concentration of this element and the latter can be monitored via the detected CsM^+ secondary ions. However the CsM^+ species can have an identical mass to another molecular complex and interferences can occur. When this occurs the secondary ion, M^+, is monitored.

Table 1 Experimental conditions for SIMS measurement.

Experiment	Primary Ion Current	Primary Ion Energy	Raster Size	Gated Area	Secondary Ions
S-SIMS	Cs^+/15nA	1.33keV	$2.5x10^{-3}cm^2$	$6.25x10^{-4}cm^2$	0 –320 amu
D-SIMS	Cs^+/15nA	1.33keV	$6.25x10^{-4}cm^2$	$1.56x10^{-4}cm^2$	CsM^+ & M^+

SIMS is often used to perform quantitative analysis of semiconductor samples. Characterisation of ZnSe by SIMS is difficult due to the existence of the large number of isotopes of both Zn and Se. They may combine with oxygen and hydrogen to create numerous interfering species.

Part of the mass spectra from a ZnSe epilayer grown on a GaAs substrate and from a piece of GaAs are shown in Figure1. The mass resolution is sufficient to permit identification of atoms and molecules containing all possible isotopes present in the samples. Most of the common matrix species are labelled and isotopic ratios have been calculated.

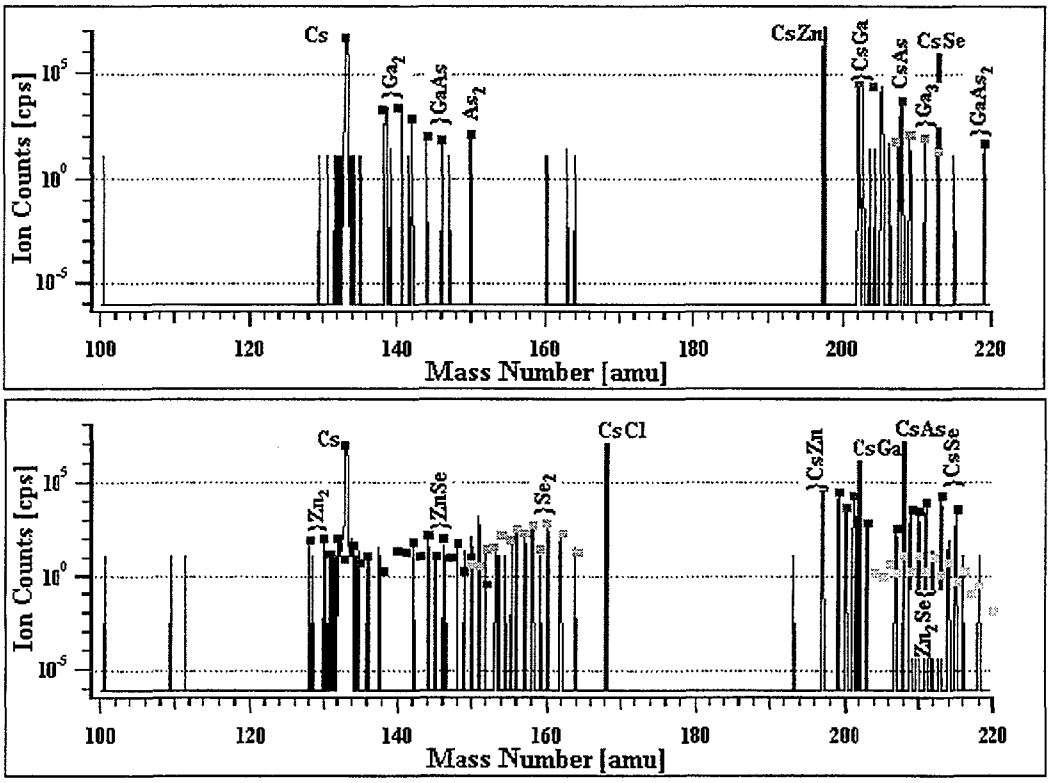

Figure 1. Positive SIMS spectrum of GaAs (Top) & Positive SIMS spectrum of ZnSe (bottom), 15nA Cs^+ primary ion beam.

For each matrix peak M^+, there is also often an accompanying hydride peak at MH^+ and less frequently an oxide peak at MO^+. The mass spectrum of the ZnSe sample is more complicated than the GaAs spectrum with a peak at almost every integer mass unit. It is possible to identify cross-matrix interferences, which can affect the results of depth profiling measurements by studying the mass spectra of the ZnSe sample and the GaAs substrate.

Quantitative SIMS depth profiling involves the use of ion-implanted standards and crater depth measurements. The depth scale is quantified by measurement of the crater after analysis using an ALPHASTEP (Tencore, Inc.) profilometer. The practical limitation to the accuracy of this measurement is either the surface roughness or the accuracy with which the sample can be levelled.

The ion-implanted standards used in this study were produced by a 1.7MeV NEC Tandem Accelerator at the Australian National University Department of Electronic Materials Engineering. Ga and As were implanted separately into ZnSe epilayers and Se and Zn were also implanted separately into GaAs substrate Samples were implanted at room temperature and were tilted 7 degrees off axis (100) to reduce the channelling effect. These standard samples were used to establish the concentration levels of Zn and Se in GaAs substrates and Ga and As in ZnSe epilayers as a function of distance from the ZnSe/GaAs interface.

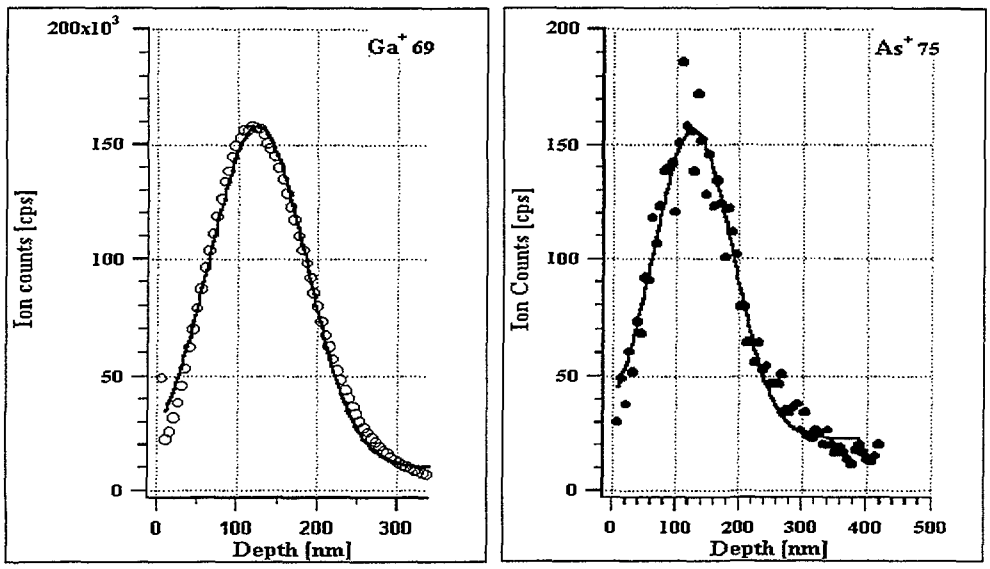

Figure 2. The original data for the Ga standard (left) and for the As standard (right).

Either the useful ion yield or corresponding sensitivity factors for Ga and As in ZnSe matrix, Zn and Se in GaAs matrix were determined by integrating over the profile of the implanted atoms. Figure 2 shows the profiles of Ga and As implanted in ZnSe epilayers. This data allows raw ion count profiles to be converted to concentration profiles.

The ZnSe/GaAs interface is not abrupt and the diffusion of Ga atoms in $ZnSe_{0.94}S_{0.04}$ layers observed by SIMS [7]. Low-temperature photoluminescence studies of undoped ZnSe grown on GaAs have suggested that the main donor impurity in ZnSe is Ga, which has diffused into the ZnSe layer from the GaAs substrate [8].

We have investigated the thermal stability of Ga from Substrate in ZnSe epilayers through the study of its thermal diffusion characteristics. Figure 3 shows the SIMS depth profiles of Ga atoms at post-annealed temperatures 400°C°, 500°C, and 600°C.

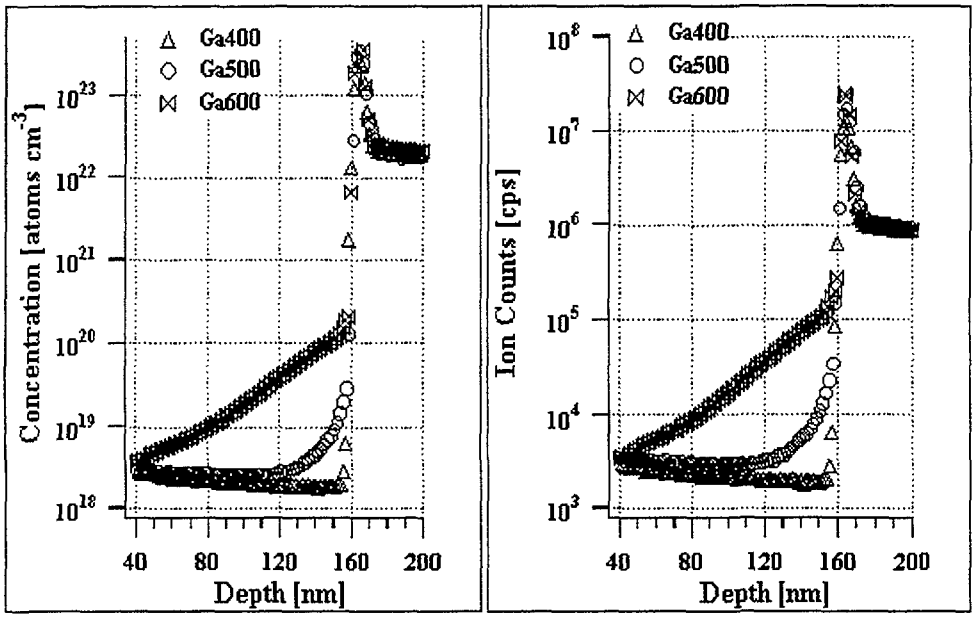

Figure 3. The raw data (right) and the quantified data (left) of SIMS depth profile of Ga atoms in ZnSe sample post-annealed for 30 minutes at three different temperatures.

The sample has been heated for 30 minutes at each above-mentioned temperature. While Ga atom diffusion could not be seen at temperatures below than 400 C° within the resolution limit of SIMS analysis, at temperature higher than 500°C diffusion of Ga atom was clearly observed. The diffusion coefficients of Ga are yet to be calculated. The diffusion of As atoms had also been investigated. The diffusion of As atoms is relatively small compare to the Ga atoms diffusion.

Acknowledgements

The Australian Institute of Nuclear Science and Engineering (AINSE) has supported this work. F.S.G. wishes also to thank the Australian government and La Trobe University for financial support.

References

S. Taniguchi, T. Hino, S. Itoh, K. Kakano, N. Kakayama, A. Ishibashi and M. Ikeda, *Electronics Lett.,* vol. 32, pp. 552, 1996

S. Nakamura, M. Senoh, S. Nagahama, N. Iwasa, T. Yamada, T. Matsushita, H. Kiyoku and Y. Sgimoto, *Jpn. J. Appl. Phys,* vol. 35, L74, 1996

A. Waag, Th. Litz, F. Fischer, H.J. Lugauer, T. Baron, K. Schull, U. Zehnder, T. Gerhardt, U. Lunz, M. Keim, G. Reuscher and G. Landwehr, *J. Cryst. Growth,* vol. 184/185, pp. 1, 1998

W. Faschinger, W. Spahn, J. Nurnberger, A. Gerhard, M. Korn, K. Schull, D. Albert, H. Ress, R. Ebel, R. Schmitt, B. Olsowi, M. Ehinger and G. Landwehr, *Phys. Stat. Solid,* vol. 202, pp. 695, 1997.

Benninghoven A et al. *Secondary Ion Mass Spectrometry SIMS IX*, Ed. Wiley, Chichester, pp. 377-425 1994

Y. Gao, J. W. Erickson, R.A. Hockett *Secondary Ion Mass Spectrometry SIMS X,* Ed. Wiley, pp. 339-342 1996

B. Cockayne, P.J. Wright, G.W. Blackmore, J.O. Williams and T. L. Ng, *J. mater. Sci.* 19, pp.3726, 1984

H. A. Mar and R. M. Park, *Jpn. J. Appl. Phys.* 27, L1728, 1988

Shallow surface depth profiling with atomic resolution

J. Xi, P.C. Dastoor, B.V. King and D.J. O'Connor

Department of Physics, The University of Newcastle, Callaghan, NSW 2308, Australia

Introduction

It is possible to derive atomic layer-by-layer composition depth profiles from popular electron spectroscopic techniques, such as X-ray photoelectron spectroscopy (XPS) or Auger electron spectroscopy (AES). When ion sputtering assisted AES or XPS is used, the changes that occur during the establishment of the steady state in the sputtering process make these techniques increasingly inaccurate for depths less than 3nm. Therefore non-destructive techniques of angle-resolved XPS (ARXPS) or AES (ARAES) have to be used in this case. In this paper several data processing algorithms have been used to extract the atomic resolved depth profiles of a shallow surface (down to 1nm) from ARXPS and ARAES data.

Methods

It is generally assumed that the solution of composition depth profiles C(x) can readily be reduced to the well-known inversion of Laplace transforms if an appropriate set of experimental measurements is available. However, it has been proven both mathematically and practically that typically there exists a host of possible solutions for C(x) for any given experimental dataset [1]. Thus, the challenge is to obtain the true solution for C(x) from a set of possible solutions and a number of different algorithms for achieving this goal are outlined below.

I. Simple search method [1]

One approach to this problem is to minimise the difference between the experimental measurements and the calculated intensities by searching for C(x), when the depth profile shapes are modelled with the benefit of a priori information about the system. For multilayer systems, however, as little as 1% of simulated noise added to the data can produce unphysical results. In order to overcome this problem the structure can be fitted by only allowing the composition of the fitted structure to vary one layer at a time. Thus, initially only the surface composition is searched with the composition of the rest of the surface held equal to the substrate composition. Then, using the fitted top-layer composition, the subsurface composition is searched with the composition of the rest of the surface equal to the substrate composition. This process is continued iteratively until the surface composition is obtained.

II. Regularisation method

Another way to eliminate the simulated noise is to regularise data; that is to filter the unwanted higher spatial frequency components of C(x) by sacrificing the depth resolution. In this case there is no need for prior information about the depth profile shape and thus this algorithm is often considered to be only a semi-quantitative technique [2].

III. Self-ratio method

Gries [3] linked the peak intensity to the moments of the depth distribution of an analyte based on the Gries-Wybenga moment equation. By means of this equation the first algebraic moment of any distribution (ie. the centroid depth) was shown to be of overriding importance and the higher central moments (variance, skewness, kurtosis. etc.) to be of rapidly decreasing significance. Hence, ARXPS or ARAES data alone is practically never sufficient for a unique

reconstruction of the depth distribution, unless the shape of the depth distribution is known. Therefore, Gries has developed a self-ratio procedure to extract the depth profile information. In this procedure the Gries-Wybenga moment equation is used to produce a chart of the model peak intensities at different emission angles for a series of depth profile shape. Then compare it with the ratios of the signal intensities at the same angles to obtain the most likely depth profile.

IV. Partial intensity method

Tilinin [4] proposed that the Laplace transform only holds when the photoemission anisotropy and elastic scattering of ejected electrons is ignored. A more realistic model is incorporated in the algorithm recently developed by Werner [5], which extracts the depth profile directly from the measurement spectrum by solving a set of linear equations derived from a Boltzmann-type kinetic equation. This kinetic equation describes the emission process of an electron after several inelastic and elastic collisions within the surface. However, adequate a priori information about the depth profile shapes is required.

Results and Discussion

The model system used to reconstruct the depth profiles is based upon the Cu_3Au system, whose well-ordered depth profile at atomic level is known to be 0.5/1.0/0.5/1.0... for Cu and 0.5/0.0/0.5/0.0... for Au. As the contributions from the deeper atomic layers to the electron emission yields decrease exponentially, it is reasonable to assume that the compositions of deeper atomic layers approach that of the bulk. Figure 1 shows the results of the simple search method and includes the assumption that the sums of the concentration of Cu and Au are unity for all depths (which further restrains the search range).

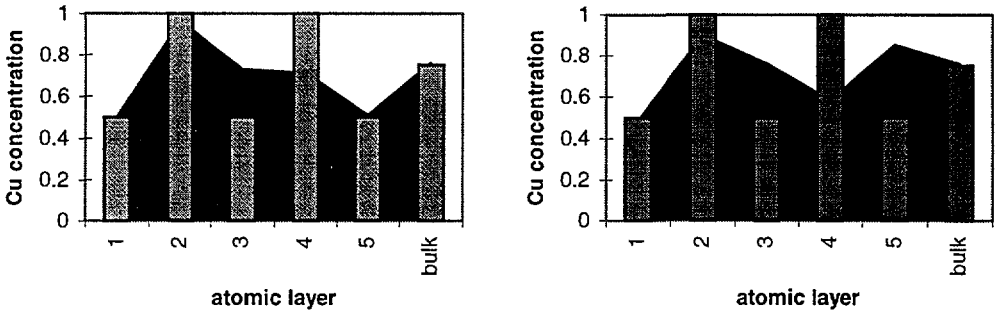

Figure1 Reconstructed depth profiles on the simulated data with 1% (left) and 5% (right) error compared with the assumed depth profile (bar)

Figure 1 demonstrates that the concentrations could be well reconstructed for only the top two atomic layers and the substrate. This is understandable since the attenuation of contributions to the peak intensity from the deeper layers increases exponentially and thus the algorithm is much less sensitive to the variation in those layers' concentration, while the contribution from the substrate is always be bigger than that from single atomic layer.

Figure 2 represents the restored depth profile results with the regularisation method using Tyler's algorithm [2]. From the left graph, we see that the Cu concentration drops from the surface layer to the second layer (at a depth of about 0.2nm) while that of Au rises, following the trend in the assumed depth profile. However, the algorithm smears the features in deeper layers out. Using smaller regularisation parameters led to instabilities in the reconstructed profiles, as illustrated in the right graph of figure2.

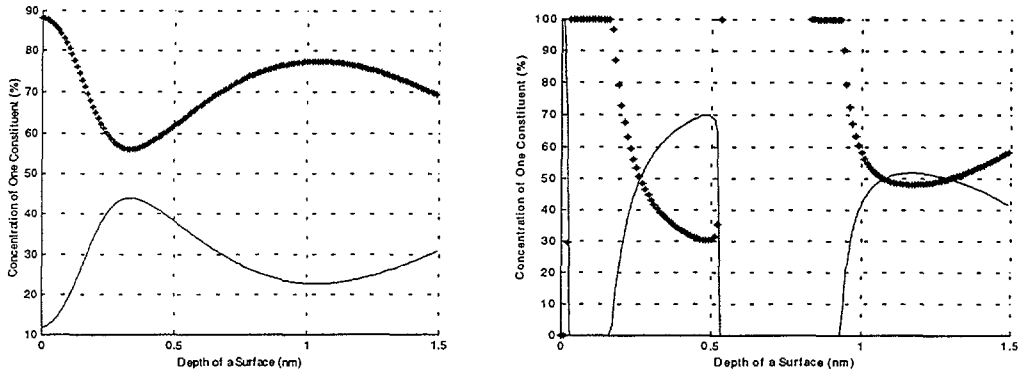

Figure2 Reconstructed depth profiles with Regularisation Method. The left graph is the profile with the large regularisation parameter, and the right one is with the small parameter, where the solid lines represent Cu and the dash lines Au.

Figure 3 shows the results of the depth profiles reconstructed using the self ratio method. It appears that more uncertainties in composition are introduced when the simulated intensities contain more noise. However, the advantages of Gries' method are that it is easily understood, accurate in error analysis and transparent in data handling.

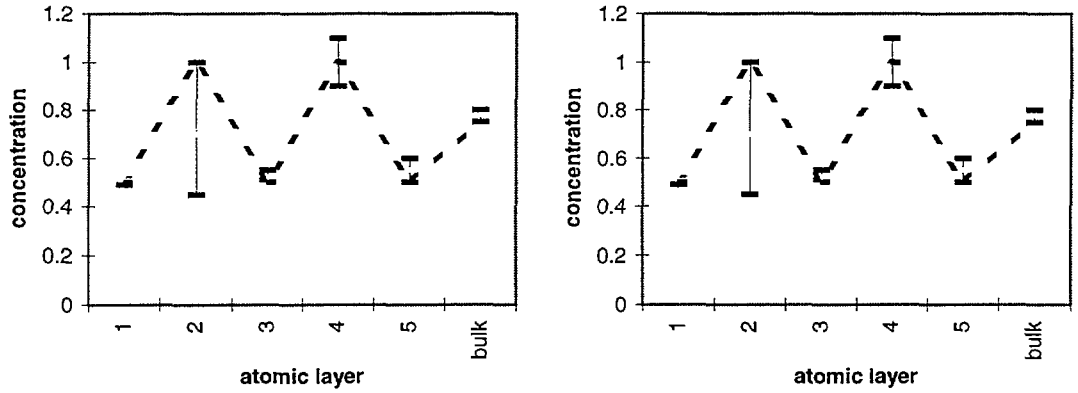

Figure3 The reconstructed concentrations with 1% (left graph) and 5% (right graph) error introduced at top five atomic layers (error bar) compared with the assumed ones (dash line)

Table 1 showed the reconstructed concentrations by the partial intensity method. It is interesting to note that the restored depth profile became unstable when only 0.1% error is introduced in the simulated intensities. This is because the expected depth resolution of this method is more than the depth of the surface.

	layer 1	layer 2	layer 3	layer 4
assumed	0.5	0	0.5	0
restored (no error)	0.5143	-0.1128	0.602	-0.0491
restored (0.1% error)	-6.89	4.626	-6.291	3.051

Table 1. Comparison of assumed and restored depth profiles with the partial intensity analysis

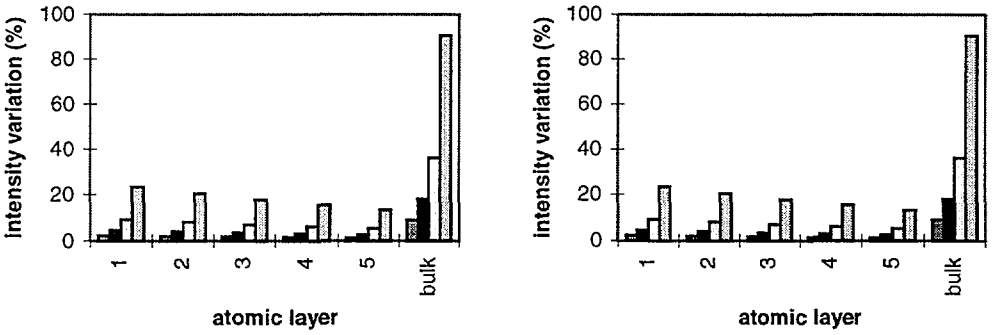

Figure 4 Intensity variation due to the concentration change (for 0.05, 0.1, 0.2 and 0.5 respectively) of different atomic layers, where the left graph is for 90 degree take-off angle and the right is for 10 degree angle.

Figure 4 shows the degree of depth profile information the ARXPS or ARAES could actually deliver, where the concentrations of other atomic layers are assumed to be unchanged, when the concentration at one atomic layer is varied. From this, it is seen that the measured intensities would experience significant changes only when the concentrations of the top two layers or substrate are changed. The deeper the atomic layer is located, the less the intensity varies, and hence, the more uncertainty there is in the concentration of the layer. This is in agreement with the work of Mroz [6], who extracted the top two atomic layers' concentration with the uncertainty of 0.05 and 0.20 respectively. It is well known that the shallow region of the surface dominates the contribution from the ejected electrons from the lower take-off angle.

Conclusions

It is possible for the simple search method to extract the composition concentration for the top two atomic layers from angle resolved electron spectroscopic measurements, and for the self ratio method to obtain such information for up to the fifth atomic layer (albeit with reduced accuracy). Atomic resolved depth profiles appear to be too fine for the regularisation and the partial intensity methods to extract meaningful compositional information. The limit of the depth profile information, that the angle resolved electron spectroscopy is able to extract, is also demonstrated.

References

[1] T.D. Bussing and P.H. Holloway, J. Vac. Sci. Technol. A 3(5), 1973-1981 (1985)

[2] B.J. Tyler, D.G. Castner and B.D. Ratner, Surf. Interface Anal. 14, 443 (1989)

[3] W.H. Gries, Appl. Surf. Sci. 100/101, 41-46 (1996)

[4] I.S. Tilinin, A. Jablonski and W.S.M. Werner, Prog. Surf. Sci. 52, 193-335 (1996)

[5] W.S.M. Werner, Surf. Interface Anal. 23, 737-752 (1995)

[6] S. Mroz and A Mroz, Vacuum, 49, 2, 101-105 (1998)

MeV Ion-induced Electron Emission from Carbon Allotropes.

D. I. Hoxley, D. N. Jamieson, S. Prawer,
Microanalytical Research Centre, School of Physics, University of Melbourne, Victoria 3010, Australia.
daewe@physics.unimelb.edu.au

R. Kalish
Physics Department and Solid State Institute, Technion-Israel Institute of technology, Haifa 3200, Israel.

Introduction

Diamonds are radiation-hard, low-noise semiconductors with unusual surface electronic properties. They have powerful applications in situations where high electron emission or multiplication is desired, such as particle detectors [1], cold cathodes [2] and vacuum switching[3]. Interest has intensified with the increasing availability of doped, conducting, synthetically grown diamond films. High electron emission has been observed for many types of radiation[4, 5]; this may be correlated with the Negative Electron Affinity (NEA) of some diamond surfaces [6]. Little work, however, has been done on ion-beam induced electron emission from diamond. We investigate the electron emission stimulated by MeV light ions, and examines the effect of the removal of the NEA surface. We apply a novel experimental technique to successfully measure the electron emission.

Experiment

Two conductive B-doped CVD diamond films were investigated: a thin (5 μm) film deposited on a conducting, p-doped Si (100) substrate, and a thicker $\sim$ 500 μm free-standing film. The diamond surface was made to be either H-terminated (by microwave H plasma) or O- terminated (by acid treatment). For comparison, a polycrystalline Au film was evaporated onto a Si (100) wafer. The samples were introduced into the target chamber of the Melbourne MP2 microprobe [7] which was then evacuated to 5×10^{-7} Torr. A $\sim 5\mu$m beam of 1 MeV H^+ was then scanned over an area of 800 μm^2 and the ion-beam induced electron yield measured using a modification of the method outlined in [8].

The electron yield γ is defined as the number of electrons escaping the surface of a target per incident ion. To obtain γ, two measurements were made: firstly, the sample was biased positive so that the vast majority of electrons emitted were attracted back to the sample, and the sample current was thus due to the beam only. The integrated charge on the sample (A_+) and the backscattered proton yield (Y_+) were recorded. The bias polarity was then reversed, so that all electrons leaving the surface were swept to the earthed walls of the chamber, and the charge (A_-) and backscattered yield (Y_-) were measured. The purpose of measuring the backscattered yield (Y) is that it is largely unaffected by the sample bias, and can therefore be used to normalise the variations in beam current. The yield is then

$$\gamma = \frac{(A_-)(Y_+)}{(A_+)(Y_-)} - 1. \quad (1)$$

It should be noted that this method uses only the standard ion microprobe instrumentation; simple software allows the instant calculation of γ upon the completion of

each pair of scans.

Results and Discussion

Nature of Surface	γ (electrons/ion)
Polycrystalline Au	1.8
Sample 1: thick H-terminated diamond	30.9
Sample 2: thin H-terminated diamond	11.1
Sample 3: thick O-terminated diamond	5.2
Sample 4: thin O-terminated diamond	5.2

Table 1: Yield for different surfaces.

The electron yields, γ, for various surfaces under 1 MeV H^+ ion bombardment are shown in Table 1. It is clear that the B-doped, H-terminated diamond surface exhibits an exceptionally high yield, an order of magnitude greater than most metal surfaces ($\gamma \sim 1-2$ for 1 MeV H^+). High yields ($\gamma \sim 25$) have been reported previously for 100-300 keV H^+ irradiation of similar films [9], but the role of the surface termination was not explicitly addressed. It is well established that H termination of CVD diamond creates a surface with negative electron affinity (NEA), we can see here that NEA is not the sole factor responsible for the high yields. Replacement of the H termination with O termination creates a positive electron affinity surface [9], and it can be seen that while this reduces the yield significantly, it is still higher than for typical surfaces. The thick film is high-quality commercially grown diamond, exhibiting larger crystals and fewer grain boundaries than the thin film. The higher crystal quality may account for the dramatically higher yield of the thicker film surface when H-terminated.

The yield from the polycrystalline Au surface compares well with values found in the literature. *In-situ* cleaned Au surfaces have a slightly lower yield than we measured ($\gamma = 1.35$ [8]), but films exposed to air before analysis show similar values ($\gamma = 1.9$) [9]. This result is consistent with the presence of an adsorbed hydrocarbon overlayer, which deposits almost immediately on the sample from the ambient whilst being transferred to the target chamber [8]. This effect is not large enough to account for the high yields seen from the diamond surfaces.

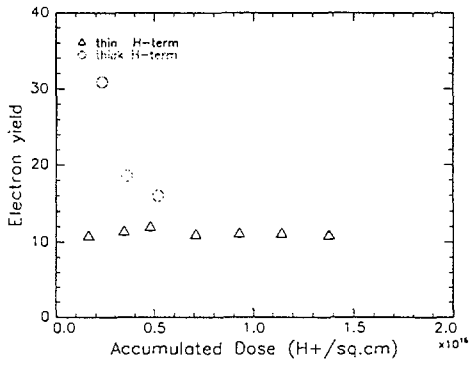

Figure 1: Variation of γ with dose for H-terminated diamond surfaces.

The high yield characteristics of the thin film were unaffected by increasing dose up to 1.5×10^{16} ions.cm^{-1} (Figure 1). The thick film at first glance appears to show a strong

yield dependence, but in fact the measured backscattered yield is artificially inflated by large sample charging , allowing more low energy backscattered protons to be detected. This can clearly be seen from the scan with the sample biased positive. There was no evidence for charging on the thin diamond film. The high electron yield is thus stable for large doses, a very desirable property for radiation measurement applications. Since removing the H-termination lowers the yield by half, we conclude that the H-termination is not removed by doses of up to 1.5×10^{16} ions.cm^{-1}. When measuring the emission of diamond surfaces, care must be taken to avoid sample charging.

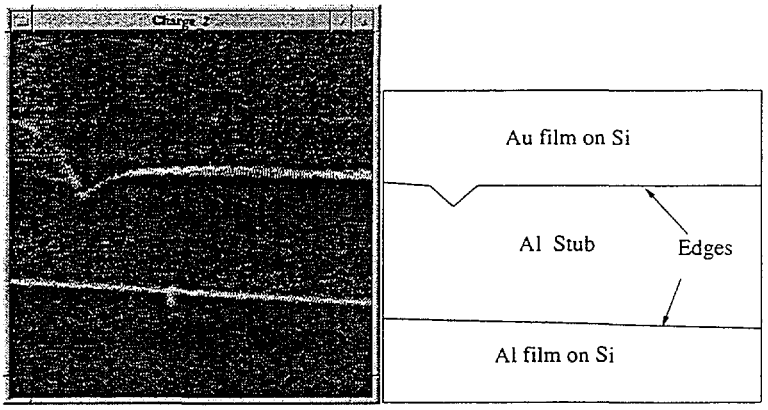

Figure 2: Charge map from Al and Au coated Si wafers mounted adjacent on Al stub.

This technique for measuring γ can easily be combined with pre-existing microprobe scanning software to provide high spatial resolution. Figure 2 shows the variation of integrated charge at each point on an inhomogeneous sample when the sample is biased negative and subject to 1 MeV H^+ ions. A schematic is shown alongside; the samples consist of two metal-coated Si wafers mounted adjacent to each other on an Al stub. Increased emission from the sharp edges of the wafers is clearly visible. The secondary electron yield can be extracted from a desired area using software; in this case the Al and Au surfaces had γ of 2.0 and 2.5 respectively.

Conclusion

We have found H-terminated, B-doped diamond exhibits very high ion-induced electron yields ($\gamma = 30.9$). Removal of the H-termination reduces the yield dramatically, ($\gamma = 5.2$) but it is still higher than metals under the same conditions. This is consistent with the downward band bending characteristic of the p-doped diamond surface. This result indicates that the negative electron affinity, while significant, is not the sole factor leading to high electron emission from diamond surfaces. The method used is a simple yet powerful extension of standard ion microprobe techniques, offering accurate measurements with high spatial resolution.

Future experiments are planned to further explore the mechanism responsable for the high electron emission from diamond, and extend this work to other high-emission forms of carbon.

REFERENCES

[1] S.F. Kozlov, R. Stuck, M. Hage-Ali, and P. Siffert. *IEEE Trans. Nuc. Sci.*, 22:160, 1975.

[2] R.U. Martinelli and D.G. Fisher. *Proc. IEEE*, 62(10):1139, 1974.

[3] K. Bergmann, R. Lebert, J. Kiefer, and W. Neff. *Appl. Phys. Lett.*, 71(14):1936, 1997.

[4] A. Breskin, R.Chechik, E. Shefer, D. Bacon, Y. Avigal, R. Kalish, and Y. Lifshitz. *Appl. Phys. Lett.*, 70(25):3446, 1997.

[5] A. Shih, J. Yater, P. Pehrsson, J. Butler, C. Hor, and R. Abrahms. *Jnl. Appl. Phy.*, 82:1860, 1997.

[6] F.J. Himpsel, J.A. Knapp, J.A. van Vechten, and D.E. Eastman. *Phys. Rev. B*, 20:624, 1979.

[7] D.N. Jamieson. *Nucl. Inst. Meth. B*, 136-8.

[8] D. Hasselkamp. *Kinetic Electron Emission from Solid Ssurfaces under Ion Bombardment*, pages 1–81. Springer-Verlag, 1991.

[9] R. Kalish, V. Richter, E. Cheifetz, A. Zalman, and P. Yona. *Appl. Phys. Lett.*, 73(1):46, 1998.

A Novel Method for Fabricating Quantum Wires in Silicon.

A. C. Y. LIU and J. C. McCALLUM
Microanalytical Research Centre, School of Physics, University of Melbourne, Parkville, Victoria 3010, Australia, amelia@mozart.ph.unimelb.edu.au

Solid phase epitaxy (SPE) has been extensively studied in silicon. The parameters for the Arrhenious behaviour of the SPE rate have been determined with extreme accuracy in the intrinsic case through the use of extended and buried amorphous layers[1]. SPE has also been observed to proceed laterally if the amorphous volume is constrained to the plane of the crystal template. Thus far lateral SPE has only concerned radial growth outward from a crystal seed. It has been found in this case that the velocity of the interface depends strongly on the direction of growth[2]. Introduced species influence the rate of SPE. Gold, for example, has been found to enhance the rate of SPE in silicon by as much as 50 times. It has been noted that the introduced gold is zone refined in the amorphous volume and finally precipitated at the interface[3].

We propose to incorporate the phenomena of lateral SPE and the zone-refinement of the coinage metals in the available amorphous volume during SPE to create wire-like structures in bulk silicon with lateral dimensions of nanometres and lengths of several microns. The processing steps are enumerated in Figure 1. A multi-energy self-implant through a nickel grid amorphises regions of the silicon to a depth of $5\mu m$. The period and aperture size of the grid results in an array of these amorphous "wells" separated by $12\mu m$ and approximately $2\mu m$ in diameter. Metal impurity atoms are then implanted through the grid at an energy of $500keV$ and a fluence of above $5 \times 10^{14}/cm^2$. An intermediate anneal at $480°C$ (not shown) diffuses the metal atoms evenly throughout the amorphous volumes of the "wells". A final anneal at temperatures in the vicinity of $600°C$ crystallises the amorphous "wells" and impels the metal atoms into the core region.

Implants were performed using the NEC ion implanter at the Electronic Materials Engineering laboratory at ANU. All implants were performed at liquid nitrogen temperatures to minimise the effects of thermal swelling of the grids. The atomic force microscope (AFM) has been found to be an ideal tool for characterising the topography of these samples. Amorphous silicon is less dense than crystalline silicon by roughly a couple of percent. This implies that the amorphous "well" regions should be apparent on the sample surface as "hillocks". The topography obtained with the AFM shown in Figure 2 confirms this expectation. As can be seen the period of the structures is $12\mu m$ and their diameters are around $2\mu m$. The fact that the "well" regions are square confirms that the grid used for the implants was stable throughout the process. Hence the "well" array is an apparent negative of the mask. The survey of heights taken as a profile across several of these "wells" indicates that the structures protrude some $80nm$ above the surface, and that they are, to all indications, uniform over the implanted area. Figure 3 is an AFM topography of one "well" showing some slight divergence from the ideal sharp square shape. A raised skirt region may be seen on one side of the protrusion which may be due to some slight instability of the grid in this direction.

Confocal Raman spectroscopy in a backscattering configuration was performed on a sample at several stages of its processing using the Dilor Confocal Raman spectroscope at the University of Melbourne. The sample contained gold implanted at a dose of $5 \times 10^{14}/cm^2$, and the annealing was interrupted at several stages to gauge the progress of lateral SPE. The amorphous "wells" in this sample were considerable larger and

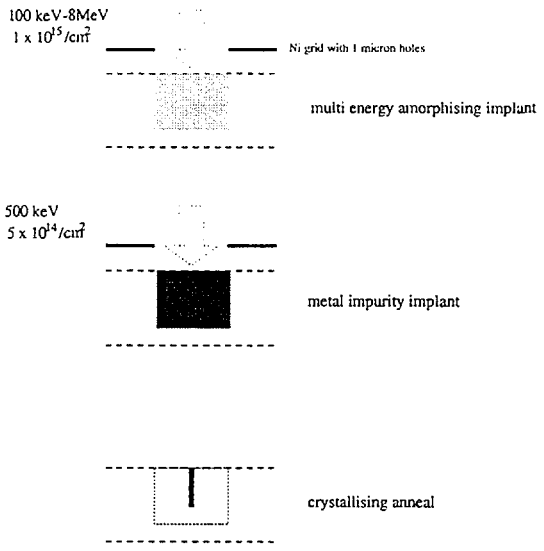

Figure 1: The process of making quantum wires in silicon.

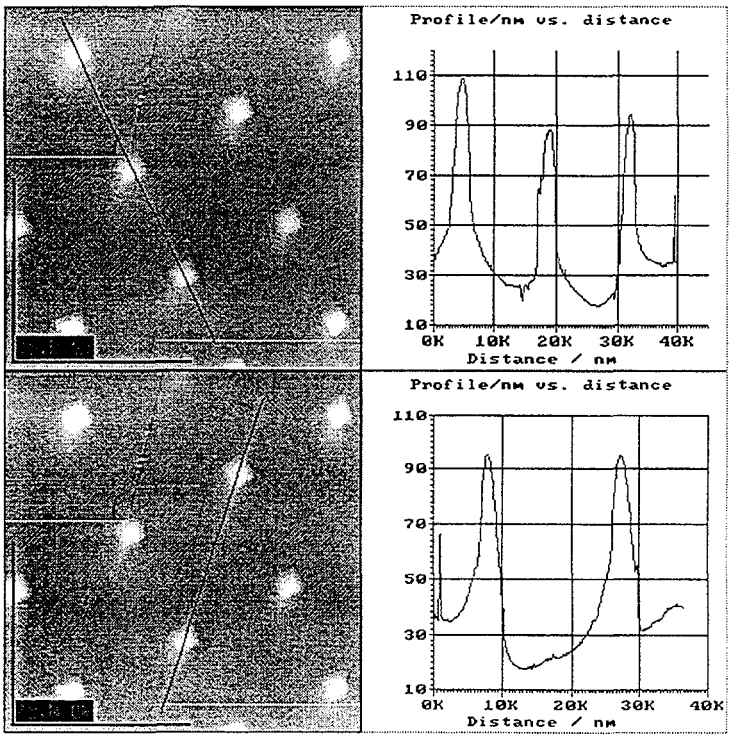

Figure 2: AFM topography of an asimplanted amorphous "well" array.

less symmetric than those depicted in Figure 2. Raman spectroscopy is a sensitive measure of the structure of silicon. In particular the position, intensity and width of both the crystalline and amorphous TO and TO-like peaks respectively are powerful determinants of parameters like the RMS bond angle distortion. In this case the argon

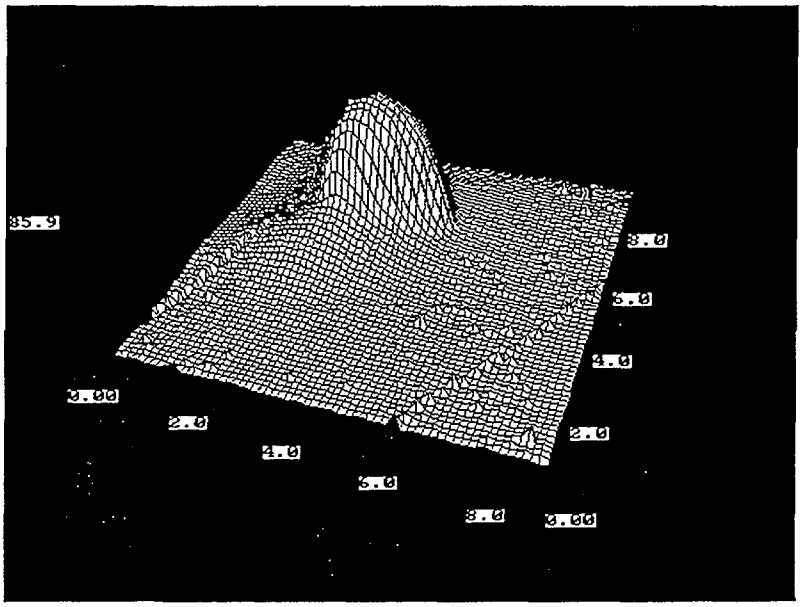

Figure 3: The AFM topography of a single "well" indicating a slight asymmetry.

laser beam ($\lambda = 514.5nm$) was focussed to a $1\mu m^2$ spot size on the sample surface and scanned across the sample in $1\mu m$ steps. The Raman spectrum was obtained at each position and deconvolved into Gaussians accounting for the amorphous and crystalline peaks. The crystalline TO peak occurs at $520cm^{-1}$ and is permitted by selection rules while the amorphous peak centres on $470cm^{-1}$ and is broader, the amorphous spectrum being representative of the full vibrational density of states. The background was subtracted using a broad Gaussian. The particulars of both the amorphous and crystalline peaks obtained from the fits can be used to generate maps of the sample, differentiating between crystalline and amorphous, and relaxed amorphous regions.

In Figure 4 two such maps are shown, obtained from plotting the crystal peak intensity against position on the plane. The area scanned was in each instance $15 \times 15\mu m^2$ which is enough to visualise one "well" in some detail. The map on the left is the as-implanted case. As can be seen there is virtually no intensity from the crystalline peak in the centre of the amorphous "well". However, variations in the intensity of the TO peak are seen over a large area, indicating a large degree of strain in the surrounding crystalline material. Such an interpretation must be made carefully, however, since the spot size is estimated to approximate the size of the structures, and so, a good deal of spatial broadening of the signal is expected to have occurred, rendering the implanted area apparently larger than it really is. The map on the right was made of the same sample after a $480°C$ relaxing anneal. While absolute intensity cannot be compared between the two maps due to variations in laser intensity on subsequent occasions, relative intensity changes are interesting. For example, it is clear that the "well", having been subject to the relaxing anneal has a sharper interface region, with the intensity of the crystalline peak changing more rapidly at the perimeter. The size of the "well" has not laterally decreased, as expected, for an anneal at such a moderate temperature.

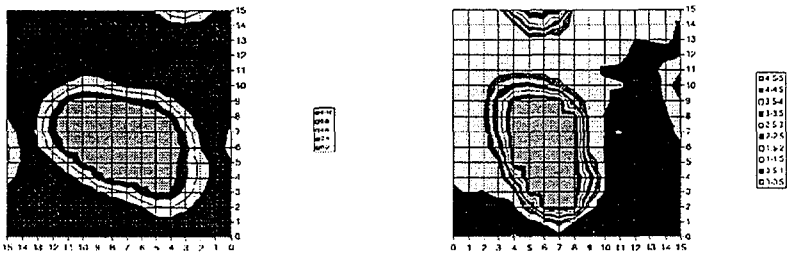

Figure 4: $15 \times 15 \mu m^2$ Raman maps obtained from plotting the crystalline peak intensity for an as-implanted sample (left) and a sample which has undergone a relaxing anneal. The interface is significantly sharpened by the anneal at the moderate temperature.

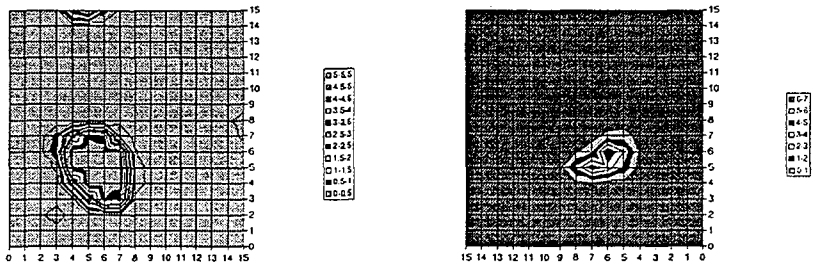

Figure 5: $15 \times 15 \mu m^2$ Raman maps obtained from plotting the crystalline peak intensity for a sample annealed at $600°C$ for $7mins$ (left) and $15mins$ (right) Lateral SPE is observed at such a temperature.

Figure 5 displays two similar such maps for the same sample having been annealed at a crystallising temperature for $7mins$ and $15mins$ respectively. Annealing at such an elevated temperature induces SPE as seen in the figure by the decreasing size of the amorphous region. It is interesting to remark that initial asymmetry in this sample is retained during the epitaxy suggesting an almost constant interface velocity, independent of direction over this range. While analogous maps may be generated with other fitted parameters, like the width and positions of the peaks, these are less striking, suggesting that the fitting routine is not yet an accurate reflection of the data.

The results of this survey of these most interesting systems is far from complete. Additional studies with the AFM and cross-sectional transmission electron microscopy are required to fully resolve the complex behaviour of these slight subjects.

REFERENCES

[1] J. C. McCallum, Nuc. Instr. Meth. B 148 (1999) 350-354.

[2] H. Yamamoto, H. Ishiwara and S. Furukawa, Jap. J. App. Phys. 25(5) (1986) 667-672.

[3] D. C. Jacobson, J. M. Poate and G. L. Olson, Appl. Phys. Lett. 48 (2) (1986) 118-120.

SESSION 9

Chair – Chris Ryan

Ion Beam Analysis-2

Hydrogen isotope profiling of functionalised polystyrene blends using RBS/ERD and RBS/NRA with simulated annealing data analysis

E.Wendler[1], C.Jeynes[1], N.P.Barradas[1,4], R.L.Thompson[2], R.Smith[3], R.P.Webb[1]

University of Surrey Ion Beam Centre, Guildford, GU2 5XH, England
Interdisciplinary Research Centre in Polymer Science and Technology, University of Durham, DH1 3LE, England
Department of Physics, University of Surrey, GU2 5XH, England
Now at Instituto Tecnologico e Nuclear, E.N. 10, 2686-953 Sacavem, Portugal

The behaviour of thin surface–active polystyrene (PS) films on silicon is being investigated. These films have amine functional groups which are attracted to the solid interface if they are fluorinated (N-PSF), and to the air interface if they are not (N-PS). To determine the interface enrichment of the species a "sandwich" of deuterated- (DPS) and hydrogenated (HPS) films was prepared. 1.5MeV ^{4}He ERD/RBS together with 0.7MeV ^{3}He NRA to determine the D profile were applied to the films, and a self consistent analysis of all three spectra using the simulated annealing algorithm was made for each sample. The ERD data contains both H and D recoils, but the D profile does not have such good depth resolution as in the NRA data. The results are combined with data from neutron reflectivity.

1. **N.P.Barradas, C.Jeynes, R.P.Webb**
Simulated annealing analysis of Rutherford backscattering data
Appl.Phys.Lett. 71 (1997) 291-3

2. **P.K.Marriott, M.Jenkin, C.Jeynes, N.P.Barradas, R.P.Webb, B.J.Sealy**
Rapid accurate automated analysis of complex ion beam analysis data
CP475, *Applications of Accelerators in Research and Industry* (eds. J.L.Duggan, I.L.Morgan) AIP 1999, pp592-595

3. **N P Barradas and R Smith**
Simulated annealing analysis of Nuclear Reaction Analysis measurements of polystyrene systems
J. Phys. D: Appl. Phys. 32 (1999) 2964-2971

High Resolution Detection Of Hydrogen In Thin Films

R.G. Elliman*, H. Timmers*+, T.R. Ophel+, L.S. Wielunski# and G.L. Harding#

* Department of Electronic Materials and Engineering+, Department of Nuclear Physics
Research School of Physical Sciences and Engineering,
ANU Canberra 0200.

CSIRO, Telecommunications and Industrial Physics, Lindfield, NSW.

INTRODUCTION

It is well known that elastic recoil protons can be detected with high energy resolution, and therefore optimum depth resolution, using magnetic spectrometers. Moreover, substantial acceptance is obtained with spectrometers that allow kinematic compensation.

The measurements to be described illustrate the potential capabilities of the ANU Enge split-pole spectrometer for high resolution surface depth profiling. They are presented to stimulate possible application by the NTA community.

SPECTROMETER INSTRUMENTATION

The ANU Enge split-pole spectrometer, installed in 1976, supported active programs, mainly relating to heavy ion reactions, for some fifteen years. More recently, reaction measurements have been largely replaced by various projects in the bailiwick of NTA, including AMS.

Several focal plane detectors, developed for reaction work, make it possible to detect back-scattered, low energy heavy ions with good energy resolution [1]. One of them is well-suited to high resolution detection of light ions, including protons. Position resolution of 2 mm along the focal plane for protons, which would correspond to an energy resolution of 4 keV for 2 MeV protons (the energy of elastic recoils produced at 45 degrees by a 200 MeV ^{197}Au beam), has been achieved in the past [2]. The active length of the detector is either 53 or 70 cm, depending on the nature of auxiliary information (such as angle of entry and energy loss measurements) required. Thus it spans a more than adequate range of about a factor of two in proton energy. In general, depth resolution deteriorates rapidly with film depth because of multiple scattering. Thus the advantages of using a spectrometer become far less pronounced for the detection of protons originating from depths that produce energies well within this spectrometer dynamic range. Simpler alternative methods are preferable to probe greater depths.

PRESENT MEASUREMENTS

Measurements are reported of two samples prepared at CSIRO, North Ryde. One sample had two hydrocarbon layers deposited onto a silicon substrate, with an aluminium layer 400 nm thick separating them. The thickness of the surface hydrocarbon layer was 40 nm, while that of the deeper layer was 60 nm. The second sample was made up of four layers of

hydrocarbon, 10 nm thick, each separated by an aluminium layer 40 nm thick. No particular effort was made to optimize the resolution of the focal plane detector, since the object was merely to obtain illustrative measurements. Even so, the position resolution was 4 mm. Improvement to at least 2 mm and possibly 1 mm is merely a procedural detail.

A beam of ^{197}Au at 154 MeV was used. Recoil protons were detected at an angle of 19 degrees, with the samples inclined at 28.5 degrees to the beam direction. The choice of scattering angle was determined by the spectrometer design. The kinematic energy variation with angle of the recoils is close to the maximum that can be corrected for by a split-pole, given the geometrical constraints imposed on movement of the focal plane detector. At the angle used, kinematic compensation obtained, making acceptances of 2 and 4 msr feasible.

Measurements of the double layered hydrocarbon sample (Figure 1) demonstrate the impressive dispersion of the spectrometer and clearly are superior to similar measurements with the same samples of the elastic recoils, produced either by 4 MeV alpha particle beam with a surface barrier detector, or by a 154 MeV ^{197}Au beam using a gas ionization detector.

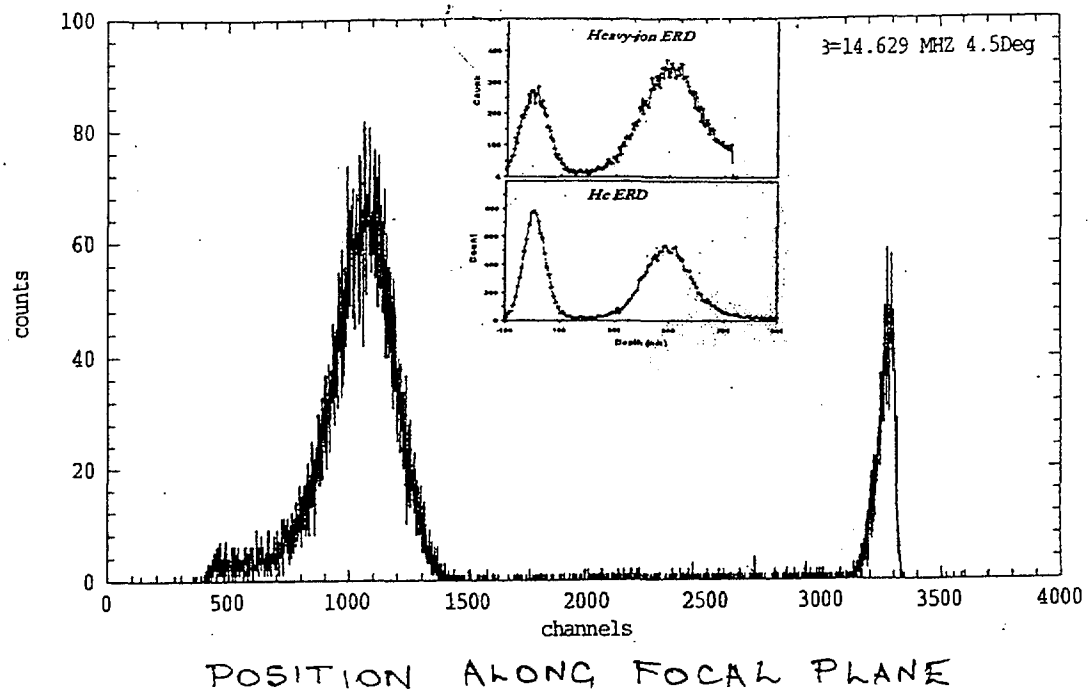

Figure 1. Position spectrum of elastic recoil protons from the double-layered sample. Details of the inset data are given in the text. They are plotted in reverse, i.e. depth increases from left to right.

A better illustration of the surface resolution capabilities is provided by the results for the second, multi-layered sample. An acceptance of 2 msr was used for the data shown in Figure 2. No significant degradation of surface resolution was observed at 4 msr, confirming that the conditions for kinematic compensation were correctly established. Even with the less than optimum detector conditions, the depth resolution for the surface edge is 10 nm. The anticipated deterioration of depth resolution with sample thickness is noteworthy.

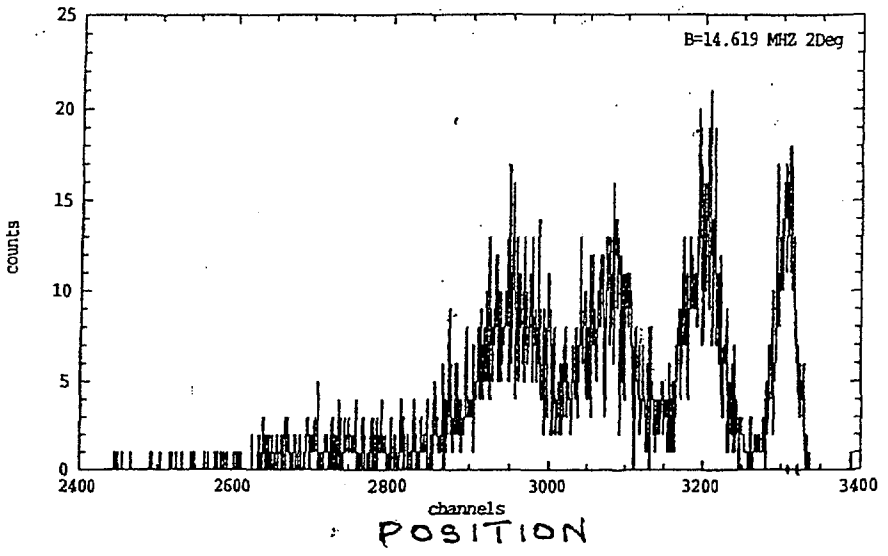

Figure 2. Position spectrum measured for the multi-layered sample. The surface hydrocarbon layer is 10 nm thick.

SUMMARY

A facility for high resolution surface studies of hydrogen is available at the ANU. Further development and application await interested users requiring surface analysis with 2 - 5 nm resolution.

REFERENCES

[1] T.R. Ophel and I.V. Mitchell, Proc. 9th Australian Conference on Nuclear Techniques of Analysis (1995) 80.

[2] T.R. Ophel and A. Johnston, Nucl, Inst. & Meth., 157 (1978) 461.

Characterisation of magnetron sputtered $SmCo_5$ thin films

Y. Wang, M. K. Ghantasata*, D. K. Sood and Kothari

Department of Communication and Electronic Engineering, * Department of Electrical Engineering, RMIT University, 124, La Trobe Street, Melbourne, 3000, Australia

K. T. Short, P. J. Evans and K. Prince

Australian Nuclear and Technology Organisation, Lucas Heights Research Laboratory, Private Mail Bag. 1, Menai, 2234, Australia

Abstract: $SmCo_5$ thin films were deposited using DC magnetron sputtering on single crystal silicon substrate with chromium and SiO_2 top layers. Deposition was carried out at three different substrate temperatures: room temperature, 400°C and 600°C. Films were characterised by using Rutherford Backscattering Spectroscopy (RBS), X-ray Diffraction (XRD), Secondary Ion Mass Spectrometry (SIMS) and SQUID magnetometer. RBS analysis indicated that the films have excellent stoichiometry with the Sm to Co ratio of 1:5. This analysis also showed that the films deposited or annealed at high temperatures ($\geq$ 600°C) indicated significant inter-diffusion at the interface between the barrier layer and the film. Oxygen was found to be the major impurity in the films. XRD data indicated that the films formed 1:5 and 2:17 phases under different deposition conditions. The preliminary studies of these films using magnetic force microscopy revealed the presence of magnetic domains.

1. Introduction

Permanent magnetic films play an important role in the realisation of many Micro Electromechanical System (MEMS) devices. One of the major requirements for such applications is the need to deposit permanent magnetic films with high coercivity and large energy products on silicon substrates. Among the rare earth group of permanent magnetic films, SmCo films typically offer both excellent intrinsic and extrinsic magnetic properties, rendering them suitable for small and compact designs where higher operating temperature and higher corrosion and oxidation resistance are crucial. Cadieu et al.[1] showed that $SmCo_5$ films directly crystallised on to a heated substrate have a coercivity (Hc) of about 23kOe. The reason for this high coercivity was associated with the high magnetic anisotropy and the fine grain structure. $SmCo_5$ films deposited on a Cr underlayer are reported to have shown a coercivity value of 3kOe at room temperature [2]. Malhotra et al [3] reported a coercivity of about 500 ~ 2800Oe for as-deposited SmCo films with a Cr underlayer, but after annealing at 500°C a coercivity of as high as 31kOe for SmCo/Cr films. The large increase in coercivity for the annealed films is attributed to the growth of the crystallites. Okumura et al.[4] confirmed similar properties and found a much higher coercivity Hc=3.6kOe for Co rich $Sm_{15}Co_{85}$/Cr films. It is clear that Hc of SmCo/Cr films depends strongly not only on the sputtering conditions, such as substrate temperature and Ar gas pressure, but also on the ratio of Sm/Co concentration, and their values are always larger than those of SmCo films deposited directly on to glass substrate. Liu et al.[5-6] reported systematic analyses of the nanostructured SmCo films on Cr underlayer, and concluded that these films is composed of crystallites of about 5 nanometres in diameter distributed discontinuously in amorphous matrix. The grain-like structure in some of the SmCo films is inherited from the Cr underlayers. This indicated that Cr underlayer plays an important role to the high coercivity of SmCo/Cr films. The volume fraction of the crystallites in the films decreases from 91% to 54% as the argon gas pressure is increased from 5mTorr to 30mTorr.

These studies indicated that the deposition of optimisation of deposition conditions to deposit the stoichiometric $SmCo_5$ films. Moreover, it has also been very clear from the literature that

these films need to be deposited at a temperature greater than at least 300°C to attain the right crystal structure. However, our earlier studies showed that the films deposited directly on silicon substrate at high temperatures resulted in the interdiffusion between the film and substrate, indicating the necessity for a barrier layer. Hence, in the present study we have investigated the suitability of two different films, chromium and silicon dioxide for possible barrier layers. SmCo films were deposited at two different temperatures 400°C and 600°C separately and the film properties such as structure, composition and some of the magnetic properties were studied.

2. *Experimental Procedure*

$SmCo_5$ thin films were deposited using DC magnetron sputtering technique. Films were deposited on silicon substrate having two different top layers with 1.5μm thick SiO_2 layer and a 0.1μm thick chromium layers. Deposition was carried out at two temperatures, 400°C and 600°C. During sputtering argon gas pressure was maintained at around 4×10^{-2}Torr. Discharge current was kept constant during all the runs at 0.5A.

The composition and structure of these films were analysed using Rutherford Backscattering Spectroscopy (RBS), and X-ray diffraction (XRD) methods, respectively. RBS was performed using a 2MeV He^{2+} beam accelerated by a Van de Graaff generator. Film composition was estimated by using standard simulation methods and comparing it with the experimental Rutherford Backscattering Spectrum [7].

3. *Results and Discussion*

The RBS spectra of the films deposited on silicon substrate with chromium top layer at 400°C and 600°C is shown in figure1. It may be observed that the film deposited at 600°C (460nm) is slightly thicker than the one deposited at 400°C (410nm). Both the films deposited were almost stoichiometric with a Sm to Co composition ratio of 1:5 within an accuracy of ±2%. Oxygen has been the major impurity in these films to an extent of around 20%. The analysis of the spectra obtained from the film deposited at 400°C indicated a chromium layer thickness of 110nm, which is the thickness of the chromium layer deposited before coating the SmCo film.

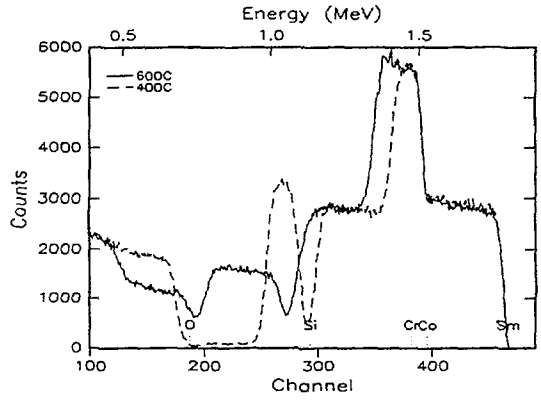

Figure 1 The RBS spectra of the films deposited on silicon substrate with chromium top layer at 400°C and 600°C, respectively.

In contrast, the film deposited at 600°C showed a considerable increase in chromium layer thickness as indicated by the broadening of the peak representing the chromium thickness. It is also interesting to note that this peak transformed into a flat topped distribution, which could be considered as a consequence of diffusion of chromium. This has been confirmed by the presence of chromium in the SmCo film layer.

Figure 2 shows the RBS spectra of the films deposited on silicon substrate with a 1.5μm thick SiO_2 layer maintained at 400°C and 600°C separately. Film prepared at 600°C is thicker than

the one deposited at 400°C, which is similar to that observed in figure1. Oxygen has been the major impurity in these films also. From the spectra of the film deposited at 400°C, it is clearly seen that the lower energy edge of Co peak represents the interface between the film and substrate. The sharpness of this edge (channel ~310) may be considered as an indication of the absence of any possible interdiffusion between the film and substrate.

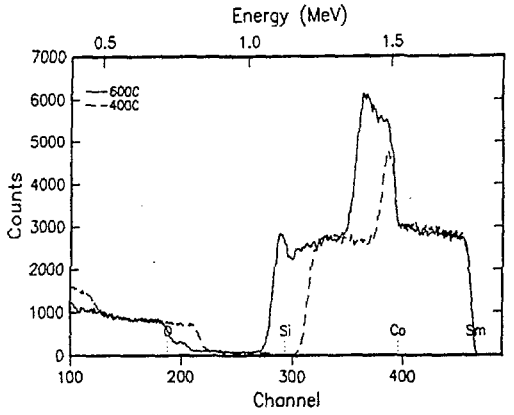

Figure 2 The RBS spectra of the films deposited on silicon substrate with SiO_2 top layer at 400°C and 600°C, respectively.

This edge in the spectrum of the film deposited at 600°C is slightly modified. Analysis of this spectrum using RUMP showed the presence of silicon in a narrow region of the film (~60nm) at the interface. However, compared to the interdiffusion noticed with the chromium barrier layer, the interaction observed between the SiO_2 and SmCo film is relatively small.

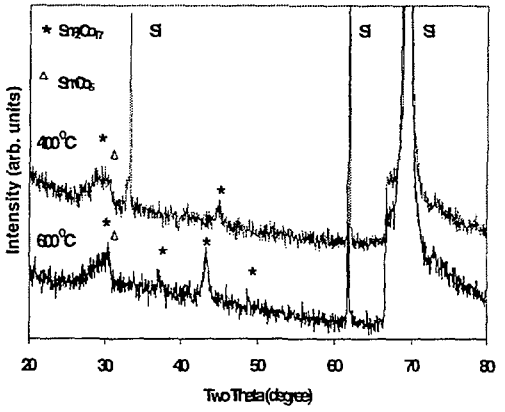

Figure 3 (a) XRD pattern of the films deposited on silicon substrate with chromium top layer at 400°C and 600°C, respectively.

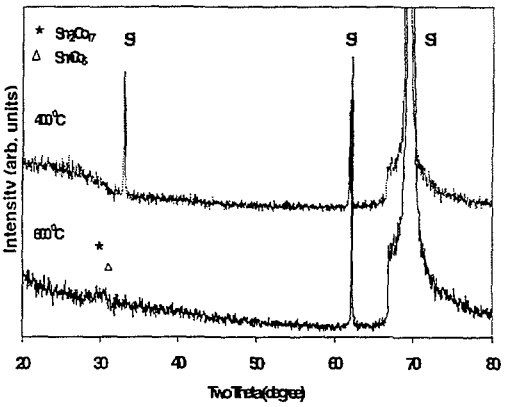

Figure 3 (b) XRD pattern of the films deposited on silicon substrate with SiO_2 top layer at 400°C and 600°C,

Figure3 compares the XRD pattern of the films deposited at 600°C and 400°C on silicon substrate with both the barrier layers mentioned above. XRD pattern of the films deposited on silicon with chromium top layer at 400°C and 600°C are shown in figure3 (a). The film deposited at 400°C indicated the formation of Sm_2Co_{17} phase. The peak at $2\theta = 45.05^\circ$ seems to represent the (111) plane of 2:17 phase, while the peaks at 2θ values of 30° and 30.65° coincide with the d-values of the (101) plane of both 2:17 and 1:5 phases respectively. In contrast, the XRD pattern of the film deposited at 600°C exhibited the (222) and (110) peaks at the 2θ values of 48.7° and 37.15° respectively in addition to those observed in the film

deposited at 400°C. Surprisingly, XRD analysis did not indicate the formation of any impurity phases due to the interdiffusion between chromium and SmCo film, which was evident in RBS data especially at 600°C. This might suggest that the impurities could still be in an amorphous state. However, this needs further investigation to ascertain the nature of impurities and their effect on the magnetic properties of the film. In figure3 (b), we have compared the XRD patterns of the films deposited at 400°C and 600°C on silicon substrate with SiO_2 top layer. In this case, while the film deposited at 400°C is still amorphous, film deposited at 600°C showed a single broad peak at 2θ values of 30.05° and 30.9°. This essentially means that this may need further annealing at a slightly higher temperature.

SIMS analysis also indicated that the films deposited at 400°C on both Cr and SiO_2 layers have sharp interfaces without any interdiffusion characteristics. However, films deposited on SiO_2 layer at 600°C seem to be relatively less prone to interdiffusion compared to those deposited on chromium layer. The study of the magnetic characteristics of these films is currently in progress.

4.Conclusions

Stoichiometric SmCo thin films were deposited in all deposition conditions with oxygen as the main impurity. Films deposited at 400°C on chromium layer appear to be micro crystalline and did not show any interdiffusion. At 600°C though the film crystallinity has improved, RBS analysis indicated possible interdiffusion between the film and chromium layer. Films deposited on SiO_2 layer indicated only the onset of crystallinity even at a substrate temperature of 600°C. It needs further investigation to understand the growth kinetics and crystallisation characteristics of the films.

Acknowledgments

This work is supported by an AINSE grant and an ARC large grant.

References

[1] F. J. Cadieu, T. D. Cheung, and L. Wickramasekera, J. Appl. Phys. 57, 4161 (1985)

[2] E. M. T. Velu, D. N. Lambeth, J. T. Thornton, and P. E. Russell, J. Appl. Phys. 75, 6132(1994)

[3] S. S. Malhotra, Y. Liu, Z. S. Shan, S. H. Liou, D. C. Stafford, and D. J. Sellmyer, J. Appl. Phys. 79, 5958 (1996)

[4] Y. Okumura, H. Fujimori, O. Suzuki, N. Hosoya, X. B. Yang, and H. Morita, IEEE Trans. Magn. 30, 4038 (1994)

[5] Y. Liu, Richard A. Thomas, S. S. Malhotra, Z. S. Shan, S. H. Liou, and D. J. Sellmyer, J. Appl. Phys. 83, 6244 (1998)

[6] Y. Liu, B. W. Robertson, Z. S. Shan, S. Malhotra, M. J. Yu, S. K. Renukunta, S. H. Liu, and D. J. Sellmyer, IEEE Trans. Magn. 30, 4035 (1994)

[7] L. R. Doolittle, Nuclear Instruments and Methods in Physics Research B9 (1985) 344

SESSION 10

Chair – Leszek Wielunski

Ion Beam Analysis-3

Simplifying position-sensitive gas-ionisation detectors for heavy ion elastic recoil detection

H. Timmers[a,b], T.R. Ophel[a], R.G. Elliman[b]

Departments of Nuclear Physics[a] and Electronic Materials Engineering[b]
Research School of Physical Sciences and Engineering ANU, Canberra, ACT 0200

1. Introduction

The use of gas-ionization detectors for Elastic Recoil Detection (ERD) [1-3] is advantageous when very heavy ion projectile beams are used. In contrast to solid state detectors, they are not affected by radiation damage. An energy resolution better than 1% can be achieved and large acceptance solid angles are possible, since position detection may be readily incorporated into the detector and kinematic energy broadening thus corrected. This is an advantage over time-of-flight systems [4-6] where the acceptance solid angle is generally limited due to the requirement for a reasonable distance between start and stop detector. Even when large area position-sensitive detectors are employed in a time-of-flight system [7], the acceptance solid angle is typically only of the order of 1-2 millisteradian.
The operation of position-sensitive gas-ionization detectors currently used for heavy ion ERD and subsequent data analysis can be considerably improved [8-10] by implementing a number of design modifications, which are discussed in this paper.

2. Conventional position-sensitive detectors for heavy ion ERD

Experiments have been carried out at the Australian National University to study design aspects of position-sensitive gas-ionization detectors for heavy ion ERD. Drawings of the original and the modified detector are shown in figure 1. Ions enter through a 70μg.cm^{-2} thick Mylar foil window, which is mounted on a cylindrical assembly. The acceptance solid angle is 5 millisteradian. Tungsten collimators can be moved in front of the detector window.
Originally, shown in figure 1a, the detector had a design similar to that of other detectors commonly employed [1,2]. The anode (+150V, 70mm wide), consisted of three sections, 30mm, 60mm and 120mm long, labeled in the figure as ΔE_1 , ΔE_2 and E_{res}, respectively. The Frisch grid (0 V) was located 10mm below the anode. The cathode, 70mm wide and 210mm long, was divided into a *Left* and a *Right* section using a sawtooth geometry. The window assembly was positioned centrally between Frisch grid and cathode, protruding 3.6mm within the edges of the electrodes.
Operation of this detector soon produced results comparable to those obtained with its counterparts in other laboratories. However, the commissioning highlighted problems, among them, field distortions by the window potential, non-linear position information and the complexity of the energy calibration, which are detrimental to measurement and data analysis. The collection of electrons on ΔE_1 and ΔE_2 is influenced by the voltage applied to the window assembly, which causes a distortion of the electric field in the entrance region [8,11]. Both ΔE signals depend on the height (y-coordinate) of the ion track. The sum of ΔE_1 and ΔE_2 is not affected. For a window voltage of –280V, which is 70% of cathode bias, the effect is smallest and this setting was used.
The recoil position is determined in two spatial directions using a cathode with sawtooth sections *Left* and *Right* (x-coordinate), and the signal ratio *C/A* of cathode and anode (y-coordinate). This information is necessary to correct the kinematic energy change with angle. Assuming a linear electric field and that the signals are calibrated relative to each other, the position is independent of energy and particle: y is proportional to *C/A* and x is proportional to *(Left - Right)/(Left + Right)*. However, it is known that this is not strictly true for actual detectors [1,8,12].

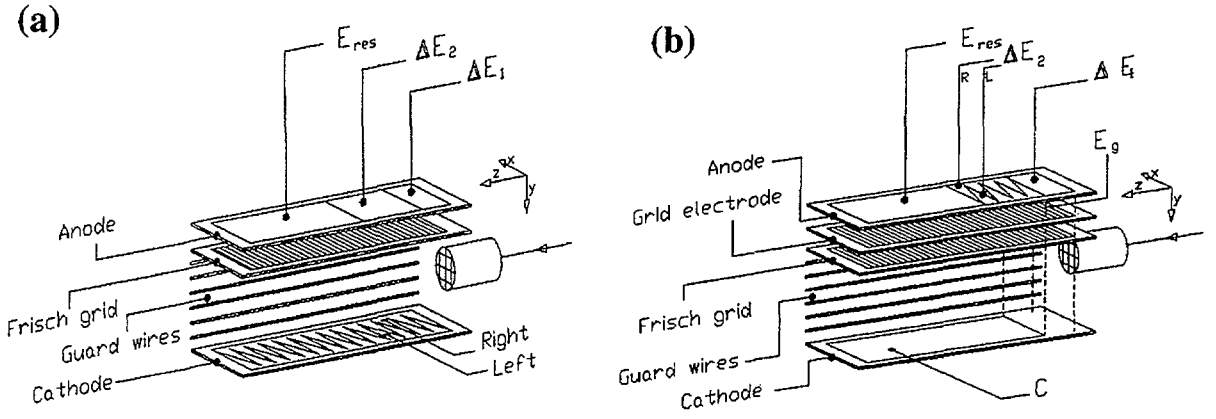

Figure 1 **(a)** The original position-sensitive gas-ionisation detector. **(b)** The modified design. The guard wires are only shown for one side.

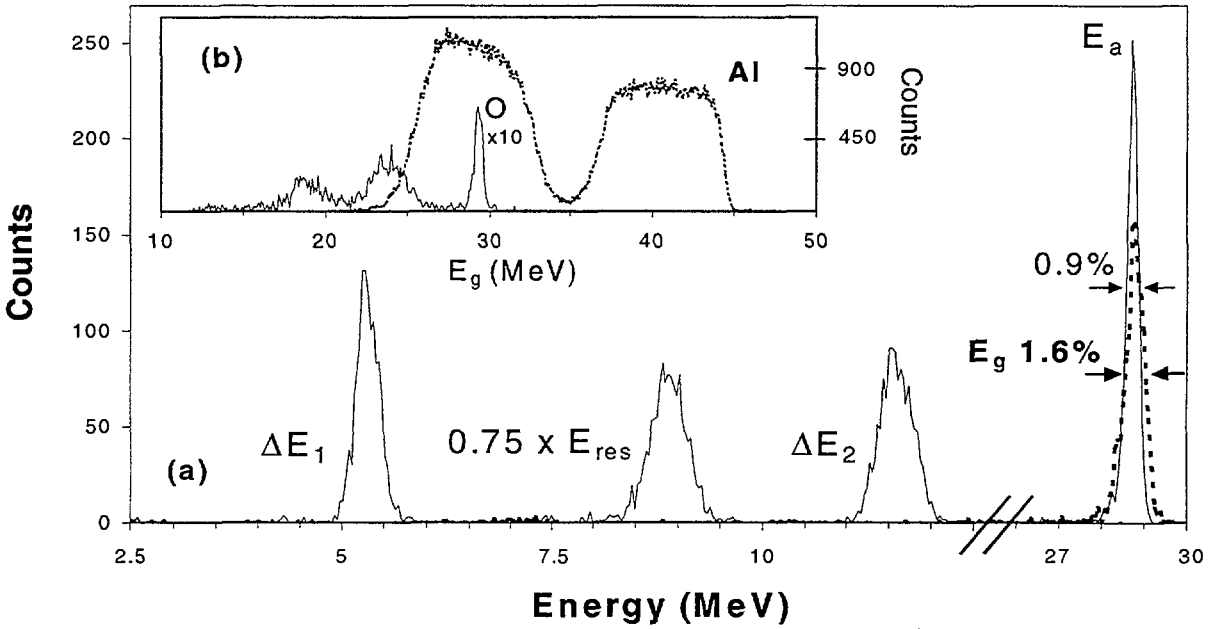

Figure 2 **(a)** Response of the modified detector for 30MeV ^{16}O ions scattered from a thin Au target. The detector was collimated to eliminate kinematic energy broadening. Shown are the anode signals ΔE_1 ,ΔE_2 , E_{res} , their sum E_a (solid) and the signal from the grid electrode E_g (dotted). The energy resolution of E_a and E_g is indicated. **(b)** Kinematically corrected energy spectra for Al (dotted) and O (solid). Heavy ion ERD was performed with a 216MeV ^{197}Au beam using the full acceptance angle.

3. New design features

The points raised in the previous sections have been addressed with the modified detector design [9,10] shown in Fig 1b.

Field calculations suggested an effective solution to the field distortions caused by the window assembly [8]. In the modified detector design the window is located off-centre, 10mm above the central detector axis and 2.6mm before the leading edge of the electrodes, as shown in figure 1b. In addition, the cathode was shortened by truncating the first 30mm, where it was found to be essentially insensitive. This effectively eliminates the variation of the two ΔE signals with height observed with the original design.

The modified detector features a grid electrode for total energy measurement. Although grid electrodes have been used in the past for other purposes [13], their effectiveness for energy measurements was not clear. An optimum configuration was found with the grid electrode biased at 58% of the anode voltage (e.g. anode + 450V and grid + 263V). The pulse height of the signal from the grid electrode is then about half of that obtained when all electrons are collected on the grid (e.g. grid and anode both at + 263V).

Figure 2a shows the ΔE_1, ΔE_2, E_{res}, E_a and E_g signals obtained for 30MeV ^{16}O ions scattered to 45° from a thin Au foil, where the subscript *"a"* refers to the combined anode signal and *"g"* refers to the total energy signal from the grid electrode, respectively. The resolution for E_a is 0.9%. This is slightly better than the value 1.6% for E_g, which is however sufficient for ERD analysis, where the resolution is largely determined by multiple scattering of the ions in the sample.

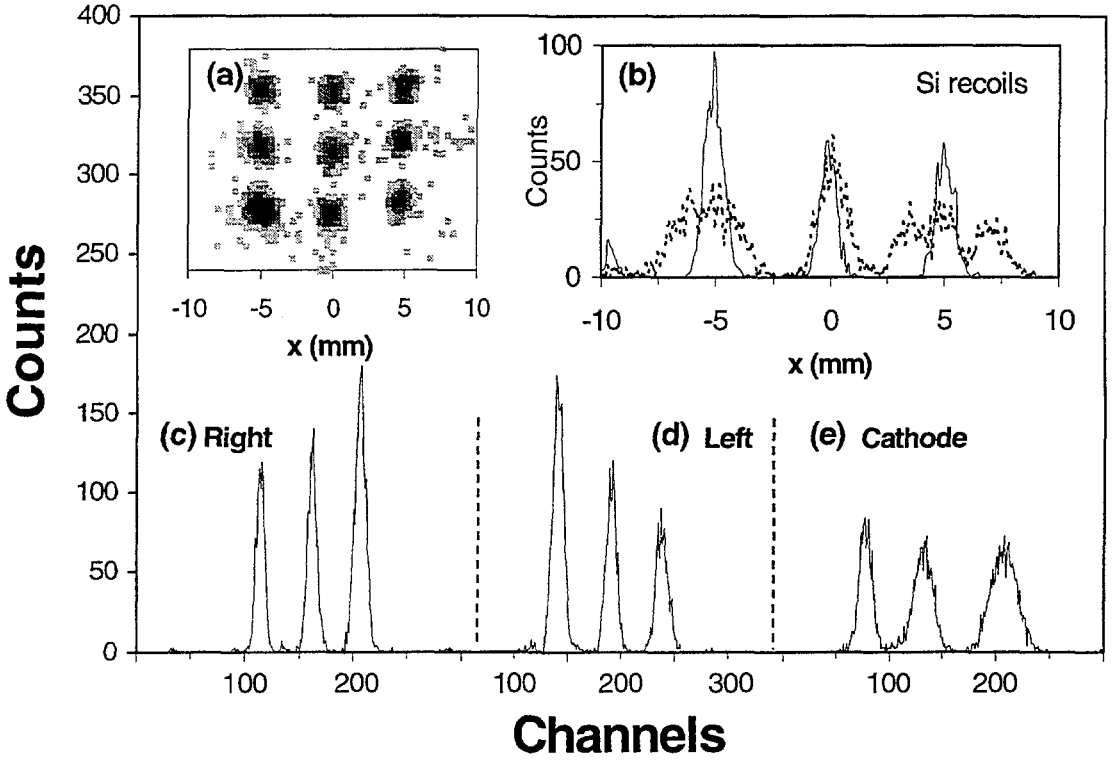

Figure 3 Position measurement with the modified detector. (**a**) x-y projection as detected through a mask with a rectilinear pattern of holes for 30MeV ^{16}O ions. (**b**) The x-position of Si recoils from the surface of a sample as detected with the old design (dotted) and the modified design (solid). (**c-e**) The individual signals corresponding to the data in (a).

This is illustrated in figure 2b using the example of a double layer of aluminium, separated by a hydrogenated carbon layer and deposited on silicon. The oxygen signal is due to surface oxidation of the aluminium layers and the silicon substrate.

With the modified design, position detection is greatly simplified obviating complex calibrations and corrections of non-linearities. This is demonstrated in figure 3, which shows position measurements for 30MeV ^{16}O and 45MeV Si ions. A mask with a rectilinear pattern of nine holes was placed in front of the window. The x-position is measured using a sawtooth division of the ΔE_2 section of the anode. The position resolution is 0.8mm [10]. This corresponds to an angular resolution of close to 0.18° for a distance of 250mm between sample and detector. The y-position of the ion is related to the ratio of the truncated cathode relative to the combined ΔE_2 and E_{res}. signals. The non-linear behaviour, obvious in figure 3e and observed previously [8], is effectively compensated by taking the square root of this ratio.

4. Summary

Elastic recoil detection of heavy ions with position-sensitive gas ionisation detectors can be greatly simplified by implementing a number of new design features. The subdivision of the energy loss electrode, together with a carefully chosen position of the entrance window to maintain optimum resolution for two ΔE signals, enable light and heavy ions to be resolved at the same gas pressure. Total energy information can be obtained by adding the signals from the anode electrodes, but also directly from a grid-electrode, obviating the need for the relative calibration of the anode electrodes. Position information independent of particle and energy, and with sufficient linearity in both spatial directions, can be measured using a sawtooth electrode within the ΔE_2 section of the anode and a truncated cathode, shortened to match the length of the combined ΔE_2 and E_{res} sections. The improved position detection allows the detection solid angle to be considerably increased without a sacrifice of resolution. It should also simplify and improve the accuracy of blocking measurements.

References

[1] W. Assmann, H. Huber, Ch. Steinhausen, M. Dobler, H. Glueckler, A. Weidinger, Nucl. Instr. Meth. B 89 (1994) 131-139.

[2] J.S. Forster, P.J. Currie, J.A. Davies, R. Siegele, S.G. Wallace, D. Zelenitsky, Nucl. Instr. Meth. B 113 (1996) 308.

[3] H. Timmers, R.G. Elliman, G.R. Palmer, T.R. Ophel, D.J. O'Connor, Nucl. Instr. Meth. B 136-138 (1998) 611.

[4] A. Oed, P. Geltenbort, F. Goennenwein, T. Manning, D. Souque, Nucl. Instr. Meth. 205 (1983) 455-459.

[5] H.J. Whitlow, G. Possnert, C.S. Peterson, Nucl. Instr. Meth. B 27 (1987) 448-457.

[6] J.W. Martin, D.D. Cohen, N. Dytlewski, D.B. Garton, H.J. Whitlow, G.J. Russell, Nucl. Inst. Meth. B 94 (1994) 277-290.

[7] W. Bohne, J. Roehrich, G. Roeschert, Nucl. Inst. Meth. B 136-138 (1998) 633-637.

[8] T.R. Ophel, H. Timmers, R.G. Elliman, Nucl. Instr. Meth. A 423 (1999) 381-393.

[9] H. Timmers, T.R. Ophel, R.G. Elliman, in print, Nucl. Instr. Meth. B.

[10] H. Timmers, T.R. Ophel, R.G. Elliman, submitted to Nucl. Instr. Meth. A.

[11] F. Naulin, M. Roy-Stephan, E. Kashy, Nucl. Instr. Meth. 180 (1981) 647-650.

[12] H. Huber, Diplomarbeit, Ludwig-Maximilians-Universitaet, Munich (1993) 47.

[13] H. Sann, H. Damjantschitsch, D. Hebbard, J. Junge, D. Pelte, B. Povh, D. Schwalm, D.B. Tran, Nucl. Instr. Meth. 124 (1975) 509.

Ion beam induced amorphisation in semiconductors studied using perturbed angular correlations

A.P. Byrne[1], E. Bezakova[2],
Department of Nuclear Physics, Research School of Physical Sciences and Engineering, Australian National University, Canberra, ACT 0200, Australia
C. J. Glover and M.C. Ridgway
Department of Electronic Materials Engineering, Research School of Physical Sciences and Engineering, Australian National University, Canberra, ACT 0200, Australia

1. Introduction

Ion implantation is an increasingly important technique in the fabrication of semiconductor devices. The understanding of irradiation produced disorder is thus of important scientific and technological significance. While many techniques have been applied to the study of semiconductor materials, no single method can provide a full characterisation and a detailed understanding of the physical processes relies on the application of a diverse range of complimentary techniques. In this paper we discuss the application of the Perturbed Angular Correlation technique to the study of ion beam amorphisation in semiconductor materials. The Perturbed Angular Correlations (PAC) method uses radioactive atoms at very low concentrations to provide information about the local electronic or magnetic structure around the probe atom. It relies on the change in the radiation pattern observed when an excited nucleus decays in an extra-nuclear field. A good description of the fundamental principles of the PAC method and its application to semiconductors is provided by the recent review of Wishart (1). The current measurements have used the ^{111}In probe nucleus. This nucleus decays via electron capture to the daughter, ^{111}Cd which is formed in an excited state. This nucleus then de-excites by the emission of two γ-rays. It is the perturbation of the γ–γ angular correlation of these two γ–rays by the presence of non zero electric field gradients at the probe site which is observed in the current measurements.

2. Implantation of ^{111}In

For the current series of measurements ^{111}In was produced in heavy-ion reactions, using beams from the 14UD tandem accelerator at Australian National University, then directly implanted into semiconductor samples positioned behind the target.

The following nuclear reactions were used for production:

^{103}Rh(^{12}C, p3n) ^{111}Sn; (35min) ^{111}In and ^{103}Rh(^{12}C, 4n)^{111}Sb; (1.5min) ^{111}Sn ; (35min) ^{111}In

with both dominant reactions leading to ^{111}In. An average production cross-section of approximately 600mb was obtained using a 69MeV carbon beam and 2.5 μm rhodium foil.

A schematic of the irradiation facility is indicated in figure 1. In this arrangement most of the carbon beam passes through the target without significant dispersion, with an average exit angle of approximately 1° The indium ions, on the other hand, have a much larger average exit angle of approximately 20°, and exit from the back of the target foil with average energy of around 4.0MeV.

The samples were mounted approximately 2 cm behind a the target with the edge offset by about 1.7 mm from the beam axis, allowing the undeflected beam to pass between them. Up to 60% of all ^{111}In nuclei that leave the target, foil can be collected on the samples. The

---

[1] Joint Appointment Department of Physics, The Faculties ANU.
[2] Present Address: Department of Medical Physics Royal Adelaide Hospital Adelaide

typical activity of each sample after implantation was about 0.1MBq, with TRIM calculations indicating that most of the ^{111}In ions come to rest within 1 to 2.5 microns.

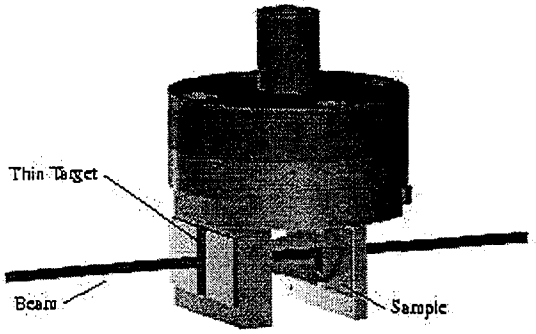

Figure 1. Irradiation facility at the 14UD accelerator.

3. PAC Measurements

3.1. Amorphisation measurements in InP

^{111}In was implanted into LEC semi-insulating (100) InP(Fe) wafers using the direct production and recoil-implantation technique. After the implantation the samples were annealed using rapid thermal annealing (RTA) (800°, 10 s) before subsequent processing. Off-line PAC measurements on annealed samples confirmed that the samples were undamaged (no electric field gradients present) prior to implantation sequences designed to produce amorphisation.

Ion beam amorphisation of the samples was performed on the ANU 1.7MeV ion implanter, by implanting ^{74}Ge beams with dose concentrations between $2x10^{12}$ and $150x10^{12}$ ions/cm^2 at liquid nitrogen temperature. These doses give a range of samples (11 in total) from unperturbed to completely amorphous material. A range of ion beam energies was used for each implantation dose in order to produce uniform depth profile of damage from the surface to 2.5 μm depth. The samples were tilted at 7° during implantation to avoid channeling.

Figure 2. Time differential ratio functions for ^{111}In in amorphised InP

After implantation, PAC measurements were performed using a spectrometer, with four BaF_2 detectors arranged in a plane, at close geometry at angles 0°, 90°, 180° and 270°. The samples were positioned perpendicular to the detector plane and at 45° with respect to the detectors. The time differential intensity of the correlation pattern is measured for all possible detector pairs.

The ratio function, R(t), was formed from the data after the background subtraction and time alignment of the spectra (1). The ratio function removes the effect of the exponential lifetime of the intermediate state and produces a signal directly proportional to the nuclear perturbation function. Some of the ratio functions are shown in figure 2.

The spectrum for the unimplanted sample shows no change in time, indicating that the

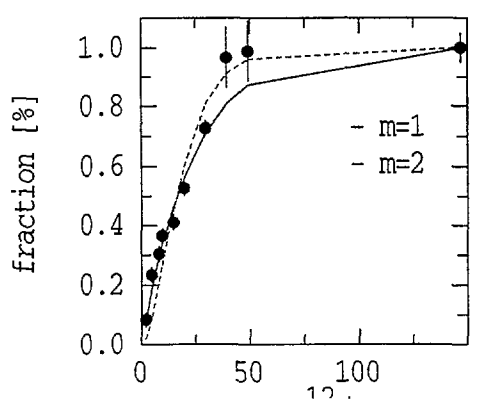

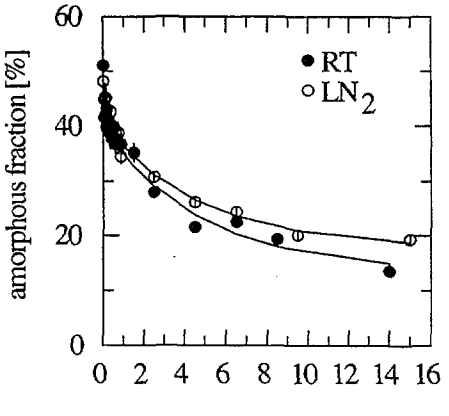

damage caused by the introduction of the radioisotope into the sample has been removed by the RTA and that the probe nuclei are now situated at substitutional sites where they experience no net electric field gradient. At low implantation dose a very gradual loss of alignment is observed consistent with the presence of long range disorder, similar to previous measurements of residual disorder in annealed heavily doped InP samples (2). As the implantation dose is increased a very rapid loss of alignment occurs, before the ratio function returns to the "hard-core" value. The measured spectra show a smooth transition from crystalline to amorphous behaviour as a function of implantation dose. Two regimes can be delineated, one where the ^{111}In sits on a weakly disturbed site and the other related to a very damaged (amorphous) environment. Accordingly, the spectra were fitted with the ``two fraction" perturbation function: $G_2(t) = f_1G_2(\omega_1,t) + f_2G_2(\omega_2,t)$, where fractions, f_1 and f_2 correspond to the number of indium nuclei associated with amorphous and non-amorphous fractions and $G_2(\omega_1,t)$ and $G_2(\omega_2,t)$ describe quadrupole interactions, with a Lorentzian distribution of transition frequencies centered around ω_1 and ω_2 at these sites. The transition frequency of the amorphous site was found to be 197 MHz (with a distribution of 69 MHz). The low-damage site was associated with the distribution of frequencies (up to 15 MHz) around zero. The current PAC measurements show that the disorder in InP is a result of the coexistence of regions resulting from simple defect production and the amorphisation processes. The initial linear dependence of the amorphised fraction on the implantation dose shown in figure 3 indicates that heterogeneous nucleation is probably the main mechanism of amorphisation at least up to doses resulting in amorphisation of 70% of the irradiated volume.

Figure 3 Amorphous fraction vs dose. **Figure 4.** Relaxation of amorphous fraction.

Existing amorphisation models can be characterized by the number of hits, m, required to produce amorphisation. Figure 3 shows the fit to the experimental data using a direct amorphisation model (m=1) (3). It confirms that the amorphisation of InP is achieved by accumulation and overlap of amorphous and heavily damaged clusters.

Deviation of the experimental data at implantation doses around $40x10^{12}$ ions/cm^2 indicates that other processes may also be involved, for example the increased overlap of simple defected regions (4) or a growth of an amorphous phase stimulated by the defective crystalline surroundings. The fit for m=2 is also shown.
We have also performed more conventional Rutherford Backscattering measurements on a samples with the same amorphising doses. A comparison the two methods (5) indicates that the PAC method may provide a greater effective resolution, particularly at high doses.

3.3. Structural relaxation measurements in InP

Structural relaxation effects resulting from room temperature annealing have also been measured in InP with the measurement of PAC spectra in damaged samples as a function of time. This work has identified two relaxation lifetimes, with the decay curves shown in figure 4, one on the order of 6 hours and the second on the order of 5 days (6). The exact origins of these lifetimes are not known. The short lifetime is probably the result of local recombination of point defects and the longer lifetime is associated with the migration of vacancies and other defects further into the lattice.

3.3. Amorphisation measurements in Ge

A similar methodology to the InP study has been applied for the PAC study of amorphisation in Ge. Amorphisation was achieved using Ge beams at energies chosen to reproduce the depth distribution of the ^{111}In. While similar differentiation into fractions associated with highly damaged amorphous and disordered environments and also be distinguished here additional features can be identified in the Ge case which are absent in the InP measurements. In particular, two additional, well defined frequencies, 49 and 390 MHz, can be distinguished for the implant dose of $2x10^{12}$ ions/cm^2 which can be associated with specific defect

configurations. The results are similar to those seen in a recent PAC study by Haesslein *et al.* of point defects introduced into Ge by electron irradiation (7). We have also performed extended X-ray absorption fine structure spectroscopy (EXFAS) and RBS measurements on a similar range of samples to more fully characterize the effect of ion beam induced damage (8).

[1] Th. Wichert Hyperfine Interactions, **97-98** 135 (1996)

[2] M.C. Ridgway *et al.* Proc. 1996 OEMMD Conf. Ed. C. Jagadish, (IEEE, Piscataway) 1997

[3] J.F. Gibbons, Proc. IEEE **60** (1972) 1062

[4] J.R. Denis and E.B. Hale, J. App Phys. **49** (1978) 1119

[5] E. Bezakova, A.P. Byrne, M.C. Ridgway, C.J. Clover and R. Vianden, App. Phys. Lett **75** (1999) 1923

[6] E. Bezakova, A.P. Byrne, M.C. Ridgway, C.J. Clover and R. Vianden, Hyp. Inter. (In Press)

[7] H. Haesslein, R. Sielemann and C. Zistl, Phys. Rev. Lett. **80** (1998) 262

[8] C.J. Clover *et al* See these elsewhere in this conference.

A new high-energy (e,2e) spectrometer for the study of the electronic structure of materials

M. Vos, G. P. Cornish A.S Kheifets and E. Weigold

Atomic and Molecular Physics Laboratories,
Research School of Physical Sciences and Engineering, The Australian National University, Canberra

Electron momentum spectroscopy (also called (e,2e) spectroscopy) is a very direct method of studying the electronic structure of materials. Using only the elemental laws of energy and momentum conservation this spectroscopy measures the probability that an electron in a target has a binding energy ε and momentum $\boldsymbol{q}$. Over the last 5 years this technique was used with considerable success at Flinders University. This type of experiment is done in a transmission geometry, using extremely thin samples. However, even for the thinnest samples multiple scattering is a severely complicating factor, hampering a genuinely quantitative interpretation of the Flinders University data. In order to completely exploit the potential of the technique it is necessary to employ a scattering geometry in which all electrons involved have an energy of at least 20keV. A new spectrometer was build at the ANU working in this energy range. Here we show the first results and compare the actual performance of the spectrometer with the design specifications.

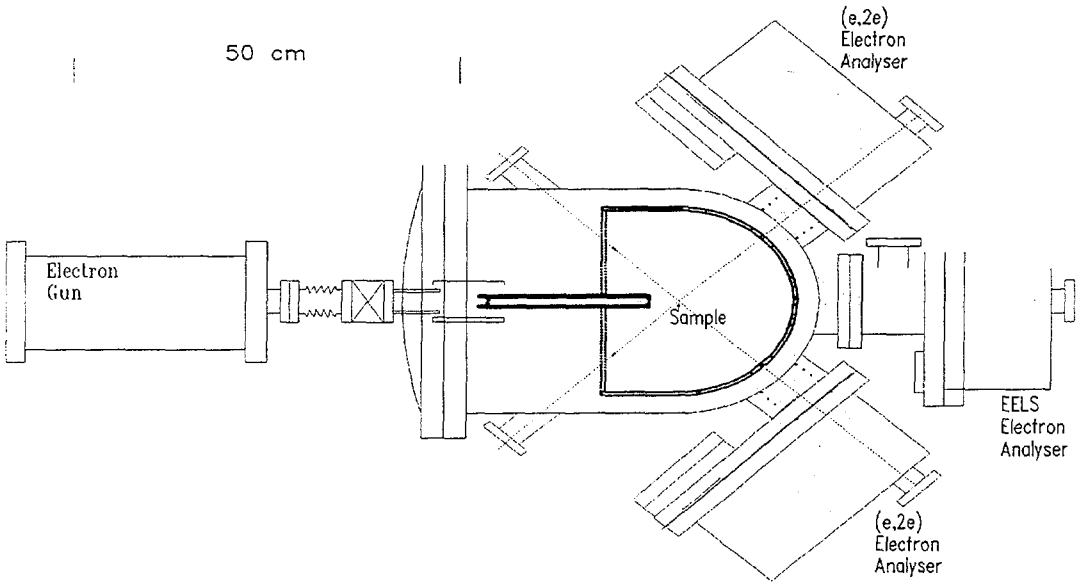

Figure 1. An outline of the ANU high-energy (e,2e) spectrometer. The positive high-voltage area containing the sample is indicated with thick lines. The electron detectors are shown using dotted lines.

In figure 1 we show an outline of the spectrometer. It uses the same symmetric scattering geometry as the spectrometer described by Ritter, but electron analysers with position sensitive electron detection as developed at Flinders University. In brief, 20keV electrons are generated in an electron gun. The target itself is inside a hemisphere that is at a potential of + 20keV. Thus incoming electrons with an energy of 40keV interact with the target. A small fraction of these electrons will undergo a collision with a target electron and some of these electrons will transfer half their energy to a target electron. In the symmetric scattering geometry both detected electrons have the same energy. Our analysers are thus tuned to measure two electrons in an energy range near 20keV emitted at polar angles close to 45° relative to the incident direction. The electrons are de-accelerated to a few 100eV kinetic energy (250eV in this work) in the lens stack preceding the hemispherical analysers. This

means that the hemispherical analyser and the channel plates/resistive anode combinations used for detection are at a convenient potential, close to ground.

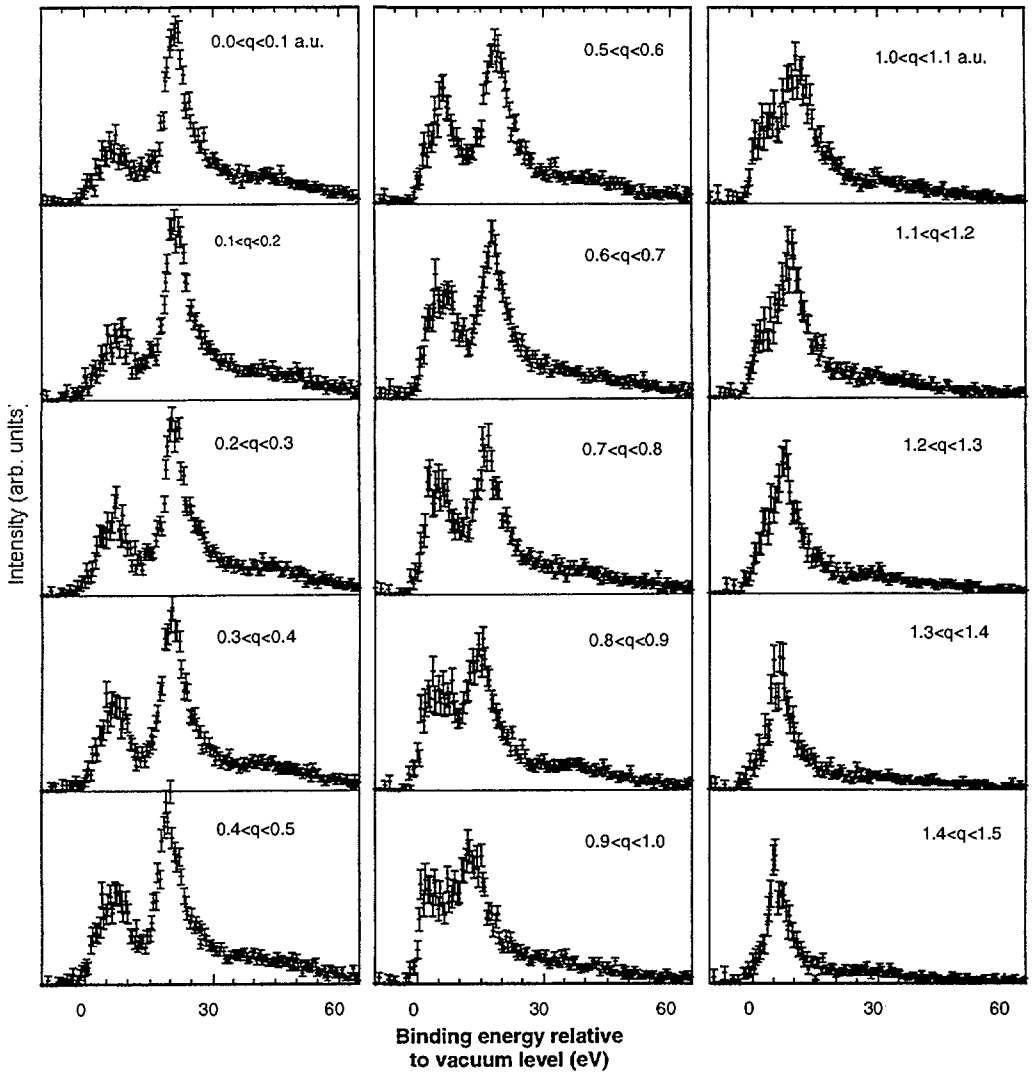

Figure 2. The (e,2e) spectra of a 35Å thick amorphous carbon film for different momenta q as indicated. Note the small background at high binding energy. All plots have the same vertical scale.

The high momentum transfer for these symmetric (e,2e) events means its cross section is low. In order to maintain an acceptable count rate we have to measure simultaneously a large angular and energy range. The hemispherical energy analysers work at a pass energy of 250eV and electrons are detected by the channel plate over an energy range of 50eV. In the azimuthal angular direction a range of +/- 4.5 degrees is projected on the channel plates, corresponding to a range of measured momenta of +/- 3 au for each detector. The central angular ranges of the two analysers are separated by 180° in azimuth. For the thinnest samples the thickness of the sample is now smaller than the mean free path of the incoming and outgoing electrons. Thus the large majority of the observed (e,2e) events will be without additional elastic and inelastic scattering events for the incoming and outgoing trajectories. This simplifies greatly the quantitative comparison of theory and experiment

The spectrometer allows measurement under a range of conditions. Slits of different sizes and angle calibration apertures are mounted on a turntable and can be changed without breaking the vacuum. In this way one can change the momentum resolution and by adjusting the pass energy one can change the energy resolution. Count rates vary from ≈ 600 counts a minute

using 0.5mm wide slits, and 500eV pass energy to ≈ 40 counts a minute using 250eV pass energy and 0.2mm slits for 100Å carbon films. The target beam current is typically 1μA.

Extreme care is taken to ensure sufficient stability of the 20kV power supplies. Both the positive and negative high voltages are measured using a precision resistor divider, and using a feed-back system it is ensured that the magnitude of the negative high voltage is equal to the magnitude of the positive high voltage within a fraction of a volt. A capacitive divider is used to measure any ripple, which is again suppressed by a feed-back network. In this way we can make long-term measurements with 1eV energy resolution using 40keV incoming electrons. After conditioning there is no arcing, which seems to indicate that we can run the spectrometer at higher energies. This will be explored in the future.

In order to test the spectrometer a sample of extremely thin amorphous carbon (about 35Å thick) was measured. The sample was annealed in order to ensure sufficient conductivity to prevent charging during the experiment.

In figure 2 we show the results for an annealed amorphous carbon film. These data were acquired over a two-day period. Near zero momentum there are two peaks one at 21eV (σ band) and one around 7eV binding energy (the π band). Both structures disperse to lower binding energy with increasing momentum. The results are similar to those published before as far as dispersion is concerned, but there is a large difference in the background level. At high binding energies (and also for high momentum values, not shown) the measured intensity drops off to very small values. This is due to the fact that the thickness of the film is now smaller than the mean free path of the electrons detected and hence both elastic and inelastic multiple scattering are relatively small effects.

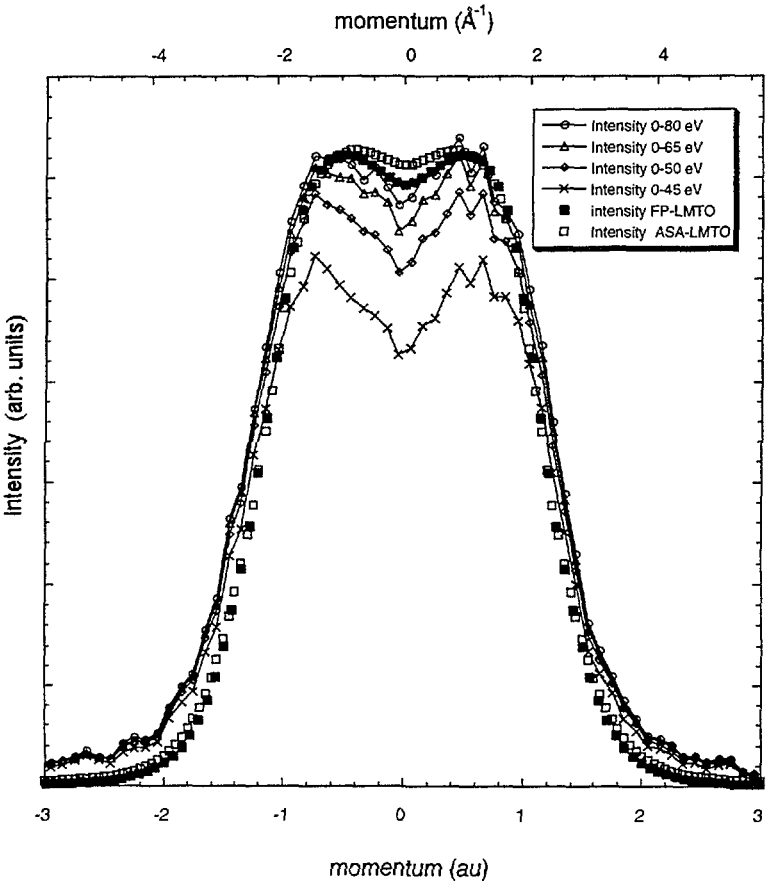

Figure 3. The experimentally obtained momentum density of the graphite film. If we choose the binding energy range large enough the obtained results become independent of the upper integration limit. These results compare favorably with the LMTO calculations.

The much smaller multiple scattering makes a quantitative comparison of theories and experiment much simpler. In figure 3 we show the energy-integrated intensity and compare this with the theoretical quantity obtained from linear-muffin-tin orbital (LMTO) calculations.

A previous comparison of the momentum density as measured by (e,2e) spectroscopy with theory was somewhat inconclusive due to the large contribution of elastic and inelastic scattering. Now the measurements compare well with the same theory. The small tail in intensity at higher momentum values is probably still due to elastic scattering.

The experimental results favors the parameter-free full potential calculation (FP-LMTO) above the more crude atomic-sphere approximation(ASA-LMTO) .

Of course the goal is to compare our results with theory directly without integrating over energy. Previous work on aluminium has shown that meaningful comparison is only possible using theories describing life-time broadening of the quasi-particle peaks and their satellites.[1]

Such calculations are currently being undertaken.

In summary, we have shown that the new ANU (e,2e) spectrometer has the capability of measuring energy-resolved momentum densities with a greatly reduced multiple scattering background, without significantly sacrificing the data acquisition rate, momentum or energy resolution.

Surface studies: corrosion, hydrogen content and charge transport in materials and devices

David N. Jamieson[1]
[1]School of Physics, Microanalytical Research Centre, University of Melbourne, Parkville, 3052

Introduction

Presented here is a review of recent applications of the Melbourne nuclear microprobe applied to the study of surface phenomena in a variety of materials over the past two years. In addition to these applications, numerous improvements to the Melbourne system were initiated over the same period. These have been mainly directed at improvements in the spatial resolution through the installation of shielding to reduce stray magnetic fields and commissioning of a new event-by-event data acquisition system that can handle high count rates from up to four detectors with full dead time correction. In 1999 an ARC Research Infrastructure and Facilities Program grant has allowed us to perform a major upgrade of the Pelletron 5U accelerator. Major components of this upgrade include: a new ion source in the terminal, replacement of the column corona needles with resistors, replenishment of the SF6 gas supply and installation of a Danfysik analysing magnet power supply. In the near future we will also test some proposals to increase the ion source brightness based on reduction of the gas load on the column from the ion source.

Many of the applications of the Melbourne nuclear microprobe over the past two years have employed the classic techniques of Ion Beam Analysis including PIXE and RBS [1]. However the role of Ion Beam Induced Charge (IBIC) has risen in significance over the past two years. This reflects the major importance of electronic materials in the materials research program of MARC. In this direction, the role of hydrogen is becoming more significant in the group's research program. Pilot studies of involving the mapping of hydrogen in polysilicon solar cells has been done with the technique of elastic recoil detection analysis (ERDA). Finally, we have also continued to study the visible light emitted from the specimen during ion irradiation. This can be collected to form images by ionoluminescense (IL). IL is an emerging technique for use with a nuclear microprobe that offers new insights into the presence of optically active defects in materials. A review of all these techniques, with many applications, is available [2]. Several recent reviews of past applications of nuclear microprobes to materials analysis are available [3,4].

Applications

1. CVD Diamond

The synthesis of diamond is a challenging task. The specimen shown here were synthesised in a chemical vapour deposition (CVD) reactor and had a peculiar greenish colour to the unaided eye. Maps of the elemental distribution of the contaminant elements are shown in figure 1. The contaminant elements appear to have different distributions suggesting more than one source of contamination.

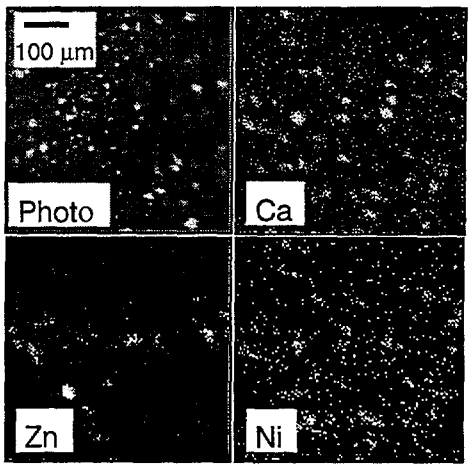

***Figure 1** Trace elements maps in CVD diamond. White to black=high to low yield, PIXE with 3MeV H.*

An insight could be obtained into the nature of the defects introduced into the diamond by performing IL [5] along with the RBS and PIXE measurements. In diamond, the most usual luminescence is contributed by to the A-band (blue to the unaided eye). However in the present specimen, the strength of this band was dwarfed by orange luminescence, see figure 2. The origin of this strong orange luminescence is a colour centre based on a vibronic band with a zero phonon line at 2.156eV [6]. The band associated with this centre is known in the literature as the "575nm" or "T1" band and is usually attributed to a single interstitial nitrogen atom bound to a vacancy along the <001> axis [7]. The IL has provided complimentary information about the contaminants to that from PIXE that cannot detect low Z elements like nitrogen.

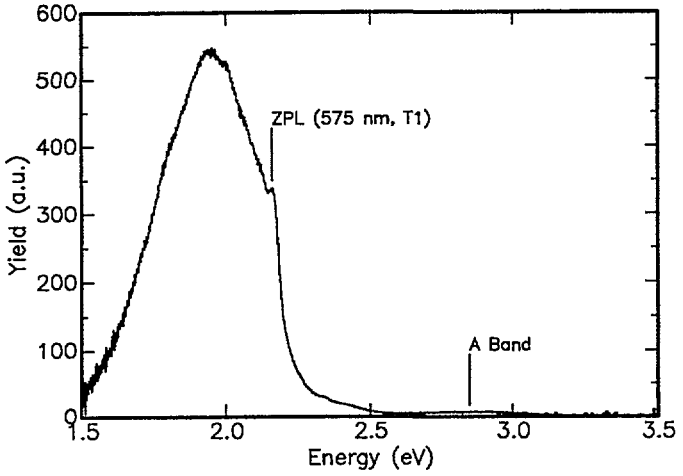

Figure 2: IL spectrum from the contaminated diamond showing strong orange luminescence.

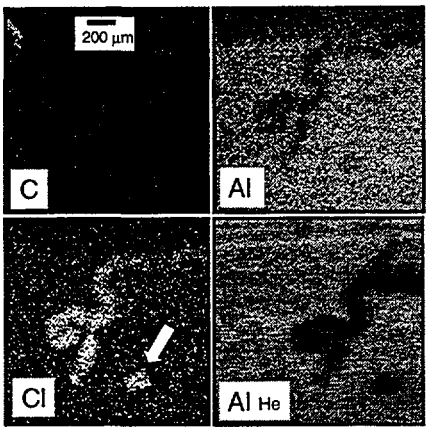

Figure 3 3MeV H RBS (C, Al), 3MeV PIXE (Cl) and 2MeV He RBS (Al He) images of a filoform. Arrow indicates growth head.

2. Filoform corrosion in aluminium alloys

The corrosion of aluminium alloys often displays filoforms [8,9] where corrosion is nucleated, possibly by a reaction involving a chlorine compound, and then grows across the surface leaving behind a characteristic meandering trail of oxide. A variety of trace elements are responsible for the growth of the filoform and the precise mechanism for the catalysis of the growth are a matter of active research. However PIXE has sufficient sensitivity to map chlorine which is one of the most important of the trace elements in the growth of filoforms. In the example shown in figure 3, images were obtained with 3MeV H^+ and 2MeV He^+ beams in order to measure the thickness and the stoichiometry of the corrosion products respectively in 2024 aluminium alloy [10]. The present specimens were prepared by deliberate scratching through the anti-corrosion coating, followed by exposure to a corrosive ambient to induce growth of the filoforms.

The images clearly show the oxide residue of the filoform from the reduced yield from Al. Spectra extracted from the filoform itself revealed the stoichiometry of the oxide to be $Al_1O_{2.15}Cu_{0.02}$. However the oxide contained numerous voids and other non-uniformities. The excess oxygen over Al_2O_3 is most likely due to the inclusion of water in the oxide. It is clear that chlorine is incorporated into the corrosion products themselves as can be seen from the Cl map in figure 3. But what is more interesting is the significant concentration of chlorine in the head of the filoform (arrow in Figure 2). This confirms the essential role of chlorine anions in triggering filoform corrosion [13] and the PIXE image has allowed the chlorine distribution to be measured directly from the induced x-rays.

3. Hydrogen profiling and trace elements in solar cell material

Contamination of materials used for photovoltaic cells can cause problems related to charge trapping and recombination. However most contaminants cannot be tolerated in concentrations high enough to be detected by ion beam analysis. Elemental maps of complete devices can reveal the distribution of contaminants that results from contact layer spill and other manufacturing or environmental influences [14].

Although trace metal contamination usually has a detrimental effect on solar cell performance, deliberate inclusion of hydrogen improves performance. The role of hydrogen, in various devices, including solar cells, is to passivate defects that would otherwise be responsible for charge trapping. The surface and depth hydrogen distribution may be measured on the nuclear microprobe by ERDA with a focused He probe. This requires the incident He beam to be at a glancing angle to the specimen surface so that the forward recoiling H atoms, dislodged from the sample surface, can be detected in a surface barrier detector at a forward scattering angle. This detector is also fitted with a thin foil filter in order to stop forward scattered incident beam particles which would otherwise overwhelm the data acquisition system. ERDA with He ions allows elemental analysis and depth profiles with about 5nm depth resolution [15]. The glancing angle geometry required for ERDA makes good spatial resolution difficult to achieve with a nuclear microprobe, but below 10μm in polycrystalline silicon is possible in some circumstances [16].

A recent example of how ERDA can be used to map the H distribution in solar cells is shown in figure 3. In this case the surface passivation layer of the cell has been removed to expose the underlying polycrystalline silicon absorber layer. It is very clear that most of the hydrogen is located in the grain boundaries of the absorber, as expected. More details about the experimental parameters of this measurement have been published [27]. Quantitative analysis of the data used to produce the image in figure 4 reveals 8 at% H in the bulk of the grains with about 20 at% H in the grain boundaries. The distribution of hydrogen seen here is quite different to the previous work on hydrogen distributions reported by Churms et al [16] where segregation of the hydrogen to the grain boundaries was not observed, instead hydrogen was seen to be widely and more uniformly distributed. This result was attributed to environmental contamination. This problem was avoided for the present measurement by removing the surface layer to expose a fresh surface prior to analysis.

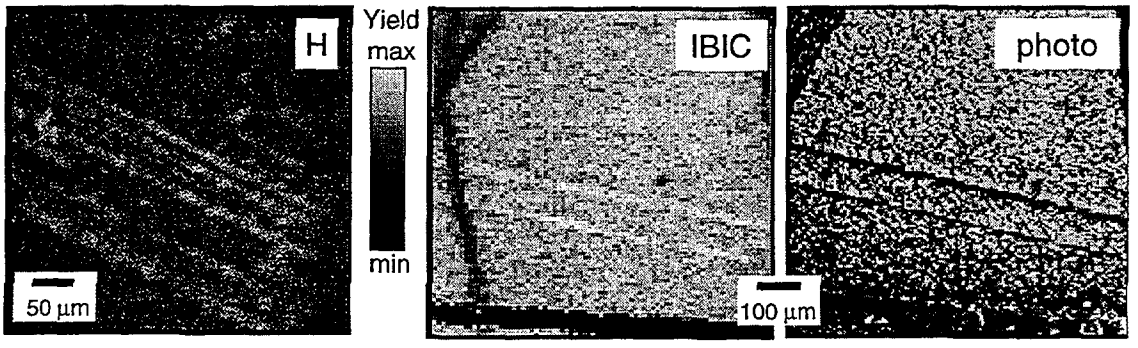

Figure 4 Images from a commercial solar cell. (left to right) 2MeV He ERDA image of the H distribution, 2MeV He IBIC image of a nearby region and a photograph of the same region.

It will be of interest to combine hydrogen distribution measurements, taking appropriate precautions to minimise the effects of beam damage, with high sensitivity ion beam induced charge [28] images from the same region of interest. An IBIC image of a different region is shown for comparison in figure 4. The parallel grain boundaries show a higher than average charge collection efficiency and the similarity to the structures seen in the ERDA hydrogen

map are suggestive of the beneficial role of hydrogen in this device. The impressive ability of IBIC to show both surface and buried features is shown by the IBIC images of figure 5. Here a PERL cell fabricated at the University of New South Wales is mapped with a 2.5MeV He beam with the specimen held at 100K. The scan size was approximately 500 x 500μm.

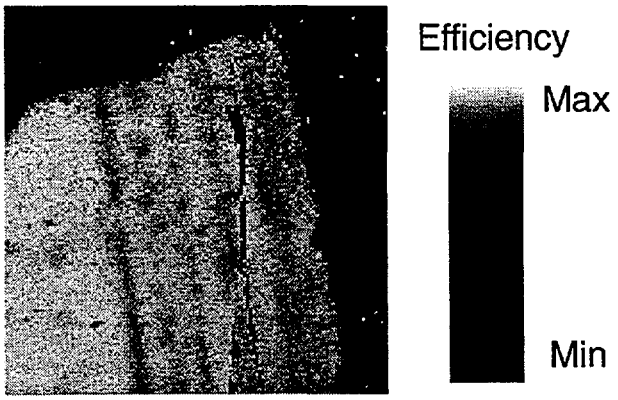

***Figure 5** IBIC images of a PERL cell. The fine stippling is not an image artefact, it arises*

Conclusion

It has been shown that the nuclear microprobe is useful in elucidating the surface structure and composition of a variety of specimens where information can be obtained about corrosion products, trace element contamination and the distribution of hydrogen. In most of these examples, a number of different measurements (such as depth distribution, stoichiometry, trace element distribution or hydrogen content) were done with the same apparatus with the specimen in situ. This versatility is a characteristic of the use of focused MeV ion beams for materials analysis.

Acknowledgments

This work was supported by grants from the Australian Research Council and the University of Melbourne visiting scholar scheme. We are grateful to Roland Szymanski for operation of the Melbourne Nuclear Microprobe system, to Peter Patterson and George Theodossiou of the Royal Melbourne Institute of Technology for alerting us to the interesting problem of filoforms and for providing the aluminium corrosion specimen and finally to Lachlan Witham for providing the IBIC image of the solar cells.

References ??check numbers??

[1] J.R. Bird and J.S. Williams, eds, Ion Beams for Materials Analysis, Academic Press (1989).

[2] M.B.H. Breese, D.N. Jamieson and P.J.C. King, *Materials Analysis with a Nuclear Microprobe*, Wiley, New York (1996).

[3] D.N. Jamieson, Nucl. Instr. Meth. B130 (1997) 706.

[4] D.N. Jamieson, Nucl. Instr. Meth. B136 (1998) 1.

[5] A A Bettiol, D N Jamieson, S Prawer and M G Allen, *Nucl. Instr. and Meth* **B85** 775 (1994)

[6] J. Walker, Rep. Prog. Phys., 42 (1979) 2607-1659.

[7] A.T. Collins and S.C. Lawson, J. Phys. Condensed Matter, 1(39) (1989) 6929-6937.

[8] R.T. Ruggeri and T.R. Beck, Corrosion, 49 (1983) 452.

[9] A.T.A. Jenkins and R.D. Armstrong, Corrosion Science, 38 (1996) 1147.

[10] Nominal composition by wt %: 3.8-4.9 Cu, 1.2-1.8 Mg, 0.3-0.9 Mn, 0.5 Si, 0.5 Fe, 0.15 Zn, 0.15 Ti, 0.1 Cr.

[13] A. Bautista, Progress in Organic Coatings 28 (1996) 49.

[14] J. L'Écuyer, C. Brassard, C. Cardinal, J. Chabal, L. Deschênes, J.P. Labrie, B. Terrault, J.G. Martel and R. St-Jacques, K. Appl. Phys. 47 381 (1996)

[15] L.C.G. Witham, D.N. Jamieson, R.A. Bardos and A. Saint, Nucl. Instr. Meth. B136/138 (1998) 1361.

[16] C.L. Churms, V.M. Prozesky, T.K. Marais, R. Pretorius, W.F. van der Weg and W. Sinke, CP392, Application of Accelerators in Research and Industry, J.L. Duggan and I.L. Morgan, eds, AIP press, New York, 1997.

[27] C. Yang, K.K. Lee, E. Teo, D.N. Jamieson and F. Watt, presented at the 6th international Conference on Nuclear Microprobe Technology and Applications, Capetown, South Africa, 1998.

[28] D.N. Jamieson, D.R. Beckman, A.A. Bettiol, J.S. Laird, K.K. Lee, S. Prawer, A. Saint and L.C.G. Witham, presented at the 6th international Conference on Nuclear Microprobe Technology and Applications, Capetown, South Africa, 1998.

SESSION 11

Chair – Rainer Siegele

Isotopic Techniques

Precision Pb and S isotopic ratio measurements by microbeam AMS

S.H. Sie, D.A. Sims, F. Bruhn, G.F. Suter, G. Cripps and T.R. Niklaus

Heavy Ion Analytical Facility, CSIRO Division of Exploration and Mining,
P.O. Box 136, North Ryde, NSW 2113, Australia

Introduction

The AUSTRALIS (AMS for Ultra Sensitive TRAce eLement and Isotopic Studies) system recently commissioned at CSIRO is a microbeam AMS system dedicated to geochemical and geochronological applications [1-4]. Unlike conventional AMS systems, where detection of rare isotopes is the main objective, AUSTRALIS is designed to perform in-situ microanalysis of stable and radiogenic isotopes with high precision and freedom from mass interference. The required high precision of better than 1 permil for geochronology is comparable to the best results obtained by AMS for the $^{13}C/^{12}C$ ratio[5,6]. This has been achieved thus far only in bulk radiocarbon measurements using the recombinator method or fast bouncing at the injector combined with a multi-Faraday cup detection.

The AUSTRALIS microbeam source incorporates a facility for viewing the sample at high magnification, essential for geological applications. The conventional bouncing method is used at the low energy side for sequential isotope switching. In order to achieve the high precision the effect of source and beam transport instabilities must be minimised. A novel bouncing method has been developed for the high energy side, allowing complete E/q and m/q analysis for all isotopes of interest, that can be driven at a high rate[7].

First results [8,9] indicated the need to drive the bouncer faster than 150 ms/isotope, which was the limit of software based driver, in order to achieve better than 0.5% precision in isotopic measurements. The breakdown of the accelerator around mid 1998, interrupted the development of a faster, hardware based driver. This resumed after the refurbishment of the accelerator was completed in early 1999. The present paper describes the result of tests of the new driver system.

Isotope Ratio Measurements

The mass spectrum of the secondary ions is first measured in either a Faraday cup or an ion counter at the image point of the low energy magnet. The mass range is unrestricted when measured by scanning the magnetic field, but for the actual measurement, a finite mass region of interest is measured by fixing the magnetic field and scanning the bouncing voltage. With all slits open and the magnet image slits set at 300μm, a mass resolution of ~850 is obtained routinely for beam spot size between 30 to 100μm. Allowing a total magnification of ~2 for the extraction and beam transport system, and dispersion of 60cm for the magnet, the observed mass resolution indicates the presence of significant aberration effects. This resolution however already results in suppression of neighbouring isotopes by $\sim 10^{-15}$, which is more than adequate for most isotopic ratio measurements in the absence of isobaric interference.

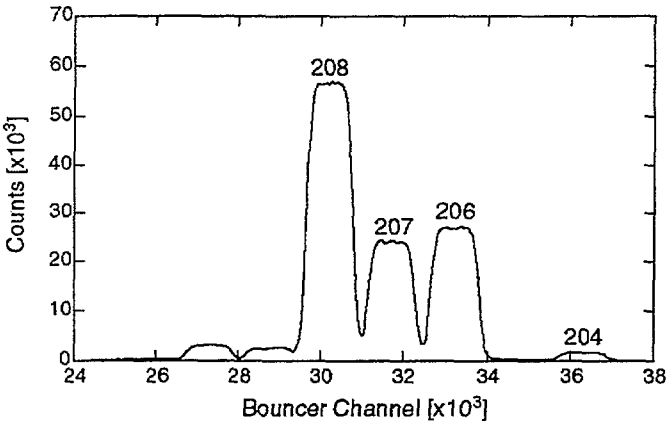

Figure 1. Mass spectrum in the region of the PbS- ions measured in the ion counter at the low energy spectrometer, by scanning the low energy bouncer. Note that the mass scale descends with higher bouncer channel.

The magnet image slits setting can be widened to allow 'flat top' transmission to reduce the effect of energy drift in the beam. Figure 1 shows a mass spectrum obtained from galena,

obtained at 500μm slit width, using the bouncing mode showing the PbS-peaks corresponding to the 204, 206, 207 and 208 isotopes at mass resolution of 850. This spectrum illustrates the problem of molecular interferences in secondary ion mass spectrometry: the $^{208}Pb^{32}S$ peak overlaps with $^{206}Pb^{34}S$, $^{207}Pb^{33}S$ and $^{207}Pb^{32}SH$ peaks, requiring extremely high (hence not practically achievable) mass resolution. Any corrections, even if known or measurable, will degrade the precision required for isotopic ratios measurements.

All measurements to date have been conducted at 1.5 MV terminal voltage, which is more than sufficient to break up the molecular ions into their atomic constituents after acceleration and charge exchange collisions in the tandem accelerator terminal. Fragments of the different isotopes are resolved with mass resolution of 2600 at the high energy analysing magnet. This 1.3m radius, 90° bend magnet, operated in the double focusing and unity magnification mode, is corrected to the second order. The beam is ultimately focused after two 22.5° bend, 3m radius spherical ESAs separated by an electrostatic doublet, into the detector chamber. As in the low energy system, the beam intensity can be measured in either a Faraday cup or an ion counter, and when necessary in a gas proportional counter with segmented anode for particle identification. The high energy bouncing system consists of two sets of deflecting plates, 40cm long with 4cm gap, at the entrance and the exit ports of the magnet box. The different isotopes are deflected transversely in the orbit plane by entrance plates, and returned to the main axis by the exit plates by applying common appropriate voltages, with the magnetic field kept constant.

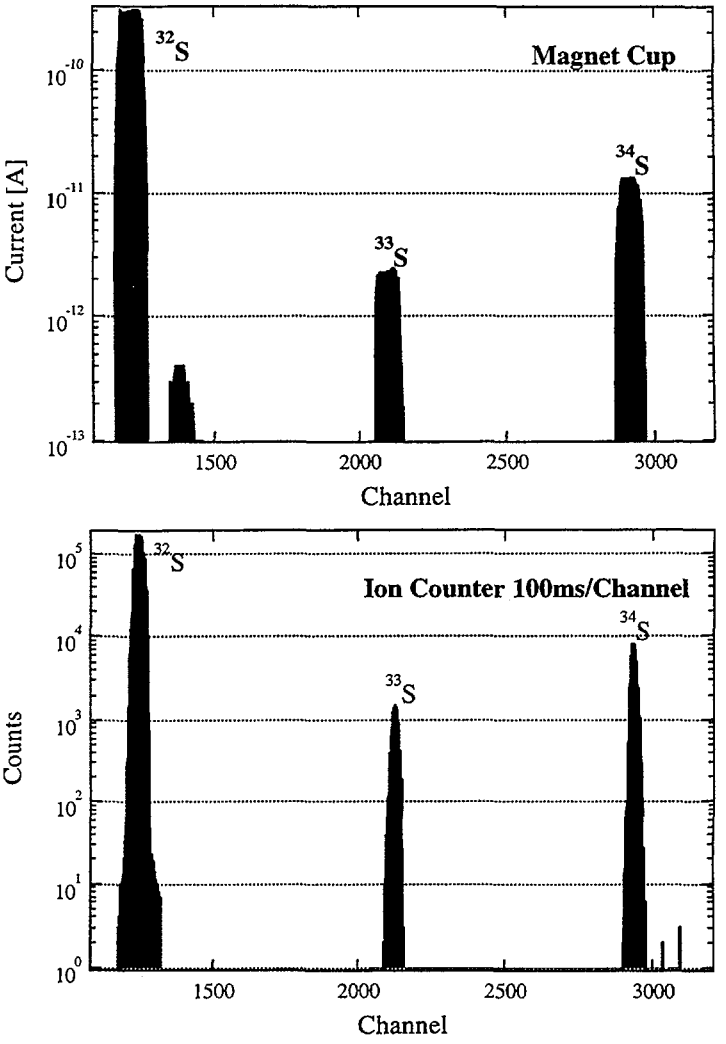

Figure 2. Composite spectrum of sulfur isotopes measured as a function of mass represented by the high energy bouncer channel, in the high energy magnet Faraday cup (top), and in the high energy ion counter (bottom).

The high energy system also shows flat top transmission characteristics, evident when Faraday cups are used to detect the ions. This is demonstrated in the S isotopes measurements, as shown in figure 2. The top shows a composite spectrum of $^{32}S^{4+}$, $^{33}S^{4+}$ and $^{34}S^{4+}$, from injected S^- ions, showing the flat top response when measured as currents in the Faraday cup. The lower figure shows the same spectrum measured in the ion counter. The flat top is not as evident due to the fact that the counter aperture is only just larger than the beam diameter.
The isotopes of interest are measured sequentially by synchronising the low energy and high energy bouncer settings. For example in the case of Pb isotopes, the high energy bouncer is set to detect $^{208}Pb^{4+}$ when injecting $^{208}Pb^{32}S^-$. Beam stability affects the precision directly, and the sputtering process as well as instabilities in the beam transport sys-tem can be the main source of fluctuations.

The new hard-ware based bouncer system permits switching time as low as 1ms per isotope. Figure 3 shows the raw counts of the Pb isotopes for a single run of measurement of a galena sample indicating significant variation due to beam instabilities. Figure 4 shows the ratios, indicating very little variation with the $^{207}Pb/^{206}Pb$ varying by only ~1 permil. Repeat measurements of the same sample, different analytical points, and the ratio shows a standard deviation of only 0.4 permil (figure 5). These measurements demonstrate the effectiveness of fast bouncing to circumvent the beam instabilities problem.

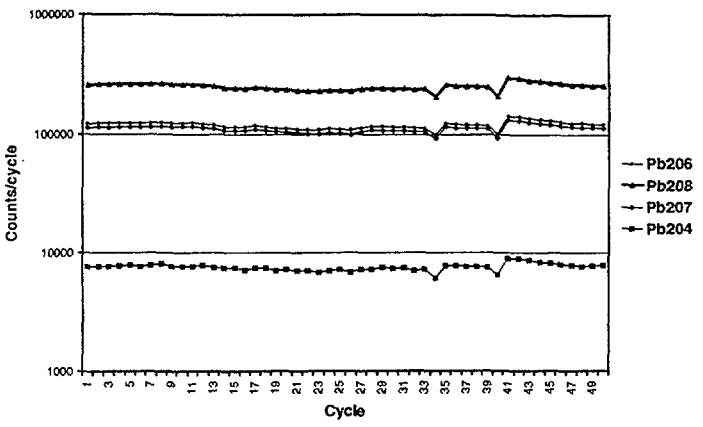

Figure 3. Raw counts of Pb isotopes in a measurement sequence can show large fluctuation. With fast cycling, the variation is reflected in all isotopes.

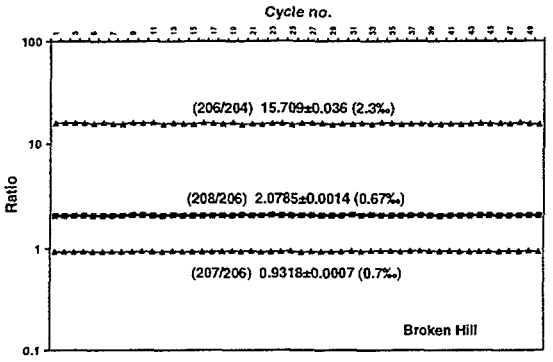

Figure 4. Pb isotopic ratios from data in figure 3, showing that the ratios are not affected by the large fluctuations in the beam intensity

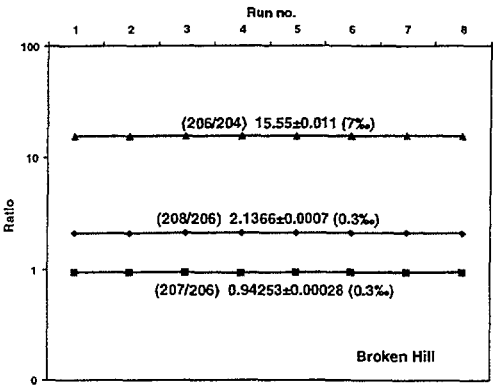

Figure 5. Repeat measurements on the same sample as in figure. 4.

Fractionation effect is deduced from measurements on known samples. Defining R as the measured ratio divided by the actual value, the fractionation factor f =1-R. In a linear fractionation model, f is proportional to the mass difference of the isotopes involved in the ratio. For example, f ($^{208}Pb/^{206}Pb$) would be twice that of f ($^{207}Pb/^{206}Pb$) and would be the same but opposite sign to f ($^{206}Pb/^{204}Pb$). However, unlike in single stage mass spectrometry where this linear model usually applies, the fractionation effect can be very non-linear with mass especially when the bouncer is operated near the limits where transmission efficiency declines rapidly.

We have used galena from Broken Hill ($^{208}Pb/^{206}Pb$ = 2.2287, $^{207}Pb/^{206}Pb$ = 0.9619, $^{206}Pb/^{204}Pb$ = 16.007) and South Farrell Mine (2.072, 0.841 and 18.57 respectively) to investigate the effect. Figure 6 shows the fractionation effect for Pb isotopes for a series of measurements covering an 8 week period. Within a series of measurements, ie. with the same accelerator setup, the fractionation factors are within the precision of the measurements. Over longer period with different conditions of the accelerator a variation of the order of 1 to 2% was observed for all ratios. The non-linearity can be seen where the f (208/206) is more than

twice f (207/206) and appears unrelated to f (206/204). The variation observed may be attributable to the slightly different condition of the transmission through the accelerator, in turn possibly due to that of the extraction of the secondary ions. The reproducibility of the beam transport conditions will be improved when the last few items (eg. the low energy stand high energy steerers) are put under computer control.

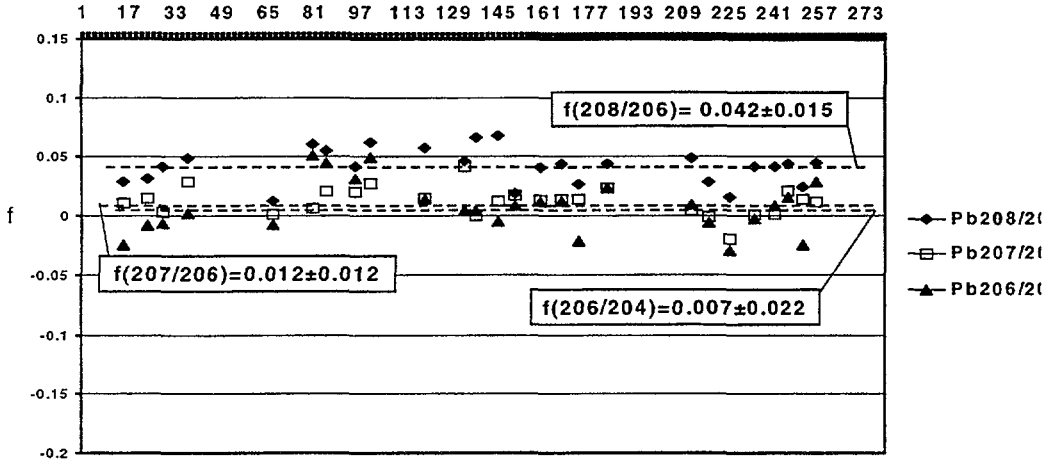

Figure 6. Fractionation factor f for Pb isotopic ratios over a period of 8 weeks. The factors are not linear with mass difference (see text).

Conclusions

A microbeam AMS system designed mainly for in-situ geochronology applications has been constructed. Tests demonstrate that a fast bouncing system is essential for achieving the high precision required in isotopic measurements. In tests on Pb and S isotopes, precision as good as 0.04% has been achieved. Long term reproducibility is still of the order of 1-2%, and is expected to be improved with better control of the beam transport components. The system paved the way for applications in geochronology previously not feasible by the in-situ method.

References

[1] Sie, S.H. , *Nucl. Instr. Meth.*, B130, 592-607 (1997).

[2] Sie, S.H. and Suter, G.F., *Nucl. Instr. Meth.*, **B92,** 221-226 (1994), Sie, S.H., Niklaus, Th.R. and Suter G.F., *Nucl. Instr. Meth.* **B123**, 112-121(1997)

[3] Sie, S.H., Niklaus, Th.R. and Suter G.F., *Nucl. Instr. Meth.*, **A382,** 299-308 (1996).

[4] Sie, S.H., Niklaus, Th.R. and Suter G.F., *Nucl. Instr. Meth.* . **B123**, 558-565 (1997)

[5] Nadeau , M.J. et al., *Nucl. Instr. Meth.* **B123**, 22-30 (1997)

[6] van der Borg, K., et al., *Nucl. Instr. Meth.* **B123**, 97-101(1997)

[7] Niklaus, Th.R., Sie, S.H. and Suter G.F., CP392, *Applications of Accelerators in Research and Industry*, ed. Duggan, J.L and Morgan I.L., AIP Press, New York 1997, pp.779-782.

[8] Sie, S.H., Niklaus, Th.R., Suter G.F. , Bruhn, F. and Cripps, G., *10th AINSE NTA Conference Proceedings* (1997)3pp.

[9] Sie, S.H., Niklaus, Th.R., Suter G.F. and Bruhn, F., *Rev. Sci. Instr.* **69**, 1353-1358 (1998)

^{10}Be concentrations in recent firn and ice from Law Dome Antarctica

A.M. Smith[1], D. Child[1], G. Elliot[1], D. Fink[1], C. Mifsud[1], Vin Morgan[2], M. Curran[2], B. Smith[2] D. Etheridge[3] and V.A. Levchenko[4]

[1]Australian Nuclear Science and Technology Organisation [ANSTO], [2]Australian Antarctic Division [AAD], [3]Commonwealth Scientific Industrial Research Organisation [CSIRO], [4]Joint Fellow [ANSTO, AAD & CSIRO]

ANSTO has been collaborating with the AAD Glaciology Program and CSIRO Atmospheric Research over the last six years on the measurement of cosmogenic isotopes from Law Dome ice sheet, East Antarctica.. In this paper we present our first results of ^{10}Be concentrations measured in the ice and firn from samples spanning this century and taken from three cores with up to a seven-fold variation in accumulation rate. In combination with a well established ice chronology, this has enabled a study of the relationship between the snow accumulation rate and the measured ^{10}Be concentration. Preliminary results suggest that, for Law Dome, the ^{10}Be concentration is independent of accumulation rate and that most ^{10}Be is incorporated into the ice sheet as a result of 'wet' precipitation.

Questions concerning the degree to which ^{10}Be is adsorbed on dust particles or present as a soluble form have complicated the interpretation of the ^{10}Be record in Northern Hemisphere ice cores. To better understand the implications for Law Dome ice we have undertaken two pilot experiments. One experiment involved measurement of the short lived radioisotope ^{7}Be along with ^{10}Be in surface snow samples in an attempt to elucidate transport effects. The second experiment was aimed at determination of the partitioning of ^{10}Be among terrestrial dust particles of different

Ultra-sensitive detection of technetium-99 by accelerator mass spectrometry

P. A. Hausladen (a), L. K. Fifield (a), R. G. Cresswell (a), M. L. Di Tada (a),
R. S. Carling (b) and J. P. Day (b)

(a) Department of Nuclear Physics, Australian National University, Canberra, ACT, 0200
(b) Department of Chemistry, University of Manchester, Manchester M13 9PL, UK

Technetium-99 is among the most prolific as well as the most long-lived ($T_{1/2}$=211 ka) fission products. It has been released in hundred-kilogram quantities from nuclear reprocessing plants, particularly that at Sellafield in the U.K. The dispersion of these releases in the North Atlantic and North Sea represent a public health issue as well as a potentially valuable oceanographic tracer experiment in this climactically important region of the world's oceans.

Techniques for the detection of ^{99}Tc with ultra-sensitivity using accelerator mass spectrometry have been developed at the ANU's 14UD accelerator. A combination of sophisticated chemical pretreatment and novel AMS techniques have permitted sensitivities at the 10fg level to be achieved. The principle challenges facing the AMS techniques are the lack of a stable technetium isotope and the existence of the stable isobar ^{99}Ru, while the advantages include sensitivity at least 2 orders of magnitude better than achieved with conventional β-decay counting or ICP-MS, and sample sizes typically 3 orders of magnitude smaller than those required for other techniques.

Developing a method for the retrospective estimation of radon exposure from in vivo measurements of ^{210}Pb activity in bone

Raymond J McKenzie*, Peter N Johnston*, Stephen B Solomon**, Peter A Burns**, Joseph R Statham** and John R Peggie**

* Department of Applied Physics, Royal Melbourne Institute of Technology, Melbourne Australia

** Australian Radiation Protection and Nuclear Safety Agency, Yallambie, Victoria

Abstract

Radon is a naturally occurring radioactive gas which has been linked to lung cancer in occupationally exposed uranium mine workers. Where monitoring of an individual's exposure to radon and radon progeny has not occurred or is incomplete, it may be possible to determine this exposure retrospectively by the measurement of the long lived decay product ^{210}Pb which accumulates in the bones of exposed individuals. This paper describes a method being developed at the whole body monitor (WBM) facility of the Australian Radiation Protection and Nuclear Safety Agency (ARPANSA) to estimate the time integrated exposure to radon over a period of up to several decades from the *in vivo* measurements of ^{210}Pb activity in the knee of human subjects. Initial work has concentrated on characterising the WBM facility for this work using artificial bone phantoms. This project will serve as a test of the feasibility of the method before undertaking further studies on human subjects.

Introduction

Radon (^{222}Rn) is a naturally occurring decay product of radium-226 (^{226}Ra), a member of the uranium-238 (^{238}U) series, and takes the form of an inert gas [1]. The presence of both ^{238}U and ^{226}Ra in most soils and rocks in varying concentrations, and the consequent escape of radon into surrounding air and water, creates the potential for significant exposure of the human population to radon. Radon decays with a half-life of 3.82 days [1] but exists in the atmosphere in various stages of equilibrium with its decay progeny, some of which have much shorter half-lives. For exposure to atmospheres containing radon and radon progeny, inhalation of the short lived alpha emitting radon progeny (^{214}Pb, ^{218}Po and ^{214}Bi) can lead to irradiation of the respiratory tract [1]. Radon progeny exposure may be elevated for those workers who are occupationally exposed in mines, underground service pits, or caves, and radon progeny exposure has been linked to the development of lung cancer in some underground uranium mine workers [1] [2].

Radiation dose to the lung due to α-particles from radon and its progeny occurs within a relatively short time (minutes to days) after inhalation and is usually estimated, using various models, from the measurement of radon and radon progeny concentration in the atmosphere in the vicinity of the worker. Where this monitoring has not occurred, or where exposure data is otherwise incomplete, it may be possible to determine radon dose retrospectively by the measurement of the long lived radioactive decay product lead-210 (^{210}Pb) which accumulates in the skeleton with an effective half-life of approximately 15 years [3].

Since *in vivo* measurement of ^{210}Pb activity involves the detection of a weakly emitted 46.5keV γ-ray which is strongly absorbed in the bone and soft tissue of the body, the efficiency of the detection of this γ-ray becomes a critical issue in determining the success of this technique. *In vivo* measurements are normally conducted on the skull or knee where significant bone mass lies close to the surface of the body thereby minimising absorption of the γ-ray in the body. The project reviewed here undertakes to determine and optimise the efficiency of the ARPANSA WBM for the detection of ^{210}Pb in bone. This study concentrates on the knee rather than the skull because of the expectation of greater ongoing uptake due to

body wear and repair mechanisms. The optimum detector geometry will be determined and the level of background interference assessed. This will be achieved through measurements in the WBM on an artificial knee phantom incorporating a ^{210}Pb radioactive source.

Experimental

The Australian Radiation Protection and Nuclear Safety Agency (ARPANSA) operates a WBM facility at their Yallambie laboratory in Victoria. The WBM consists of a large shielded chamber containing a bed on which the subjects lie, a suite of four high purity germanium (HPGe) detectors mounted as two hinged pairs (figure 1), and a mechanical arrangement to allow scanning of the detectors along the length of the body. These detectors input to a Canberra data acquisition system running on a DEC workstation for spectral data acquisition and processing.

To undertake the characterisation of the WBM, a simplified artificial knee phantom was constructed using several 12mm thick square shaped (250mm × 250mm plates of bone equivalent plastic (PVC). The plates can be stacked on top of one another to simulate knees of varying thickness. A disc shaped source was manufactured in the ARPANSA workshop using a filter paper substrate onto which a known quantity of reference ^{210}Pb solution was deposited. A schematic representation of the knee phantom is shown in Figure 1.

While two sources are shown above and below the bone material, only one is in fact used. However, two measurements are taken, one with the (single) source placed against the top surface of the knee and one with the source placed against the bottom surface of the knee. Following the methods used by Laurer et al [4] the geometric mean of these two results is taken to represent the count that would be obtained if the activity of the source were distributed uniformly throughout the volume of the knee. This then provides the calibration reference. The efficiency of different measuring geometries was explored by varying the

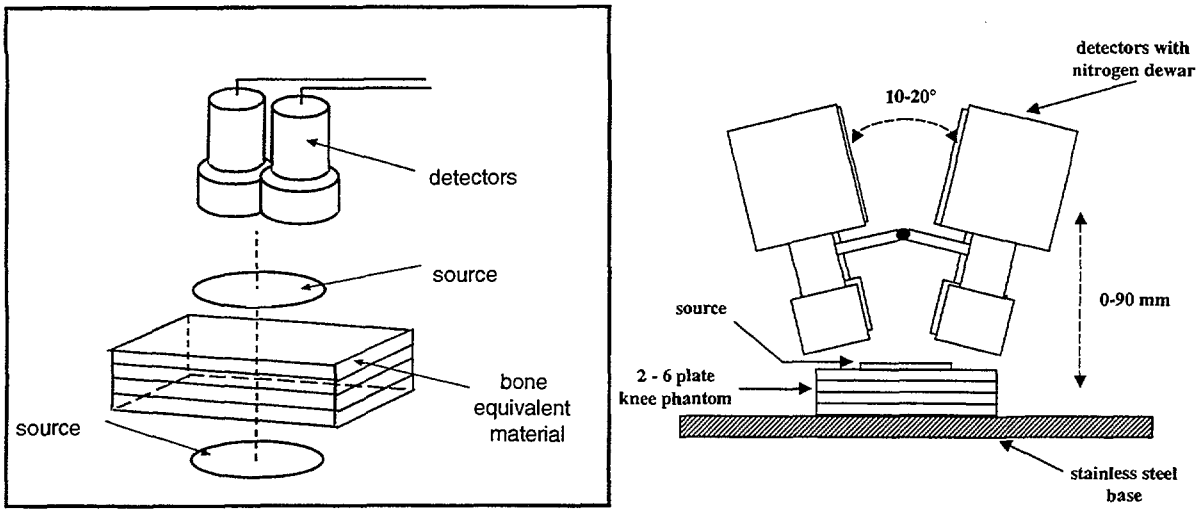

Figure 1. Schematic illustration of construction of simple knee phantom with its two source positions and the experimental arrangement from the side view showing the pairs of detectors hinged above the phantom with the source in the higher position.

detector height above the knee and the angle between the detectors. Note that for simplicity only two detectors are shown, but as previously mentioned, the ARPANSA WBM facility in fact uses a suite of four detectors.

The minimum detectable amount (MDA) of ^{210}Pb activity that it is possible to reliably detect in the WBM is also determined in this work. The MDA of the WBM in a given energy range depends on the background counts contributed by the WBM in that energy range. These

counts arise from the materials from which the chamber is constructed, the atmosphere in the chamber and from the human subjects or other objects in the chamber [5]. The MDA is thus determined by undertaking a long background count with all intentional radioactive sources removed from the chamber.

Results

Figure 2 shows the variation of count rate obtained for an average sized knee when the height of the detectors above the knee, and the included angle between the detectors, is varied over a range of values. The descriptors MinAngle, MedAngle and MaxAngle refer to the included angles of 10°, 15° and 20° respectively. The figure shows that while count rate always increases as the angle between the detectors is increased (so that they point more directly at the centre of the source), the height above the knee at which the maximum count rate is achieved depends on this angle. It is postulated that this is due to collimation effects within the detector which causes the source to be obscured at close distances. Highest overall count rates always occur for the maximum included angle at a height of 30mm above the knee.

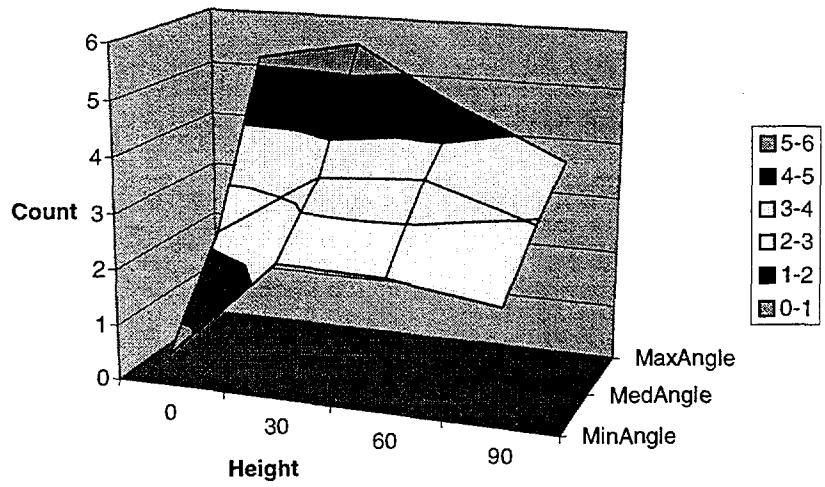

Figure 2. Variation of count rate with detector angle and height for average knee

The count rates achieved for the average sized knee are quite low. The calibration factor determined for the this knee is only $1.57 \pm 0.03 \times 10^{-4}$CPSBq^{-1}. The low sensitivity is thought to be the result of assuming a uniform volumetric distribution of ^{210}Pb in bone. Animal studies have shown the ^{210}Pb is concentrated at the surface of bone [6], which effectively makes the bone appear much thinner since less of the activity is absorbed in the volume of the bone. It is estimated that assuming a distribution of ^{210}Pb that is limited to the top 1mm of the bone surface would improve the sensitivity determined above by a factor of approximately 25.

The MDA determined for a 2 hour count in the ARPANSA WBM is 1.55×10^{-2}CPS at the 95% confidence level using the convention for detection limits established by Currie et al [7]. Using the more reasonable surface distribution assumption, this is equivalent to a ^{210}Pb activity in bone of approximately 4Bq. For measurements on the knee, which represents approximately 10% of human bone mass [8], this is equivalent to a total body burden of approximately 40Bq. It is estimated that the human background for ^{210}Pb in the general public due to ingestion from food, water, air and smoking is approximately 12Bq [3,4], so the

sensitivity of the technique as estimated here is only sufficient for measurements on subjects whose exposure is considerably in excess of that expected for the general public. However, the knee model used is obviously very crude, and considerable improvement in detection efficiency (and hence calculated MDA, which is affected by the calibration factor) may be expected from using a more anatomically realistic knee model.

Conclusion

The ARPANSA Whole Body Monitor (WBM) facility has been characterised for the *in vivo* measurement of ^{210}Pb in bone as part of the development of a method to estimate the retrospective radon exposure of human subjects from measurements on this long lived decay product. The most efficient measurement geometry for measurements on the knee has been determined using an artificial knee phantom, and the calibration factor and MDA for these measurements in the ARPANSA WBM have been determined.

Assuming a realistic distribution of ^{210}Pb in bone, it is determined that the ARPANSA WBM is suitable for determining ^{210}Pb in subjects whose radon exposure is several times that expected for the general public, and that sensitivity is likely to be considerably improved using a more anatomically realistic knee model.

References

[1] Committee on the Biological Effects of Ionising Radiations, "Health Risks of Radon and Other Internally Deposited Alpha Emitters", BEIR IV, National Academy Press, Washington, 1988

[2] NAS/NRC, "Effects of Inhaled Radioactive Particles", 1961

[3] Scheler R, Dettmann R Brose, "Retrospective Estimation of Exposure to Short Lived ^{222}Rn Progeny by Measurements of ^{210}Pb in the Skull", Radiation Protection Dosimetry Vol 79, Nos 1-4, 1998

[4] Laurer R, Estrada J, Cohen N, "Lung Exposure from Inhalation of Radon Progeny: Calculated from In Vivo Measurements of ^{210}Pb in the Skull", Health Physics, Vol 76, No 4, 1999

[5] Estrada J, Laurer G, "A Method to Obtain Subject Background for Low-Level *In-Vivo* Measurements of the Head", Health Physics, Vol 65-3, 1993

[6] Salmon P, Arola E, Clayton R, Thomas P, Henshaw D, "Age and Microdistribution of Pb-210 at Caribou Bone Surfaces", International Journal of Radiation Biology, Vol 3, No 1, 1998

[7] Currie L, "Limits for Qualitative Detection and Quantitative Determination", Analytical Chemistry, Vol 40 No 3, 1968

[8] Spitz H, University of Cincinnati, Health Physics Program, Private Communication, 1999

The latest news from the ANTARES AMS facility

David Fink, Michael Hotchkis, Ewan M. Lawson, Andrew M. Smith, and Ugo Zoppi

Physics Division, Australian Nuclear Science and Technology Organisation Lucas Heights Science and Technology Centre Private Mail Bag 1, Menai NSW 2234, Australia

The ANTARES AMS Facility is now well established with respect to routine measurement of the long-lived radioisotopes ^{14}C, ^{10}Be, ^{26}Al, ^{36}Cl, and ^{129}I, and supports a rich research program in environmental science, with emphasis on archaeology, global climate change and nuclear safeguards. New directions in applications of AMS to biomedicine and health studies are in progress. In addition, over the past 3 years a concerted effort in the development of an AMS measurement capability for actinide isotopes has recently been realised with the successful detection of ^{236}U.

The broad picture of this diverse activity – in applications and methodology - will be covered in order to bring you the latest news.

POSTERS

Elemental analysis of artefacts — establishing external beam PIXE

Andrew Alves, Peter Johnston, Robert Short and Ian Bubb.

Department of Applied Physics, Royal Melbourne Institute of Technology,
GPO Box 2476V, Melbourne 3001

Abstract

The development of an external PIXE facility on the 1 MV Tandetron accelerator at RMIT has led to a wide range of research possibilities. A proton beam, generated inside a vacuum is brought into air via an Au coated Kapton foil exit window (thickness 8μm, diameter 0.35mm). Monitoring of the beam intensity is achieved by detecting backscattered protons from the inside Au coating on the window. Artefacts, which may be too large to be placed inside the vacuum, are positioned in the beamline opposite the exit window. An optical system consisting of a CCD camera, alignment laser and two mirrors allows viewing of a region of the target 10mm x 10mm. This technique provides quantitative analysis of elements in the pigments used in paintings and on ceramics, which is a valuable tool in art conservation and authentication. Application of the technique to a ceramic sample from the historic house 'Viewbank' is described.

Introduction

In the study of artistic and historically significant artefacts procedures such as dating, authentication and conservation can be made easier by the determination of elemental composition. External beam PIXE (Proton Induced X-ray Emission) is an ideal analysis technique for this application because it is usually non-destructive. The artefact remains intact, does not need to be introduced into a vacuum and the ambient gas around the artefact allows heat and charge conduction.. Analysis at any point on the surface of an artefact can be achieved by positioning it in the path of an external proton beam. Elements in the irradiated region of the artefact with an atomic weight greater than Al may be quantitatively determined. The technique also has the advantage of being fast. Qualitative analysis is generally possible after only seconds of exposure to the beam.

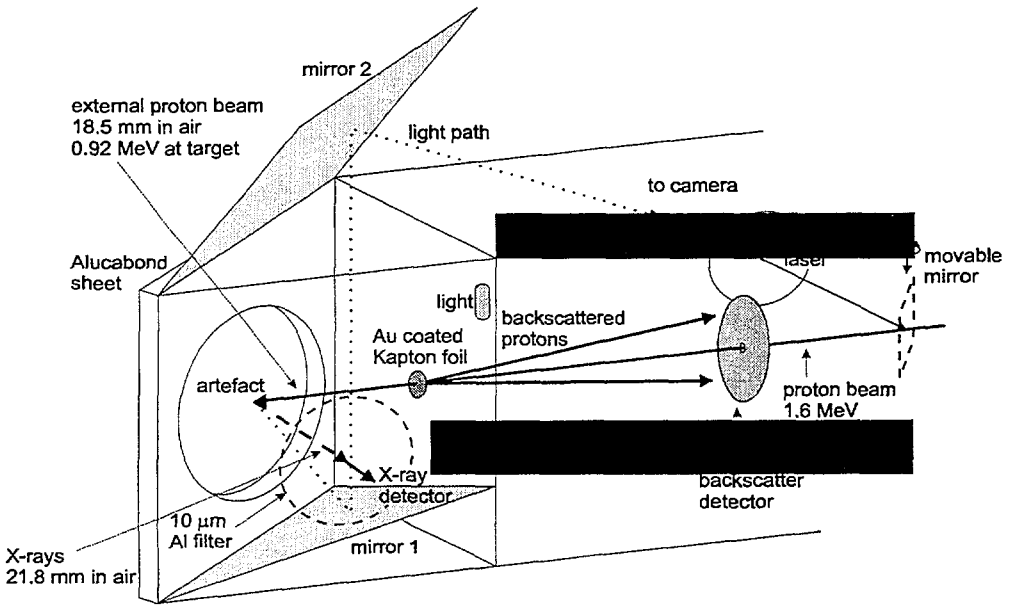

Figure 1. External PIXE apparatus.

Experiment

There are four main requirements in order to achieve a working external PIXE facility. (1) A source of protons. (2) A window between a region of high vacuum and atmospheric pressure which allows transmission of protons. (3) An X-ray detector and data acquisition electronics. (4) A means of mounting the artefact and aligning the target region. See the schematic in Figure 1 for the current setup.

In the current work, the proton beam is produced by the 1 MV Tandetron accelerator at RMIT, which provides a focused beam of 1.6MeV protons inside the vacuum chamber. The transport of the beam through the exit window and air causes the energy at the target to be reduced. The simulation package TRIM [3] is used to calculate the energy loss of the protons through the window and air. An 8μm Kapton foil coated with a 20nm Au layer on both sides is used as the window between the vacuum chamber and the atmosphere. Monitoring of the transmission of protons through the window is achieved by backscatter analysis of protons from the inner Au layer using an annular backscatter detector. The exposure is normalised by counting the backscattered protons as the X-ray spectrum is collected. For quantitative analysis, one needs to know the overall charge to which the sample has been exposed. It is therefore necessary to relate the beam intensity passing through the exit window and hitting the target to the count of backscattered protons. As the thickness of the Au layer varies from one window to another, a calibration is necessary for each new window. A 99% pure Ni standard is used as the target for the window calibration. The Ni is exposed to the beam for a range of Au counts. Using the known composition of the Ni standard, the software package PIXAN [4] is used to calculate the beam intensity (figure 2). The lifetime of the windows was found to be from 4 to 10 hours of irradiation. It was found that the lifetime of the window increases with Au coating on both sides of the foil. This is ascribed to the Au inhibiting surface diffusion as the beam passes through the window.

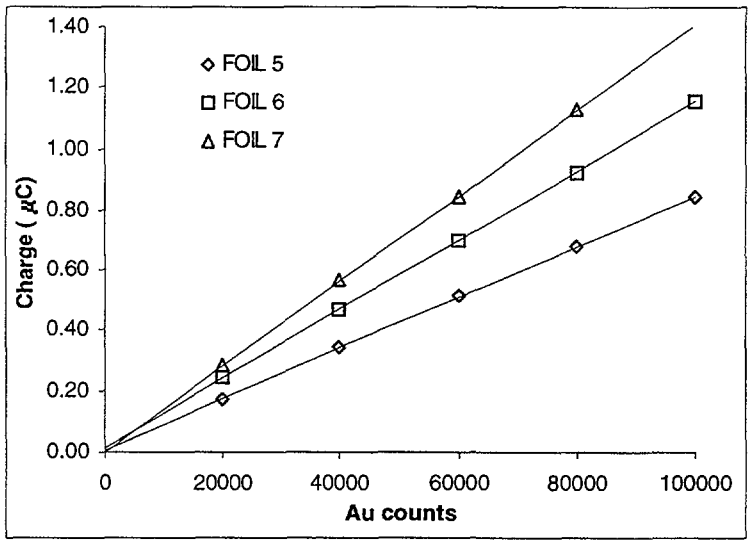

Figure 2. Charge vs Au counts for foils 5, 6 and 7.

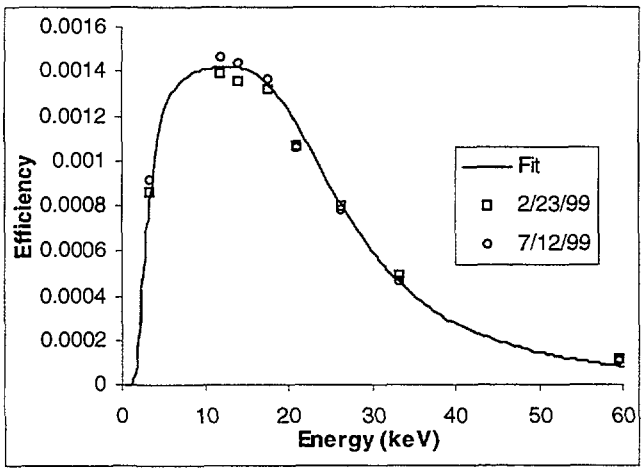

Figure 3. Si(Li) X-ray detector efficiency.

The X-ray detector used is a PGT Si(Li) X-ray detector of 30mm^2 with a resolution of 150eV at 5.9keV The efficiency of the detector is calibrated over the complete energy range being considered using a calibrated ^{241}Am source and known X-ray peak intensities [5]. (figure 3). Artefacts are mounted behind an Alucabond sheet mounted on a positioning stage with horizontal and vertical adjustments. The region of the artefact to be analysed is exposed to the beam via a 40mm diameter hole in the Alucabond. Viewing of the target beamspot is

achieved by an optical system consisting of two mirrors and a digital CCD camera. An image of a 10mm x 10mm target area is obtained and can be saved digitally. As protons do not cause fluorescence in all materials the exact position of the beamspot is aligned using a laser. A removable mirror inside the vacuum chamber reflects the laser beam along the beamline. The beamspot position shows up as a dot on the artefact, which allows the beam to be placed accurately on the artefact using the positioning stage.

Results

Artefacts studied were a number of ceramic pottery fragments from Heritage Victoria. Figure 4 shows X-ray spectra from ceramic sample 8. Visual inspection of the samples indicated that they appeared to have a glaze over different coloured patterns. Because the ceramics were broken the ceramic substrate was exposed at the edge. The aim was to determine if in fact the glaze was lead based and what elements were used in the pigments in the patterns. The elements present are P, Cl, K, Ca, Ti, Cr, Mn, Fe, Co, Cu, Zn and Pb. The spectra show the Pb L X-rays more prominently from the glazed surfaces. Therefore we conclude that the glaze is lead based. Al and Ar also appear in all spectra however must be disregarded. Al is used as the filter for the detector and gives rise to additional X-ray fluorescence at the energy of the Al K series. The presence of Ar in the atmosphere gives rise to an Ar peak.

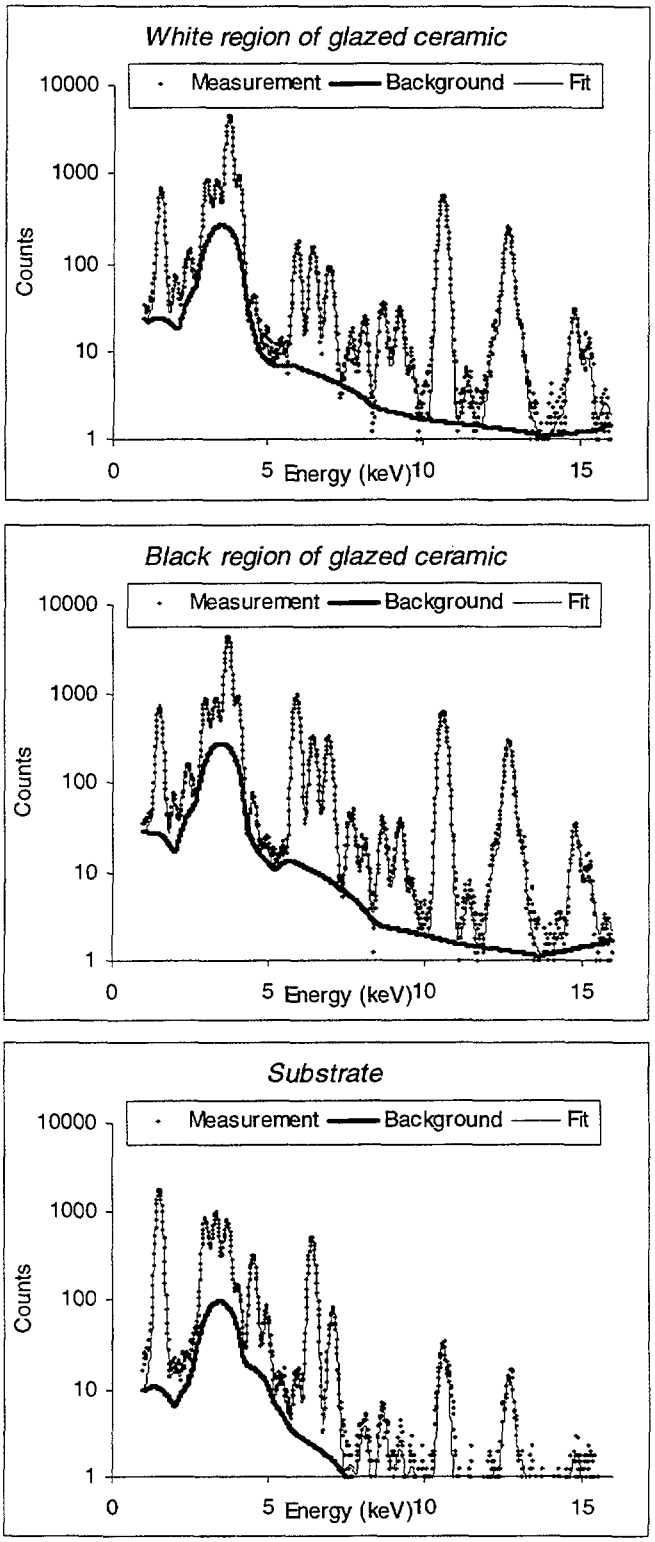

Figure 4. Spectra from ceramic sample 8.

Analysis

Once the PIXE spectrum has been collected qualitative analysis can be made by recognition of the characteristic X-ray peaks. Quantitative analysis of the elements in the artefact was performed using the analysis package PIXAN. The analysis is broken up into two parts. Firstly a curve is fitted to the spectrum based on known X-ray energies. The best fit is acquired by qualitatively determining elements in the sample and the corresponding electronic transitions, Kα, Kβ, Lα, etc. Secondly a theoretical yield (peak area / atomic percentage) for each element is determined based on the known efficiency of the X-ray detector and the concentration of one or more major elements. The peak area divided by the yield gives the atomic percentage in parts per million (PPM). The atomic percentage for the major

elements should match the original value used to calculate the yield. An iterative procedure is used to calculate the actual atomic percentage.

Figure 5 is a quantitative composition of the elements present in the sample, using peak areas and yields generated by PIXAN. Due to the low efficiency of the detector at low energies the uncertainty in the calculation of the yield is high for elements P, Cl and K. By comparing the substrate with the two glazed regions, elements Ca, Mn, Co, Cu, Zn and Pb feature more prominently in the surface material, glaze and/or pigments. Elements Ti, Cr and Fe are more prominent in the substrate. The similarity in atomic percentage of Ca, Cu, Zn, and Pb between white and black regions of the glazed ceramic indicate these elements are present in the glaze. Differences in the composition of the two glazed surfaces indicate that the proton beam penetrates and allows analysis of a greater depth than the thickness of the glazing. Elements Mn, Co and possibly Fe are present in the black pigment.

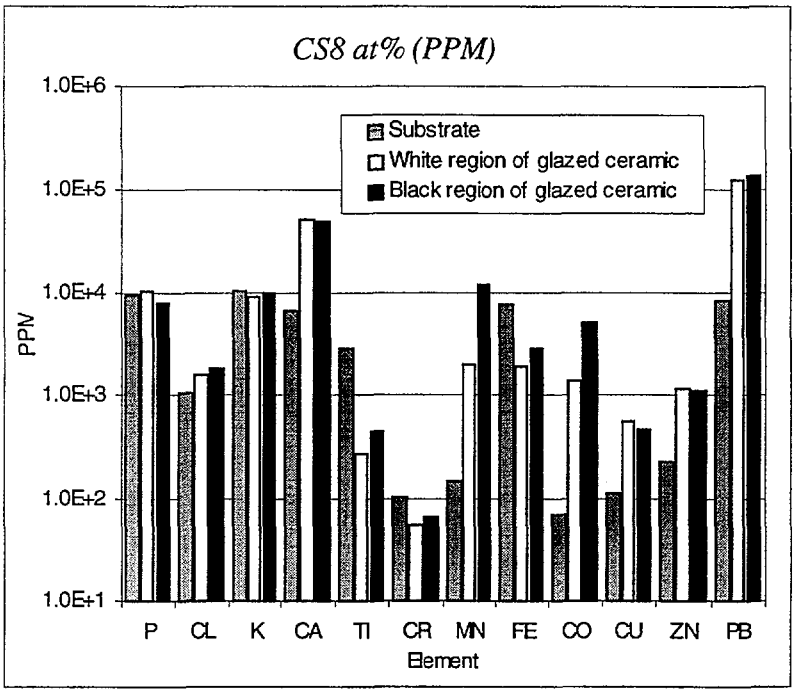

Figure 5. Composition of the ceramic sample CS8

Conclusions

The design of the external PIXE facility at RMIT for the analysis of paintings and ceramics has been described.

The application of the techniques to a ceramic sample from the historic house 'Viewbank' has shown that the analysis is capable of discerning the key elements in the ceramic substrate, glazing and pigments.

References

[1] M. Moser, I. F. Bubb, P. N. Johnston, M. El Bouanani, W. B. Stannard and R. C. Short, Nucl. Instr. Meth. B 136-138 (1998) 841-845; Nucl. Instr. Meth. B139 (1998) 164-168.

[2] M.A. Respaldiza and J. Gómez-Camacho, Applications of Ion Beam Analysis Techniques to Arts and Archaeometry, Universidad de Sevilla, 1997.

[3] J. F. Ziegler and J. P. Biersack, The Stopping and Range of Ions in Solids, Pergamon Press, New York 1985 with Software TRIM 95.9, IBM Research, New York 1995.

[4] E. Clayton, Australian Atomic Energy Commission Report AAEC/-M113 (1986), Nucl. Instr. Meth., B22 (1987) 64.

[5] D. D. Cohen, Nucl. Instr. Meth. A267 (1988) 492-498.

U-Th-Pb chemical dating of monazites using the proton microprobe

F. Bruhn[1,*], S. H. Sie[1], A.Möller[2] and B. Hensen[2],

[1]HIAF Laboratory, CSIRO Exploration and Mining, PO Box 136, North Ryde, NSW 2113.
[2]Department of Applied Geology, University of New South Wales, Sydney, NSW 2052.

1. Introduction

Chemical dating of U and/or Th bearing minerals, ie age determinations using the elemental concentrations rather than isotopic ratios, was used in the early days of geochronology[1], but subsequently superseded by the more accurate isotopic methods of dating. The method has more recently been revived, particularly for monazite dating using the electron microprobe[2-8].

The two prerequisites for the method are : (1) The concentration of non-radiogenic Pb can be neglected and (2) the system has remained closed with respect to these elements after mineral formation, i.e. the concentrations of U, Th and Pb have only changed due to radioactive decay. Under these circumstances, which are accepted to be a relatively common feature of monazites [3] the age (τ) can be calculated by resolving the following equation [3].

$$Pb = (Th/232)\ \{\exp(\lambda^{232}\tau)-1\}\ 208 + (U/238.04)\ [\ 0.9928\ \{\exp(\lambda^{238}\tau)-1\}\ 206 + 0.0072\ \{\exp(\lambda^{235}\tau)-1\}\ 207\ ]$$

Pb, U, and Th are the concentrations inppm, and λ^{232}, λ^{235} and λ^{238} are the radioactive decay constants of ^{232}Th, ^{235}U and ^{238}U, respectively. Due to the transcendental nature of the equation it can only be resolved by iteration.

2. Analytical procedures

We have used micro-PIXE to determine the chemical composition of polished monazite grain separates at the HIAF. A typical X-ray spectra obtained with a 20 – 30μm beam of 3MeV protons using a Si(Li) detector oriented at 135° to the beam direction, through a 100μm Al filter is shown in figure 1. Count rates were kept in the range of 2 to 4K counts per second to minimise pile-up effects. A single analysis using a 1.5nA beam took about 5 to 10 minutes for an accumulated charge of 0.5 to 1μC. Detection limits (99 % confidence) were typically 10 to 20ppm for U, Th and Pb, and <1000ppm for the rare earth elements. A ll quoted errors in chemical concentrations and ages are two standard deviations.

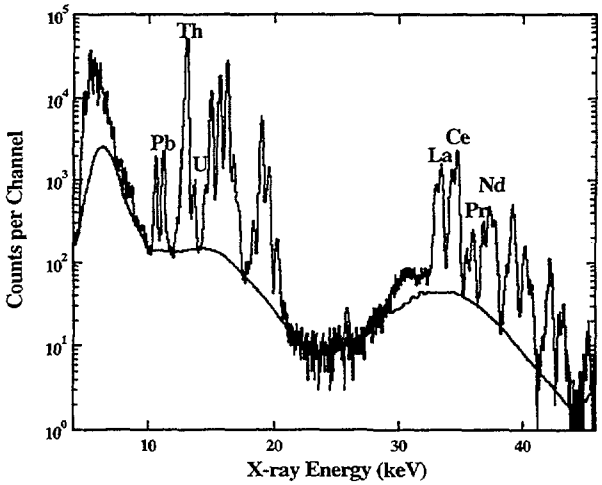

Figure 1. An example of a PIXE spectrum from a monazite with ~1500ppm Pb, obtained with a 3MeV proton beam and 1.5 μC integrated charge. A 100 μm Al filter was used for this measurement.

3. Results

A total of 54 samples of both standards and unknown sample material (cf. Table 1 and Figure 2) have been performed. The standard samples are well characterized with known ages derived from other dating techniques. The unknown as samples have also been analysed using the SHRIMP ion microprobe [9] for comparison. The samples are: (a) *MAD* standard monazite used for SHRIMP ion microprobe analyses at Curtin University, Perth [10], with 1500ppm Pb and an age of 514 million years (Ma), (b) Madagascan monazite *F6*, with an age of 557±20 Ma derived from electron microprobe analysis [3,11], (c) monazite *Moacir*, with an age of 501±48 Ma, derived from electron microprobe analysis [3], and (d) samples with unknown ages (*NH13, NH35, NH49*) from granites and granulite facies metasediments in the Northampton Block, Western Australia [12].

Results of micro-PIXE analyses of the standard MAD yielded ages between 493±31 and 528 ± 31 Ma. The average of 512 ± 32 Ma coincides well with the reference age of 514 Ma used for SHRIMP calibration. Seventeen measurements of Madagascan monazite *F6* result in ages between 474 ± 90 and 567 ± 40 Ma. The average of 514 ± 32 overlaps with the age of 557 ± 20 Ma derived from electron microprobe dating [3]. Nine spots have been measured in sample *Moacir*, and yield ages between 437 ± 63 and 479 ± 47 Ma. The average of 454 ± 41 Ma overlaps with the age of 501 ± 48 Ma derived from electron microprobe dating [3]

The ages for the unknown samples are derived from measurement of individual monazite grains in 3 different batches. Sample *NH13* consists of 7 grains with ages between 1068 ± 79 and 1143 ± 68 Ma and an average of 1094 ± 58 Ma. The independent SHRIMP $^{207}Pb/^{206}Pb$ age of 1068 ± 7 Ma for this population overlaps with the proton microprobe age. Sample *NH35* is a batch of 4 grains with ages between 1084 ± 76 and 1167 ± 70 Ma and an average of 1141 ± 71 Ma, overlapping with the independent SHRIMP $^{207}Pb/^{206}Pb$ age of 1076 ± 4 Ma. Thirteen grains have been analyzed from sample *NH49*, yielding ages between 1056 ± 70 and 1174 ± 129 Ma with an average of 1110 ± 39 Ma. This coincides with the independent SHRIMP $^{207}Pb/^{206}Pb$ age of 1082 ± 5 Ma.

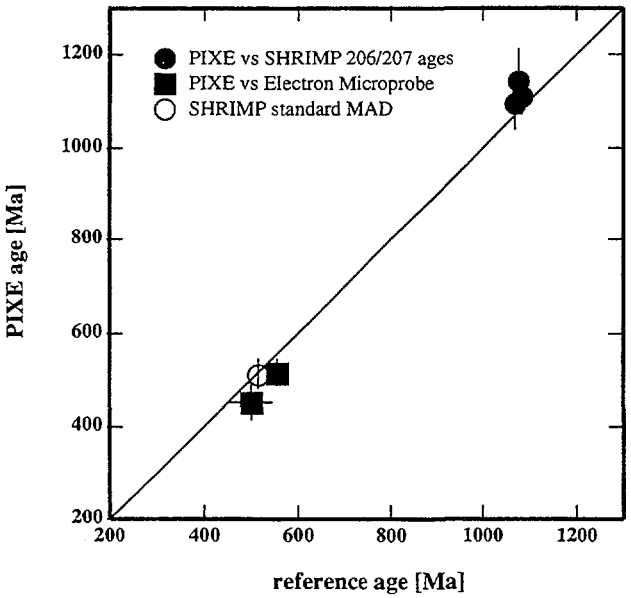

Figure 2. Comparison of ages derived from chemical U-Th-Pb proton microprobe dating and other geochronological methods as a reference. Error bars are 2 standard deviations.

4. Discussion and implications for geochronology

The results of this initial study demonstrate that proton microprobe analysis of monazite can be used as a straightforward and accurate tool to obtain meaningful ages. It thus offers considerable benefit to geochronological issues. Given a measurement time of 5 min per grain

Table1: Results of PIXE analyses for U-Th-Pb datings.

	Th [%]		U [%]		Pb [%]		τ (Ma)
Analysis	conc	2σ	conc	2σ	conc	2σ	
MAD.1[1]	6.23	0.23	0.108	0.013	0.1514	0.0034	510±33
MAD.2[1]	6.27	0.23	0.109	0.013	0.1541	0.0036	517±33
MAD.4[1]	6.52	0.20	0.116	0.014	0.1643	0.0038	528±31
MAD.5[1]	6.35	0.22	0.113	0.013	0.1490	0.0036	493±31
NH49.1[2]	8.71	0.36	0.333	0.017	0.4964	0.0090	1104±65
NH49.2[2]	8.94	0.27	0.283	0.023	0.5108	0.0096	1129±59
NH49.5[2]	8.12	0.26	0.330	0.028	0.467	0.013	1106±69
NH49.8[2]	9.02	0.33	0.273	0.027	0.488	0.012	1076±69
NH49.10[2]	8.78	0.36	0.414	0.036	0.502	0.010	1080±70
NH49.22[2]	9.26	0.25	0.305	0.206	0.553	0.011	1174±129
NH49.25[2]	8.86	0.27	0.296	0.262	0.512	0.016	1135±167
NH49.34[2]	9.15	0.31	0.274	0.016	0.512	0.014	1112±68
NH49.35[2]	8.79	0.26	0.265	0.020	0.497	0.011	1123±60
NH49.39[2]	9.78	0.26	0.492	0.038	0.602	0.019	1149±72
NH49.43[2]	7.20	0.29	0.344	0.026	0.4028	0.0096	1056±70
NH49.54[2]	10.50	0.31	0.477	0.029	0.635	0.013	1145±60
NH49.58[2]	9.09	0.31	0.505	0.041	0.537	0.016	1088±74
NH35.39[2]	5.75	0.15	0.717	0.044	0.4343	0.0086	1155±63
NH35.57[2]	5.58	0.16	0.563	0.037	0.401	0.010	1167±70
NH35.69[2]	5.35	0.20	0.364	0.029	0.3259	0.0092	1084±76
NH35.71[2]	5.23	0.08	0.447	0.028	0.355	0.011	1148±78
NH13.3[2]	6.07	0.21	0.625	0.050	0.405	0.013	1082±80
NH13.4[2]	6.56	0.22	0.191	0.021	0.366	0.011	1112±77
NH13.8[2]	6.53	0.19	0.491	0.042	0.4291	0.0092	1143±68
NH13.9[2]	5.44	0.19	0.775	0.056	0.394	0.012	1068±79
NH13.10[2]	6.46	0.20	0.701	0.052	0.445	0.013	1100±75
NH13.11[2]	4.92	0.18	0.491	0.039	0.3256	0.0090	1083±79
NH13.14[2]	4.49	0.17	0.048	0.008	0.2257	0.0090	1044±83

	Th [%]		U [%]		Pb [%]		τ (Ma)
analysis	conc	2σ	conc	2σ	conc	2σ	
F6.1.1[3]	11.1	0.4	0.145	0.023	0.267	0.021	513±63
F6.1.2[3]	11.4	0.4	0.141	0.023	0.265	0.019	497±57
F6.1.3[3]	11.2	0.4	0.145	0.023	0.267	0.018	509±55
F6.1.5[3]	11.0	0.4	0.144	0.022	0.269	0.019	521±57
F6.2.1[3]	10.9	0.4	0.14	0.022	0.262	0.021	513±63
F6.2.2[3]	11.1	0.4	0.135	0.021	0.258	0.021	497±61
F6.2.4[3]	10.82	0.38	0.142	0.022	0.264	0.019	521±58
F6.2.5[3]	11.0	0.4	0.144	0.025	0.262	0.018	508±56
F6.3.1[3]	11.0	0.4	0.148	0.013	0.268	0.017	519±55
F6.3.3[3]	11.1	0.7	0.152	0.027	0.247	0.031	474±90
F6.3.4[3]	11.1	0.7	0.158	0.030	0.252	0.031	483±92
F6.3.5[3]	11.0	0.7	0.154	0.026	0.248	0.034	480±98
F6.3.6[3]	11.2	0.7	0.154	0.029	0.250	0.032	476±92
F6.3.7[3]	11.1	0.7	0.154	0.020	0.250	0.033	480±98
F6.3.8[3]	11.1	0.7	0.152	0.028	0.248	0.031	476±92
F6.3.9[3]	11.1	0.7	0.136	0.022	0.271	0.025	520±81
F6.3.10[3]	11.08	0.39	0.126	0.015	0.294	0.001	567±40
moacir.1[4]	6.49	0.26	0.128	0.018	0.140	0.014	451±66
moacir.2[4]	6.10	0.24	0.102	0.019	0.127	0.013	440±64
moacir.3[4]	6.54	0.27	0.136	0.022	0.141	0.019	447±76
moacir.4.2[4]	6.58	0.25	0.135	0.020	0.140	0.013	444±61
moacir.5[4]	6.55	0.24	0.131	0.019	0.150	0.008	479±47
moacir.6[4]	6.46	0.27	0.124	0.019	0.143	0.013	464±64
moacir.7[4]	6.35	0.26	0.0612	0.013	0.131	0.012	446±61
moacir.8.1[4]	6.59	0.17	0.137	0.012	0.138	0.013	437±63
moacir.8.2[4]	6.64	0.28	0.134	0.018	0.144	0.014	453±64

[1] SHRIMP standard *MAD*
[2] unknown samples from the Northampton Block, Western Australia
[3] electron microprobe standard *F6* [3]
[4] electron microprobe standard monazite lens *Moacir* [3]

grain, as many as 100 measurements can easily be performed in the course of an 8 hours working day. As is the case for electron microprobe analyses, sample preparation is quite straightforward. Mineral separates as well as polished thin sections can be used, the latter having the advantage that the petrographic position of the analysed grain is known. Although precision and accuracy of coventional TIMS analysis are at least one order of magnitude better than that of any *in-situ* method, this drawback is compensated for by the necessity of labour intensive and costly chemical separation inherent with conventional TIMS. In contrast to electron microprobe analyses with typical detection limits of 200ppm using a wavelength dispersive system [3], PIXE measurements with the proton microprobe yield considerably lower detection limits of about 10ppm for Pb, Th and U. Furthermore, owing to the use of an energy dispersive detector, additional information on the sample chemistry, e.g. rare earth elements, is readily available. The low detection limits, in principle, make micro-PIXE analyses viable for the investigation of phases containing lower concentrations of Pb, U, Th (e.g. zircon, sphene [13]) and young monazites (<100Ma) that have accumulated less radiogenic Pb than the older ones. However, peak overlaps and lower Pb and U concentrations in the case of zircon may cause lower precision. Studies to test these applications are in progress. A possible disadvantage of the PIXE method is the relatively high effective depth of analysis (~30μm), and care must be taken when analysing samples with intense chemical/isotopic zonation (Figure 3).

Combined with cathodoluminescence and backscatter electron studies used to investigate chemical zonation, the method is of great potential use when discriminating different age populations and thus source areas of clastic rocks within the framework of provenance studies.

Acknowledgement

The authors wish to thank j.-c. Montel for providing monazite samples measured by electron microprobe, p.d. kinny for the possibility to use the mad standard and l.m. kriegsmann for providing samples from western australia. Financial support from the deutsche forschungsgemeinschaft (dfg) and australian geodynamics cooperative research centre (agcrc) is gratefully acknowledged

References

[1] G. Faure, Principles of Isotope Geology (John Wiley & Sons, New York, 1986).
[2] J.-M. Montel, M. Veschambre and C. Nicollet, C.R. Acad. Sci. Paris 318 (1994) 1489.
[3] J.-M. Montel, S. Foret, M. Veschambre, C. Nicollet and A. Provost, Chem. Geol. 131 (1996) 37.
[4] I. Braun, J.-M. Montel, and C. Nicollet, Chem. Geol. 146 (1998) 65.
[5] K. Suzuki, M. Adachi and T. Tanaka, Sed. Geol. 75 (1991) 141.
[6] K. Suzuki, M. Adachi and I. Kajizuka, Earth and Planet. Sci. Lett. 128 (1994) 391.
[7] K. Suzuki and M. Adachi, J. Metamorph. Geol. 16 (1998) 23.
[8] D. Rhede, I. Wendt and H.-J. Förster, Chem. Geol. 130 (1996) 247.
[9] I.S. Williams, Transact. Royal Soc. Edinburgh 83 (1992) 447.
[10] P.D. Kinny, Curtin University of Technology, School of Physical Sciences, Report No. SPS 693/1997/AP72 (1997).
[11] J.-L. Paquette, A. Nedelec, B. Moine and M. Rakotondrazafy, J. Geol. 102 (1994) 523.
[12] L.M. Kriegsman, A. Möller, D.R. Nelson and B.J. Hensen, unpublished data.
[13] R. Frei, V.M. Prozesky and W. Przybylowicz, Nucl. Instr. and Meth. B130 (1997) 676.

Chlorine-36 in the great artesian basin

Richard Cresswell (a), Keith Fifield (a), Bruce Radke (b),
Jim Ferguson (b), Tim Ransley (b) and Rien Habermehl (b)

Department of Nuclear Physics, Australian National University, Canberra, ACT, 0200
(b) Land and Water Sciences Division, Bureau of Resource Sciences, Canberra, ACT, 2609

The Great Artesian Basin is a confined groundwater basin, which underlies arid and semi-arid regions across 1.7 million km^2 or one-fifth of Australia. The basin's groundwater resources were discovered around 1880, and their development allowed the establishment of an important pastoral industry. Pastoral activity, town water supplies, mining and petroleum ventures are all totally dependent on artesian groundwater. Understanding the age, and thus the flow-rates, of groundwater across the basin is crucial in the management of this vital resource.

The GAB has become a classic example of the use of the naturally occurring radio-isotope chlorine-36 as a groundwater dating tool in large confined aquifers. The validity of using chlorine-36 to trace groundwater flow from recharge to discharge through the basin has been questioned, however, with suggestions that mixing and stagnation can also explain the ^{36}Cl data, and flow models are not appropriate.

We now have over 300 $^{36}Cl/Cl$ determinations for the Great Artesian Basin, with 183 analyses identified from the main Jurassic aquifer. The emerging picture is naturally more complex than either simple through-flow, or mixing, or stagnation. We can thus distinguish stream-lines of rapid through flow, as well as regions of relative stagnation and areas where mixing is dominant.

An overview of the results will be presented, and will highlight the need for integrated studies. In this case, hydro-geological, hydro-chemical and hydro-geophysical interpretations are required before the radio-isotope data can be meaningfully interpreted.

RBS cross-section of MeV ions channeling in crystals from quantum theory

J. L. den Besten*†, D. N. Jamieson†, L. J. Allen and P. G. Spizzirri†

School of Physics, University of Melbourne, VIC, 3010, AUSTRALIA

Abstract

We present an alternative approach to describing Rutherford Backscattered (RBS) angular yield scans. The Bloch wave method to formulate the cross-section is a fundamental approach originating from Schrödinger's equation. This quantum formulation is often used when describing various aspects of electron diffraction including Backscattering, EDX and TEM but has seen little application to the very short wavelength regime of MeV ions. It offers several significant advantages. Great freedom is given to crystal properties and structure in the theory allowing a fundamental insight into the channeling phenomena and hence the crystal itself. We have calculated both planar and axial channeling scans and these maps are shown to be in good agreement to their experimental counterparts. There is excellent correlation between the theoretical and experimental results for both χ_{min} and $\psi_{1/2}$. Further investigation is required into the area of absorption or dechanneling. This phenomenon requires different mechanisms for electron and ion scattering differ greatly.

Introduction

Much debate was generated in the late 1960s[1, 2i] when the first suggestions were made about using a quantal approach to describe the channeling of a proton or heavier ion in a periodic crystal lattice as opposed to the newly formulated classical method generated by Lindhard[3]. This suggestion was motivated by the newly successful quantal approach describing the diffraction of the *electron* in a periodic potential. The outcome of this debate was simply that the theory is correct for both electrons and protons yet for protons, the calculation is computationally difficult and expensive and, to a large extent, experimental conditions reduces the possibility of observing any quantal effects[4]. Chadderton[5], in a review of this discussion, acknowledged this but went on to say that if the classical method is used, the calculation will not be correct if the situation is approaching the quantal realm as any quantal effects will never be described by the calculations. Alternatively, if one uses the quantal method, the classical limit may be approached, hence the calculation will always be correct and will reflect both the classical and quantal effects. Nip and Kelly[6, 7, 8] then proceeded to formulate the Bloch wave equations taking into consideration the properties of an ion in a crystal potential and any experimental conditions. They investigated the limits at which the proton no longer needs be considered quantum mechanically.

* Corresponding Author: jdb@ph.unimelb.edu.au

† MicroAnalytical Research Centre

The classical limit

The classical limit for the scattering of charged particles in a crystal lattice as given by Chadderton[5] and formulated by Nip and Kelly[8] is described as *the small-transverse-wavelength limit*. This means

$$\lambda_{xy} << \tfrac{1}{2} a_{xy} \qquad \text{Eq 1}$$

for classical mechanics to be applicable. In this case λ_{xy} is the transverse de Broglie wavelength defined by

$$\lambda_{xy} = \hbar / m\left(v_x^2 + v_y^2\right)^{1/2} \qquad \text{Eq 2}$$

where m is the mass of the projectile, v_x and v_y are the velocities of the projectile in the transverse x and y planes respectively and a_{xy} is the smallest transverse interplanar spacing of the crystal lattice.

This is equivalent to

$$a > 200\lambda / \psi_c \qquad \text{Eq 3}$$

derived from the Uncertainty Principle. a is the interplanar spacing, λ is the de Broglie wavelength and ψ_c is the critical scattering angle derived by Lindhard[3]. Depending on the experimental conditions this may hold true for "heavy" particles while for electrons it will never be the case and must be treated wave mechanically. Hence the proton is very close to the transition between quantal and classical mechanics.

Theory

The Schrödinger equation is solved to determine the wave function, $\Psi(\mathbf{K},\mathbf{r})$, of an ion traversing through a crystal lattice[9] using the elastic scattering potential of the crystal lattice, $V(\mathbf{r})$, the potential representing absorptive scattering, $W(\mathbf{r})$, and the properties of the ion, the energy, E, and the reduced mass of the system, m. The crystal potential is periodic, hence the wave function can be given as a linear superposition of Bloch states[10],

$$\Psi(\mathbf{K},\mathbf{r}) = \sum_i \alpha^i \sum_{\mathbf{g}} C_{\mathbf{g}}^i \exp\left[i\left(\mathbf{K} + \lambda^i \hat{\mathbf{n}} + \mathbf{g}\right)\cdot\mathbf{r}\right] \qquad \text{Eq 4}$$

where $\mathbf{K}$ is the wave vector in a crystal corrected for refraction, α^i is the excitation amplitude of the ith Bloch wave, $C_{\mathbf{g}}^i$ are the Bloch wave coefficients, λ^i are the complex eigenvalues which contains the absorption coefficient, $\hat{\mathbf{n}}$ is the surface normal directed inwardly and $\mathbf{g}$ is the reciprocal lattice vector.

The crystal potential is derived from a screened Coulomb atomic potential, where the screening function used is the Universal screening function[11] which is considered to be the best fit to the full spectrum of data[12].

The total scattering cross section, σ, can be defined as the rate of absorption of ions in a crystal of volume V. Therefore the cross section is proportional to the integral of the rate of flux loss per unit volume[13]

$$\sigma = \frac{2m}{\hbar^2 k} \int_V W(\mathbf{r}) \left|\Psi(\mathbf{r})\right|^2 d\mathbf{r} \qquad \text{Eq 5}$$

Hence the cross section for a single process, such as Rutherford Backscattering, can be obtained by using the appropriate component of $W(\mathbf{r})$, i.e. $W^{RBS}(\mathbf{r})$[14]. Note that the wave function is complete and that all absorptive processes have been considered in formulating the wave function. For a more complete derivation and discussion of the theory, the reader is referred to the references 15 and 16.

Results

Experiments-

The Melbourne University microprobe was used to generate the RBS 1-D and 2-D angular scans of the <100> axis and constituent planes for Ni and FeS_2 crystals. 1MeV protons were used in an unfocussed, collimated beam. An angular resolution of 0.1° was used over a range of $\pm 2^\circ$ about the axis. The scanning was done using the G-Paq data acquisition package developed within the Microanalytical Research Centre.[17]

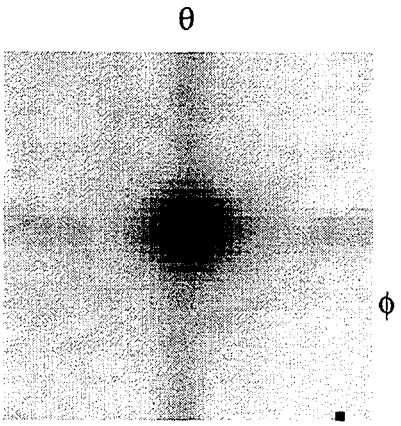

Figure 1 **2-D angular scan of the <100> axis of FeS_2**

Calculations-

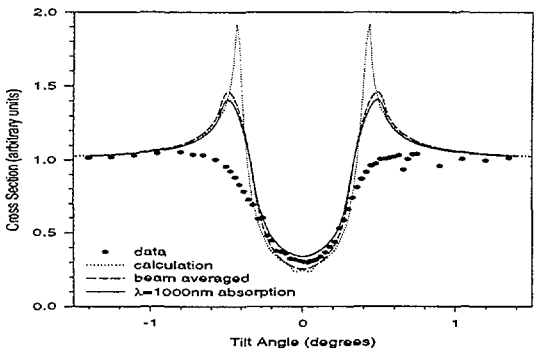

Figure 2 Calculated angular yield curves for {100} nickel for a depth of 250nm compared to experiment (circles). Also show the variation from the initial calculation to taking into account beam convergence and including a mean absorption.

We present the quantal RBS calculation of a heavy charged MeV particle in a crystal lattice. The examples mentioned in the Experiments section have been simulated using the program CPBW (Charged Particle Bloch Wave). This program gives great freedom in its parameters in order to simulate the experimental conditions as closely as possible. The temperature, thickness of the sample, the type of crystal including multiple elements and concentration of impurities and angular resolution are all considered. Both the crystal potential and the RBS cross section can be calculated for both the planar orientation and the axial orientation for any combination of parameters mentioned above. In this work we present both planar and axial angular scans of the RBS cross section. For the axial orientation this includes both 2-D scan about the axis and 1-D scan through the axis at a chosen angle to ϕ. For the RBS calculations, the scans can be calculated for a particular element only or all constituent elements which make up the compound.

Comparison-

We get excellent agreement when comparing the experimental angular scans with those simulated by CPBW[15,16], especially the χ_{min} and $\psi_{1/2}$, the minimum depth and the half width at half maximum. The shoulder region is overestimated but with a suitable absorption or dechanneling mechanism these shoulders are reduced. The beginnings of this can be seen in reference 15 using a mean absorption. Clearly a stronger absorption is required in the

shoulder region and hence the absorption needs to be angular dependent. This is still being investigated, as the Einstein model, used with electrons, for thermal diffuse scattering, the major contributor to absorption, is not as applicable for protons.

Conclusions

The results from the calculations when compared to the RBS experimental data provide very encouraging and promising results. Further work is required in the area of absorption or dechanneling in which case the properties of electrons and protons differ greatly in the mechanisms for absorption and the properties effecting these mechanisms.

References

[1] L. T. Chadderton, Phys. Letts., **23** (1966) 303.

[2] R. E. De Wames, W. F. Hall and G. W. Lehman, Phys. Rev., **148** (1966) 181.

[3] J. Lindhard, Mat.-Fys. Medd. Dan. Vidensk. Selsk., **34** no. 14 (1965).

[4] J. M. Cowley, Phys. Letts., **A26** (1968) 623.

[5] L. T. Chadderton, J. Appl. Cryst., **3** (1970) 429.

[6] H. C. H. Nip and J. C. Kelly, Phys. Rev. **B5** (1972) 813

[7] H. C. H. Nip and J. C. Kelly, Phys. Rev. **B5** (1972) 1797

[8] H. C. H. Nip and J. C. Kelly, Phys. Rev. **B5** (1972) 2425

[9] C. J. Humpreys, Rep. Prog. Phys., **42** (1979) 122.

[10] L. J. Allen and C. J. Rossouw, Phys. Rev., **B39** (1989) 8313.

[11] J. F. Ziegler, J. P. Biersack and U. Littmark, *The Stopping and Range of Ions in Solids* (Pergammon, New York, 1985) p.41.

[12] D. J. O'Connor and J.P. Biersack, Nucl. Instr. Meth., **B15** (1968) 14.

[13] H. D. Heidenreich, J. Appl. Phys., **33** (1962) 2321.

[14] L. J. Allen and T. W. Josefsson, Phys. Rev., **B52** (1995) 3184.

[15] J. L. den Besten, L. J. Allen and D. N. Jamieson, Phys. Rev., **B60** (1999)

[16] J. L. den Besten, D. N. Jamieson and L. J. Allen, to be published in Nucl. Instr. Meth. **B**.

[17] P. G. Spizzirri, J. L. den Besten and D. N. Jamieson, presented at the 11th AINSE Nuclear Techniques of Analysis Conference and the 6th Vacuum Society of Australia Congress, (1999)

Recent developments in ion-assisted deposition techniques for multilayer optical thin films

Svetlana Dligatch, Roger P. Netterfield and David J. Drage

CSIRO Telecommunications and Industrial Physics, PO Box 218, Lindfield, NSW 2070, Australia
Tel: +61-2-94137000 Fax: +61-2-94137200,
svetlana.dligatch@tip.csiro.au, roger@tip.csiro.au, davidd@tip.csiro.au

Introduction

Ion Assisted Deposition (IAD) has become a well-established technique in the manufacture of high quality optical coatings. It has been demonstrated that IAD surpasses conventional Physical Vapour Deposition on a number of points. Ion bombardment during film deposition permits intrinsic stress modification, improves adhesion and durability, reduces porosity and hence moisture adsorption and vacuum-to-air shifts of the films. It allows production of multi-layer optical components with low absorption and stable refractive index (1-3).

Extensive work on the development of this technique has been carried out at CSIRO Telecommunications and Industrial Physics over the last two decades (4-6). A variety of optical components including edge, band pass, notch and laser filters, anti-reflection coatings, enhanced mirrors, beamsplitters and polarisers has been successfully manufactured. All these product types require high level control of the numerous deposition parameters in order to achieve reproducibility and uniformity of the films. In the last two years significant improvements have been made in IAD and in film deposition control which allow accurate manufacture of optical thin film designs with a very demanding performance specification.

Deposition System

Our deposition system is equipped with a conventional oil diffusion pumping system. Base pressures of ~10^{-6} Pa (rising to a 10^{-2} Pa during deposition) are reached after a low temperature bake-out.

The system is equipped with two types of evaporation source. Material is evaporated either from an electron beam evaporator or from a thermal evaporation source. The substrates are mounted in a rotating workplate 400 mm above the source and are bombarded with a beam of ions produced by a gridless end-Hall ion source. A rotating shutter is used to ensure thickness uniformity of film across the workplate.

The optical properties of the growing film can be monitored in-situ by a spectrophotometer and/or ellipsometer. Ellipsometric monitoring is carried out at an angle of incidence of 70° at a single wavelength and measures relative polarisation state, hence is independent of drift. It allows the calculation of the refractive index and thickness of the film and this information can be used to adjust deposition conditions or to re-optimise coating design if necessary (7). Other advantages of ellipsometry are high thickness sensitivity and no dead zones at turning points. It can also be used to control deposition rate.

Dispersion of refractive index for all materials is measured ex-situ using a spectroscopic ellipsometer and obtained values are used in optical design calculation.

Some examples of manufactured optical components

Over the years a wide range of optical components had been produced at CSIRO using ion-assisted deposition. Several examples presented below give some indication of our design and production capabilities.

Some of the multi-layer coatings are quite complicated and become feasible with the development of advanced computer programs. These programs have been developed to the stage where they are capable of producing optical thin film designs of 100 layers or more to meet the most demanding performance specification. A measured result of such a design is the edge filter shown in Fig. 1. with high transmittance in visible range and blocked NIR region.

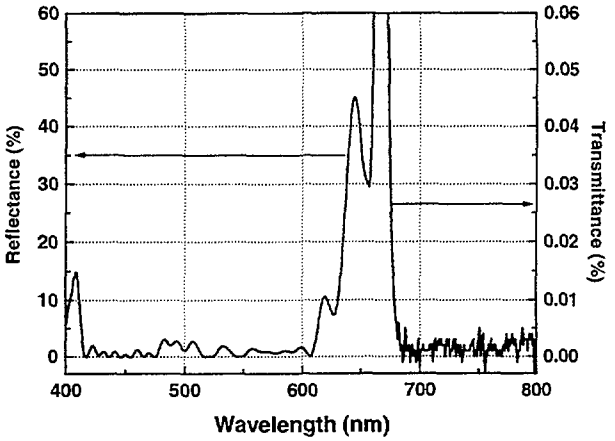

Figure 1. Edge filter Measured reflectance of 50- layer edge filter.

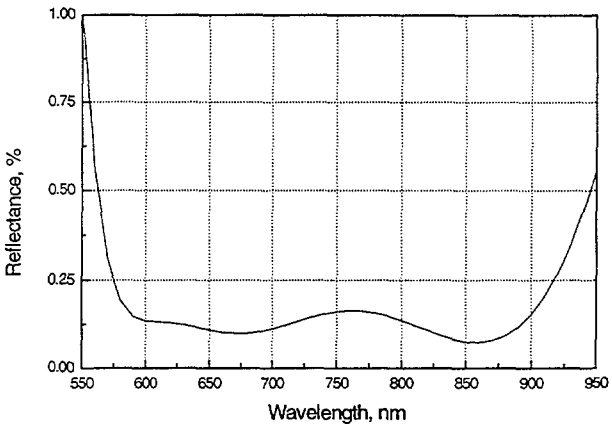

Figure 2. 4- layer anti-reflection coating

This is a 50-layer design of alternating high and low refractive index materials where the difference in optical thickness between successive layers of each material is mostly very small ie. within 2%. Therefore, to reproduce this design requires close control of the deposition conditions (deposition rate, ion bombardment, gas pressure) and accurate monitoring of the optical thickness of the growing film. The latter is achieved with ellipsometric monitoring which gives control of thickness and refractive index deviation within 1% of a target design.

An example of anti-reflection coating for the 600 to 900nm wavelength range is presented in Figure 2. Coating consists of 4 alternating layers of TiO_2 and SiO_2 and reduces reflection to 0.2%. For a two layer single wavelength filter the best result we have achieved so far is 0.01%.

Optical design of the colour corrected 532nm notch filter with blocked IR region is much more complicated and requires 60 layers of alternating high and low refractive index material. The optical transmittance of this filter is illustrated in Figure 3.
Figure 4. shows transmittance (T) and reflectance for illumination from the either side of a substrate (R and R') of a coating developed at CTIP for use in the LIGO project to measure the figure of optical components having reflectance from 100% to 3.5% at 1064nm.(8) The spatial variations across the working aperture in physical thickness of the two materials used to coat the reference surface were determined to an accuracy better than 1nm using a single wavelength ellipsometer operating at 633nm. Variations across the aperture of the phase changes on reflection from both sides of the substrate and on transmission were estimated. Plate distortion due to stress in the coatings has also been measured.

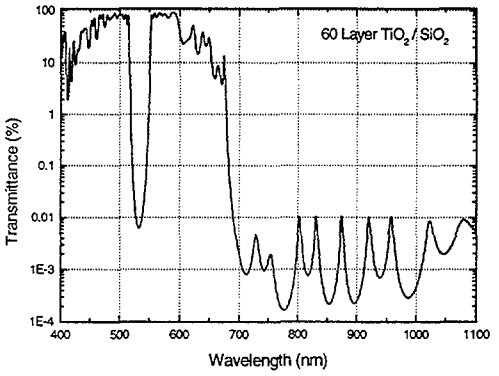

Figure 3. 60- layer 532nm notch plus IR blocker colour corrected filter

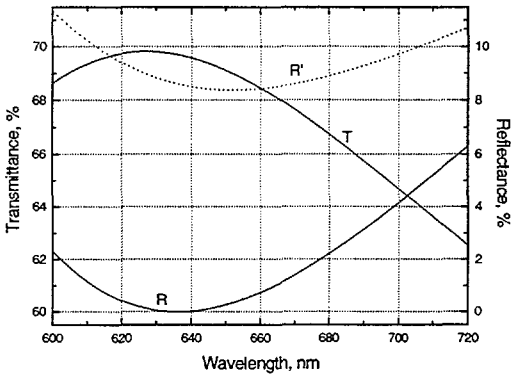

Figure 4. Transmittance and Reflectance of the Clapham-Dew coating

Fizeau interferometers have long been used to determine the surface figure of uncoated optics. Collimated monochromatic light is directed towards a pair matching surfaces which are mounted parallel to one another and normal to the beam and the resulting interfering (essentially two beam) fringes are viewed in reflection. Since the reflectances from the two surfaces are equal (and approximately 4% for glass) the intensity of the fringe minimum is zero so the fringe contrast is unity. If the same reference surface is used to measure the figure of a higher reflecting (coated) surface the fringe minimum intensity is no longer zero and the fringe contrast decreases, eventually reaching zero for 100% reflecting optics.

Clapham and Dew(9) described a solution whereby the reference surface was coated with a lossy reflecting surface (consisting of dielectric and absorbing films) having a transmittance T of 0.35, a reflectance at the glass-film interface R' of 0.10 and at the air-film interface R of 0.05. Good contrast fringes were obtained for measurements of an aluminised test flat, as well as giving reasonable fringe contrast for uncoated glass surfaces. A similar requirement has occurred in the Laser Interferometer Gravitational-wave Observatory (LIGO) project where the surface figure of all the optical surfaces from essentially 100% reflecting to uncoated must be critically evaluated. So that the reference surface can be fully characterised, it is essential that the variation in physical thickness of the coating across the working aperture is known to an accuracy better than 1nm. Variations across the aperture of the phase changes on reflection from both sides of the substrate and on transmission are estimated.

Further Improvements

In spite of significant increase in our production and design capabilities there is still room for improvement, and there are a number of technical challenges. This type of deposition is very labour intensive and requires complex fixturing and monitoring and regular system maintenance. Our next goal is computer automation of the deposition process and improved monitoring, control and adjustment, thickness verification and design re-optimisation. This will allow us to maintain more consistent deposition rate and improve repeatability.

Introduction of multi-wavelength ellipsometric monitoring in combination with spectroscopic photometry will also improve system capabilities.

Conclusions

With the effort and time that has been spent on the development of the IAD technology and characterisation of the process parameters our ability to produce increasingly more difficult optical designs has advanced significantly. However, some amount of work is still necessary to obtain fully predictable system performance and reproducibility

References

[1] J.J Cuomo, J.M.E. Harper, C.R. Guarnieri, D.S. Yee, L.J. Atanasio, J. Angilello C.T. Wu, and R. H. Hammond, *J. Vac. Sci. Technol.* **20**, 349 (1987).

[2] F.A. Schmidt, "Use of ion beam assisted deposition to modify the microstructure and properties of thin films", *Int. Mater. Rev.*, 35 (1990) 61-128.

[3] M.L. Fulton, "Application of ion-assisted –deposition using a gridless end-Hall ion source for volume manufacturing of thin-film optical filters," in *Optical Interference Coatings,* ed. F. Abeles, Proc. SPIE 2253, (1994) 374-393.

[4] R.P. Netterfield, "Ion-assisted processes in optical thin film deposition", Proc. SPIE 678, Optical Thin Films II: New Developments, (1986), pp. 14-23.

[5] R.P. Netterfield, P.J. Martin, C.G. Pacey, W.G. Sainty, D.R. McKenzie and G. Auchterlonie,."Ion assisted deposition of mixed TiO_2-SiO_2 films", *J. Appl. Phys.* 66 (4), 1989, pp. 1805-1809.

[6] P.J. Martin and R.P. Netterfield, "Optimisation of deposition parameters in ion-assisted deposition of optical thin films", *Thin Solid Films,* 199, (1991), pp. 351-358.

[7] D.J. Drage and R.P. Netterfield, "In-situ ellipsometric monitoring of a dielectric multilayer edge filter ", Optical Interference Coatings Tech. Digest Series Vol. 9, Tucson, pp430-432, (June 1998).

[8] R.P. Netterfield, D.J. Drage, C.H. Freund, C.J. Walsh, A.J. Leistner, J.A. Seckold and B.F. Oreb, "Coating requirements for the reference flat ot a Fizeau interferometer used for mesuring from uncoated to highly reflecting surfaces," Proc. SPIE 3738, (1999) pp. 128-135.

[9] P.B. Clapham, and G. D. Dew, "Surface-coated reference flats for testing fully aluminized surfaces by means of the Fizeau interferometer", *J. Sci. Instrum.* 44, pp. 899-902, (1967).

Effect of annealing on nonlinear optical properties of Ge nanocrystals in fused silica

A. Dowd[a], M. Samoc[b], R. G. Elliman[a]

[a]Electronic Materials Engineering Department, and [b]Laser Physics Centre,
Research School of Physical Sciences and Engineering, Australian National University Canberra ACT 0200

Introduction

The novel optical properties of glasses containing a suspension of semiconducting or metallic nanocrystals have resulted in them being the subject of considerable attention over the past few years. Such materials exhibit a large optical nonlinearity with a rapid response, which makes them potential candidates for new technologies based around optical signal processing[1-3]. Several techniques exist to synthesise the nanocrystals such as co-sputtering[4,5], chemical vapour deposition[6], sol-gel synthesis[7] and ion implantation[8,9]. The latter technique offers the advantages of a very flexible process, no restriction to any particular impurity and the possibility to produce high volume fractions of nanocrystals.

Glasses containing metallic nanocrystals have been widely studied. The local field enhancement reaches a maximum at the surface plasmon resonance at which wavelength the samples exhibit resonant absorption and an enhancement of the third order optical nonlinearity[7,10-12]. The increase in absorption is however undesirable for practical materials[13]. Semiconductor systems show much reduced absorption and nonlinearities of the same order of magnitude as the metal systems[14-17]. In this case however the material response is less well understood.

Experimental

Substrates were 1mm thick fused silica plates. These were implanted with 1.0MeV Ge or 400keV Si ions to a dose of 3×10^{17}cm^{-2} at 77K. The mean projected range of the ions was ~ 0.6μm, the FWHM of the distribution was ~ 0.5μm and the peak concentration was less than 10 at. % as determined by Rutherford backscattering measurements. Subsequent annealing was performed at 1100°C with a forming gas (95% N_2 and 5% H_2) ambient for 60 minutes. The size distribution of the Ge nanocrystals was determined using transmission electron microscopy (TEM) on a Philips CM 300 operating at 300keV. Cross sectional samples for TEM were prepared by mechanical polishing, dimpling and ion milling.

Optical nonlinearity measurements were undertaken with time resolved degenerate four wave mixing (DFWM) using the forward scattering geometry[13]. The samples were characterised using laser pulses at a wavelength of 800nm, a pulse duration of 600 fs and a repetition rate of 30Hz. The laser beams were focused which resulted in a spot size about 3×10^{-4}cm^2 and a peak light intensity of 300GW cm^{-2}. The nonlinear refractive index of the implanted layer $|n_2^{layer}|$ was calculated using the following equation:

$$\left|n_2^{layer}\right|^2 = \left|n_2^{silica}\right|^2 \left(\frac{I_{npm}}{I_{pm}}\right)\left(\frac{L^{silica}}{L^{layer}}\right)^2 \qquad (1)$$

$|n_2^{silica}|$ is the nonlinear refractive index of silica (= 3×10^{-16}cm^{2}W^{-1}), I_{npm} is the measured non phase matched DFWM signal dominated by the contribution from the implanted layer, I_{pm} is the phase matched signal dominated by the contribution from the silica substrate, L^{layer} is the effective sampling length for the implanted layer taken to be the FWHM of the highest dose

distribution and L^{silica} is the effective sampling length in the silica substrate, which was experimentally determined to be 700 μm.

Results and Discussion

Using TEM imaging, no nanocrystals are observed in the samples before heat treatment. After annealing at high temperature, nanocrystals can be easily seen at the depth of the projected range. The nanocrystals are single crystal and approximately spherical. The nanocrystals range in diameter from 2.0nm to 6.0nm with an average diameter of 3.0nm. A high-resolution bright field image of a Ge nanocrystal in the annealed sample is shown in figure 1. One can clearly see the lattice fringes corresponding to the {111} planes of the Ge crystal with the usual bulk diamond structure.

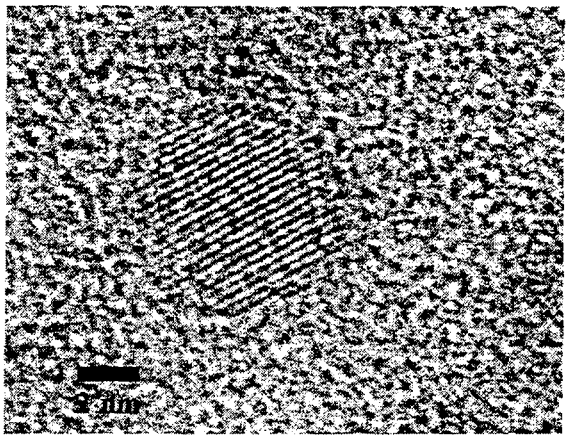

Figure 1 TEM micrograph of single Ge nanocrystal in silica showing fringes corresponding to {111} lattice planes.

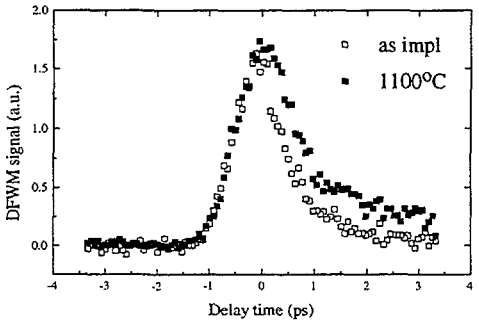

Figure 2 DFWM data for a sample implanted with $3x10^{17}Ge.cm^{-2}$ before annealing (open squares) and after annealing at 1100°C (solid squares).

Figure 2 shows the time resolved DFWM signals for a sample implanted with $3x10^{17}Ge.cm^{-2}$ as implanted and after annealing at 1100°C with an incident light intensity of 9μJ. The nonlinear refractive index ($|n_2|$) of each sample is calculated at the maximum peak height using equation (1). The magnitude of the nonlinear refractive index measured in both cases is large, and the nonlinearity of the as implanted sample ($|n_2| = 5.2x10^{-13}cm^2W^{-1}$) is within experimental error the same as the nonlinearity of the annealed sample ($|n_2| = 5.2x10^{-13}cm^2W^{-1}$). The nonlinear response of the samples shows a rapid relaxation both before and after annealing. Analysis of this temporal response determined by fitting the curves assuming a $sech^2$ laser pulse showed for both samples an instantaneous response ($\tau < 100fs$) and a delayed response ($\tau \sim 3ps$).

If interband transitions within the nanocrystals were responsible for the nonlinear response of the Ge implanted silica, one would expect a large difference in the magnitude of $|n_2|$ between the two systems. Quantum confinement theory predicts among other things an increase of the energy gap of semiconductors as the size decreases. According to an effective mass calculation[18] the largest Ge nanocrystals in the annealed sample (d = 6nm) should have an

energy gap of 1.4eV, and as such it should be possible to excite interband transitions in these nanocrystals with the 1.55eV photons used in the DFWM experiment. On the other hand, nanocrystals if they exist in the as implanted sample would be of such a size that the energy gap would far exceed 1.55eV. The fact that we do not observe a significant difference in the nonlinearity before and after annealing excludes interband transitions as the dominant mechanism responsible for the large optical nonlinearity.

Defects may contribute to the nonlinear response of semiconductor nanocrystals by providing alternative channels for carrier excitation and relaxation. This is consistent with the fast relaxation times observed. Carrier lifetimes in pure bulk Ge and Si are in the μs range, however the presence of defects can significantly reduce the lifetimes to the ps range[19]. Therefore the fast relaxation time measured by DFWM could be another indication of defect-mediated recombination.

Defects in silica caused by ion implantation are known to be annealed out by 500°C[20,21]. Since these samples are annealed at 1100°C we can assume that these defects will be present in the as implanted sample but not in the annealed sample. Therefore the similar nonlinear refractive index of the two Ge implanted samples is unlikely to be due to defects in the bulk silica.

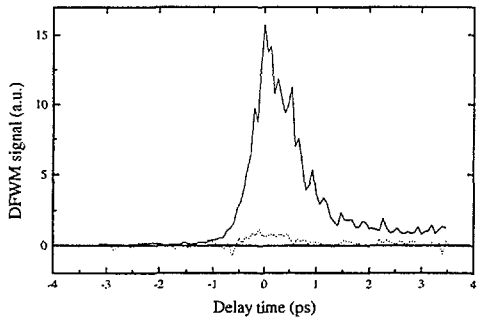

Figure 3 DFWM signal for sample implanted with Ge (solid line) and Si (dotted line).

It is interesting to compare the response of Ge implanted silica with other group IV semiconductor systems. Figure 3 compares the DFWM signals (incident intensity = 15μJ) of samples implanted with Ge or Si ions to a fluence of $3\times10^{17}cm^{-2}$ and subsequently annealed. The nonlinearities are $|n_2| = 6.5\times10^{-13}$ and $2.6\times10^{-13}cm^2W^{-1}$ for Ge and Si samples respectively. Clearly the response of the Si implanted sample is small compared to that of the Ge implanted sample. We believe therefore that the defects are somehow associated with the presence of Ge.

Conclusions

The nonlinear optical properties of silica ion implanted with Ge before and after annealing were examined. The magnitude of the nonlinear refractive index $|n_2|$ of the as implanted sample was found to be large and of the same order as the annealed sample. The relaxation time constant of the nonlinearity was also the same in both cases. The magnitude of the nonlinearity of silica implanted with Si is ~ 3 times lower than the nonlinearity of silica implanted with Ge. We propose that the large nonlinearity observed may be a consequence of Ge related defect-mediated recombination of photoexcited carriers.

References

[1] Y. Maeda *et al.*, Appl. Phys. Lett. **59,** 3168-70 (1991).

[2] T. Matsumoto *et al.*, Jpn. J. Appl. Phys. 2 **33,** L 35-L 36 (1994).

[3] F. Z. Henari *et al.*, Appl. Phys. Lett. **67,** 323-325 (1995).

[4] S. Takeoka, M. Fujii, S. Hayashi and K. Yamamoto, Phys. Rev. B **58,** 7921-7925 (1998).

[5] W. K. Choi *et al.*, J. Appl. Phys. **86,** 1398 (1999).

[6] H. Kumomi and F. G. Shi, Phys. Rev. Lett. **82,** 2717 (1999).

[7] M. Y. Lee, T. S. Kim and Y. S. Choi, Journal of Non-Crystalline Solids **211,** 143-149 (1997).

[8] Y. Kanemitsu, H. Tanaka, K. S. M. T. Kushida and H. A. Atwater, J. Appl. Phys. **86,** 1762 (1999).

[9] S. Guha, M. D. Pace, D. N. Dunn and I. L. Singer, Appl. Phys. Lett. **70,** 1207-1209 (1997).

[10] D. Ricard, P. Roussignol and C. Flytzanis, Opt. Lett. **10,** 511-513 (1985).

[11] W. Schrof *et al.*, Advanced Materials **3,** 338-341 (1998).

[12] J. M. Ballesteros, J. Solis, R. Serna and C. N. Alfonso, Appl. Phys. Lett. **74,** 2791 (1999).

[13] M. Samoc *et al.*, J. Opt. Soc. Am. B **15,** 817-825 (1998).

[14] R. G. Elliman, B. Luther-Davies, M. Samoc and A. Dowd, Mater. Res. Symp. Proc. **438**, 423 (1997)

[15] S. Vijayalakshmi, M. A. George and H. Grebel, Appl. Phys. Lett. **70,** 708-710 (1997).

[16] E. Vanagas *et al.*, J. Appl. Phys. **81,** 3586-3591 (1997).

[17] A. Dowd, R. G. Elliman, M. Samoc and B. Luther-Davies, Appl. Phys. Lett. **74,** 239-241 (1999).

[18] T. Takagahara and K. Takeda, Phys. Rev. B **46,** 15 578-81 (1992).

[19] A. Chin, K. Y. Lee, B. C. Lin and S. Horng, Appl. Phys. Lett. **69,** 653-655 (1996).

[20] A. Polman, J. Appl. Phys. **82,** 1 (1997).

[21] S. Guha, J. Appl. Phys. **84,** 5210-5217 (1998).

The use of RBS technique in characterising RF-magnetron sputtered perovskite films

H.V.Duong, D.K. Sood, P.K. Srivastava* and S.P.S.Badwal*

Department of Communication and Electronic Engineering, RMIT University, Melbourne 3000
* Ceramic Fuel Cells Limited, 170 Browns Road, Noble Park 3174

Introduction

Solid Oxide Fuel Cell (SOFC) is an alternative method for electricity generation by electrochemical means. The materials used in the interconnect component of a fuel cell stack must meet stringent requirements. Some perovskites such as $La_{1-x}Ca_xCrO_3$ (LCC) have been used as the interconnect in SOFC, however it high costs have made it economically unsuitable for commercial use. A possible alternative material is stainless steel. The main weakness in this material is that it rapidly corrodes in air at the high operating temperatures required for SOFC. Furthermore, a number of studies[1,2,3] have found that chromia forming alloy when used as an interconnect released chromium-oxide gaseous species which caused severe degradation of the fuel cell. Therefore, a ceramic protecting layer on the alloy could help to minimise or prevent this effect.

Sputtering deposition of perovskite materials on an alloy have not been reported in literature, however, spray-painted of $La_{1-x}Sr_xCrO_3$ on a chromium forming alloy had been carried out[4] but with limited success in minimising the corrosion of the alloy at high temperatures. In this work, a RF-magnetron sputtering technique was used to deposit different thicknesses of LCC on silicon and on stainless steel substrates at various deposition parameters. Rutherford Backscattered Spectroscopy (RBS) and the RUMP program was then used to characterise the deposited films.

Experimental

The target used in the sputtering of LCC on the substrate had the composition of $La_{0.85}Ca_{0.15}CrO_3$ with 99.9% purity. The composition of the steel substrate was 71wt% Fe and 27wt%Cr. Si(100) substrates were also used to facilitate RBS analysis. Prior to deposition, the steel was polished to 1200 SiC grade paper and was then polished again to mirror finish using 0.3μm alumina suspension. Sputtering parameters for the deposition of the LCC on the substrates are shown in Table 1 below. RBS analyses of the films were carried out using 2MeV $^4He^{++}$ ions beam at a scattering angle of 169°.

Results and Discussion

Sample no./substrate	Power W	Ar:O_2 ratio	Substrate temperature °C	Deposition time min/h	Film thickness μm	Film composition
LCC27/Si	200	2:1	600	10 min	0.06	$La_{0.85}Ca_{0.15}CrO_3$
LCC28/Si	300	2:1	room temp.	9 min	0.10	$La_{0.64}Ca_{0.15}Cr_{0.75}O_3$
LCC34/steel	200	2:1	800	4 h	1.6	$La_{0.85}Ca_{0.15}CrO_3$
LCC36/steel	200	2:1	800	8 h	>2.6	$La_{0.85}Ca_{0.15}CrO_3$

Table 1 Deposition parameters and characteristics of the films deposited on the silicon and the steel substrates

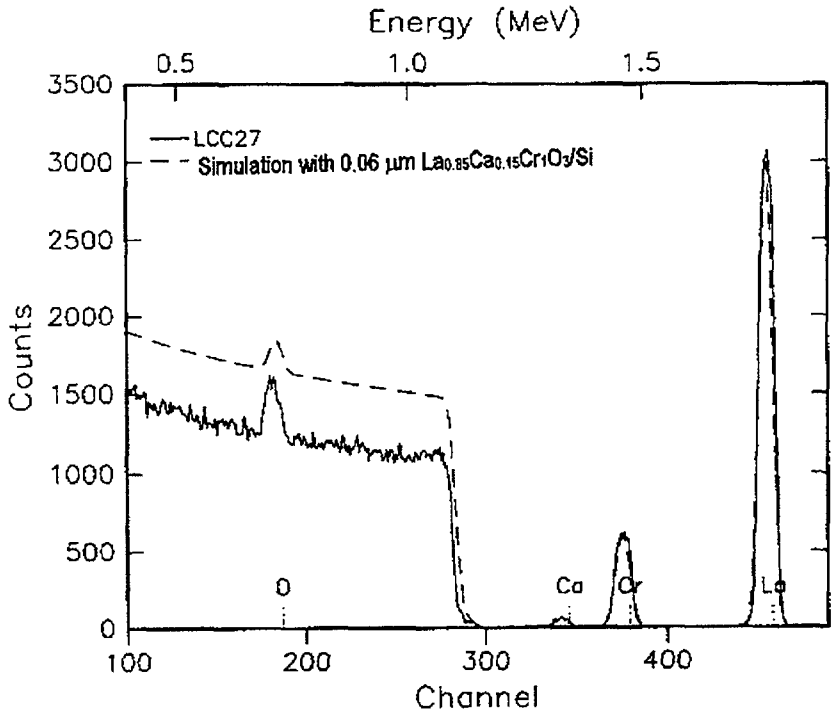

Figure 1. RBS and simulated spectra of the LCC27 sample

Figure 1 shows the presence of La, Cr, Ca and O on the film at energy level of 1.78, 1.47, 1.34 and 0.73MeV respectively. The silicon substrate energy edge is at 1.13MeV. Simulated RBS spectrum of the film gave closest fit when the thickness of the film was 0.06μm as shown in Table 1 with a composition of $La_{0.85}Ca_{0.15}CrO_3$. This had the same composition as the target LCC. The simulated region for the substrate portion of the spectrum was higher than the experimental spectrum. This was due to channelling effect in the single crystal silicon substrate.

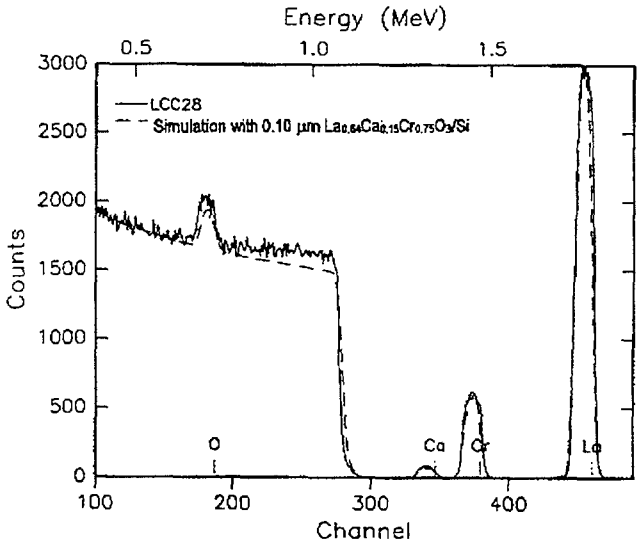

Figure 2. RBS and simulated spectra of the LCC28 sample

Figure 2 shows a similar RBS spectrum as in Figure 1 although the simulated spectrum gave the composition of the film to be $La_{0.64}Ca_{0.15}Cr_{0.75}O_3$ with film thickness of 0.1μm. This showed that temperature of deposition had a significant effect on the composition and thickness of the film produced.

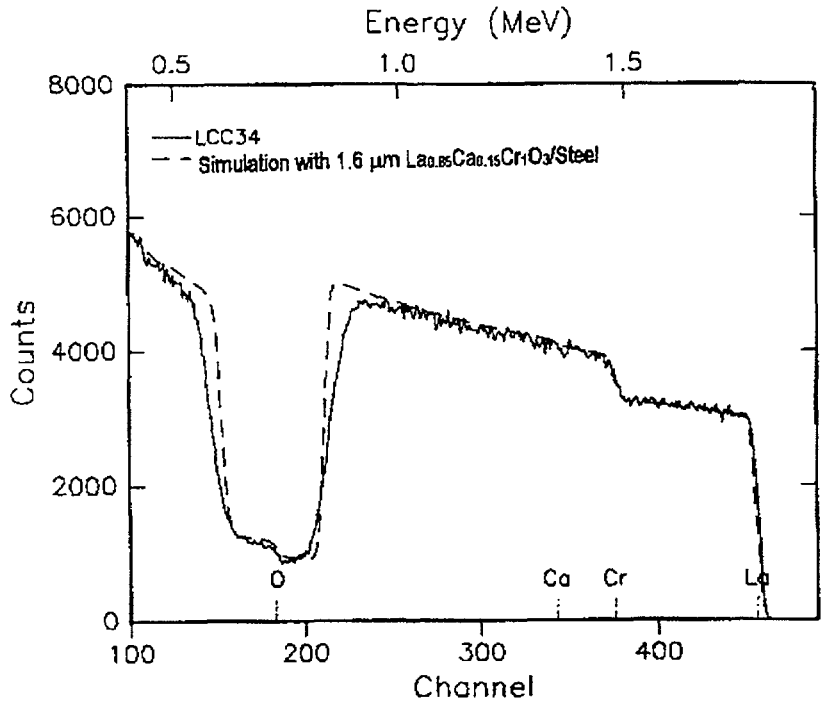

Figure 3 RBS and simulated spectra of the LCC34 sample

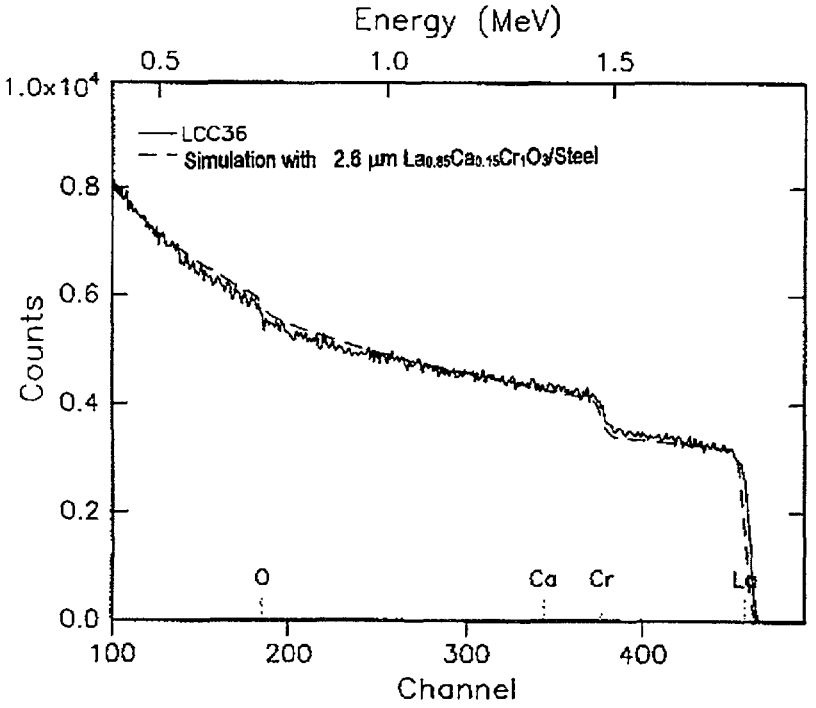

Figure 4 RBS and simulated spectra of the LCC36 sample

Figures 3 and 4 show spectra of LCC deposited on the steel substrate which were at different conditions to the films deposited on the silicon substrate. The simulated RBS spectra of the films fit closely with the experimental spectra giving the thickness of the film to be 1.6μm and >2.6μm for the 4h and 8h deposition respectively. An accurate thickness of the 8h deposited film could not be determined since the simulated spectrum was no longer sensitive to thick films. Both films have the same composition as the target.

Conclusion

The LCC films that were deposited on the silicon and the steel substrates were found to be stoichiometric and have the same composition as the target. On the other hand, deposition at room temperature produced a nonstoichiometric film. The thickness of the LCC films was strongly dependent on deposition time. Deposition power and the type of substrate used were not found to effect the chemical composition of the films produced with respect to the target. These RBS results were very crucial in optimising the deposition conditions to obtain proper stoichiometry and thickness of LCC required for use in SOFC applications.

Acknowledgments

Thanks to Mr Rhys Hildebrandt for preparing the steel substrates. This work was supported by AINSE and ARC grants.

References

[1] Linderoth S., Hendriksen P. V., Mogensen M., and Langvad N., *Journal of Materials Science*, **31**(1996), 5077-5082.

[2] Quakdakkers W. J., Greiner H., Hansel M., Pattanaik A., Khanna, A. S. and Mallener W., *Solid State Ionics*, **91**(1996), 55-67.

[3] Badwal S.P.S., Deller R., Foger K., Ramprahash Y., and Zhang J. P., *Solid State Ionics*, **99**(1997), 297-310.

[4] Linderoth S., *Surface Coating Technology*, **80**(1-2)(1996), 185-189.

Simultaneous hydrogen detection with an ERD gas ionization detector

R.G. Elliman[a], H. Timmers[a,b], T.R. Ophel[b], T.D.M. Weijers[a,b], L.S. Wielunski[c] and G.L. Harding[c]

Departments of [a]Electronic Materials Engineering and [b]Nuclear Physics, Research School of Physical Sciences and Engineering, Australian National University, Canberra, Australia

[c]CSIRO, Telecommunications and Industrial Physics, Lindfield, Australia

1. Introduction

The use of high-energy heavy primary ions increases the range of elements that can be detected in an elastic-recoil detection (ERD) experiment and provides improved detection sensitivity and depth resolution[1-5]. Large solid-angle position-sensitive gas ionization detectors are well suited to the detection of heavy recoils but recoiled protons are generally detected with an additional surface barrier detector. This study examines the possibility of simultaneously detecting protons and heavy-ions with a gas ionisation detector.

2. Experimental Details

Heavy-ion ERD experiments were conducted at the Australian National University 14 UD tandem accelerator facility using the 2m scattering chamber[6]. Recoiled ions were detected with a novel gas ionization detector described elsewhere[7,8]. The detector incorporates a segmented anode that consists of two ΔE electrodes and a residual energy (Eres) electrode. The second of the ΔE electrodes is further partitioned to provide position information in the scattering plane which is used to correct the kinematic energy spread of ions entering the detector. A grid electrode is incorporated between the Frisch grid and the anode to provide an independent total energy signal. The detector was operated with a flowing propane ambient and a 0.5μm thick Mylar entrance window. A symmetrical scattering geometry was employed in both cases with a scattering angle of 45°.

Two modes of operation were explored for hydrogen detection. A transmission mode in which the energy loss of the protons was detected as they passed through the detector, and a stopped mode in which the protons were stopped within the gas detector. In transmission mode, 214 and 241MeV Au ions were used to analyze Ge- and Sn-doped silica films deposited on a silicon substrate. The layers varied in thickness from 900nm to ≥ 1700nm. The propane pressure in the detector was 70 mbar. To illustrate the stopped mode, 140MeV Au ions were used to analyze an Al bilayer containing thin hydrogenated amorphous carbon (H:C) layers at the surface and at a depth of 470nm. This sample was fabricated by depositing a 495nm Al layer (containing 3.2% Zn) onto a Si substrate, followed by a 60nm H:C layer, a second 470nm Al layer (containing 2.4% Zn), and finally a 40nm H:C surface layer. The propane pressure in the detector was 100 mbar.

For comparison with the heavy-ion measurements, conventional ERD analysis was performed on the Al bilayer sample using 4.6MeV He ions and a surface barrier detector located at a scattering angle of 30°. Scattering was symmetrical, with the incident and exit beams inclined at 15° to the sample surface. A 25 μm thick Mylar stopping foil was used to exclude scattered primary ions.

3. Results and Discussion

3.1 Transmission Mode

Figure 1 shows results for the transmission mode measurement. Sn, Si and O recoils from the doped silica film are readily resolved in the two-dimensional (ΔE vs Energy) spectrum. The inset plot shows the energy-loss for hydrogen obtained from the Eres and Grid electrodes and amplified with high gain. Hydrogen is confined to the doped silica film and the total hydrogen content can be directly determined from these data. Information about the hydrogen depth distribution can also be deduced.

Figure 2 shows a Eres spectrum for protons extracted from the inset in Figure 1. This can be converted to a depth profile from knowledge of the detector geometry and stopping powers. This can be simplified by measuring the response of the detector to a known hydrogen distribution. Figure 2 shows such a response function obtained using a Kapton sample with a uniform hydrogen content. Dividing the thin film spectrum by the response function effectively normalizes the energy loss spectrum, accounting for geometric effects and energy loss in the detector. The depth scale can then be calculated directly from knowledge of energy losses in the sample. This is illustrated by the black circles on the response curve, the separation of which corresponds to equal depth increments of ~280nm in SiO_2. The sampling depth is ~2.5μm.

3.2 Stopped Mode

A measurement of an Al bilayer sample, in which the recoiled protons were fully stopped in the detector, is shown in Figure 3. In this case the experimental conditions are not ideal for detection of heavier elements. Despite this, the two dimensional (ΔE_1 versus ΔE_2) spectrum enables the distinction of the lighter elements such as C, N and O, highlighting the advantage of the initial ΔE_1 electrode. These measurements employed a rectangular aperture (15mm x 5mm) in front of the detector to reduce the kinematic energy spread of the detected protons.

The inset in Figure 3 shows the hydrogen signal derived from the Eres and Grid electrodes after amplification with high gain. The two hydrogenated layers are clearly evident in this projection and energy spectra can be directly extracted by projecting the data onto the Eres or Grid axes, with the former having better resolution. In both cases the measurement is analogous to that of a surface barrier detector with a stopping foil. The proton energies detected by the Eres electrode fall in the range 900keV to 1.4MeV, corresponding to a probing depth of ~1.2 μm for films composed of low atomic number elements, such as SiO_2 or Al. This sampling depth is considerably less than that for transmission mode measurements.

Figure 4 compares the Eres spectrum for protons from the inset of Figure 3, with that measured for the same sample using conventional He ERD analysis with 4.6MeV He primary ions. For the ionization detector, the FWHM of the surface peak is 64keV and that of the second peak is 148keV. For the surface barrier detector the corresponding values are 50keV and 104keV, respectively. Thus the energy (depth) resolution is comparable for the two detection methods under the conditions employed. However, the actual resolution [Energy width of the surface peak divided by the maximum recoil energy of the protons] is better for the He-ERD due to the higher hydrogen recoil energy in this case, 2.6MeV compared to 1.4MeV with Au at 140MeV as a primary ion.

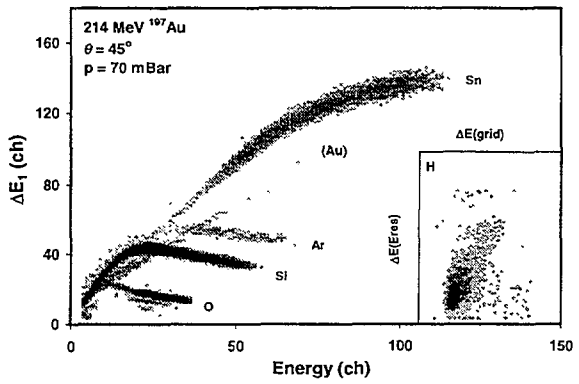

Figure 1: Two-dimensional projection of the ΔE_1 (energy loss) and Grid (total energy) signals measured for a Sn-doped silica film on a Si substrate. The inset shows the H signal detected in transmission mode using the Eres and Grid electrodes.

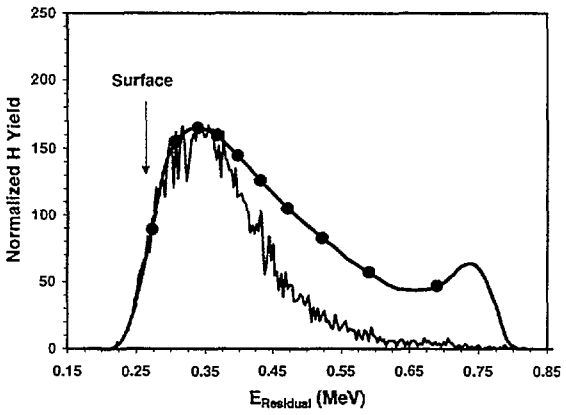

Figure 2: Eres spectrum extracted from the inset in Figure 1 together with a response function of the electrode for H (thick line). The circles on the response function indicate equal thickness (

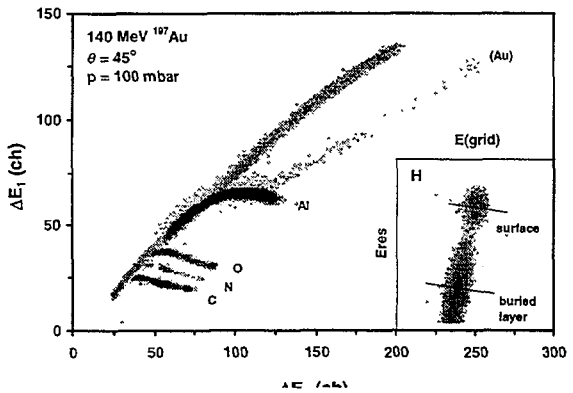

Figure 3: Tw o-dimensional projection of the ΔE_1 and ΔE_2 signals measured for an Al bilayer sample. The inset shows proton events detected using highly amplified Eres and Grid signals.

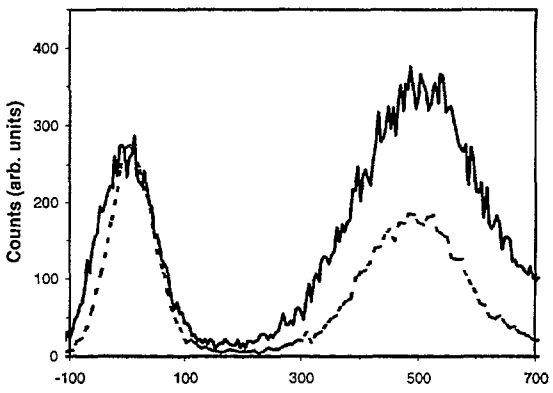

Figure 4: H distribution obtained for the Al bilayer sample. Residual energy spectrum (Eres) extracted from the inset in Figure 3 (solid) and that measured with He-ERD (dashed). Note that the relative heights of the two peaks are different for the two measurements because they have not been corrected for variations in scattering cross-section or stopping power.

The results presented in Figure 4 illustrate that a gas-ionization detector can be used to measure hydrogen distributions with a depth resolution comparable to that attainable with conventional He-ERD during simultaneous analysis of heavier recoils. No attempt has been made to optimize the depth resolution of the hydrogen measurement in either case since such optimization depends on the sample, and in the heavy ion case, on what other information is required.

4. Conclusions

It has been shown that gas-ionization detectors can be used for the simultaneous detection of hydrogen during heavy ion recoil analysis. Two modes of operation were demonstrated: a) a *transmission mode*, where the experimental conditions were optimized for heavy-ion detection and hydrogen was detected from an energy-loss signal, and b) a *stopped mode*, where protons were fully stopped within the detector and their energy determined from a residual energy signal. Both modes were shown to be suitable for measuring the total hydrogen content of thin films. The transmission mode provides greater analysis depth whilst the stopped mode provides superior depth resolution. Both modes enable simultaneous detection of heavier recoils.

5. References

1 W. Assmann, P. Hartung, H. Huber, P. Staat, H. Steffens, and C. Steinhausen, Nucl. Instr.Meth. B85 (1994) 726-731

2 W. Assmann, J. A. Davies, G. Dollinger, J. S. Forster, H. Huber, T. Reichelt, and R. Siegele, Nucl. Instr. Meth. B118 (1996) 242-250

3 J. S. Forster, P. J. Currie, J. A. Davies, R. Siegele, S. G. Wallace, and D. Zelenitsky, Nucl. Instr. Meth. B113 (1996) 308-311

4 J. A. Davies, J. S. Forster, and S. R. Walker, Nucl. Instr. Meth. B139 (1998) 120-127

5 J. A. Davies, J. S. Forster, and S. R. Walker, Nucl. Instr. Meth. B138 (1998) 594-602

6 H. Timmers, R. G. Elliman, G. R. Palmer, T. R. Ophel, and D. J. O'Connor, Nucl. Instr. Meth. B138 (1998) 611-615

7 H. Timmers, T. R. Ophel, and R. G. Elliman, Nucl. Instr. and Meth. A (In Press) (1999)

8 H. Timmers, T. R. Ophel, and R. G. Elliman, Proceedings of the 14th Ion Beam Analysis Conference, Nucl. Instr. Meth. (In Press) (1999).

Structure and low temperature thermal relaxation of amorphized germanium.

C.J. Glover[1], M.C. Ridgway[1], A.P. Byrne[1], K.M Yu[2], G.J. Foran[3], C. Clerc[4], J.L Hansen[5] and A. Nylandsted Larsen[5]

1 Research School of Physical Sciences and Engineering, Australian National University, Canberra, ACT 0200 Australia; 2 Materials Science Division, Lawrence Berkeley National Laboratory, Berkeley, USA; 3 Australian Nuclear Science and Technology Organisation, Menai, Australia; 4 Centre National de Recherche Scientifique, Orsay, France; 5 Institute of Physics and Astronomy, Aarhus University, Aarhus, Denmark

The structure of implantation-induced damage in amorphized Ge has been investigated using high resolution extended x-ray absorption fine structure spectroscopy (EXAFS). EXAFS data analysis was performed with the Cumulant Method, allowing a full reconstruction of the inter-atomic distance distribution (RDF). For the case of MeV implantation at –196 °C, for an ion-dose range extending two orders of magnitude beyond that required for amorphization, a dose-dependent asymmetric RDF was determined for the amorphous phase including an increase in bond-length as a function of ion dose. Low-temperature thermal annealing resulted in structural relaxation of the amorphous phase as evidenced by a reduction in the centroid, asymmetry and width of the RDF. Such an effect was attributed to the formation (and subsequent annihilation) of three- and five-fold co-ordinated atoms, comparing favourably to theoretical simulations of the structure of a-Ge.

Introduction

Despite many years of intensive research a thorough understanding of the structure and dynamical process occurring in amorphous materials is still lacking. For example, it is unclear as to whether differences in the structural properties of amorphous semiconductors prepared by different methods are artefacts of their respective preparation methodology, or is it possible that a continuum of metastable states *allowed*?. Structural relaxation of amorphous semiconductors [1] has also been studied in order to understand the characteristic structure of these materials. For example, studies of amorphous Ge [2] and Si [3] have suggested two possible models for structural relaxation. From Raman and neutron diffraction studies [4] it was thought that this relaxation was due the rearrangement of bond angle distortions throughout the amorphous network. Later, a combination of DSC and Raman measurements, Roorda [3] determined a relationship between the kinetics of relaxation for amorphized Si with defect annealing in lightly damaged crystalline Si. Those studies concluded that the relaxation was due to annihilation of point defects in the amorphous phase, however a model incorporating bond angle re-ordering gave equally good fits to the data. It stands to reason that the annihilation of defects would necessarily involve rearrangements of bond angles on a local scale. EXAFS measurements of amorphous material are relatively insensitive to distortion in the bond angle distribution for the first co-ordination shell and can thus provide information about the bondlength changes on relaxation [5].

The goal of the present work has been to determine the structural parameters of ion-implantation induced amorphized *and* relaxed Ge, to aid the understanding of these intriguing materials systems by comparison to relevant theoretical works.

Experimental

Transmission EXAFS measurements of the Ge K-edge were performed at 10K on beamlines 2-3 and 4-3 of the Stanford Synchrotron Radiation Laboratory and 20-B of the Photon Factory. Samples were prepared by implanting ~ 2 μm thick crystalline films. ^{74}Ge implantations were performed at –196 °C, at 7° incidence. Multiple-energy, multiple-dose

MeV implantation sequence was utilised to produce a near-constant distribution of energy deposition in vacancy production over depths of ~0.2-2.2 μm. A low ion flux (power density ~ 0.5 W/cm^2) was utilised to avoid beam induced heating [6]. Selected samples were relaxed by annealing at 200 C for 1hr in an air ambient.

The EXAFS data was extracted from an absorption spectrum in the conventional manner [7], utilising the SPLINE code [8] for interactive background subtraction.

The EXAFS data, was k^3-weighted (where k is the photoelectron momentum), as shown in Figure 1a for crystalline and amorphous Ge samples. A single modulated sinusoid in the amorphous spectrum, indicates scattering from a single atomic shell, as consistent with the Fourier Transform (FT) (Figure 1b) which is comprised of a single peak.

The cumulant method [9,10] is a model-independent technique based on the expansion of EXAFS amplitudes and phases as a series of cumulants of the interatomic distance distribution. The cumulants were determined by comparing the EXAFS amplitude and phase of the implanted samples (s) to that of a known reference (r) in this case a crystalline sample. The difference in the cumulants $\Delta C1$ and $\Delta C3$ were obtained from a fit to the phase difference as given by eq. 1, and $\Delta C0$, $\Delta C2$ and $\Delta C4$, (where $\Delta Ci = Ci_s - Ci_r$) from a fit to the logarithm of the amplitude ratio (eq. 2),

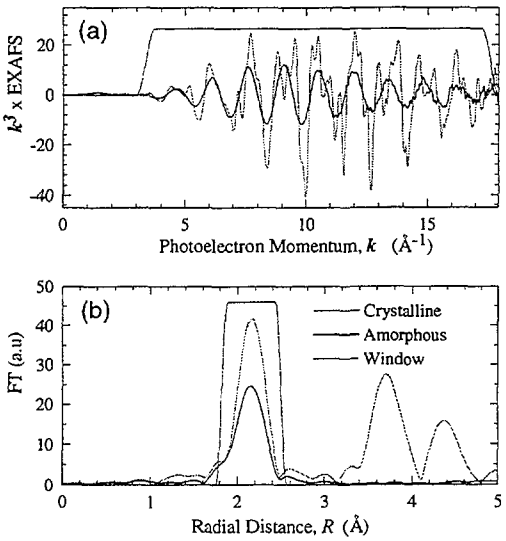

Figure 1. EXAFS (a) and Fourier-transformed (b) spectra comparing crystalline and amorphised Ge.

$$\Phi_S(k) - \Phi_r(k) = 2k\Delta C1 - \frac{4}{3}k^3\Delta C3 + \ldots\ldots \qquad 1$$

$$\ln\frac{A_S}{A_r} = \ln\frac{N_S}{N_r} + \Delta C0 - 2k^2\Delta C2 + \frac{2}{3}k^4\Delta C4 + \ldots \qquad 2$$

Absolute magnitudes for the sample cumulants were obtained from the reference cumulants of the crystalline spectra, the latter determined assuming a Gaussian interatomic distance distribution. The electron mean free path, λ, was set at 5Å independent of k, and the structural parameters were then be obtained from the cumulants using eqs. 3 and 4.

$$\Delta C0 = -2\frac{\Delta C1}{\lambda} - 2\left(\ln C1_S - \ln C1_r\right) \qquad 3$$

$$R_S = C1 + \frac{2C2}{C1}\left(1 + \frac{C1}{\lambda}\right) \qquad 4$$

Specifically, $C0$ is a normalisation factor, $C1$ is related to R_s, $C2$ is the mean square displacement of the backscattering atoms to absorbing atoms, $C3$ measures asymmetry of the interatomic distance distribution, and $C4$ is connected to the width and shape of the distribution. The real interatomic distance distribution was determined from the Fourier Transform of the reconstructed characteristic function in the range $-25 : k : 25\text{Å}^{-1}$.

Results

Figure 2 shows the ion-dose dependence of the EXAFS-determined bondlength, R, and asymmetry parameter, $C3$, for amorphized Ge. For all samples, the experimental R and $C2_s$ values ($\geq$2.458 $\pm$ 0.002Å and $\geq$0.0028 $\pm$ 0.0005Å^2, respectively) exceeded those of the crystalline reference (2.4496Å and 0.0018 $\pm$ 0.0003Å^2, respectively), consistent with the presence of structural disorder in the amorphous phase. Shown in Figure 3 are the reconstructed real RDF's for selected samples, compared to the crystalline reference. Clearly the increase in bondlength is manifested by a shift to generally higher bondlengths, with an exaggeration of the large R tail, due to the presence asymmetry. It should be noted that analysis by the so-called standard method with a Gaussian RDF does not reveal this important detail (not shown).

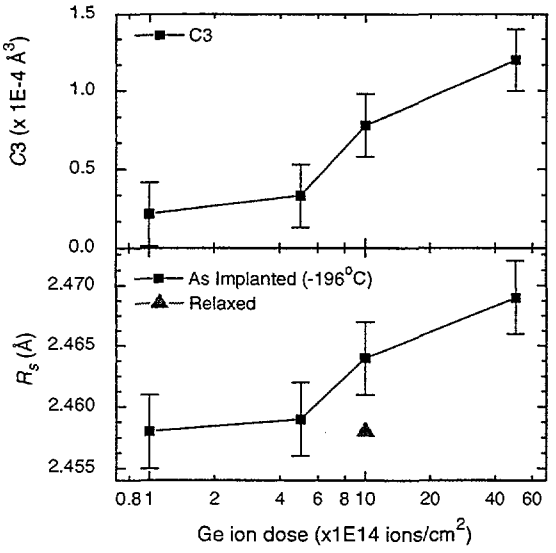

Figure 2. Nearest-neighbour a-Ge bondlength R, and asymmetry parameter $C3$, as functions of ion dose

The observed trends in structural evolution were entirely consistent with an implantation-induced increase in the fraction of defective inter-atomic configurations. *Ab-initio* molecular-dynamics calculations [11] have predicted that amorphous Ge is comprised of three-, four- and five-fold coordinated atoms. The three- and five- fold coordinated atoms in the amorphous phase may be envisaged as analogues to the fundamental crystalline defects - a vacancy and interstitial, respectively. The presence of the three- and five-fold coordinated atoms, with bondlengths of 2.52 and 2.57Å respectively, exceeding that of the tetragonal site (2.47Å), would produce a dose dependant shift to longer bondlengths, as observed. This can considered to be evidence for the increase of the defective site population (ie point defects) with increasing ion bombardment.

The reconstructed RDF for the structurally relaxed a-Ge is shown in Fig 3. Readily apparent was a reduction in bondlength, Debye-Waller factor and asymmetry of the RDF. The RDF for the annealed sample clearly shows a reduction in mainly longer bondlength components,

indicative of a change in the short range ordering of the amorphous network. This appears to be the reverse of the dose dependant trend, indicating the removal of the ion implantation produced point defects, fully supporting the defect annihilation model for structural relaxation [3]. Further, the determined structural parameters for the relaxed sample were identical to that of the lowest dose implanted sample (a dose slightly greater by ~ 1e13 ions/cm^2 than the amorphization threshold). It is proposed that the measured structure for the relaxed and low dose implanted samples may thus be characteristic of an ideal continuous random network [12]. Such a result appears surprising due to the highly non-equilibrium nature of ion implantation.

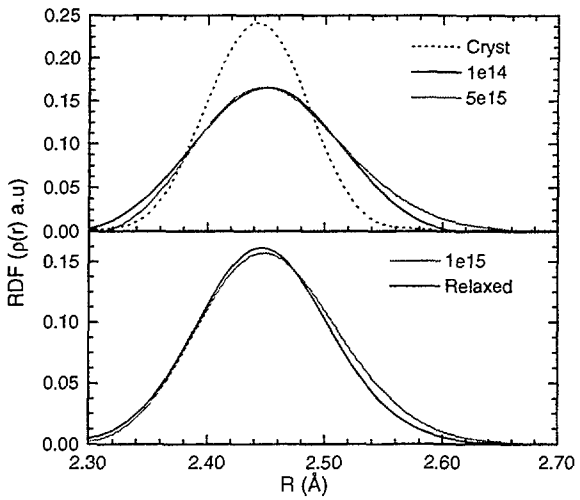

Figure 3. Real a-Ge inter-atomic distance distribution for a pair of nearest-neighbor atoms as a function of ion dose and relaxed at 200°C.

Conclusion

EXAFS has been used to characterize atomic-scale structural modifications in amorphous Ge produced by ion implantation. The inter-atomic distance distribution of amorphised Ge was shown to *continuously evolve* as a function of ion dose. Ion-dose dependent increases in bondlength and asymmetry in the inter-atomic distance distribution were observed. For an implant temperature of -196°C, we suggest these micro-structural modifications resulted from an implantation-induced increase in the three- and five-fold coordinated atom fractions and represented a mechanism of accommodating vacancies and interstitials within the amorphous phase. Subsequent structural relaxation showed changes in the RDF which were attributed to a reduction of the three- and five-fold coordinated atom fractions, thus supporting a model for relaxation via point defect annihilation. The usefulness of ion implantation as a technique for the preparation of amorphous semiconductor samples for structural studies has also been shown.

Acknowledgments

MCR, CJG and GJF acknowledge support from the Australian Synchrotron Research Program, funded by the Commonwealth of Australia via the Major National Research Facilities Program. Work done (partially) at SSRL which is operated by the Department of Energy, Office of Basic Energy Sciences.

References.

[1] E. P. Donovan, F. Spaepen, D. Turnbull, J. M. Poate, and D. C. Jacobson, J. Appl. Phys. **57,** 1795 (1985).

[2] J. Fortner and J. S. Lannin, Phys. Rev. B **37,** 10154-8 (1988).

[3] S. Roorda, W. C. Sinke, J. M. Poate, D. C. Jacobson, S. Dierker, B. S. Dennis, D. J. Eaglesham, F. Spaepen, and P. Fuoss, Phys. Rev. B **44,** 3702-25 (1991).

[4] J. Fortner and J. S. Lannin, Phys. Rev. B **39,** 5527- 30 (1989).

[5] C. E. Bouldin, R. A. Forman, M. I. Bell, and E. P. Donovan, Phys. Rev. B **44,** 5492- 6 (1991).

[6] M. C. Ridgway, C. J. Glover, H. H. Tan, A. Clark, F. Karouta, G. J. Foran, T. W. Lee, Y. Moon, E. Yoon, J. L. Hansen, A. Nylandsted-Larsen, C. Clerc, and J. Chaumont, in *Amorphous semiconductor sample preperation for transmission EXAFS measurements.*, 1998 (Proc. Mat. Res. Soc.).

[7] D. E. Sayers and B. A. Bunker, in *X-Ray Absorption: Principles, Applications and Techniques of EXAFS, SEXAFS and XANES*, edited by D. C. Koningsberger and R. Prins (Wiley, New York, 1988), p. 211-253.

[8] P. J. Ellis, PhD Thesis, University of Sydney, 1995.

[9] G. Bunker, Nucl. Instrum. Methods **207,** 437-44 (1983).

[10] G. Dalba, P. Fornasini, M. Grazioli, and F. Rocca, Phys. Rev. B **52,** 11034-43 (1995).

[11] G. Kresse and J. Hafner, Phys. Rev. B. **49,** 14251 (1994).

[12] D. E. Polk, J. Non-Cryst. Solids **5,** 365-76 (1971).

Characterisation of a new alkoxide sol-gel hydroxyapatite

D. D. Green, G. S. K. Kannangara, A. Milev and B. Ben-Nissan

Department of Chemistry, Materials and Forensic Science
University of Technology, Sydney PO BOX 123, Broadway, NSW 2007, Australia

Introduction

Hydroxyapatite (HAp) coatings have been used to promote bone growth and fixation towards implant surfaces to encourage faster recovery times for the recipient. Current coating processing techniques, capable of producing thin HAp layers are pulsed-laser deposition [1] and sputtering (high-temperature processing). Other technologies are *in vitro* methods [2], electrodeposition [3] and sol-gel [4-5], due to the fact that these techniques utilise lower processing temperatures they avoid structural instabilities of HAp at elevated temperatures [6]. The term sol-gel encompasses any process of producing ceramic materials (single and mixed oxides, as well as non-oxides e.g. nitrides) from solutions. The sol-gel process was first identified by Ebelman [7], and has been used to produce ceramic powders, coatings, and bulk materials including glasses. The implementation of a sol-gel methodology enables increased stoichiometry and homogeneity, while having the ability to coat complex shapes.

Sol-gel hydroxyapatite reported by Chai *et al.*[8] employed tri ethyl phosphite [$P(OEt)_3$] as the staring phosphorus alkoxide precursor, whereby it was established that in order to obtain monophasic hydroxyapatite upon firing there must be a 24 hour ripening period. The ripening period was determined to be an equilibrium step whereby the equilibrium intermediate phase lied in favour of a diethyl phosphite arrangement (species) within the sol.

Therefore, the work here under taken was to produce hydroxyapatite using diethyl phosphite [$HOP(OEt)_2$] as a starting alkoxide precursor with a final aim to reduce or eliminate the ageing period as observed by Chai *et al* in $P(OEt)_3$ solutions [8].

Materials and Methods

The work employs a conventional alkoxide route which has been modified from Chai *et al.*[8]. Calcium alkoxide precursor solution was prepared by dispersing calcium diethoxide [$Ca(OEt)_2$, Kojundo Chemical Lab., Saitama, Japan] in absolute ethanol [Et(OH), Riedel-de Haen, Germany] followed by the addition of ethylene glycol [$Et(OH)_2$, Aldrich, USA] to dissolve $Ca(OEt)_2$ while maintaining vigorous stirring. Phosphorus precursor solution was then prepared by diluting $HOP(OEt)_2$ (Aldrich, USA) in absolute Et(OH) while stirring. After complete dissolution of the $Ca(OEt)_2$, a stoichiometric quantity of the phosphorus precursor solution was added drop-wise to the calcium precursor solution to avoid concentration gradients within the sol. Vigorous stirring was maintained throughout the addition and for a further 10 minutes thereafter. All vials were capped to avoid volatisation. Due to the hygroscopic nature of the reactants, all preparation was carried out in a glove box containing a dry nitrogen atmosphere. The sol's were aged over a period of 24 hours.

After the sol's were aged (3 and 24 hours), they were poured into petri dishes and hydrolysed in a convection oven (Labec, Australia) at 70°C for approximately 72 hours. On completion of hydrolyses, gel's were crushed via mortise and pestle and fired in a muffle furnace (Ceramic Engineering, Australia), where the ramp rate was set at 150°C/ hour in a stagnate air atmosphere. Temperatures of 250, 450, 700, and 900°C were chosen as soaking temperatures where soaking took place for one hour. This was to effectively remove any organic residue within the gel.

Resultant fired gels were compositionally analysed via XRD on a Siemens D-5000 (Karlsruhe, Germany), employing CuKα radiation. The diffraction pattern was collected over

the 2θ range of 29–40°, acquisition time of 2s at a 0.02° step size. Particle and sintering characterisation of the fired particles was performed on a Joel 35C SEM (Joel, Japan)

Results and Discussion

All resultant hydrolysed gel were similar in appearance after their prescribed ageing period, gels had a crystal like formation with a slight yellow hue to them. Fired gel's had undergone some sintering and were white in appearance.

XRD results of the fired gel's for 3 and 24 hour ageing periods are given in figure 1. The major phase for both ageing periods is hydroxyapatite (JCPDS 9-432) with minor accompanying phases of CaO (JCPDS 13-1497) and β–TCP (JCPDS 9-169). Over the 24-hour ageing period, XRD results indicate a slight lowering of intensity of the CaO peak and to a lesser extent β–TCP with respect to HAp intensity. The reason being thought for the presence of the minor phases is that the reactants have not had efficient time to react over a 24 hour period. Alternately, there may be the effects of dehydroxylation or decomposition of the HAp, due to high temperature firing or lack of stoichiometry between the starting precursors, resulting in the presence of CaO and β–TCP [9].

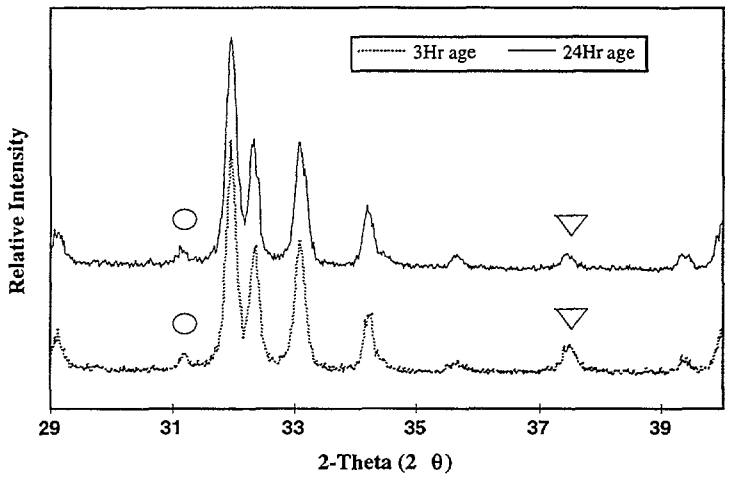

Fig: 1 XRD patterns of 3 and 24Hr ageing – minor phases of CaO and β–TCP do not differ greatly over the 24Hr period – crystal phases are CaO (∇) and β–TCP (O) unassigned peaks belong to HAp

SEM pictures of the 3 hour aged powders are given in figure 2a and 2b. Both ageing times showed no difference in the morphology of the fired gels. It can be seen in both figures that the particles are spherical in appearance, Fig: 2a, represents the particles that have started to agglomerate and started to undergo active sintering. Figure: 2b shows that the particle size is approximately 100nm. The nano-sized particles explain the progression of agglomeration and sintering at the firing temperature of 900°C.

Conclusion

The work thus far undertaken has illustrated that it is possible to produce hydroxyapatite via diethyl phosphite route. Ageing the sol does not appear to effect the composition of the fired gel. It could be possible that the reactants do not react together stoichiometrically or the nano-sized particles are extremely reactive (under sintering conditions) and are already undergoing the effects of decomposition and/or dehydroxylation. Further work into this system will help to enable the optimal conditions for monophasic or biphasic hydroxyapatite synthesis without the need for ageing.

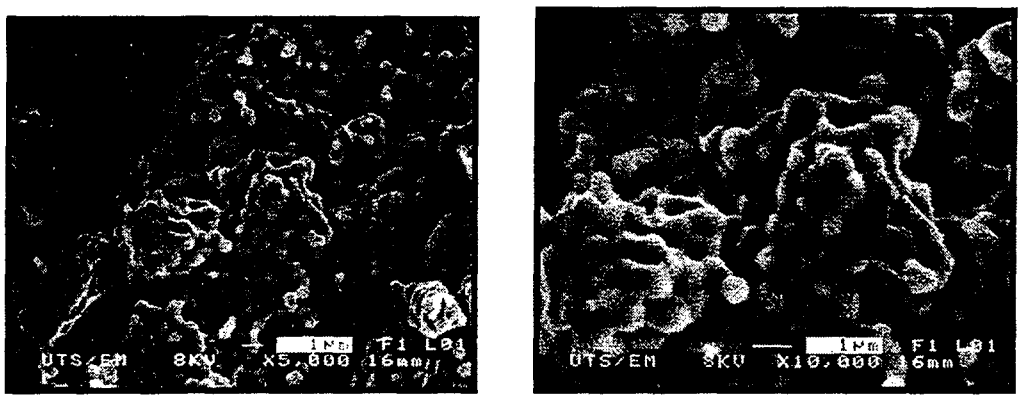

(a) (b)

Figure 2 – SEM micrographs of 3hr. aged powder fired to 900°C – particles are spherical in appearance. The agglomerations and sintering are shown in 2(a), 2(b) shows the nano-sized particles after firing.

References

[1] C. M. Wolke, K. De Groot and J. A. Jansen, *J. Biomed. Mater. Res.* **39** (1998) 524.

[2] H. Dasarathy, C. Riley and H. D. Coble, *J. Biomed. Mater. Res* **27** (1993) 477.

[3] M. Shirkhanzadeh, *J. Mater. Sci. Mater. Med.* **6** (1995) 90.

[4] B. Ben-Nissan, C. S. Chai and K. A. Gross, in "Bioceramics 10" edited by L. Sedel and C. Rey (Elsevier Science, London, 1997) p.175

[5] W. Weng and J. L. Baptista, *J. Mater. Sci. Mater. In Med.*. **9** (1998) 159.

[6] W. Van Raemdonck, P. Ducheyne and P. Demeester, in "Metal and Ceramic Biomaterials", Vol. 2, edited by P. Ducheyne and G. W. Hastings (CRC Press, Boca Raton, FL, 1984) pp. 143-66.

[7] Ebelman M. Untersuchungen uber die Verbindung der Borsaure und Kieselsaure mit Aether. *Ann Chim Phys,* **57** (1846) 319-55

K. A. Gross, C.S. Chai, G. S. K. Kannangara and B. Ben-Nissan, *Journal of Materials Science: Materials in Medicine* **9** (1998) 839.

B. Ben-Nissan, C. S. Chai and L. Evans, in "Encyclopedic Handbook of Biomaterials and Bioengineering", Vol. 1, edited by D. L. Wise *et al.* (Marcel Dekker, Inc, 1995) pp202-05.

Acknowledgments:

The authors would like to thank the Microstructural Unit of UTS for the use of XRD and SEM equipment, and the funding from the Australian Research Council-Small Grant is gratefully acknowledged.

Ion beam modification of thermal stress resistance of MgO single crystals with different crystallographic faces

V. N. Gurarie[1], P. H. Otsuka[1], D. N. Jamieson[1], J. S. Williams[2], M. Conway[2]

[1]School of Physics, MARC, University of Melbourne, Parkville VIC. 3052
[2]Department of Electronic Materials Engineering, Research School of Physical Sciences and Engineering, ANU, Canberra, 0200

Abstract

Ion beam modification of thermal shock stress and damage resistance of MgO single crystals with various crystallographic faces is investigated. The most stable crystal faces in terms of stress and damage resistance are established. Ion implantation is shown to reduce the temperature threshold of fracture for all crystal faces tested. The (111) face is demonstrated to be of highest stability compared to (110) and (100) faces in both implanted and unimplanted crystals. At the same time ion implantation substantially increases the microcrack density for the faces tested and reduces the degree of fracture damage following thermal shock. The microcrack density is found to be highest in the crystals with (110) face in comparison with the (001) and (111) faces. The effect is analysed using fracture mechanics principles and discussed in terms of the implantation-induced lattice damage.

Introduction

High temperature resistance of ceramic materials makes them suitable for a number of applications for which metals are not appropriate. However, an important consideration is their brittle nature, which causes them to fracture readily under sufficiently high stresses, in particular under dynamic loading. Surface modification by ion implantation has been shown to lower the fracture threshold in ceramic materials, allowing fracture to be initiated at lower surface temperatures. At the same time, ion implantation produces a higher density of cracks, but such cracks penetrate smaller distances into the material. This effectively raises the damage resistance parameter and therefore should result in higher durability following damage by thermal shock [1].

The observed modification of fracture behavior is due to the formation of surface energy-absorbing layers which are known to improve the impact and thermal shock resistance of ceramic materials. Ion implantation has been shown to be effective in producing such layers. Numerous fine cracks developed in the layers limit the strength of the material, but provide an effective mechanism for absorbing strain energy during thermal shock and preventing catastrophic crack propagation [2]. The elastic energy produced under the applied stress in the layer is transformed into the surface energy of propagating cracks. Multiple microcracking in the layer is needed to make the energy absorption more effective in the near-surface thus decreasing the depth of crack propagation and hence the degree of damage to the material.

With this in view it is important to establish major factors that are capable of optimising the properties of the ion beam-produced surface energy absorbing layers in brittle ceramics. In this study we investigate the morphology, stability and resistance to damage of the layers in MgO single crystals with various crystallographic faces.

Experimental

The (001), (110) and (111) faces of MgO monocrystals were implanted with 86KeV Si^- ions to a dose of $5x10^{16}cm^{-2}$ at room temperature. Only half of the crystal surface was subjected to implantation to compare the response to thermal shock of implanted and unimplanted regions.

This allows both the implanted and unimplanted regions to be tested under similar thermal conditions.

Thermal shock was produced by exposing the sample surface of ~ 1.5 x cm^2 to a plasma jet produced by a plasma gun [1]. The plasma pulse duration is ~40μs. The samples were placed at some distance from the gun with the plasma jet propagating perpendicular to the sample surface. The surface layer is under compressive strain during the heating stage followed by tensile stresses arising during the cooling stage of the plasma pulse. In these experiments the surface peak temperature is calibrated by measuring the size of fragments, bounded by cracks, and the gap between them [1]. This gap is formed as a result of the contraction of adjacent fragments on cooling from the fracture temperature. Thus, by the end of cooling the relative temperature deformation of the fragment is $\Delta b/b$, where Δb is the gap between the fragments and b is the fragment size. On the other hand, the relative temperature deformation is known to be equal to $\Delta b/b = \alpha (T_f - T_o)$, where α is the thermal expansion coefficient, T_f is the fracture temperature, at which a crack separating adjacent fragments originates, and T_o is the initial sample temperature. The fracture temperature is then determined from the expression: $T_f = T_o + \Delta b / b \alpha$. Details of this treatment are given elsewhere [1]. The gaps between fragments are often very small, particularly between small fragments and at low peak temperatures, so it is difficult to resolve them under an optical microscope and a SEM is used in these cases.

Results and Discssion

Thermal stress resistance of (001), (110) and (111) faces for MgO crystals.

The thermal stresses analysis for MgO crystals with (001), (110) and (111) faces is done using the continuum mechanics equations appropriate for cubic crystals: Hooke's equations with the temperature term, equilibrium and compatibility equations. Assuming fracture starts when stresses in cleavage planes reach the tensile strength σ_b, the stress resistance parameter ΔT_b is computed which represents the maximum temperature variation sustained by the crystal face without fracture. The results of computations are given in Table I. Table I also shows numerical values for the stress resistance parameter for the (001), (110) and (111) faces of MgO crystals. The values are obtained using the tensile strength for MgO of $\sigma_b = 1.55*10^9$Pa, which is calculated using the experimental value ΔT_b =500Kfor the (001) face.

Table I: Theoretical stress resistance parameter for MgO crystals.

Face	ΔT_b (K)	% relative to (110) face	ΔT_b (K)
(001)	$3.2268*10^{-7} \sigma_b$	6%	500
(110)	$3.0346*10^{-7} \sigma_b$	0	470
(111)	$3.9898*10^{-7} \sigma_b$	31.4%	620

The theoretical results in Table I indicate that the stress resistance of the (111) face is ~30% higher in comparison with the (110) face which has the lowest stress resistance.

The experimental results of the ion beam effect on the stress resistance for different crystal faces are given in table II. Experimentally the stress resistance parameter ΔT_b was measured at the edge of the fracture zone where the temperature variation is just sufficient to originate fracture.

Table II: Experimental data for stress resistance parameter ΔT_b in implanted and unimplanted MgO crystals with various faces.

Face	ΔT_b (K) – Unimplanted	ΔT_b (K) - Implanted
(001)	500	250
(110)	400	200
(111)	750	600

As can be seen from Tables I and II there is an adequate correspondence between experimental and theoretical values for ΔT_b in unimplanted crystals. Table II indicates that the stress resistance parameter is lowered for all faces due to ion implantation, in particular for (001) and (110) faces. The (111) face demonstrates much smaller reduction in the stress resistance following ion implantation.

The data are discussed in terms of the structural changes induced by ion implantation and their effect on crystal properties. According to theoretical data the quantity ΔT_b depends on elastic constants and the tensile strength σ_b. The latter quantity is obviously highly sensitive to the implantation-induced lattice damage. It is known from fracture mechanics that $\sigma_b = K/(\pi a)^{1/2}$ where a is the crack length and K is the fracture toughness. Both quantities K and a in the equation are affected by ion implantation.

In brittle solids the size a of the preexisting microcracks is of particular importance. For the same brittle material σ_b can statistically vary in a wide range depending the size of the preexisting defects. Ion implantation is known to produce a substantial lattice damage in the form of dislocations, vacancies and interstitial atoms [3]. These defects can generate a number of crack-nucleating centers in the form of micropores and voids. Because ion implantation decreases the stress resistance parameter it is obvious that the implantation-induced crack-nucleating defects are larger than the preexisting ones in the unimplanted crystal. Since for the (001) and (110) faces the fracture stress is halved due to implantation one can assume that ion implantation generates microcracks which are roughly 4 times the size of the preexisting ones.

The other quantity which is affected by ion implantation is the fracture toughness K. This property depends on the energy absorbed at the tip of the propagating crack. The energy absorption is related to the surface energy and plastic flow at the crack tip. The ion beam effect on these properties is complex. There are indications that fracture toughness of MgO crystals can be substantially increased due to ion implantation [3]. At the same the high dislocation density which is produced by ion implantation reduces the dislocation mobility and thus by suppressing plasticity can reduce fracture toughness. Obviously, the size a of the implantation-induced defects is a major factor which determines the reduction in fracture stress and hence in the stress resistance parameter ΔT_b. It is quite possible that ion implantation damage also changes the anisotropy of the elastic constants which contributes to the effect observed.

Crack density and degree of damage for various crystal faces

Previous experiments show that ion implantation damage generates high-density microcrack systems. High-density microcracking is known to be effective in toughening brittle ceramics. Toughening by crack tip shielding by microcracking takes place because the elastic energy at the crack tip is transformed into the surface energy by multiple microcracking [2]. This process decreases the range of the propagating cracks. Therefore, in the heavily microcracked material the degree of fracture damage under mechanical or thermal shock loading is decreased.

Crack density, measured as the number of fragments per unit area at the face, for unimplanted and implanted MgO samples is presented in Table III.

Table III.

Face	Fragment density, mm^{-2}, unimplanted	Fragment density, mm^{-2}, implanted	Ratio, impl./unimpl.
(001)	204	918	4.5
(110)	1647	7220	4.38
(111)	339	1455	4.29

The table indicates that ion implantation substantially increases the density of cracks and crack-nucleating centers, by 4-5 times for all faces. The data suggest that for the implantation parameters used in the experiments the implantation-induced lattice damage responsible for crack nucleation is dependent on the crystal face. The microcrack density and resistance to fracture damage is maximum for the (110) face. The data are discussed involving the energy-based approach and the ion-beam effect on interatomic potential energy.

Conclusions

Ion implantation is shown to reduce the stress resistance parameter for all crystal faces in MgO single crystals. The minimum reduction is observed for the (111) face which exhibits the maximum stability compared to the (001) and (110) faces. On the other hand the microcrack density and resistance to damage is shown to be highest for (110) face. The effects are discussed in terms of the implantation-induced lattice damage on various faces.

References

[1] V.N. Gurarie, A.V. Orlov, J.S. Williams, NIMB, *Beam Interactions with Materials and Atoms*, B 127/128, 1997, 616-620; B 147, 1999, 221-225.

[2] J.B. Wachtman, *Mechanical Properties of Ceramics*, J. Wiley & Sons, 1996.

[3] C.W. White, C.J. McHargue, P.S. Sclad, L.A. Boatner and G.C. Farlow, *Ion Implantation and Annealing of Crystalline Oxides*, North-Holland Publ., 1989.

Actinides Analysis by Accelerator Mass Spectrometry

M.A.C. Hotchkis, D. Child, D. Fink, G.E. Jacobsen, P.J. Lee, N. Mino,
A.M. Smith and C. Tuniz

Australian Nuclear Science and Technology Organisation
PMB 1, Menai, NSW 2234, Australia

Introduction

At the ANTARES accelerator at ANSTO a new beamline has been commissioned, incorporating new magnetic and electrostatic analysers, to optimise the efficiency for Actinides detection by Accelerator Mass Spectrometry (AMS). The detection of Actinides, particularly the isotopic ratios of uranium and plutonium, provide unique signatures for nuclear safeguards purposes. We are currently engaged in a project to evaluate the application of AMS to the measurement of Actinides in environmental samples for nuclear safeguards. Levels of certain fission products, Actinides and other radioactive species can be used as indicators of undeclared nuclear facilities or activities, either on-going or in the past. Other applications of ultra-sensitive detection of Actinides are also under consideration.

Here we report on the first application of the system: the measurement of ^{236}U in environmental media including soil and sediment. A detailed paper has been prepared [1].

The Actinides AMS system

The ANTARES AMS system has been described elsewhere (see for example [2]). The design of the new beamline for actinides analysis was discussed at the last NTA conference [3]. A schematic is shown in Figure 1. The beam is focussed by an electrostatic quadrupole at the exit of the accelerator tube and steered through 12° by an electrostatic deflector, bringing the beam to a focus where the charge states emerging from the accelerator are resolved. The selected charge state of the beam is then energy-analysed by a high-resolution electrostatic analyser. This spherical (double-focussing) 90° analyser with radius 2.5m has a maximum rigidity of 8 MeV/q (±80kV across the 25mm gap). The nominal resolving power of 5000 is sufficient to enable rejection of molecular-type interferences. When a molecule containing a neighbouring mass isotope is injected into the accelerator along with the isotope of interest (e.g. $^{235}U^{17}O$ molecule with $^{236}U^{16}O$), the break-up of the molecule in the accelerator terminal stripper leads to a small energy difference between the positive ions (1 in 1500 difference for $^{235}U^{5+}$ and $^{236}U^{5+}$).

The beam is then mass analysed in a 90° double-focussing magnet with radius 2 m, pole gap 50mm and maximum rigidity ME = 250 MeV-amu. At the image plane the actinide isotopes are separated by 16mm. An adjustable array of detection devices, including Faraday cups and secondary electron multiplier detectors for low intensity beams, is situated in this plane,. One mass position allows particles through to a time-of-flight (TOF) leg, followed by a gas detector, for high sensitivity identification of very rare isotopes.

The actinides facility includes a sample preparation laboratory in which we have tested methods for the extraction and separation of actinides from matrices such as soils. Samples are totally dissolved by NaOH fusion and HF digestion and the Actinides are separated by ion exchange chromatography using TRU-Resin. The uranium fraction is then eluted and co-precipitated with iron oxide. The iron oxide matrix is mixed with an equal mass of niobium powder to make material which performs optimally in the AMS ion source.

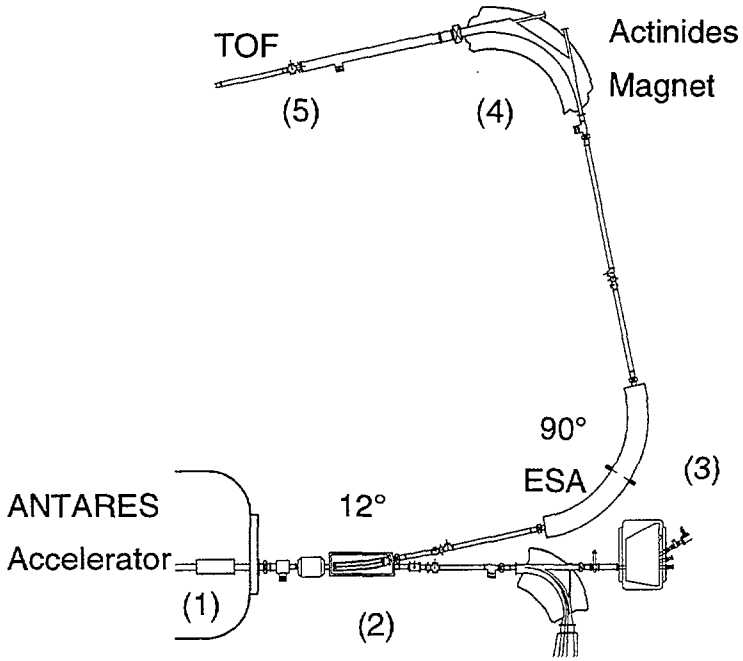

Figure 1. Schematic diagram of the actinides AMS beamline on the ANTARES accelerator showing (1) the electrostatic quadrupole lens, (2) 12° deflector, (3) 90° electrostatic analyser, (4) 90° magnet, and (5) isotope detection station.

^{236}U measurements and results

The results for 236:238 ratios are shown in Table 1. The New Brunswick Laboratory (NBL) uranium isotopic standards U010 and U005-A have ^{236}U:^{238}U isotopic ratios in the 10^{-5} range. To avoid cross-contamination in the ion source we diluted them to approximately 1:100 with the natural uranium material from NIST (4321C). In Table 1, the diluted U010 standard is used to normalise the other results. The other NBL standards yield the expected ratios. The NIST 4321C reference material is natural uranium and is expected to have a very low ^{236}U content (ratio ~10^{-10}) [4]. Our present results are consistent with this; a scan of the injection magnet field demonstrated that the detector count rate observed for this sample originates from ^{235}U. However, the TOF system was not used for the present measurements; with the TOF system in operation, a much lower background level could be achieved.

Our first chemistry and accelerator tests were performed with samples made from a uranium elemental standard solution supplied by Aldrich. We found it had somewhat anomalous ^{235}U:^{238}U and ^{234}U:^{238}U ratios (~0.5% and 0.004% respectively), and a high level of ^{236}U (see Table 1). Subsequently the supplier informed us that it is made from depleted uranium. Contamination with ^{236}U could have occurred in the enrichment plant if some recycled uranium had been used as feed material.

The IAEA 375 soil reference material is a contaminated soil containing various radionuclides including plutonium, from a site in Russia about 100 km from Chernobyl. While the uranium concentration is predominantly of natural origin (as evidenced by the activity ratios of the other isotopes), it is expected that ^{236}U would accompany Pu contamination. For measurement of the ^{236}U:^{238}U ratio of this material we required only 1g of the soil, yielding a sample with 2μg of uranium. The result of 2.45×10^{-6} for the ^{236}U:^{238}U ratio gives a ^{236}U activity of 11 mBq/kg in the soil. The Pu activity is 300 mBq/kg, hence a Pu:^{236}U activity ratio of 27. If both activities originate from contamination by nuclear fuel residues, the

expected activity ratio would be in the range 1000 to 3000. The anomaly may be due to other sources of ^{236}U or due to differing transport characteristics.

Table 1. ^{236}U in uranium isotopic standards, reference materials and others.

Sample	*Uranium mass in sample* [1] *(mg)*	*Total sample mass (mg)*	*$^{238}U^{5+}$ typical current (pA)*	*236:238 isotopic ratio ($\times 10^{-9}$)*	*Expected 236:238 ratio ($\times 10^{-9}$)*
NBL U010 isotopic standard [2]	0.1	15.6	200	(588.7) [3]	630.7
NBL U005-A isotopic std [2]	0.5	15.4	500	117±19	97.9
NBL U005-A isotopic std [2]	0.1	15.7	150	140±30	97.9
NBL U030-A isotopic std	0.1	16.6	60	6300±310	6180
NBL U0002 isotopic std	0.1	14.4	200	< 9	<100
NIST 4321C natural uranium	0.085	15.9	150	< 7	-
IAEA 375 soil (Chernobyl area)	0.002	4.6	25	2450±120	-
IAEA 135 sediment (Irish Sea)	0.004	7.0	10	1480±370	-
IAEA 300 sediment (Baltic Sea)	0.015	10.7	3	< 15	-
Fe_2O_3 procedural blank	-	6.9	<0.2	-	-
Aldrich uranium solution [4]	0.1	20.0	100	2670±120	-

[1] Assuming 100% yield from the extraction procedure.

[2] The ^{236}U:^{238}U ratio is diluted by approximately 100:1 using natural uranium solution (NIST 4321C); the expected ratio is calculated assuming that the NIST solution is free of ^{236}U.

The IAEA 135 sediment from the Irish Sea contains a clear ^{236}U signal due presumably to the proximity of the Sellafield reprocessing plant or resulting from the 1957 Windscale accident. Relating the ^{236}U to the Pu activity in this sample is difficult due to the various possible origins of each; as well as site emissions, both Pu and U have been dumped in the Irish Sea in the past. The Baltic Sea sediment (IAEA 300) yielded no ^{236}U signal above the background level of these measurements.

Conclusions

We have successfully demonstrated the measurement of ^{236}U in small environmental samples. These measurements have been made relative to available uranium isotopic standards. The

soil and sediment reference materials we have measured provide a starting point in the measurement of ^{236}U in environmental media. In contrast to 'traditional' AMS, the method requires only micrograms of the major isotope (^{238}U in this case). This opens the way to measurement of ^{236}U:^{238}U ratios in a wide range of media, including, for example, sea water, which contains 3μg/l U.

We believe that ^{236}U has great potential as a signature of irradiated nuclear material or as a tracer. Further measurements of ^{236}U in a variety of samples are in progress. Studies of its distribution are required to evaluate fully its potential as a nuclear signature. We also plan to use the system described in this paper for measurements of Pu and other U isotopes in environmental media.

[1] M.A.C. Hotchkis, D. Child, D. Fink, G.E. Jacobsen, P.J. Lee, N. Mino, A.M. Smith and C. Tuniz, submitted to Nucl. Inst. & Meth.

[2] C. Tuniz et al., Nucl. Instr. & Meth. B123 (1997) 73 and references therein.

[3] M.A.C. Hotchkis et al., in Proc. 10th Aust. Conf. NTA, Canberra, 24-26 Nov 1997.

[4] X.-L. Zhao, M.-J. Nadeau, L.R. Kilius and A.E. Litherland, Nucl. Instr. & Meth. B92 (1994) 249.

Monte-Carlo simulation of heavy ion elastic recoil detection analysis data to include the effects of large angle plural scattering

P.N. Johnston[1], R.D. Franich[1], I.F. Bubb and M. El Bouanani[2], D.D. Cohen[3], N. Dytlewski[3] and R. Siegele[3]

[1]Department of Applied Physics, Royal Melbourne Institute of Technology, GPO Box 2476V, Melbourne 3001,
[2]Current address Department of Physics, Univeristy of North Texas, Denton, USA
[3]Australian Nuclear Science and Technology Organisation, PMB 1, Menai 2234, Australia.

Abstract

Heavy Ion Elastic Recoil Detection Analysis (HIERDA) is becoming widely used to study a range of problems in materials science, however there is no standard methodology for the analysis of HIERDA spectra. Major impediments are the effects of multiple and plural scattering which are very significant, even for quite thin (~100nm) layers of very heavy elements. To examine the effects of multiple scattering a fast FORTRAN version of TRIM has been adapted to simulate the spectrum of backscattered and recoiled ions reaching the detector. Two problems have been initially investigated. In the first, the detector is positioned beyond the critical angle for single scattering from a pure V target where traditional slab analysis would not predict any scattered yield. In the second, a thin Au layer on a Si substrate is modelled for two different thicknesses of the substrate to investigate the effect of the substrate chosen. The use of multiple processors enabled the acquisition of statistically reasonable simulation spectra for scattered and recoiled ions. For each target modelled, 10^9 incident ions were tracked. The results of the simulations are compared with experimental measurements performed using ToF-E HIERDA at Lucas Heights and show good agreement except in the long tails due to Plural Scattering.

Introduction

Heavy Ion Elastic Recoil Detection Analysis (HIERDA) is an increasingly popular analytical technique for materials analysis. It is limited in part by a lack of a standard data analysis method. Slab models of various levels of sophistication have been used widely to yield quantitative results from HIERDA, but because of the high probability of multiple interactions of a given incident ion, these fail to simulate all the features of measured spectra.

In a previous paper we described our first attempts to use Monte-Carlo ion transport using the 'TRIM' code to simulate the spectrum from HIERDA [1]. In that work we showed that Monte-Carlo simulation reproduces important features of HIERDA spectra including (i) the low energy sides of features broadened by small angle multiple scattering, (ii) the long tails due to large angle plural scattering and (iii) particles of higher energy than single scattering due to multiple scattering where the product of kinematic factors is greater than the kinematic factor for single scattering.

In this paper we apply a similar method to two problems. The first is the simulation of recoil and scattered spectra for a case where scattering is beyond the critical angle for scattering. In this case the scattered ions only arise from multiple scattering and so traditional 'slab' analysis would not predict any scattered yield. The second problem is an investigation of the phenomenon recently identified by Li and O'Connor [2] where they have seen that modelling of the substrate has a pronounced effect on the magnitude of tailing in medium energy ion scattering.

Experiment

The experimental data presented in this paper were obtained using 60MeV $^{81}Br^{8+}$ and 60MeV $^{127}I^{9+}$ ions from the ANTARES 8 MV FN Tandem accelerator at the Lucas Heights laboratories of the Australian Nuclear Science and Technology Organisation. The HIERDA measurements were made using a ToF-E detector telescope with a flight path of 495mm and with carbon foils of 25.3μg/cm^2 as described elsewhere [1]. The targets were a pure V sample and a well characterised layer of Au, 60nm thick, on Si substrates. The samples were irradiated at 67.5° to the surface normal.

Time spectra were used as these have better resolution for heavy elements than the energy spectra exhibit [3] as well as being subject to a far simpler and more direct calibration process. Time calibration is established using samples which span a wide range of atomic masses as described by El Bouanani et al [4].

The signals from backscattered and recoiled ions were extracted from the raw data using the PAW analysis code [5] complemented with a suite of macros called TASS [6]. Time spectra were extracted after the individual elemental signals were identified and separated using Mass versus Energy projections.

Monte-Carlo Simulation

Monte-Carlo simulations were performed using a fast FORTRAN version of TRIM [7] compiled with Lahey FORTRAN 90 on Pentium and similar computers with processor speeds from 120 to 350 MHz. More details of the simulations and the virtual detector are given in [1]. Briefly, the virtual detector is made much larger than the real detector by accepting ions where (i) the scattering angle was between 44° and 46° and (ii) the azimuthal angle was restricted so that the excess path length in the exiting ion's path is less than 10%.

In the first problem, the scattered and recoiled spectra generated by 60MeV ^{81}Br ions incident at 67.5° to the surface normal of a pure V sample are modelled. This aims to compare the simulated spectrum of scattered ions beyond the single scattering limit with experimental measurements. 10^9 incident ^{81}Br ions were simulated assuming a minimum ion target nuclear transfer energy (T_{min}) of 5eV. As numerous computers were used, it is instructive to give a benchmark result for one computer. Simulation of 10^6 ion paths took 4600 s on a Pentium II 350MHz computer.

In the second problem 60MeV ^{127}I ions are incident on a sample of Au 75nm thick on a Si substrate. The Au layer is made 75nm thick to give equivalent energy loss to that observed experimentally in measurements on the 60nm Au layer mentioned previously. This is because of a deficiency in the stopping powers. The substrate thickness of Si is modelled with 2 thicknesses: 1nm and 500nm to explore the possibility of a significant difference in the scattered I spectrum. At least 10^9 ions were simulated in each of these cases.

The ion energies were then corrected for energy loss in the first timing foil and converted to time over the known flight length. These flight times were then converted to a time histogram (simulated spectrum) using the experimental time calibration bin width and offset.

Results and Discussion

Fig 1 shows a comparison of experimental data with simulated spectra for scattered and recoiled ions from 60MeV ^{81}Br ions on V. The recoiled spectrum shows reasonable agreement with experimental data and is used to normalise the data set. A comparison of experimental data and simulation for the backscattered spectrum shows a similar magnitude and shape, but the simulation significantly exceeds the experimental data at flight times above 110ns.

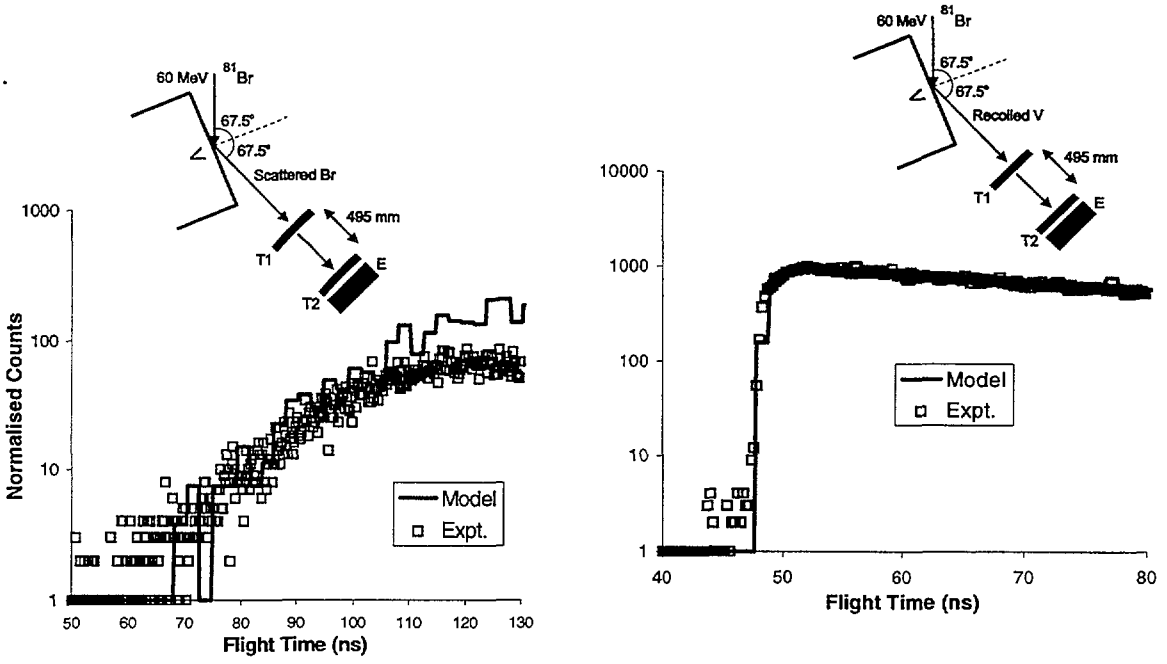

Figure 1. (**a**) Comparison of the scattered Br spectrum (□) from a pure V sample with a Monte-Carlo simulation, and (**b**) comparison of the recoiled V spectrum (□) with a Monte-Carlo simulation which has been used for normalisation.

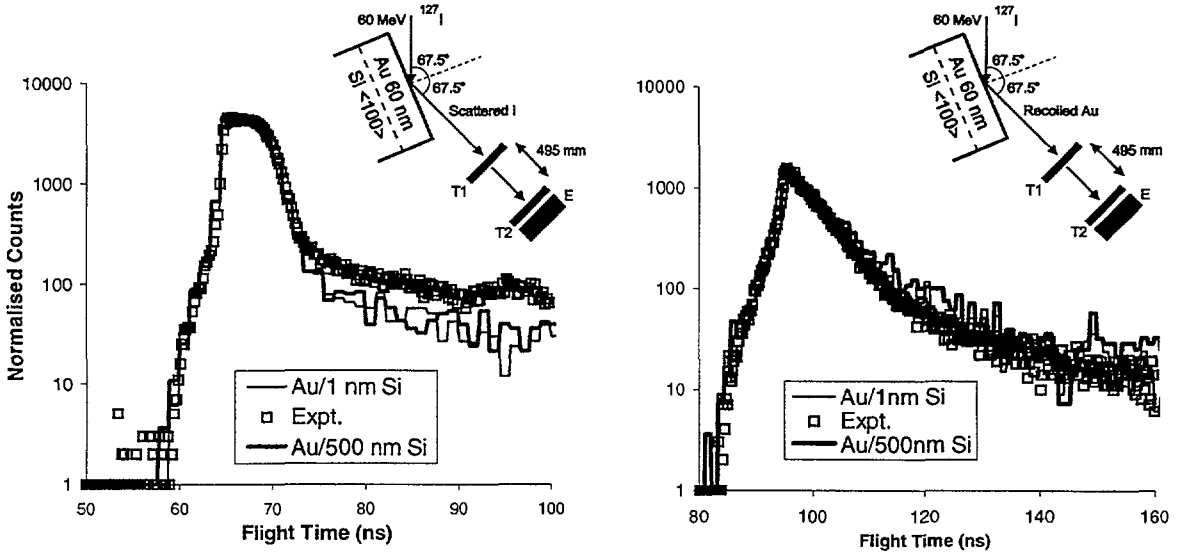

Figure 2. (**a**) Comparison of the scattered I spectrum (□) from a 75nm Au on Si sample with a Monte-Carlo simulation assuming a substrate thickness of 1nm (thin) and a substrate thickness of 500nm (thick), and (**b**) comparison of the recoiled Au spectrum (□) with a Monte-Carlo simulation assuming a substrate thickness of 1nm (thin) and a substrate thickness of 500nm (thick).

Figure 2 compares experimental data from the 60nm Au layer on Si with simulated spectra of a 75nm Au layer on Si considering two substrate thicknesses. The two simulations are in agreement but both give tailing contributions well below the experimental data. The critical angle for single scattering of I ions from Si is much less than 45° and other experimental work demonstrated that multiply scattered I from Si alone would have a very small direct contribution.

Conclusion

- Monte Carlo simulation of spectra from HIERDA can reproduce most of the features of the spectra.
- Simulation of the spectrum of multiply scattered ^{81}Br ions from a V sample reproduces the basic features of the measured spectrum however the simulation exceeds the measured data for lower scattered ion energies.
- In comparing experimental and modelled HIERDA spectra from a thin layer of Au on Si, there is a substantial discrepancy between the tailing as observed and modelled. This cannot be attributed to substrate effects of the type observed by Li and O'Connor [2].

Acknowledgement

Supported by the Australian Institute of Nuclear Science and Engineering.

References

[1] P.N. Johnston, I.F. Bubb, M. El Bouanani, D.D. Cohen and N. Dytlewski, American Institute of Physics Conference Proceedings 475, AIP Press, New York (1999), Editors J.L. Duggan and I.L. Morgan, p.517.

[2] M.M. Li and D.J. O'Connor, Nucl. Instr. and Meth. B 149 (1999) 460-468.

[3] P.N. Johnston, M. El Bouanani, W.B. Stannard, I.F. Bubb, D.D. Cohen, N. Dytlewski and R. Siegele, Nucl. Instr. and Meth. B 136-138 (1998) 669.

[4] M. El Bouanani, M. Hult, L. Persson, E. Swietlicki, M. Andersson, M. Östling, N. Lundberg, C. Zaring, D.D. Cohen, N. Dytlewski, P.N. Johnston, S.R. Walker, I.F. Bubb and H.J. Whitlow, Nucl. Instr. and Meth. B 94 (1994) 530-536.

[5] CERN, PAW Manual Version 1.14, (Application Software Group, Computing and Networks Division, CERN, Geneva, Switzerland, 1992).

[6] H.J. Whitlow, TASS, Internal Report, (Dept. Nuclear Physics, Lund Institute of Technology, Sölvegatan 14 S-223 62 Lund, Sweden, 1993).

[7] H. Hay, Department of Electronic Materials Engineering, Australian National University (1995) derived from the original TRIM [8].

[8] J.P. Biersack, and U. Littmark, 'The Stopping and Range of Ions in Solids', Pergamon, New York (1985).

Initial stages of Ni deposition and diffusion in Ag(001)

D. Karpuzov[1], H.J. Kang[2] and D.J. O'Connor[3]

1 Institute of Electronics, Bulgarian Academy of Sciences, Sofia, 2 Department of Physics, Chunkbuk University, Korea, 3 Department of Physics, University of Newcastle, Callaghan, NSW 2308

Abstract

The distribution of Ni deposited in UHV on a Ag(001) surface has been studied with Low Energy Ion Scattering. Previous studies using Low Energy Electron Diffraction have concluded that the Ni preferentially forms clusters and is located below the surface.

In this study, from polar scans and from sputter profiling, it is evident that Ni is present both on the surface and below it with a preference for a subsurface site. Upon deposition, the crystallographic structure of the surface is somewhat disordered suggesting that although there is high mobility of the Ni atoms, it is not sufficient to ensure a well ordered surface.

Sputter profiling shows a higher yield in the subsurface region and this concentration then tails off into the bulk.

Introduction

The study of Ni deposition on Ag(001) was prompted by an attempt to explore novel atomic properties of Ni grown epitaxially on Ag. The motivation was to form a surface alloy (one to two atomic layers thick) which would have physical and chemical properties not found in bulk material. Previous studies [1] have suggested that the Ni does not form a sharply segregated layer but instead there evidence for clustering of the Ni below the surface (figure 1) are white. This is the model which has been inferred from from previous measurements.

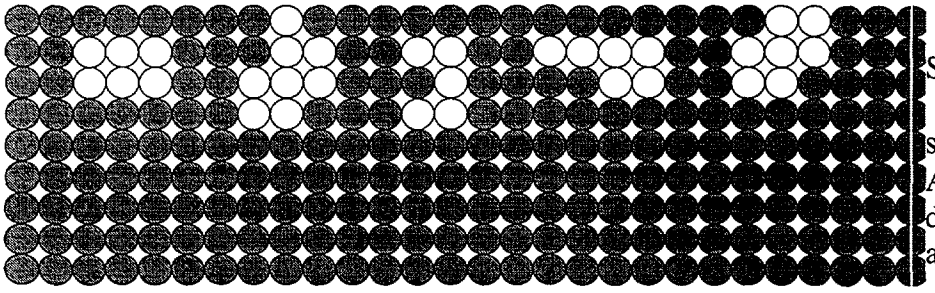

Figure 1 Side view of an Ag(001) surface. The Ag atoms are dark and the Ni atoms

The current study used Low Energy Ion Scattering of 2keV Li+ and Ne+ to determine the structure and composition of the surface and near-surface region. The sample was sputter cleaned until no evidence of contamination was found using LEIS. It was then annealed and the cooled to room temperature before depositing approximately one monolayer of Ni on the surface by thermal evaporation from a filament. Analysis was performed by depth profiling as well as polar and azimuthal scans using LEIS.

Results

The preliminary results from sputter profiling of the sample under low fluence (fig two) revealed that the subsurface concentration of Ni was greater than the surface concentration. This supports the previous findings that Ni did not form a surface alloy (one to two atomic layers thick) but instead diffused to form a macroscopic subsurface layer.

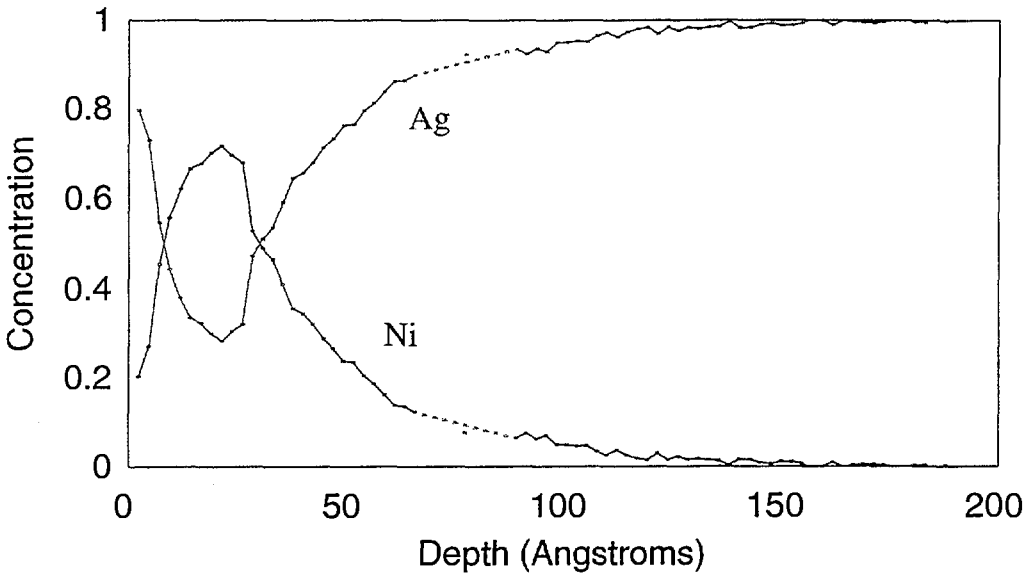

Figure 2

Amorphous zone evolution in Si during Ion bombardment

Sergei O. Kucheyev

Department of Electronic Materials Engineering, Research School of Physical Sciences and Engineering, Australian National University, Canberra, Australia, E-mail: sok109@rsphysse.anu.edu.au

1. Introduction

Heavy ion induced damage in crystalline Si has been extensively studied for the last several decades. It has been experimentally ascertained that if the damage level in the collision (sub)cascade volume exceeds some threshold value, an amorphous zone in a crystalline matrix can be created (see, *e.g.*, Refs.[1-5]).

Such amorphous zones (a-zones) have been directly observed by transmission electron microscopy (TEM) for the low dose heavy ion bombardment of Si at relatively low temperatures (at room temperature and below). Such a-zones in a surrounding crystalline matrix are also expected to be formed during ion bombardment at elevated temperatures (T ~ 200-550 °C), but their direct post-implantation observation is difficult because of dynamic annealing of displacement damage during implantation. Dynamic annealing can occur via both direct thermal and ion beam assisted processes. These processes are rather effective since the annealing temperatures for a-zones have been shown to be much lower than those required for crystallization at a planar amorphous-crystalline (a/c) interface for thermal [2,5,6] and ion beam induced crystallization [4,7-10]. This reduction of the annealing temperature has been successfully explained on the basis of the additional driving force available for crystallization from the derivative of the surface free-energy density of a curved phase boundary [11-13].

Although a lot of work has been undertaken to understand the formation and stabilization of a-zones in Si, very little effort has been made to study their thermal and, especially, ion / electron beam induced evolution.

Isolated amorphous zone evolution during direct thermal annealing has been theoretically studied based on a modified Gibbs-Thomson approach [11-13] and by molecular dynamics simulation [14]. However, the consideration of ion beam mediated annealing has remained a matter of uncertainty, particularly as to the micro-mechanism of non-equilibrium ion beam induced crystallization and the inapplicability of purely thermodynamic approaches. For example, molecular dynamics simulations are questionable due to the long time scale of dynamic annealing processes and the large number of atoms in the collision cascades produced by high energy ions. Furthermore, ion beam induced a-zone growth which is expected to occur for certain implant conditions (low sample temperature and high ion flux) has not yet been studied.

In this report a-zone evolution in Si is considered based on a point defect diffusion model for ion beam induced crystallization and amorphization in Si [15,16] modified to take into account purely thermal annealing and the additional interfacial driving force for crystallization. In addition, the previously unconsidered problem of determination of the a-zone size distribution under different implant conditions is addressed and solved for a possible case of a-zone annealing behavior. Possible experiments necessary to test this theoretical treatment are also proposed.

Although in the present study the main emphasis will be on the a-zone evolution in crystalline Si during ion bombardment, the developed formalism can be applied as well to a more general problem of grain evolution in two phase elemental systems and especially to the crystalline zone evolution in an amorphous matrix [17].

2. *Isolated Zone Evolution*

In the present discussion all a-zones are assumed to be spherical and amorphous, *i.e.*, homogeneous regardless of the real structure, defect types and concentrations in amorphous Si [18]. Of interest is the time dependence of the a-zone radius *dr/dt*, which is assumed to consist of direct thermal annealing $(dr/dt)^{th}$ and ion beam mediated crystallization / amorphization $(dr/dt)^{ion}$ terms: $dr/dt = (dr/dt)^{th} + (dr/dt)^{ion}$.

Based on the simple model [15,16], the ion beam induced amorphous-crystalline phase transition rate is proportional to a linear superposition of the point defect fluxes from the crystalline part of the structure to the a/c interface. If the activation energies for defect migration are higher than those for defect recombination at the a/c interface – an assumption which is not unreasonable – the model [15,16] yields:

$$(dr/dt)^{ion} = - \alpha_1(T)/(2 \cdot r), \quad \text{for } r > r_0, \tag{1}$$

where r_0 is a minimum a-zone radius; the coefficient α_1 depends on the irradiation conditions (ion species and energy, temperature, beam flux) determining the quasi-stationary concentrations of point defects during ion bombardment. It is interesting to note that the possible dependence of the a/c interface recombination rates for point defects on the a-zone radius due to the additional interfacial driving force does not influence the form of Eq. (1), which is determined by the diffusion limited radius dependence of the point defect concentrations at a spherical a/c interface.

Based on a modified Gibbs-Thomson formalism [11-13], the direct thermal annealing rate can be described as $(dr/dt)^{th} = - [\beta(T) + \alpha_2(T)/(2 \cdot r)]$, where $\beta(T)$ is a radius independent term corresponding to thermal crystallization at a planar a/c interface. Because we are interested in crystallization at relatively low temperatures ($T < 500$ °C) when direct thermal crystallization at a planar a/c interface in Si is almost negligible, but thermal shrinkage of amorphous inclusions with curved a/c boundaries does take place [2,5,6], the following annealing law will be assumed: $(dr/dt)^{th} = - \alpha_2(T)/(2 \cdot r)$.

Therefore, the final a-zone radius behavior can be written as

$$dr/dt = (dr/dt)^{th} + (dr/dt)^{ion} = -\alpha(T)/(2 \cdot r), \tag{2}$$

where $\alpha = \alpha_1 + \alpha_2$. It is interesting to note that *dr/dt* has the same dependence on the a-zone radius, *r*, for both direct thermal and ion beam assisted regimes. The Eq. (2) leads to the following evolution expression for a spherical a-zone during ion bombardment:

$$r(t) = [r(0)^2 - \alpha(T) \cdot t]^{1/2}, \tag{3}$$

where $\alpha > 0$ corresponds to a-zone shrinkage and $\alpha < 0$ to its growth. For large $r(0)$, the a-zone radius linearly depends on the irradiation dose:

$$r(t) \approx r(0) - [\alpha(T)/(2 \cdot r(0))] \cdot t, \quad \text{for } r(0)^2 >> \alpha(T) \cdot t. \tag{4}$$

Although general features of the obtained *dr/dt* expression – the zones with smaller radii anneal faster than those with bigger ones – is consistent with the results of the semi-quantitative TEM study of amorphous zone evolution during room temperature 60 keV He^+ ion bombardment reported by Abroyan and Nikulina [8,9], to the present author's knowledge, no direct measurements of $r(t)$ dependence have yet been done during elevated temperature ion bombardment, and, therefore, the preceding analysis cannot yet be verified.

On the other hand, the experimental results of Battaglia *et al.* [7] on the Rutherford backscattering (RBS) study of 600 keV Kr^+ induced annealing and damage accumulation in Si crystals with pre-existing disorder produced by low dose 150 keV Au ions support the $r(t)$ dependence given by Eq. (4). However, using such RBS results to test the theoretical result is rather complicated because 150 keV Au ions create a-zones with a relatively broad radius distribution. Consequently, the approach developed below is recommended.

3. Zone Size Distribution

During elevated temperature bombardment of Si monocrystals by heavy or intermediate mass ions, a-zones are generated directly in collision (sub)cascades and dynamically annealed at the same time. To my knowledge, this process has not been described theoretically in the literature and, hence, is considered below.

The radius distribution of a-zones is proposed to be governed by the following kinetic partial differential equation:

$$\frac{\partial f}{\partial t} + \left(\frac{dr}{dt} \right) \cdot \frac{\partial f}{\partial r} = G(r), \tag{5}$$

where $f(r,t)$ is the a-zone radius distribution function ($f(r,t)\cdot dr$ represents the instantaneous concentration of a-zones with $r \in [r, r+dr]$); $G(r)$ is the a-zone generation function which is assumed to have a maximum and meet the following requirements: $G(r) \rightarrow 0$ when $r \rightarrow 0, \infty$. The latter limit ($r \rightarrow \infty$) is quite obvious, while the former limit ($r \rightarrow 0$) comes from TEM measurements of the a-zone radius distribution after ion bombardment [8,9] and is consistent with the simple vacancy out-diffusion model for a-zone formation [19].

A number of analytical functions $G(r)$ meet the conditions given above, one of the possible functions being

$$G(r) = A \cdot r \cdot \exp(-r/R_m) \cdot h(t) \cdot h(r-r_0), \tag{6}$$

where A and R_m are the parameters describing a-zone generation, and $h(x)$ is the Heaviside's function ($h(x) = 0$ for $x < 0$, and $h(x) = 1$ for $x \geq 0$). With dr/dt and $G(r)$ in the forms of Eqs. (2) and (6) the solution of the differential equation (5) in the stationary regime for the case when a-zone formation and dynamic annealing are balanced gives

$$f(r,\infty) = (2 \cdot A \cdot R_m/\alpha) \cdot \exp(-r/R_m) \cdot [r^2 + 2 \cdot r \cdot R_m + 2 \cdot R_m^2]. \tag{7}$$

It is assumed in Eq. (7) that all temperature dependencies are contained in the factor $(2 \cdot A \cdot R_m/\alpha)$.

In a number of cases it is convenient to describe the real continuous a-zone radius distribution by the average radius $\langle r \rangle$, which can be easily calculated provided that $f(r,t)$ is known, although its direct experimental determination during elevated temperature ion bombardment is rather difficult. Equation (7) gives $\langle r \rangle = 2 \cdot R_m$, which coincides with the mean radius for the proposed generation function (Eq. (6)). This result seems rather surprising: $\langle r \rangle$ is independent of temperature, which, on the other hand, is consistent with recent results of the computer simulation of ion beam induced epitaxial crystallization and amorphization in Si where all disordered regions generated and dynamically annealed during ion irradiation were assumed to be described by a certain average radius [15]. Moreover, using several algebraic and exponential $G(r)$ functions and Eq. (5), we have shown that $\langle r \rangle$ is temperature independent and greater or equal to the mean radius for the generation function. The latter feature is determined by the simple fact that the zones with smaller radii anneal faster than those with bigger ones. The obtained $\langle r(T) \rangle$ behavior, however, is due to the assumed simple form for dr/dt (Eq. (2)). More complex analytical dr/dt expressions have been shown to give a weak temperature dependence of the average a-zone radius in the stationary regime.

As mentioned above, in order to describe the RBS results on the ion beam induced annealing of the pre-existing damage produced by heavy ion bombardment [7], one should take into account the a-zone radius distribution. In this case, Eq. (5) can be used with $G(r) = 0$ and the following obvious initial and boundary conditions: $f(\infty,t) = 0$ and $f(r,0) = G_1(r) \cdot t_1$, where $G_1(r)$ is the a-zone generation function for heavy ions, and t_1 is the time of irradiation by heavy ions. For example, Eq. (5) with the initial a-zone distribution, $G_1(r) \cdot t_1$, given in the form of Eq. (6) yields:

$$f(r,t) = A \cdot t_1 \sqrt{r^2 + \alpha t} \exp\left[- \frac{\sqrt{r^2 + \alpha t}}{R_m} \right], \tag{8}$$

which can be used to fit the effective number of scattering centers obtained by RBS. Nevertheless, this approach only seems to be useful to test the dr/dt dependence if we know the numerical values of A and R_m. The exact determination of these parameters is difficult due to the ill-posed nature of this

mathematical problem, given the accuracy of the experimental results and the theoretical assumptions made.

4. Conclusions

The understanding of a-zone evolution during ion bombardment is of great importance in micro- and nanoelectronics. In such applications, amorphous region generation and simultaneous annealing should be taken into account for a correct prediction of the damage distribution and for a correct consideration of radiation damage processes in general.

In order to verify the theoretical results presented in this report, the following experiments could be proposed.

(1) TEM study of the stabilized a-zone size distribution after heavy ion bombardment at different temperatures.

(2) *In situ* TEM study of isolated a-zone evolution (zone shrinkage and growth) during ion / electron irradiation. It should be noted that the work reported by Jencic *el al.* [20,21] was more focused on the a-zone shrinkage in Si during irradiation by electrons with the energy lower than the threshold energy required to produce atomic displacements.

(3) *In situ* TEM study of the a-zone radius distribution during heavy ion bombardment at elevated temperatures for the case when a-zone production and dynamic annealing are balanced.

References

[1] J.W. Mayer, L. Eriksson, J. Davies, Ion Implantation in Semiconductors, Academic Press, 1970.

[2] L.M. Howe, M.H. Rainville, Nucl. Instr. and Meth. B 19/20 (1987) 61.

[3] J. Washburn *et al.*, Nucl. Instr. and Meth. 209/210 (1983) 345.

[4] M.O. Ruault *et al.*, Phil. Mag. A 50 (1984) 667.

[5] L.M. Howe, M.H. Rainville, Nucl. Instr. and Meth. 182/183 (1981) 143.

[6] G.L. Olsen, J.A. Roth, Mater. Sci. Rep 3 (1988) 1.

[7] A. Battaglia, F. Priolo, E. Rimini, G. Ferla, Appl. Phys. Lett. 56 (1990) 2622.

[8] I.A. Abroyan *et al.*, in: Abstracts of All-Russian Conf. "Ion Beam Modification of Materials," Chernogolovka, Russia, 1987, p. 217.

[9] L.M. Nikulina, Ph.D. Thesis, Leningrad Polytechnical Institute, 1987.

[10] R.G. Elliman *et al.*, Nucl. Instr. and Meth. B 19/20 (1987) 435.

[11] G. Carter, Phil. Mag. A 68 (1993) 1091.

[12] G. Carter, Phil. Mag. A 69 (1994) 583.

[13] G. Carter, M.J. Nobes, R.G. Elliman, Vacuum 45 (1994) 1197.

[14] M.J. Caturla *et al.*, Phys. Rev. B 54 (1996) 16683.

[15] A.I. Titov, S.O. Kucheyev, in: Proceedings of XIV International Conference on Ion-Surface Interactions, Zvenigorod, Russia, 1999.

[16] A.I. Titov, S.P. Voskoboynikov, S.O. Kucheyev, Bull. Russian Acad. Sci., Phys. 62 (1998) 867.

[17] C. Spinella, S. Lombardo, S.U. Campisano, Appl. Phys. Lett. 57 (1990) 554.

[18] S. Knief, W. von Niessen, T. Koslowski, Phys. Rev. B 58 (1998) 4459.

[19] F.F. Morehead, B.L. Crowder, Rad. Eff. 6 (1970) 27.

[20] I. Jencic *et al.*, J. Appl. Phys. 78 (1995) 974.

[21] I. Jencic *et al.*, Nucl. Instr. and Meth. B 148 (1999) 345.

Simulation studies of the optimal depth resolution of heavy ion ERDA for H/D profiling in silicon

M.M.Li and .J.O'Connor

Department of Physics, University of Newcastle Callaghan, NSW 2308, Australia

Instruction

The heavy ion Elastic Recoil Detection Analysis (ERDA) technique has been extensively employed for profiling light elements including H and D in the thin film. In analysis of depth profiling, the most concerned parameter is the depth resolution, which is limited by a number of factors such as the kinematic effects, the energy resolution of a detector, and the energy straggling of the recoiled ions. While there have been some experimental and theoretical studies of the optimal depth resolutions using He, C and Ne ions, a comprehensive survey of optimizing depth resolution for more heavy projectiles with conjunction of a specific sample has not been reported yet. In this work, the optimization conditions of depth resolution for heavy projectile ($17 \leq Z_1 \leq 79$) ERDA were studied by extensive simulation calculations.

Simulation

The depth resolution δx at a sample depth x is given by

$$\delta x = \delta E / [S]$$

where [S] is the energy loss factor and δE is the total energy spread, which has contributions from the beam itself spread, geometry, straggling in target of projectile, multiple scattering and energy resolution of the detector. A detailed description of these terms of energy spread can be found in literature [1,2]. It is readily demonstrated that the depth resolution δx depends on the incident energy E of projectile, the identity Z_1 of species and geometry condition and these factors are not independent. To attain an optimal depth resolution a wide range of possible values of atomic number of projectile, incident energy and geometry parameters should be investigated. In order to optimize these parameters, a comprehensive theoretical investigation has been made to compare the performance of heavy projectiles (Cl, I, Ni and Au) over the energy range of 1—60MeV by extensive simulation calculations using MDEPTH code [3]. The possible optimization conditions also are influenced by the recoil scattering cross section and the detectable energy range, which need to be considered comprehensively. In the simulation study, a Si surface within a small level of hydrogen and deuterium is chosen to be an example of a target. The energy resolution is assumed to be 1%, which is a typical value for some detector systems, for example an electrostatic spectrometer. We give a comprehensive evaluation on contributions to depth resolution and recoil cross-section from ion species, incident energy and geometry conditions.

Results and Discussion

The recoil cross section is proportional to $\cos^{-3}\Theta$, where Θ is recoil scattering angle. It is obvious that the bigger recoil angle is used, the larger recoil cross section is obtained and hence the more yield of recoil sample atoms. However, the recoil energy has a strong dependence on the recoil angle, which can be approximately written as $\Delta E_r/E_r = -2\tan\Theta\Delta\Theta$. The large kinematic energy spread will limit the total energy resolution. Besides, it is also necessary to consider selecting an appropriate Θ angle to make the energy of recoil particles in the region of maximizing stopping power of recoil. These factors have been included in this study. Figure 1 and figure 2 show the depth resolution curves for deuterium in Si against projectile energy by simulation calculations. It can be seen that for both small and large incident angles the optimal depth resolutions lie at lower energy positions. With increase of

incident energy, the depth resolutions for light projectiles increase more sharply than heavier ions for the large incident angles. For small incident angle α, there is not significant difference for the depth resolution of Au and I. As the heavy projectile may cause severe irradiation damage for certain target materials, projectile Au can be replaced by I ions without losing the optimal feature of depth resolution in the case of small incident angle, when it is required.

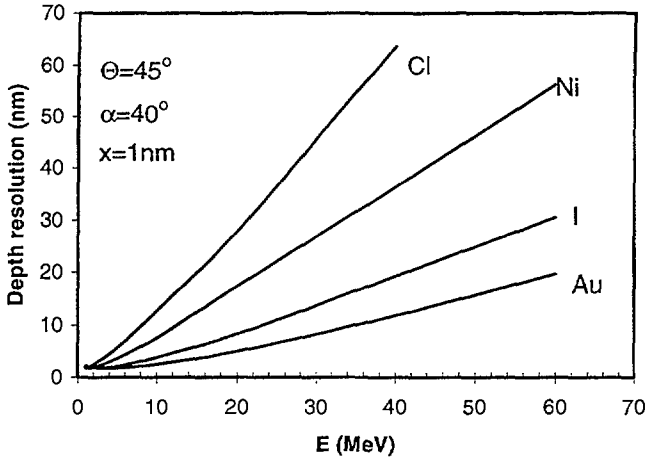

Figure1 Simulated ERDA depth resolution for D in Si near surface (x=1nm) as a function of incident energy at large incident angle α. Θ is the recoil scattering angle

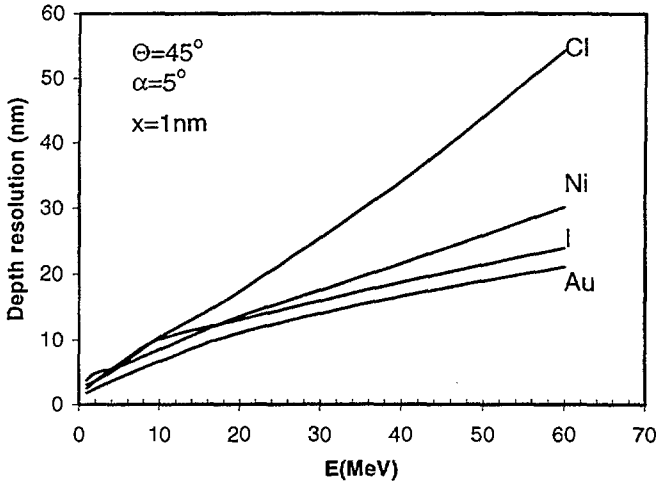

Figure2 Simulated ERDA depth resolution for D in Si near surface for D in Si near surface (x=1nm) as a function of incident energy at small incident angle.

Figure3 compares the simulated depth resolution for four species (Cl, Ni, I and Au) as a function of the geometry at a fixed energy. The better depth resolutions are achieved at larger α. This is informative for the geometric set-up in an ERDA experiment. Figure4 shows calculation results of depth resolutions at depth 100nm, where the better depth resolution is obtained by using lighter projectiles at small incident angle.

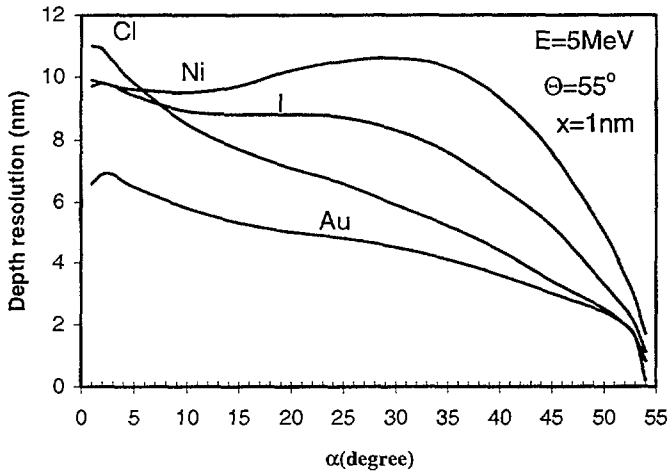

Figure3 Simulated depth resolution variation with incident angle α for D in Si near surface (x=1nm).

Due to the greater damage induced by irradiation of heavy projectile, special consideration should be given to increase recoil cross section and hence to shorten the irradiation times in order to reduce irradiation effect. The larger recoil cross section due to an appropriate combination among various conditions has been taken into account to achieve a good statistics.

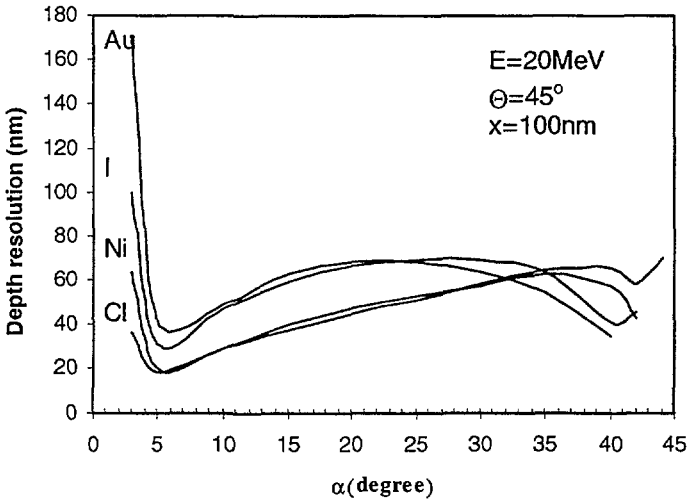

Figure4 Simulated depth resolution variation with incident angle α for D in Si at depth 100nm.

References

[1] D.J.O'Connor and Tan Chunyu, Nucl.Instr. and Meth. B 36 (1989) 178.

[2] F.Paszti, E.Szilagyi and E.Kotai, Nucl.Instr. and Meth. B 54(1991) 507.

[3] E.Szilagi, F.Paszti and G.Amsel, Nucl.Instr. and Meth. B 100(1995) 103.

A study of charge state approach to the stopping power of MeV B, N, and O ions in carbon

M.M. Li[1], D.J. O'Connor[1], H. Timmers[1] and P.C. Dastoor[1], Robert A. Langley[2]

[1]Department of Physics, University of Newcastle, Callaghan, NSW 2308, Australia
[2]Oak Ridge Scientific Consultants, Kingston, TN 37763, USA

Abstract

The charge state approach has been applied to treat the electronic stopping powers of swift O, N and B ions in carbon foil. According to the charge state model, the contributions to the electronic stopping power of energetic projectiles passing through solid targets are due to collisional interactions and from the charge exchange process. The definition of fractional effective charge from Brandt and Kitagawa has been combined into the current charge state model. Extensive applications of this approach require data of the equilibrium charge state distributions and knowledge of charge-exchange cross sections—involving electronic capture and loss processes. Both measured data and empirical calculations of the equilibrium charge state fraction are used in the study, and the electronic capture cross sections are obtained with the eikonal Brinkman-Kramers approximation (EBK). By comparing the numerical results with the latest experimental data as well as empirical values, it is shown that the present approach slightly overestimates the energy loss at the intermediate velocity region.

1.Introduction

The advent of MeV ion implantation and the application of heavy ion beams for surface analysis have stimulated a renewed interest of the stopping power of ions in solids. In the past, a large amount of experimental data has been accumulated. Based on these data, comprehensive compilations and empirical formulas for stopping power have been produced [1]. Among the data in the compilations, those corresponding to high and low velocity regime are reasonably accurate, however, some experimental data in the intermediate velocity region are less accurate. In the intermediate velocity region, where the projectile velocity is around $Z^{2/3}v_0$, the interaction between a projectile and the target atom is complicated and the mechanism of charge-exchange process is only now becoming clearly understood.

The charge state approach has been successfully applied almost exclusively for the case of light ions in aluminium [2], but so far few other systems have been investigated yet. The reason is possibly due to difficulties for determining precisely the charge-exchange cross section of heavy ions in a solid target. The purpose of the present study is to calculate the stopping powers for B, N and O ions in carbon over the intermediate and high velocity regime by the charge state approach, and to compare them with the experimental results.

2.Charge state approach

In the charge state model, the fractional stopping power of singly charged projectiles can be obtained by scaling to that of the bare nucleus of the projectile. The collision term in the stopping power is determined from all individual charge states weighted by their equilibrium charge fraction. The total stopping power consists of the collision term and charge-exchange term as follow [3]

$$S = \sum_{Q} f_Q \zeta^2 S_{q=1} + \sum_{Q} \sum_{Q' \neq Q} f_Q \sigma_{Q \to Q'} U_{Q \to Q'} \qquad (1)$$

where Q is the charge state from +1 to +Z, f_Q the equilibrium charge state fraction, $\sigma_{Q \to Q'}$ the charge exchange cross section from the charge state Q to Q′, and $U_{Q \to Q'}$ is the energy transfer

in the related charge exchange processes. The fractional effective charge ζ is a function of ionization fraction q and solid property, which can be derived from the Brandt and Kitagawa theory [4].

3.Charge exchange parameters and calculations of stopping power

It can be seen from the charge state description of stopping power that the equilibrium charge fraction f_Q as well as the charge exchange cross section are the two most important parameters to describe the charge exchange process of energetic ions moving in the solid target. The measured data of equilibrium charge distribution have been compiled by Shima et al. [5]. Although a wealth of experimental data for various heavy ions passing through thin carbon foils have been available from compilations, some data for a given projectile only cover a few sparse energy values. For unavailable data at some energy position, the Shima empirical method [5] has been utilized to calculate the equilibrium charge distribution in the study. In addition, we have performed some measurements about O and B ions in carbon.

Another important parameter is the charge exchange cross section, which involves the electron capture and loss processes. Three different charge transfer processes—Auger process, Resonant process and Shell process, have been proposed to understand electronic charge exchange mechanisms [6]. Full calculations of the electronic capture and loss cross sections for the three processes are very complicated. Fortunately, in the case of high projectile energies, the problem appears relatively simple, because it has been demonstrated that the capture cross section is dominated by the shell process while the loss cross section is mainly due to the resonant process, whilst the above three processes can occur inside the target simultaneously. The capture cross section of the shell process can be calculated with eikonal Brinkman-Kramers approximation (EBK). On the other hand, the electron loss cross section can be obtained by considering the single-electron process. For single-electron processes there exists a relationship between electron capture and loss cross section

$$f_Q \sigma_{Q \to Q+1} = f_{Q+1} \sigma_{Q+1 \to Q} \qquad (2)$$

4. Results and discussions

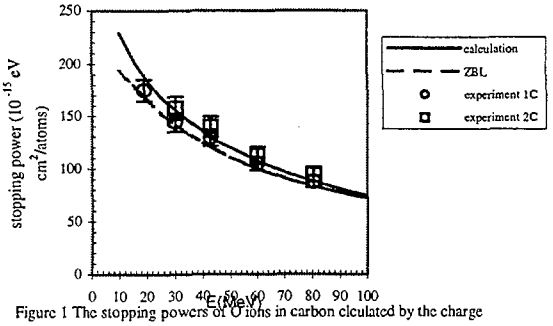

Figure 1 The stopping powers of O ions in carbon clculated by the charge state model approach and compare with the ZBL and experimental values.

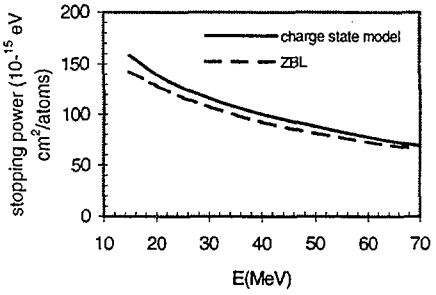

Figure 2 Comparison of stopping powers by the charge state approach calculations with the ZBL for N ions in C.

Using the charge state fractions and EBK cross sections as well as the fractional effective charge values, the stopping powers for swift O, N and B ions in carbon have been calculated . The results are shown in figures 1-3, along with the latest measured data [7]. Measurements of stopping power with O ions (beam 19, 30, 43, 60 and 80MeV) through carbon foils with two sets thickness have been performed recently at the Australian National University [7]. From figure 1, the data of different thickness sample are reasonably consistent within the uncertainties of the foil thickness. The measured data for O ion in carbon are higher from 1.4% to 7.5 % than Ziegler et.al. (ZBL) [1] values in the case of one carbon foil, and higher around 14% for the case of two carbon foils. The calculated results from the charge state

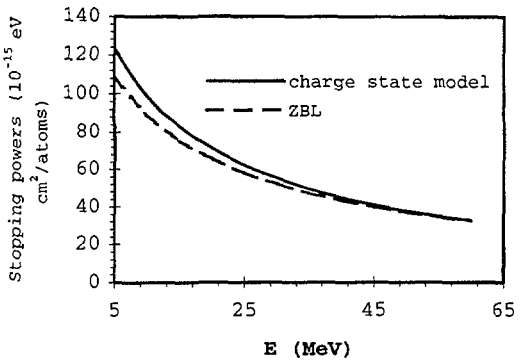

Fig.3 Comparison of stopping powers by the charge state model calculations with the ZBL [1] for B ions in C.

model agree with the latest measurements well. On the other hand, the calculated stopping power are higher from 3% to 18.5% than ZBL values, depending on the incident energy of projectile. The greater deviation between calculated and the ZBL values for those below 15MeV may be attributed to the BK model of effective charge being a poor approximation at the lower boundary edge of the intermediate velocity regime. From figure 1, it is also obviously seen that the charge exchange contribution to stopping power is small at high energies. This is a tendency as expected, as the projectile is stripped increasingly till fully stripped with higher incident energy and meantime the charge-exchange decreases to zero.

The wide application of the charge state approach requires comprehensive knowledge of the equilibrium charge distribution and charge-exchange cross sections. Since equilibrium charge state distributions for any combination of projectile and solid material are incomplete, extensive calculations using this approach seem seriously being hampered. However, a recent experiment [8] reveals that the equilibrium charge state distributions of energetic ions through target depend very weakly on the target material. If more experimental evidences confirm this conclusion, it will shed a light for extending the charge state model to calculate stopping power of any combination of incident ion and target material.

References

[1] J.F.Ziegler, J.P.Biersack and U.Littmark, The Stopping and Range of Ions in Solids (Pergamon, New York, 1985).

[2] A.Arnau etc, Nucl. Instr. and Meth. B 69 (1992) 102.

[3] Q.Yang, Phys.Rev.A 49 (1994) 1089.

[4] W.Brandt and M.Kitagawa, Phys.Rev. B 25 (1982) 5631.

[5] K.Shima, T.Mikumo and H.Tawara, At.Data Nucl.Data Tables 34 (1986) 357.

[6] F.Sols and F.Flores, Phys.Rev. A 37 (1988) 1469.

[7] M.M.Li and H.Timmers etc. ANU Annual Report 1998,

[8] W.Jiang, Ph.D thesis, the Institute of Ion Beam Physics and Materials Research, 1998

Combined atomic force microscopy (AFM), X-ray photoelectron spectroscopy (XPS) and quartz crystal microbalance (QCM) studies of glucose oxidase (GOx) immobilised onto self-assembled monolayer on the gold film

Dusan Losic, [1] J. Justin Gooding, [2] Joe Shapter[1] Paul Erokin[2] and Ken Short [3]

[1] Faculty of Science and Engineering, The Flinders University of South Australia, Adelaide 5001
[2] School of Chemistry, The University of New South Wales, Sydney 2052
[3] Materials Division, ANSTO, Lucas Heights, NSW 2234

Summary

In fabrication of biosensors, self-assembled monolayers (SAM) are an attractive method of immobilizing enzymes at electrode surface since it allows precise control over the amount and spatial distribution of the immobilized enzyme. The covalent attachment of glucose oxidase (GOx) to a carboxylic terminated SAM chemisorbed onto gold films was achieved via carbodiimide activation of the carboxylic acids to a reactive intermediate susceptible to nucleophilic attack by amines on free lysine chains of the enzyme. Atomic force microscopy (AFM), X-ray photoelectron spectroscopy (XPS) and quartz crystal microbalance (QCM) measurements were used for characterization of GOx modified gold surfaces. Tapping mode AFM studies have revealed that GOx molecules form slightly disordered arrays of pentagonal or hexagonal clusters. Observed features of immobilised GOx are distributed as a submonolayer on the SAM surface which has allowed visualisation of native and unfolded enzyme structure. The presence of the SAM and enzyme on the gold surface was detected by XPS spectroscopy. Spectra show typical peaks for the C 1s, O 1s and N 1s regions. A kinetic study of the adsorption of GOx onto activated SAM using in-situ QCM allowed determination the amount of immobilised GOx on the layer and consequently the optimal immobilisation conditions. Performance parameters of the biosensor such as sensitivity to glucose concentration as a function of enzyme loading were evaluated amperometrically using the redox mediator *p*-benzoquinone.

Introduction

Biosensors are increasingly becoming practical and useful tools in medicine, food quality control, environmental monitoring and research. The coupling of biorecognition molecules such as enzymes, antibodies or whole cells with either electrochemical, optical or piezoelectric signal transducer is the basis of a biosensor.[1] Immobilisation of the biological molecule is a particularly demanding aspect of the fabrication biosensors as the immobilisation procedure must reproducibly maintain the biorecognition molecule close to the transducer surface while retaining its biological activity.[2] Many physical and chemical methods for immobilising enzymes on solid electrode surface, like adsorption and physical entrapment within membranes, have been widely used.[1] Recently covalent attachment on self-assembled monolayer (SAM) has been investigated as a new, promising strategy for fabrication of a variety of biosensors.[2] Self-assembled monolayers (SAM) can potentially provide a reproducible and robust method of fabricating immobilised enzyme layers with considerable control over the orientation and distribution of the enzyme[2]. The well-ordered monolayers formed by alkanthiols on metal surfaces can be used to immobilise of single layer of enzymes close to an electrode surface with a high degree of control over the molecular architecture of the recognition interface[3] Some techniques such as electrochemistry [4, 5], ellipsometry [6], scanning tunneling microscopy (STM)[7], atomic force microscopy (AFM) [8], FTIR and X-ray photoelectron spectroscopy (XPS) [9], surface plasmon resonance [10],

quartz crystal microbalance (QCM) [11] have been employed for examination of covalent immobilisation of enzyme onto the SAM.

Glucose oxidase (GOx) is a common enzyme used in electrochemical biosensors for determination of glucose in medical and industrial situations. Our pervious studies [3,4,11] have been concerned with optimilisation of a procedure to ensure reproducible enzyme loading and defined morphology which may result in fabrication of more reproducible devices.

This abstract presents study of glucose oxidase electrode as a biosensor fabricated by direct covalent attachment of GOx onto SAMs. A combination of techniques are used, such as AFM, XPS and QCM, for the characterization of the sensing interface in an attempt to correlate the surface structure with the amperometric response of the resultant enzyme electrode.

Experimental Section

The enzyme electrodes were fabricated by the self-assembly of 3-mercaptopropionic acid (MPA) onto gold from an ethanolic solution as described previously [2,5] (see Figure 1).

Figure 1 Schematic representation of the immobilisation of GOx to a SAM on a gold surface

Gold films were prepared by gold evaporation onto silanised glass slides by (3-mercaptopropyl) trimethoxysilane (MPS). [12]. The carboxylic acid terminated SAM was immersed in a solution of 1-ethyl-3(3-dimethylaminopropyl) carbodiimide hydrochloride (EDC) and N-hydroxysuccinimide (NHS) to activate the SAM for enzyme immobilisation. The activated electrodes were then exposed to an enzyme solution where free amine groups on the enzyme surface nucleophilically attacked the succinimidyl-terminated SAM thus giving covalent attachment of the enzyme. Applied concentrations of GOx enzyme were 0.2 μg/mL, 2μg/mL, 10μg/mL, 25μg/mL, 120μg/mL, 300μg/mL, 480μg/mL and 600μg/mL with incubation times of 5, 30, 60, 90 and 120 minutes. Electrodes were thoroughly rinsed with the buffer solution and water and then dried and stored in a desiccator.

A Dimension 3100 AFM (Digital Instrument, Santa Barbara, CA) using Si_3N_4 cantilevers was used for imagining using tapping mode where tip lightly "taps" on the sample surface during scanning, contacting the surface at the bottom of its swing, see Figure 2.

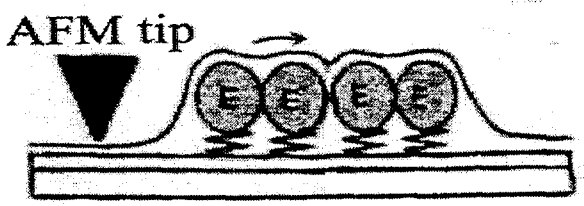

Figure 2 Idealized illustration of contact AFM tip and GOx enzyme covalently attached onto the SAM.

AFM images of bare gold, MPA modified gold and MPA-modified gold with immobilised with different concentration of GOx were obtained in air with optimally adjusted parameters of force curve, tip frequency, scan size and scanning speed. High-resolution images were difficult to achieve due to high interaction of tip as well as the highly flexible and soft surface of the GOx interface.

The enzyme electrode employed in the XPS studies were formed as described earlier. The analysis took place 1-3 days after the samples were prepared using XPS spectrometer with X–ray source of monochromated Al Kα line (1486.6eV).

The kinetics of the adsorption of GOx onto EDC/NHS-activated self-assembled monolayer of MPA were monitored in situ using a home made QCM. The enzyme loading was estimated by using a "dip-and-dry" method that involved the measurement of the resonant frequency of a quartz crystal before and after enzyme immobilisation. Additionally, the amount of GOx immobilised was determined by stripping the active center from the enzyme, flavine adenine dinucleotide (FAD) out of the enzyme and fluorometrically measuring the concentration of FAD in solution [4].

The response of the enzyme electrode to glucose concentration was monitored amperometricaly at

+ 500 mV vs Ag/AgCl reference electrode in phosphate buffer with p-benzoquinone employed as a redox mediator.

Results and Discussion

AFM characterisation

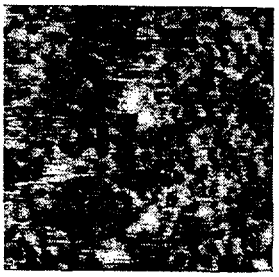

Surfaces of different samples of fabricated enzyme electrode made using different concentrations of GOx were studied by taping mode AFM in air. A typical image is presented in Figure 3 which shows the presence of array of pentagonal to hexagonal clusters with size of about 50nm in diameter.

Figure 3. A typical image of GOx enzyme immobilised on SAM concentration of 300µg/ml and deposition time of 60 minutes, scanning area 1um²

Profile analysis of enzyme surface shows an average height of 2-3nm which is much less then native GOx molecule. This may indicate that structures are in unfolded form but could also be an artifact of the AFM tip to provide a true profile of the surface relief. This is further confirmed by the apparent larger molecular size of individual GOx molecule in the AFM images. From the magnified images of linked group of clusters and isolated clusters shown in Figure 4a, 4b and 4c, a proposed model of immobilised GOx is shown in Figure 4d. Five to six GOx molecular units are linked in one ring and linked with other clusters to give an array structure of enzyme monolayer.

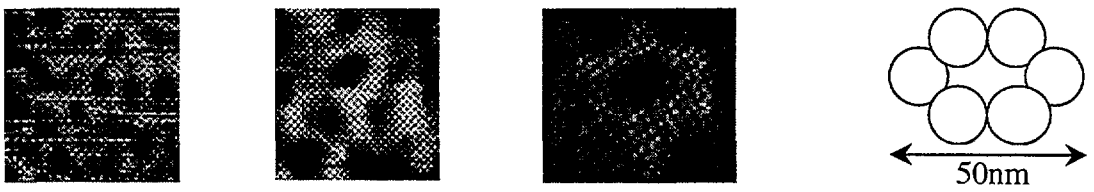

a) b) c) d)

Figure 4 . Magnified AFM images of GOx clusters with linked a) ten clusters b) two clusters c) one isolated hexametric cluster d) and proposed model.

This observation is in agreement with other studies of native GOx molecular structure[7,13] where the enzyme is described as dimeric protein containing one tightly bound flavin dinucleotide (FAD) per monomer and has ellipsoid shape with average diameter of 10nm per molecule. Similar images with same features are obtained for all samples with different concentration of GOx except for concentration of 0.2µg/ml which demonstrates that immobilisation from this concentration did not make uniform enzyme monolayer onto SAM. It is possible that small areas of assembled enzyme still exist on the surface but these were not

observed in the present experiment. Control experiments where the surface was repeatedly washed and then imaged with the AFM showed the clusters were robustly adhered to the surface. Furthermore, the AFM images obtained of bare gold, gold films with adsorbed MPA and activated MPA by coupling agent EDC/NHS did not show any of these surface features and possessed significantly different tip-sample interaction , thus providing strong evidence that these clusters are due to immobilized GOx.

The AFM images obtained in this way clearly distinguish arrays of linked GOx enzyme molecules which constructs a single monolayer on the SAM. These results correlate well with data from QCM and amperometric characterisation of electrode which shows good enzyme sensitivity to glucose as measured by a mediator redox system.

XPS, QCM and functional characterization

The steps in fabrications of enzyme electrode from assembly of MPA, activation with EDC/NHS and finally immobilisation of enzyme were assessed using XPS. The appearance of a N 1s signal (centered at 400.3eV) after activation step, a new component in the C 1s region (centered at 286.6eV) assigned to carbon atoms linked to sulfide group of NHS and an O 1s peak (centered at 531.6eV) assigned to oxygen atoms in the sulfonate group indicates that NHS was present on the surface. The presence of GOx immobilized on the surface of the SAM could be confirmed by changes of peaks in C 1s region attributed to the presence amino acid side chains of polypeptide backbone and in cabrbohydrate residues of its polysaccharide shell. The N 1s peak at 400.1eV was assigned to nitrogen atoms present in the amide bonds in the polypeptide chain, amino acid chain and N-acetylglucosamine residues.

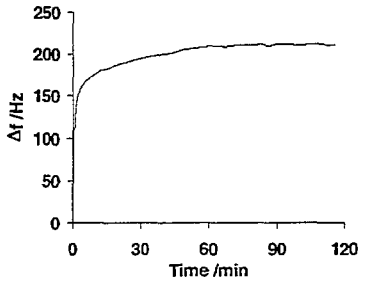

Figure 5. Response frequency change as function of time for adsorption of GOx

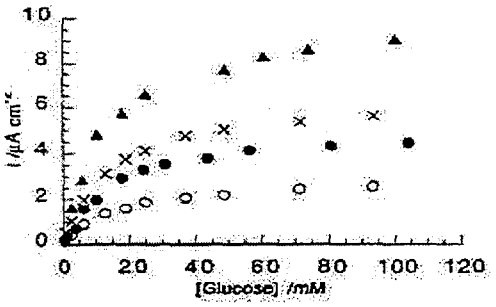

Figure 6. Influence of enzyme loading on the response to glucose concentration

The QCM study of kinetics of the adsorption of GOx onto DDC/NHS activated self-assembled monolayer of MPA monitored in situ is shown in Figure 5. These adsorption experiments indicate that extreme care must be taken when selecting the condition for enzyme immobilisation for reproducible sensor fabrication. It is clear that an initial 30 minute immersion period would have been insufficient to result in complete monolayer coverage. The optimal enzyme immobilisation procedure was chosen to be 90 minutes incubation in 480μg protein/ml of pH 5.5 buffer. These conditions would ensure complete monolayer coverage without a significant extension of the incubation period. Using this enzyme incubation time between electrode variability was reduced to less than 10%, reproducibility superior to that achieved with polymer immobilization [13]. Finally, the electrode prepared using optimised conditions exhibited a significantly improved reproducibility compared to those previously fabricated as illustrated in Figure 6 which shows the influence of enzyme loading (o) 0.08pmol/cm ^{2}, (•) 0.13pmol/cm^2, (x) 0.019pmol/cm^2 and (_) 0.29pmol/cm^2 versus the response of the enzyme electrode to glucose monitored amperometricaly with p-benzoquinone as a redox mediator.

Conclusions

AFM images of glucose oxidase covalently attached to self-assembled monolayers on gold were obtained. These give useful qualitative information about immobilized layer of the enzyme. Molecules of enzyme are assembled in single layer which shows pentametric or hexametric cluster structures of about 50nm in diameter which suggest a native and unfolded enzyme structure. In correlation with other techniques such as QCM, XPS and amperometric examination, it was shown that reproducibility and sensitivity of biosensor depends significantly on the procedure used in immobilisation of enzyme to the electrode. The covalent immobilisation of enzyme with alkanthiols is very promising immobilisation technology in fabrication of biosensors.

Acknowledgment

This work was supported by an AINSE grant which provided time on AFM facilities at ANSTO. We would also like to acknowledge financial support from the ARC.

References

Hall, E.A.H., Biosensors, 1990, Buckingham, Open University Press

J.J. Gooding, D.B. Hibert, TrAC, 18 (1999) 525.

J.J. Gooding, P. Erokhin, L. Pugliano, D.B. Hibbert, Conference Proceeding, Australian International Symposium on Analytical Science, Melbourne July 4^{th}-9^{th} (1999).

J.J. Gooding, M. Situmorang, P. Erokhin, D.B. Hibert, Anal. Commun., 36(1999) 000

J.J. Gooding, V.G.Prag, E.A.H. Hall, Anal. Chem., 70 (1998) 2396

G.P. Lopez, H.A. Biebuyck, R. Harter, A. Kumar, G.M. Whitesides, J.Am.Chem.Soc.,115(1993)10774

Q. Chi, J. Zhang, S. Dong, E. Wang, J.Chem. Soc. Faraday Trans., 90(1994)2057

A. Ikai, Surface Science Report, 26(1996)261

A. J. Guiomar, J. T. Guthrie, S. D. Evans, Langmuir 15(1999) 1198

M. Mrksich, G.B. Sigal, G.M. Whitesides, Langmuir 11(1995) 4383

K. Gaus, E.A.H. Hall., J. Colloid Interface Sci. 194(1997)364

R. Wilson, A.P.F. Turner, Biosensor & Bioelectronics 7(1992)165

E.A.H. Hall, J.J. Gooding, Mikrochim. Acta 121 (1995) 119.

A Clean Measurement of the Hydrogen Retardation of the Rate of Solid Phase Epitaxy in Silicon.

A. C. Y. LIU and J. C. McCALLUM
Microanalytical Research Centre, School of Physics, University of Melbourne, Parkville, Victoria 3052, Australia, amelia@mozart.ph.unimelb.edu.au

The rate retarding effects of the impurity hydrogen on solid phase epitaxy (SPE) in silicon have yet to be completely understood. Existing measurements of this behaviour do not coincide exactly, however, several features have attained prominence. Firstly, a linear decrease in the SPE rate is detected up until a certain concentration of hydrogen. Subsequent to this point the rate remains almost constant at around half the intrinsic rate. It is conjectured that the hydrogen bonds to and passivates the defects whose agency enables the incorporation of atoms from the amorphous phase to the crystalline. This rate reduction increases until the defect population is saturated. At this point the reduction in rate ceases. Secondly, a dependence on temperature has not been consolidated, in contrast with the trends observed with the doping species[1].

Here a method is proposed for producing a controlled concentration of hydrogen for the advancing amorphous/crystalline interface to encounter during epitaxy. A bubble layer is formed in crystalline silicon approximately $0.6\mu m$ beneath the surface through the implantation of hydrogen at $65keV$ with fluences of $4 \times 10^{16}/cm^2$ and $3 \times 10^{16}/cm^2$ and annealing for $1hr$ at $850°C$ in dry argon. The anneal doesn't outgas all the introduced hydrogen, leaving a remnant gas pressure in the bubbles. The hydrogen implants at the two fluences should yield two samples with different amounts of hydrogen trapped in the bubbles. A buried amorphous layer is created to encompass the bubble layer containing this residual contaminant through silicon self implantation at appropriate energies and fluences. The progress of the front interface of the buried amorphous layer is monitored by time resolved reflectivity (TRR) as SPE is effected at various temperatures[2].

It is known that the diffusion of hydrogen occurs in a similar temperature regime to that required for SPE. Thus at the temperatures associated with epitaxy, the hydrogen may diffuse distances of the order of several hundred nanometres. The complexities that arise from measuring the movement of an interface encountering an ever evolving profile are large, and hamper attempts to measure cleanly the influence of the contaminant. In this case the additional step of trapping the introduced species at the bubble layer pins the hydrogen at that depth, as initial sputtering ion mass spectroscopy (SIMS) studies of samples implanted with hydrogen at $4 \times 10^{16}/cm^2$ and partially crystallised at $600°C$ indicate. The results of these studies are seen in Figure 1.

The initial hydrogen profile after amorphisation demonstrates that the hydrogen has retained its peak concentration at around half a micron, avoiding potential problems with smearing associated with the amorphising implant. The data set labelled "before" represents a SIMS analysis of a sample that has been annealed to the point where the front interface has just encountered the hydrogen. It should be noted that while the annealing time and temperature for this sample has been sufficient for a significant intrusion of hydrogen from the surface to be apparent, the introduced hydrogen profile remains distinct from that of the infiltrating hydrogen. Contemporary studies indicate that the bubbles themselves are largely destroyed by an amorphisation of the material, yet the evidence presented here suggests that while this may be the case the hydrogen is still predominantly trapped at whatever sites it was originally bound to.

This is surprising since it is known that implanted hydrogen diffuses quite rapidly in amorphous silicon. Indeed an analysis of hydrogen's diffusing behaviour in amorphous silicon indicates that for the times and temperatures used in this study the characteristic diffusion length, $\sqrt{Dt}$, where D is the coefficient of diffusivity and t is the annealing time, would be greater than $5000\mathring{A}$[3]. Some of the hydrogen clearly conforms to this diffusion routine as is evident from the "tail" that extends from the peak hydrogen concentration into the amorphous layer, accounting for more than half of the implanted hydrogen. However, this leaves a significant portion trapped at the initial bubble layer. The curve denoted "after" is from a sample in which the interface has been permitted to pass through the hydrogen rich layer. Again the hydrogen profile is peaked, but as shown in the graph it has been picked up by the interface and displaced before it. The amount still trapped at $0.6\mu m$ is less than half that in the peaked region carried by the interface. The portion which has diffused into the layer is still more than half that which is variously trapped, either at the original depth, or conveyed by the interface. It is interesting to note that in both the "before" and "after" cases, the integrated implanted hydrogen concentrations exceed that of the original implanted concentration by a factor of approximately 2 suggesting that the quasi-infinite hydrogen reservoir at the surface has fed the diffusion into the amorphous layer. While the diffusion of the hydrogen is apparently complex, to all indications a controlled and virtually constant hydrogen concentration profile is encountered by the interface over the depth range sampled. This promises a precise measurement of the retarding effects of this contaminant.

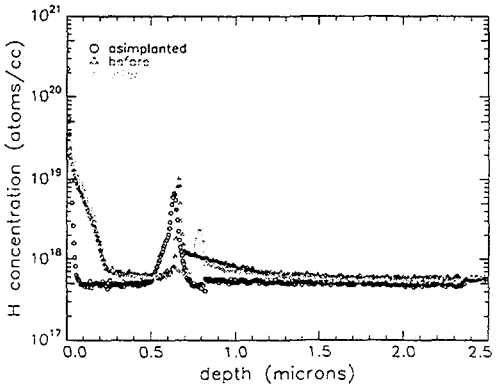

Figure 1: SIMS analyses of an asimplanted sample, a sample in which the interface has just encountered the hydrogen, and a sample in which the interface has been permitted to pass through the interface.

Figure 2 shows a representative TRR trace of a sample implanted with $4 \times 10^{16}/cm^2$ hydrogen and an intrinsic buried layer case for comparison. The reflectivity data was collected during an anneal at 580^oC in each instance. For the sample containing hydrogen the point at which the hydrogen is encountered by the interface is clear from the collapse in amplitude of the trace. This amplitude deflation is generally associated with the interface losing planarity. It may also be noted that the period of the curve decreases after this, indicating a decrease in the rate of crystallisation. Such a point is not distinguishable for the $3 \times 10^{16}/cm^2$ sample (not shown). These differences are illustrated quantitatively in Figure 3 which plots the velocity of the interface against depth, again obtained from anneals at 580^oC. The sudden decline in the velocity of the interface at $6000\mathring{A}$ is clear in the case of the $4 \times 10^{16}/cm^2$ sample. The slight collapse in the velocity as the interface reaches the remnant bubble layer in the $3 \times 10^{16}/cm^2$

case is a subtle, yet present, effect. It is curious that for the $3 \times 10^{16}/cm^2$ hydrogen implanted sample a recovery in interface velocity is seen.

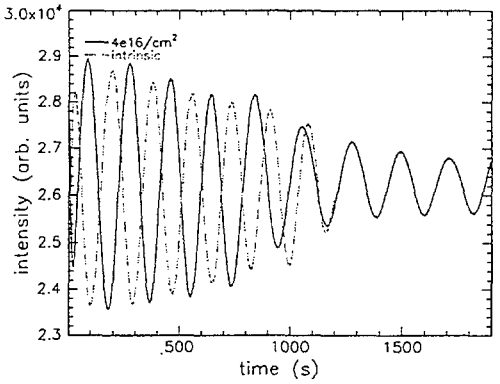

Figure 2: Typical TRR traces of a sample implanted with $4 \times 10^{16}/cm^2$ hydrogen and the intrinsic case. In this case annealing was performed at $580°C$. It is obvious from the sudden extinction of the amplitude at $1250s$ in the trace from the contaminated sample that the interface has encountered the residual bubble field. The lengthening of the period of this trace subsequent to this event is a more subtle effect.

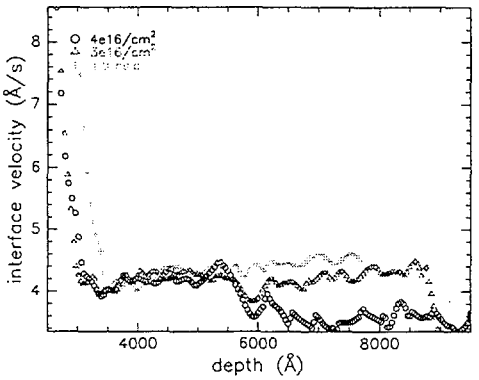

Figure 3: The effect of the hydrogen rich layer on epitaxy is more obvious in this display of interface velocity against depth. The sudden decline in velocity at the prescribed depth is apparent in both the samples containing hydrogen. It is curious that a recovery in epitaxial rate is seen in the $3 \times 10^{16}/cm^2$ case.

The results of the temperature series' ($500°C$ to $660°C$ in $20°C$ intervals) are shown in Figure 4. A self-normalised data set was prepared for each of the hydrogen implanted samples in which the "after" interface velocity was normalised to the "before" interface velocity. This may be done since as seen in the graph of interface velocity against position, the velocity of the interface prior to encountering the hydrogen does not significantly differ from the intrinsic case for both of the contaminated samples prepared. In the case of the $3 \times 10^{16}/cm^2$ hydrogen implanted sample the normalised interface velocity is 1 to within experimental error over the entire temperature range sampled. This indicates that the concentration threshold for retardation is not present in this sample. There is an unmistakable trend with temperature for the $4 \times 10^{16}/cm^2$ case. with lower temperatures yielding a more greatly retarded SPE rate. It is hard to account for the detail seen here without knowing the impact of residual bubble structure, or

having replicated points which may be suspect.

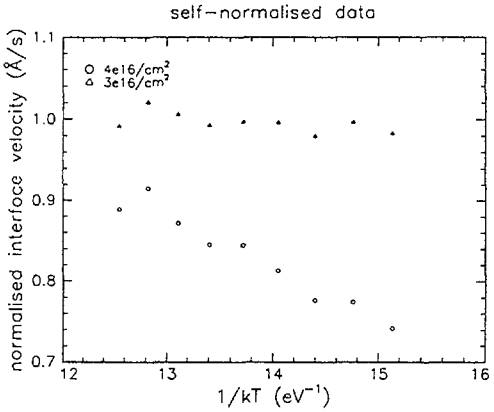

Figure 4: Normalised interface velocity for a range of temperatures. The implantation of $3 \times 10^{16}/cm^2$ hydrogen and subsequent treatment seems not to provide enough hydrogen to realise any substantial effect on SPE. A trend with temperature is clear for the sample implanted with $4 \times 10^{16}/cm^2$ hydrogen. Here the lower temperatures result in a more marked reduction in SPE rate.

While the results of this study are inconclusive, several points that warrant further study have emerged. Interestingly, the cited concentration threshold of $1 \times 10^{19}/cm^3$ hydrogen for an onset of retardation was not achieved for the sample implanted with hydrogen at a fluence of $4 \times 10^{16}/cm^2$, as shown by the SIMS analysis. However, the observed reduction in SPE rate may in part be due to the effect of any remaining bubble structure, a parameter which may in future be explored through the use of helium filled bubbles. Helium is expected to have significantly less inherent effect on epitaxy in silicon, and so an experiment of this kind would depend more on the residual structure and yield a normalising data set. The strikingly different behaviours of the samples implanted with the two fluences suggests that further SIMS analysis is needed to establish that in the $3 \times 10^{16}/cm^2$ sample the hydrogen profile remains similarly distinct under annealing conditions and to ascertain the concentration of hydrogen that is trapped by the remnant bubble layer. A clear temperature dependence has been established in the hydrogen retardation of SPE in silicon, despite the fact that the data obtained thus far is limited. This supports the idea that the slowing of the interface may be linked to alterations in the band structure. This in turn may be linked to a passivation of dangling bonds by hydrogen, "freeing" the Fermi level from the defect band. Further work with different concentrations of hydrogen is needed to clarify this pertinent issue.

REFERENCES

[1] G. L. Olson and J. A. Roth, *Handbook of Crystal Growth*, ed. D. T. J. Hurle, Elsevier Science, 1994, Chapter 7.

[2] J. C. McCallum, Appl. Phys. Lett. 69 (7) (1996) 925-927.

[3] G. L. Olson and J. A. Roth, *Handbook of Crystal Growth*, ed. D. T. J. Hurle, Elsevier Science, 1994, Chapter 7.

Isostructural exclusion of elements between aragonite and calcite layers in the shell of the Pacific oyster *Crassostrea gigas*

A. Markwitz[1], R. W. Gauldie[1], W. J. Trompetter[1], D. N. Jamieson[2], J. Pithie[1], S. K. Sharma[3]

1. Institute of Geological & Nuclear Sciences Ltd., PO Box 30-312, Lower Hutt, New Zealand2. Micro analytical Research Centre, School of Physics, University of Melbourne, Australia3. Hawaii Institute of Geophysics and Planetology, School of Ocean, Earth Sciences and Technology, University of Hawaii, 2525 Correa Road, Honolulu, HI 96822, USA

Sections of the shell of the farmed Pacific oyster *Crassostrea gigas* that are available commercially in Wellington, New Zealand, showed a distinct alternating pattern in the shell mineral when observed by reflected light (Figure 1).

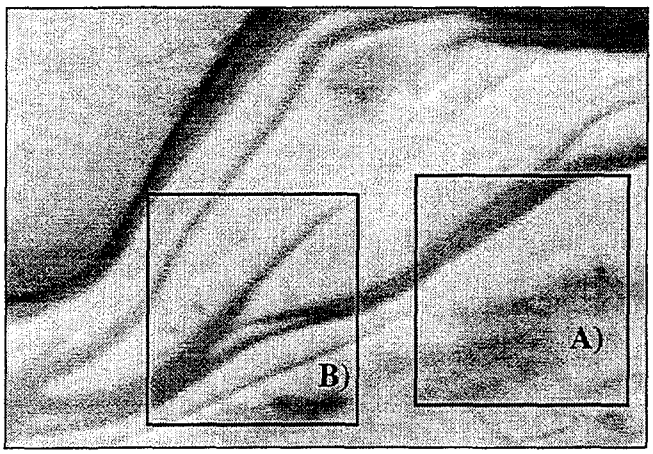

Figure 1: Distinct alternating pattern in the shell mineral observed by reflected light. The positions where two 2D maps were measured are indicated by the regions A and B

The layers were identified by Raman scattering as alternating bands of the calcite and aragonite mineral forms of calcium carbonate using the micro-Raman facility at the Hawaii Institute of Geophysics and Planetology [1]. The differences in the unit cell structure of calcite and aragonite favour different trace elements in the two minerals. Aragonite is iso-structural with Strontianite $SrCO_3$, and calcite is isostructural with Smithsonite $ZnCO_3$ [2]. As a result, Sr deposition should be favoured in the aragonite layer and is excluded from the calcite layer; and, conversely, Zn deposition should be favoured in the calcite layer and is excluded from the aragonite layer. However, up to today, significant differences in the pattern of Sr and Zn in microprobe scans are not discovered.

In order to obtain high-resolution two dimensional (2D) maps of the trace elements proton microprobe scans were performed using the microprobe facility in Melbourne [3]. The proton beam was focused to 6μm in diameter and particle induced X-ray emission (PIXE) analyses were made across the calcite and aragonite layers of the shell of C. gigas.

The measurements show sharply divided boundaries reflecting the inverse occurrence of Zn and Sr. The 2-D target area of the shell cross section was a 400μm thick section mounted in Zn-, Sr-free resin on glass.

Figures 2 to 4 show Ca, Sr, and Zn maps measured at position A (refer to figure 1.). The Ca map of the 2-D cross section in figure 2 shows only minor Ca density changes corresponding to the pattern (viewed by reflected light) of the light (calcite) and dark (aragonite) layers.

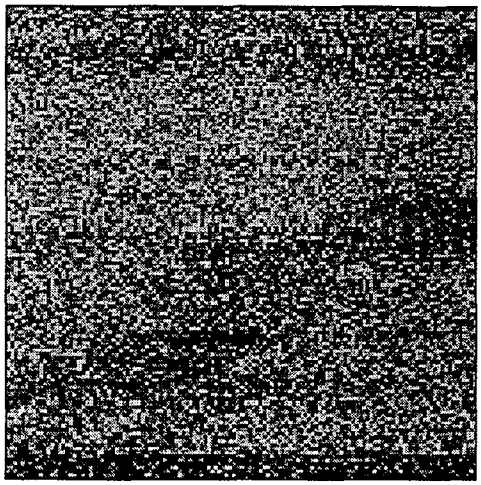

Figure 2: Ca map of the 2-D cross section

However, the Sr map in figure 3 shows clear Sr peaks occupying the dark layer areas in figure 1. The Zn map in figure 4 shows clear Zn peaks occupying the light layer areas in figure 1.

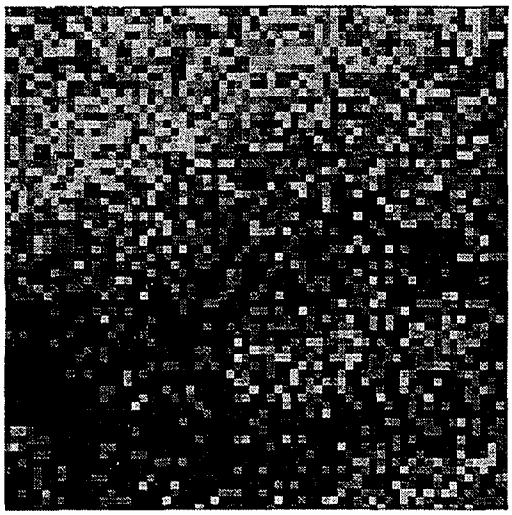

Figure 3: Sr map of the 2-D cross section

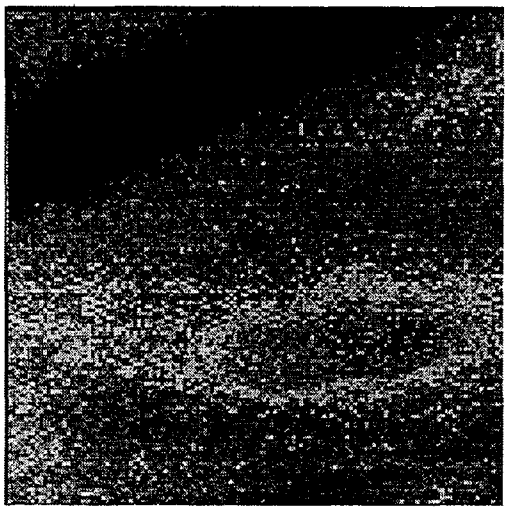

Figure 4: Zn map of the 2-D cross section

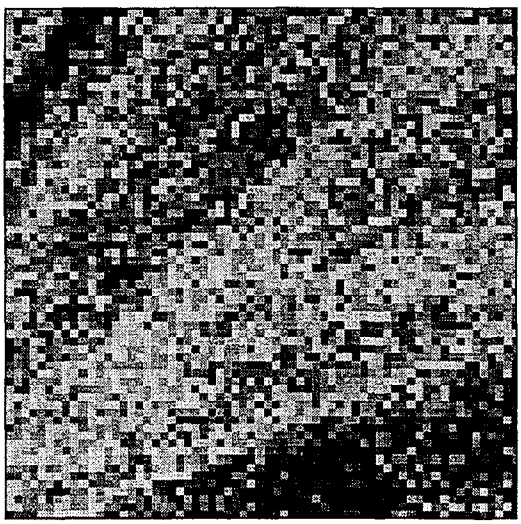

Figure 5: Sr map of the 2-D cross section

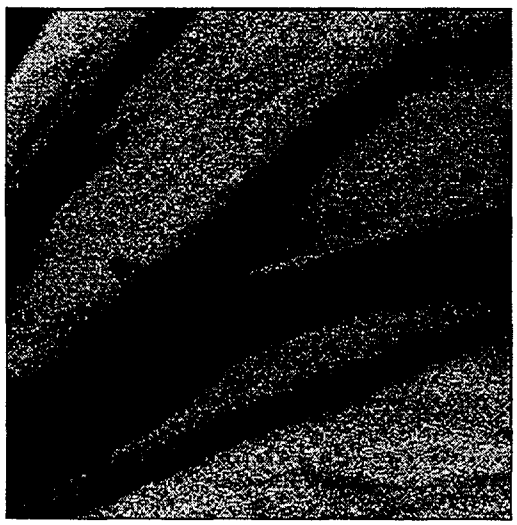

Figure 6: Zn map of the 2-D cross section

Additional maps were recorded to confirm the findings described in figures 3 and 4. Figures 5 and 6 show Sr and Zn maps measured at position B (refer to figure 1).

By the ion microprobe analysis of the oyster shell it is shown that differences in the unit cell structure of calcite and aragonite definitively favour different trace elements in the two minerals. The microprobe maps confirm that aragonite is iso-structural with $SrCO_3$, and calcite is isostructural with $ZnCO_3$.

References:

[1] Gauldie, R. W., S. K. Sharma and E. Volk. 1997. Micro-Raman spectral study of vaterite and aragonite otoliths of the Coho salmon *Oncorhynchus kisutch.* Comp. Biochem. Physiol. 118: 753-757

[2] Mason, B. and Berry, L. G. 1968. Elements of Mineralogy. W. H. Freeman and Company, San Francisco. 330 pp

[3] D.N. Jamieson, Nuclear Instruments and Methods B 136-138 (1998) 1-13

Investigation of iron oxide film-substrate interfaces using Rutherford backscattering and channeling techniques

S. Maheswaran*, S. Thevuthasan†

*School of Science, University of Western Sydney, Nepean, Kingswood, NSW 2747, Australia
†Environmental Molecular Sciences Laboratory, Pacific Northwest National Laboratory, Richland, WA 99352, U.S.A.

Abstract

Thin films of α-Fe_2O_3(0001) (hematite) were epitaxially grown on Al_2O_3(0001) substrates using the new molecular beam epitaxy (MBE) system at the Environmental Molecular Sciences Laboratory (EMSL). We have investigated the interface between the hematite films and sapphire substrates using Rutherford Backscattering (RBS) and channeling experiments. Theoretical simulations were performed using VEGAS code to investigate the surface and interface structural properties of the films.

Introduction

There is growing interest in the synthesis of model oxides as thin films on various oxide and metal substrates to obtain high-quality surfaces. The growth of iron oxides thin films with good crystalline quality is of increasing interest due to their applications in heterogeneous catalysis, magnetic thin films, surface geochemistry, corrosion, and integrated microwave devices [1-6]. Several high-quality well-oriented single crystal iron oxide films with various stoichiometry have been synthesized using the Molecular Beam Epitaxial (MBE) growth method and the structural properties of these have been analyzed by various surface and bulk sensitive techniques [6-12]. The physical and chemical properties of interfaces play a major role in the growth of high-quality thin films. We have used Rutherford backscattering (RBS) and channeling techniques to investigate the nature of the interface between epitaxially grown α-Fe_2O_3(0001) thin films and α-Al_2O_3(0001) substrate. Both α-Al_2O_3 and α-Fe_2O_3 exhibit a rhombohedral corundum crystal structure with metal +3 cations located in distorted oxygen octahedra. The lattice parameters along the c-axis are 4.76 and 5.03A°, for α-Al_2O_3 and α-Fe_2O_3 respectively, resulting in a lattice mismatch of 5.4%. The growth of this film on this substrate is expected to be complex due to the strain associated with this large lattice mismatch. In fact, it has been shown that the initial growth was a layer by layer growth up to the thickness of ~10A° and the growth was then transformed into an island growth mode [13]. Finally the islands coalesce to create a well-ordered uniform thin film. In this paper, we summarize our investigation of the characterization of the film-substrate interface of epitaxially grown 7A°, 70A° and 700A° thick α-Fe_2O_3(0001) films on α-Al_2O_3(0001) substrates using RBS and channeling techniques.

Experimental

The films were grown using procedures described elsewhere [9]. After growth, the samples were carefully removed from the MBE system and introduced into the channeling end station at the accelerator facility. The details of the accelerator facility and the end stations are described elsewhere [14]. The samples were heated to 200-250°C to desorb hydrocarbons from the surface. The samples were then mounted on a molybdenum backing plate using Ta clips and a conventional alumel-chromel thermocouple was attached to the backing plate close to the sample for temperature measurements. The standard dose of helium ions for one spectrum was 4.4×10^{15} ions/cm^2. The backscattering spectrum was collected using a silicon surface barrier detector at a scattering angle of 150°. The primary energy of the ions was 1.04MeV and the incident ion beam was directed along the normal to the sample surface.

Theoretical simulations of surface peak area were simulated using VEGAS program. This computer program uses Monte Carlo calculations and a Moliere screened potential to simulate the ion scattering interactions and it is described elsewhere [15]. The root mean square vibrational amplitudes are calculated using the Debye temperature, reported for Fe_3O_4 [9] and the vibrations are assumed to be isotropic.

Results and Discussion

Aligned and random RBS spectra using 1.04MeV He^+ beam for the 700A° thick film is shown in Fig. 1. The minimum yield (χ_{min}) for the film is determined to be 2.7 ± 0.3 %. In general, the crystalline quality of the film seems to be very good and the minimum yield is accordingly very low. The first three peaks (at the high energy side) visible in the aligned spectrum correspond to the front Fe surface peak, Fe atoms open to ion beam at the interface (back surface of the film) and Al atoms at the interface (substrate surface) respectively. Since the Fe and Al atoms are visible to ion beam at the interface, there must be some disordering of the iron oxide film at the interface or there must be substrate-film mixing present at the interface. Although mixing of the substrate and the film is possible at the interface, no evidence for mixing has been observed in the random spectrum within the experimental resolution and uncertainties. It could be that the lattice mismatch between the substrate and the film is too large (5.4%) to allow a continuous transition between the two crystal structures at the interface.

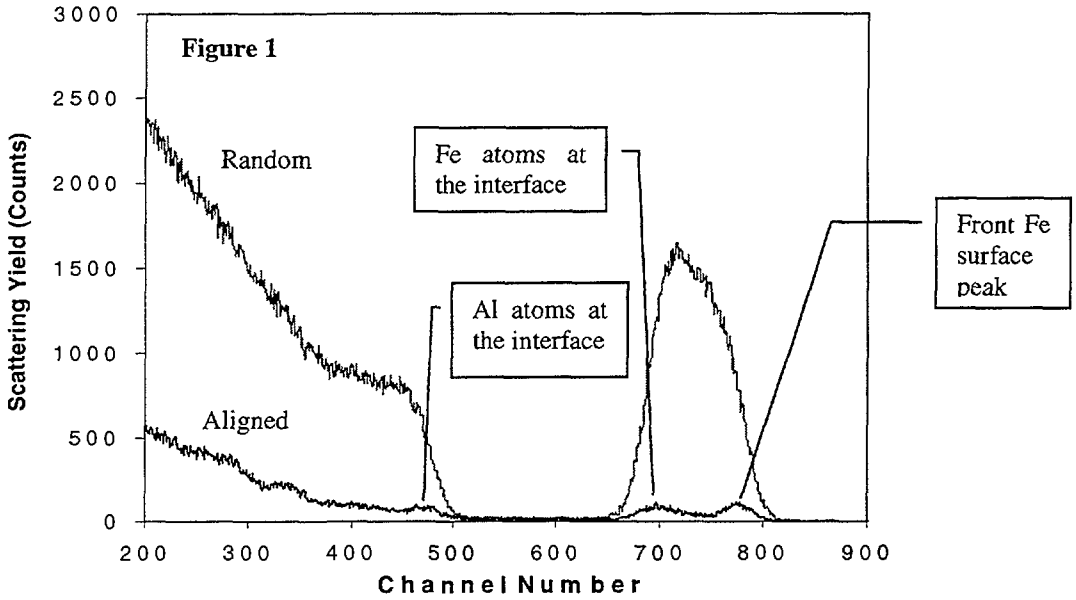

The experimental peak area of the front Fe surface peak is determined to be 2.3 atoms/row and this area is approximately same as the area of the back Fe surface peak. The simulated surface peak area using VEGAS code was 2.7 atoms/row and there is a reasonable agreement between the experimental and theoretical surface peak areas. A single Fe-layer terminated bulk like hematite structure with appropriate surface relaxations [16] was used in this simulation. Simulation of the back surface peak using disordered interface structures is currently in progress.

Figure 2 shows the aligned and random spectra for the 70A° thick film and only one peak is visible in the aligned spectrum. Since the film thickness is much smaller than the thicker (700A°) film, a single peak is possible due to the overlap of two peaks from the Fe atoms present at the front and the back surfaces of the thin film. The experimental area of this peak is approximately 2.5 atoms/row. The simulated surface peak area using VEGAS code was 2.6 atoms/row which is in a good agreement with the experimental value.

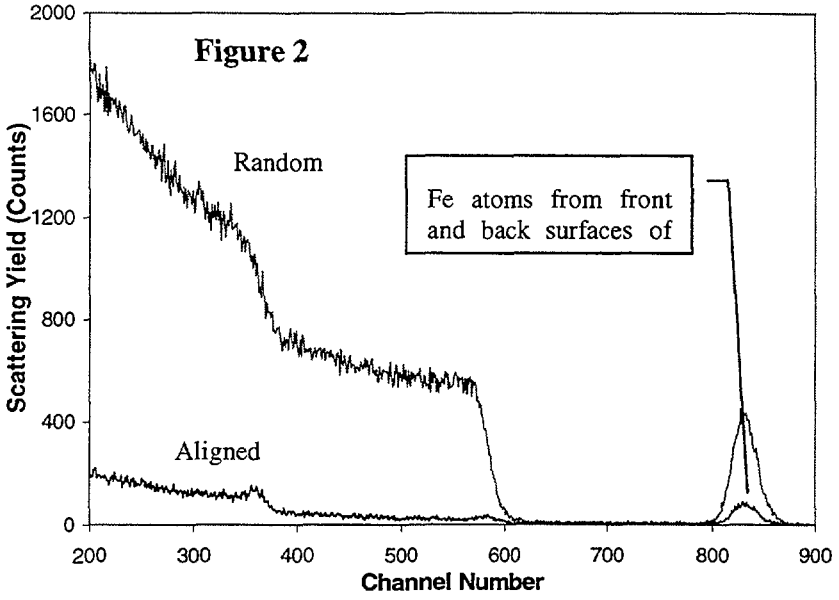

The aligned and random spectra from the 7A° thick film is presented in Fig. 3. The experimental peak area was determined to be 1.1 atoms/row using the hematite structure. The simulated surface peak area using the bulk Fe_2O_3 structure, which was used to simulate the surface peak area in the thickest film, was 1.9 atoms/row. Since this area doesn't agree with the experimental surface peak area, the non-common iron oxide phase reported for this film [17] is currently under investigation.

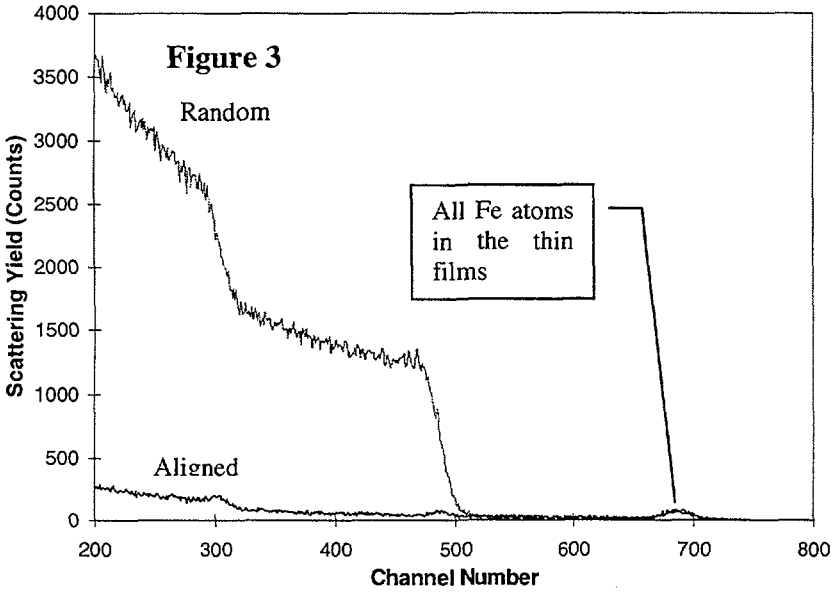

Conclusion

We have used RBS along with the channeling techniques to investigate the interfacial properties between hematite films and sapphire substrates. A disordered phase due to the lattice mismatch between the film and the substrate exists at the interface. Surface peak areas were simulated using VEGAS program and reasonable agreement was found between the experimental and the simulated surface peak areas in the case of thick films. Simulations on the thinnest film with the non-common iron oxide phase are in progress.

Acknowledgements

Pacific Northwest National Laboratory is a multi-program national laboratory operated for the U.S. Department of Energy by Battelle Memorial Institute under contract No. DE-AC06-76RLO 1830. The authors gratefully acknowledge partial support from the US Department of Energy, Offices of Basic Energy Sciences, and Biological and Environmental Research - Environmental Management Science Program. UWS-Nepean Staff Development Fund (School of Science) is also greatly acknowledged for providing travel fund to one of the authors for the experimental work.

References

[1] J. W. Geus, Appl. Catl. 25 (1986) 313.

[2] H. H. Kung, *Transmission Metal Oxides: Surface Chemistry and Catalysis* (Elsevier, New York, 1989).

[3] T. Fujii, M. Takano, R. Katano, and Y. Bando, J. Appl. Phys. 66 (1989) 3168.

[4] T. D. Waite, Rev. Mineral, 23 (1990) 559.

[5] R. K. Wild, in *Surface Analysis: Techniques and Applications, Special Publication 84*, edited by D. R. Randell and W. Neagle (Royal Society of Chemistry, London, 1990).

[6] D. M. Lind, S.D. Berry, G. Chern, H. Mathias, and L.R. Testardi, Phys. Rev. B45 (1992) 1838.

[7] J. F. Anderson, M. Kuhn, U. Diebold, K. Shaw, P. Stoyanov, and D. Lind, Phys. Rev. B 56 (1997) 1134.

[8] J. M. Gaines, P.J.H. Bolemen, J.T. Kohlhepp, C.W.T. Bulle-Lieuwma, R.M. Wolf, A. Reinders, R. M. Jungblut, P.A.A. van der Heijden, J.T.W.M. van Eemeren, J. aan de Stegge, W. J.M. de Jonge, Surf. Sci. 373 (1997) 85.

[9] Y. J. Kim, Y. Gao, and S.A. Chambers, Surf. Sci. 371 (1997) 358.

[10] Y. Gao, Y.J. Kim, S. Thevuthasan, P. Lubitz, and S.A. Chambers, J. Appl. Phys. 81 (1997) 3253.

[11] Y. Gao, Y.J. Kim, S.A. Chambers, and G. Bai, J. Vac. Sci. Technol. A 15 (1997) 332.

[12] Y. Gao and S.A. Chambers, J. Cryst. Growth 174 (1997) 446.

[13] S.I. Yi, Y. Liang, S. Thevuthasan, and S.A. Chambers, accepted to Surf. Sci.14. S. Thevuthasan, C.H.F. Peden, M.H. Engelhard, D.R. Baer, G.S. Herman, W. Jiang, Y. Liang, and W.J. Weber, Nucl. Instr.Meth. A, (1998) in press.

[14] J. W. Frenken, R. M. Tromp, and J. F. Van der Veen, Nucl. Instrum. Methods B 17 (1986) 334.

[15] S. Thevuthasan, Y.J. Kim, S.I. Yi, S.A. Chambers, J. Morais, R. Denecke, C.S. Fadley, P. Liu, T. Kendelewicz, and G.E. Brown Jr. Surf. Sci. 425 (1999) 276.

[16] S.I. Yi, S. Thevuthasan, and S.A. Chambers, submitted to Surf. Sci. Lett.

The Kinetics of Solid Phase Epitaxy in As-Doped Buried Amorphous Silicon Layers

J. C. McCALLUM
Microanalytical Research Centre, School of Physics, University of Melbourne, Parkville, Victoria 3052, Australia, jcm@physics.unimelb.edu.au

Introduction

Ion implantation is the principal method used to introduce dopants into silicon for fabrication of semiconductor devices. The damage which accumulates during ion implantation may lead to amorphisation of the silicon over the depth range of the ions. To activate the dopants and make a useful device the damaged or amorphous material must be crystallised by thermal annealing. In the case of amorphous silicon layers, crystallisation can be achieved by a solid-state process called solid phase epitaxy (SPE) in which the amorphous layer transforms to crystalline silicon (c-Si) layer by layer using the underlying c-Si as a seed. Unlike liquid phase epitaxy, SPE occurs under conditions where the atomic mobility is comparatively low and crystallisation occurs by highly localised bond breaking and rearrangement processes. The bond breaking process is thought to be mediated by a defect which is present at the amorphous/crystalline (a/c) interface, however, the exact nature of this defect is unknown. One of the key observations which may lead to identification of the defect is the fact that moderate concentrations of dopants enhance the SPE crystallisation rate while the presence of equal concentrations of an n-type and a p-type dopant (impurity compensation) returns the SPE rate to the intrinsic value. This provides crucial evidence that the SPE mechanism is sensitive to the position of the Fermi level in the bandgap of the crystalline and/or the amorphous silicon phases and may lead to identification of an energy level within the bandgap that can be associated with the defect.

The crystallisation via solid phase epitaxy of a-Si surface layers formed by self-ion implantation into single-crystal (c-Si) substrates has been studied extensively [1, 2] and various models have been proposed to explain the SPE growth process and its observed dependence on parameters such as substrate orientation [3], impurity type and concentration [4] and pressure [5]. The studies of dopant-enhanced SPE are of particular importance because they provide insight into the fundamental mechanism responsible for the crystallisation process [1]. Significantly, the experiments of Walser and co-workers showed that for dopant concentrations less than ~ 0.1 at.% the SPE rate increases linearly with concentration [6] and several different models of the SPE process that can accommodate this observation have been proposed [5–8]. However, Olson and Roth [9] have shown that the SPE rate in thin (< 4000 Å) surface a-Si layers like those used by Walser et al. is affected by the presence of hydrogen even when the measurements are performed in vacuum. They found that H present in the surface oxide infiltrates the a-Si layer during annealing and that for thin layers this results in a nearly constant H concentration of $\sim 2 \times 10^{19}$ cm^{-3} at the amorphous/crystalline (a/c) interface throughout the SPE process, causing retardation of the growth rate. They also showed that the intrinsic SPE rate can be obtained by using a-Si layers several microns thick and measuring the growth rate during the early stages of crystallisation before significant concentrations of H have penetrated to the a/c interface [1]. However, thick amorphous surface layers are not very convenient for studies of dopant-enhanced SPE and the degree of H infiltration must always be considered. Recently, we have shown that buried a-Si layers provide an alternative environment in which the intrinsic [10] and dopant-enhanced [11] growth kinetics of a-Si can be studied free from the rate-retarding influence of H and that a two laser time resolved reflectivity technique can be used to measure the instantaneous crystallisation rates in these layers. The overlying crystalline Si layer provides a barrier to H infiltration. This paper gives details of SPE measurements in As-doped buried a-Si layers and discusses the implications of these data for models of the SPE process.

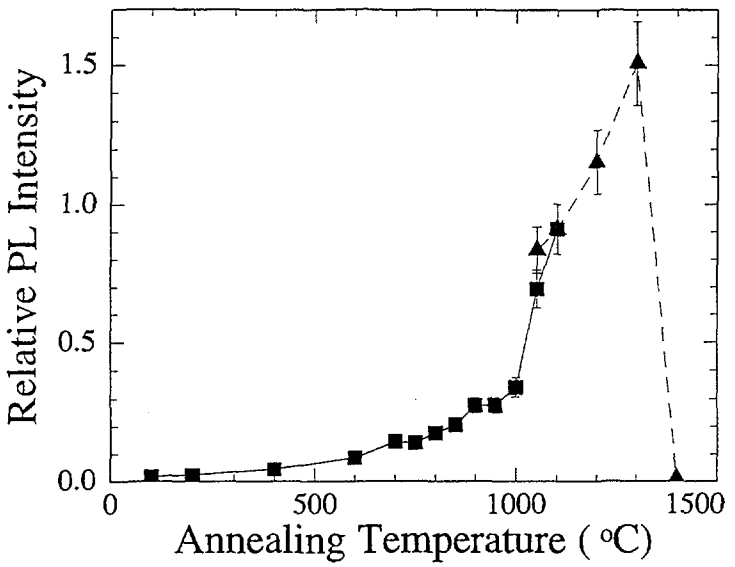

Figure 1: (a) Schematic representation of the reflected signals for the 632.8 nm laser used in the TRR measurements. (b) TRR trace for crystallisation of a buried a-Si layer at 580°C.

Experiment

For the dopant-enhanced SPE studies, uniform concentration profiles were produced over the depth range $\sim$ 0.4–0.7 μm by implantation of As ions at four different energies in the range 450–1200 keV with the substrates held at 77 K. Following As implantation, the samples were annealed at 580°C, 1 hr under UHV conditions in the implantation chamber to fully crystallize the implanted layer. Buried a-Si layers were then formed using self-ion implantation [10]. The SPE rates were determined in air by mounting the samples on a resistively heated vacuum chuck and using time resolved reflectivity at wavelengths of $\lambda = 1152$ nm and $\lambda = 632.8$ nm to measure the a/c interface motion during crystallisation. Further details of the experimental procedure are given elsewhere [10, 11].

Results

Figure 1(a) shows a schematic representation of the laser reflections from the sample interfaces for the 632.8 nm laser used in the TRR measurements of the SPE rates in the buried a-Si layers. During crystallisation, the front and back a/c interfaces of the buried amorphous layer approach each other with growth rates represented by v_f and v_b. For much of the crystallisation process, the 632.8 nm reflectivity signal is only sensitive to motion of the front a/c interface because the laser light is strongly absorbed in the amorphous layer. Figure 1(b) shows a typical 632.8 nm TRR trace collected during SPE of a buried a-Si layer at a temperature of 580°C in air. During SPE, the front a/c interface recedes from the surface region and the

REFERENCES

[1] For a review, see G. L. Olson and J. A. Roth, *Chapter 7: Solid Phase Epitaxy*, Handbook of Crystal Growth **3**, 255, ed. D. T. J. Hurle, Elsevier, Amsterdam (1994).

[2] O. Hellman, Materials Science and Engineering Reports **R16**, 1, (1996).

[3] F. Spaepen and D. Turnbull, *Laser-Solid Interactions and Laser Processing*, eds. S. D. Ferris, H. J. Leamy and J. M. Poate, AIP Conf. Proc. No. 50 (New York: AIP), 73 (1979).

[4] W. W. Park, M. F. Becker and R. M. Walser, Appl. Phys. Lett. **52**, 1517 (1988).

[5] G. Q. Lu, E. Nygren and M. J. Aziz, J. Appl. Phys. **70**, 5323 (1991).

[6] R. M. Walser and Y. J. Jeon, Mater. Res. Soc. Symp. Proc. **205**, 27 (1992) and references therein.

[7] J. S. Williams and R. G. Elliman, Phys. Rev. Lett. **51**, 1069 (1983).

[8] M. Wautelet, Semicond. Sci. Technol. **4**, 685 (1989).
[9] J. A. Roth, G. L. Olson, D. C. Jacobson, J. M. Poate, and C. Klinschbaum, Mater. Res. Soc. Symp. Proc. **205**, 45 (1992).
[10] J. C. McCallum, Appl. Phys. Lett. **69**, 925 (1996).
[11] J. C. McCallum, Mat. Res. Soc. Symp. Proc. **438/439**, 119 (1997) .
[12] Y. J. Jeon, M. F. Becker and R. M. Walser, Mater. Res. Soc. Symp. Proc. **157**, 745 (1990).
[13] P. A. Stolk, F. W. Saris, A. J. M. Berntsen, W. F. van der Weg, L. T. Scaly, R. C. Barklie, G. Krötz and G. Müller, J. Appl. Phys. **75**, 7266 (1994).
[14] P. Gortmaker, Ph.D. Thesis, ANU (1997).

Doping-Dependence of Solid Phase Epitaxy in Boron Implanted Amorphous Silicon Layers

J. C. McCALLUM
Microanalytical Research Centre, School of Physics, University of Melbourne, Parkville, Victoria 3010, Australia, jcm@tauon.ph.unimelb.edu.au

Ion implantation is the principal method used to introduce dopants into silicon for fabrication of semiconductor devices. During ion implantation, damage accumulates in the crystalline silicon lattice and amorphisation may occur over the depth range of the ions if the implant dose is sufficiently high. As device dimensions shrink, the need to produce shallower and shallower highly-doped layers increases and the probability of amorphisation also increases. To achieve dopant-activation, the amorphous or damaged material must be returned to the crystalline state by thermal annealing. Amorphous silicon layers can be crystallised by the solid-state process of solid phase epitaxy (SPE) in which the amorphous layer transforms to crystalline silicon (c-Si) layer by layer using the underlying c-Si as a seed. The atomic mechanism that is responsible for the crystallisation is thought to involve highly-localised bond-breaking and rearrangement processes at the amorphous/crystalline (a/c) interface but the defect responsible for these bond rearrangements has not yet been identified. Since the bond breaking process necessarily generates dangling bonds, it has been suggested that the crystallisation process may solely involve the formation and migration of dangling bonds at the interface. [1] One of the key factors which may shed further light on the nature of the SPE defect is the observed dopant-dependence of the rate of crystallisation. It has been found that moderate concentrations of dopants enhance the SPE crystallisation rate while the presence of equal concentrations of an n-type and a p-type dopant (impurity compensation) returns the SPE rate to the intrinsic value. This provides crucial evidence that the SPE mechanism is sensitive to the position of the Fermi level in the bandgap of the crystalline and/or the amorphous silicon phases and may lead to identification of an energy level within the bandgap that can be associated with the defect.

There have been a number of studies in which an attempt has been made to quantify the dopant-dependence of SPE in relation to impurity type and concentration. [2] However, Olson and Roth [3] showed that these experiments were affected by the presence of hydrogen which infiltrated the a-Si layer from the native surface-oxide layer during annealing causing retardation of the growth rate. Recently, we have shown that buried a-Si layers provide a suitable environment in which the intrinsic [4] and dopant-enhanced [5, 6] growth kinetics of a-Si can be studied free from the rate-retarding influence of H and that a two laser time resolved reflectivity technique can be used to measure the instantaneous crystallisation rates in these layers. The overlying crystalline Si layer provides a barrier to H infiltration. Furthermore, we have shown for As-doped buried a-Si layers, the concentration and temperature dependence of the dopant-enhancement is consistent with the Generalised Fermi Level Shifting model (GFLS) after suitable extension of the model to include degenerate semiconductor statistics. [6] The Fermi Level Shifting model was originally proposed by Williams and Elliman [7] in 1983 and then resurrected as the GFLS model by Lu et al. [8] in 1991 but until our recent measurements, the quality of the data was not sufficient to determine whether or not the

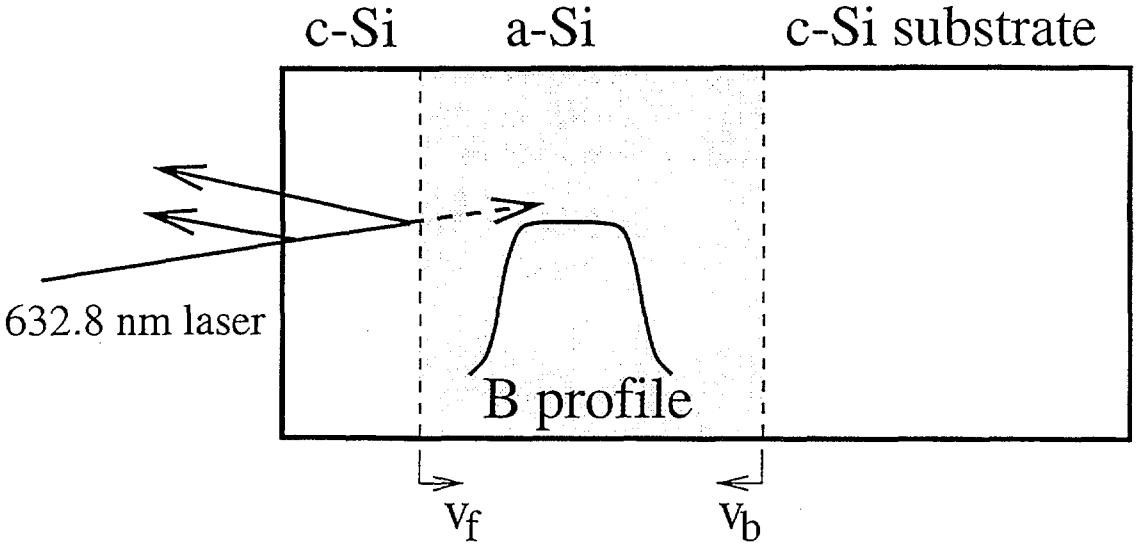

Figure 1: Schematic representation of the sample geometry and the reflected signals for the 632.8 nm laser used in the TRR measurements.

model correctly described the dopant-dependence of SPE. In this paper, we present preliminary results for dopant-enhanced SPE measurements in B-doped buried a-Si layers and show that the GFLS model once again provides a good description of the observed trends. Importantly, these results together with the previous As study show that the GFLS model works for both n and p-type dopants.

For the dopant-enhanced SPE studies, uniform concentration profiles were produced over the depth range $\sim$ 0.8–1.2 μm by implantation of B ions at four different energies in the range 350–560 keV into pre-amorphised Si(100) substrates. The substrates were held at 77 K throughout the various implantation steps. Following B implantation, the samples were annealed at 580°C, 1 hr under UHV conditions in the implantation chamber to fully crystallize the implanted layer. Buried a-Si layers were then formed using self-ion implantation [4]. The SPE rates were determined in air by mounting the samples on a resistively heated vacuum chuck and using time resolved reflectivity at wavelengths of λ = 1152 nm and λ = 632.8 nm to measure the a/c interface motion during crystallisation. Further details of the experimental procedure are given elsewhere [4, 5].

Figure 1 shows a schematic representation of the sample geometry and the laser reflections that are used in the time resolved reflectivity measurements (TRR) to monitor the interface motion during crystallisation. During crystallisation, the front and back amorphous/crystalline (a/c) interfaces of the buried amorphous layer approach each other with growth rates represented by v_f and v_b. For much of the crystallisation process, the 632.8 nm reflectivity signal is only sensitive to motion of the front a/c interface because the laser light is strongly absorbed in the amorphous layer. As it passes through the depth range $\sim$ 0.8–1.2 μm the front a/c interface encounters the B-doped region and the crystallisation rate increases.

The TRR measurements are further illustrated in Fig. 2. Figure 2(a) shows a typical 632.8 nm TRR trace collected during SPE of an intrinsic buried a-Si layer at a temperature of 540°C in air. Each oscillation in the reflectivity signal corresponds to movement of the front a/c interface over a distance of 780 Å. The interface velocity as a function of

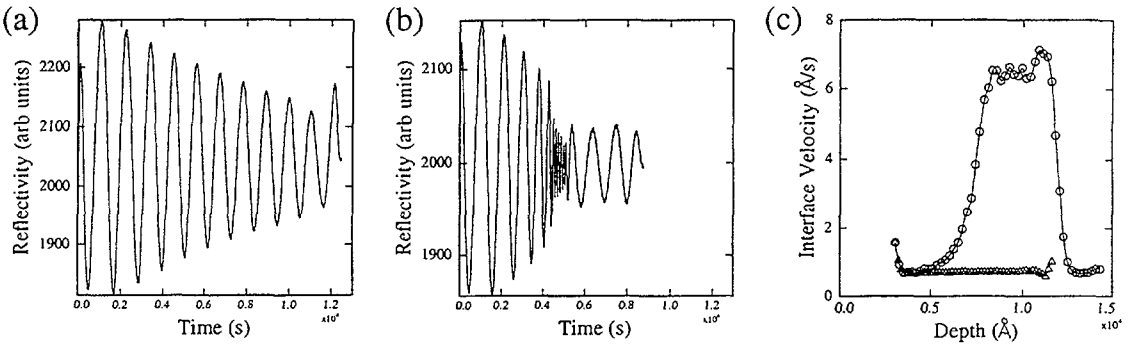

Figure 2: TRR traces for SPE of (a) an intrinsic buried a-Si layer and (b) a buried a-Si layer doped with 1×10^{20} B.cm^{-3}. (c) Interface velocity versus depth profiles extracted from the intrinsic (triangles) and B-doped (circles) TRR data.

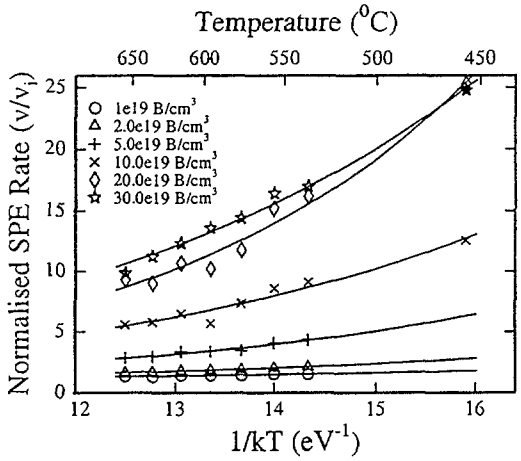

Figure 3: Dopant-enhanced SPE rates for the front a/c interfaces of buried a-Si layers normalized to the corresponding intrinsic SPE rate. Data are shown for six different B concentrations in the range $1\text{–}30\times10^{19}$ cm^{-3}. The solid lines are obtained by fitting Eq. 1 to the data.

time or depth can be extracted from the TRR trace as illustrated in Fig. 2(c). For the intrinsic sample (triangles), the interface velocity is constant at 0.7 Å.s^{-1} throughout most of the crystallisation time. Figure 2(b) shows the corresponding reflectivity trace for SPE of a buried a-Si layer doped with 1×10^{20} B.cm^{-3}. When the a/c interface encounters the B-doped region the period of the oscillations decreases quite dramatically. The amplitude of the signal also decreases and this is usually associated with a loss of interface planarity. The interface velocity versus depth for this sample is also shown in Fig. 2(c) (circles). In this case, the SPE rate in the B-doped sample is enhanced over the intrinsic rate by more than a factor of 9.

SPE rates were measured over the temperature range 460–660°C for buried a-Si layers containing six different B concentrations spanning the range $1\text{–}30\times10^{19}$ cm^{-3}. Figure 3 shows the dopant-enhanced SPE rates normalised to the intrinsic rate. In the GFLS model of Lu et al.[8] which is based on an earlier model by Williams and Elliman [7], SPE is assumed to occur through motion at the a/c interface of a neutral

defect, D^0 and its negatively and/or positively charged counterparts, $D^{\pm}$, and it is assumed that these defects are in thermal and electronic equilibrium, with the latter being determined by the band structure and density of states of the crystal. For p-type doping, for example, as the dopant concentration increases, the Fermi level shifts towards the valence band edge and the concentration of D^+ increases. If each charge state is equally efficient in promoting SPE, then the following expression can be derived for the normalised SPE rate [8]:

$$\frac{v}{v_i} = \frac{1 + \frac{[D^+]}{[D^0]}\Big|_{\text{doped}}}{1 + \frac{[D^+]}{[D^0]}\Big|_{\text{intrinsic}}} = \frac{1 + g\exp(\frac{E^+ - E_F}{kT})}{1 + g\exp(\frac{E^+ - E_{F,i}}{kT})} \tag{1}$$

where $[D^0]$, $[D^+]$ are the concentrations of D^0, D^+, respectively, E_F, $E_{F,i}$ are the Fermi levels in the doped and intrinsic c-Si respectively, and E^+ is an energy level associated with the defect responsible for SPE and g is the degeneracy factor.

The Fermi level, E_F, as a function of temperature and total B concentration, N_B, is found by solving the charge neutrality condition: $n + [B^-] = p$ where n, p and $[B^-]$ are the electron, hole and ionised acceptor concentrations, respectively. [6] Then, the only two free parameters in Eq. 1 are the degeneracy factor, g, and energy level, E^+, of the defect. The solid lines in Fig. 3 are fits of Eq. 1 to the data obtained with values of $g = 0.3 \pm 0.2$ and $E^+ = 0.23 \pm 0.03$ eV above the valence band edge. These values are thoroughly reasonable and although at present they cannot be linked to a particular defect, we believe that the quality of the fits provides compelling evidence that the GFLS model gives an accurate picture of the dopant-dependence of SPE.

CONCLUSIONS

The kinetics of dopant-enhanced solid phase epitaxy (SPE) have been measured in buried a-Si layers doped with B. The dopant-enhanced SPE data can be modelled by an extension of the Generalised Fermi Level Shifting model to include degenerate semiconductor statistics on the crystalline Si side of the interface. The quality of the fits provides compelling evidence that the GFLS model gives an accurate picture of the dopant-dependence of SPE. We believe this picture can be further improved through detailed examination of the band structure at the a/c interface.

REFERENCES

[1] F. Spaepen and D. Turnbull, *Laser-Solid Interactions and Laser Processing*, eds. S. D. Ferris, H. J. Leamy and J. M. Poate, AIP Conf. Proc. No. 50 (New York: AIP), 73 (1979).

[2] R. M. Walser and Y. J. Jeon, Mater. Res. Soc. Symp. Proc. **205**, 27 (1992) and references therein.

[3] G. L. Olson and J. A. Roth, *Chapter 7: Solid Phase Epitaxy*, Handbook of Crystal Growth **3**, 255, ed. D. T. J. Hurle, Elsevier, Amsterdam (1994).

[4] J. C. McCallum, Appl. Phys. Lett. **69**, 925 (1996).

[5] J. C. McCallum, Mat. Res. Soc. Symp. Proc. **438/439**, 119 (1997).

[6] J. C. McCallum, Nucl. Instr. and Meth. in Phys. Res. B **148**, 350 (1999).

[7] J. S. Williams and R. G. Elliman, Phys. Rev. Lett. **51**, 1069 (1983).

[8] G. Q. Lu, E. Nygren and M. J. Aziz, J. Appl. Phys. **70**, 5323 (1991).

Coating of the orthopaedic titanium alloys with sol-gel derived hydroxyapatite

A. Milev, D. Green, C. S. Chai and B. Ben-Nissan

Department of Chemistry, Materials and Forensic Science, University of Technology, Sydney, PO Box 123, Broadway NSW 2007, Australia E-mail: Adriyan.Milev@uts.edu.au

Introduction

Hydroxyapatite (HAp) is known to be both biocompatible and bioactive material, however, due to its poor mechanical properties and design limitations is not suitable for applying as a load bearing implant. This could be overcome by using appropriate metallic substrates covered with HAp, derived *via* different techniques. These coatings allow improved adhesion strength of the load bearing substrate to the bone, resulting in shorter healing periods as well as predictable behaviour of the implant for longer periods of time.

There are different techniques of producing HAp appropriate for coating purposes. Due to the small particle size of the grains derived, sol-gel route is preferable where lower sintering temperatures are of primary importance.

For better adhesion between substrate and hydroxyapatite coating, the surface of titanium substrate, in this study, was converted to titanium nitride and/or oxynitride. Sintering temperatures of 900°C have been used for producing crystalline HAp coatings. The control of sol-gel solutions and the analysis of the coatings were carried out using XRD, SEM and DTA techniques. Results obtained indicate high quality HAp coatings can be produced on titanium substrates especially with complex shapes that benefits over the other coating methods.

Materials and Methods

Solution Preparation

Solution preparation was conducted in a moisture free atmosphere due to the hygroscopic nature of the reactants. High purity calcium diethoxide was dissolved with the assistance of a magnetic stirrer in a vial containing ethanol and ethanediol. Independently triethyl phosphite was added to another vial consis ethanol. The phosphite solution was then added dropwise to the calcium containing solution to obtain a Ca/P molar ratio of 1.67/1, and the reaction mixture was stirred for a period of 30 minutes at ambient temperature. This solution was allowed to age for periods up to 24 hours [1, 2].

Characterisation of the Precursor Sols and Gels

The gels were crushed in a mortar and pestle and analysed with thermo-gravimetric analysis and differential thermal analysis using a SDT 2960 simultaneous thermal analyser (TA Instruments, Newcastle, USA). The powder was heated at 10°C/min to 1200°C in a stagnant air atmosphere.

Coating Production

Titanium and Ti6Al4V coupons were ground and polished to a surface finish of 0.05 microns and used as substrates. Before coating substrates were ultrasonically cleaned twice with acetone and then twice in ethanol. A quantity of 0.05 ml of aged unhydrolysed solution was taken from the vial and placed on the polished coupon surface. A spin coater (Headway Research, Garland, USA) was used at a speed of 2500 r.p.m.for 10 seconds to produce the coating. The applied layer was hydrolysed in an oven at 70°C for 15 minutes and then prefired

at 500°C for 15 minutes. A total of 5 layers were deposited before final firing to 600, 700, 800 and 900°C for 120 minutes.

Characterisation of Coatings

Coatings were analysed using X-ray diffraction with a grazing angle attachment (0.5°). The crystallisation temperature determined in differential thermal analysis was confirmed with X-ray diffraction on a Siemens D-5000 diffractometer (Karslruhe, Germany) with Cu Kα radiation. The diffraction pattern was collected over the 2θ range of 20-40° with an acquisition time of 5 seconds at each step of 0.02°.

Scanning electron microscopy was performed in a JEOL JSM-6300 using a field emission gun as the electron source. Coatings fired to different temperatures were coated with carbon before analysis.

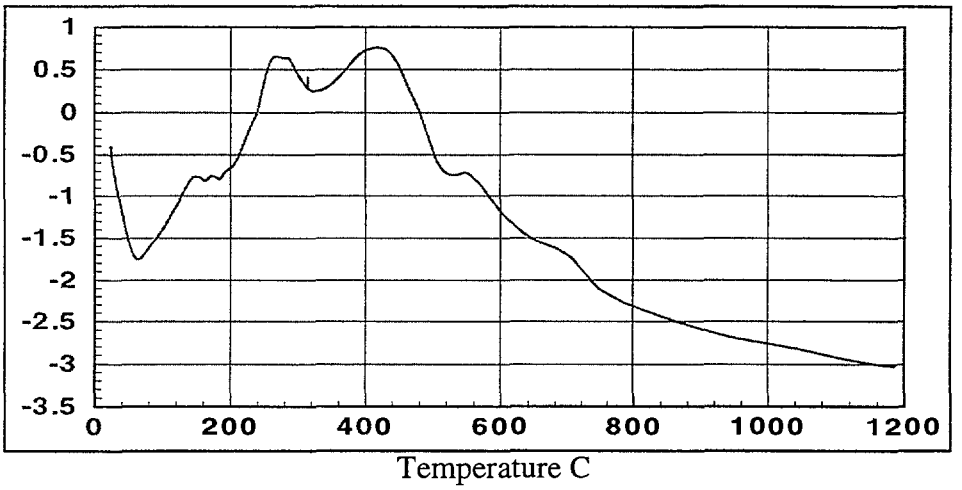

Figure 1.Thermal analysis showing conversion of hydrolysed gel into Hydroxyapatite

Results and Discussion

Differential thermal analysis of the aged samples shows an endotherm followed by three exotherms positioned at 240, 400 and 550°C, (Figure 1). The endothermic reaction at low temperature is related to the removal of alcohols and adsorbed water. The first two exotherms correspond to polycondensation and the release of organics, thus requiring a prefiring temperature of 500°C. The exothermic peak at 550°C suggests crystallisation of an amorphous calcium phosphate. Coatings fired to temperatures between 500 and 900°C and analysed by X-ray diffraction indicates that crystallisation occurs between 500 and 600°C, (Figure 2). The release of heat on crystallisation is small suggesting that small atomic arrangements of the calcium and phosphate species are required for crystallisation. Indeed the coatings were crack free with average size 500nm.

X-ray diffraction of the coatings heated to the various temperatures indicated that initially the titanium substrate was observed which oxidised at temperatures starting at 800°C. Based on the possible phase transformation in the metallic substrate, the occurrence of oxidation and very little weight loss after 800°C, it is suggested that this temperature is suitable for manufacturing sol gel hydroxyapatite coating. The resulting microstructure is a nano-grained hydroxyapatite coating with an average grain size of 500nm (Figure 3). Densification of the coating can then be obtained with a longer firing temperature at 800°C.

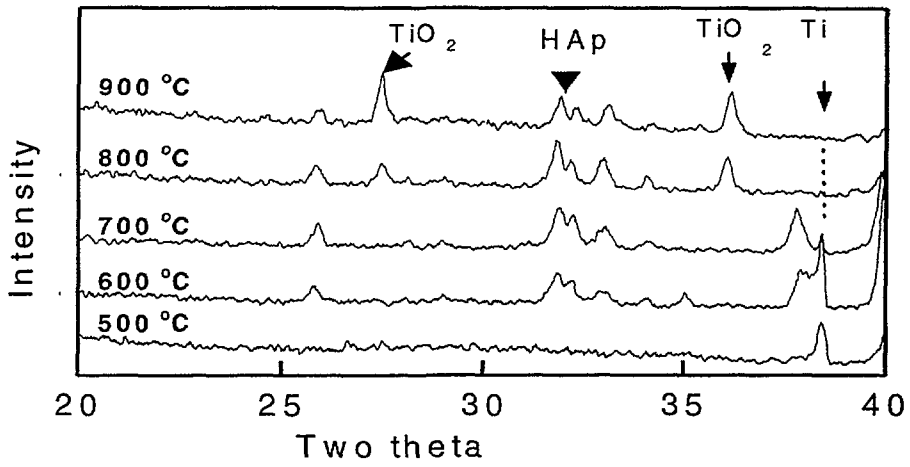

Figure 2. XRD plots of HAp coatings on Ti substrate calcified at various temperatures

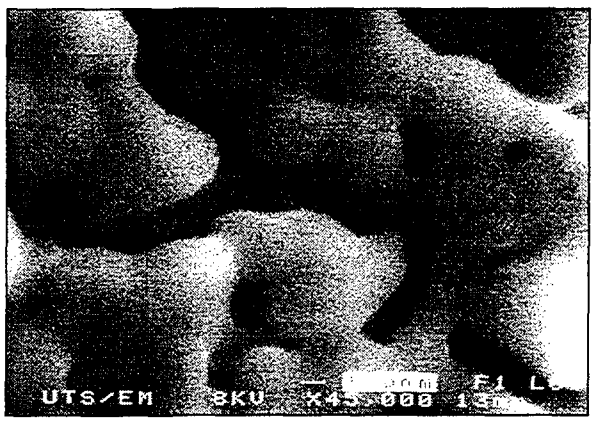

Figure 3. SEM micro-graph of HAp on Ti substrate, calcified at 800°C for 2 hours

Conclusions

Nanocrystalline thin films coatings have been composed *via* sol-gel alkoxide route. Coating thickness ranges from 100 to 1000nm depending on the number of applied layers. Solutions were noticed to wet substrates well and produced crystalline HAp coatings. A final firing temperature of 800°C is required to remove most of the organic material and to produce thin homogeneous coatings. SEM examination revealed the growth of dense coatings consisting of grains with medium size 500nm after sintering at 800°C.

References

K. A. Gross, C.S. Chai, G. S. K. Kannangara and B. Ben-Nissan, *Journal of Materials Science: Materials in Medicine* **9** (1998) 839.

C.S. Chai, K. A. Gross and B. Ben-Nissan, *Biomaterials* **19** (1998) 2291.

Imaging of fluid flow in porous rocks by neutron radiography

Mike F. Middleton

School of Applied Geology, Curtin University of Technology, Perth, 6845 WA, Australia;
email: middlem@lithos.curtin.edu.au

Dynamic neutron radiography (DNR) is a tool that has been used for some years for the non-destructive testing of mechanical equipment, especially where fluid flow is involved (Lindsay et al., 1989; Balaskó & Sváb, 1996). The method is particularly valuable as it can present a visualization of the fluid flow. However, applications of this method to petroleum exploration and production have not been reported extensively in the literature until recently (Middleton & Pázsit, 1998a, 1998b, 1999; Balaskó et al., 1999). Because the technique is capable of producing "real-time" images of fluid flow in rocks, quantities of geological interest, such as flow rate, fluid mixing and rock inhomogeneities, can be observed. Quantitative estimates of porosity, permeability, fluid saturation and capillary pressure can also be made from the neutron-attenuation images of a porous reservoir rock.

Previous studies have shown that DNR can (i) highlight inhomogeneities in fluid flow patterns in porous rocks, and (ii) provide a good estimate of relative fluid saturation, if "heavy water" is displaced by oil, in porous reservoir sandstones (Middleton & Pázsit, 1998a). The power of DNR over NMR (nuclear magnetic resonance) computer-aided-radiography/tomography is that the resultant image is not distorted by the presence of iron, or other magnetic minerals, in the sample. The aim of this paper is to demonstrate the ability of this method to delineate (1) "effective porosity" (pore space involved in fluid flow), versus (2) total porosity (total pore space in the rock)..

The attenuation of thermal neutrons, which are low-energy neutrons of energy of about 0.025 ev, can be described well by the exponential rule:

$$I = I_o \exp(-\mu \rho h), \qquad (1)$$

where I is the intensity of the transmitted neutron beam, I_o is the intensity of the incident neutron beam, μ is the neutron attenuation coefficient, ρ is the density of the rock sample, and h is the thickness of the sample. The attenuation coefficient, μ, used herein reflects the total attenuation, due to both the scattering and capture processes for thermal neutrons.

For the types of experiments that we are doing in the present study, a dry sandstone is either (i) fully saturated with water under a vacuum, or (ii) partially saturated due to the passage of water through the sample under low pressure. Based on equation (1), one can write simple expressions for the attenuated neutron intensity of (i) a dry sample, (ii) a partially saturated sample and (iii) a fully saturated sample:

Dry sample:

$$I_{dry} = I_o \exp(-\mu_1 \rho_1 h) ,$$

with

$$\mu_1 \rho_1 h = [\mu_m \rho_m (1-\phi)] h , \qquad (2)$$

where μ_m is the attenuation ceofficient of the matrix, ρ_m is matrix density, ϕ is porosity and h is the sample thickness. Note that the air in the pore space has negligible contribution to the attenuation of the incident neutron beam.

Partially saturated sample:

$$I_{partial} = I_o \exp(-\mu_1 \rho_1 h) ,$$

with
$$\mu_1 \rho_1 h = [\mu_m \rho_m (1-\phi) + \mu_w \rho_w V_w] h , \quad (3)$$

where μ_w is the attenuation coefficient of water, ρ_w is the density of water and V_w is the volume fraction of the water in the rock. In this case, the volume frction of the water is less than the porosity ($V_w < \phi$).

Fully saturated sample:

$$I_{sat} = I_o \exp(-\mu_1 \rho_1 h) ,$$

with
$$\mu_1 \rho_1 h = [\mu_m \rho_m (1-\phi) + \mu_w \rho_w \phi] h . \quad (4)$$

In this last case, the volume fraction of the water is equal to the porosity ($V_w = \phi$). Middleton & Pázsit (1998a) have shown how these expressions can be extended to porous rocks containing multi-phase fluids.

One can relate the above cases to fluid flow in a porous reservoir rock by remembering that, while a reservoir rock may be fully saturated, only those pores with "connectivity" will allow fluid to flow. Thus, if water is allowed to flow in an initially dry rock, full saturation may not be reached for some considerable time. Indeed, if the applied pressure forcing fluid flow through the sample is insufficient, the porous sample may retain a degree of "residual air saturation" during the whole experiment. We, therefore, submit that once a stable flow of water is attained in the sample, the volume fraction of water (V_w), calculated using equation (3), should be a reasonable approximation of the "effective permeability" (ϕ_{eff}) of the sample.

The dynamic neutron image produced by our experiments is captured from the "converter screen" by a super-VHS video camera. This video image, which is essentially a "black and white" photograph, can then be converted into a "grey-scale" digital image using a conventional software package. Each pixel on the digital image will have a grey-scale intensity, which is proportional to the original attenuated image intensity. Provided the experiment was performed in such a way that a dry image was initially captured, we can reproduce the sample image on a pixel by pixel basis with a relative neutron intensity for each pixel given by $(I_{dry} - I)/(I_o - I_{dry})$, where I is either $I_{partial}$, or I_{sat} , for each pixel on the digital image. Depending on the type of experiment carried out, we can solve equations (2) to (4) in conjunction with the observed ratio $(I_{dry} - I)/(I_o - I_{dry})$ to derive either ϕ_{eff} or ϕ for each pixel on the image.

This whole conversion process from relative neutron intensity to porosity can be carried out using a standard image processing software package. The new porosity image can then be displayed as a colour-enhanced image to aid interpretation of the porosity structure of the sample.

We have carried several dynamic neutron intensity experiments on a well studied high-porosity, high-permeability sandstone from the Visingsö Formation in Sweden. The petrophysics of the sandstone has been studied in detail by Jakobsson (1989), and also by Middleton & Pázsit (1998b). The sample used for this study had a porosity of approximately 20 %, determined by the gas-expansion and the imbibition methods, and a permeability of approximately 1.5 Darcy (10^{-12} m^2), measured by the air-permeability and liquid-constant-head methods.

Two dynamic neutron radiography experiments were carried out on the sample slab with dimensions thickness of 1 cm, width of 5 cm and length of 10 cm. The 5cm x 10 cm face

was exposed to the incident neutron beam, which was attenuated over the 1 cm thickness of the sandstone slab. The sides of the sample were sealed with adhesive aluminium coating to prevent escape of water, and inlet and outlet tubes were fitted (over the aluminum seal) at the top and bottom to allow introduction and escape of the water.

The sample was initially imaged in a dry state, as a reference for the porosity calculations. Water was then flowed in a horizontal direction through the sample under a pressure of approximately 0.02 MPa. The water flood experiment was imaged continuously by DNR, and 10 images were selected after stable fluid flow was achieved for further analysis. These 10 images were then summed to eliminate statistical variations in the neutron beam, and the ratio $(I_{dry} - I_{partial})/(I_o - I_{dry})$ was determined for each pixel. Finally, the effective porosity (ϕ_{eff}) was calculated for each pixel, and a colour image formed (Figure1a).

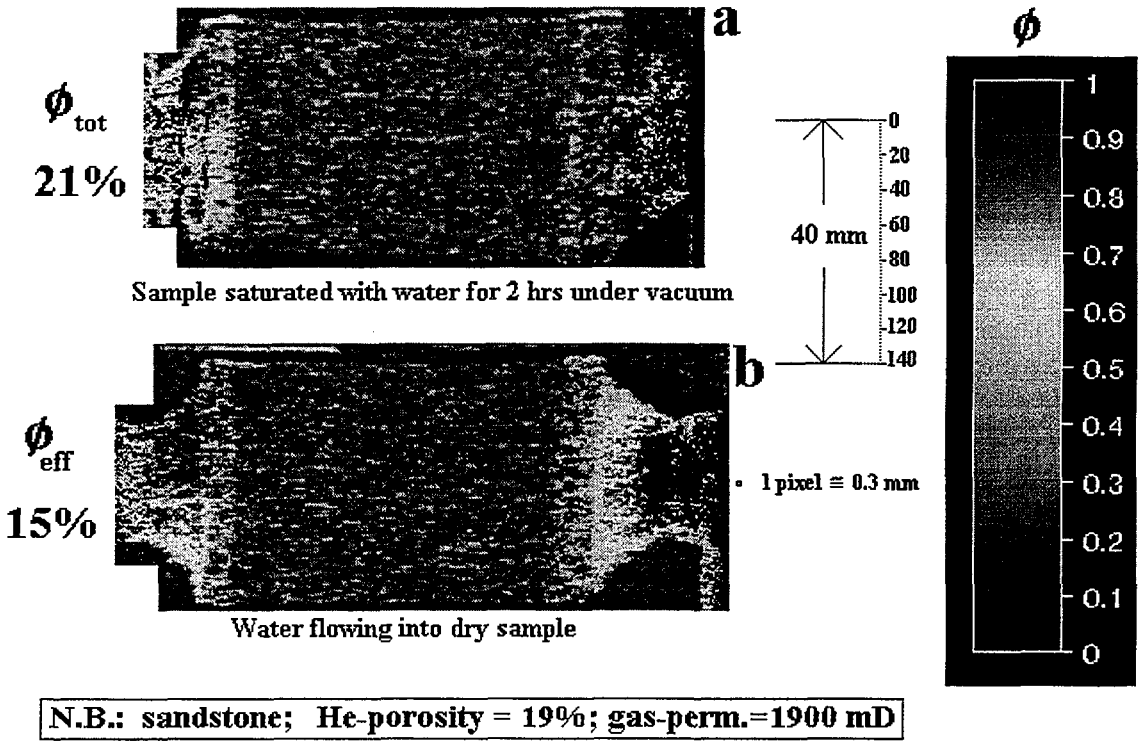

Figure 1: Dynamic neutron radiographic image converted to (a) "total porosity", which represents the total pore space in the sandstone, and (b) "effective porosity", which represents the pore space that can accommodate fluid flow in the sandstone.

The sandstone sample was then fully saturated under a vacuum for 2 hours, and a final DNR image made. No flow occurred during this experiment, and the top and bottom inlets were sealed to trap fully the interstitial water. The same processing was carried out to form the colour image of the total porosity (Figure1b).

Close examination of both images show significant differences in the porosity structure. An average porosity for each of the images can be performed using the image processing package by summing all pixels and dividing by the total number of pixels. The partially saturated (water flood) experiment gave an average porosity of 15 %, and the fully saturated sample yielded an average porosity of 21 %. The latter value agrees reasonably well with the 20 % total porosity determined by the conventional porosity techniques. The lower 15 % "effective porosity" indicates that a considerable number of pores did not contain water during the flow experiment.

References

Balaskó, M. & Sváb, E., 1996, Dynamic neutron radiography instrumentation and applications in Central Europe: Nuclear Instruments & Methods in Physics Research A, vol. **377**, pp.140-143.

Balaskó, M., Körösi, F. & Sváb, E., 1999, Modelling of oil inflitration and distribution in sandstone applying dynamic neutron radiography: Abstract Volume, Sixth World Conference on Neutron Radiography, Osaka, Japan, May 1999, pp.200-201.

Jakobsson, H., 1989, Geologisk documentation av en sandsten från Visingsöformationen: Chalmers Tekniska Högskola och Göteborgs Universitet, Geologiska Institutionen, Publ. B 330.

Lindsay, J.T., Kauffman, C.W., Fogler, H.S. & Last, J., 1989, Neutron radiography applications at the University of Michigan, Phoenix Memorial Laboratory: *in* Proceedings of The Third World Conference on Neutron Radiography, May 14-18, Osaka, Japan, Kluwer Academic Publishers, Dordrecht.

Middleton, M.F. & Pázsit, I., 1998a, Neutron Radiography: A technique to support reservoir analysis, *Exploration Geophysics*, vol. 29, pp.512-515.

Middleton, M.F. & Pázsit, I., 1998b, A study of the Visingsö Sandstone using neutron radiography, Nordic Petroleum Technology Series III, Research in Petroleum Technology, pp.139-148.

Middleton, M.F., Pázsit, I. & Solymar, M., 1999, Petrophysical Applications of Neutron Radiography, Proceedings of the Sixth World Conference on Neutron Radiography, Osaka, Japan, *in press*.

The effect of band structure on sputtering

Ming Tan and B.V. King

Physics Department, University of Newcastle, NSW 2308, Australia

Abstract

Using one-color two step ionisation schemes, we have measured using resonant ionisation spectroscopy (RIS) the number of Ni atoms ejected in the ground state (a^3F_4) and an electronically excited state (a^3D_3) state from both Ni_3Al and pure Ni surfaces. The ratio of the RIS signal from the a^3D_3 state to that from the a^3F_4 state is 1.07±0.03 for Ni_3Al and 1.05±0.08 for pure Ni. To within experimental error, we saw no difference between pure Ni and the alloy in the relative sputter yield of Ni atoms in the excited a^3D_3 state compared to ground a^3F_4 state. There is a difference in the electronic band structure between pure Ni and Ni_3Al. The above result indicates the different band structure does not influence the relative sputter yields of excited states.

Introduction

When bombarded by energetic ions, metal surfaces emit various particles including secondary ions, clusters and ground and excited state atoms. During sputtering, classical momentum transfer between the incident ion and target atoms takes place. In addition target atoms may be electronically excited or ionised. The momentum transfer leads to sputtering of particles. Electronic events occurring near the surface can determine the formation of secondary ions or excited secondary neutrals. An understanding of the basic mechanisms related to these electronic events is of fundamental and practical interest.

It is however difficult to analyse ejected secondary neutrals, either in the ground or excited states, because a mass spectrometer cannot directly detect them. In order to analyse secondary neutrals, the ejected neutrals must be ionised, typically by an electron beam, electron gas or laser. Of these techniques, laser postionisation is the most sensitive. It also allows state-selective ionisation so that both ground state and electronically excited neutrals may be separately measured. Results from laser postionisation measurements [1] on Ni show that the magnitude of the excitation energy, the electronic configuration and the character of the band structure play an important role in the formation of the excited atoms. For example in pure Ni, there are more atoms sputtered into the excited states a^3D_3 and a^3D_2 than the ground state a^3F_4. This observation has been explained by the resonant electron transfer model [2-4]. The aim of this study is to examine the resonant electron transfer model by measuring the ratio of atoms sputtered in the a^3D_3 state to those in the a^3F_4 state from pure Ni and from Ni_3Al, using RIS.

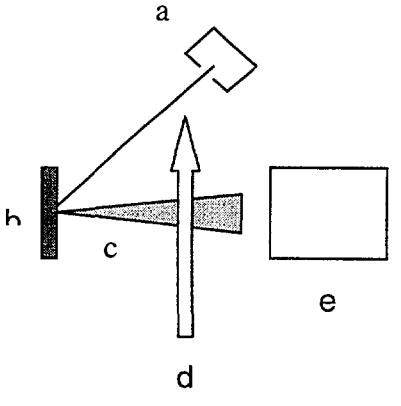

Figure 1. Schematic diagram of a laser postionisation mass spectroscopy: (a) primary ion source, (b) target, (c) ejected particles, (d) laser pulse beam, (e) mass spectrometer

Experimental procedure

Figure 1 schematically shows the basic setup of a laser postionisation mass spectroscopy. Argon ions are produced in the ion source and electrostatically accelerated to 4keV and then focused at 45° incidence onto a 3mm spot on the target. A laser pulse of 8 ns with a cross section of 1mm x 8mm was positioned 12mm above the target surface. Neutral atoms sputtered in a specific quantum state are selectively ionised by tuning the laser wavelength and extracted into a time-of-flight mass spectrometer and subsequently counted by a microchannel plate detector. One-color two step schemes were employed to ionise sputtered atom, as shown in Figure 2. The a^3F_4 is the ground state of Ni atoms and the a^3D_3 and a^3D_2 are excited states. The $a^3F_3^0$ is the resonant intermediate state and IP stands for the ionisation potential. For such ionisation schemes, two photons are required to ionise one atom. One photon excites an atom to the resonant intermediate state and subsequently this excited atom absorbs a second photon from the same laser field and become ionised. The ionisation efficiency depends mainly on the ionisation cross section.

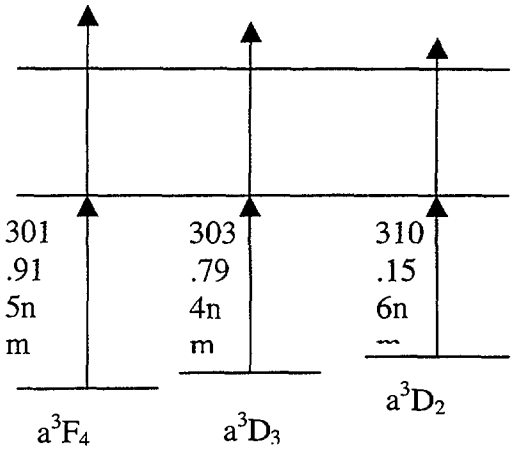

Figure2. One-color two step ionisation schemes used in this study

Figure 3 shows a timing scheme for detecting RIS signal. The flight time of primary ions from the ion source to the target is 10μs. τ_D is the delay time between the primary ion pulse and the laser pulse. $\Delta\tau_I$ is the width of ion pulse. τ_E is a flight time of sputtered atoms from the target to the laser beam and τ_m is a flight time of laser-ionised atom in the extraction field. Sputtered atoms have a distribution of velocity. Faster sputtered atoms have a smaller τ_E and after being ionised, they take less time to reach MCP owing to their higher initial velocities at which they enter the extraction field and τ_m is correspondingly shorter. The τ_m of photoions of different initial velocities was measured by changing the delay time (τ_D) between the primary ion pulse and the laser pulse. When $\Delta\tau_I$ is 200ns and τ_D is chosen to be 11μs, atoms whose τ_E is 0.8-1.0μs are ionised and a RIS peak appears at τ_m = 4.8μs. When τ_D is 18μs, τ_E values of measured atoms range from 7.8-8.0μs and a RIS peak was observed at τ_m = 6.6μs. In the RIS intensity measurements, the MCP is switched on 4.8μs and off 6.8μs after laser fires. This MCP gate can detect photoionised atoms whose τ_E ranges from 0.9 to 8.0μs. The kinetic energy is roughly estimated to be 54eV and 0.68eV for atoms sputtered with an τ_E of 0.9μs and 8μs, respectively. The RIS measurements were performed by changing the delay time (τ_D) between the primary ion pulse and the laser pulse. From the RIS versus τ_D measurements, the relative intensity of atoms ejected in a specific atomic state can be determined.

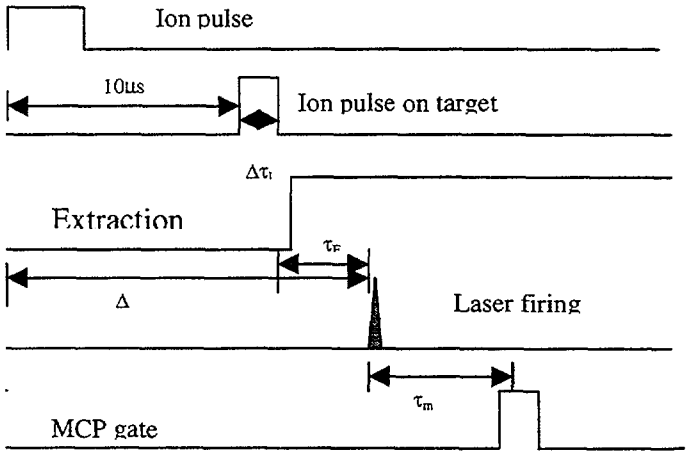

Figure 3. Timing scheme for RIS

The base pressure of the UHV chamber in which the target and MCP detector are assembled is 1.4 x 10^{-9}mbar and the operating pressure is 2.1 x 10^{-8}mbar. The time required that a clean metal surface adsorbs a monolayer of contamination under this base pressure is theoretically estimated to be 15 min. In order to reduce contamination, the measurements were done with a 2μs pulse. The measurement time is shorter than 3 min.

We examine the cleanliness of a target surface by measuring the RIS intensity. The RIS intensity increases as the surface contamination decreases. The ion beam was continuously rastered across a surface area of 5.7mm x 5.7mm, and subsequently the RIS intensity was measured. The cleaning and RIS measurement was repeated until the RIS intensity was found to stay unchanged. Then the target was believed to be clean and measurements were performed.

Results

Figure 4 shows τ_D distributions of the RIS of Ni atoms ejected in a^3F_4 and a^3D_3 states from Ni_3Al. Most of Ni atoms sputtered in a^3F_4 and a^3D_3 states were observed at τ_D of 11.5 – 17.5μs, which is identical to τ_E of 1-7μs.

We have measured the RIS intensity of atoms sputtered in a^3F_4 and a^3D_3 states from pure Ni and Ni_3Al single crystals, with τ_E ranging from 1 to 7μs (kinetic energies being 0.9 - 44eV. Four independent measurements were performed for all the RIS intensities. The laser power for these measurements is 1.0 – 1.2mJ/pulse. Table 1 gives normalised RIS intensities and shows that the a^3F_4 RIS intensity is almost equal to the a^3D_3 intensity for Ni_3Al and pure Ni. The RIS ratio of a^3D_3 to a^3F_4 is 1.046 for pure Ni, and 1.074 for Ni_3Al.

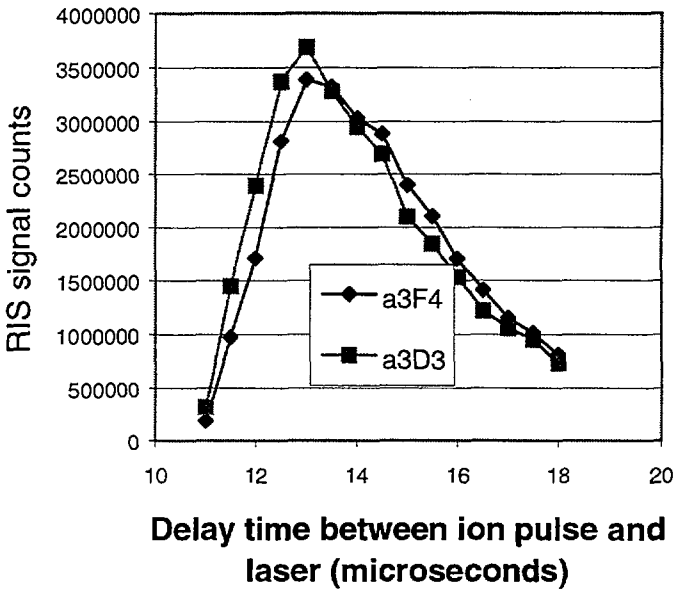

Figure 4 RIS intensity versus delay time for ground and excited states in Ni_3Al

4. Discussion

The resonant electron model assumes that the formation of a sputtered atom can be regarded as a departing ion picking up an electron from the valence band and that the orbital energy and shape of the valence electron is preferentially preserved. Consequently, the population of atoms sputtered in a specified quantum state can depend not only on the excitation energy but also on the coupling between the valence electron and the final state of the atom. The electronic configuration of Ni atoms ejected in the a^3D_3 and a^3D_2 states ($3d^94s^1$) is closer to the valence electron of Ni ($3d^{9.4}4s^{0.6}$) than that of the ground state ($3d^84s^2$). Due to the weaker coupling of the ground state to the valence electron, the ground state a^3F_4 is less populated than the a^3D_3 and a^3D_2 states.

Table 1 RIS signal of Ni atoms ejected in a^3F_4 and a^3D_3 states from Ni_3Al and Ni

Ni_3Al		Pure Ni	
a^3F_4	a^3D_3	A^3F_4	a^3D_3
43.2	48.1	35.1	41
44.2	47.7	37.6	37.8
43.8	46.8	39.2	39.5
47.4	48.9	36.8	37.2
Average 44.6	Average 47.9	Average 37.2	Average 38.9

The valence electron configuration of Ni_3Al is calculated to be $3d^{8.4}4s^{1.6}$ [5]. The difference in electronic structure between the Ni_3Al band ($3d^{8.74}4s^{1.26}$) and the atomic ground state a^3F_4 ($3d^84s^2$) is much smaller than that between the Ni band ($3d^{9.4}s^{0.6}$) and the a^3F_4 state. According to the resonant tunneling model, the probability of a valence electron resonantly transferring into the a^3F_4 state ($3d^84s^2$) in the Ni_3Al single crystal should be larger than in the Ni single crystal due to the stronger coupling of an atomic ground state with the valence band of the alloy. Therefore, if the model holds true, the population ratio of a^3D_3 to a^3F_4 in the Ni_3Al crystal should be smaller than in the Ni crystal.

The RIS intensity is given by I = nVP where n is the population density that indicates the number per unit volume at the laser beam region of atoms ejected in a specific quantum state, V is the sampling volume and P is the ionisation probability of one atom. Since the experimental conditions for the Ni_3Al alloy are the same as those for the Ni metal, the V and P ratios of a^3D_3 to a^3F_4 for the alloy are identical to those of the metal. Therefore, the population ratio change is reflected in the RIS signal intensity ratio. However, the expected decrease in the RIS ratio was not observed in Ni_3Al. Much research is required to confirm the resonant electron transfer model.

5. Summary

The RIS ratio of a^3D_3 to a^3F_4 in Ni_3Al is almost identical to that in pure Ni. We did not observe the band structure effect on sputtering of Ni atoms in a^3F_4 and a^3D_3 states from Ni_3Al and pure Ni. The band structure effect of sputtering is awaiting further examinations.

6. References

[1] B.J. Garrison, N. Winograd, R. Chatterjee, Z. Postawa, A. Wucher, E. Vandeweert, P. Lievens, V. Philipsen, R. Silverans, Rapid Commun. Mass Spectrom. 12, 1266(1998).

[2] C. He, Z. Postawa, S. Rosencrance, R. Chatterjee, B.J. Garrison, and N. Winograd, Phys. Rev. Lett 75, 3950(1995).

[3] E. Vandeweert, V. Philipsen, W. Bouwen, P. Thoen, H Weidele, R. Silverans, and P. Lievens, Phys. Rev. Lett. 78, 138(1997).

[4] E. Veje, Phys. Rev. B28, 5029(1983).

[5] Zs. Kovcs, et al, Phys. Rev. B54, 8501(1996).

RBS and XRD analysis of silicon doped titanium diboride films

S. Mollica[a], D.K. Sood[a], M. K. Ghantasala[a], R. Kothari[a], P.Evans[b], G. Collins[b]

[a]Department of Communication and Electronic Engineering, RMIT University, 124 LaTrobe Street, Melbourne 3000, Australia, [b]Australian Nuclear and Science Technology Organisation, Lucas Heights Research Laboratory, Private Mail Bag 1, Menai 2234, Australia

Abstract

Titanium diboride is a newly developed material suitable for protective coatings. Its high temperature oxidation resistance at temperatures of 700°C and beyond is limited due to its poor oxidative behaviour. This paper presents a novel approach to improving the coatings' oxidative characteristics at temperatures of 700°C by doping with silicon. Titanium diboride films were deposited onto Si(100) wafer substrates using a DC magnetron sputtering system. Films were deposited in two different compositions, one at pure TiB_2 and the other with 20%Si doping. These samples were vacuum annealed at 700°C at $1x10^{-6}$Torr to investigate the anaerobic behaviour of the material at elevated temperatures and to ensure that they were crystalline. Samples were then oxidised in air at 700°C to investigate their oxidation resistance. Annealing the films at 700°C in air results in the oxidation of the film as titanium and boron form TiO_2 and B_2O_3. Annealing is seen to produce only minor changes in the films. There is some silicon diffusion from the substrate at elevated temperatures, which is related to the porous nature of the deposited film and the high temperature heat treatments. However, silicon doped films showed relatively less oxidation characteristics after annealing in air compared with the pure TiB_2 samples.

Introduction

Titanium diboride is a ceramic material that has attracted much interest for applications such as a protective coating against oxidative wear because of its high hardness, high melting point and good electrical properties. It has recently been used as a protective coating in crucibles and electrodes for aluminium reduction. TiB_2 also displays remarkably good conductivity at elevated temperatures, a characteristic observed in relatively few other recently developed coating materials. It displays a potential for use as a coating for stainless steel interconnects within a ceramic fuel cell (CFC). However, it is unstable at elevated temperatures, and as reported previously [1] will form B_2O_3 and TiO_2 at elevated temperatures. Previous work [2] from the authors presented results of implantation with Ti and Ta ions to investigate the self-ion damage effects and the effects of implanting a higher valency ion on the crystal lattice. Implantation of Ti and Ta resulted in improved oxidation resistance of the films. This paper presents the details of our results on the doping of silicon in to the TiB_2 films by co-sputtering process.

Experimental

TiB_2 films were deposited onto Si(100) wafers by DC magnetron sputtering at an argon pressure of $3.2x10^{-3}$ Torr. Silicon doping was performed using silicon pieces (of a calculated area according to the required dopant concentration in the film) attached to the target with silver adhesive paste. This ensured that the silicon was co-sputtered with the TiB_2 to give the desired silicon concentration throughout the entire thickness of the films. After deposition, selected films were vacuum annealed for four hours at 700°C and then subjected to oxidation at the same temperature for four hours. These films were analysed for composition and structure using Rutherford Backscattering Spectrometry (RBS) and X-Ray Diffraction (XRD) respectively. RBS was performed using a 2-MeV He^{2+} beam (collimated to 1.5mm diameter) backscattered at 169° to the beam direction. Spectra were accumulated for a total charge of

20μC measured with a sensitive Faraday cup arrangement. XRD was performed using a SIEMENS D500 Diffractometer using CoKα radiation.

Results and Discussion

The two analytical tools employed for the investigation are Rutherford Backscatering Spectrometry (RBS) and X-Ray Diffraction (XRD). Figure 1 refers to the RBS spectra of pure TiB_2 films. It shows three different spectra corresponding to the asdeposited pure TiB_2 film, annealed at 700°C and oxidised at 700°C. It may be observed from the film that the thickness of the asdeposited film is less than the annealed and oxidised films. This may be due to the thickness variation of the film during deposition. Oxygen has been the main impurity in these films. Previous work, [3] explains an unavoidable level of oxygen contamination, and that there seems to be a tendency for these films to form TiO_2 in the presence of oxygen. We also noticed a small quantity of aluminum present in the film. This could have been sputtered from the clamping ring that was holding the TiB_2 target to the holder. In the subsequent experiments the magnetron holder has been modified to eliminate the possibility of any aluminum impurity in the films. The 0%Si-doped oxidised TiB_2 film displays a greatly reduced thickness of Ti and greatly increased silicon and oxygen concentrations. However, the reduction in the thickness of deposited titanium may be attributed to two reasons. In addition to the non-uniformity of the deposition process, the presence of increased oxygen signal might also have contributed to this behaviour. It is difficult to state unequivocally the exact boron concentration in the asdeposited films and also any changes occurred in its composition due to heat treatments because of its low atomic number.

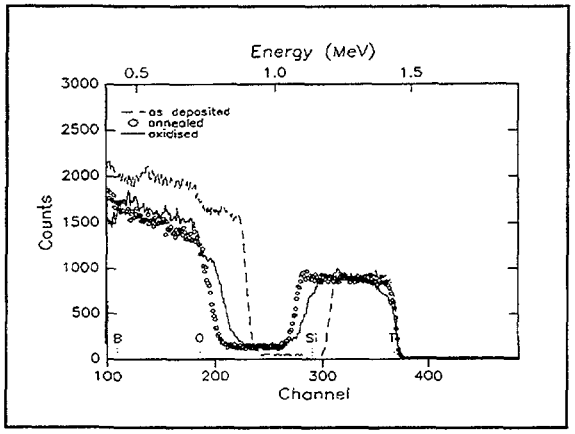

Figure 1. RBS Spectrum of Pure TiB_2 films

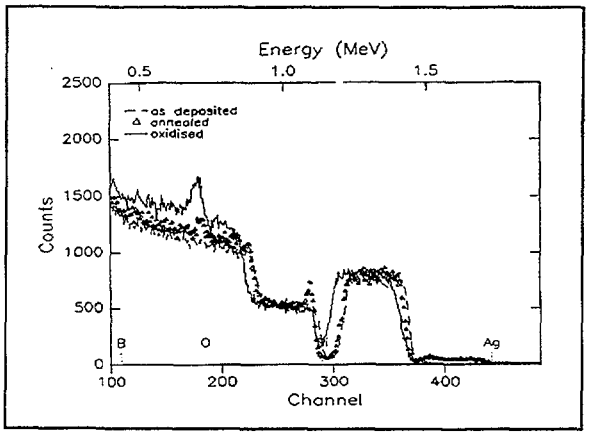

Figure 2 RBS Spectrum of 20%Si-doped TiB_2 films

Figure 2 refers to the 20%Si-doped films. The asdeposited film displays the deposited titanium, silicon signals along with a small concentration of oxygen and some silver. The silver is observed because it is present in the adhesive paste used in attaching the silicon pieces to the target. In spite of the care taken not to expose any silver paste adhesive directly to the plasma, apparently there has been some sputtering at the edges and corners, which resulted in the inclusion of a minimal quantity of silver (< 0.8 %) in the films. The vacuum annealed TiB_2 film exhibits relatively little change as far as the RBS data is concerned. Though there is no oxygen present in the asdeposited and vacuum annealed films, some amount of oxygen is present in the oxidised film over a thinner surface layer. Thickness of the oxygen signal is certainly less than one fifth of the total thickness of the film as indicated by the titanium signal at the channel number 368. This essentially means that the bulk of the TiB_2 film is still intact without oxidation, which may be attributed to the presence of silicon in the film. A noted reduction in the silver concentration is observed after the treatment. It is difficult to observe the boron concentration due to the reasons explained above.

Figures 3 and 4 give a good comparison of the XRD spectra of pure (0%Si-doped) TiB_2 films with that of 20%Si-doped films. In figure 3, the asdeposited sample clearly displays the formation of the $TiB_2(100)$ and $TiB_2(101)$ peaks at approximate 2-theta angles of 34.5° and 44.5° respectively. These are in agreement with the standard values reported in the powder diffraction file data for TiB_2 phase (PDF 35-741). There are two large peaks at 2-theta values of approximately 61.8 and 68.9 that represent different planes of the silicon substrate. The XRD (not shown in the figure) of the vacuum annealed sample (700°C for 4 hours) has also indicated the formation of same peaks. In contrast, the XRD spectra of oxidised sample shown in figure 3 exhibits the formation of many different peaks. In addition to the substrate silicon peaks, we observe the following peaks at the approximate 2-theta angles: 32°, 36°, 54.5°, 39.5°, 41.5°, 44.5°, 61.5° and 63°. These peaks are mainly attributed to three different phases: TiB_2, B_2O_3 and TiO_2. In specific, the peaks at 32° ,36° and 54.5° can be attributed to (222), (400) and (600) planes of B_2O_3 phase, while the peaks at 39.5°, 41.5° are identified to belong to the (200) and (111) planes of TiO_2 rutile phase. Interestingly, a peak corresponding to the (204) plane of TiO_2 anatase phase is also seen at a 2-theta value of 63°. Rest of the peaks are that of (100) and (110) planes of TiB_2 phase. This is clearly indicating the oxidation of the film. The oxidised spectrum is in agreement with the RBS data also. As large amount of oxygen presence is seen from the RBS spectra of both asdeposited and annealed films, it is not surprising to see the formation of different oxide phases after oxidation. However, at this stage the role of oxygen in the oxidation of the film is not clearly understood.

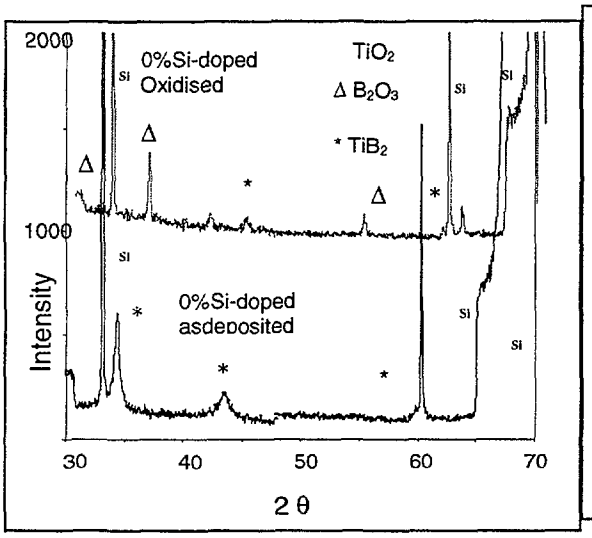

Figure 3 XRD Spectrum of 0%Si-doped TiB_2 Oxidised Film

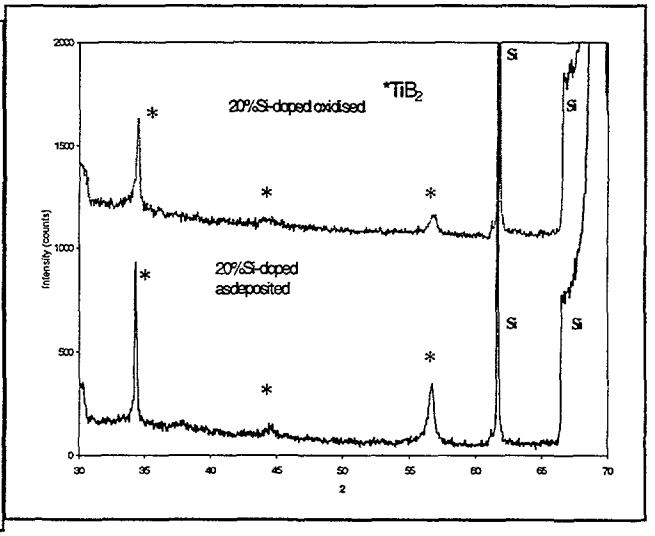

Figure 4 XRD Spectrum of 20%Si-doped TiB_2 Oxidised Film

Fig.4 represents the xrd spectra of the films deposited with around 20% silicon doping. Bottom spectra in this figure belongs to the xrd of the asdeposited film while the top one is that of the oxidised film. It is very clear from these spectra that there is not much change between the xrd spectra of the asdeposited and oxidised films. Though the peaks remained the same even after oxidation, their intensities varied. Overall, there have been no indications of any oxide formation in these films compared to the pure TiB_2 films without any doping.

Conclusions

This paper presented the results of our investigation on the silicon doping of TiB_2 films deposited by DC magnetron sputtering. Pure TiB_2 films oxidise to TiO_2 and B_2O_3 when annealed in the presence of oxygen at 700°C for four hours. Silicon doping via co-sputtering has a positive effect in reducing the oxidation of TiB_2 to TiO_2 and B_2O_3 when annealed in the presence of oxygen under the same conditions. The evidence presented in both XRD and RBS spectra support these conclusions. However, the oxidation mechanism under the silicon doping conditions need further investigation.

Acknowledgments

This work is supported by an AINSE and ARC small grant.

References

[1] A. Kulpa, Ttroczynski, J. Am. Ceram. Soc. 79 (1996) 518.

[2] D.K. Sood, S.Mukherjee, G. Katselis, I.G. Brown, K.E. Prince, K.T. Short, P.J. Evans, Surf. Coat. & Tech. 103-104 (1998) 304.

[3] J.R. Shappirio, J.J. Finnegan, Thin Solid Films, 107, (1983) 81

[4] W.A. Zdaniewski, J. Wu, S.C. Gujrathi, K. Oxthorn, J. Mater. Res. 6 (1991) 1066.

The creation of Ti: Sapphire by Ion Implantation of $\gamma - Al_2O_3$

M. J. Norman, L. D. Morpeth, J. C. McCallum
Microanalytical Research Centre, School of Physics, University of Melbourne, Victoria 3010, Australia, mjn@physics.unimelb.edu.au

Introduction

Sapphire (Al_2O_3), being transparent to the visible spectrum, is an excellent optical material. The ability of Al_2O_3 to hold a range of optically active ions makes it a good laser host, hence sapphire films doped with such ions are of interest because of their potential applications in planar optoelectronic devices. That is, where optical and microelectronic components are integrated on the same wafer. This would involve depositing the optically active film onto a silicon substrate (the basis for most electronic devices.)

The aim of this experiment was to investigate the possibility of forming optically active Ti^{3+} by ion co-implantation of Ti and O ions directly into buried polycrystalline cubic ($\gamma - Al_2O_3$) sapphire layers, as a means of forming a Ti:Sapphire waveguide laser. To date, there has been little research on the doping of $\gamma - Al_2O_3$.

The materials produced were characterised by two methods. Structure was probed by the use of Rutherford Backscattering Spectrometry (RBS) and Ion Channeling (RBS-C) techniques. Optical properties were verified by photoluminescence (PL) measurements using a Raman Spectroscopy laser system.

Experiment

Single crystals of $\alpha - Al_2O_3$ were obtained from Crystal Systems, Inc. The disk specimens, as supplied, were polished on one side. These were annealed at 1400°C in air for 48 hours to remove any residual defects induced by the mechanical polishing process. All samples were implanted at liquid nitrogen ($N_{2(l)}$) temperature using the 1.7 MeV NEC implanter at the Department of Electronic Materials Engineering ANU. They were mounted to the sample stage with silver dag to ensure good thermal contact. $N_{2(l)}$ temperature was used for a number of reasons. First, for stoichiometric implants of Al and O, relatively low doses are needed to amorphise sapphire. Second, in $\alpha - Al_2O_3$ there is evidence to suggest that $N_{2(l)}$ temperature implantation of Ti and O ions encourages formation of Ti^{3+} more readily [4]. It is anticipated that the result will be similar for $\gamma - Al_2O_3$.

Figure 1 shows a schematic of the implantation and annealing process in the formation of Ti:sapphire in the γ phase.

Fig. 1 (a) A buried amorphous layer was formed by implantation of a stoichiometric ratio of Al and O ions. The implantation schedule was as follows: Al (1.2 MeV, $5 \times 10^{16} cm^{-2}$) and O (1.4 MeV, $5 \times 10^{16} cm^{-2} + 1.18$ MeV, $2.4 \times 10^{16} cm^{-2}$). We performed two oxygen implants (at different energies and doses) for each sample to obtain a relatively constant profile over the depth range required. The energies and doses required for this profile were derived with the aid of the PROFILE [5] code. The dimension of the implantation region on each disk was 1.6 cm × 1.9 cm.

Fig. 1 (b) The samples were then annealed at 900°C for one hour in O_2 to transform the buried amorphous layer to $\gamma - Al_2O_3$ [1]. Greater temperatures would result in the rapid epitaxial regrowth of the α phase, connecting at the interfaces between the γ layer

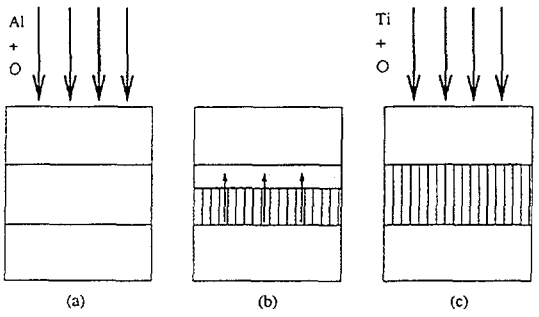

Figure 1: Schematic representation of the implantation process: (a) formation of an amorphous sapphire layer in bulk $\alpha - Al_2O_3$, (b) annealing to form $\gamma - Al_2O_3$ and (c) implantation of titanium and oxygen into the buried $\gamma - Al_2O_3$ layer.

and the surrounding $\alpha - Al_2O_3$ bulk. At 900°C, the regrowth of the α phase is limited to a few tens of Ångstroms per hour [2, 3].
Fig. 1 (c) A series of varying Ti and O doses followed. Again, the PROFILE code was used to calculate the energies and doses required to obtain a constant implant profile for both Ti and O, which overlapped the depth range of the γ layer. First, we performed a Ti dose series, maintaining the O/Ti ratio at 3:2. This is the ratio of atoms in the Ti_2O_3 molecule, which has titanium in the 3+ oxidation state, and which we hope to form within the sample. The implantation schedule for 0.1 atomic percent (at. %) Ti was as follows: Ti (2.5 MeV, 4.12 $\times 10^{16} cm^{-2}$ + 1.8 MeV, $2.06 \times 10^{15} cm^{-2}$) and O (1.4 MeV, 3.25 $\times 10^{15} cm^{-2}$ + 1.2 MeV, $9.73 \times 10^{14} cm^{-2}$ + 1.1 MeV, $9.73 \times 10^{14} cm^{-2}$ + 1.0 MeV, $9.73 \times 10^{14} cm^{-2}$). We also implanted Ti to 0.2 and 0.05 at. % , with doses scaled accordingly. A series of implants were then performed, where the atomic percentage of Ti was held constant (0.1 at. %) in the sample, while the ratio of titanium to oxygen was varied (doses scaled accordingly).

Before PL was performed, the Ti + O implanted samples were further annealed in order to both encourage the formation of Ti^{3+} and remove any optical defects. Defect centres can absorb photons as well as emitting their own characteristic light. The anneals were varied in duration (1 - 4 hrs) and annealing ambient - O or forming gas (4 % H + 96 % Ar). Again, care was taken to use annealing temperatures and times that precluded $\alpha - Al_2O_3$ from forming.

PL was performed on the samples using a Raman Microprobe with the 514.5 nm line of an Ar^+ ion laser as the excitation source. The intensity at the expected emission peak of Ti^{3+} was measured for each sample in the Ti + O implantation series. A more complete spectrum, of the emission band, was also taken for each.

RBS was performed using 2.8 MeV He^{++} ions. This was performed post-amorphisation and on a sample annealed to form $\gamma - Al_2O_3$. As yet, it has not been performed on Ti implanted samples.

Results and Discussion

The RBS spectrum in Fig. 2 was collected from an amorphised sample. No annealing had occured at this stage. The channeled spectrum (triangles) exhibits relatively high yields in the near-surface regions of the Al + O parts of the spectrum. This indicates the presence of implantation damage near the surface. The amorphous layer appears

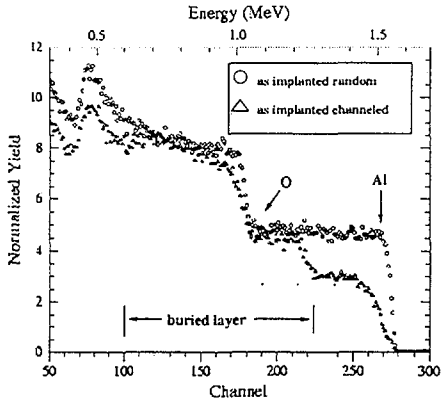

Figure 2: RBS spectrum of a sample with a buried $\gamma - Al_2O_3$ layer

to begin about half-way between the Al and O edges, with a sharp increase in yield. The back edge of the amorphous layer appears to be the first dip in the yield after the O edge. RUMP [6] simulations indicate that this RBS spectrum is produced by an amorphous Al_2O_3 layer about 10,300Å thick, beginning at a depth of about 4,000Å. The annealed sample produced a similar channeled spectrum. The front and back edges of the layer, as described above, appear to be slightly steeper, indicating a sharpening of the interface between the layer and the bulk sample. This is consistent with the formation of $\gamma - Al_2O_3$. It is hoped that further investigations using X-ray techniques will be more conclusive.

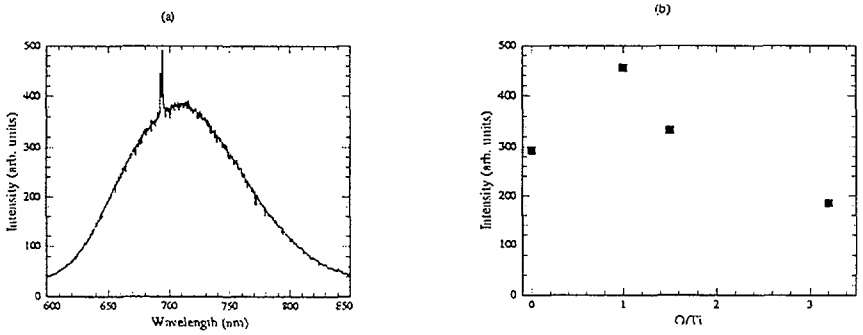

Figure 3: Photoluminescence Data: (a) A typical spectrum, showing the broad luminescence of Ti:sapphire, with two thin chromium peaks and (b) the peak luminescence of the Ti:O ratio series.

Photoluminescence data is shown in Fig. 3. Fig. 3(a) shows a typical spectrum, taken in the region of the broad emission band of Ti:sapphire. This sample was implanted with 0.2 at. % Ti with a ratio of O to Ti of 3:2 and was subsequently annealed in O for 4 hrs. There is a distinct decrease in the efficiency of the optics and CCD camera in the Raman Microprobe above $\approx$ 700 nm. This tends to skew data towards lower wavelengths and we have not attempted to correct for it. The spikes near the top

of the spectrum are due to chromium impurities in the sample. This impurity is part of the manufacturing process.

PL Intensity data were taken around the emission peak (700 nm) for each sample in the Ti + O implantation and anneal series. They suggest that annealing for 1 hr at 900°C increases the PL signal by two orders of magnitude. Anneals of longer duration (4 hrs) at 900°C increase the PL signal only fractionally from the 1 hr anneals. The data also indicate that annealing ambient does not affect the PL signal. This was expected, since the gamma layer was buried well below the surface of the sample, and diffusion of ambient atoms into the layer would have been unlikely.

The concentration series peak data appear to have a profile as found in studies [4] of $\alpha - Al_2O_3$, and will not be commented on. The peak data pertaining to the O/Ti ratio series are shown in Fig. 3(b). This data is quite different to that of Ti/O implantation into $\alpha - Al_2O_3$. The data in Ref. [4] show an increase in peak intensity until the O/Ti ratio reaches 2:1. A marked decrease is seen for ratios above this. Our data show a different trend, although more investigation of the mid-points is needed. The PL signal is relatively high for an implant of Ti alone. The greatest PL intensity appears to be when the O/Ti ratio is near 1:1, although a smaller fraction may yield a higher peak intensity. For ratios greater than 1:1, there is a gradual roll-off in peak intensity.

Conclusion

We have created buried $\gamma - Al_2O_3$ layers in bulk $\alpha - Al_2O_3$. We have found that co-implantation of Ti and O ions into the buried $\gamma - Al_2O_3$ layers forms Ti in the active (3+) oxidation state. Further, the Ti^{3+} is formed most effectively when the ratio of implanted O to Ti is 1:1. This is unlike $\alpha - Al_2O_3$, where the the most productive ratio is 2:1. Futher studies need to be done to determine more precisely the structure of the buried layer. The possibility that Ti^{3+} is formed more readily, by co-implantation ratios with less oxygen than titanuim, also needs to be investigated. At this stage, $\gamma - Al_2O_3$ is comparable to $\alpha - Al_2O_3$ in its ability to form Ti^{3+} and, hence, may be a good waveguide laser host.

REFERENCES

[1] C. W. White, L. A. Boatner, P. S. Sklad, C. J. McHargue, G. C. Farlow and M. J. Aziz, "Ion Implantation and Annealing of Crystalline Oxides and Ceramic Materials", *Nuc. Inst. and Methods B* **32** (1988), pp. 11 - 22.

[2] D. R. Clarke, "Epitaxial Phase Transformations in Aluminium oxide", *Phys. Stat. Sol. A* **166** (1998), pp. 183 - 196.

[3] J. C. McCallum and T. W. Simpson, "Time Resolved Reflectivity Measurements of the Amorpohous-to-gamma and Gamma-to-alpha phase transistions in ion implanted Al_2O_3", *Nuc. Inst. and Methods B* **91** (1994), pp. 60 - 62.

[4] J. C. McCallum and L. D. Morpeth, "Synthesis of Ti:sapphire by Ion Implantation", *Nuc. Inst. and Methods B* **148** (1999), pp. 726 - 729.

[5] PROFILE CODE, Implant Sciences Corporation, USA.

[6] RUMP, RBS analysis package, M. O. Thompson, Cornell, Ithaca, N. Y.

LEIS studies of a Pt deposited Rh(100) surface

C.P. Oliver, B.V. King, D.J. O'Connor
Department of Physics, University of Newcastle, Callaghan 2308 NSW

Catalysts are widely used in industry and the search is always on for cheaper and more efficient catalytic materials. Pt and Rh are found in many applications because of their excellent catalytic properties, outstanding thermal stability and their resistance to corrosion. In particular, the so called three-way catalyst is used for the decontamination of automobile exhaust gases. This catalyst can simultaneously remove carbon monoxide (CO), nitric oxides NO_x and hydrocarbons. The catalytic activity of any alloy or bimetallic system is strongly influenced by its surface composition and structure. To investigate the surface, low energy ion scattering (LEIS) has been used along with low energy electron diffraction (LEED). These surface sensitive techniques reveal surface order, surface composition and atomic positions to more fully characterize and understand the PtRh surface and its catalytic nature.

LEIS involves the use of a probe ion (usually noble gas or alkali) of energy from 100eV to a few keV being scattered from a surface. The energy and angular distribution of the scattered ions or recoils is then measured. These quantitative measurements give short range structural information about the surface, thus complementing long range order LEED measurements. LEIS is very powerful since it is a real space technique, and can be described with simple concepts based on classical collision phenomena such as shadowing and blocking. It can measure distances between atoms with an accuracy of 0.1 Å and determine surface elemental compositions to 1 %. The technique owes its surface sensitivity to the high neutralization probability of the incident ion. Noble gas ions scattered from the top layer are neutralized with a probability of greater than 90%. The main drawback of LEIS is the damaging effect of the incident probe on the surface structure. Thus the incident current needs to be limited to an acceptable value.

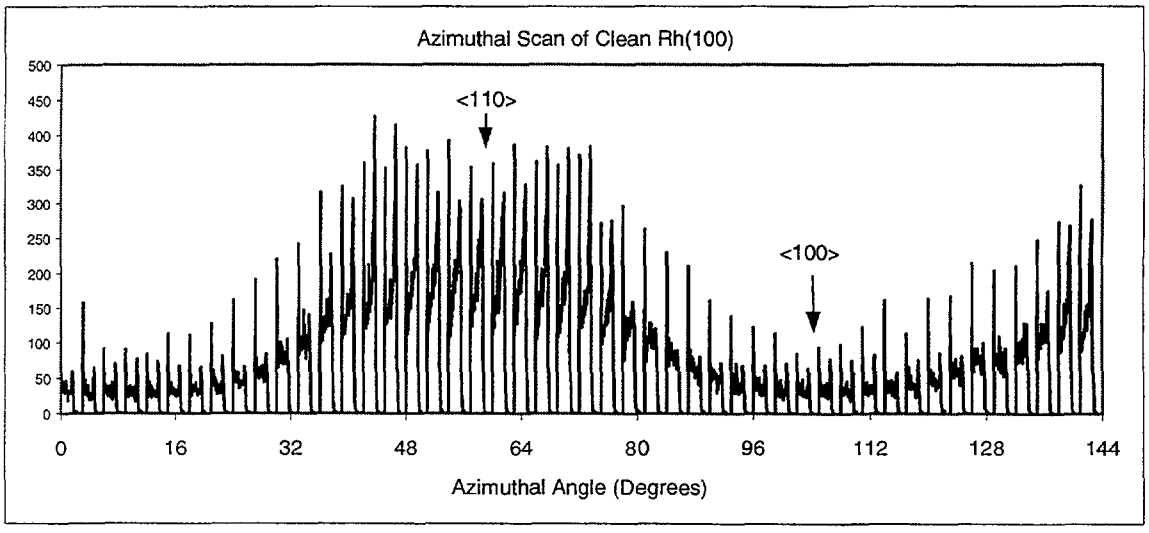

Figure 1. Azimuthal Scan of Clean Rh(100)

Figure 1 is an azimuthal scan of the clean Rh(100) surface. The incident ion was Li, angle of incidence 45 degrees and scattering angle 90 degrees. As the FCC crystal is rotated, the background and surface peak can be seen to move through systematic minima and maxima. The angles at which the crystal was aligned along the <100> and <110> directions are indicated. Along the <100> direction the system is in the so called 'double alignment'

configuration. In this scenario, all ions recoiling from layers other than the surface layer should be blocked and thus we should see a minimum in the background yield. This phenomena can be seen in Figure 1. The surface peak is also periodically changing. This is due to the focusing and shadowing of the first layer atoms onto second layer and sometimes third layer atoms.

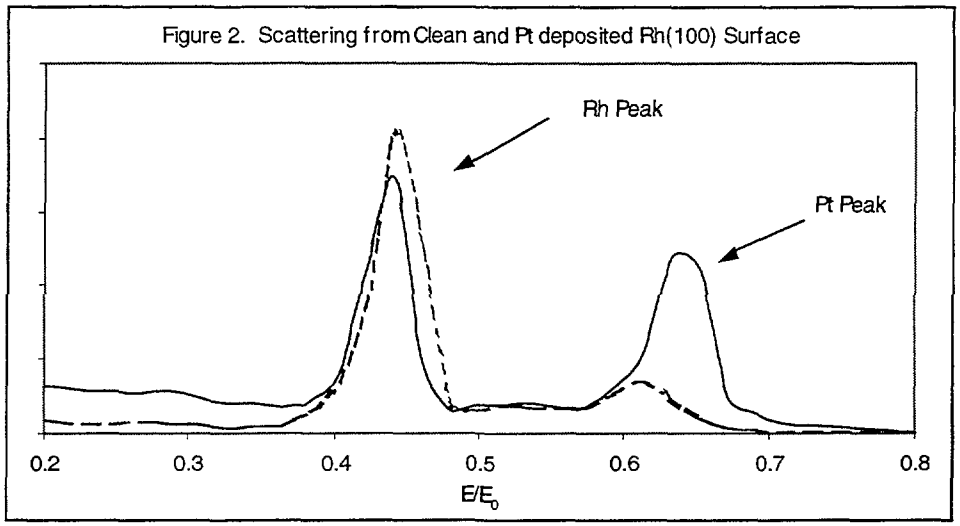

Figure 2. Energy Spectra from Clean and Pt deposited Rh(100) Surface

Figure 2 shows single energy scans using Ar^+ ions scattered from a clean (continuous line) and Pt deposited (broken line) Rh(100) surface. The angle of incidence is 45 degrees and scattering angle 90 degrees. Using classical binary collision models the predicted E/E_0 value for Rh is 0.44 and 0.66 for Pt. This is in excellent agreement with the peaks as seen in Figure 2. The spectrum from the clean surface has a small contribution at approximately 0.61 E/E_0 as a result of double scattering of Ar^+ ions from pairs of Rh atoms.

Extensive research has been conducted on PtRh(100) alloys. In recent years temperature dependence on surface and near surface concentrations has been widely investigated. The surface of the alloy has been shown to be sensitive to annealing temperature with a generally increasing Pt presence on the surface at higher temperatures [2]. However, the alloy is a random alloy [3] and thus Pt and Rh atoms may randomly occupy FCC lattice sites. When the surface is heated in the presence of O_2, a p(3×1) LEED structure is observed. This p(3×1) structure has also been observed when a Pt deposited Rh(100) surface was heated to 600K in 1×10^{-7} Torr oxygen [3]. It is thought that the p(3×1) pattern reflects the ordered arrangement of Rh-O on a Pt(100) like Pt-layer which in turn sits on the Rh(100) surface. Thus we have a Rh-O/Pt/Rh(100) structure. This model is also proposed for the alloy surface, and the Rh-O overlayer thought to be the active surface for the PtRh catalyst.

The reconstruction of atoms to fit the p(3×1) is not fully known and many models have been proposed. LEIS will be used to determine atomic structure and concentration to verify or refute currently proposed models. Only then can the high catalytic activity of the PtRh(100) surface start to be fully understood.

References

[1] M. Drager, "*Aluminium Deposition on a Ni(100) Surface, A Low Energy Ion Scattering Study* ?? of Newcastle, (1995).

[2] E. Platzgummer et al, *Temperature-dependent segregation on $Pt_{25}Rh_{75}$(111) and (100)*, **419**, (1999), 236-248.

[3] K. Tanaka et al, *Chemical Reconstruction of Pt-Rh(100) Alloy and Pt/Rh(100), Rh/Pt(100) Bimetallic Surfaces*, **42**, (1995), 303-307.

Caesium diffusion through cement paste cured at different temperatures

V.K. Peterson[1], K.E Prince[2], A. Ray[1], W.K. Bertram[2] & L.P Aldridge[2]

[1]University of Technology Sydney, Dept. of Chemistry, Material and Forensic Science.
[2]Australian Nuclear Science and Technology Organisation

Abstract

Cs^+ diffusivity through ordinary Portland cement (OPC) samples was investigated using Inductively Coupled Plasma Mass-Spectrometery (ICP-MS) and Secondary Ion Mass-Spectrometry (SIMS). Intrinsic diffusivites were calculated using modified diffusion equations. The intrinsic diffusivities of Cs^+ through OPC and cemented clinoptilolite samples cured at 25°C, 60°C and 150°C were compared. As expected, Cs^+ diffusivity was found to increase with increasing cure temperature of OPC. Cs^+ diffusivity through cemented clinoptilolite also varied with cure temperature. The addition of clinoptilolite to OPC reduced Cs^+ diffusivity through the sample, and this effect was more pronounced at greater cure temperatures.

Introduction

Cement and cement-zeolite mixtures have been commonly used in the disposal of low to medium level radioactive wastes. The processes controlling the retention of Cs^+ in a cemented wasteform are not completely understood. Non retained caesium ions are free to migrate through the encapsulant matrix, making it difficult to predict the long-term retention of waste ions by the wasteform. The diffusion phenomena of Cs^+ through its encapsulant matrix is therefore important. The diffusivity of ions through cementitious materials is affected by both the permeability of the hardened cement paste, as well as the sorption and interaction of the ions with the matrix. It has been found that variations in cure temperature of the cement matrix changes the retention of Cs^+. Cemented clinoptilolite has significant advantages in the retention of Cs^+ over OPC because the Cs^+ has been shown to bind with the zeolite [1]. The effect of the binding of Cs^+ to the clinoptilolite should result in less diffusivity of Cs^+ within the matrix. The diffusivity of an ion can be assessed using the diffusion cell test method and penetration profiles. [2]. The diffusion cell test method involves the construction of concentration-time profiles, whilst the penetration profiles involve concentration – depth profiles.

Experimental

The cement samples were prepared from a single batch of OPC. To ensure workability superplasticizer was added to each sample, which were normalized to equal viscosities. Two different cement samples were prepared, containing 0 and 50 wt.% of zeolite with respect to total dry ingredients from the Werris Creek deposit in NSW. The samples were cured for four weeks. Disks were cut from each sample. For concentration – time profile construction, 2mm disks were cut, and for penetration depth experiments, 35mm thick samples were cut. The disks were sandwiched between two solution chambers, one containing a 0.6MCs^+, the other containing counter ions. Cs^+ diffused from the left-hand cell chamber across the sample to the right-hand cell chamber. For concentration – time profiles, solution aliquots were removed from each cell chamber daily. Aliquots were analysed for Cs^+ using ICP-MS, and concentration – time profiles constructed. At the end of a three-week diffusion period, a small sample was cut through the solid in the axial diffusion direction, polished, and gold coated for SIMS analysis by a Cameca IMS 5f ion microprobe. SIMS results were semi-quantitative as

the sputtering ratio of the beam was dependent on the sample matrix, which was unable to be matrix matched in standards. An O^- 12.5keV primary beam was focussed on a spot of diameter size range 50-70μm, corresponding to a primary beam current of approximately 10nA. Each spot was sputtered for 600s, and the average of the last eight readings recorded.

Results

An increase in OPC cure temperature resulted in increased Cs^+ diffusivity through OPC. This was thought to have been caused by an increase in permeability.

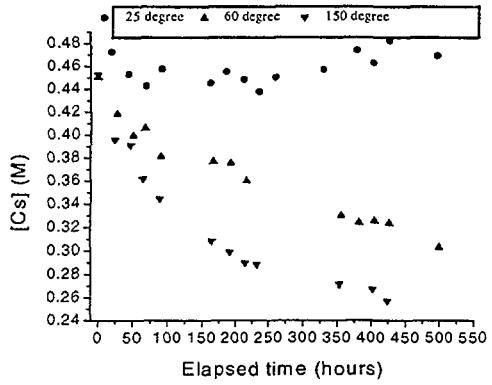

Figure 1a: [Cs] in left-hand chamber with OPC cured at various temperatures.

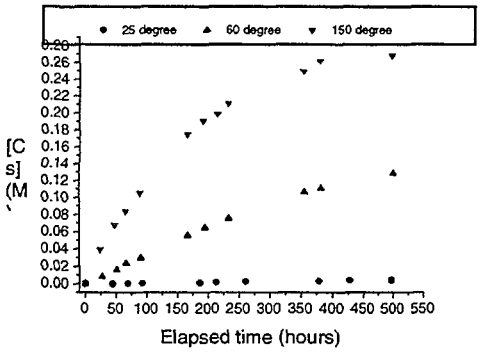

Figure 1b: [Cs] in right-hand chamber with OPC cured at various temperatures.

Table 1: Cs^+ diffusivity through OPC.

Cure Temperature (° C)	Calculated diffusivity ($m^2.hour^{-1}$)
25	1.32×10^{-9}
60	5.36×10^{-8}
150	2.01×10^{-7}

The addition of zeolite to OPC in 25 degree-cured samples resulted in no clear alteration to Cs^+ diffusivity through OPC. Initial sections of the concentration – time profiles for Cs^+ diffusion out of the cemented zeolite samples appeared flat when compared to the corresponding OPC sample. The final Cs^+ diffusivities through these samples were however very similar. These results suggested that Cs^+ may have initially bound to sites in the zeolite, but this did not affect the diffusivity of the Cs^+ once these sites were occupied.

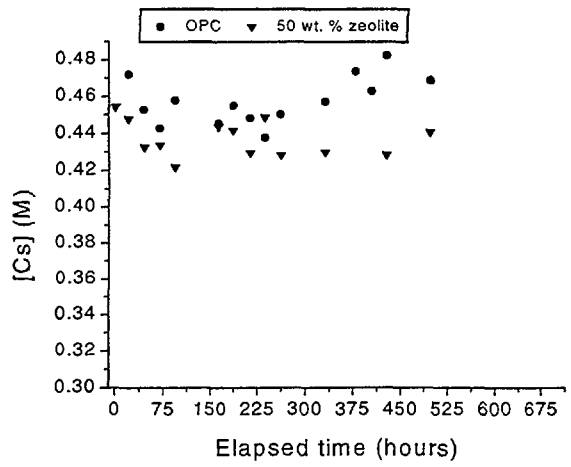

Figure 2a: [Cs] in left-hand chamber with OPC and various zeolite loadings cured at 25 degrees.

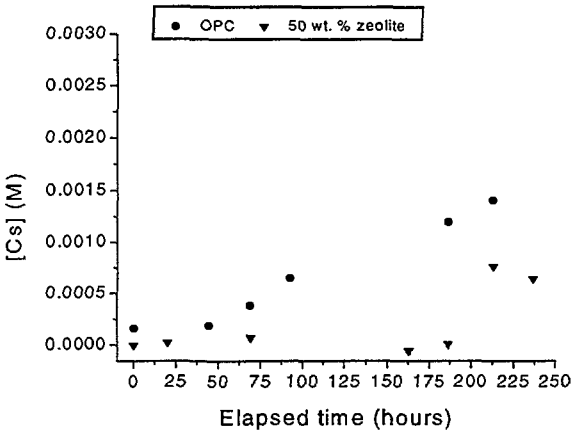

Figure 2b: [Cs] in right-hand chamber with OPC and various zeolite loadings cured at 25 degrees.

Table 2: Cs^+ diffusivity through OPC and cemented zeolite cured at 25 degrees.

Sample	Calculated diffusivity ($m^2.hour^{-1}$)
OPC	1.32×10^{-9}
50 wt. % zeolite and OPC	1.91×10^{-9}

The addition of zeolite to OPC in 60 degree cured samples resulted in decreased Cs^+ diffusivity through OPC.

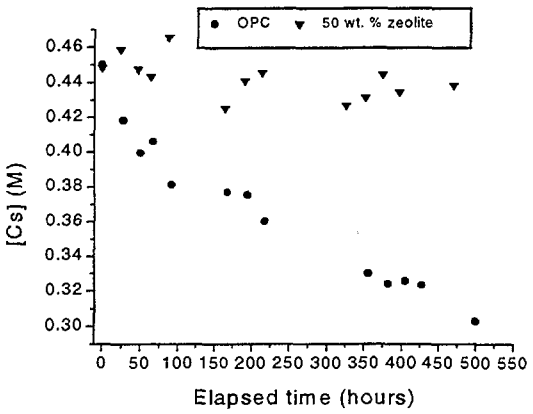

Figure 3a: [Cs] in left-hand chamber with OPC cemented zeolite cured at 60 degrees.

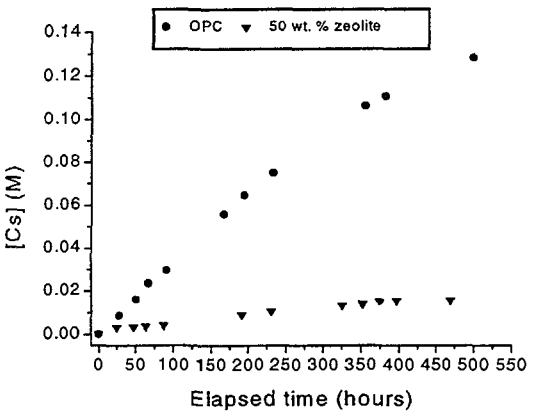

Figure 3b: [Cs] in right-hand chamber with OPC and cemented zeolite cured at 60 degrees.

Table 3: Cs^+ diffusivity through OPC and cemented zeolite cured at 60 degrees

Sample	Calculated diffusivity ($m^2.hour^{-1}$)
OPC	5.36×10^{-8}
50 wt. % zeolite and OPC	5.48×10^{-9}

Penetration depths closely reflected results given by diffusivity measurements. Figure 4 shows a typical SIMS penetration profile.

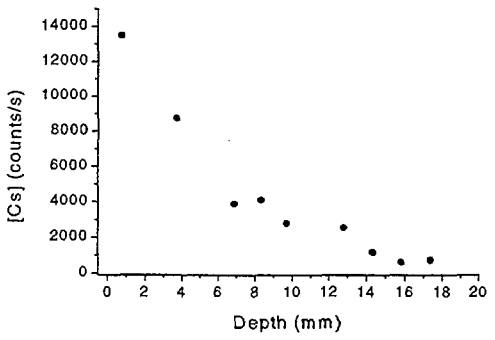

Figure 4: [Cs] in OPC solid cured at 25 degrees.

Table 4: Cs^+ penetration depth in OPC cured at various temperatures.

Sample	Penetration depth (mm)
25 degree cured OPC	5.0
60 degree cured OPC	16.0
150 degree cured OPC	18.0
25 degree cured OPC and 50 wt. % zeolite	1.4
60 degree cured OPC and 50 wt. % zeolite	2.4
150 degree cured OPC and 50 wt. % zeolite	15.0

Conclusion

Cs^+ diffusivities were successfully calculated using the diffusion cell test. Penetration depths were also measured using SIMS, and these reflected results obtained in the diffusion experiments. The addition of clinoptilolite to OPC improved the retention of Cs^+ within the matrix.

Acknowledgment

This work was supported by AINSE grant 99/123.

References

1. K. Stevenson, Materials Science Degree Thesis, Univ. Tech. Sydney, (1997).

2. W. K. Bertram; P. Rougeron, and L. P. Aldridge, J. Aust. Ceram. Soc. **35,** 73-78 (1999)

3 A. Atkinson and A. Nickerson, Nuclear Technology **81,** 100-113 (1988).

4. L. P. Aldridge; R. A. Day, S. Leung; A. S. Ray; M. G. Stevens; R. S. Knight, and C. F. Mapson, in K. L. Scrivener and J. F. Young, Mechanisms of Chemical Degradation of Cement-based Systems London: E & FN Spon; 358-365 (1997)

5. K. Prince; P. Rougeron and L. P. Aldridge, in Proceedings Australian Institute of Nuclear Science and Engineering 10th Australian Conference on Nuclear Techniques of Analysis; Canberra. NTA 3. (1997)

6. F.P. Glasser, Adv, Cement. Research. (1990).

Strontium binding to cement paste cured at different temperatures

V.K. Peterson[1], R. Siegele[2], A. Ray[1], W.K. Bertram[2] & L.P Aldridge[2]

[1]University of Technology Sydney, Dept. Chemistry, Materials and Forensic Science.
[2]Australian Nuclear Science and Technology Organisation

Abstract

Concentration – depth profiles were measured using Proton Induced X-ray Emission (PIXE). These results were used as a measure of the Sr^{2+} retention abilities of each matrix. Ordinary Portland cement (OPC) and cemented clinoptilolite samples were cured at 25°C, 60°C and 150°C. As expected, the Sr^{2+} penetration depth increased with increasing OPC cure temperature. Surprisingly, the penetration depths of Sr^{2+} increased with the addition of clinoptilolite to the OPC, however the increase in penetration depth was reduced in samples cured at higher temperatures.

Introduction

Cement waste forms are often used to immobilise mixtures of Sr^{2+} and Cs^{+}. The diffusion phenomena of Sr^{2+} through cement and cement-zeolite matrixes are important to the immobilisation of radioactive strontium within cementitious materials. The diffusivity of ions through cementitious materials is affected by both the permeability of the material, as well as the sorption and interaction of the ions with the matrix. It has been found that variations in cement cure temperature cause changes to the products of the reactions occurring in setting cement and cement – zeolite mixtures. This results in alterations to sample permeability and to the sorption of ions within the matrix.

Cement based wasteforms are often used for the immobilisation of radioactive waste Sr^{2+} in a low to intermediate concentration range. Sr^{2+} binds to cement, and to crystalline tobermorite, which forms in cement systems cured above 100°C [1]. Zeolites such as clinoptilolite, which bind with Sr^{2+} are often added to cement encapsulant systems [2]. However some calcium hydroxide released as cement hydrates can react to destroy the zeolite and form calcium silicate hydrate in the well-known pozzolanic reaction. The pozzolanic reaction has been shown to increase with cure temperature [3].

This work compared the measured penetration depths of Sr^{2+} between cement and cement – zeolite systems in order to assess the amount of Sr^{2+} binding within the system.

Experimental

The cement samples were prepared from a single batch of OPC. Superplasticiser was added to ensure workability of the cement samples, which were normalised to equal viscosities. The cement zeolite samples were prepared, containing 50 wt.% zeolite from the Werris Creek deposit in NSW. The samples were allowed to hydrate for 28 days. Cylinders approximately 35mm in length were cut from each sample. The cylinders were sandwiched between two solution chambers, one containing 0.6M Sr^{2+}, the other containing counter ions. Sr^{2+} diffused from the left-hand cell chamber across the sample to the right-hand cell chamber. At the end of a three-week diffusion period, a small sample was cut representative of diffusion in the axial diffusion direction, for analysis by PIXE. Penetration profiles were measured using a small diameter, 2.5MeV beam with a target current range of 1 - 2nA and with a 50μm aperture. This gave a beam of diameter approximately 50μm and total charge of 0.192μC. A perspex filter was used to absorb a large percentage of low energy X-rays, and avoided count

rate interferences from the characteristic X-rays of Ca and Si, both of which are major constituents of cement.

Results and discussion

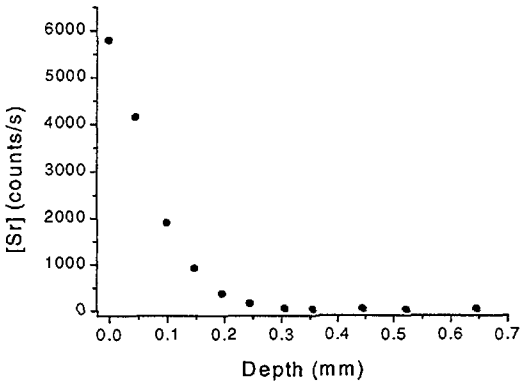

Fig. 1: Sr^{2+} penetration profile in 25°C – cured OPC

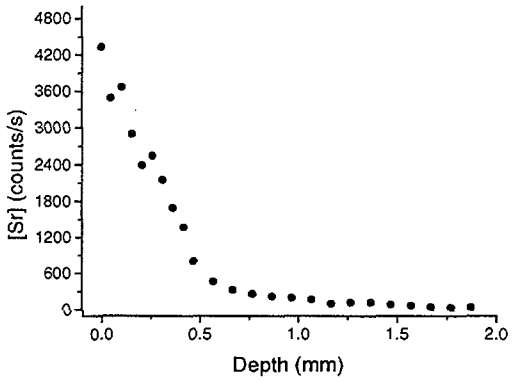

Fig. 2: Sr^{2+} penetration profile in 60°C – cured OPC

Penetration depths derived from Figures 1, 2 and 3 are given in Table 1. Table 1 showed that increased cure temperature of OPC resulted in an increase in the Sr^{2+} penetration depth These results were consistent with previous results [4] that showed an increase in the permeability of OPC with increased cure temperature

Comparison of Figures 4 with 5 illustrates the effect of cure temperature on Sr^{2+} penetration in cemented zeolite.

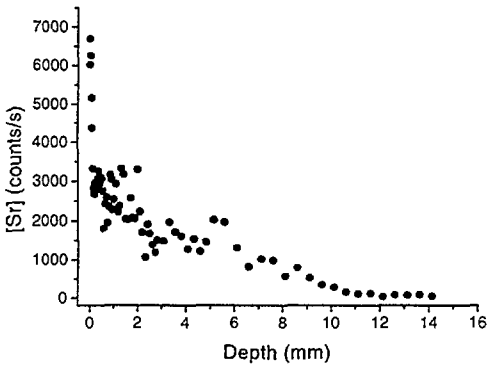

Fig. 3: Sr^{2+} penetration profile in 150°C – cured OPC

Table 1: Sr^{2+} Penetration in OPC cured at various temperatures.

Sample	Sr^{2+} penetration depth (mm)
25°C – cured OPC	0.3
60°C – cured OPC	1.0
150°C – cured OPC	11.0

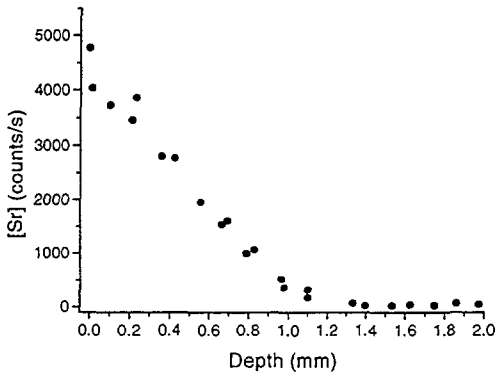

Fig. 4: Sr^{2+} penetration profile in OPC and 50 wt. % zeolite cured at 25°C.

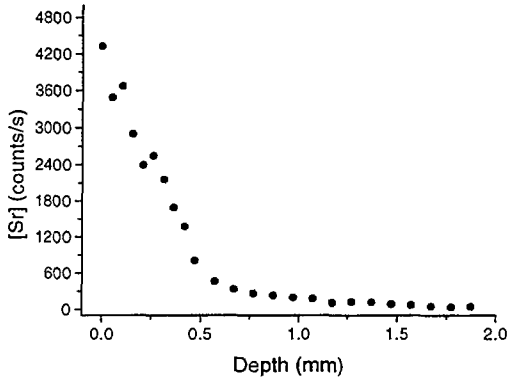

Fig. 5: Sr^{2+} penetration profile in OPC and 50 wt. % zeolite cured at 60°C.

Table 2: Effect of zeolite addition on the penetration depth of Sr^{2+} in OPC cured at various temperatures.

Cure temperature (°C)	Sr^{2+} penetration in OPC with 50 wt. % zeolite (mm)	% increase in penetration depth upon zeolite addition
25	1.4	367%
60	1.6	60%

The increase in penetration depth of Sr^{2+} in OPC caused by the addition of zeolite was thought to be caused by the higher water : cement ratio in the cemented zeolite samples. Samples containing zeolite had a water : cement ratio of 0.52, which was larger than that of the OPC samples which had a ratio of 0.32. An increase in the water : cement ratio of OPC has been shown to result in an increase in sample permeability [4]. The fact that the increase in penetration depth was not as prominent in samples cured at 60°C when compared to those cured at 25°C, could be explained in two ways. The first was that the increase in cure temperature accelerated the pozzolanic reaction, which would have resulted in the production of cementitious material that may have reduced sample permeability [3]. The second was that the pozzolanic reaction may have caused increased Sr^{2+} binding as this reaction has been shown to cause the release of aluminium from the zeolite framework, and the addition of aluminium phases into OPC has previously been shown to increase Sr^{2+} retention in OPC systems [5].

Werris Creek zeolite has been shown to resist the pozzolanic attack of cement at room temperature [6] and to retain more caesium than other zeolites. Stevenson [2] has shown that the addition of this Australian zeolite helps cement retains more Sr. However the penetration profiles results indicate that there is significant difference in binding between Sr and the cement – zeolite cured at different temperatures. This effect should be better understood and the cemented zeolite examined by XRD to find if the amount of pozzolanic reaction has generated the differences postulated on the basis of the penetration profile results.

The results do show the applicability of the techniques introduced by Atkinson and Nickerson [7] and modified by Siegele et al [8] for understanding the retention of ions such as Sr that interact with the cement paste. These results can be used with the theory of Bertram et al [9] to explain the variation of retention of strontium in cement pastes. Further work is now in progress to model these results and obtain XRD of the samples.

Conclusion

Increased cure temperature of OPC caused an increase in Sr^{2+} penetration thought to be caused by an increase in sample permeability. The addition of zeolite also caused an increase in Sr^{2+} penetration in OPC, and this was also thought to have been caused by an increase in sample permeability. Without XRD information, no further conclusion could be made concerning the exact effect of cure temperature variation on the retention of Sr^{2+} in cemented zeolite.

Acknowledgment

This work was supported by AINSE grant 99/123.

References

[1] F.P. Glasser, *Adv, Cement. Research.* (1990).

[2] K. Stevenson, Materials Science Degree Thesis, Univ. Tech. Sydney, (1997).

[3] M. J. Angus, R. W. Crawford, F. P. Glasser, C. E. McCulloch and A. A. Rahman, *Advances in Ceramics Volume 8 Nuclear Waste Management.* G. G. Wicks and WQ. A. Ross, 429-40. Columbus, OH (USA) Am. Ceram. Soc. (1984)

[4] A. Kumar and D. M Roy, *J. Am. Ceram. Soc.,* **69** 356-60 (1986).

[5] S. Hoyle. and M. W. Grutzeck, in 3rd. Int. symp. on ceramics in nuclear waste management. Am. Ceram. Soc. Inc. 275-284.; (1986).

[6] L. P. Aldridge; R. A. Day, S. Leung; A. S. Ray; M. G. Stevens; R. S. Knight, and C. F. Mapson, in K. L. Scrivener and J. F. Young, Mechanisms of Chemical Degradation of Cement-based Systems London: E & FN Spon; 358-65 (1997)

[7] A. Atkinson and A. Nickerson, *Nuclear Technology 81,* 100 (1988).

[8] R. Siegele, P. Rougeron, L. P. Aldridge; D. D. Cohen and E. Stelzer. in Proceedings Australian Institute of Nuclear Science and Engineering 10th Australian Conference on Nuclear Techniques of Analysis.; Canberra. P1.34 (1997).

[9] W. K. Bertram; P. Rougeron, and L. P. Aldridge, *J. Aust. Ceram. Soc.* **35,** 73-78 (1999)

The Effect Of Ion Implanted Yttrium On The High Temperature Corrosion Behaviour Of A Chromia Forming Alloy

S.Shamsili, D.K. Sood, Microelectronics and Materials Technology Centre, Department of Communication and Electronics Engineering, Royal Melbourne Institute of Technology, Vic.
S.P.S. Badwal, Ceramic Fuel Cells Limited, 170 Browns Road, Noble Park Vic. 3174
P.J.Evans, ANSTO, Menai NSW 2234

1. Introduction

Solid oxide fuel cells convert gaseous fuels via an electrochemical process directly into electricity with high efficiency and very low pollution. In a fuel cell, several single cells are joined together through an interconnect material to form a stack for desired power output. The interconnect material is required to meet stringent specifications of matching thermal expansion coefficient with other fuel cell components, low material and fabrication costs, high electrical and thermal conductivity, chemical stability, high strength and ductility and high corrosion resistance at 800-900°C.

To fulfil these criteria several different materials from ceramics to metals have been evaluated. More recently the use of alloys has been gaining popularity. The most commonly used high temperature oxidation resistant alloys contain chromium (Cr) which on exposure to oxidising environments at high temperatures form a protective layer of chromia (Cr_2O_3). This layer inhibits further oxidation of the metal. The major drawback of chromia forming alloys is the formation of the volatile Cr-oxide and hydroxide species [1]. These species are a potential source for long term cell degradation, due to deposition at the cathode interface and formation of new crystalline phases. However, minor additions of reactive elements such as Ce, La or Y improve considerably the overall oxidation resistance of these alloys. A spectacular improvement in the oxide scale adherence by the addition of these elements are commonly observed [2]. Reactive elements may be doped to the bulk material in various ways. They are normally incorporated at levels less than about 1at.% as an alloying addition. Alternatively ion implantation which is a highly controllable and reproducible technique, can be used. However, formation of physical defects in the implanted regions can be a drawback [3]. Our previous studies on high temperature corrosion of La [4] and Ce [5] implanted alloys show that a substantial improvement in oxidation behaviour is achieved by implantation. Especially a remarkable decrease in oxide thickness is observed.

The present research addresses the effect of Y implantation on the high temperature oxidation of Fe-24Cr alloy. Results on oxidation kinetics, oxide morphology and their temperature dependence are discussed.

2. Experimental

Ferritic stainless steel TP 446 (72.37% Fe, 26.16% Cr, 0.77% Mn, 0.51% Si) specimens (13mmx13mm) were polished to 2400 mesh grit with SiC paper and thoroughly cleaned. Ions of Y were implanted on steel samples using MEVVA ion implanter at an extraction voltage of 40 kV, to a dose of 1x1016 and $1x10^{17}$ ions/cm^2 at nominal room temperature. Each sample had about 4mm wide unimplanted region for comparison. After implantation, samples were oxidised in air for 1-360h at 800°C, or at 900°C for 0.5-360h. Heating rate was 100°C/h. Specimens were characterised by Optical Microscopy, Scanning Electron Microscopy (SEM/EDX), Normal X-Ray Diffraction (XRD), and Rutherford Backscattering Spectrometry (RBS). An analysis beam of 2.0-MeV ^4He was used for RBS, at a scattering angle of 165°.

3. Results and Discussion

3.1 SEM-EDX Analysis

SEM analysis provided information on the surface morphology of the specimens, while EDX analysis gave information on the element composition of the oxide layer(s) formed.

Figure 1 illustrates the effect of the implantation dose on grain growth at 800°C. Oxidation time was 1h. On the unimplanted sample (Figure 1a), the grain size in the oxide layer was between 0.2 and 1μm. When the sample was implanted with Y at a dose of $1x10^{16}$, the grain size reduced to between 0.15 and 0.5μm (Figure 1b). As the dose was increased to $1x10^{17}$ the grain size decreased remarkably (Figure 1c), and fully shaped grains as evident in Figures 1a and b were no longer present. At 900°C a similar effect was observed.

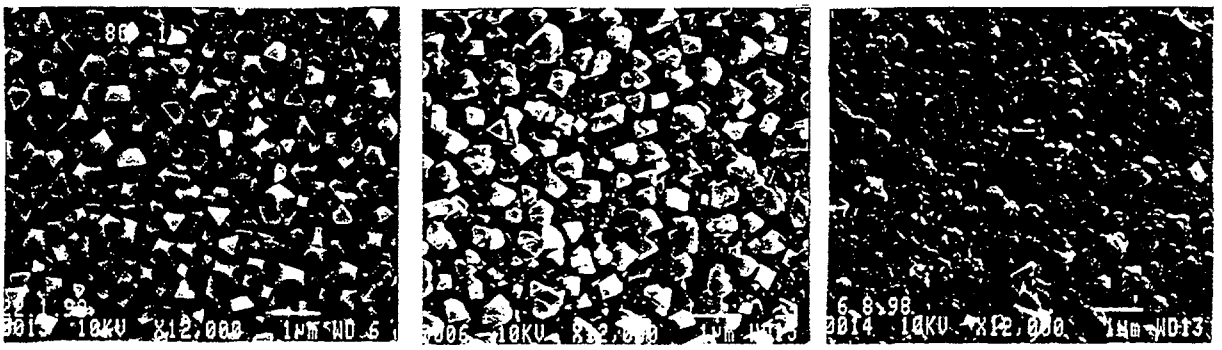

a) b) c)

Figure 1: SEM image, oxidation at 800°C, 1h. a) Unimplanted b) Implanted, $1x10^{16}$, c) Implanted, $1x10^{17}$.

Figure 2 shows micrographs of samples which are oxidised at 800°C for 360h. On the unimplanted samples, at higher oxidation times, 120h and 360h, spallation of the oxide layer was observed (Figure 2a). This phenomena was not seen on the implanted ones even at 900°C. As the implantation dose was increased to $1x10^{17}$ (Figure 2b), the grain size was reduced dramatically. The sword like formations which were formed on the unimplanted samples were not observed. On these formations only Mn and O were detected by EDX analysis. Neither Fe nor Cr were present.

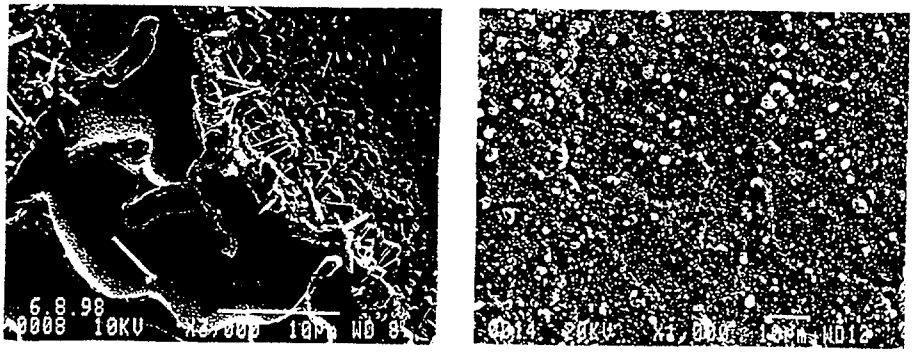

a) b)

Figure 2: SEM image, oxidation 800°C, 360h. a) Unimplanted b) Implanted, $1x10^{17}$.

3.2 XRD and RBS Analysis

Both short term and long term oxidised samples were analysed by XRD. Table 1 shows the identified phases.

Fe-Cr alloy was identified in all cases , indicating that the steel specimens were not fully oxidised even after 120h of oxidation. On the unimplanted samples Cr_2O_3 and Fe_3O_4 were identified at both temperatures. At 800°C Y implantation had a significant effect on Cr and Fe oxide formations. At the implantation dose of $1x10^{16}$ only the major XRD peaks of Cr_2O_3 and Fe_3O_4 phases were observed, indicating a significant reduction in the oxide thickness. At the higher dose, $1x10^{17}$, Cr_2O_3 peaks were no longer detectable; however at 120h of oxidation two major peaks of Fe_3O_4 were detected. At this dose Y implantation most probably inhibits the Cr_2O_3 formation at the external surface of the alloy. It also slows down Fe_3O_4 formation. At 900°C, the effect of Y implantation was still significant for short term oxidation. On the samples which were oxidised for 0.5h only the major XRD peaks of Fe_3O_4 phase was observed, indicating a decrease in the oxide thickness.

Table 1: Phases identified by XRD

Heat Treatment		**Unimplanted**	**Y-imp. 1E16**	**Y-imp. 1E17**
800°C	1h	Fe-Cr Alloy	Fe-Cr Alloy	Fe-Cr Alloy
	24h	Fe-Cr Alloy, Cr_2O_3, Fe_3O_4, other	Fe-Cr Alloy, Cr_2O_3(100%) $Fe_3O_4$100%,30%	Fe-Cr Alloy
	120h	Fe-Cr Alloy, Cr_2O_3, Fe_3O_4, other	Fe-Cr Alloy, $Cr_2O_3$100%,70% $Fe_3O_4$100%,30% other	Fe-Cr Alloy, $Fe_3O_4$100%,30%
900°C	0.5h	Fe-Cr Alloy, Fe_3O_4	Fe-Cr Alloy, $Fe_3O_4$100%	Fe-Cr Alloy, $Fe_3O_4$100%
	120h	Fe-Cr Alloy, Cr_2O_3, Fe_3O_4	Fe-Cr Alloy, Cr_2O_3, Fe_3O_4, other	Fe-Cr Alloy, Cr_2O_3, Fe_3O_4, other

Analysis of oxide layers by RBS gave some additional information on the oxide phase formations and oxide thicknesses.

Figure 3 shows RBS spectra of as implanted and oxidised samples at 800°C and 900°C. The implantation dose was $1x10^{17}$. On the as implanted sample Y signal had a Gaussian distribution with a peak at 1.66MeV, while the substrate appeared as a step with leading edge at 1.49MeV. After the oxidation at 800°C Y peak was no longer shallow and its height decreased as the oxidation temperature was increased. Y was redistributed during oxidation. An increase in the oxide thickness was observed as the temperature was increased to 900°C. The oxide film thickness caused a shift in the Fe edge ΔE=184keV at 800°C and ΔE=210keV at 900°C. This increase in ΔE values indicates an increase in the oxide thickness.

Some RBS spectra were simulated by using the knowledge gained by XRD analysis. Simulations done on different spectra showed that the oxide layer was formed by an Fe/Cr containing oxide and Fe_3O_4. An example is given in Figure 4 where the best fit is obtained (thinner curve) with the data , for a duplex oxide layer. This duplex layer consisted of a top

surface layer of ~500A and composition of $Fe_{1.5}O_3Cr_{0.5}$, below which a second layer of Fe_3O_4 with a thickness of ~2750A was formed. Simulation work is still in progress to obtain a better fit.

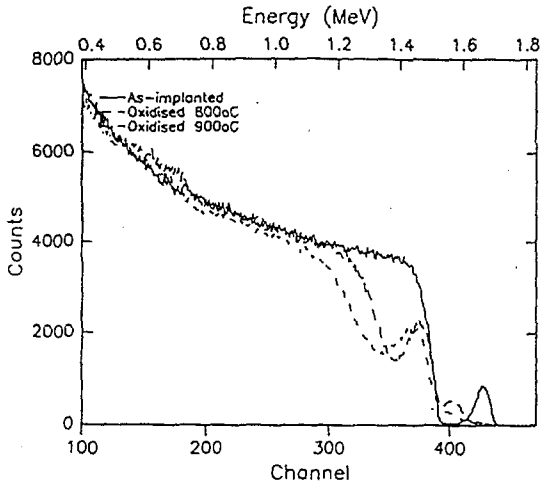

Figure 3: RBS spectra of as implanted and oxidised samples.

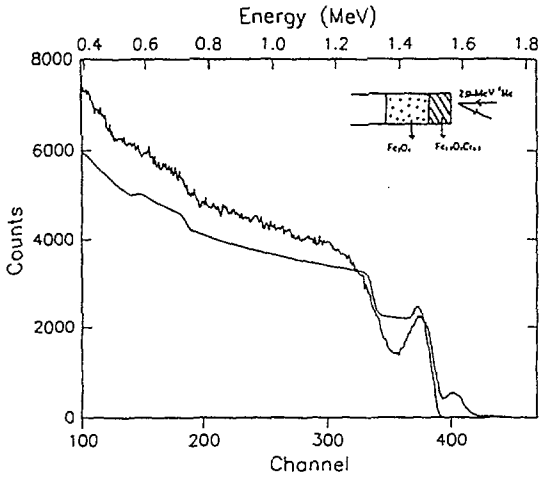

Figure 4: Simulation of an RBS spectrum Oxidation at 800°C, 1h, dose $1x10^{17}$

4. Conclusion

The experimental results show: 1) Oxidation behaviour of TP446 stainless steel improved with Y implantation. 2) The grain size of the oxide layer decreased as the implantation dose increased. 3) Increase in the oxidation time encouraged grain growth, and it probably caused the formation of new oxide phases. 4) At both temperatures several oxide phases eg. Cr_2O_3, Fe_3O_4 appear to grow on the steel surface, acting as a protective layer. 5)Y oxide phases were not detected. 6) Y implantation caused an improvement in the adherence of the oxide scale.

5.Acknowledgments

Mr.Les Bennet, Kodak Australasia Research Laboratories Vic., is acknowkledged for his help in taking the SEM pictures. This work was supported by AINSE and ARC grants.

6.References

1) S.P.S.Badwal, R.Deller, K.Foger, Y.Ramprahash and J.P.Zhang, "Interaction Between Chromia Forming Alloys and Air Electrode of the Solid Oxide Fuel Cell", Solid State Ionics, vol.99, pg.297-310,1997
2) H.Hindam, D.P.Whittle, "Microstructure, Adhesion and Growth Kinetics of Protective Scales on Metals and Alloys.", Oxidation of Metals, Vol.18, Nos.5/6, pg.245-284, 1982
3) V.Sirinivasan, A.W.Nusorvik, A.K.Rai, Oxidation and Sulfidation of Implanted and Unimplanted AISI446 Steel.", Oxidation of Metals, Vol.34, Nos.5/6,1990
4) S.Shamsili, D.K.Sood, S.P.S.Badwal, P.J.Evans, "Modification of High Temperature Oxidation Behaviour of Chromia Forming Alloys by Ion Implantation.", Proceedings of 10th Australian Conference on Nuclear Techniques of Analysis, 1997
5) S.Shamsili, D.K.Sood, S.P.S.Badwal, P.J.Evans, "Corrosion Behaviour of Cerium Implanted Stainless Steel as a Potential Interconnect Material for Solid Oxide Fuel Cells.", Proceedings of 18th Australian Ceramics Conference, 1998

Analysis of NdFeB thin films prepared by facing target sputtering

L.Shivalingappa, S.Mohan

Department of Instrumentation, Indian Institute of Science,

Bangalore – 560 012 (India)

Muralidhar K. Ghantasala and Dinesh K. Sood*,

Department of Electrical Engineering, *Department of Communication and Electronic Engineering, RMIT University, 124, La Trobe Street, Melbourne – 3000 Australia

Abstract

In this paper, we present the details of our work on the deposition and characterization of NdFeB thin films. These films were prepared using facing target sputtering technique. The silicon(100) substrates were maintained at a substrate temperature of 400 to 600°C during deposition. Film structure, composition and magnetic properties are analyzed using Rutherford Backscattering Spectroscopy (RBS) and X-ray Diffraction (XRD) techniques. Films deposited below 400°C were x-ray amorphous, while the onset of crystallinity was observed with the films deposited at 500°C. Typical film composition was Nd : Fe : B = 2.2 : 12.5 : 2. Film composition appear to be a function of deposition conditions. Oxygen has been found to be the main impurity in the films. Oxygen content in the film reduced as the substrate temperature is increased.

Introduction

NdFeB and SmCo are the commonly used permanent magnetic materials for a wide variety of applications. Since the discovery of $Nd_2Fe_{14}B$ in 1984 [1], numerous studies in $Nd_2Fe_{14}B$ based materials have been conducted to obtain a better understanding of their excellent intrinsic properties and develop better fabrication process for permanent magnets. With the rapid development of micromechanical systems, microelectronics and integrated electromagnetic devices, applications of permanent magnetic films are becoming more significant [2]. Miniaturised magnetic sensors, actuators and motors are some of the areas that can benefit from the development of film type magnets [3].

$Nd_2Fe_{14}B$ films have been prepared by thin film processes such as magnetron sputtering [4], molecular beam epitaxy and pulsed laser deposition [5-6]. The magnetic properties of these films depend mainly on growth technologies, texture control and microstructure. To the author's knowledge, there has been no report on the growth of NdFeB thin films using facing target sputtering (FTS) till now. Films prepared using FTS have got many advantages namely uniform films over large areas [7] with smooth dense and columnless microstructure [8], properties which are highly desirable in the magnetic films. Hence, an attempt has been made in this work to deposit these films using FTS technique and study their structural and compositional properties. Films have been prepared at different substrate temperatures in the temperature range 400 to 625°C and the film properties were investigated.

Experimental

The schematic of the FTS system is shown in figure 1. It consists of a vacuum pumping assembly, a control panel for the pumping system, a vacuum chamber designed to accommodate two sets of facing targets and a substrate holder with heater assembly (described in detail in ref.9).

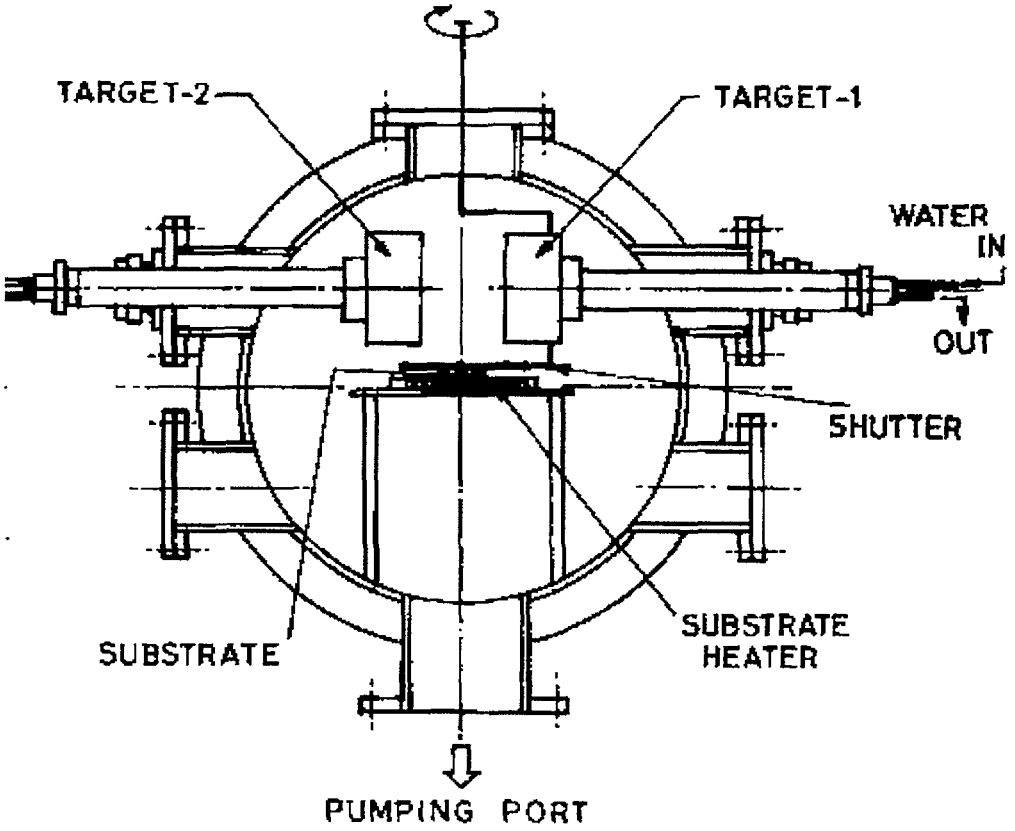

Figure1 : Schematic of the Facing target sputtering system chamber

The pumping module consists of a conventional 4.5" diffstack diffusion pump having a pumping speed of 230 l/sec backed by a direct drive rotary pump. The ultimate vacuum that has been achieved with liquid nitrogen trap is 2 x 10^{-6} mbar.

The inter target distance was maintained at 65 mm and the target to substrate distance was kept at 60 mm throughout these investigations. Prior to deposition, substrates were heated to the deposition temperature and kept at that value for a few hours to ensure a uniform and equilibrium temperature over the entire substrate surface. Films were deposited on to silicon (100) and copper substrates in pure argon atmosphere at pressures 0.04 mbar for discharge current of 50 mA. Deposition was carried out by maintaining the substrate temperature at ambient and at 500 to 625°C. The substrate heater was fabricated in the laboratory using suitable kanthal wire. The whole heater assembly is enclosed in a stainless steel holder with suitable insulator. The maximum temperature obtained in the heater is 650°C.

The composition and structure of the films were analysed using Rutherford back-scattering spectroscopy (RBS) and X-ray diffraction technique. The composition of the film was determined by using standard simulation methods and comparing it with the experimental Rutherford back-scattering spectrum using a RUMP program.

Results and Discussion

Figure 2 shows the x-ray diffraction pattern of $Nd_2Fe_{14}B$ films deposited at 550, 570, 600 and 625°C at 50 mA discharge currents. The peak representing the (331) plane is more intense for the films deposited at 550 and 570°C substrate temperature. The intensity of this peak gradually reduces as the substrate temperature is increased to 600 and 625°C. Further study of XRD pattern for different discharge currents and pressure are still under progress. Films

prepared at substrate temperature less than 500°C are found to be amorphous in nature.

Tsai et al [10] deposited $Nd_2Fe_{14}B$ films by dc magnetron sputtering on Si(111) wafer. Films were deposited at ambient temperature and postannealed in a high vacuum with a temperature between 480–600°C. They observed the peaks representing planes (204) and (410) from XRD analysis. Kanekjyo et al [11] prepared $Nd_2Fe_{14}B$ films by single role melt-spinning technique under an argon pressure. The XRD analysis revealed the $Nd_2Fe_{14}B$ formation of (331), (204), (214), (313), (224), (410), and (314) planes.

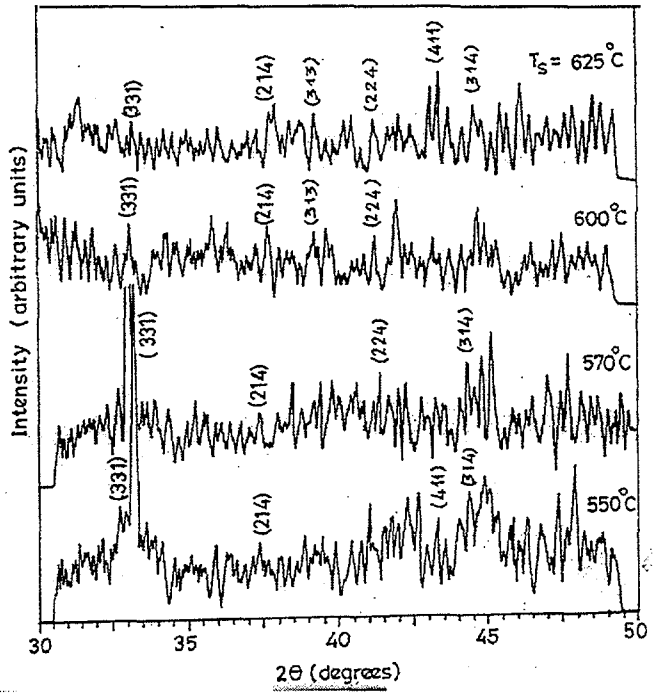

$Nd_2Fe_{14}B$ films were prepared by Yu et al [12] by magnetron sputtering technique. The asdeposited films were annealed at 500°C. The XRD analysis showed $Nd_2Fe_{14}B$ crystallites isotropically oriented in the annealed film.

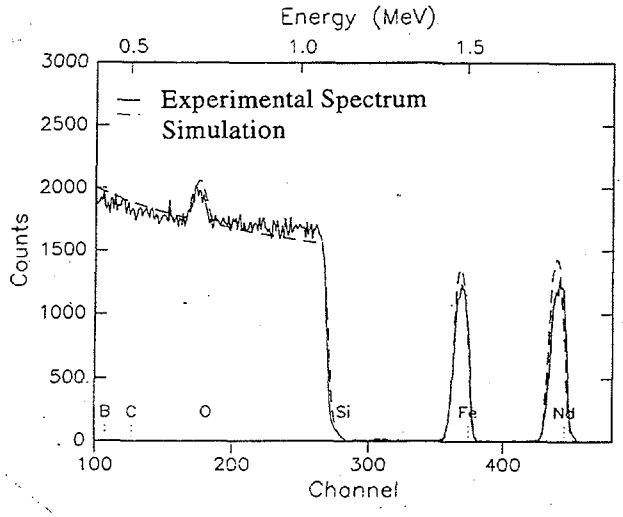

Figure 3 shows the typical RBS spectrum of the film deposited at 570°C. Figure compares the simulated and experimental spectrum. Nominal film compositional ratio equals Nd:Fe:B = 2.2:12.5:2. However, oxygen has been found to be the major impurity in the films. Though the film composition is similar at all substrate temperatures, oxygen impurity content has reduced at higher substrate temperatures. Further, at higher substrate temperatures, there has

been some evidence of significant interdiffusion between the film and substrate. Further studies are in progress to optimize the deposition conditions.

Summary

NdFeB thin films were deposited by facing target sputtering technique. Films were deposited at different substrate temperatures in the range 400 to 625°C. These films were analysed for the structure and composition using the XRD and RBS techniques. These films showed a nominal composition of Nd:Fe:B – 2:12:1 and have indicated the formation of crystalline stoichiometric phase above 500°C. Further studies are in progress to understand the growth kinetics of these films.

Acknowledgements

This work is supported by an AINSE grant and an ARC large grant

References

[1] M.Sagawa, S.Fujimura, M.Togawa, H.Yamamota and Y.Matsuura, J.Appl. Phys. 55, 2083 (1984).

[2] J.F. Herbst, Rev. Mod. Phys, 63, 819 (1991).

[3] F.J. Cadieu, T.D. Cheung and L.Wickramasekara, J.Magn. & Mag. Mater., 54-57,535(1986)

[4] G.K. Muralidhar, B.Window, D.K.Sood and R.B.Zmood, J. Mat. Sci., 33, 1349 (1998).

[5] .B.A.Kapitanov. N.V. Komilov, Ya.L.Linetsky and V.Yu. Tsvetkov, J.Magn. & Mag.Mater., 127, 289 (1993).

[6] K.D. Ayleswarth, Z.R. Zhao, D.J. Sellmyer and G.C. Hadjipanayis, J.Magn & Mag. Mater., 82, 48 (1989).

[7] Qshua Fan, J.Vac.Sci. Technol., A10, 3371 (1992).

[8] H. Ho, and M. Naoe,IEEE Trans. Mag. 26, 181 (1990).

[9] M. Swarnalatha and S.Mohan, Vacuum 48, 15 (1997).

[10] J.L. Tsai, T.S. Chin, S.K. Chen and E.Y. Huang, J.Appl. Phy. 83, 6241 (1998).

[11] H. Kanekiyo and S. Hirosawa, J.Appl. Phys. 83, 6265 (1998).

[12] M. Yu, Y. Liu, S.H. Liou and D.J. Sellmyer, J. Appl. Phys, 83, 6611 (1998).

G-paq: a motion control and data acquisition package for ion beam analysis

P. G. Spizzirri, J. L. den Besten and D. N. Jamieson

School of Physics, Microanalytical Research Centre. University of Melbourne, Parkville, VIC, 3052, Australia.

Introduction

The analysis of crystalline materials using nuclear microprobe techniques is now commonplace. Channeling contrast microscopy (CCM) [1] and Rutherford Backscattering (RBS) angular two-dimensional scans, which are used to study defects, strain, surface effects and the presence of impurity atoms in crystalline materials, can benefit from automation through computer control. Important criteria for a computer controlled instrument such as this are: suitable operating system (eg. Microsoft® Windows), a graphical user interface (GUI), readily available components, cost effectiveness, ease of use, flexibility and scalability. While there are a number of effective RBS channeling angular scanning solutions in use throughout the microprobe community, few can provide this level of application abstraction.

Recent trends in software and hardware development have seen the emergence of desktop/laptop personal computer (PC) based virtual instruments (VI's) [2]. It has been said that the PC is now the most powerful and cost effective approach to building instruments because they can outperform "blackbox" solutions in computing power, data transfer rates, memory, data storage, graphics, ease of use and familiarity. Other benefits stem from the availability of commercial-off-the-shelf (COTS) [3] components (hardware) that can often provide complex functionality and third party analysis software that can extend the instrument's use beyond the vendor defined limits.

This paper discusses a general purpose, data acquisition and motion control solution, G-Paq, based upon the National Instruments® LabVIEW hardware and software development environment. Locally developed, this solution uses a minimum of customised components, is compatible with the principals of Good Laboratory Practice (GLP) [4], is easy to use, has a graphical user interface and is flexible. While it has been developed for nuclear microprobe based channeling contrast microscopy using a specimen stage goniometer, its application to general motion control applications is also possible.

Experimental

The G-Pac virtual instrument depicted in Figure 1, was interfaced to a 'Hodges' 4 axis eucentric goniometer [5] as found on the Melbourne Nuclear Microprobe which has been described previously [6]. The software makes extensive use of menus, dialog boxes and a setup utility to maximise online 'real-estate' which depicts instrument *state* information. The digital interface controls the four Radio Spares (RS 440-442) stepping motors using RS (332–098) stepping motor drive cards mounted in a Eurocard rack. While configured for four axis control in this experiment, the software has provision for six axis control. It also allows axis labeling, conversion units and backlash correction to be fully user configurable with I/O line assignment through drop-down menus. Stepping motor speed control is also user configurable through the setup menu. In addition, some experimental control has been incorporated using the digital I/O although at this stage, they only allow remote switching of a faraday cup.

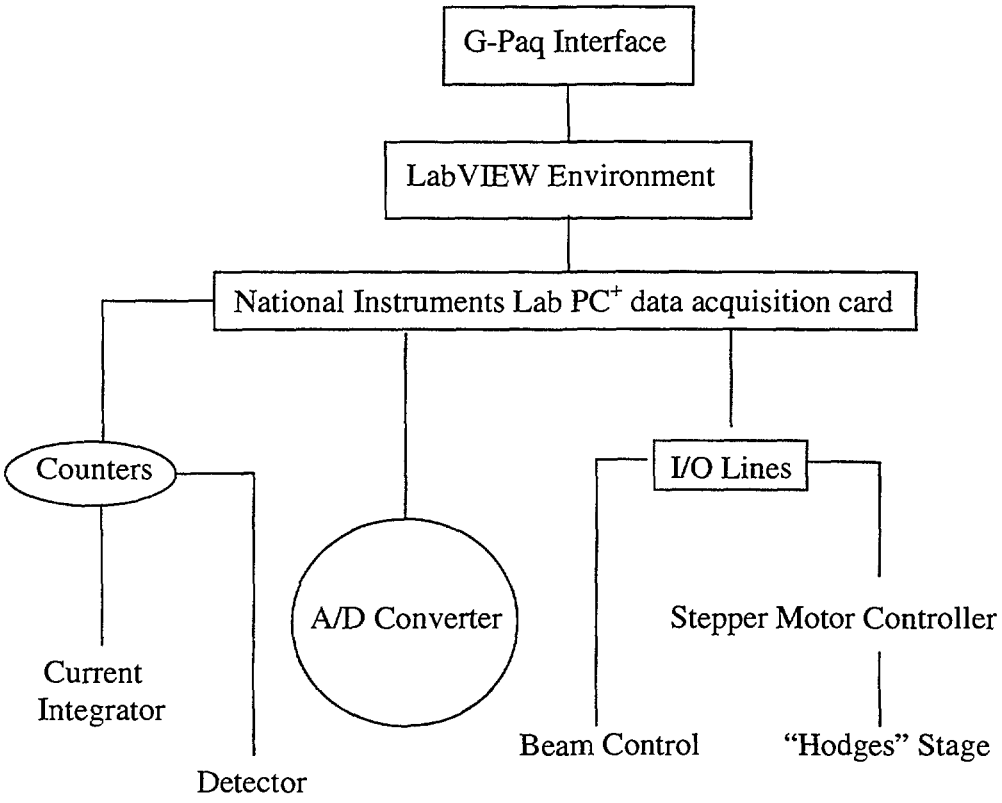

Figure 1. G-Paq functional diagram

Data acquisition is facilitated by the two 16 bit counters integral to the interface card. They can be aligned with time or event driven dwell periods allowing true charge integration (as applied to angular scans) with only a minimum of additional custom hardware. This ability to dwell and integrate signal at any location in an angular scan allows the user to define the required measurement statistics. A multiplexed analog-to-digital converter is also available for input although it was not used in this application. In total, a maximum of four input channels are catered for with each completely user configurable allowing any combination of analog or digital signals to be measured with user defined labels and conversion units.

The personal computer comprising the other hardware components of this VI is a 100MHz Intel® 486 with 36MB of Ram and a 1.2GB hard disk drive. Although using the Microsoft® Windows 95 operating system, this application has also successfully operated on the Microsoft® Windows for Workgroups 3.11 and Microsoft® Windows 98 platforms. Additionally, National Instruments® can provide a Microsoft® Windows NT version of the LabVIEW development and run-time environment. In any case, the user interface shown in Figure 2 is unchanged.

Data acquired with this VI is saved to disk (either locally or to a remote computer via computer network) in a readily readable, tab delimited, ASCII text format. In this file, all data acquisition and motion control parameters are saved in accordance with the principals of Good Laboratory Practice. This allows third party analysis solutions to be applied to data acquired with this instrument. To illustrate this feature, results reported below have been processed using Microsoft® Excel or Powerpoint and the MARC AGP and Nuwave packages.

Results

The following results demonstrate the ability of this VI to perform angular scans of crystals to find the major axis for channeling purposes. Using 1MeV H^+, an angular scan of a Nickel

crystal is shown exhibiting the major <100> axis and (100) and (110) planes in Figure 3. The ±2° Phi and ±2.5° Theta angular scan range using 0.1° increments has resulted in a high resolution map which enables the analyst to identify and orient an unknown crystal.

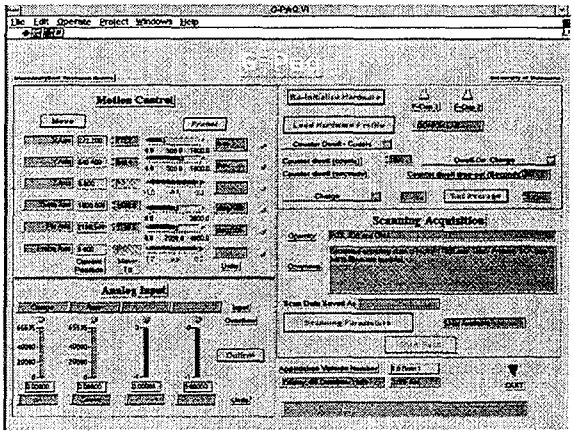

Figure 2. G-Paq Virtual Instrument User Interface

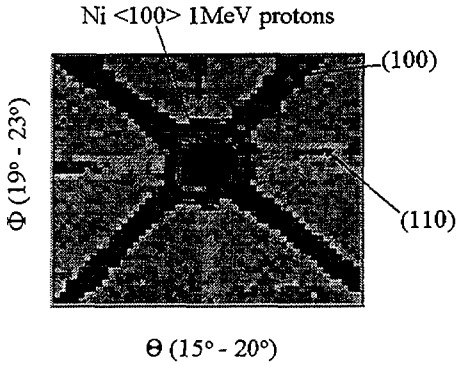

Figure 3. A Channeling angular scan about the <100> axis of a Nickel crystal. This image shows the signal from the surface down to 80nm (nominal) of the crystal as a function of the angular range as indicated with 0.1° resolution and a dose of 10nC per pixel. The analysis beam was 1MeV H^+ with a detector of 25msr at a scattering angle of 150°.

An accompanying experimental azimuthal scan about the <100> axis of the same Nickel crystal sample is illustrated in Figure 4 below. In this case, an azimuthal scan was synthesised from the appropriate orthogonal tilts of our four axis goniometer.

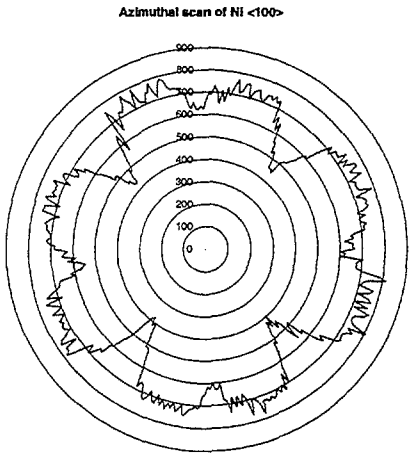

Figure 4. An experimental azimuthal scan about the <100> axis of a Nickel crystal using the same ion analysis beam parameters and detector as in figure 3 above. The backscattered yield is plotted along the radius of the polar coordinate, with maximum intensity towards the centre.

Conclusions

The G-Paq VI proposed herein has been shown to be capable of performing multidimensional RBS angular scans of crystalline samples for the purpose of axis identification. With both linear and circular motion control of up to six axes, this COTS package provides both a flexible and user friendly solution to nuclear microbeam analysis.

Future developments of this VI include the incorporation of RS232 and GPIB control of other COTS motion control systems and interfacing to the MARC MPSYS nuclear microprobe data acquisition package to allow spectral measurements at each position in the angular scan.

References

[1] J.C. McCallum, C.D. McKenzie, M.A. Lucas, K.G. Rossiter, K.T. Short and J.S. Williams, Appl. Phys. Letts. 42(9):827, 1983.

[2] J. Truchard, IEEE Spectrum, 35(1), 12, January, 1998.

[3] J. Voas, IEEE Software, 15(2), 16, March 1998.

[4] L. Huber, "Good Laboratory Practice and Current Good Manufacturing Practice", Hewlett Packard Press, 1996 (5963-2115E).

[5] D.N. Jamieson, R.A. Brown, C.G. Ryan and J.S. Williams, Nucl. Instr. and Meth. B 54, 213, 1991.

[6] M.B.H Breese, D.N. Jamieson and P.J.C. King, "Materials analysis using a nuclear microprobe", John Wiley and Sons, New York, 1996.

Thermally stimulated currents in polycrystalline diamond films and their application to ultraviolet dosimetry

Elizabeth Trajkov and Associate Professor Steven Prawer

Microanalytical Research Centre, School of Physics, The University of Melbourne, Parkville

Introduction

Quantifying individual exposure to solar ultraviolet radiation (UVR) is imperative to understanding the epidemiology of UVR related skin cancer. The development of personal UVR dosimeters is hence essential for obtaining data regarding individual UVR exposure, which can then be used to establish appropriate protective measures for occupational and recreational exposure.

Because diamond is a tissue equivalent material and has a wide band-gap, CVD polycrystalline diamond has been proposed for use in solar-blind UV dosimetry. It has been reported that the photoconductivity in polycrystalline diamond films is enhanced after UV illumination.[1] Photo-generated carriers can be trapped at some deep levels after illumination. Because these levels are deep the thermal release of carriers is a slow process at room temperature. Therefore the new arrier distribution reached after illumination can result in a metastable state because the temperature is too low to restore the initial equilibrium. The sample can be bought back to initial equilibrium by heating. If the current is recorded during heating of the samples one can observe current peaks corresponding to the thermal release of trapped carriers, the so-called thermally stimulated currents (TSC).

From first-order kinetics, we find that the TSC intensity is proportional to the initial density of trapped carriers, n_{to}. Since n_{to} varies with the radiation dose, the measurement of TSC can find an application in radiation dosimetry since the measurement of TSC gives a direct measure of that dose.

Nitrogen can be used to introduce deep traps in diamond. This investigation will involve examining the affect of the nitrogen concentration on the irradiation response of the films. Furthermore, we will analyse the fading rate of the TSC signal. If diamond films are to have a practical application in UVR dosimetry, then ideally we require a linear relationship between the dose response and the TSC, and we also require a low fading rate. From this investigation we hope to find the optimum nitrogen concentration which yields the desired results.

Experimental

Thin CVD polycrystalline diamond films grown under different conditions and of varying nitrogen concentration were used for the investigation of TSC in diamond. The four diamond samples in increasing nitrogen content are NRL134, NRL212, NRL176 and NRL224. They were fabricated at the Naval Research Laboratory using microwave plasma enhanced chemical vapour deposition To determine the quality of the four different diamond samples, Raman analysis was performed.

The photoluminescence and Raman spectra were excited using the 514.5 line from an Argon ion laser and collected using a DILOR XY confocal micro-Raman spectrometer. Figure 1 shows the Raman spectra for the four different diamond samples.

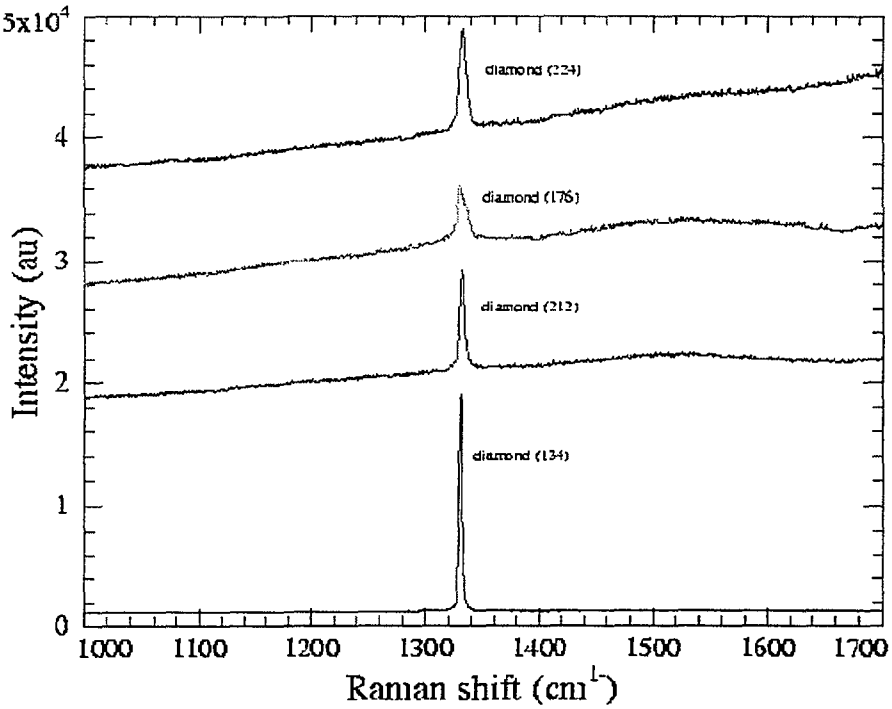

Figure 1: Raman spectra from four different CVD polycrystalline diamond films excited at 514.5nm. The curves have been displaced vertically for clarity.

From the spectra, the diamond peak occurs at about 1332cm^{-1} as expected. NRL134 has the highest quality, whereas NRL176 is of the poorest quality since the diamond peak is broad compared to the others.

Photoluminescence Raman spectra were used to determine the type of impurities in the four samples. From the photoluminescence spectra (Figure 2) we found that the diamond samples NRL134, NRL212 and NRL176 had luminescence peaks at about 2.15eV, 1.94eV and 1.7eV. According to the literature,[2] the 2.15eV centre is a vacancy – interstitial nitrogen complex and the 1.94eV centre is a vacancy trapped next to a single substitutional nitrogen. The 1.7eV peak is due to silicon in the sample.[3] The diamond sample NRL224 showed all the above photoluminescence peaks except for the 1.7eV peak. One possible explanation for this is that for higher N concentrations, the N quenches the Si photoluminescence peak. [4]

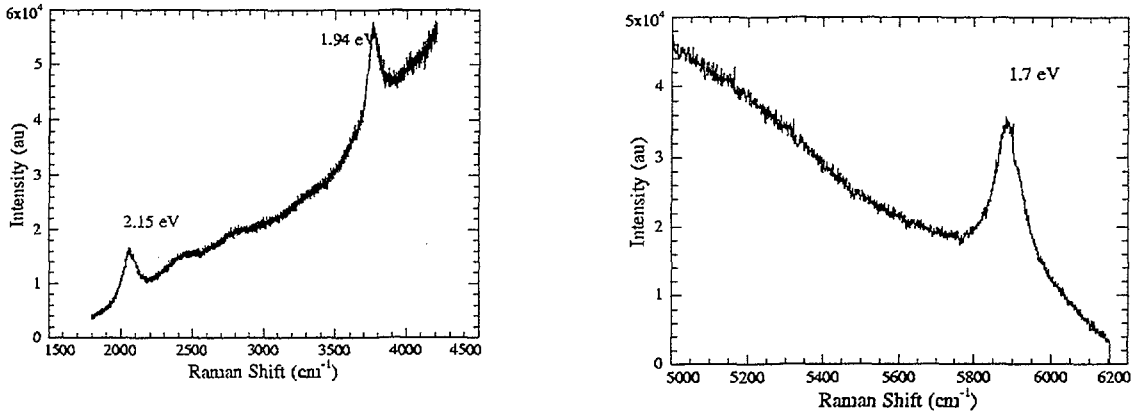

Figure 2: Typical photoluminescence spectra for CVD polycrystalline diamond

Further Work

The next stage will be to deposit Mo/Au electrical ohmic contacts to the diamond samples to study the dark conduction and UV photo-induced conductivity in the four different diamond samples.

The dark conduction investigation will involve measuring the current-voltage, *I(V)*, characteristics at different temperatures (300 – 600 K) and also measuring the current-temperature, *I(T)*, characteristics for different electric fields. From this study we hope to verify that Poole-Frenkel conduction is the mechanism governing dark conduction in CVD diamond.

The *I(V)* and *I(T)* characteristics of the diamond samples will then be measured after they have been irradiated with ultraviolet light. Also, the TSC glow curve obtained with different heating rates will be plotted for each sample.

To determine the potential of these four different diamond samples for UV radiation dosimetry we will investigate their dose response. We hope to find a sample whose TSC signal increases linearly with the irradiation dose over a large response time. Furthermore, the TSC decay at different storage temperatures will be analysed.

References

[1] P. Gonon, S. Prawer, Y. Boiko & D. Jamieson, *Diamond Relat. Mater.* 6, 1997, 860 - 864

[2] A. Collins, *Conference Proceedings Vol. 52 "Eurodiamond '96"*, edited by C.Manfredotti & E. Vittone, Bologna, 1996

[3] P. Gonon, S. Prawer and D. Jamieson, *Appl. Phys. Lett.*, 70(22), 1997

[4] S. Prawer, T. McCormick, W. Alexander, L. Seitzman, J. Butler, *Nitrogen Doping of CVD Diamond*, source unknown

Characterisation of amorphous silicon alloys by RBS/ERD with self consistent data analysis using simulated annealing

N.P.Barradas[1,3], E.Wendler[1], C.Jeynes[1], S.Summers[2], H.S.Reehal[2]

University of Surrey Ion Beam Centre, Guildford, GU2 5XH, England
School of Electrical, Electronic & Information Engineering, South Bank University, London SE1 0AA, England
Now at Instituto Tecnologico e Nuclear, E.N. 10, 2686-953 Sacavem, Portugal

Hydrogenated amorphous silicon films are deposited by CVD onto insulating (silica) substrates for the fabrication of solar cells. 1.5MeV ^{4}He ERD/RBS is applied to the films, and a self consistent depth profile of Si and H using the simulated annealing (SA) algorithm was obtained for each sample. The analytical procedure is described in detail, and the confidence limits of the profiles are obtained using the Markov Chain Monte Carlo method which is a natural extension of the SA algorithm. We show how the results are of great benefit to the growers.

1. **N.P.Barradas, C.Jeynes, M.Jenkin, P.K.Marriott**
Bayesian Error Analysis of Rutherford Backscattering Spectra
Thin Solid Films **343-344** (1999) 31-34

2. **N.P.Barradas, C.Jeynes, R.P.Webb, U.Kreissig, R.Grötzschel**
Unambiguous automatic evaluation of multiple ion beam analysis data with simulated annealing
Nucl. Instr. and Methods **B149** (1999) 233-237

Insertion Devices and Beamlines for the Proposed Australian Synchrotron Light Source

Richard F. Garrett and John W. Boldeman
Australian Synchrotron Research Program
ANSTO, PMB 1, Menai, NSW, 2234

The proposed Australian synchrotron light source, Boomerang, is a third generation 3 GeV storage ring which is designed to provide for the great majority of Australian requirements for synchrotron radiation well into the next century. The storage ring could accommodate up to 60 experimental stations, including beamlines from 9 insertion devices, which far exceeds the projected Australian requirements over the life of the faciltiy. Undulator radiation will be available up to 20 keV.

The first phase construction of Boomerang includes funding for 9 beamlines, comprising 5 bending magnet and 4 insertion device beamlines. The beamline complement has been chosen to cater for approximately 95% of the current and projected Australian demand for synchrotron radiation over the first 5 years operation of the facility. Details will be shown of the performance of the proposed insertion devices, and the initial beamline complement will be presented.

Richard Garrett, FAX (02) 9717 3145, garrett@ansto.gov.au

LIST OF PARTICIPANTS

(as at date of printing)

ANSTO

P Airey
J Boldeman
P Bourke
D Cohen
A Croal
P Evans
J Fallon
D Fink
H Garnett
R W Garrett
D Garton
M A Hotchkis
Q Hua
S Jane
R A Jeffree
P C Lee
G McOrist
H Noorman
K Prince
A Sarbutt
R Siegele
A Smith
E Stelcer
R Szymczak
M Zaw
U Zoppi

Australian Geological Survey Organisation

A Radlinski

Australian National University

A P Byrne
S Cheylan
R Cresswell
S Deenapanray
A Dowd
C Glover
P Hausladen
S Jones
S Kucheyev
T R Ophel
H Timmers
M Vos
T Weijers

Coherent Scientific Pty Ltd

P Dall'Armi-Stoks

CSIRO

F Bruhn
S Dligatch
C Ryan
S H Sie

Curtin University of Technology
M Middleton

Flinders University
M Ford
D French
D Losic
V Sashin

Indian Institute of Science
L Shivalingappa

Institute of Atomic Physics
B Constantinescu

Institute of Geological & Nuclear Sciences, NZ
B Trompetter

La Trobe University
F Gard
J Riley

Royal Melbourne Institute of Technology
A Alves
A Brus
I F Bubb
R Franich
M Ghantasala
P Johnston
K Kivits
R McKenzie
S Mollica
S Shamsili
D Sood
M van der Vleuten
H Van Duong
Y Wang

Thin Film Center Inc, USA
A Macleod

University of Melbourne
J den Besten
V Gurarie
D Hoxley
H Jackson
D Jamieson
B Johnson
A Liu
J McCallum
L Morpeth
M Norman
J Orwa
P Otsuka
P Spizzirri
E Trajkov

University of New South Wales
R Clark
N Paris
N Singh

University of Newcastle
A Bilic
P Dastoor
M Gladys
B King
M Li
J D O'Connor
C Oliver
J Quinton
M Tan
J Xi

University of Surrey, UK
E Wendler

University of Technology Sydney
B Ben-Nissan
D Green
J Hu
A Milev
V Peterson
J Russell

University of Western Sydney Nepean Campus
S Maheswaran

Victoria University of Technology
K Lawlor